



## AVERTISSEMENT

Ce document est le fruit d'un long travail approuvé par le jury de soutenance et mis à disposition de l'ensemble de la communauté universitaire élargie.

Il est soumis à la propriété intellectuelle de l'auteur. Ceci implique une obligation de citation et de référencement lors de l'utilisation de ce document.

D'autre part, toute contrefaçon, plagiat, reproduction illicite encourt une poursuite pénale.

Contact : [ddoc-theses-contact@univ-lorraine.fr](mailto:ddoc-theses-contact@univ-lorraine.fr)

## LIENS

Code de la Propriété Intellectuelle. articles L 122. 4

Code de la Propriété Intellectuelle. articles L 335.2- L 335.10

[http://www.cfcopies.com/V2/leg/leg\\_droi.php](http://www.cfcopies.com/V2/leg/leg_droi.php)

<http://www.culture.gouv.fr/culture/infos-pratiques/droits/protection.htm>

**Ecole Doctorale RP2E**  
**Ressources, Produits, Procédés et Environnements**

Thèse  
présentée pour l'obtention du titre de  
Docteur de l'Université Henri Poincaré, Nancy  
Spécialité : Géosciences

par  
Isabelle DUHAMEL

**Caractérisation des sources d'uranium à l'Archéen**  
**Mécanismes de genèse des gisements d'uranium**  
**les plus anciens (3,0 à 2,2 Ga) et des**  
**préconcentrations uranifères paléoprotérozoïques**

Soutenance publique le 4 juin 2010

**Membres du jury :**

Rapporteurs	<b>Laurence ROBB</b>	Professeur, Université d'Oxford, Angleterre
	<b>Jean-François MOYEN</b>	Professeur, Université Jean Monnet, St-Etienne
Directeur de thèse	<b>Michel CUNEY</b>	Directeur de Recherche CNRS, Nancy
Examineurs	<b>Christian MARIGNAC</b>	Professeur, Ecole Nationale Supérieure des Mines de Nancy
	<b>Anne-Sylvie ANDRE-MAYER</b>	Maître de conférences, HDR, UHP-G2R, Nancy
	<b>Christoph GAUERT</b>	Professeur, Université de l'Etat Libre, Afrique du Sud
	<b>Claude CAILLAT</b>	Ingénieur géologue, AREVA
	<b>Jean-Pierre MILESI</b>	Géologue, AREVA



---

## AVANT-PROPOS

---

La problématique de cette thèse a été pensée dès l'année 2005 par trois personnes qui auront joué un rôle majeur dans ma formation sur la géologie de l'uranium : mon directeur de recherche **Michel Cuney** (DR. CNRS, UMR G2R-CREGU), mon ancien patron **Serge Genest** (anciennement président d'Omégalpha Inc. devenu AREVA-Québec au Canada) et **Claude Caillat** (ingénieur AREVA). Après quatre années passées au Canada pour suivre un master de recherche à l'UQÀM et travailler dans l'exploration de l'uranium au Québec pour Omégalpha Inc., je suis revenue en France en juin 2006 afin de me lancer dans cette recherche passionnante sur la géologie de l'uranium à l'Archéen. Je remercie ces trois grands géologues qui m'ont fait confiance et j'espère mettre acquitté honorablement de la tâche qui m'était impartie.

Ces travaux ont été financés conjointement par le **CREGU** (Centre de Recherche et Étude sur la Géologie de l'Uranium) et par le groupe **AREVA**.

Les recherches ont été menées au sein du Laboratoire de Géologie et de Gestion des Ressources Minérales et Énergétiques (**G2R**) à l'Université Henri Poincaré (Nancy, France) et de l'École Doctorale **RP2E**.

Ce travail n'aurait pu aboutir sans les nombreuses collaborations développées avec les universités et les entreprises minières qui ont su abolir les frontières et partager gracieusement leurs informations, leurs données et leurs échantillons :

- **Denis Thiéblemont** (BRGM, Orléans, France)
- **Martin Van Kranendonk** (Geological Survey of Western Australia)
- **Marieke Van Lichtervelde** (BGR, Hanovre, Allemagne)
- **Christopher Gauert** et **Ulrike Rantzch** (Université de l'Etat Libre, Bloemfontein, Afrique du Sud)
- **Laurence Robb**, **Carl Anhaeusser**, **Judith Kinnaird** et **Gillian Drennan** (Université du Witwatersrand, Johannesburg, Afrique du Sud)
- **Richard Stewart** (Uranium One, Dominion Mine, Afrique du Sud)
- **Falk Koenemann** (Aachen, Allemagne)
- **Patrick Enright** (Pele Mountain Ltd, Toronto, Ontario, Canada)
- **Michel Gauthier** et **Normand Goulet** de l'Université du Québec à Montréal (Québec, Canada)
- le laboratoire **A. P. Karpinsky Russian Geological Research Institute (VSEGEI)** à Saint-Petersburg (Russie)

---

## REMERCIEMENTS

---

Mes remerciements vont tout d'abord à mon directeur de recherche **Michel Cuney** qui est venu me trouver au Canada et a su voir en moi une apprentie géologue prometteuse. Il m'a permis de me dépasser en me donnant de grandes ambitions et toujours plus d'échantillons de ses innombrables expéditions à travers le monde ... Il a aussi été le seul professeur au cours de mes dix années d'université à avoir pu m'expliquer l'importance de la géochimie et à me la faire apprécier. Merci beaucoup Michel, j'espère que la relève sera à la hauteur de tes espérances !

Je remercie les membres du jury qui ont accepté de lire et d'évaluer mes recherches : **Laurence Robb** (professeur à l'Université d'Oxford et professeur émérite de l'Université du Witwatersrand), **Jean-François Moyen** (professeur à l'Université Jean Monnet, St-Etienne), **Christoph Gauert** (professeur à l'Université de l'Etat Libre), **Christian Marignac** (professeur à l'Ecole Nationale Supérieure des Mines de Nancy), **Anne-Sylvie André-Mayer** (Maître de conférences à l'UHP de Nancy) et les examinateurs du groupe AREVA, **Claude Caillat** et **Jean-Pierre Milesi**.

Je tiens à remercier toutes les personnes qui ont contribué à la collecte des échantillons à travers le monde et plus particulièrement : le professeur **Judith Kinnaird** pour son accueil et son aide à l'Université du Witwatersrand, **Christopher Gauert** et **Ulrike Rantzch** pour leur aide sur le terrain et le partage des données sur les reefs du Dominion, **Marieke Van Lichtervelde** pour son aide sur l'interprétation de la minéralogie de la pegmatite de Tanco, **Richard Stewart** et ses collègues de la mine du Dominion ainsi que **Patrick Enright** et le personnel de Pele Mountain Ltd à Toronto pour leur aide respective dans leurs carothèques, **Bernard Poty** pour les échantillons de la mine Denison et du Central Rand, **Falk Koenemann** pour les échantillons du champ aurifère de West Rand, **Denis Thiéblemont** pour l'échantillonnage des granitoïdes de Guinée, **Anne-Sylvie André** et **Léonid Serov** pour l'échantillonnage de la péninsule de Kola.

Je remercie tout le personnel de recherche et les techniciens des différents laboratoires sans qui les données ne se seraient pas accumulées : **Marc Brouand** pétrographe du groupe AREVA, **Cédric Demeurie** du laboratoire de lithopréparation lamellaire de Nancy Université, **Alain Kohler**, **Johan Ravaux**, **Sandrine Mathieu** et **Robert Lallement** du Service Commun de Microanalyses, **Michel Champenois** et **Denis Mangin** du CRPG.

Je tiens à remercier toutes les personnes du G2R qui m'ont « supporté » au cours de ces trois années, qui m'ont soutenu et offert leur amitié. Je ne saurais toutes les citer car elles sont nombreuses, aussi ne soyez pas triste de ne pas lire votre nom... je nommerais donc l'essentiel avec bien sûr les thésards du « gang des uraninistes » car ce sont les meilleurs(!), en commençant par mes deux collègues de bureau **Julien Mercadier** et **David Salze**, **Jeremy Neto**, **Antonin Richard**, **Jessica Bonhoure**, **Sandrine Cinelu**, **Olivier Cardon**, **Christophe Rozsypal** et **Ahlam Ibrahim**, vient ensuite le « gang des beloteurs », **Olivier Belcourt**, **Olivier Pierron**, **Gaëtan Hubert**, **Anne-Laure** et **Vincent Girard**, puis tous les autres thésards, **Apolline Lefort**, **Junying Ding**, **Stéphane Renard** et **Michaël Franiatte**. Enfin, merci aux autres personnes du G2R et du CREGU pour leur aide et j'en oublie probablement : **Pierre Schuhmacher**, **Michel Cathelineau**, **Marie-Christine Boiron**, **Karine Pistre**, **Roland Mairet**, **Patrick Lagrange**, **Christine Léonard**, **Laurence Moine** et **Chantal Peiffert**.

Je remercie les étudiants de licence, de master ou d'école ingénieure ainsi que les stagiaires qui ont participé à mon projet de thèse et j'espère ne pas les avoir trop traumatisés : **Guillaume Kern**, **Johan Bergé**, **Stéphanie Fleurance**, **Antoine Hudault**, **Caroline Demange**, **Guillaume Thomas**, **Pierre-Jean Misson** et **Vincent Cuney**.

Enfin, je voudrais remercier tous les membres de ma famille pour leur aide et leur soutien : merci aux **Duhamel** et aux **Achin** !

*Je dédie ce mémoire à mon fils Arthur  
qui aura été là depuis le début...  
dans la joie et la bonne humeur !*

---

# TABLE DES MATIÈRES

---

<b>AVANT-PROPOS</b>		<b>3</b>
<b>REMERCIEMENTS</b>		<b>4</b>
<b>TABLE DES MATIÈRES</b>		<b>6</b>
<b>INTRODUCTION GÉNÉRALE</b>		<b>9</b>
1.	<b>Objectifs de l'étude</b>	<b>11</b>
2.	<b>Cibles</b>	<b>11</b>
3.	<b>Méthodologie</b>	<b>13</b>
4.	<b>Plan du mémoire</b>	<b>14</b>
<b>CHAPITRE 1</b>	<b>CONNAISSANCES SUR L'ARCHÉEN ET TRANSITION VERS LE PALÉO- PROTÉROZOÏQUE</b>	<b>15</b>
1.	<b>Introduction : l'échelle des temps</b>	<b>17</b>
2.	<b>Géodynamique archéenne et genèse des continents</b>	<b>18</b>
3.	<b>Nature, répartition et potentiel uranifère des roches archéennes</b>	<b>23</b>
4.	<b>Atmosphère primitive et « oxyatmoversion »</b>	<b>29</b>
5.	<b>Gisements d'uranium de type paléo-placer et origines possibles</b>	<b>33</b>
6.	<b>Conclusion : problématique et approche de cette étude</b>	<b>37</b>
	<b>Références bibliographiques de l'introduction et du chapitre 1</b>	<b>39</b>
<b>CHAPITRE 2</b>	<b>SOURCES MAGMATIQUES ARCHÉENNES DE L'URANIUM</b>	<b>47</b>
	<b>Introduction</b>	<b>48</b>
<b>Partie 2.1</b>	<b>Evolution of the magmatic rock composition from the West African Craton (Guinea) between 3.5 and 2.0 Ga: evidence of U and Th fractionation during progressive differentiation</b>	<b>49</b>
<b>Partie 2.2</b>	<b>U, Th and REE mobility during Ca-metasomatism of Archean K-rich granites from the Pilbara Craton, Western Australia</b>	<b>91</b>
<b>Partie 2.3</b>	<b>Geochemical characterization of U-bearing minerals from the Archean TANCO pegmatite, Manitoba, Canada: Magmatic origin and later hydrothermal remobilization ...</b>	<b>139</b>
<b>Partie 2.4</b>	<b>Uranium occurrences associated to partial melting and metasomatism in Precambrian granitoids from the Baltic Shield</b>	<b>177</b>
	<b>Synthèse et discussion sur les sources magmatiques archéennes de l'uranium</b>	<b>233</b>

---

<b>CHAPITRE 3</b>	<b>PALÉO-PLACERS URANIFÈRES</b>	<b>241</b>
<hr/>		
Introduction	.....	243
Partie 3.1	Mineralogy and Geochemistry of uranium mineralization in the Archean quartz-pebble conglomerate deposits of the Witwatersrand Basin, South Africa .....	245
Partie 3.2	Hydrothermal vs. detrital uraninite origin in the Elliot Lake quartz pebble conglomerates, Ontario, Canada: a chemical characterization using EMPA and SIMS .....	313
Partie 3.3	Geochemistry and Mineralogy of post-GOE Quartz Pebble Conglomerates: example of the thoriferous Jatulian Formation from the Baltic Shield (2.3-2.15 Ga) ....	357
Synthèse et discussion sur les minéralisations uranifères des conglomérats à galets de quartz	.....	389
<b>CONCLUSIONS GÉNÉRALES</b>		<b>397</b>
<hr/>		
<b>LISTE DES ABRÉVIATIONS</b>	.....	<b>401</b>
<b>LISTE DES FIGURES</b>	.....	<b>403</b>
<b>LISTE DES TABLEAUX</b>	.....	<b>417</b>
<b>ANNEXE 1 : MÉTHODOLOGIE ANALYTIQUE</b>		<b>423</b>
<hr/>		
1.	Géochimie sur roche totale .....	425
1.1	Préparation des échantillons .....	425
1.2	Protocole chimique .....	425
2.	Etude minéralogique .....	425
2.1	Lithopréparation lamellaire .....	425
2.2	Autoradiographie .....	425
2.3	Microscopie optique .....	426
2.4	Microscopie électronique à balayage (MEB) .....	426
2.5	Microsonde électronique (CAMECA SX100 et SX50) .....	429
2.5.1	Caractérisation de la composition des minéraux par microanalyses <i>in situ</i> .....	429
2.5.2	Application à la géochronologie .....	430
3.	Etudes isotopiques .....	430
3.1	Principe de fonctionnement de la microsonde ionique (CAMECA IMS-3F) .....	431
3.2.	Préparation des échantillons .....	432
3.3	Datation isotopique U-Pb des uraninites .....	432
3.4	Mesures des teneurs en Y et REE des uraninites .....	433
Références citées dans les annexes analytiques	.....	434

<b>ANNEXE 2 :    DONNEES GEOCHIMIQUES EXTERNES</b>	<b>435</b>
<b>RÉSUMÉ / ABSTRACT</b> .....	<b>441</b>

---

# **INTRODUCTION GÉNÉRALE**

---

Les paléo-placers uranifères, dont l'âge de mise en place remonte à 3,09 Ga pour les concentrations du Bassin du Witwatersrand en Afrique du Sud, sont les plus anciens gisements d'uranium que l'on trouve sur Terre. Ces gisements représentent près de 11% de la production mondiale d'uranium et environ 5,5 % des réserves mondiales encore exploitables dans les occurrences connues (Figure 1; données 2007 de l'IAEA d'après Cuney, 2009). Les minéralisations sont principalement sous la forme de grains d'uraninite accumulés dans des horizons de minéraux lourds riches en pyrite et matières carbonées. La teneur en uranium varie entre 0,015-0,03 % U dans les conglomérats à Au-U du bassin de Witwatersrand en Afrique du Sud où l'uranium est exploité en sous-produit, à un maximum de 0,14 % U dans le gisement d'Elliot Lake au Canada (Cuney and Kyser, 2008).

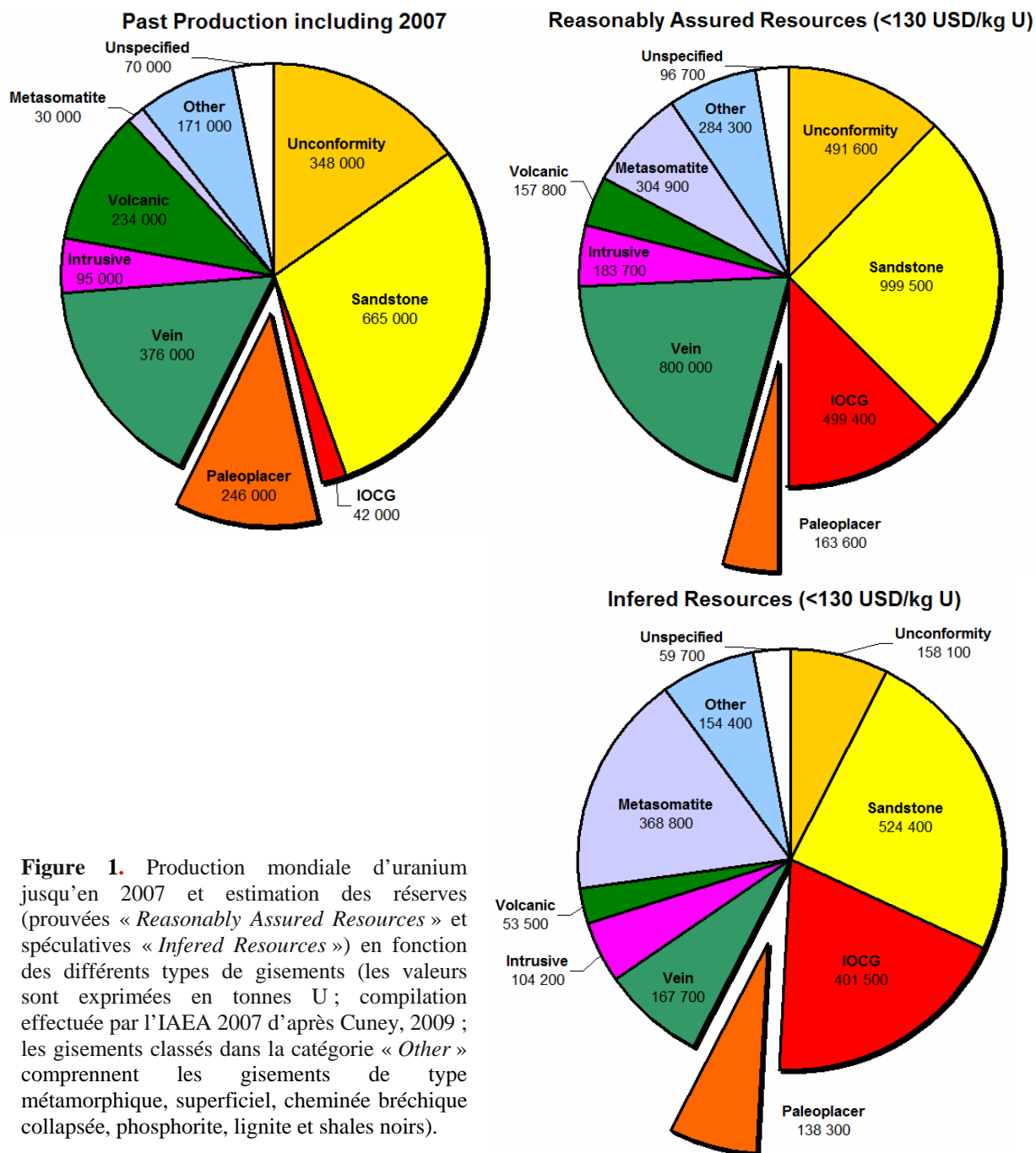


**Figure 1.** Production mondiale d'uranium jusqu'en 2007 et estimation des réserves (prouvées « Reasonably Assured Resources » et spéculatives « Inferred Resources ») en fonction des différents types de gisements (les valeurs sont exprimées en tonnes U; compilation effectuée par l'IAEA 2007 d'après Cuney, 2009; les gisements classés dans la catégorie « Other » comprennent les gisements de type métamorphique, superficiel, cheminée bréchique, phosphorite, lignite et shales noirs).

Compte tenu de la fluctuation du marché du prix de l'uranium ces dix dernières années et dans un souci permanent pour la recherche de matière première énergétique dont le manque croissant se fait sentir actuellement, il est important de comprendre la métallogénie de ces gisements. Or, nombre de questions restent encore à élucider sur ces paléo-placers, notamment concernant leur origine (détritique ou hydrothermale) et la provenance des minéralisations (source magmatique). La vocation beaucoup plus large de cette étude est d'appréhender la géologie du globe dans son ensemble, à savoir l'existence d'une atmosphère primitive réductrice à l'Archéen et la nature des processus géodynamiques qui prévalaient à cette époque, précurseurs de la formation la croûte continentale et des premiers magmas enrichis en uranium dont découle la genèse de tous les autres types de gisements.

## 1. OBJECTIFS DE L'ÉTUDE

L'objectif général de ce travail est de comprendre les mécanismes de fractionnement de l'uranium à l'Archéen avant l'apparition de l'oxygène libre dans l'atmosphère. L'étude pétrographique et géochimique des granitoïdes archéens enrichis en uranium et le suivi de leur évolution jusqu'au Paléoproterozoïque permettront 1) de caractériser la nature de ces magmas et leur environnement géodynamique, 2) d'identifier les phases minérales uranifères, 3) de déterminer quels sont les mécanismes responsables de cet enrichissement (différenciation ou fractionnement magmatique, fusion partielle, métasomatisme...), 4) puis quels sont les processus physiques ou chimiques liés à la mobilisation de ces toutes premières concentrations. L'étude de plusieurs paléo-placers formés entre 3,09 et 2,2 Ga servira ensuite à déterminer les paragenèses minéralogiques associées aux minéralisations uranifères ainsi que leurs signatures chimiques afin de les comparer à celles de différents socles archéens. Le but ultime est de déterminer si l'uranium est d'origine hydrothermale ou détritique, et enfin, pour les minéralisations détritiques, d'évaluer la contribution relative de chacune des sources magmatiques potentielles.

## 2. CIBLES

Afin d'avoir une vue globale du cycle de l'uranium à l'Archéen, plusieurs cibles ont été sélectionnées (Figure 2) :

- 5 cibles dans les granitoïdes des boucliers Canadien (pegmatite de Tanco, Manitoba), Baltique (région de Carélie en Finlande et péninsule de Kola en Russie), d'Afrique de

l'Ouest (craton de Kenema Man en Guinée), et d'Australie Occidentale (craton de Pilbara) ;

- 2 cites dans des paléo-placers uranifères majeurs, les conglomérats archéens du bassin du Witwatersrand dans les Groupes du Dominion (3,09-3,07 Ga) et du Central Rand (2,91-2,71 Ga) en Afrique du Sud, ainsi que les conglomérats du district minier d'Elliot Lake ou Blind River (Ontario, Canada) appartenant au Super-Groupe Huronien (2,45-2,22 Ga) ;
- et enfin la dernière cible correspondant à un paléo-placer thorifère plus récent (post-oxyatmoverion), dans les séries gréseuses et conglomératiques jatuliennes (2,3-2,15 Ga) échantillonnées en Russie afin de marquer l'évolution des conditions de formation des concentrations détritiques d'uranium au cours du temps.

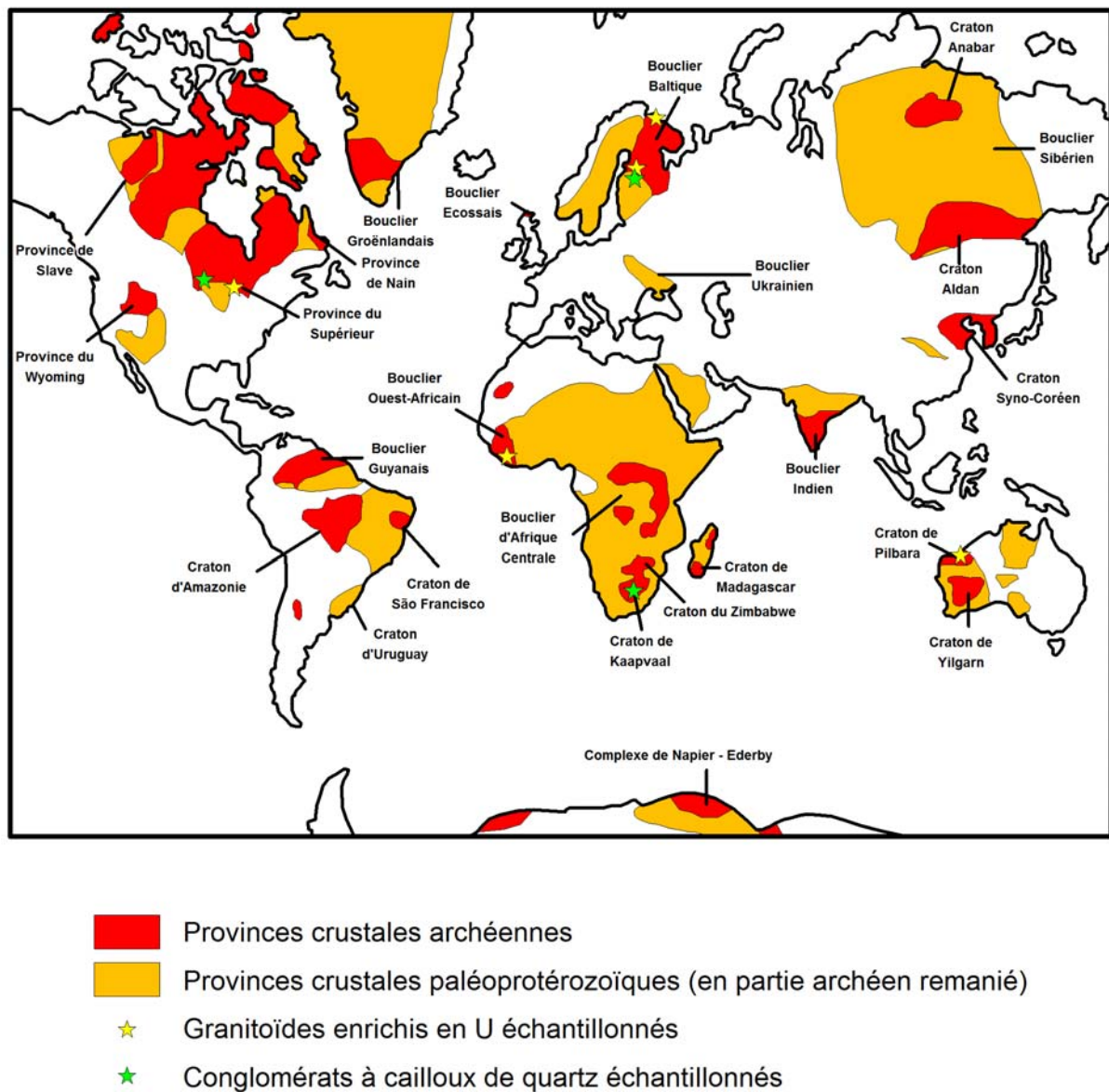


**Figure 2.** Répartition géographique des provinces archéennes et protérozoïques dans le monde (modifiée de Rämö and Haapala, 1996) et localisation des granitoïdes et paléo-placers échantillonnés dans cette étude.

### 3. METHODOLOGIE

L'étude systématique développée pour chacun de ces cites a consisté tout d'abord en une synthèse bibliographique des travaux antérieurs afin de compiler les données géologiques, minéralogiques et géochimiques déjà existantes.

La prise de contact avec différents intervenants extérieurs ayant travaillé sur ces cites (voir avant-propos) ainsi que les missions de terrain en Afrique du Sud (2005 et 2007) et au Canada (2007) ont permis de récolter un éventail assez large d'échantillons pour cette étude. La méthodologie analytique appliquée sur les échantillons est respectivement la même pour chacun des cites étudiés et les différents instruments utilisés sont présentés de façon plus détaillée en Annexe 1.

Tout d'abord, les échantillons de granitoïdes et les conglomérats minéralisés sont analysés par géochimie sur roche totale (concentrations en éléments majeurs et traces par ICP-MS et ICP-OES) afin de caractériser la nature de la roche et les teneurs en radioéléments. Deuxièmement, l'étude minéralogique (microscopie optique en lumières transmise et réfléchie, MEB-EDS) permet d'identifier et de comparer la paragenèse des phases minérales uranifères et des phases accessoires associées caractéristiques de chacun des domaines. Une première approche comparative permet de définir les composantes détritiques des roches sédimentaires par rapport à la composition des roches sources érodées dont elles sont issues. La chronologie relative de cristallisation des minéraux peut être déterminée par la paragenèse associée, la forme, la texture ou encore le recoupement des phases minérales entre elles. Elle permet de séparer les minéraux détritiques des phases épigénétiques dans les conglomérats ou les minéraux d'origine magmatique ou métasomatique dans les granitoïdes. Enfin, les analyses chimiques et isotopiques *in situ* des minéraux, respectivement à la microsonde électronique et à la sonde ionique, permettent de déterminer les compositions précises et les âges de cristallisation des différentes phases accessoires.

## 4. PLAN DU MEMOIRE

Cette thèse est divisée en quatre chapitres.

Le premier chapitre est une synthèse bibliographique des connaissances sur l'Archéen nécessaire à la compréhension de cette étude et permettant de définir la problématique du sujet et les axes de recherche engagés par la suite.

Le second chapitre regroupe les résultats de l'étude minéralogique et géochimique des différents domaines magmatiques archéens à paléoprotérozoïques étudiés et représentant les sources potentielles des minéralisations uranifères détritiques des paléo-placers. Ces résultats sont classés suivant la nature des roches étudiées, depuis les séries les moins évoluées de type TTG et granitoïdes calco-alcalins potassiques (granitoïdes de Guinée du craton Ouest Africain et du craton de Pilbara en Australie) vers les termes les plus différenciés (pegmatite peralumineuse de Tanco, Manitoba, Canada et granites de type S et métasomatites du Bouclier Baltique).

Le troisième chapitre est dédié à l'étude des paléo-placers ordonnés suivant leur âge de dépôt, de l'Archéen (de 3,09 Ga pour le Groupe de Dominion à la base du Bassin de Witwatersrand) au paléoprotérozoïque pour les sédiments les plus récents (les dépôts jatuliens de Russie). Le cortège de minéraux présent dans chacun des paléo-placers sera comparé aux paragenèses minérales observées dans les sources magmatiques étudiées dans le chapitre précédent aussi qu'à leurs caractéristiques chimiques.

La conclusion finale permettra de dresser les implications tant sur la métallogenèse des premières concentrations en uranium sur Terre que sur les conséquences géodynamiques qui découlent de ces travaux.

---

**CHAPITRE 1 :**  
**CONNAISSANCES SUR**  
**L'ARCHÉEN**  
**ET TRANSITION VERS**  
**LE PALÉOPROTÉROZOÏQUE**

---



Ce premier chapitre est consacré à la synthèse bibliographique des connaissances sur la géologie, la géodynamique et la géochimie des roches à l'Archéen, sur les changements liés à la transition Archéen-Paléoprotérozoïque et sur les premières concentrations en uranium formées sur Terre à cette époque. Cette première partie de l'étude permet de comprendre la problématique et les enjeux de ce travail.

## 1. INTRODUCTION : L'ÉCHELLE DES TEMPS

L'Archéen est la période géologique comprise entre 3,8 et 2,5 Ga (Figure 1.1). Cet intervalle de temps marque une période importante de l'évolution terrestre.

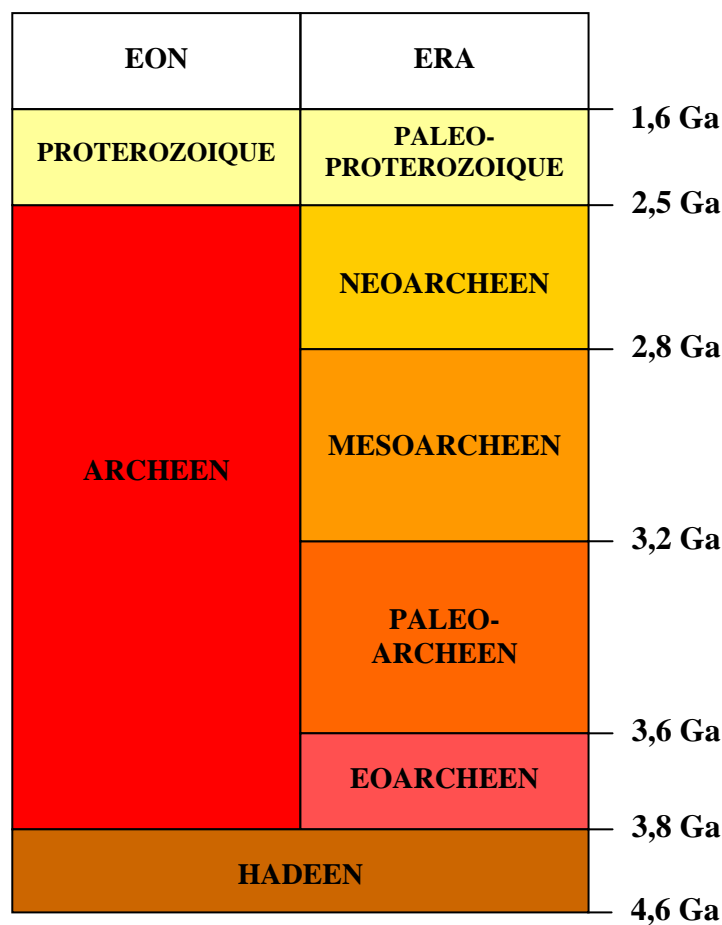


Figure 1.1. Chronologie de l'Archéen

Il marque tout d'abord la fin de l'intense bombardement météoritique qui avait lieu à l'Hadéen (Baldwin, 1974 ; Sleep *et al.*, 1989 ; Moorbath, 2005). Il correspond aussi à l'existence indéniable des océans à la surface de la Terre confirmée par la présence d'unités métasédimentaires telles que celle de l'île d'Akilia, au Groenland, datées par la méthode Pb-Pb sur zircon entre  $3865 \pm 11$  Ma et  $3840 \pm 8$  Ma (Nutman *et al.*, 1997), et de structures en

coussinets (en anglais « *pillow lava* ») dans les amphibolites d'Isua de 3,7-3,8 Ga découvertes également au Groenland (Komiya *et al.* 1999). L'initialisation de la tectonique des plaques telle que nous la connaissons actuellement est marquée par l'apparition à l'Archéen de la croûte continentale (c.f. partie 2) composée essentiellement de roches de type tonalites-trondhjémites-granodiorites (TTG) qui prendraient naissance dans des arcs volcaniques associés à des zones de subduction (de Wit, 1998) mais dont l'origine reste controversée (c.f. partie 3). Les roches sédimentaires archéennes recèlent aussi les plus anciennes traces de vie, du carbone d'origine organique ( $\delta^{13}\text{C} = -28 \text{ ‰}$ ) dans les roches métamorphiques du gisement de fer d'Isua au Groenland qui sont datées à 3,8 Ga (Mojzsis *et al.*, 1996 ; van Zuilen *et al.*, 2003). Ces roches sédimentaires ont enregistré le changement des conditions anoxiques de l'atmosphère à la transition entre l'Archéen et le Paléoproterozoïque (c.f. partie 4). Enfin, c'est aussi à l'Archéen que l'on trouve les plus vieux gisements d'uranium de type paléo-placer dans les conglomérats à cailloux de quartz du bassin de Witwatersrand en Afrique du Sud (c.f. partie 5). Les auteurs s'accordent à dire que ces gisements ont subi l'influence du changement global de la composition atmosphérique au Paléoproterozoïque mais nous verrons que de nombreuses questions restent encore en suspens.

## 2. GÉODYNAMIQUE ARCHÉENNE ET GENÈSE DES CONTINENTS

La géodynamique de la croûte terrestre à l'Archéen reste encore obscure actuellement. D'après Condie (2006), la tectonique des plaques serait le principal mécanisme de refroidissement de la Terre au cours de son histoire et aurait déjà été active à l'Archéen voir même avant. Cependant, cette théorie est basée sur le principe d'uniformitarisme selon lequel les processus géodynamiques qui régissent la tectonique du globe de nos jours (tectonique des plaques, rhéologie, convection mantellique...) se sont exercés par le passé et sont applicables afin d'appréhender la géologie de l'Archéen. Or, certains paramètres contrôlant la dynamique de la Terre étaient sensiblement différents à cette époque. Tout d'abord, la production de chaleur radiogénique du manteau était environ trois à quatre fois plus importante qu'elle ne l'est actuellement et le manteau était donc plus chaud (Brown, 1985 ; Pollack, 1997). Compte tenu de la température plus élevée du manteau, sa viscosité devait être plus faible et les mouvements convectifs plus rapides (Korenaga, 2006). Ceci expliquerait la production de grands volumes de roches mafiques dans les zones extensives préservées au sein des cratons. Cependant, la présence de grandes structures de déformation en dômes et bassins montrent aussi l'existence d'une dynamique verticale particulière à l'Archéen.

Quatre mécanismes retenus dans la littérature peuvent induire les mouvements lithosphériques verticaux et horizontaux à l'Archéen :

- la **sagduction** (d'après Gorman *et al.*, 1978, puis repris par Martin, 2005) contrôlée par la différence de densité entre les roches ;

Le principe de sagduction est expliqué par la Figure 1.2 où des komatiites très denses ( $D = 3,3$ ) se mettent en place en formant de grands épanchements sur des granitoïdes de densité inférieure de type TTG ( $d = 2,7$ ) et créent des mouvements gravitaires verticaux induisant la morphologie des terrains archéens couramment observée en dômes et bassins.

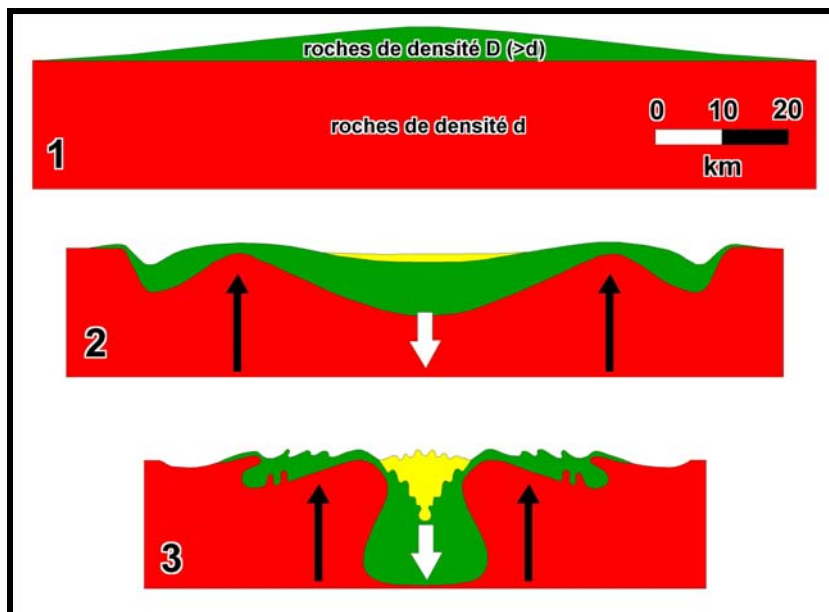


**Figure 1.2.** Le principe de sagduction (d'après Gorman *et al.*, 1978 et Martin., 2005) permet d'expliquer les mouvements lithosphériques verticaux observés à l'Archéen entre les unités granito-gneissiques anciennes de type TTG formant des dômes par mouvements ascendants (flèches noires) dans des roches volcaniques plus jeunes et plus denses constituant les ceintures de roches vertes qui s'enfoncent par mouvements gravitaires.

- la **subduction** de la croûte océanique hydratée (Martin, 1986 ; Calvert *et al.*, 1995 ; de Wit, 1998 ; Kamber and Collerson, 2000) ;

La Figure 1.3 illustre ce phénomène qui diffère des zones de subduction actuelles. Le gradient géothermique élevé à l'Archéen (flèche rouge) permettait en effet la fusion de la croûte océanique à de faibles profondeurs ( $\sim 50$  km) et la formation de granites de type TTG par fusion partielle de roches basaltiques hydratées laissant dans le résidu de fusion grenat et amphibole (domaine en rose). Le gradient géothermique actuel (flèche bleue), plus faible en température qu'à l'Archéen, permet au contraire la déshydratation de la croûte océanique (domaine hachuré vert) vers 90-100 km de profondeur, avant qu'elle n'ait atteint son point de fusion. Cette déshydratation dans les zones de subduction actuelles provoque le métasomatisme du manteau, l'abaissement du solidus mantellique (courbe orange) et finalement la fusion partielle dont les

produits vont enrichir la croûte continentale en formant des magmas riches en potassium et autres éléments incompatibles dont l'uranium.

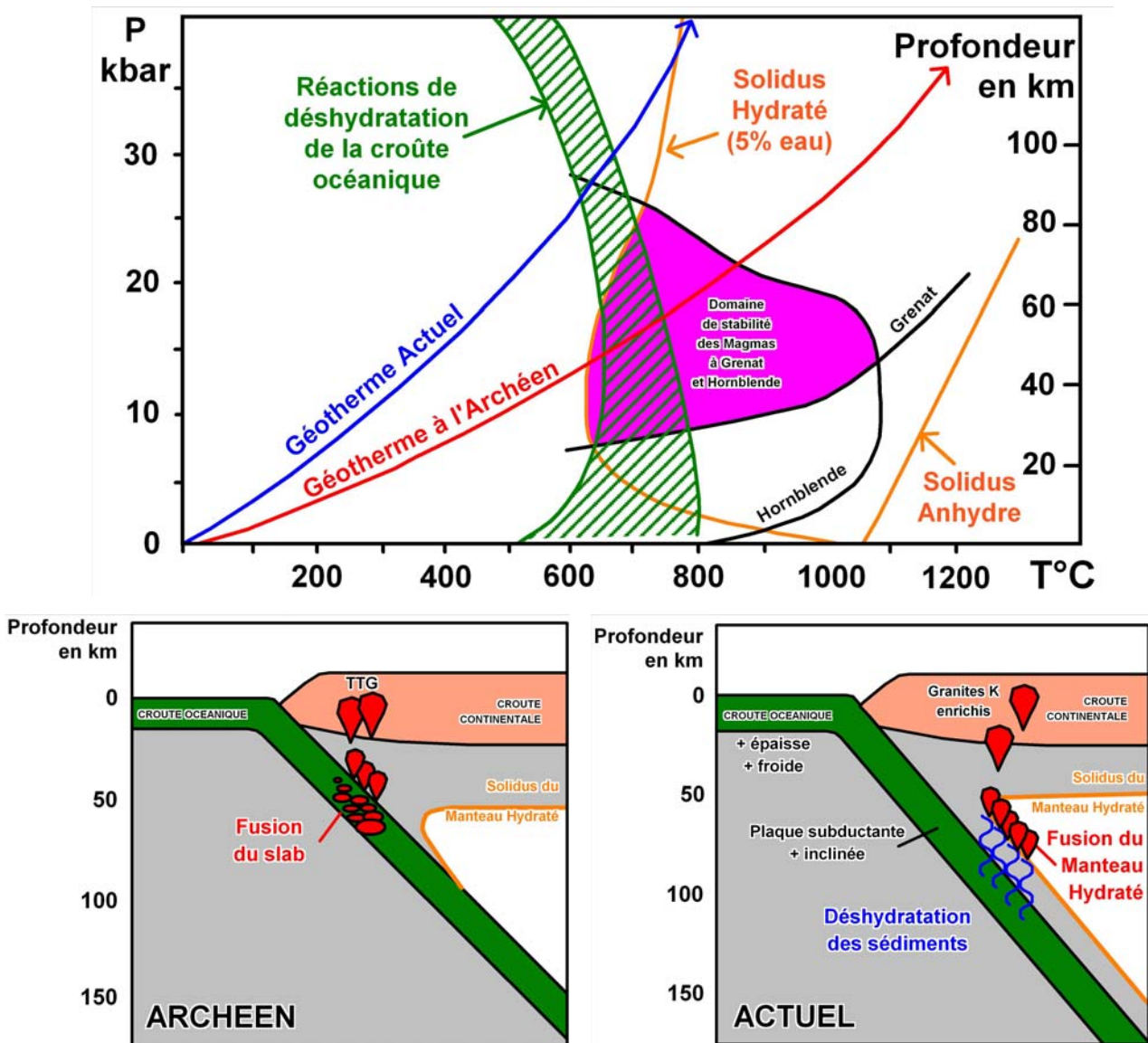


**Figure 1.3.** Diagramme pression-température et coupes schématiques des zones de subduction montrant la formation de la croûte continentale à l'Archéen et à notre époque (modifié de Martin, 2005).

- la **délamination** de la croûte océanique, soit celle subductante qui crée une remontée de plume mantellique depuis la discontinuité sismique D'' à 660 km de profondeur (Condie, 2000 et 2004), soit de la partie inférieure du plateau océanique qui permet la fusion de la proto-croûte mafique par relâchement de pression (Zegers and Keken, 2001) présentée par la Figure 1.4 ;

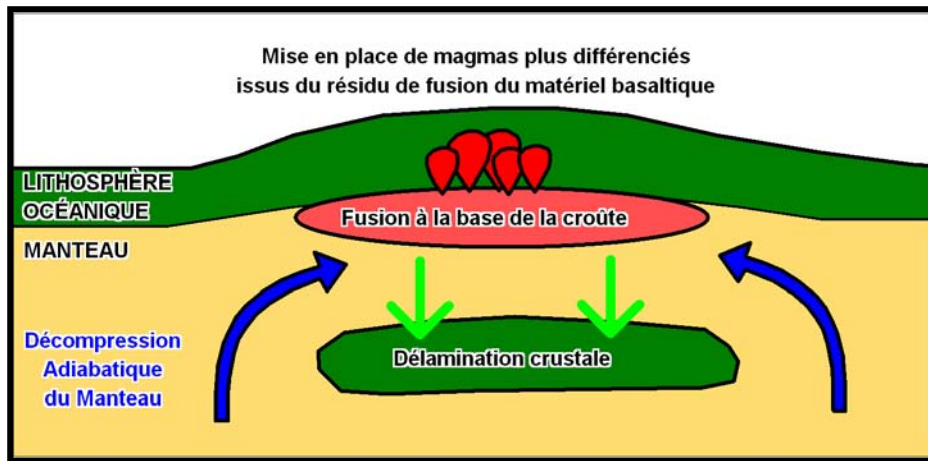


Figure 1.4. Schéma simplifié d'une délamination crustale.

- et enfin, la remontée de **panaches mantelliques** profonds (Figure 1.5) qui engendre la formation en surface de grands volumes de croûte océanique qui peuvent fondre à la base et donner naissance aux TTG (Condie, 2001 et 2004 ; Ernst and Buchan, 2003 ; Wyman and Kerrich, 2002).

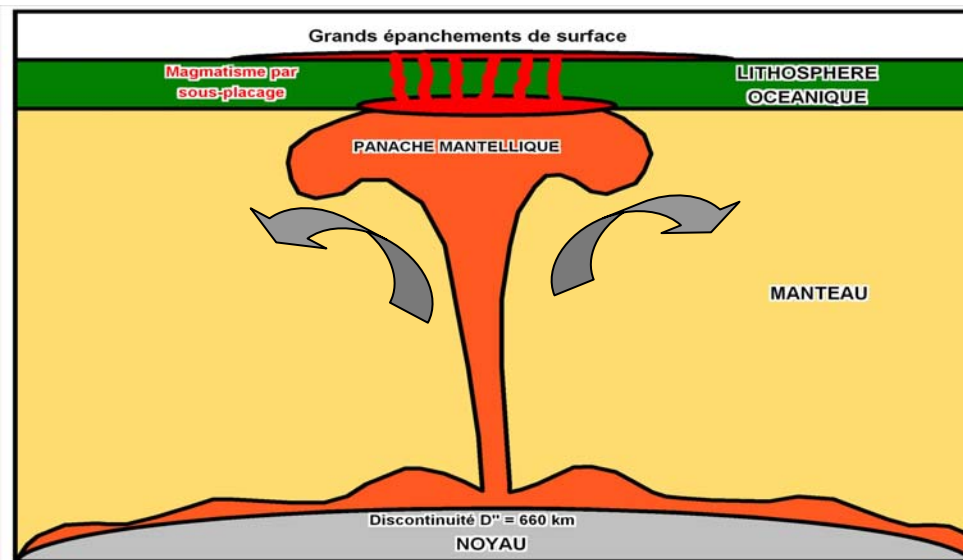


Figure 1.5 Schéma simplifié d'une remontée de plume mantellique.

L'intense activité magmatique à l'Archéen auraient permis l'extraction des trois quart du volume de la croûte continentale actuelle du manteau primitif formant les premiers continents. Cependant, une croûte continentale pré-archéenne aurait peut être été présente dès l'Hadéen (Wilde *et al.*, 2001 ; Harrison *et al.*, 2006). En effet, des zircons extraits de métasédiments à Jack Hills en Australie occidentale et datés à 4,404 Ga sont caractérisés par un fort taux de  $\delta^{18}\text{O}$  et comprennent des micro-inclusions de  $\text{SiO}_2$  qui seraient issus de l'interaction de roches supracrustales avec une hydrosphère précoce (Wilde *et al.*, 2001). Ces zircons représenteraient les reliques d'une roche felsique de composition granitique ayant existée à l'Hadéen. Cette première

croûte continentale aurait toutefois été rapidement recyclée dans le manteau (Harrison *et al.*, 2006).

La distribution des âges U-Pb sur zircons dans les roches vertes archéennes prélevées autour du globe indiquerait qu'il y aurait eu trois pics majeurs de création de croûte continentale au Précambrien à environ 2,7 Ga, 1,9 Ga et 1,2 Ga (Condie, 1995 et 2000). La formation de grands volumes de croûte continentale serait épisodique et une étude géochimique récente (Campbell, 2003) suggère qu'environ 70 % de la masse continentale actuelle aurait été créée avant 3 Ga. Les pics de création de croûte continentale observés par Condie (1995 et 2000) correspondraient aux âges de formation de supercontinents : Kenorland et Zimvaalbara entre 2,7 et 2,6 Ga, Columbia entre 1,8 et 1,7 Ga et Rodinia entre 1,1 et 1,0 Ga.

La reconstitution de l'assemblage des continents au Néoarchéen reste encore extrêmement spéculative. Compte tenu de l'absence d'un enregistrement des contraintes paléomagnétiques (position des pôles et polarité) dont l'intervalle de temps serait bien défini dans une séquence sédimentaire archéenne, il est difficile de positionner les supercontinents autour du globe à cette époque. D'après la présence de niveaux d'impactites datées à 3.47 Ga (U-Pb sur zircon) dans les cratons de Kaapvaal en Afrique du Sud et de Pilbara en Australie, ces deux noyaux continentaux devaient être réunis entre 3.5 et 3.1 Ga en un supercontinent appelé Vaalbara (Byerly *et al.*, 2002). Le supercontinent Kenorland lui aurait succédé vers 2.9 Ga et rassemblerait les boucliers Baltique, Sibérien et celui d'Amérique du Nord d'après les corrélations géochronologiques, stratigraphiques et sédimentologiques établies dans les roches sédimentaires des provinces de Rae, de Hearne, du Wyoming, de l'Ontario ainsi que de la Finlande et de l'ouest de la Russie (Aspler and Chiarenzelli, 1998). Le troisième supercontinent, Zimvaalbara, aurait probablement coexisté avec Kenorland entre 2,9 et 2,65 Ga et rassemblait les cratons archéens de Kaapvaal, de Pilbara et du Zimbabwe (Stanistreet, 1993 ; Aspler and Chiarenzelli, 1998 ; Barley *et al.*, 2005). Les cratons de São Francisco au Brésil, de Gawler au sud de l'Australie, de l'Antarctique, de la Chine ainsi que les blocs archéens de l'Inde se seraient ensuite ajoutés entre 2,6 et ~ 2,42 Ga par accrétions successives (Aspler and Chiarenzelli, 1998 ; Barley *et al.*, 2005).

Les supercontinents archéens se seraient ensuite désolidarisés sous l'effet de superplumes mantelliques qui les auraient scindés en plusieurs plaques par des rides médio-océaniques (Barley *et al.*, 2005). La fragmentation du supercontinent Kenorland entre 2,45 et 2,10 Ga est marquée par la présence d'essaim de dykes mafiques et de bassins sédimentaires liée à des rifts sur plusieurs continents (Pesonen *et al.*, 2003). Les cratons archéens se seraient ensuite rassemblés à la faveur d'orogènes successifs entre 2,1 et 1,8 Ga qui ont abouti à l'accrétion des

roches vertes et granitiques et à l'assemblage des continents sous une nouvelle configuration, le supercontinent Columbia (aussi appelé Hudsonland, Nuna ou Nena), entre le Paléo- et le Mésoprotérozoïque (Zhao *et al.*, 2002 ; Pesonen *et al.*, 2003). La reconstitution de ce supercontinent (figure 1.6) a été réalisée principalement grâce aux données paléomagnétiques, lithostratigraphiques et géochronologiques. Entre environ 1,9 et 1,6 Ga, il rassemblait les boucliers précambriens Laurentia (Amérique du Nord et Groenland), Baltique, de la Sibérie, de l'Australie et de l'Antarctique, ainsi que de la Chine, de l'Inde et de l'Afrique mais ces trois derniers avec plus de réserves (Zhao *et al.*, 2002 ; Pesonen *et al.*, 2003).

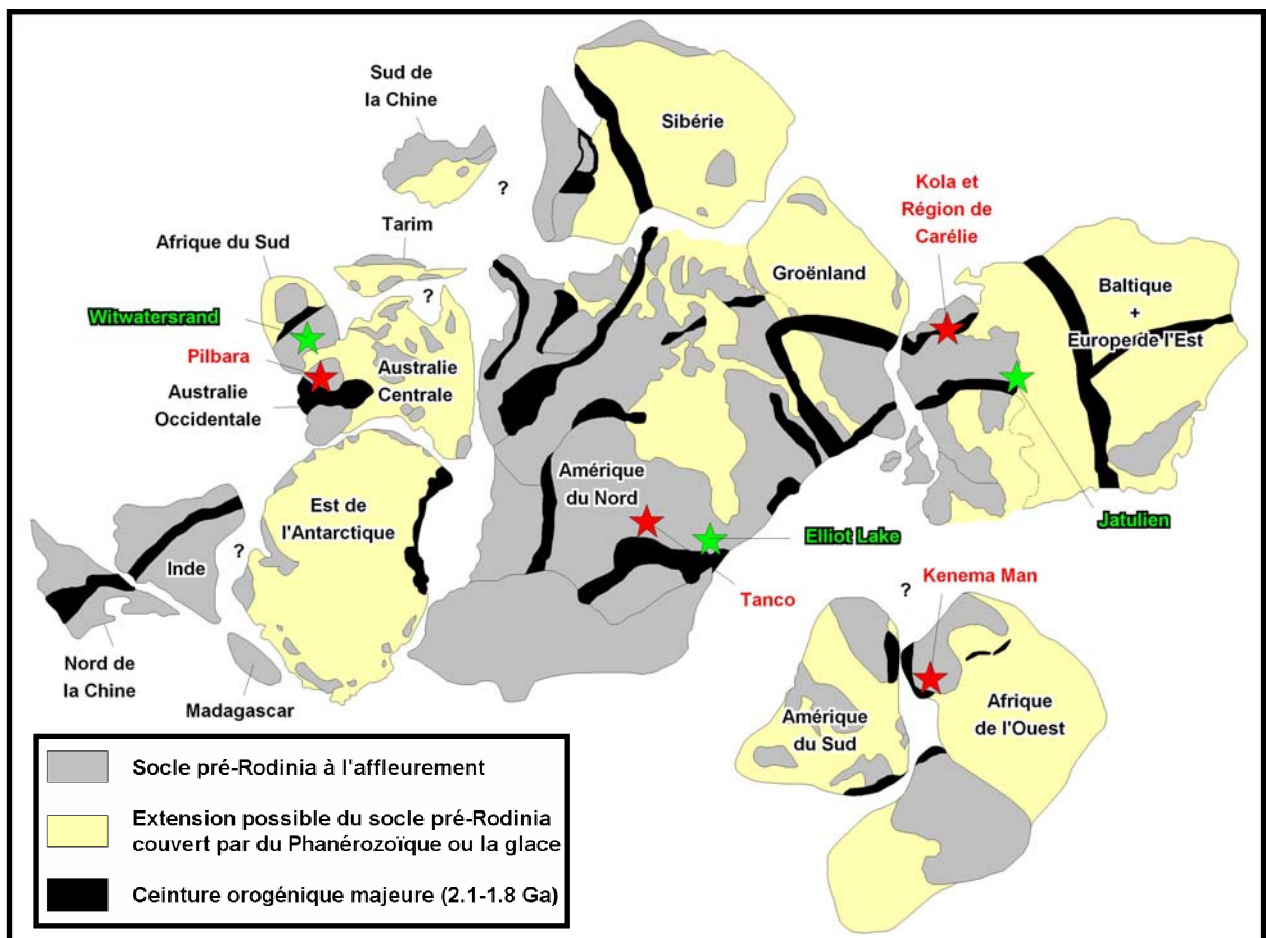


**Figure 1.6.** Reconstitution du supercontinent Columbia au paléo-mésoprotérozoïque issu de collisions entre les blocs cratoniques archéens et protérozoïques lors des orogènes entre 2,1 et 1,8 Ga (modifié de Zhao *et al.*, 2002). La localisation des zones d'étude est reportée par des étoiles : en rouge les zones de socle archéen et en vert les paléo-placers.

### 3. NATURE, RÉPARTITION ET POTENTIEL URANIFÈRE DES ROCHES ARCHÉENNES

Les provinces archéennes exposées actuellement représentent environ 5 à 7,5% de la surface continentale (Nisbet, 1987 ; de Wit, 1998). Elles sont réparties sur tous les continents, sont étroitement associées aux provinces protérozoïques constituées en partie de roches

archéennes remaniées, et l'ensemble forme les grands boucliers précambriens (c.f. Figure 2 de l'introduction générale).

D'après Martin (2005), les terrains archéens sont composés essentiellement de dômes granito-gneissiques de roches de type TTG (~85%), séparés par des ceintures de roches vertes volcano-sédimentaires (~5%) et intrudés par des granitoïdes tardifs (~10%).

- ***Les granitoïdes archéens***

Les roches de type tonalites-trondhjémites-granodiorites (TTG) représentent le plus grand volume de roches archéennes actuellement préservées dans les cratons, soit près de 90% de la croûte continentale juvénile formée entre 4,0 et 2,5 Ga (Jahn *et al.*, 1984 ; Martin *et al.*, 2005). Le plutonisme felsique serait apparu dès le Paléoarchéen d'après la présence de tonalite, de trondhjémite, de diorite, de granodiorite et de leucogranite datés entre 3870 et 3625 Ma dans le complexe gneissique d'Itsaq au Groenland (Nutman *et al.*, 1996). Les roches de type TTG se formeraient par la fusion à haute pression de roches basaltiques issues d'une croûte océanique subductée (Drummond and Defant, 1990 ; de Wit, 1998 ; Martin, 1999 ; Martin *et al.*, 2005). Ces magmas sont essentiellement constitué de quartz ( $\text{SiO}_2 > 64$  wt%) et de plagioclases ( $\text{Na}_2\text{O}$  entre 3 et 7 wt%), ils sont pauvres en ferromagnésiens avec cependant la présence de biotite et de hornblende, et le plus souvent ils sont dépourvus de feldspath potassique. Les TTG sont pauvres en Rb, Th, U, K et en HREE (Sm, Tb, Yb) par rapport à la croûte continentale actuelle (Tableaux 1.1 et 1.2). Cette composition évolue au cours du temps en montrant une augmentation progressive en Mg, Ni, Cr, Sr, et ( $\text{CaO} + \text{Na}_2\text{O}$ ) suggérant une interaction croissante avec le manteau péridotitique inexistante avant 3,3 Ga (Martin *et al.*, 2005). Le gradient géothermique élevé à l'Archéen permettait en effet à la plaque océanique subductante de fondre avant sa déshydratation à la différence de ce qui se produit actuellement avec la croûte océanique (Figure 1.3). Cependant, le processus de formation des TTG est toujours débattu. Les roches de type TTG d'âge inférieur à 3 Ga ont des compositions qui diffèrent des adakites échantillonnées dans les zones de subduction actuelles et s'approcheraient plus de celles des granites riches en Na phanérozoïques formés par fusion partielle de matériaux basaltiques hydratés à la base d'une croûte océanique épaissie (Smithies, 2000). Condie (2005) propose un modèle mettant en jeu des remontées de plumes mantelliques sous la croûte océanique qui provoqueraient cet épaississement crustale et la genèse de ces magmas. L'étude géochimique et pétrographique des magmas de type TTG du craton de Barberton en Afrique du Sud conforterait plutôt la formation de ces roches en contexte tectonique compressif associé à une phase d'accrétion et parallèlement

d'amincissement de la croûte (Clemens *et al.*, 2006). L'origine des granitoïdes de type TTG reste donc encore controversée.

La composition des granitoïdes évolue finalement à la fin de l'Archéen vers des roches plus riches en Na<sub>2</sub>O, K<sub>2</sub>O, MgO et REE tels que les granites de type Closepet observés au sud de l'Inde ou les sanukitoïdes du Japon (Martin and Moyen, 2005 ; Tableau 1.2). Ces granitoïdes tardifs sont intrusifs dans les ceintures de roches vertes et les roches de type TTG. Ils sont appauvris en silice par rapport aux TTG, ils sont métalumineux, modérément à fortement potassiques (Figure 1.7) et sont caractérisés par un spectre en éléments des terres rares enrichi en éléments légers (LREE, Figure 1.8). Ces roches plutoniques intrusives seraient le produit de la fusion des TTG préexistants et du métasomatisme du matériel péridotitique profond induit par la libération des fluides d'une croûte subductante sous-jacente (Martin *et al.*, 2005). Cette évolution magmatique, avec l'apparition des granites d'affinité calco-alcaline, marque la transition vers le Paléoprotérozoïque et le changement important de la dynamique terrestre à cette époque associé au refroidissement de la planète. Les granites tardi-archéens sont aussi plus riches en éléments incompatibles que les TTG précoces et notamment en U et Th avec un rapport Th/U plus grand (5,4) que la moyenne crustale proche de 4 (Tableau 1.1).

**Tableau 1.1.** Comparaison des teneurs en uranium et thorium (ppm) de la croûte continentale à l'Archéen par rapport à la composition actuelle

	TTG Archéens Précoces*		TTG Archéens Tardifs*		Croûte Continentale Archéenne**	Croûte Continentale Actuelle**	Croûte Continentale Actuelle Supérieure**
	Moyenne (n=212)	1σ	Moyenne (n=831)	1σ	Moyenne	Moyenne	Moyenne
Th (ppm)	4,10	2,40	8,10	5,30	2,9	3,5	10,7
U (ppm)	1,20	0,49	1,50	0,99	0,75	0,91	2,8
Th/U	3,42		5,40		3,87	3,85	3,82

**Références :** \* Condie (2005) ; \*\* Taylor and McLennan (1985) ; **Notes :** 1σ = écart-type sur la moyenne ; n = nombre d'analyses utilisées pour le calcul de la moyenne.

**Tableau 1.2.** Composition moyenne des roches de type TTG, des sanukitoïdes et des granites de type Closepet (extrait de Martin *et al.*, 2005)

	TTG >3.5 Ga		TTG 3.5 Ga<t<3 Ga		TTG <3 Ga		Sanukitoïdes <62%SiO2		Closepet <62% SiO2	
	Moyenne (n=108)	1σ	Moyenne (n=320)	1σ	Moyenne (n=666)	1σ	Moyenne (n=31)	1σ	Moyenne (n=43)	1σ
wt%										
SiO <sub>2</sub>	69,59	3,1	69,65	3,5	68,36	3,8	58,76	2,9	56,39	3,5
TiO <sub>2</sub>	0,39	0,3	0,36	0,2	0,38	0,2	0,74	0,3	1,2	0,5
Al <sub>2</sub> O <sub>3</sub>	15,29	0,9	15,35	1,3	15,52	1,1	15,8	0,9	15,79	1,4
Fe <sub>2</sub> O <sub>3T</sub>	3,26	1,2	3,07	1,6	3,27	1,6	5,87	1,5	7,34	1,7
MgO	1	0,5	1,07	0,6	1,36	0,9	3,9	1,3	3,38	1,9
CaO	3,03	0,9	2,96	1,2	3,23	1,1	5,57	1,5	5,45	1,4
Na <sub>2</sub> O	4,6	0,5	6,64	0,8	4,7	0,8	4,42	0,7	3,94	0,8
K <sub>2</sub> O	2,04	0,8	1,74	0,7	2	0,8	2,78	0,8	3,17	0,8
P <sub>2</sub> O <sub>5</sub>	0,13	0,09	0,14	0,09	0,15	0,1	0,39	0,1	0,72	0,3
MnO	0,04	0,03	0,06	0,05	0,05	0,05	0,09	0,02	0,13	0,08
ppm										
Ni	12	9	15	12	21	21	72	35	38	43
Cr	34	22	21	19	50	111	128	85	50	58
V	39	24	43	26	52	32	95	19	129	44
Y	12	9	14	19	11	16	18	11	37	13
Zr	166	64	155	76	154	131	184	129	323	109
Nb	8	7	6	4	7	5	10	8	18	7
La	35,3	19	31,4	25	30,8	24	59,9	28	90,9	46
Ce	61,7	33	55,1	35	58,5	400	126	47	188	80
Nd	25,8	14	19,6	14	23,2	19	54,8	16	84,9	34
Sm	4,2	2	3,3	3	3,5	2	9,8	3	14,5	6
Eu	1	0,39	0,8	0,36	0,9	0,45	2,3	0,62	3,2	1,09
Gd	3,2	2,2	2,4	1,3	2,3	1,4	6	1,4	9,2	2,1
Dy	1,8	1,1	1,9	1	1,6	0,9	3,2	0,8	5,6	1,1
Er	0,77	0,7	0,77	0,4	0,75	0,5	1,41	0,5	2,68	0,7
Yb	0,78	0,4	0,63	0,4	0,63	0,4	1,32	0,7	2,05	0,8
Lu	0,2	0,12	0,13	0,1	0,12	0,1	0,26	0,1	0,34	0,1
Rb	79	39	59	29	67	51	65	22	93	37
Ba	449	323	523	327	847	555	1543	563	1441	653
Sr	360	116	429	178	541	252	1170	638	978	350
(La/Yb) <sub>N</sub>	26,85		32,86		32,52		29,92		29,32	
Sr/Y	30,45		31,44		51,1		63,98		26,58	
Mg#	0,38		0,41		0,45		0,57		0,48	
K <sub>2</sub> O/Na <sub>2</sub> O	0,44		0,38		0,43		0,63		0,8	

**Notes :** 1σ = écart-type sur la moyenne ; n = nombre d'analyses utilisées pour le calcul de la moyenne ; références utilisées pour les TTG (Martin, 1994 ; Martin and Moyen, 2002), pour les sanukitoïdes (Shirey and Hanson, 1984, 1986 ; Querré, 1985 ; Balakrishnan and Rajamani, 1987 ; Stern and Hanson, 1991 ; Krogstad *et al.*, 1995 ; Smithies and Champion, 1999 ; Stevenson *et al.*, 1999 ; Moyen *et al.*, 2003a) et pour les granites de Closepet (Jahn *et al.*, 1988 ; Barton *et al.*, 1992 ; Jayananda *et al.*, 1995 ; Frost *et al.*, 1998 ; Moyen *et al.*, 2001, 2003b).

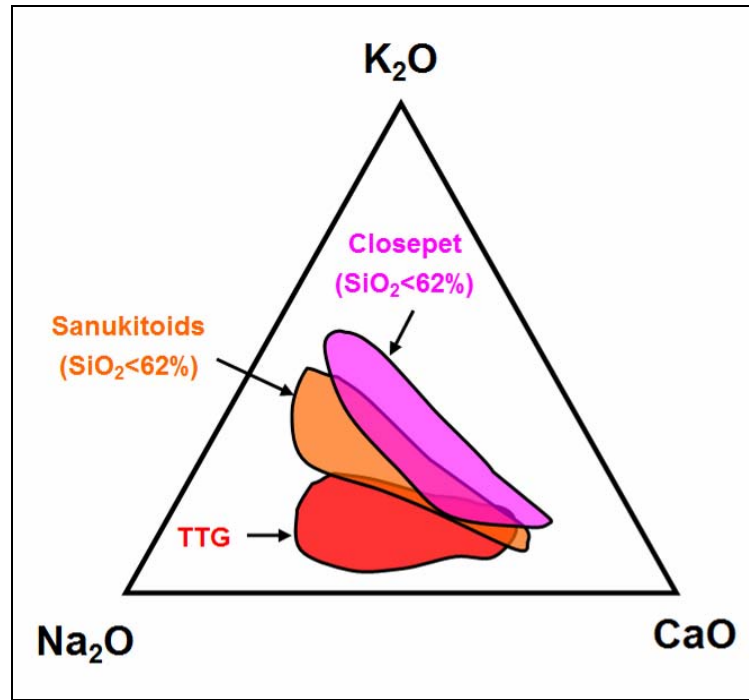


**Figure 1.7.** Diagramme ternaire K<sub>2</sub>O-Na<sub>2</sub>O-CaO montrant l'évolution de la composition des granitoïdes archéens (TTG, sanukitoïdes et granites de type Closepet) modifié de Martin and Moyen (2005).

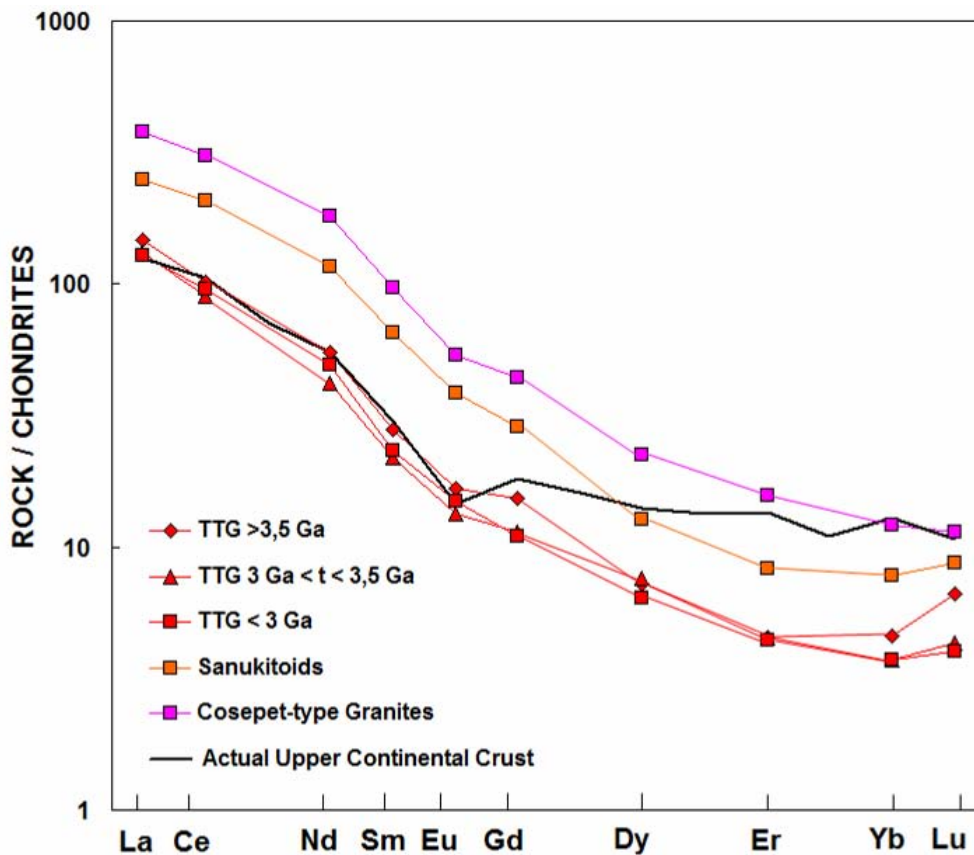


**Figure 1.8.** Spectre des REE normalisées aux chondrites (valeurs chondritiques C1 de Sun and McDonough, 1989) pour les granitoïdes archéens (TTG, sanukitoïdes et granites de type Closepet) d'après les compositions du Tableau 1.2 (Martin *et al.*, 2005) comparés à la composition moyenne de la croûte continentale actuelle (Taylor and McLennan, 1985).

- *Les ceintures de roches vertes*

Les ceintures de roches vertes sont composées de roches volcano-sédimentaires métamorphisées.

Les roches volcaniques basaltiques sont d'affinité tholéitique et de composition mafique à ultramafique (komatiites, andésites, amphibolites, gabbros...). Ces roches volcaniques sont caractérisées par des spectres en REE plats et elles sont extrêmement pauvres en éléments incompatibles avec généralement  $U < 0,5$  ppm et  $Th < 1,5$  ppm (Polat and Kerrich, 2000). Elles constituent les reliques métamorphisées de la croûte océanique archéenne directement issues de la fusion du manteau primitif.

Les roches sédimentaires se déposent dans les paléo-vallées et les bassins intracratoniques entre les dômes granito-gneissiques. Les sédiments correspondent le plus souvent à des grès immatures de type greywackes issue de l'érosion des roches volcaniques et des grès riches en quartz provenant des roches plutoniques et métamorphiques. Les plateformes carbonatées représentant une sédimentation de faible profondeur se sont formées autour des cratons stables et des premiers continents, suivi à plus grande profondeur par le dépôt de shales noirs et de formations ferrifères rubanées (ou BIF de l'anglais « *banded iron formation* » ; Barley *et al.*, 2005). Les BIF n'ont pas d'équivalent actuel mais ils correspondraient à la précipitation de fer ferreux au fond de l'océan primitif anoxique saturé en  $Fe^{2+}$  dissous (Holland, 1984). Généralement, les BIF se présentent sous la forme d'une alternance entre des lits riches en fer et des lits de chert. Les teneurs en U et Th des sédiments archéens sont grandement variables et dépendent principalement de la roche source dont ils proviennent, puis des processus de sédimentation (séparation granulométrique et tri sélectif des particules en fonction de leur densité, effets de l'altération lors du transport, solubilité et résistance des minéraux détritiques, taux d'érosion et rapidité de la sédimentation...) et enfin des processus post-sédimentaires qui peuvent influencer le fractionnement des éléments (métamorphisme, diagenèse, altération météorique ou hydrothermale).

Les différentes lithologies qui viennent d'être présentées sont le reflet d'une croûte primitive dont le contexte géodynamique et les processus de formation restent encore incertains. La figure **1.9** présente une compilation des analyses géochimiques de roches archéennes dont les abondances en uranium et en thorium ont été mesurées (base de données « GEOROC » ; Sarbas, 2008). La croûte continentale, dont les 3/4 se sont formés à l'Archéen, constitue le principal réservoir en U et Th de la Terre. La genèse des premiers granitoïdes potassiques est donc un point capital pour la compréhension du fractionnement de l'uranium et des premiers maillons du

cycle de l'U. Ce sont en effet ces granitoïdes tardifs qui semblent être les plus riches en éléments incompatibles à cette époque.

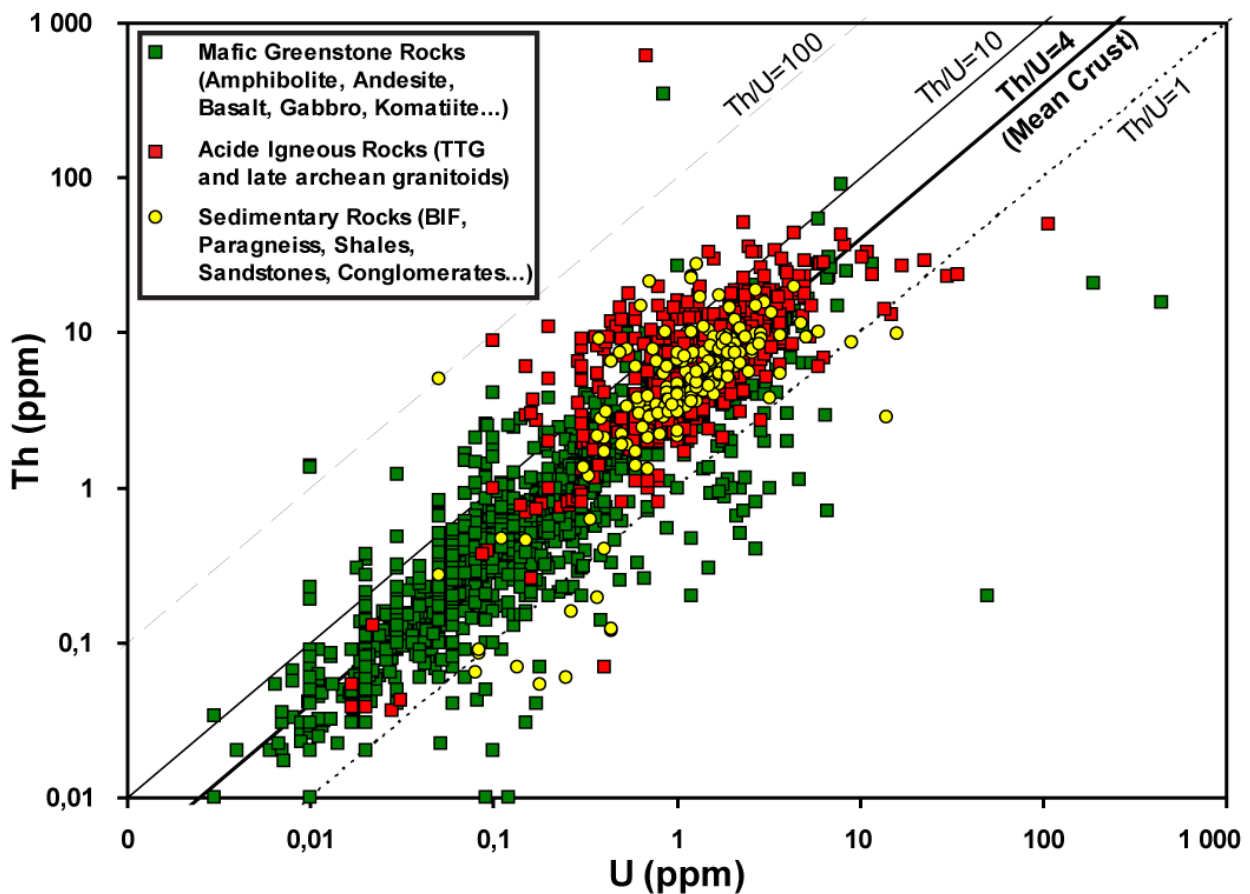


**Figure 1.9.** Teneurs en uranium et thorium (ppm) des roches archéennes d'après une compilation des analyses géochimiques des différents cratons référencées dans la base de données « GEOROC » (3094 analyses: 2236 roches mafiques, 649 roches acides et 209 roches sédimentaires, extrait du site <http://georoc.mpch-mainz.gwdg.de/georoc/>).

#### 4. ATMOSPHÈRE PRIMITIVE ET « OXYATMOSPHÈRE »

Les roches sédimentaires archéennes contiennent les plus anciennes traces de vie découvertes à ce jour d'après leur composition isotopique (Mojzsis *et al.*, 1996) ainsi que des traces fossiles vieilles de 3,2 Ga (Rasmussen, 2000). Ces roches révèlent une complexification des organismes vivant depuis les bactéries méthanogènes et méthanotrophes les plus simples, jusqu'aux organismes capables d'effectuer la photosynthèse comme les cyanobactéries et les organisations algaires plus complexes telles que les colonies stromatolitiques vers 2,7 Ga (Brock *et al.*, 2003). Le développement de la vie et la biodiversité à l'Archéen seraient à l'origine de l'apparition de l'oxygène dans l'hydrosphère puis dans l'atmosphère. Cependant, deux théories sont discutées quant à la composition de l'atmosphère archéenne par rapport à l'évolution de son taux d'oxygène libre.

Une première école de pensée (Cloud, 1972 ; Kasting, 2001 ; Holland, 2006) soutient l'hypothèse que l'hydrosphère et l'atmosphère primitives seraient anoxiques. L'atmosphère primitive réductrice provenant du dégazage des volcans et des magmas avant 2,45 Ga serait essentiellement composée de H<sub>2</sub>, de méthane (CH<sub>4</sub>) et d'ammoniaque (NH<sub>3</sub>) avant la formation du noyau terrestre, puis de vapeur d'eau, de CO<sub>2</sub>, et de N<sub>2</sub> avec des concentrations mineures en H<sub>2</sub> et CO après la différenciation (Kasting, 1993 ; Catling and Claire, 2005). La concentration en O<sub>2</sub> de l'atmosphère archéenne serait inférieure à 10<sup>-5</sup> PAL (rapport au taux de l'atmosphère actuelle, de l'anglais « *Present Atmospheric Levels* », d'après Barley *et al.*, 2005 ; figure **1.10**). L'apparition d'organismes phototrophes tels que les cyanobactéries à l'Archéen est supposée être le mécanisme prédominant ayant conduit à l'augmentation progressive de l'oxygène libre dans l'atmosphère grâce à leur faculté de libérer de l'oxygène en produit de la réaction de la photosynthèse (CO<sub>2</sub> + H<sub>2</sub>O → CH<sub>2</sub>O + 2O<sub>2</sub> où CH<sub>2</sub>O représente la matière organique synthétisée; Catling and Claire, 2005 ; Frimmel, 2005 ; Yamaguchi, 2005). Le taux d'O<sub>2</sub> dans l'atmosphère pourrait aussi augmenter grâce à l'échappement d'hydrogène dans l'espace lors de la photolyse du méthane dans la haute atmosphère (CO<sub>2</sub> + 2H<sub>2</sub>O → CH<sub>4</sub> + 2O<sub>2</sub> → CO<sub>2</sub> + O<sub>2</sub> + 4H<sub>(espace)</sub>) ; d'après Catling *et al.*, 2001). La concentration en oxygène aurait donc augmenté au cours du Paléoprotérozoïque, entre 2,4 et 2,3 Ga (Bekker *et al.*, 2004) jusqu'à atteindre des valeurs comprises entre 0,02 et 0,04 atm vers 1,85 Ga (Holland, 2006). Ce phénomène est appelé l'oxyatmoversion ou encore le G.O.E. (de l'anglais « *Great Oxidation Event* »).

Une seconde école soutient l'hypothèse d'une atmosphère archéenne oxygénée (Ohmoto, 1996, 2003 et 2004 ; Lasaga and Ohmoto, 2002). La concentration en oxygène de l'atmosphère serait restée constante au cours du temps (Figure **1.10**) dès que les organismes capables de réaliser la photosynthèse seraient apparus vers 3,5 Ga voir dès 4,0 Ga (Lasaga and Ohmoto, 2002). Toutefois, cette seconde hypothèse est loin d'être soutenue par la majorité (Rye and Holland, 1998 ; Holland, 1999 ; Kasting, 2001 ; Frimmel, 2005).

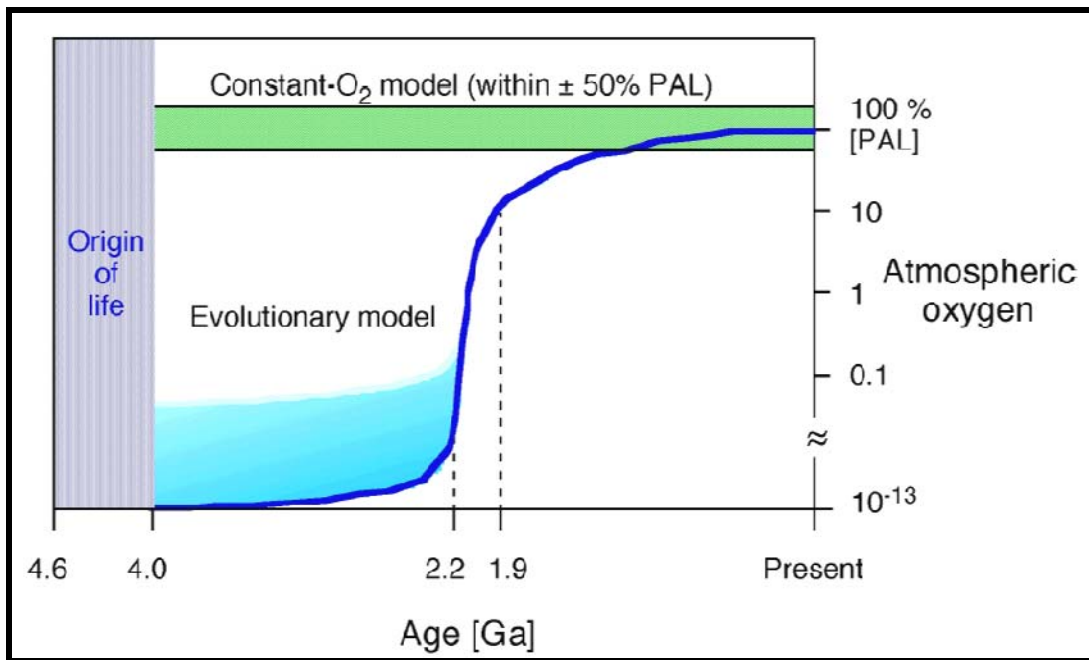


**Figure 1.10.** Composition de l'atmosphère au cours du temps (d'après Yamaguchi, 2005) : **en bleu** - modèle pour une atmosphère archéenne réduite avec la courbe de l'évolution de  $pO_2$  augmentant progressivement avec la complexification des organismes vivants et l'oxyatmoverision entre 2,2 et 1,9 Ga dès l'apparition des organismes phototrophes (hypothèse soutenue par Kasting, 1987 et 2001, Rye and Holland, 2000, Pavlov *et al.*, 2001, Bekker *et al.*, 2004, Barley *et al.*, 2005, Holland, 2006), et **en vert** - modèle pour une atmosphère archéenne oxygénée (d'après Ohmoto, 1996, 2003 et 2004 ; Lasaga and Ohmoto, 2002).

En effet, l'hypothèse d'une atmosphère archéenne acide et anoxique est soutenue par différents arguments géologiques et géochimiques. Tout d'abord, l'argument majeur consiste en la disparition des formations de fer rubanée de l'enregistrement géologique après 1,8 Ga (Holland, 1999 ; Klein, 2005). Le dépôt des BIF nécessite l'accumulation et le transport de fer ferreux ( $Fe^{2+}$ ) qui n'est stable que sous conditions anoxiques. Le changement des conditions d'oxydation se serait traduit par la production de fer ferrique ( $Fe^{3+}$ ) qui aurait précipité rapidement sous la forme d'hydroxyde de fer et limiterait ainsi l'accumulation de fer et la formation des BIF. D'autre part, cette atmosphère réductrice permettait aussi la préservation de cortèges de minéraux à uraninite, pyrite, sidérite et magnétite concentrés dans les sédiments détritiques continentaux archéens (Roscoe, 1969 et 1973 ; Pretorius, 1981 ; Rasmussen and Buick, 1999). Les grains d'uraninite et de pyrite sont insolubles en conditions anoxiques et ils sont très instables en milieu oxygéné, tout comme les grains de sidérite détritiques observés dans les grès archéens (3250-2750 Ma) du craton de Pilbara en Australie (Rasmussen and Buick, 1999). Les dépôts protérozoïques plus récents passent à des cortèges où prédominent les oxydes de fer, sans pyrite ni uraninite détritique (Roscoe, 1969 et 1973 ; Pretorius, 1981) confortant l'hypothèse de l'augmentation en oxygène de l'atmosphère après l'Archéen. L'apparition de paléosols riches en hématite entre 2,2 et 2,0 Ga (Rye and Holland, 1998 ; Murakami *et al.*, 2001 ; Yang and Holland, 2003), de niveaux oxydés de type « *redbeds* » après 2,3 Ga (Barley *et al.*,

2005) et de sulfates ( $\text{CaSO}_4$ ) dans les évaporites postérieures à 1,9 Ga (Melezhik *et al.*, 2005) suggèrent un taux d'oxygène suffisamment élevé pour entraîner l'oxydation de fer et du soufre. Enfin, le fractionnement des isotopes du soufre indépendamment de la masse (MIF) dans les sulfates des roches sédimentaires archéennes démontrerait que l'atmosphère primitive riche en composés volcaniques soufrés n'était pas protégée des rayonnements ultraviolets contrairement à l'atmosphère actuelle composée d'une couche d'ozone (Farquhar and Wing, 2003 ; Pavlov *et al.*, 2003). Tous ces arguments sont donc en faveur d'une atmosphère archéenne anoxique et d'une augmentation de la concentration en oxygène libre dans l'atmosphère entre 2,2 et 1,85 Ga (Figure 1.11).

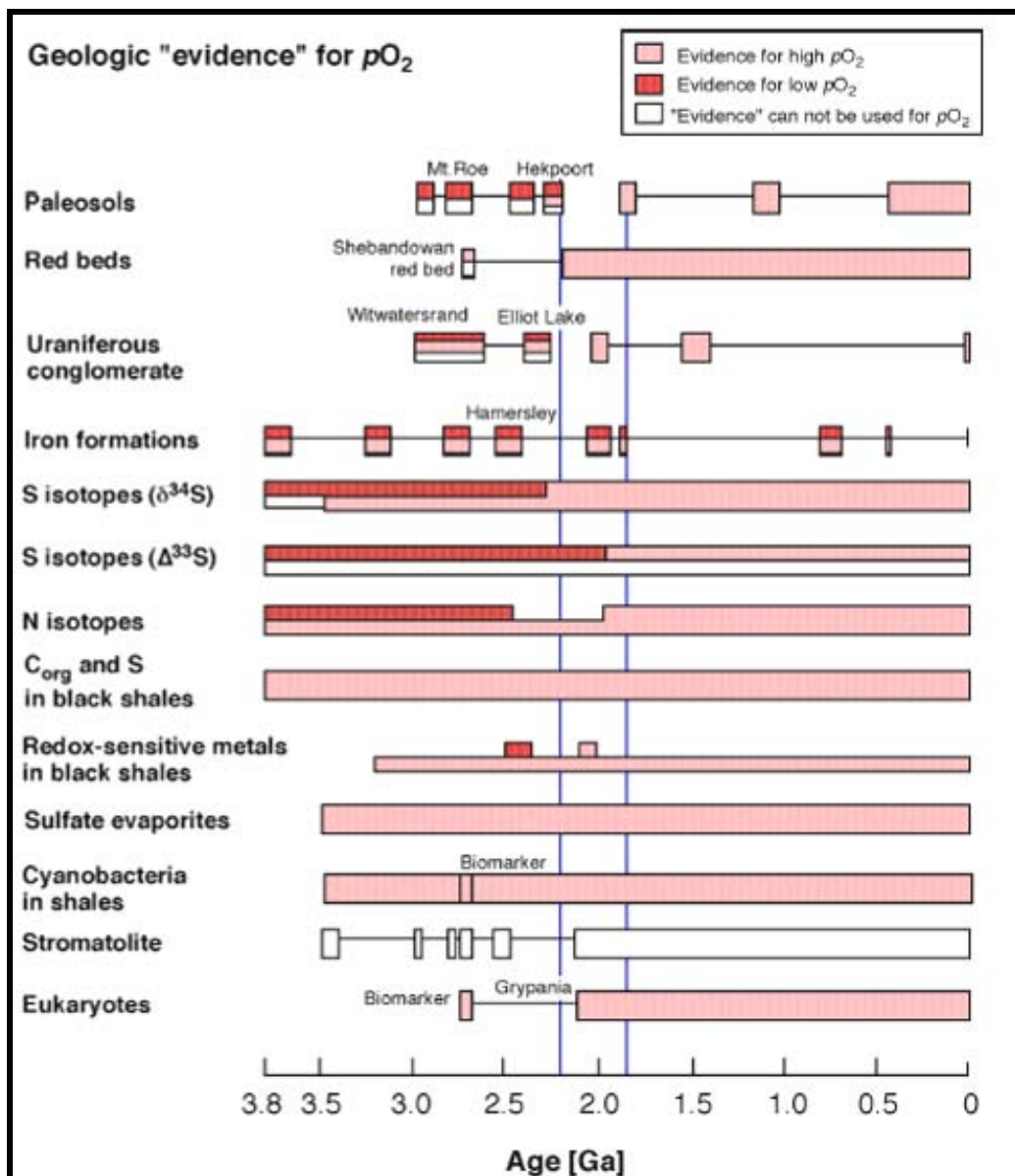


**Figure 1.11.** Résumé des « évidences » de l'oxyatmoversion, l'augmentation de l'oxygène libre dans l'atmosphère entre 2,2 et 1,85 Ga symbolisée par les traits bleus (extrait de Yamaguchi, 2005 ; modifié de Holland, 1994 et Phillips *et al.*, 2001).

L'argumentation pour une atmosphère oxygénée à l'Archéen est basée principalement sur la découverte de niveaux latéritiques sur des paléosols âgés d'environ 2,3 Ga (Ohmoto, 1996 ; Ohmoto *et al.*, 1999), sur la découverte de paléosols oxydés vieux de 2,7 Ga (Kimberley and Grandstaff, 1986), sur l'existence d'uraninite et de pyrite détritiques préservées dans des dépôts sédimentaires Phanérozoïques (Maynard *et al.*, 1991 ; Maynard, 1992) et sur les variations des concentrations en isotopes du fer et de l'azote dans les shales noirs archéens (Yamaguchi *et al.*, 2002 et 2003). Le débat sur l'âge de l'oxygénation de l'atmosphère reste donc encore d'actualité.

L'augmentation du taux d'oxygène dans l'hydrosphère et dans l'atmosphère a cependant des conséquences importantes sur la chimie de la surface terrestre et sur les conditions d'oxydoréduction des gisements métalliques notamment pour le fer et l'uranium. Les séquences sédimentaires détritiques et plus particulièrement les niveaux conglomératiques déposés avant 2,2 Ga sont porteurs de concentrations importantes en uraninite détritique alors que les conglomérats formés après l'oxyatmoversion sont « le plus souvent » dépourvus de minéralisation uranifère (Roscoe, 1969 et 1973 ; Pretorius, 1981 ; Maynard *et al.*, 1991 ; Maynard, 1992). A titre d'exemple, les conglomérats du Tarkwa au Ghana dont l'âge maximal de sédimentation a été établi à  $2133 \pm 4$  Ma (U-Pb sur zircons ; Pigois *et al.*, 2003) contiennent des gisements d'or associés à des minéraux lourds tels que l'hématite sans aucune trace d'uranium à la différence des conglomérats du Bassin du Witwatersrand en Afrique du Sud, qui sont associés à de l'or, de l'uraninite et de la pyrite détritiques (Frimmel, 2005). Le fait que certains dépôts sédimentaires phanérozoïques puissent contenir des uraninites et pyrites détritiques (Maynard *et al.*, 1991 ; Maynard, 1992) suggère qu'il faille trouver d'autres arguments pour soutenir la théorie de l'oxyatmoversion. L'état redox de l'atmosphère reste donc un point important à élucider pour la métallogénèse des gisements d'U de type paléo-placer.

## **5. GISEMENTS D'URANIUM DE TYPE PALÉO-PLACER : ORIGINE ET SOURCES POSSIBLES**

Les gisements uranifères dans les conglomérats à cailloux de quartz des séries sédimentaires archéennes à paléoprotérozoïques sont les plus anciens gisements d'uranium connus sur Terre. Ils sont présents tout autour du globe et représentent une réserve économique importante d'uranium mais aussi en d'autres métaux de base tels que l'or ou les Eléments du Groupe du Platine (EGP). Les minéralisations uranifères sont réparties dans des niveaux conglomératiques à galets de quartz de bassins intracratoniques produits de l'érosion des reliefs continentaux archéens (Smith and Minter, 1980 ; Frimmel and Gartz, 1997). Ces conglomérats se mettent en place dans des systèmes fluvio-deltaïques et les minéralisations à or, pyrite et

uraninite principalement suivent les lits de minéraux lourds (Roscoe, 1969 et 1973 ; Pretorius, 1981).

D'après une ancienne reconstitution de la position des continents au Paléoproterozoïque (Piper, 1976), la répartition des paléo-placers semble associée spatialement et temporellement à celle des BIF (Figure 1.12 ; d'après Houston and Karlstrom, 1979). En effet, les zones de BIF peuvent être corrélées entre elles sur plusieurs centaines de kilomètres suggérant la formation d'une large plateforme continentale et une stabilisation des cratons pendant une longue période, entre le Méso- et le Néoarchéen. Les BIF se sont formés en marge des cratons stables et les paléo-placers en bordure de ces blocs archéens surélevés dans les vastes systèmes fluviaux et deltaïques associés à la formation de grands bassins intracratoniques. Cette reconstitution du supercontinent est maintenant désuète et supplantée par celle présentée en figure 1.6 corrélée par des études géologiques, géochimiques, isotopiques et géochronologiques plus récentes. Cependant, notons que les paléo-placers uranifères se sont développés préférentiellement entre 3,1 et 1,9 Ga (Pretorius, 1981) et que leur « disparition » concorde avec celle des BIF vers environ 1,8 Ga, ainsi qu'avec l'apparition de niveaux oxydés de type « *red beds* ». Ce changement important de la sédimentation précambrienne semble associée aux modifications de l'état redox de l'hydrosphère et de l'atmosphère (Houston and Karlstrom, 1979). Les paléo-placers déposés après 1,9 Ga ne contiennent généralement plus d'uraninite détritique car l'atmosphère à partir du Paléoproterozoïque était suffisamment oxydante pour rendre instable la forme réduite de l'uranium (valence  $U^{4+}$  à l'état solide dans l'uraninite  $UO_2$ , altéré en milieu oxydé et mobilisé en solution sous la valence  $U^{6+}$ ) de même que le fer ferrique pour les BIF. Les quelques rares sédiments présentant des grains d'uraninite et de pyrite détritiques au Phanérozoïque (Maynard *et al.*, 1991 ; Maynard, 1992) semblent associés à des conditions très particulières de dépôts : dans des rivières, sous des conditions froides et des terrains à hauts reliefs induisant une érosion intense sous une atmosphère raréfiée et une sédimentation et un enfouissement extrêmement rapide permettant la préservation de ces minéraux.

Les conglomérats précambriens à uraninite les plus étudiés sont les conglomérats à cailloux de quartz du Super-Groupe du Witwatersrand en Afrique du Sud datés entre environs 2,90 et 2,84 Ga (Frimmel, 2005) et les conglomérats du Super-Groupe Huronien datés entre 2,7 et 2,2 Ga dans le district minier d'Elliot Lake au Canada (Roscoe, 1973). Deux origines ont été proposées pour les minéralisations uranifères dans ces paléo-placers : une origine syngénétique (détritique) et une origine épigénétique (hydrothermale) qui sont toujours actuellement débattues.

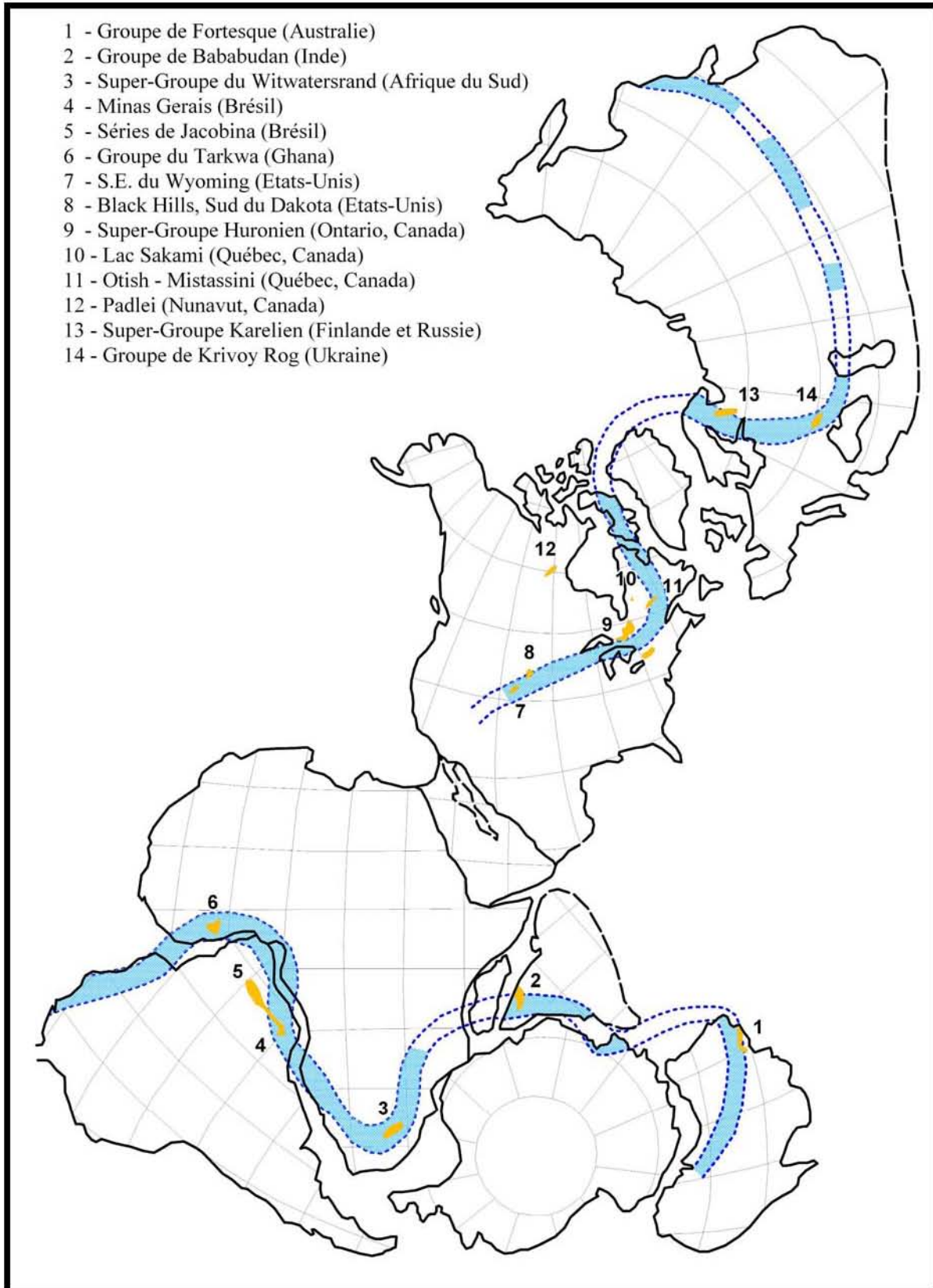


**Figure 1.12.** Répartition des paléo-placers archéens à paléoprotérozoïques (en orange) et des formations de fer rubanées (BIF de l'anglais « *Banded Iron Formation* » ; en bleu) modifiée de Houston and Karlstrom, (1979) d'après la reconstitution des continents de Piper (1976) et la distribution des BIF de Goodwin (1973).

L'origine détritique est soutenue par la forme arrondie des grains de pyrite, d'uraninite et d'or, par le contrôle de la distribution des minéraux lourds selon les structures sédimentaires primaires (Smith and Minter, 1980 ; Minter, 1999 ; Frimmel and Minter, 2002) ainsi que par les études géochronologiques effectuées sur les minéralisations (Houston and Karlstrom, 1979 ; Frimmel, 2005). L'origine détritique des grains arrondis d'uraninite dans les conglomérats du bassin du Witwatersrand en Afrique du Sud a notamment été démontrée par les datations U-Pb et Re-Os respectivement sur des grains d'uraninite et de pyrite, dont les âges obtenus sont de  $3050 \pm 50$  Ma pour l'uraninite (estimation de l'intercepte supérieur entre Discordia et Concordia d'après Rundle and Snelling, 1977) et de  $2,99 \pm 0,11$  Ga pour la pyrite (Kirk *et al.*, 2002), sont plus vieux que l'âge de dépôt maximal des roches sédimentaires estimé à 2,90 Ga (Minter, 2002 ; Frimmel, 2005). Enfin, dans les dépôts des conglomérats Huroniens à Elliot Lake, les uraninites ont des teneurs en thorium importantes, entre 4 et 12 wt% ThO<sub>2</sub>, impliquant une source magmatique et donc une origine détritique (Ono, 2001).

Cependant, l'origine hydrothermale est suggérée par des textures de dissolution des grains, par des recristallisations secondaires en surcroissance sur les minéraux primaires, par la présence de séricite dans la matrice des conglomérats, ainsi que par des minéralisations à or, pyrite ou thucholite (composé de matière organique enrichie en U et Th) dans des fractures ou sous forme de veines (Houston and Karlstrom, 1979 ; Barnicoat *et al.*, 1997 ; Mock and Ohmoto, 1997 ; Parnell, 1999). Les datations isotopiques U-Pb sur les uraninites du Witwatersrand ont aussi donné un deuxième groupe d'âges autour de  $2040 \pm 100$  Ma et la matière carbonées associée donne des âges autour de 2760 Ma pour le Groupe de Dominion à la base du bassin et entre 2540 et 2000 Ma dans le Super-Groupe du Witwatersrand (Rundle and Snelling, 1977), des âges plus jeunes que l'âge des roches sédimentaires hôtes de la minéralisation. Finalement, la théorie de paléo-placer remanié (initialement proposée par Holmes, 1957 et Robertson, 1976) est maintenant acceptée par la majorité et permet d'expliquer cette ambiguïté. Le modèle propose en effet que le gisement d'origine détritique ait été modifié par la circulation de fluides lors de la diagenèse et d'autres événements tectoniques ou thermiques post-sédimentaires (Frimmel and Minter, 2002).

Bien qu'un consensus se soit établi sur l'origine mixte des minéralisations, la provenance des uraninites détritiques des paléo-placers reste toujours une énigme. En effet, la nécessité d'avoir une source en métal pré-enrichie par rapport aux valeurs du Clarke (3-4 ppm U) dans un environnement assez proche des grands bassins détritiques où reposent ces gisements (Cuney, 2009) est contrariée par le fait que toutes les roches archéennes étudiées jusqu'à présent au pourtour de ces bassins sont de type TTG et donc pauvres en uranium. Les granitoïdes capables de cristalliser des uraninites sont de nature généralement très fractionnée tels que les granites

peralumineux, peralcalins ou encore métalumineux, calco-alcalins et fortement potassiques dont la teneur en uranium dépasse de 3 à 5 fois celle du Clarke (Cuney, 2009). Quelques rares études ont portées sur la reconnaissance de ces sources. Pour le bassin du Witwatersrand, l'étude des critères sédimentologiques et les mesures des paléo-courants ont permis de donner une première idée de la provenance des sédiments, depuis les dômes granitiques au nord, nord-ouest et sud-ouest (Els, 1998 ; Frimmel and Minter, 2002). Les études géochronologiques par la méthode isotopique U-Pb sur les grains détritiques de zircon, de xénotime, de pyrite ou d'uraninite dans les conglomérats ont permis de restreindre l'âge minimal des roches parentes entre 2,9 et 3,1 Ga pour les sédiments du Super-Groupe de Witwatersrand et ~ 3,0 Ga pour le Groupe de Dominion formant le conglomérat à la base du bassin (Burger *et al.*, 1962 ; Rundle and Snelling, 1977 ; Barton *et al.*, 1989 ; Robb *et al.*, 1990a ; Armstrong *et al.*, 1991 ; Robb *et al.*, 1992 ; Poujol *et al.*, 1999 ; Kositcin *et al.*, 2001 ; Kositcin and Krapez, 2004). Quelques rares granites âgés de 2,8 Ga situés autour du bassin du Witwatersrand présentent des enrichissements en uranium et en thorium, voir quelques rares cristaux d'uraninite disséminés dans les zones vestiges d'un paléo-régolithe (Drennan, 1988 ; Robb *et al.*, 1990b). Enfin, les caractéristiques des minéraux et des inclusions fluides des conglomérats à galets de quartz de la formation de Matinenda à Elliot Lake semblent indiquer une source de type granitique potassique ou pegmatitique de type alaskite similaire à la pegmatite de Rössing en Namibie (Robinson and Spooner, 1982). Cependant, toutes ces études restent assez succinctes quant à définir la nature des granitoïdes et l'origine des minéralisations. L'âge des granites enrichis autour du Witwatersrand reste plus jeune que les âges U/Pb des minéraux détritiques des paléo-placers. Les granitoïdes très évolués tels que les granites potassiques ou peralumineux n'apparaîtraient qu'à la fin de l'Archéen avec la différenciation progressive de la croûte continentale par fractionnement successif lors de la fusion partielle de matériaux pré-existant, ou encore par l'apport de matériaux enrichies dans les zones de subduction « évoluées » avec le métasomatisme du manteau (c.f. partie 3). La provenance, la nature des roches sources et le mode de formation des minéralisations uranifères à l'Archéen restent donc encore les sujets de nombreuses spéculations.

## **6. CONCLUSION : PROBLEMATIQUE ET APPROCHE DE CETTE ETUDE**

Les changements importants de l'environnement terrestre superficiel – géodynamique du globe, formation de la croûte continentale, genèse des granitoïdes, érosion par l'hydrosphère, sédimentation sous une atmosphère réductrice et enfin apparition de la vie et enrichissement progressif en oxygène de l'atmosphère – ont fait de l'Archéen une période importante pour la métallogénie de l'uranium. C'est en effet à l'Archéen que la croûte continentale s'est enrichie en

uranium et a formé d'assez grands volumes de roches pour permettre la formation des premières concentrations détritiques préservés dans un milieu réducteur. Ensuite, la période de transition entre l'Archéen et le Paléoprotérozoïque a influencé le fractionnement de l'uranium par l'oxydation et la mobilisation des premières concentrations.

Tous les gisements uranifères protérozoïques majeurs tels que les gisements de type discordance du Bassin d'Athabasca (Saskatchewan, Canada) trouvent leur source dans les roches du socle archéen pré-enrichies en uranium (Cuney, 2009). Cependant, le contexte géologique, la nature de la roche hôte ou encore les mécanismes physiques et chimiques qui ont amenés à la formation de ces concentrations secondaires en uranium peuvent être totalement distincts d'un gisement à l'autre. On peut donc supposer que la nature de la roche source archéenne joue un rôle essentiel dans leur formation et qu'il est aussi important de caractériser ces sources que de suivre le cheminement complexe de l'uranium jusqu'à son piège afin d'établir un modèle métallogénique complet.

Les roches archéennes et les premières concentrations en uranium sur Terre sont encore bien mal connues et restent encore très peu étudiées en comparaison des roches et des gisements protérozoïques et phanérozoïques. Afin de combler ces lacunes, deux aspects seront étudiés dans ce travail : premièrement, caractériser la nature minéralogique et chimique des roches magmatiques archéennes enrichies en uranium afin de déterminer le contexte géologique dans lequel elles se sont mises en place, l'époque et le domaine les plus propices à leur formation, d'identifier les minéraux porteurs de l'uranium et les processus permettant sa mobilisation et son enrichissement ; deuxièmement, caractériser la signature chimique des roches sédimentaires des gisements de type paléo-placer, des minéralisations en uranium et du cortège de minéraux lourds qui l'accompagne afin de retrouver la ou les sources archéennes dont ils proviennent par une étude comparative avec les roches magmatiques étudiées.

Le premier aspect de la recherche est déjà guidé par les résultats de travaux antérieurs (Roscoe, 1969 ; Rye and Roy, 1978 ; Stuckless, 1978 ; Houston and Karlstrom, 1979) qui définissent les roches felsiques du Méso- et Néoarchéen comme les plus propices à un enrichissement en uranium, alors que cet élément est quasi absent des roches volcaniques basiques à ultrabasiques des ceintures de roches vertes préférentiellement associées aux concentrations d'or et de pyrite détritiques des paléo-placers. Nos recherches seront donc portées essentiellement sur les granitoïdes archéens et plus particulièrement sur les séries les plus différenciées (granites calco-alcalins, potassiques ou encore peralumineux). Le chapitre suivant portera donc sur la caractérisation minéralogique et géochimique des roches sources potentielles et des minéraux uranifères qui les constituent. Cette recherche amènera à déterminer quels sont les domaines archéens les plus favorables à la formation de concentrations en uranium.

## RÉFÉRENCES BIBLIOGRAPHIQUES DE L'INTRODUCTION GÉNÉRALE ET DU CHAPITRE 1

- Armstrong, R. A., Compston, W., Retief, E. A., William, L. S. and Welke, H. J., 1991, Zircon ion microprobe studies bearing on the age and evolution of the Witwatersrand triad, *Precambrian Research* 53, p. 243-266.
- Aspler, L. B. and Chiarenzelli, J. R., 1998, Two Neoproterozoic supercontinents? Evidence from the Paleoproterozoic, *Sedimentary Geology* 120, p. 75-104.
- Balakrishnan, S. and Rajamani, V., 1987, Geochemistry and petrogenesis of granitoids around Kolar schist belt: constraints for crustal evolution in Kolar area, *K. Geol.* 95, p. 219-240.
- Baldwin, R. B., 1974, Was there a "terminal lunar cataclysm" 3.9-4.0 x 10<sup>9</sup> years ago? *Icarus*, 23, p. 157-166.
- Barley, M.E., Bekker, A. and Krapez, B., 2005, Late Archean to Early Paleoproterozoic global tectonics, environmental change and the rise of atmospheric oxygen, *Earth and Planetary Science Letters* 238, p. 156--171.
- Barnicoat, A.C., Henderson, I. H. C., Kniper, R. J., Yardley, B. W. D., Napler, R. W., Fox, N. P. C., Kenyon, A. K., Muntingh, D. J., Strydom, D., Winkler, K. S., Lawrence, S. R. and Cornford, C., 1997, Hydrothermal gold mineralization in the Witwatersrand Basin, *Nature* 386, p. 820-824.
- Barton, J. M., Doig, R., Smith, C. B., Bohlender, F. and van Reenen, D. D., 1992, Isotopic and REE characteristics of the intrusive charnoenderbite and enderbite geographically associated with the Matok Pluton, Limpopo Belt, southern Africa, *Precambrian Research* 55 (1-4), p. 451-467.
- Barton, E.S., Compston, W., Williams, I.S., Bristow, J.W., Hallbauer, D.K. and Smith, C.B., 1989, Provenance ages for the gold-bearing Witwatersrand Supergroup: constraints from ion-microprobe U-Pb ages of detrital grains, *Econ. Geol.* 84, p. 2012-2019.
- Bekker, A., Holland, H. D., Wang, P. L., Rumble, D., Stein, H. J., Hannah, J. L., Coetzee, L. L. and Beukes, N. J., 2004, Dating the rise of atmospheric oxygen, *Nature* 427, p. 117-120.
- Brocks, J. J., Buick, R., Summons, R. E. and Logana, G. A., 2003, Reconstruction of Archean biological diversity based on molecular fossils from the 2.78 to 2.45 billion-year-old Mount Bruce Supergroup, Hamersley Basin, Western Australia, *Geochimica et Cosmochimica Acta*, Vol. 67, No. 22, p. 4321-4335.
- Brown, G.C., 1985, Processes and problems in the continental lithosphere: geological history and physical implications, In: Snelling, N. (ed.), *Geochronology and Geological Record*, Special Publication – Geological Society of London 10, p. 326-334.
- Burger, A. J., Nicolaysen, L. O. and de Villiers J. W. L., 1962, Lead isotopic compositions of galenas from the Witwatersrand and Orange free State, and their relation to the Witwatersrand and Dominion Reef uraninites, *Geochimica et Cosmochimica Acta* Vol. 26, Issue 1, p. 25-50.
- Byerly, G. R., Lowe, D. R., Wooden, J. L. and Xie, X., 2002, An Archean impact layer from the Pilbara and Kaapvaal Cratons, *Nature* 297, p. 1325-1327.
- Calvert, A. J., Sawyer, E. W., Davis, W. J. and Ludden, J. N., 1995, Archean subduction inferred from seismic images of a mantle suture in the Superior Province, *Nature* 375, p. 670-674.

- Campbell, I. H., 2003, Constraints on continental growth models from Nb/U ratios in the 3,5 Ga Barberton and other Archaean basalt komatiite suites, *Am. J. Sci.* 303, p. 319-351.
- Catling, D. C. and Claire, M. W., 2005, How Earth's atmosphere evolved to an oxic state: A status report, *Earth and Planetary Science Letters* 237, p. 1-20.
- Catling, D. C., Zahnle, K. J., McKay, C. P., 2001, Biogenic methane, hydrogen escape, and the irreversible oxidation of early life, *Science* 293, p. 839-843.
- Clemens, J. D., Yearron, L. M. and Stevens, G., 2006, Barberton (South Africa) TTG magmas: Geochemical and experimental constraints on source-rock petrology, pressure of formation and tectonic setting, *Precambrian Research* 151, p. 53-78.
- Cloud, P. E., Jr., 1972, A working model of the primitive Earth, *American Journal of Science*, Vol. 272, p. 537-548.
- Condie, K. C., 2006, Evolving plate tectonic regimes on planet earth, 2006 Philadelphia Annual Meeting (22-25 October) Philadelphia, Pennsylvania, Paper no. 82-1 (Abstract).
- Condie, K. C., 2005, TTGs and adakites: are they both slab melts?, *Lithos* 80, p. 33-44.
- Condie, K. C., 2004, Supercontinents and superplume events: distinguishing signals in the geologic record, *Physics of the Earth and Planetary Interiors* 146, p. 319-332.
- Condie, K. C., 2001, *Mantle Plumes and Their Record in Earth History*, Cambridge, New York, 320 p.
- Condie, K. C., 2000, Episodic continental growth models: afterthoughts and extensions, *Tectonophysics* 322, p. 153-162.
- Condie, K. C., 1995, Episodic ages of greenstones: A key to mantle dynamics?, *Geophys. Res. Lett.* 22, p. 2215-2218.
- Cuney, M., 2009, The extreme diversity of uranium deposits, *Mineralium Deposita* 44, p. 3-9.
- de Wit, M. J., 1998, On Archean granites, greenstones, cratons and tectonics: does the evidence demand a verdict?, *Precambrian Research* 91, p. 181-226.
- Drennan, G. R., 1988, The Nature of the Archean Basement in the Hinterland to the Welkom Goldfield, M. Sc. Thesis of the Witwatersrand University (Johannesburg), 187 p.
- Drummond, M. S. and Defant, M. J., 1990, A model for trondjemite-tonalite-dacite genesis and crustal growth via slab melting: Archean to modern comparisons, *Journal of Geophysical Research* 95, p. 21503-21521.
- Els, B. G., 1998, The question of alluvial fans in auriferous Archaean and Proterozoic successions of South Africa, *South African Journal of Geology* 101, p. 17-25.
- Ernst, R. E., and Buchan, K. L., 2003, Recognizing mantle plumes in the geological record, *Annu. Rev. Earth Planet. Sci.* 31, p. 469-523.
- Farquhar, J. and Wing, B. A., 2003, Multiple sulfur isotopes and the evolution of the atmosphere, *Earth and Planetary Science Letters* 213, p. 1-13.
- Frimmel, H. E., 2005, Archaean atmospheric evolution: evidence from the Witwatersrand gold fields, South Africa, *Earth-Science Reviews* 70, p. 1-46.
- Frimmel, H. E. and Gartz, V. H., 1997, Witwatersrand gold particle chemistry matches model of metamorphosed, hydrothermally altered placer deposits, *Mineralium Deposita* 32, p. 523-530.
- Frimmel, H. E. and Minter, W. E. L., 2002, Recent Developments Concerning the Geological History and Genesis of the Witwatersrand Gold Deposits, South Africa, *Society of Economic Geologists, Special Publication* 9, p. 17-45.

- Frost, C. D., Frost, B. R., Chamberlain, K. R. and Hulsebosch, T. P., 1998, The late Archaean history of the Wyoming Province as recorded by granitic magmatism in the Wind River Range, Wyoming, *Precambrian Research* 89, p. 145-173.
- Goodwin, A. M., 1973, Plate tectonics and evolution of Precambrian crust, In: Tarling and Runcorn (eds.), *Implications of continental drift to the earth sciences*, London, Academic Press, vol. 2, p. 1047-1069.
- Gorman, B. E., Pearce, T. H. and Birkett, T. C., 1978, On the structure of Archaean greenstone belts, *Precambrian Research* 6, p. 23-41.
- Harrison, T. M., McCulloch, M. T., Blichert-Toft, J., Albarede, F., Holden, P. and Mojzsis, S. J., 2006, Further Hf isotope evidence for Hadean continental crust *Geochimica et Cosmochimica Acta*, Vol. 70, Issue 18, Supplement 1, August-September, p. A234.
- Holland, H. D., 2006, The oxygenation of the atmosphere and oceans, *Philosophical Transactions of the Royal Society B*, 361, p. 903-915.
- Holland, H. D., 1999, When did the Earth's atmosphere become oxic? A Reply, *Newsletter of The Geochemical Society*, 100, p. 20-22.
- Holland, H. D., 1994, Early Proterozoic atmospheric change, In: Bengtson, E. (Ed.), *Early Life on Earth*, Nobel Symposium No. 84, Columbia University Press, New York, p. 237-244.
- Holland, H. D., 1984, *The Chemical Evolution of the Atmosphere and Oceans*, Princeton, NJ, Princeton Univ. Press., 582 p.
- Holmes, S. W., 1957, Pronto Mine, In: *Structural geology of Canadian ore deposits*, Canadian Institute of Mining and Metallurgy, Special vol. 2, p. 324-339.
- Houston, R. S. and Karlstrom, K. E., 1979, Precambrian uranium-bearing quartz-pebble conglomerates: Exploration Model and United States Resource Potential, University of Wyoming Laramie, USA, prepared for the U.S. Department of Energy, 510 p.
- Jahn, B. M., Auvray, B., Shen, Q. H., Liu, D. Y., Zhang, Z. Q., Dong, Y. J., Ye, X. J., Zhang, Q. Z., Cornichet, J. and Macé, J., 1988, Archean crustal evolution in China: the Taishan complex, an evidence for juvenile crustal addition from long-term depleted mantle, *Precambrian Research* 38, p. 381-403.
- Jahn, B. M., Vidal, P., Kröner, A., 1984, Multichronometric ages and origin of Archaean tonalitic gneisses in Finnish Lapland: a case for long crustal residence time, *Contrib. Mineral. Petrol.* 86, p. 398-408.
- Jayananda, M., Martin, H., Peucat, J. J. and Mahabaleswar, B., 1995, Late Archean crust-mantle interactions in the Closepet granite, Southern India: evidence from Sr-Nd isotopes, major and trace element geochemistry, *Contrib. Mineral. Petrol.* 119, p. 314-329.
- Kamber, B. S. and Collerson, K. D., 2000, The Role of Slab Melting in Continental Crustal Growth: Trace Element Constraints from Archean TTG Gneiss Complexes and Models of Oceanic Crust Production, *Eos Trans. AGU*, 81 (48), Fall Meet. Suppl., MN: Fall Meeting 2000.
- Kasting, J. F., 2001, Earth history: the rise of atmospheric oxygen, *Science* 293, p. 819-820.
- Kasting, J. F., 1993, Earth's early atmosphere, *Science* 259, p. 920-926.
- Kasting, J. F., 1987, Theoretical constraints on oxygen and carbon dioxide concentrations in the Precambrian atmosphere, *Precambrian Research* 34, p. 205-229.

- Kimberley, M. M. and Grandstaff, D. E., 1986, Profiles of elemental concentrations in Precambrian paleosols on basaltic and granitic parent materials, *Precambrian Research* 32, p. 133-154.
- Kirk, J., Ruiz, J., Chesley, J., Walshe, J. and England, G., 2002, A major Archean gold and crust-forming event in the Kaapvaal Craton, South Africa, *Science* 297, p. 1856-1858.
- Klein, C., 2005, Some Precambrian banded iron-formations (BIFs) from around the world: Their age, geologic setting, mineralogy, metamorphism, geochemistry, and origins; *American Mineralogist*, Vol. 90, No. 10, p. 1473-1499.
- Komiya, T., Maruyama, S., Masuda, T., Nohda, S. and Okamoto, K., 1999, Plate tectonics at 3,8-3,7 Ga, Field evidence from the Isua accretionary complex, West Greenland, *Journal of Geology* 107, p. 515-554.
- Korenaga, J., 2006, Archean Geodynamics and the Thermal Evolution of Earth, In: *Archean Geodynamics and Environments*, Geophysical Monograph Series 164, the American Geophysical Union, p. 7-31.
- Kositcin, N. and Krapez, K., 2004, Relationship between detrital zircon age-spectra and the tectonic evolution of the Late Archaean Witwatersrand Basin, South Africa, *Precambrian Research* 129, p. 141-168.
- Kositcin, N., England, G. L., Rasmussen, B., Fletcher, I. R., McNaughton, N. J., Krapez, B., Groves, D. I. and Griffin, B. J., 2001, Xenotime/Zircon geochronology in the Archaean Witwatersrand Basin, *AGSO - Geosciences Australia* 2001, p 244-246.
- Krogstad, E. J., Hanson, G. N. and Rajamani, V., 1995, Sources of continental magmatism adjacent to late Archean Kolar suture zone, South India: distinct isotopic and elemental signatures of two late Archean magmatic series, *Contrib. Mineral. Petrol.* 122, p. 159-173.
- Lasaga, A. C. and Ohmoto, H., 2002, The oxygen geochemical cycle: dynamics and stability, *Geochimica et Cosmochimica Acta* 66, p. 361-381.
- Martin, H., 2005, Genesis and Evolution of the Primitive Earth Continental Crust, In: M. Gargaud et al. (Ed.), *Lectures in Astrobiology*, Springer-Verlag Berlin Heidelberg, Vol. I, p. 113-163.
- Martin, H., 1999, Adakitic magmas: modern analogues of Archean Granitoids, *Lithos* 46, p. 411-429.
- Martin, H., 1994, The Archean grey gneisses and the genesis of the continental crust, In: Condie, K.C. (Ed.), *The Archean Crustal Evolution*, *Developments in Precambrian Geology*, Elsevier, Amsterdam, p. 205-259.
- Martin, H., 1986, Effect of steeper Archean geothermal gradient on geochemistry of subduction-zone magmas. *Geology* 14, p. 753-756.
- Martin, H. and Moyen, J. F., 2005, The Archaean-Proterozoic transition: Sanukitoid and Closepet type magmatism, *Polskie Towarzystwo Mineralogiczne – Prace Specjalne Mineralogical Society of Poland – Special Papers*, Vol. 26, p. 57-68.
- Martin, H. and Moyen, J. F., 2002, Secular changes in TTG composition as markers of the progressive cooling of the Earth, *Geology* 30 (4), p. 319-322.
- Martin, H., Smithies, R. H., Rapp, R., Moyen, J. F. and Champion, D., 2005, An overview of adakite, tonalite-trondhjemite-granodiorite (TTG), and sanukitoid: relationships and some implications for crustal evolution, *Lithos* 79, p. 1-24.
- Maynard, J. B., 1992, Chemistry of modern soils as a guide to interpreting Precambrian paleosols, *J. Geol.* 100, p. 279-289.

- Maynard, J. B., Ritger, S. D. and Sutton, S. J., 1991, Chemistry of sands from the modern Indus River and the Archean Witwatersrand basin: Implications for the composition of the Archean atmosphere, *Geology* 19, p. 265-268.
- Melezhik, V. A., Fallick, A. E., Rychanchik, D. V. and Kuznetsov, A. B., 2005, Palaeoproterozoic evaporites in Fennoscandia: implications for seawater sulphate, the rise of atmospheric oxygen and local amplification of the  $\delta^{13}\text{C}$  excursion, *Terra Nova* 17, p. 141-148.
- Minter, W. E. L., 2002, Witwatersrand paleoplacer mineralogy as an indicator of the Archean atmosphere, Presented at GSA 2002 Annu. Meet., Denver.
- Minter, W. E. L., 1999, Irrefutable Detrital Origin of Witwatersrand Gold and Evidence of Eolian Signatures, *Economic Geology*, vol. 94, no. 5, p. 665-670.
- Mock, R. L. and Ohmoto, H., 1997, Nondetrital origins of uranium-bearing minerals and pyrites in Early Proterozoic quartz-pebble conglomerates of the Elliot Lake district, Ontario, Seventh Annual V. M. Goldschmidt Conference, Abstract 2273.
- Mojzsis, S. J., Arrhenius, G., McKeegan, K. D., Harrison, T. M., Nutman, A.P., Friend, C. R. L., 1996, Evidence for life on Earth before 3800 million years ago, *Nature* 384, p. 55-59.
- Moorbath, S., 2005, Oldest rocks, earliest life, heaviest impacts, and the Hadean-Archaean transition, *Applied Geochemistry*, Vol. 20, Issue 5, p. 819-824.
- Moyen, J. F., Martin, H. and Jayananda, M., 2001, Multi-element geochemical modelling of the crust-mantle interactions during late-Archean crustal growth: the Closepet granite (South India), *Precambrian Research* 112, p. 87-105.
- Moyen, J. F., Martin, H., Jayananda, M. and Auvray, B., 2003a, Late Archean granites: a typology based on the Dharwar Craton (India), *Precambrian Research* 127 (1-3), p. 103-123.
- Moyen, J. F., Nedelec, A., Martin, H. and Jayananda, M., 2003b, Syntectonic granite emplacement at different structural levels: the Closepet granite, South India, *J. Struct. Geol.* 25 (4), p. 611-631.
- Murakami, T., Utsunomiya, S., Imazu, Y. and Prasad, N., 2001, Direct evidence of late Archean to early Proterozoic anoxic atmosphere from a product of 2,5 Ga old weathering, *Earth and Planetary Science Letters* 184, p. 523-528.
- Nisbet, E. G., 1987, *The Young Earth: An introduction to Archaean geology*, Allen & Unwin, Boston and London, 402 p.
- Nutman, A. P., Mojzsis, S. J. and Friend, C. R. L., 1997, Recognition of >3850 Ma water-lain sediments in West Greenland and their significance for the early Archaean Earth, *Geochimica et Cosmochimica Acta*, Vol. 61, no. 12, p. 2475-2484.
- Nutman, A. P., McGregor, V. R., Friend, C. R. L., Bennett, V. C. and Kinny, P. D., 1996, The Itsaq Gneiss Complex of southern West Greenland; the world's most extensive record of early crustal evolution (3900-3600 Ma), *Precambrian Research* 78, p. 1-39.
- Ohmoto, H., 2004, The Archean atmosphere, hydrosphere and biosphere; In: Eriksson, P. G., Altermann, W., Nelson, D.R., Mueller, W. U., Catuneanu, O. (Eds.), *The Precambrian Earth: Tempos and Events, Developments in Precambrian Geology*, Vol. 12, Elsevier, Amsterdam, p. 361-388.
- Ohmoto, H., 2003, Gast Lecture Chemical and biological evolution of the early Earth: A minority report, *Goldschmidt 2003*, A2 (Abstract).
- Ohmoto, H., 1996, Evidence in pre-2.2 Ga Paleosols for the early evolution of atmospheric oxygen and terrestrial biota, *Geology*, Vol. 24, No. 12, p. 1135-1138.

- Ohmoto, H., Beukes, N. J., Gutzmer, J. and Nedachi, M., 1999, The formation of laterites approximately 2.3 billion years ago, *Abst. With Programs, Geol. Soc. Amer.* 31, p. 225-226.
- Ono, S., 2001, Detrital uraninite and the early earth's atmosphere: SIMS analyses of uraninite in the Elliot Lake district and the dissolution kinetics of natural uraninite, Ph.D. Thesis, The Pennsylvania State University, 195 p.
- Parnell, J., 1999, Petrographic evidence for emplacement of carbon into Witwatersrand conglomerates under high fluid pressure, *Journal of Sedimentary Research* Vol. 69, No. 4, p. 164-170.
- Pavlov, A. A., Ono, S., Rumble III, D., Kasting, J. F. and Toon, O. B., 2003, S<sub>8</sub> aerosols in the Archean atmosphere, *Goldschmidt Conference*, A377 (Abstract).
- Pavlov, A. A., Brown, L. L. and Kasting, J. F., 2001, UV shielding of NH<sub>3</sub> and O<sub>2</sub> by organic hazes in Archean atmosphere, *Journal of Geophysical Research* 106, p. 23267-23287.
- Pesonen, L. J., Elming, S. A., Mertanen, S., Pisarevsky, S., D'Agrella-Filho, M. S., Meert, J. G., Schmidt, P. W., Abrahamsen, N. and Bylund, G., 2003, Palaeomagnetic configuration of continents during the Proterozoic, *Tectonophysics* 375, p. 289-324.
- Phillips, G. N., Law, J. D. M. and Myers, R. W., 2001, Is the redox state of the Archean atmosphere constrained? *Soc. Econ. Geol. Newsletter* 47 (1), p. 9-18.
- Pigois, J. P., Groves, D. I., Fletcher, I. R., McNaughton, N. J., Snee, L. W., 2003, Age constraints on Tarkwaian palaeoplacer and lode-gold formation in the Tarkwa-Damang district, SW Ghana, *Mineralium Deposita*, Vol. 38, No. 6, p. 695-714.
- Piper, J. D. A., 1976, Paleomagnetic evidence for a Proterozoic supercontinent, *Philosophical Society of South Africa*, Vol. 1, p. 63-108.
- Pollack, H. N., 1997, Thermal characteristics of the Archaean, In: de Wit, M. J., and Ashwal, M. D. (Eds.), *Greenstone belts*: Oxford, UK, Clarendon Press, p. 223-232.
- Polat, A. and Kerrich, R., 2000, Archean greenstone belt magmatism and the continental growth-mantle evolution connection: constraints from Th-U-Nb-LREE systematics of the 2.7 Ga Wawa subprovince, Superior Province, Canada; *Earth and Planetary Science Letters* 175, p. 41-54.
- Poujol, M., Robb, L. J. and Respaut, J. P., 1999, U-Pb and Pb-Pb isotopic studies relating to the origin of gold mineralization in the Evander Goldfield, Witwatersrand Basin, South Africa, *Precambrian Research* 95, p. 167-185.
- Pretorius, D. A., 1981, Gold and Uranium in Quartz-Pebble Conglomerates, *Economic Geology*, 75<sup>th</sup> Anniversary Volume, p. 117-138.
- Querré, G., 1985, Paragenèse de la croûte continentale à l'Archéen : les granitoïdes tardifs (2,5-2,4 Ga) de Finlande orientale ; pétrologie et géochimie, *Mém. Docum. Centre Arm. Et Struct. Socles*, Université de Rennes, Rennes, 226 p.
- Rasmussen, B., 2000, Filamentous microfossils in a 3235-million-year-old volcanogenic massive sulphide deposit, *Nature* 405, p. 676-679.
- Rasmussen, B. and Buick, R., 1999, Redox state of the Archean atmosphere: evidence from detrital heavy minerals in ca. 3250-2750 Ma sandstones from the Pilbara Craton, Australia, *Geology* 27, p. 115-118.
- Robertson, J. A., 1976, The Blind River uranium deposits: the ores and their setting, Ontario Division of Mines, MP65, 45 p.

- Robinson, A. and Spooner, E. T. C., 1982, Source of the detrital components of uraniferous conglomerates, Quirke ore zone, Elliot Lake, Ontario, Canada, *Nature* 299, p. 622-624.
- Robb, L. J., Davis, D. W., Kamo, S. L. and Meyer, F. M., 1992, Ages of altered granites adjoining the Witwatersrand Basin with implications for the origin of gold and uranium, *Nature* 357, p. 677-680.
- Robb, L. J., Davis, D. W. and Kamo, S. L., 1990a, U-Pb ages on single zircon grains from the Witwatersrand Basin, South Africa: constraints on the age of sedimentation and the evolution of granites adjacent to the basin, *J. Geol.* 98, p. 311-328.
- Robb, L. J., Meyer, F. M., Ferraz, M.F. and Drennan, G.R., 1990b, The distribution of radioelements in Archaean granites of the Kaapvaal Craton, with implications for the source of uranium in the Witwatersrand basin, *South African Journal of Geology* 93, p. 5-40.
- Roscoe, S. M., 1973, The Huronian Supergroup, a Paleoproterozoic succession showing evidence of atmospheric evolution, In: Young, G. M. (Ed.), *Huronian stratigraphy and sedimentation*, The Geological Association of Canada, Special Paper 12, p. 31-48.
- Roscoe, S. M., 1969, Huronian rocks and uraniferous conglomerates in the Canadian Shield, *Geol. Surv. Can.*, Pap. 68-40, 205 p.
- Rundle, C. C. and Snelling, N. J., 1977, The geochronology of uraniferous minerals in the Witwatersrand Triad: an interpretation of new and existing U-Pb data on rocks and minerals from the Dominion Reef, Witwatersrand and Ventersdorp Supergroups, *Philosophical Transactions of the Royal Society of South Africa*, 286, p. 567-583.
- Rye, R. and Holland, H. D., 2000, Life associated with a 2.76 Ga ephemeral pond? Evidence from Mount Roe #2 paleosol, *Geology* 28, p. 483-486.
- Rye, R. and Holland, H. D., 1998, Paleosols and the evolution of atmospheric oxygen: a critical Review, *Am. J. Sci.* 298 (8), p. 621-672.
- Rye, D. M. and Roy, R. F., 1978, The distribution of thorium, uranium, and potassium in Archean granites from northeastern Minnesota, *American Journal of Science*, Vol. 278, p. 354-378.
- Sarbas, B., 2008, The GEOROC database as part of a growing geoinformatics network, in: Brady, S.R., Sinha, A.K., and Gundersen, L.C. (editors): *Geoinformatics 2008—Data to Knowledge*, Proceedings: U.S. Geological Survey Scientific Investigations Report 2008-5172, p. 42-43.
- Shirey, S. B. and Hanson, G. N., 1986, Mantle heterogeneity and crustal recycling in Archean granite-greenstone belts: evidence from Nd isotopes and trace elements in the Rainy Lake province, Ontario, Canada, *Geochimica et Cosmochimica Acta* 50, p. 2631-2651.
- Shirey, S. B. and Hanson, G. N., 1984, Mantle derived Archean monzodiorites and trachyandesites, *Nature* 310, p. 222-224.
- Sleep, N. H., Zahnle, K. J., Kasting, J. F. and Marowitz, H. J., 1989, Annihilation of ecosystems by large asteroid impacts on the early Earth, *Nature* 342, p. 139-142.
- Smith, N. D. and Minter, W. E. L., 1980, Sedimentological controls of gold and uranium in two Witwatersrand paleoplacers, *Economic Geology*, vol. 75, no. 1, p. 1-14.
- Smithies, R. H., 2000, The Archaean tonalite-trondhjemite-granodiorite (TTG) series is not an analogue of Cenozoic adakite, *Earth and Planetary Science Letters* 182, p. 115-125.
- Smithies, R. H. and Champion, D. C., 1999, High-Mg diorite from the Archaean Pilbara Craton: anorogenic magmas derived from a subduction-modified mantle, *Geol. Surv. West. Aust. Annu. Rev.* 1998-1999, p. 45-59.

- Stanistreet, I. G., 1993, Ancient and modern examples of tectonic escape basins: the Archaean Witwatersrand Basin compared with the Cenozoic Maracaibo Basin, In: Frostick, L. E., Steel, R. J. (Eds.), *Tectonic Controls and Signatures in Sedimentary Successions*. Int. Assoc. Sedimentol. Spec. Publ. 20, p. 363-376.
- Stern, R. A. and Hanson, G. N., 1991, Archean high-Mg granodiorite: a derivative of light rare earth enriched monzodiorite of mantle origin, *J. Petrol.* 32, p. 201-238.
- Stevenson, R., Henry, P. and Gariépy, C., 1999, Assimilation-fractional crystallization origin of Archean sanukitoid suites: Western Superior Province, Canada, *Precambrian Research* 96, p. 83-99.
- Stuckless, J. S., 1978, U, Th, and K concentration in three Precambrian granites from Wyoming: implications for uranium geology (abst.), In: Lageson, D. R. (ed.), *Occurrences of uranium in Precambrian and younger rocks of Wyoming and adjacent areas*, Geological Survey of Wyoming, public information circular, No. 7, p. 29-30.
- Sun, S. S. and McDonough, W. F., 1989, Chemical and isotopic systematics of oceanic basalts: implications for mantle compositions and processes, In: A. D. Saunders and M. J. Norry (Eds.), *Magmatism in the ocean basins*, Geological Society, London, p. 313-345.
- Taylor, S. R. and McLennan, S. M., 1985, *The continental crust: composition and evolution*. Blackwell, Oxford, UK., 312 p.
- van Zuilen, M. A., Lepland, A., Teranes, J., Finarelli, J., Wahlen, M. and Arrhenius, G., 2003, Graphite and carbonates in the 3,8 Ga Isua Supracrustal Belt, *Precambrian Research* 126, p. 331-348.
- Wilde, S. A., Valley, J. W., Peck, W. H. and Graham, C. M., 2001, Evidence from detrital zircons for the existence of continental crust and oceans on the Earth 4.4 Ga ago, *Nature* 409, p. 175-178.
- Wyman, D. A. and Kerrich R., 2002, Formation of Archean continental lithospheric roots: The role of mantle plumes, *Geology*, Vol. 30, No. 6, p. 543-546.
- Yamaguchi, K. E., 2005, Evolution of the atmospheric oxygen in the Early Precambrian: an updated review of geological "evidence", *Frontiere Research on Earth Evolution*, Vol. 2, p. 1-9.
- Yamaguchi, K. E., Beard, B. L., Johnson, C. M., Ohkouchi, N. and Ohmoto, H., 2003, Iron isotope evidence for redox stratification of the Archean oceans, *Geochimica et Cosmochimica Acta* 67, A550.
- Yamaguchi, K. E., Naraoka, H., Watanabe, Y. and Ohmoto, H., 2002, The Early Evolution of the Archean nitrogen biochemical cycle, *Geochimica et Cosmochimica Acta* 66, A857.
- Yang, W. and Holland, H. D., 2003, The Hekpoort paleosol profile in strata 1 at Gaborone, Botswana: soil formation during the great oxidation event, *American Journal of Science*, Vol. 303, p. 187-220.
- Zegers, T. E., and van Keken, P. E., 2001, Middle Archean continent formation by crustal delamination, *Geology*, Vol. 29, No. 12, p. 1083-1086.
- Zhao, G., Cawood, P. A., Wilde, S. A. and Sun, M., 2002, Review of global 2.1-1.8 Ga orogens: implications for a pre-Rodinia supercontinent, *Earth-Science Reviews* 59, p. 125-162.

---

**CHAPITRE 2 :**  
**SOURCES MAGMATIQUES**  
**ARCHEENNES**  
**DE L'URANIUM**

---

## INTRODUCTION

L'uranium est un élément incompatible à grand rayon ionique (voisin de 1 Å) au même titre que le thorium ou les éléments des Terres Rares. Présent en très faible quantité dans les roches volcaniques basiques, de l'ordre du ppb, il passe préférentiellement dans la phase liquide lors de la fusion partielle d'une roche et s'enrichit progressivement au cours de l'évolution d'un magma. Ainsi, les roches ignées felsiques les plus « évoluées » issues de magmas peralcalins fortement fractionnés, de magmas calco-alcalins fortement potassiques ou encore de magmas peralumineux, constituent les meilleures sources pour la formation de concentrations en uranium et la cristallisation d'uraninite (Cuney and Kyser, 2008). Dans les cratons Archéens, les roches acides les plus abondantes sont les TTG (tonalite–trondhjemite–granodiorite), des granitoïdes sodiques pauvres en uranium formées par fusion partielle d'un matériel basaltique soit en contexte d'amincissement crustal, soit dans une zone de subduction (cf. chapitre précédent). Les granitoïdes plus différenciés issues de la fusion des TTG ou des roches sédimentaires des ceintures de roches vertes sont beaucoup plus enrichis mais restent toutefois minoritaires en terme de volume dans la croûte archéenne actuellement préservée. Il est cependant probable que cet enregistrement ne soit que partiel et biaisé par les phénomènes d'érosion et de recyclage progressif de la croûte par la tectonique des plaques. Ce chapitre se propose d'étudier différents types de granitoïdes enrichis en uranium de l'Archéen au Paléoproterozoïque échantillonnés dans des contextes géologiques variés afin de caractériser la nature de ces roches, leur chimie, leur minéralogie (identification des minéraux porteurs de l'uranium et autres phases accessoires associées) et enfin les processus responsables de l'enrichissement de la croûte continentale lors de cette période critique pour l'évolution terrestre.

## PARTIE 2.1

# Evolution of the magmatic rock composition from the West African Craton (Guinea) between 3.5 and 2.0 Ga: evidence of U and Th fractionation during progressive differentiation

Isabelle Duhamel<sup>1</sup>, Michel Cuney<sup>1</sup> and Denis Thiéblemont<sup>2</sup>

<sup>1</sup> *Laboratoire de Géologie et de Gestion des Ressources Minérales et Energétiques (G2R), Nancy-Université, CNRS, CREGU, Boulevard des Aiguillettes, B.P. 239, F-54506 Vandœuvre-lès-Nancy Cedex (France)*

<sup>2</sup> *BRGM, B.P. 6009, 45060 Orléans Cedex 2, France*

---

### Abstract

The West African Craton has been formed during successive magmatic events from Paleoproterozoic to Paleoproterozoic generating various igneous rock series. Their major and trace element composition revealed that the igneous rocks emplaced in a convergent margin tectonic setting and derived from the partial melting of a subducted oceanic mafic crust and the Archean continental nucleus formed above.

The first TTGs at ca. 3.54-2.9 Ga are mostly metaluminous to weakly peraluminous in composition, from medium to high K affinity with low uranium concentrations (<1 ppm). Leonian granitoids formed ca. 3.05-2.95 Ga and Liberian granites ca. 2.85-2.7 Ga are metaluminous to peraluminous calc-alkaline series with up to 6 wt% K<sub>2</sub>O and can reach tens of ppm U but Th is still predominant rising from tens to a hundred ppm Th. Petrographic study and mineral chemical analysis indicate that uranium and thorium in Archean granitoids are distributed in refractory minerals, mainly monazite-(Ce) with some urano-thorianite inclusions and zircon. The last generation of granitoids is Paleoproterozoic in age and is represented by the ca. 2.1-2.0 Ga peraluminous high-K calc-alkaline granodiorites, granites and shoshonitic syenites formed by the partial melting of the Archean series. Monazite, zircon, apatite and titanite are common but in the most enriched granite (22.15 ppm U, 18.37 ppm Th and Th/U ~ 0.83) they totally disappear and uraninite crystallizes. Uranium oxides are characterized by high thorium contents (3.11-6.59 wt% ThO<sub>2</sub>) and chemical U-Th-Pb dating yields highly variable ages with a main population circa 1671 ± 95 Ma and a younger age at 680 ± 25 Ma reflecting radiogenic lead loss during subsequent alteration event.

Indeed the magmatic assemblage of both Archean and Paleoproterozoic Guinean granitoids has undergone post-magmatic alteration processes by late Ca-rich fluid circulation represented by authigenic deposition of epidote ± allanite widespread in all the plutonic rocks, by the transformation of monazite-(Ce) to a solid solution consisting mainly of huttonitic monazite and minor brabantite, by cationic substitutions within metamict zircon with REE replaced by slight enrichment in U+Th+Ca and also by the dissolution of uraninite (boxworks) replaced by carbonates, hematite and sulfides. Considering the radioelement mobility, the high-K calc-alkaline series of south-east Guinea may be considered as a potential source for subsequent uranium ore deposition.

---

### Key words

Guinea, West African Craton, Kénéma-Man Domain, Archean, Paleoproterozoic, high-K calc-alkaline granites, uranium thorium fractionation, zircon, monazite, uraninite.

## INTRODUCTION

The West Africa Craton is composed of two Archean to Paleoproterozoic continental crust blocks, the Leo Rise to the south and the Reguibat to the north (Fig. 2.1.1). Crustal blocks are separated by the Taoudeni Basin filled by clastic sediments deposited from Upper Paleoproterozoic ca. 1100-1000 Ma to Devonian ca. 300 Ma (Bronner et al., 1980). The Kénéma-Man domain studied in this work is part of the southern Leo Rise block and is located in south-east Guinea. This domain is made of various Archean igneous rocks aged from ca. 3.54 to 2.95 Ga (Thiéblemont et al., 2001) partly reworked during Paleoproterozoic ca. 2.1 Ga (Birimian or Eburnean event; Boher et al., 1992).

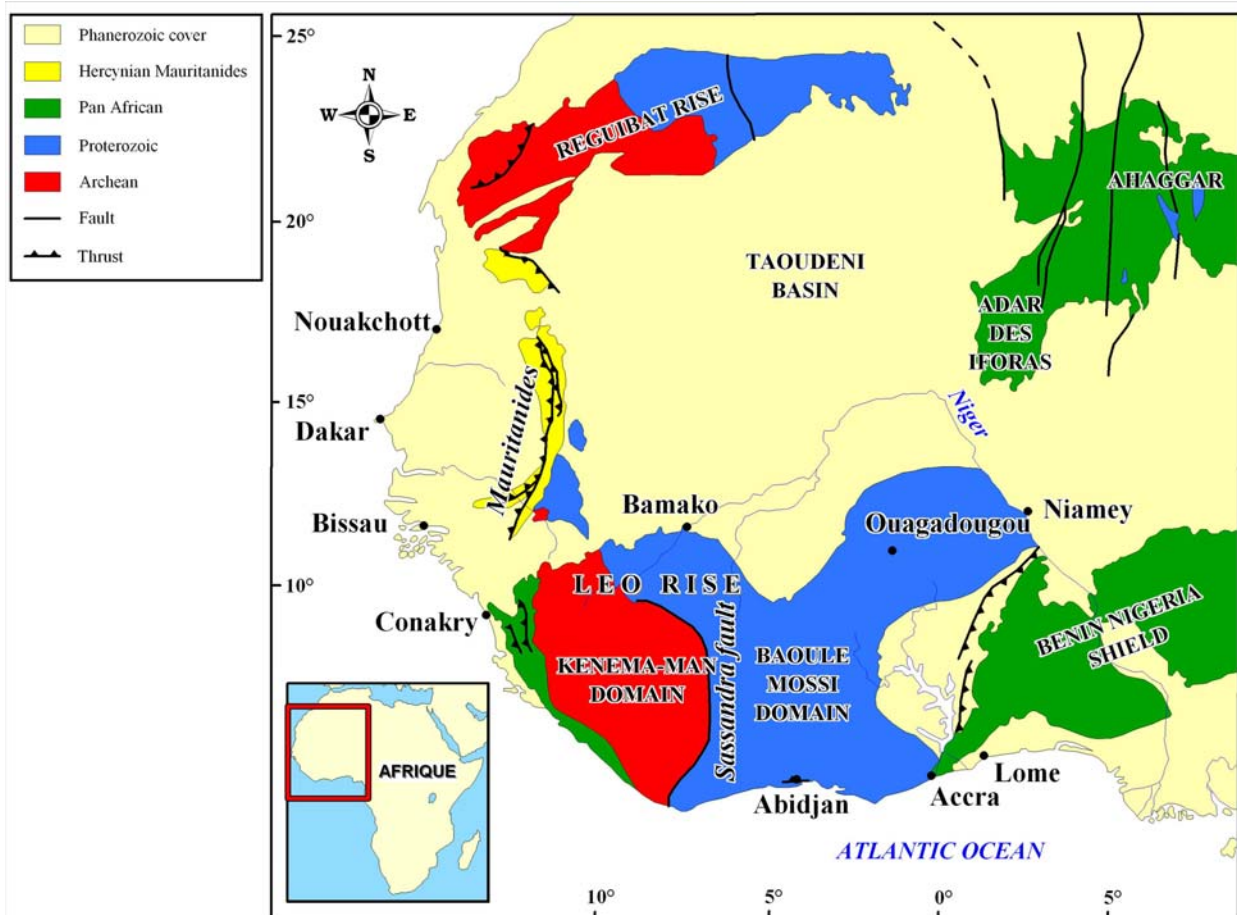


**Figure 2.1.1** Simplified geological map of the West African Craton (modified from Egal et al., 2002).

During the last decade, numerous investigations have been performed in the region combining geological mapping, geochemistry, petrology, geochronology and isotope analyses. Indeed, the Kenema-Man domain represents a continuous geological record over the Early Precambrian time, a period still poorly understood for the processes involved in the continental crust formation. Tonalites, trondhjemites and granodiorites (TTGs) represent almost 70% of the

Archean rocks presently preserved on the Earth surface and disappear progressively at the Archean-Paleoproterozoic boundary with the development of high-K granites. The geodynamic and tectonic settings of these rocks are strongly debated opposing two theories, a thickened crust with mantle plume underplating (Condie, 2000, 2001 and 2004) or a subducting ocean crust inducing devolatilization in depth of the slab and melt of the mantle wedge (Martin, 1999 and 2005). The focus of this study is in the uranium enrichment happening through the evolution of the geochemical composition of these rocks. This work presents the geochemical and mineralogical study of the different Archean to Paleoproterozoic granitoid series from the Kénéma Man domain in south-east Guinea in an attempt to better understand the fractionation of radioelements during crustal growth. The chemical criterion of granitoids is used to determine the nature of the rocks and to define the geological context of emplacement. The petrologic observations and in situ accessory mineral analyses provide the identification of the uranium and thorium bearing phases. The results will be discussed in order to explain the processes involved in the radioelement distribution and concentration in the igneous rocks.

## **GEOLOGY OF SOUTH-EAST GUINEA**

South-east Guinea geological map (Fig. 2.1.2) is covered in wide majority by magmatic rocks divided into 4 major magmatic cycles.

The first cycle comprises the Paleoarchean Guélémeta orthogneiss limited to a south-east band oriented WNW-ESE along a ridge formed by the younger Nimba banded iron formations (Birimian). The old gneisses yield isotope dating in zircon (SHRIMP) results in ages of ca.  $3535 \pm 9$  Ma and  $3542 \pm 13$  Ma and are thought to be formed during early accretion by partial melting of a basaltic protolith under eclogitic conditions (Thiéblemont et al., 2001).

The second cycle corresponds to the Leonian amphibolites, ultramafic rocks and partly migmatized gneisses of Middle Archean age distributed in a 80 km wide band oriented SSW-NNE. Isotope dating of zircon yield an age at ca.  $3050 \pm 16$  Ma (Goujou et al., 1999a-b).

The third cycle is represented by two major plutonic rock batholiths, the Macenta batholith in the northwestern part of the map and the Tounkarata batholith in south-east. These batholiths are composed of tonalites, granodiorites and granites mainly of Liberian age  $\sim 2.9$ - $2.8$  Ga (Thiéblemont et al., 2001). However, isotope dating of some zircon grains (SHRIMP) from orthogneisses included within the Macenta batholith yield an inherited age ca.  $3462 \pm 24$  Ma

with a Liberian overprint at ca.  $2868 \pm 2$  Ma (Bering et al., 1998) suggesting that granitic rocks derived from an older continental crust protolith.

The volcanic-sedimentary pile consists of metabasite, banded iron formations (BIF), quartzite and pelitic rocks which were deposited between the third and the last magmatic cycles. The NE-SW Nimba belt developed between the Guélémeta Orthogneiss of the first cycle and the Liberian Toukarata batholith, whereas the N-S Simandou sediments were deposited unconformably upon the Middle Archean migmatites and gneisses of the second cycle (Obermüller and Roques, 1946; Billa et al., 1999). Detrital zircon from quartzites give ages of ca. 2615 Ma in the Nimba belt (Billa et al., 1999) and 2711-2871 Ma in the Simandou sediments (Thiéblemont et al., 1999a-b).

The last magmatic cycle is defined by Paleoproterozoic intrusions crosscutting the Leonien rocks. The Eburnean granitoids are represented by a major batholith to the north-east mainly formed of pyroxene granodiorite emplaced at ca. 2.08-2.07 Ga (Lahondère et al., 1999a-b) and numerous younger lenses of biotite-granites and syenites interpreted as the melting products of older monzogranites and granodiorites (Thiéblemont et al., 2004). Isotope ages in the younger intrusions gave an age of ca.  $2082 \pm 7$  Ma and  $2055 \pm 13$  Ma in syenites, and ca.  $2023 \pm 57$  Ma in leucogranites (Thiéblemont et al., 1999a). The Eburnean event is responsible for high grade metamorphism leading locally to anatexis and widespread deformation in the earlier rocks with development of a general NE-SW foliation (Goujou et al., 1999a-b). A greenschist-facies retrograde metamorphism is associated with several NNE-SSW trending faults and locally folding structures that affect the different magmatic rocks, even the last emplaced syenite and granitic intrusions, attributed to a late Eburnean tectono-metamorphic event before 2040 Ma (Egal et al., 2002; Thiéblemont et al., 2004).

This part of the West African Craton was then stable during a long period. During the Jurassic tholeiitic dolerite dykes and sills were emplaced approximately 200 Ma ago and related to the opening of the Atlantic mid-oceanic ridge (Katja, 1996; Deckart et al., 1997).

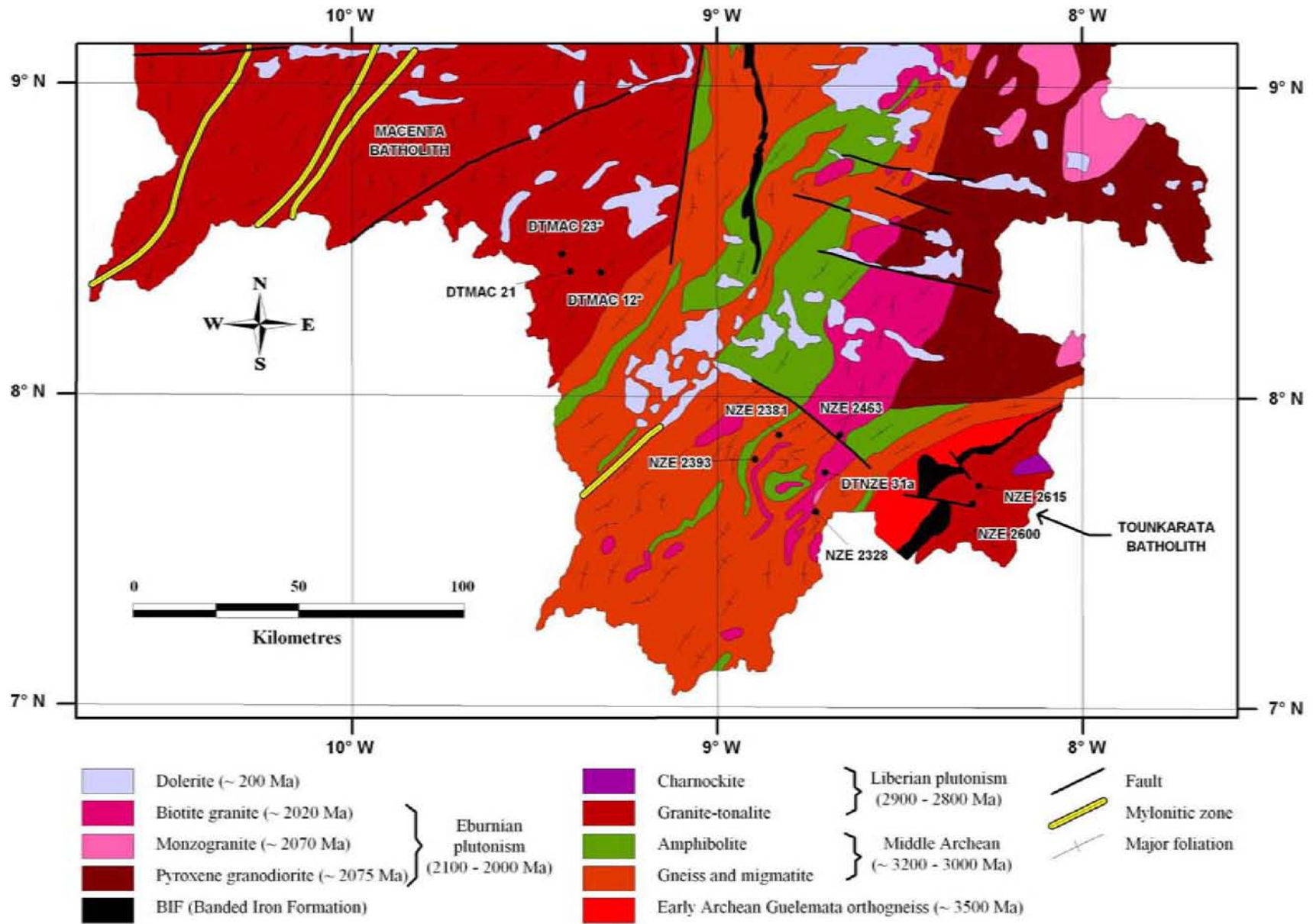


Figure 2.1.2. Geological map of south-east Guinea (modified from Thiéblemont et al., 2001) and location of studied samples.

## METHODOLOGY

### *Whole-rock geochemistry*

The whole-rock geochemical data presented in this work are from the BRGM database covering the chemical analyses performed between 1998 and 2001. The data compilation comprises a total of 105 analyses: 4 samples from the Paleoproterozoic cycle, 59 from the Leonian cycle, 38 from the Liberian cycle and 4 from Paleoproterozoic rocks. The bulk geochemical composition of the samples was analysed using inductively coupled plasma spectroscopy techniques: emission spectroscopy (ICP-AES) for major elements and mass spectroscopy (ICP-MS) for trace elements. Measurement uncertainties are generally below 5-10 % for major elements and under 2 % for trace elements.

Table 2.1.1 presents a synthesis of the chemical parameters calculated to classify the bulk rock composition and the radioelement contents. The complete analytical results are accessible in the following previous publications: Thiéblemont et al. (1999 a and b) and Goujou et al. (1999 a and b). The parameters Q [= Si/3-(K+Na+2Ca/3)], P [= K-(Na+Ca)], A [= Al-(K+Na+2Ca)] and B [= Fe+Ti+Mg] are calculated in thousands of cations from the major element contents (Debon and Le Fort, 1983 and 1988). The aluminosity index A/CNK [= (Al<sub>2</sub>O<sub>3</sub>/102)/((CaO/56)+(Na<sub>2</sub>O/62)+(K<sub>2</sub>O/94))] and the peralkaline index A/NK [= (Al<sub>2</sub>O<sub>3</sub>/102)/ ((Na<sub>2</sub>O/62)+(K<sub>2</sub>O/94))] (also called “agpaitic” when expressed as NK/Al) are calculated in molar fraction (Shand, 1947; Maniar and Piccoli, 1989). The uranium and thorium contents of the rocks (in ppm) are corrected from the alpha-decay of <sup>238</sup>U and <sup>232</sup>Th using the method of Robb et al. (1990) deriving from the radioactive decay law. For Archean rocks, the decrease of the U and Th concentrations due to radioactive decay become to be significant mainly for whole rock U contents and also for Th/U ratios, because the decay constant of Th is much larger than the one of uranium (see below). Equations (1) and (2) permit to calculate the initial radioelement concentrations are as follow:

$$(1) U^* \approx U_{\text{total at present time}} \times \left[ \frac{1}{\frac{t}{e^{-1.44 \times T^{238}U}}} \right] \text{ and } (2) Th^* \approx Th_{\text{total at present time}} \times \left[ \frac{1}{\frac{t}{e^{-1.44 \times T^{232}Th}}} \right]$$

where  $U_{\text{total at present time}}$  = actual U content of the rock (in ppm);  $Th_{\text{total at present time}}$  = actual thorium Th content (in ppm);  $t$  = approximate age of the rock (we have used the minimal age of the magmatic cycle: 3.5 Ga for Paleoproterozoic rocks, 2.9 Ga for Leonian rocks, 2.7 Ga for Liberian rocks and 2 Ga for Paleoproterozoic rocks); the radioactive decay of uranium and thorium are considered as totally dependant of <sup>238</sup>U and <sup>232</sup>Th with  $T^{238}U = 4.47$  Ga and  $T^{232}Th = 14.05$  Ga.

## Chapitre 2 : Sources Magmatiques Archéennes de l'Uranium

**Table 2.1.1.** Calculated P, Q, A and B parameters (in thousands of cations), A/CNK and A/NK (in moles),  $K_2O/Na_2O$  ratio, U and Th contents (in ppm), Th/U ratio, initial U\* and Th\* contents (in ppm) and initial Th\*/U\* ratio of the Guinean magmatic rocks (all the whole rock geochemical data from BRGM used for calculation of are given in Appendix 2, table A1). The ten bold samples refer to samples analysed petrographically in this study.

Sample	P	Q	A	B	A/CNK	A/NK	$\frac{K_2O}{Na_2O}$	U	Th	Th/U	U*	Th*	$\frac{Th^*}{U^*}$
<i>Paleoarchean Rocks (3.5 Ga)</i>													
Eclogite-KEC-81-12	-241.8	52.3	-178.6	404.0	0,62	3,88	0,39	0,14	0,38	2,71	0,24	0,45	4,15
Eclogite-KEC-81-4	-232.1	89.5	-179.8	486.1	0,58	4,41	0,14	0,34	0,71	2,09	0,59	0,84	1,71
Adamellite-NZE2629A	-65.7	184.3	42.6	27.0	1,17	1,33	0,94	0,63	14,33	22,75	1,09	17,04	0,92
Trondhjemite-NZE2578	-179.6	192.9	15.8	22.3	1,06	1,47	0,24	0,96	10,09	10,51	1,65	12,00	0,60
<i>Leonian Rocks (3.0-2.9 Ga)</i>													
Biotitic Amphibolite-NZE2066c	-269.1	59.7	-218.6	407.3	0,56	5,79	0,10	0,07	0,22	3,14	0,11	0,25	9,10
Pyroxene bearing Gneiss-NZE2317	-252.4	36.3	-175.1	304.9	0,64	2,47	0,42	0,07	0,09	1,29	0,11	0,10	9,10
Amphibolite-DL273	-243.8	82.7	-167.8	386.9	0,61	3,68	0,10	0,10	1,10	11,00	0,16	1,27	6,37
Amphibolite-DL47	-253.7	78.5	-158.6	380.8	0,66	5,17	0,13	0,10	0,80	8,00	0,16	0,92	6,37
Amphibolite-DTTIN1	-266.1	57.0	-175.5	366.8	0,63	3,84	0,12	0,10	0,46	4,60	0,16	0,53	6,37
Amphibolite-NZE2082	-196.7	115.9	-131.7	373.0	0,68	8,06	0,91	0,10	0,46	4,60	0,16	0,53	6,37
Amphibolite-pyroxenite-NZE2535	-265.5	71.0	-177.0	368.1	0,63	4,73	0,07	0,11	0,51	4,64	0,17	0,59	5,79
Mafic Amphibolite-NZE2329c	-228.6	77.9	-194.7	479.9	0,56	4,20	0,36	0,12	0,22	1,83	0,19	0,25	5,31
Amphibolite-DTNZE1	-286.1	57.0	-265.5	335.4	0,52	6,93	0,24	0,18	0,93	5,17	0,28	1,07	3,54
Mylonitic Gneiss-DL271B	-214.4	184.9	-9.6	77.5	0,97	2,14	0,08	0,20	2,20	11,00	0,31	2,54	3,19
Pyrigarnite-DTNZE3	-267.5	63.2	-183.7	368.0	0,62	4,26	0,09	0,20	0,37	1,85	0,31	0,43	3,19
Amphibolite-pyroxenite-NZE2295	-261.3	66.2	-180.4	365.8	0,61	3,53	0,10	0,22	0,81	3,68	0,35	0,93	2,90
Metagabbro-NZE2416	-251.0	77.6	-161.9	386.1	0,65	4,98	0,12	0,22	0,77	3,50	0,35	0,89	2,90
Pyrigarnite-NZE2553a	-179.2	137.5	-116.2	426.8	0,67	7,26	0,36	0,26	0,81	3,12	0,41	0,93	2,45
Amphibole and biotite bearing Granite-ID234	-214.4	118.3	-29.5	130.1	0,92	1,90	0,24	0,27	0,66	2,44	0,42	0,76	2,36
Ultrabasic-DL086	-17.6	249.8	284.6	640.5	12,20	16,97	0,20	0,30	1,50	5,00	0,47	1,73	2,12
Amphibolite-DTTIN14*	-229.7	86.4	-174.8	368.6	0,61	4,52	0,36	0,30	2,90	9,67	0,47	3,35	2,12
Biotitic Amphibolite-NZE2351d	-213.8	48.8	-197.4	388.1	0,56	2,23	0,66	0,30	1,01	3,37	0,47	1,17	2,12
Ultramafic Rock-ID350	-294.5	23.1	-377.8	425.8	0,34	2,51	0,37	0,31	0,66	2,13	0,49	0,76	2,06
Orthogneiss-ID289A	-212.3	165.9	10.2	31.3	1,03	1,62	0,16	0,33	0,36	1,09	0,52	0,42	1,93
Amphibolite-DTTIN17	-263.8	64.7	-189.0	339.1	0,62	4,23	0,25	0,38	1,39	3,66	0,60	1,60	1,68
Amphibolite-DL279	-225.6	81.4	-150.2	379.1	0,65	3,74	0,35	0,40	2,60	6,50	0,63	3,00	1,59
Orthogneiss-ID289B	-256.6	28.8	-104.6	243.5	0,77	2,06	0,27	0,44	2,99	6,80	0,69	3,45	1,45
Amphibolite-pyroxenite-NZE2329b	-246.5	57.1	-194.1	368.8	0,58	3,40	0,27	0,49	0,52	1,06	0,77	0,60	1,30
Mafic Rock-DL79B	-244.0	62.1	-159.3	378.6	0,65	3,55	0,23	0,50	0,90	1,80	0,78	1,04	1,27
Amphibolite-DTMAC2	-264.0	25.2	-204.2	341.6	0,60	2,58	0,39	0,56	1,64	2,93	0,88	1,89	1,14
Amphibolite-DL056A	-192.9	55.1	-114.5	330.1	0,73	2,39	0,71	0,60	3,30	5,50	0,94	3,81	1,06
Migmatitic Gneiss-DL147	-87.2	91.3	-57.1	163.0	0,84	1,39	1,28	0,60	30,50	50,83	0,94	35,20	1,06
Monzogabbro-ID261B	-197.2	25.9	-219.6	475.6	0,51	2,25	0,96	0,60	1,49	2,48	0,94	1,72	1,06
Amphibolite-pyroxenite-NZE2447	-167.4	156.1	-69.7	375.6	0,79	12,83	0,40	0,66	1,24	1,88	1,04	1,43	0,97
Pyroxene bearing Gneiss-NZE2257	-282.8	125.0	-362.4	227.5	0,33	3,33	0,20	0,74	2,00	2,70	1,16	2,31	0,86
Amphibolite-NZE2346	-125.6	137.6	-18.6	172.9	0,94	1,93	0,85	0,80	7,61	9,51	1,26	8,78	0,80
Mafic Gneiss- DL225A	-204.2	54.7	-65.4	169.6	0,84	1,86	0,51	0,90	5,90	6,56	1,41	6,81	0,71
Biotitic Granite-ID406	-199.4	89.7	-11.0	146.8	0,97	1,73	0,36	0,97	13,73	14,15	1,52	15,85	0,66
Hornblende and biotite bearing Gneiss-NZE2236	-106.4	137.8	-104.5	234.9	0,92	2,02	1,08	0,99	4,57	4,62	1,55	5,27	0,64
Amphibolite-NZE2565	-212.1	45.4	-245.6	236.4	0,76	1,99	0,55	0,99	2,47	2,49	1,55	2,85	0,64
Pyrigarnite-BEY2462b*	-220.1	117.9	-119.7	367.1	0,70	5,54	0,05	1,10	0,90	0,82	1,73	1,04	0,58
Microdiorite-DL109B	-230.2	5.0	-62.0	295.9	0,86	2,40	0,39	1,10	11,10	10,09	1,73	12,81	0,58
Amphibolite-NZE2379	-284.6	51.2	-144.1	173.5	0,72	3,25	0,22	1,10	2,58	2,35	1,73	2,98	0,58
Biotitic Granite-ID275	-175.5	171.5	18.2	65.8	1,06	1,70	0,29	1,15	5,40	4,70	1,80	6,23	0,55
Amphibolite- NZE2130	-185.9	119.2	-56.9	187.0	0,84	1,97	0,43	1,19	3,26	2,74	1,87	3,76	0,54
Diorite-DL150A	-176.8	22.8	-202.4	283.4	0,57	1,56	1,11	1,20	8,80	7,33	1,88	10,16	0,53
Migmatitic Granite-DL68	-67.4	180.3	12.7	43.8	1,05	1,32	1,01	1,30	36,20	27,85	2,04	41,78	0,49
Pyroxene bearing Gneiss-NZE2033	-215.6	140.8	-126.1	225.0	0,65	2,20	0,16	1,37	6,77	4,94	2,15	7,81	0,47
Pyroxene bearing Gneiss-NZE2239	-138.7	12.4	-162.8	175.6	0,66	1,65	1,62	1,61	7,01	4,35	2,53	8,09	0,40
Amphibolite-NZE2467	-272.9	81.1	-265.0	286.1	0,50	5,88	0,33	1,62	3,43	2,12	2,54	3,96	0,39
Granite-EE139	-126.3	144.4	3.2	47.9	1,01	1,33	0,65	1,70	10,80	6,35	2,67	12,46	0,37
Orthogneiss-TIN2040	-62.8	200.7	15.6	22.6	1,06	1,41	1,10	2,08	34,44	16,56	3,26	39,75	0,31
Migmatitic Gneiss-JLF.114	-69.6	196.9	14.4	16.1	1,06	1,11	0,84	2,30	29,40	12,78	3,61	33,93	0,28
Orthogneiss-DTMAC1	-135.7	191.5	10.9	50.0	1,04	1,57	0,51	2,34	17,52	7,49	3,67	20,22	0,27
Biotitic Granite-ID398	-49.6	193.1	12.1	22.3	1,05	1,29	1,18	2,36	28,76	12,19	3,70	33,19	0,27
Metatuff-NZE2066a	-140.5	158.7	4.8	117.9	1,02	1,77	0,55	2,38	5,37	2,26	3,74	6,20	0,27
Biotitic Granite-ID113	-98.4	172.6	9.2	61.9	1,03	1,46	0,82	2,43	10,67	4,39	3,81	12,31	0,26
Biotitic Granite-ID277	-88.3	173.6	11.4	28.3	1,04	1,30	0,84	3,66	19,28	5,27	5,74	22,25	0,17
Gneiss- AC.362	-32.9	166.1	8.5	32.6	1,03	1,23	1,37	3,80	50,00	13,16	5,96	57,71	0,17
Biotitic Granite-ID125	-87.7	117.8	-1.5	69.5	0,99	1,28	0,96	5,29	21,03	3,98	8,30	24,27	0,12
Granite-DL284	-9.5	170.8	9.6	20.9	1,04	1,17	1,58	7,50	46,50	6,20	11,77	53,67	0,08
<b>Qtz-Monzonite Gneiss-NZE2328</b>	<b>-84.0</b>	<b>106.3</b>	<b>-11.1</b>	<b>149.0</b>	<b>0,97</b>	<b>1,59</b>	<b>1,25</b>	<b>12,97</b>	<b>69,23</b>	<b>5,34</b>	<b>20,35</b>	<b>79,90</b>	<b>0,05</b>
Migmatitic Gneiss-ID.579	15.9	191.3	8.9	23.8	1,03	1,21	2,08	57,00	60,10	1,05	89,45	69,36	0,01

## Chapitre 2 : Sources Magmatiques Archéennes de l'Uranium

Sample	P	Q	A	B	A/CNK	A/NK	$\frac{K_2O}{Na_2O}$	U	Th	Th/U	U*	Th*	$\frac{Th^*}{U^*}$
<i>Liberian Rocks (2.8-2.7 Ga)</i>													
Granodiorite-DL247	-102.9	174.5	-6.3	50.4	0.98	1.47	0.84	0.10	4.50	45.00	0.15	5.14	6.57
Granodiorite-ID461	-112.3	160.9	13.9	36.1	1.05	1.54	0.77	0.11	0.08	0.73	0.17	0.09	5.98
Qtz-diorite-NZE2659	-263.5	68.4	-177.8	364.1	0.62	3.97	0.06	0.12	0.55	4.58	0.18	0.63	5.48
Adamellite-ID371	-73.3	123.2	-7.9	63.5	0.97	1.34	1.16	0.14	0.77	5.50	0.21	0.88	4.70
Qtz-diorite-AC.492	-257.6	79.3	-194.6	373.4	0.58	4.42	0.11	0.20	1.80	9.00	0.30	2.06	3.29
Qtz-Monzodiorite-DL259C	-163.8	76.2	-74.9	357.0	0.79	2.32	0.68	0.20	2.80	14.00	0.30	3.20	3.29
Gabbro-ID341	-260.1	49.9	-112.2	292.8	0.74	2.47	0.17	0.23	0.87	3.78	0.35	0.99	2.86
Syenite-DL251B	-92.8	8.9	-69.2	205.0	0.83	1.40	1.38	0.30	3.70	12.33	0.46	4.23	2.19
Adamellite-ID321	-62.7	166.1	12.2	19.0	1.04	1.34	1.14	0.30	0.92	3.07	0.46	1.05	2.19
Granodiorite-ID260	-129.9	162.9	12.8	68.6	1.04	1.61	0.63	0.32	38.19	119.34	0.49	43.64	2.05
Adamellite-NZE2652	-79.6	178.6	17.1	25.5	1.06	1.35	0.92	0.41	13.35	32.56	0.62	15.26	1.60
Granodiorite-ID261A	-89.0	159.6	20.1	51.4	1.07	1.47	0.92	0.44	5.76	13.09	0.67	6.58	1.49
Tonalite-IDEE425	-160.0	136.8	-8.3	76.9	0.97	1.49	0.49	0.44	1.29	2.93	0.67	1.47	1.49
Granodiorite-ID215	-122.5	166.1	18.2	45.8	1.06	1.49	0.64	0.52	3.67	7.06	0.79	4.19	1.26
Adamellite-ID333	-70.2	215.8	10.6	59.3	1.05	1.37	0.92	0.82	18.31	22.33	1.25	20.92	0.80
Granodiorite-ID278	-142.7	162.8	5.2	23.9	1.02	1.42	0.54	0.94	2.84	3.02	1.43	3.25	0.70
Qtz-Syenite-AC.497	-65.4	112.9	-39.2	123.3	0.88	1.39	1.45	1.00	17.50	17.50	1.52	20.00	0.66
Tonalite-DTMAC20	-180.6	131.3	13.4	96.6	1.04	1.74	0.37	1.03	8.02	7.79	1.57	9.16	0.64
Tonalite-ID292	-184.7	162.4	6.9	57.4	1.02	1.67	0.30	1.05	7.27	6.92	1.60	8.31	0.63
Granodiorite-MAC3075	-126.5	162.5	15.7	62.4	1.05	1.56	0.64	1.06	22.07	20.82	1.61	25.22	0.62
Qtz-diorite-ID294	-194.8	77.6	-204.4	305.5	0.54	1.89	0.83	1.21	4.14	3.42	1.84	4.73	0.54
Qtz-Monzonite-ID443	-83.4	113.2	-6.5	101.1	0.98	1.43	1.09	1.33	21.36	16.06	2.02	24.41	0.49
Syenite-ID392	-86.5	-1.9	-71.0	129.1	0.82	1.13	1.23	1.36	10.93	8.04	2.07	12.49	0.48
Tonalite-MAC3078a	-154.1	161.0	8.9	50.3	1.03	1.58	0.47	1.41	8.53	6.05	2.15	9.75	0.47
Granodiorite-ID436	-92.8	149.8	-1.7	34.9	0.99	1.09	0.78	1.63	10.93	6.71	2.48	12.49	0.40
Tonalite-NZE2603	-156.4	152.5	26.7	110.4	1.10	1.62	0.39	1.80	18.25	10.14	2.74	20.86	0.37
Qtz-Monzodiorite-ID395	-148.8	69.4	-50.1	135.6	0.87	1.49	0.78	1.86	9.20	4.95	2.83	10.51	0.35
Granodiorite-NZE2618*	-100.5	151.1	7.7	79.9	1.03	1.45	0.82	1.90	34.70	18.26	2.89	39.65	0.35
Adamellite-DTMAC9	-70.9	179.5	14.3	21.4	1.05	1.30	0.99	1.94	32.30	16.65	2.95	36.91	0.34
Granodiorite-ID179	-116.7	198.1	54.5	55.1	1.23	1.50	0.51	3.27	10.17	3.11	4.97	11.62	0.20
Granite-DL228A	-26.7	150.5	16.5	65.3	1.06	1.34	1.54	3.30	102.80	31.15	5.02	117.48	0.20
Granite-DTMAC15	3.9	174.0	16.7	42.1	1.07	1.25	1.88	3.80	83.75	22.04	5.78	95.71	0.17
Tonalite-MAC3078e	-194.0	133.8	-17.9	100.5	0.95	1.69	0.32	4.13	16.30	3.95	6.28	18.63	0.16
<b>Granodiorite-DTMAC23*</b>	<b>-135.3</b>	<b>155.5</b>	<b>7.6</b>	<b>49.0</b>	<b>1.03</b>	<b>1.44</b>	<b>0.59</b>	<b>4.20</b>	<b>15.40</b>	<b>3.67</b>	<b>6.39</b>	<b>17.60</b>	<b>0.16</b>
<b>Granite-DTMAC12*</b>	<b>-21.9</b>	<b>186.7</b>	<b>19.2</b>	<b>26.8</b>	<b>1.08</b>	<b>1.24</b>	<b>1.44</b>	<b>4.30</b>	<b>76.80</b>	<b>17.86</b>	<b>6.54</b>	<b>87.76</b>	<b>0.15</b>
<b>Tonalite-DTMAC21</b>	<b>-199.3</b>	<b>142.2</b>	<b>16.7</b>	<b>63.1</b>	<b>1.05</b>	<b>1.61</b>	<b>0.26</b>	<b>4.33</b>	<b>16.04</b>	<b>3.70</b>	<b>6.59</b>	<b>18.33</b>	<b>0.15</b>
<b>Granite-NZE2600</b>	<b>-22.7</b>	<b>186.2</b>	<b>20.7</b>	<b>16.9</b>	<b>1.08</b>	<b>1.23</b>	<b>1.41</b>	<b>8.63</b>	<b>30.48</b>	<b>3.53</b>	<b>13.13</b>	<b>34.83</b>	<b>0.08</b>
<b>Adamellite -NZE2615</b>	<b>-49.0</b>	<b>177.5</b>	<b>14.1</b>	<b>30.3</b>	<b>1.05</b>	<b>1.30</b>	<b>1.20</b>	<b>9.76</b>	<b>32.22</b>	<b>3.30</b>	<b>14.85</b>	<b>36.82</b>	<b>0.07</b>
<i>Paleoproterozoic Rocks (2.1-2.0 Ga)</i>													
Syenite-DTNZE 31a	28.5	12.2	-129.1	97.5	0.70	1.11	3.49	2.98	19.66	6.61	4.06	21.71	0.25
Granite-NZE2393	26.0	189.7	22.5	37.8	1.09	1.33	2.46	5.05	94.80	18.78	6.89	104.65	0.15
Granite-NZE2463	-5.3	185.1	15.8	23.3	1.06	1.29	1.78	12.16	63.29	5.20	16.60	69.87	0.06
Granite-NZE2381	3.4	164.6	12.4	16.5	1.04	1.29	1.97	22.15	18.37	0.83	30.22	20.27	0.03

### Sampling

Ten samples were collected by BRGM (Bureau de Recherches Géologiques et Minières) in south-east Guinea during geological fieldwork. Locations of samples are presented on the geological map (Fig. 2.1.2). GPS coordinates and rock type classifications are given in Table 2.1.2: one sample is from Leonian gneisses (NZE2328), 5 samples are from the Liberian granitoids (NZE2600, NZE2615, DTMAC12, DTMAC21 and DTMAC23) and 4 samples from the later Paleoproterozoic intrusions (NZE2381, NZE2393, NZE2463 and DTNZE31a). Geochemical data of the ten samples selected for mineralogical characterization are given in Table 2.1.3. They were chosen because their U and Th contents were over the average concentrations of the present average upper continental crust (2.8 ppm U and 10.7 ppm Th after Taylor and McLennan, 1985).

## Chapitre 2 : Sources Magmatiques Archéennes de l'Uranium

**Table 2.1.2.** Location and brief description of samples.

Age	Sample	Latitude	Longitude	Unit	Lithology
Leonian (3.1-2.95 Ga)	NZE 2328	7°37'45" N	8°43'51" W	Guinean Gneiss	Orthogneiss
	DTMAC 12*	8°23'51" N	9°19'09" W	Macenta Batholith	Granite
	DTMAC 21	8°24'00" N	9°24'08" W	Macenta Batholith	Granite
Liberian (2.9-2.8 Ga)	DTMAC 23*	8°27'21" N	9°25'31" W	Macenta Batholith	Granodiorite
	NZE 2600	7°39'24" N	8°18'05" W	Toukarata Batholith	Granite
	NZE 2615	7°42'48" N	8°17'02" W	Toukarata Batholith	Adamellite
Paleoproterozoic (2.3-2.05 Ga)	NZE 2381	7°52'29" N	8°49'51" W	Eburnean Leucogranite	Granite
	NZE 2393	7°47'46" N	8°53'50" W	Eburnean Leucogranite	Granite
	NZE 2463	7°52'34" N	8°39'50" W	Eburnean Leucogranite	Granite
	DTNZE 31a	7°45'19" N	8°42'21" W	Eburnean Karanah Syenite	Syenite

*Notes:* Latitudinal and longitudinal coordinates are given in degrees, minutes and seconds.

**Table 2.1.3.** Geochemical composition of the studied felsic igneous rocks from south-east Guinea (data from Thiéblemont et al, 1999 a and b; Goujou et al., 1999 a and b).

Age Facies Sample	Leonian			Liberian			Paleoproterozoic			
	Orthogneiss NZE 2328	Granite DTMAC 12*	Granite DTMAC 21	Granodiorite DTMAC 23*	Granite NZE 2600	Adamellite NZE 2615	Granite NZE 2381	Granite NZE 2393	Granite NZE 2463	Syenite DTNZE 31a
SiO <sub>2</sub> (%)	63.01	74.00	68.81	71.10	74.89	73.17	73.22	73.36	74.10	61.25
Al <sub>2</sub> O <sub>3</sub>	16.27	13.50	16.76	15.50	13.77	14.06	14.73	13.75	13.87	15.56
Fe <sub>2</sub> O <sub>3</sub>	4.91	2.00	3.16	2.40	0.95	1.71	0.88	2.18	1.41	4.16
MnO	0.07	0.06	0.08	0.04	0.04	0.04	0.03	0.02	0.04	0.09
MgO	3.18		0.78	0.60	0.16	0.26	0.21	0.31	0.17	1.43
CaO	3.64	0.90	3.03	2.40	0.83	1.38	1.45	1.24	1.26	4.47
Na <sub>2</sub> O	3.40	3.40	5.41	4.70	3.53	3.67	3.03	2.40	3.01	2.58
K <sub>2</sub> O	4.26	4.88	1.38	2.78	4.98	4.42	5.97	5.90	5.37	9.00
TiO <sub>2</sub>	0.65	0.14	0.33	0.32	0.08	0.19	0.02	0.22	0.11	0.78
P <sub>2</sub> O <sub>5</sub>	0.24	0.06	0.06	0.12	0.10	0.09	0.05	0.05	0.04	0.33
L.O.I.	0.36	0.50	0.49	0.40	0.30	0.55	0.30	0.47	0.19	0.26
Total	99.99	99.44	100.29	100.36	99.63	99.54	99.89	99.90	99.57	99.91
As (ppm)	0.51		0.34		0.03	0.19	0.25	0.09	0.24	0.39
Ba	1097	1550	393	1765	760	1499	765	902	697	6248
Be	3.32		1.23		1.25	2.16	1.13	0.00	0.55	0.94
Bi	0.02		0.01		0.01	0.02	0.04	0.02	0.03	0.04
Co	17.23		5.59	6.00	1.15	2.04	1.79	2.45	1.54	7.77
Cr	236	49	56	28	17	34	53	27	34	33
Cs	11.57		0.59		1.03	1.71	0.74	0.65	0.75	0.62
Cu	31.37		16.15		2.87	2.69	61.62	3.29	4.86	29.45
Ga	21.13		22.01		18.42	20.73	15.04	18.86	16.17	17.21
Hf	7.80	6.50	4.54	4.40	3.37	4.73	1.08	6.24	3.60	2.21
Mo	3.62		2.31		1.30	2.23	2.06	1.96	1.66	1.88
Nb	15.40	12.90	5.98	5.70	7.17	14.45	0.97	10.60	3.33	33.15
Ni	78.57		9.82		2.57	3.70	4.60	4.06	3.63	8.91
Pb	51.25		15.47		44.04	33.00	47.17	41.27	44.33	14.95
Rb	275	160	82	80	158	208	129	240	206	200
Sb	0.02		0.11		0.03	0.05	0.02	0.02	0.04	0.06
Sn	2.21		1.64		0.75	1.91	0.34	0.18	0.42	4.21
Sr	401	105	545	636	85	139	253	156	164	1798
Ta	1.37	0.90	0.82	0.80	0.86	1.73	0.06	0.23	0.16	4.12
<b>Th</b>	<b>69.23</b>	<b>76.80</b>	<b>16.04</b>	<b>15.40</b>	<b>30.48</b>	<b>32.22</b>	<b>18.37</b>	<b>94.80</b>	<b>63.29</b>	<b>19.66</b>
<b>U</b>	<b>12.97</b>	<b>4.30</b>	<b>4.33</b>	<b>4.20</b>	<b>8.63</b>	<b>9.76</b>	<b>22.15</b>	<b>5.05</b>	<b>12.16</b>	<b>2.98</b>
V	60.03		27.22	24.00	1.02	12.05	2.24	11.03	3.47	59.84
W	0.83		0.17		0.18	0.26	0.12	0.07	0.13	0.34
Y	14.17	13.40	9.58	20.10	35.74	16.59	4.24	8.21	7.94	26.11
Zn	58.02		59.43		24.02	35.30	9.08	28.92	20.53	55.09
Zr	317	110	218	128	97	177	34	223	123	83
La (ppm)	82.60	73.10	44.82	46.60	33.70	44.25	19.57	102.37	64.03	110.61
Ce	149	134	78	68	61	77	38	178	91	264
Pr	15.06	13.10	7.56	9.20	6.18	7.80	4.42	18.17	10.54	35.52
Nd	51.57	45.00	24.68	35.10	21.18	25.55	15.37	59.42	33.57	142.71
Sm	7.47	7.40	3.02	7.00	4.70	4.40	2.96	8.84	5.02	25.53
Eu	1.50	0.50	0.72	1.20	0.70	0.93	0.99	0.90	0.90	6.98
Gd	5.31	6.30	2.20	6.10	4.69	3.19	2.17	5.98	3.53	15.11
Tb	0.59	0.90	0.31	0.80	0.76	0.46	0.27	0.68	0.37	1.71
Dy	2.82	4.20	1.52	4.00	4.96	2.54	1.19	2.56	1.68	7.00
Ho	0.47	0.70	0.31	0.70	1.14	0.51	0.16	0.33	0.24	0.89
Er	1.27	1.40	0.89	1.50	2.80	1.47	0.29	0.88	0.64	2.19
Tm	0.19	0.20	0.13	0.20	0.46	0.25	0.03	0.07	0.07	0.22
Yb	1.12	0.70	0.85	1.20	2.76	1.46	0.15	0.44	0.44	1.49
Lu	0.18	0.10	0.15	0.20	0.41	0.23	0.02	0.08	0.08	0.20
ΣREE	319	288	165	182	146	170	85	379	212	614
[La/Sm] <sub>N</sub>	2.67	2.38	3.58	1.61	1.73	2.43	1.59	2.80	3.08	1.05
[Gd/Yb] <sub>N</sub>	3.83	7.27	2.09	4.11	1.37	1.77	11.96	11.11	6.42	8.21
Eu/Eu*	0.73	0.22	0.85	0.56	0.46	0.76	1.19	0.38	0.65	1.09
A/CNK	0.97	1.08	1.05	1.03	1.08	1.05	1.04	1.09	1.06	0.70
A/NK	1.59	1.24	1.61	1.44	1.23	1.30	1.29	1.33	1.29	1.11
Th/U	5.34	17.86	3.70	3.67	3.53	3.30	0.83	18.78	5.20	6.61

### ***Mineralogical study***

Mineralogical studies were undertaken at the University of Nancy (France) on a set of 13 polished thin sections. Autoradiography of the polished rock surfaces has been performed but no positive results were provided by this method which suggest that U and Th are probably within accessory phases with low U-content. Transmitted and reflected light microscopy was undertaken at the G2R laboratory (Géologie et Gestion des Ressources Minérales et Energétiques) with a polarizing microscope Olympus BX51.

Both scanning electron microscope (SEM) and electron microprobe (EMP) analyses of the minerals were performed at the SCMEM laboratory (Service Commun de Microscopie et de Microanalyses).

The SEM instrument Hitachi FEG-S4800 coupled with an energy dispersive spectrometer (EDS) NORAN Vantage give semi-quantitative measurements of the major components in minerals. The backscattered electron mode of the SEM provides high resolution images of the textural heterogeneities and the variations in the grey intensities within minerals are associated to changing average atomic number and to variations in the local chemical composition.

Electron microprobe analyses (EMPA) in the radiogenic accessory minerals (zircon, monazite and uraninite) were conducted on CAMECA SX100 instrument equipped with 5 wavelength-dispersive spectrometers (WDS). The measurements were performed with a current intensity of 10 nA, an accelerating voltage of 20 kV for zircon and monazite analysis or 15 kV for uraninite analysis and a beam spot size of approximately 2  $\mu\text{m}$  wide. Standard calibration, spectrometer crystals, background position and counting times on peaks used for experiments are given in Table 2.1.4. Average chemical compositions are given in weight percent of the oxides (wt.%) for each element. However, to allow comparison between the different radiogenic grains, EMPA results have been recalculate for the plots in atomic percent (at.%). In the case of the monazite, mineral group composition is calculated in end-member proportions (Bowie and Horne, 1953; Förster, 1998): the Th and Si contents are attributed to the huttonite molecule  $[\text{ThSiO}_4]$ , the Ca, U and Pb contents are included in the brabantite  $[\text{Ca}(\text{Th,U,Pb})(\text{PO}_4)_2]$  and all other REE and Y contents are part of the monazite-(Ce) molecule  $[(\text{REE,Y})\text{PO}_4]$  calculated by the difference between the total molecular fraction and the huttonite and brabantite fractions. Monazite compositions are then plotted in the ternary system defined by the species boundaries.

**Table 2.1.4.** Overview of the element set-up for the electron microprobe including analysed line, calibration standard, and background positions used during integrated analysis of zircon, monazite and uraninite

<i>Mineral analysed</i>	<i>Element</i>	<i>Line</i>	<i>Spectrometer crystal</i>	<i>Standard</i>	<i>High Back-ground</i>	<i>Low Back-ground</i>	<i>Slope</i>	<i>Peak counting time (s)</i>
<i>Zircon</i>	La	L $\alpha$	PET	LaPO <sub>4</sub>	500		1.1	20
	Ca	K $\alpha$	PET	Wollastonite	700		1.1	10
	P	K $\alpha$	PET	KTiP	400	-400		20
	Zr	L $\alpha$	TAP	Zircon	700		1.2	10
	Y	L $\alpha$	TAP	YPO <sub>4</sub>	625	-450		40
	Al	K $\alpha$	TAP	Albite	800		1.2	10
	Yb	L $\alpha$	LIF	YbCo <sub>2</sub> Si <sub>2</sub>	474	-943		20
	Er	L $\alpha$	LIF	ErNi <sub>2</sub> Si <sub>2</sub>	600		1.05	20
	Dy	L $\alpha$	LIF	DyRu <sub>2</sub> Ge <sub>2</sub>	320	-1200		40
	Fe	K $\alpha$	LIF	Fe metal	600		1.1	10
	Si	K $\alpha$	TAP	Zircon	500		1.2	20
	Hf	M $\alpha$	TAP	Hf metal	600	-550		30
	Ti	K $\alpha$	LPET	MnTiO <sub>3</sub>	600		1.1	10
	U	M $\beta$	LPET	UO <sub>2</sub>	793	-1447		30
	Th	M $\alpha$	LPET	ThO <sub>2</sub>	726	-1274		30
Pb	M $\beta$	LPET	PbCrO <sub>4</sub>	970	-900		30	
<i>Monazite</i>	Ce	L $\alpha$	PET	CePO <sub>4</sub>	450		1.2	10
	La	L $\alpha$	PET	LaPO <sub>4</sub>	500		1.1	10
	Ca	K $\alpha$	PET	Wollastonite	700		1.1	20
	Pb	M $\beta$	PET	PbCrO <sub>4</sub>	1700		1.05	60
	Zr	L $\alpha$	TAP	ZrO <sub>2</sub>	700		1.2	20
	Y	L $\alpha$	TAP	YPO <sub>4</sub>	625	-450		30
	Al	K $\alpha$	TAP	Albite	800		1.2	20
	Gd	L $\beta$	LIF	GdTiGe	450	-400		60
	Fe	K $\alpha$	LIF	Hematite	700		1.1	20
	Mn	K $\alpha$	LIF	MnTiO <sub>3</sub>	600		1.1	20
	Sm	L $\alpha$	LIF	SmPO <sub>4</sub>	600	-600		60
	P	K $\alpha$	TAP	CePO <sub>4</sub>	800		1.2	20
	Si	K $\alpha$	TAP	Orthose	800		1.2	20
	Nd	L $\beta$	LPET	NdPO <sub>4</sub>	700		1.15	20
	Pr	L $\beta$	LPET	PrPO <sub>4</sub>	750	-370		20
	Ti	K $\alpha$	LPET	MnTiO <sub>3</sub>	600		1.1	10
	U	M $\beta$	LPET	UO <sub>2</sub>	793	-1447		60
Th	M $\alpha$	LPET	ThO <sub>2</sub>	726	-1247		30	
<i>Uraninite</i>	Ce	L $\alpha$	PET	CePO <sub>4</sub>	500		1.2	20
	Ca	K $\alpha$	PET	Wollastonite	700		1.1	20
	U	M $\beta$	PET	UO <sub>2</sub>	500		1.1	20
	K	K $\alpha$	PET	Orthose	600		1.1	10
	Pb	M $\alpha$	PET	PbCrO <sub>4</sub>	1700		1.05	50
	Zr	L $\alpha$	TAP	ZrO <sub>2</sub>	700		1.2	20
	Si	K $\alpha$	TAP	Orthose	800		1.2	20
	Al	K $\alpha$	TAP	Albite	800		1.15	10
	Fe	K $\alpha$	LIF	Fe metal	600		1.1	20
	Mn	K $\alpha$	LIF	MnTiO <sub>3</sub>	600		1.1	20
	V	K $\alpha$	LIF	V	600		1.05	20
	P	K $\alpha$	TAP	LaPO <sub>4</sub>	600		1.15	20
	Y	L $\alpha$	TAP	YPO <sub>4</sub>	775	-450		40
	Mg	K $\alpha$	TAP	Olivine	1200		1.2	40
	Na	K $\alpha$	TAP	Albite	500		1.05	10
	La	L $\alpha$	LPET	LaPO <sub>4</sub>	500		1.1	20
	Ti	K $\alpha$	LPET	MnTiO <sub>3</sub>	600		1.1	20
	Th	M $\alpha$	LPET	ThO <sub>2</sub>	500		1.1	60
	S	K $\alpha$	LPET	SrS	600		1.05	20
	Mo	L $\alpha$	LPET	Mo	500		1.1	20

*Notes:* TAP – thallium acid phthalate crystal; LPET – large pentaerythriol crystal; PET – large pentaerythriol crystal; LIF – Lif crystal; PC1 – multilayered W-Si crystal; Background positions refer to number of wavelength, expressed as  $\sin \theta 10^3$ , above and below the peak position or derived by line regression with the slope indicated. Background counting time is equivalent to half of the peak counting time for each element.

U, Th and Pb concentrations measured by electron microprobe in uranium oxides are used to calculate chemical ages of the minerals using the method of Pommier et al. (2002) and Cocherie and Albarède (2001) corresponding to iteration for finding a solution to the following equation (modified from Bowles, 1990):

$$(3) \quad C_{Pb} = C_{Th}[0.897(e^{\lambda_{232} \cdot t} - 1)] + C_U[0.859(e^{\lambda_{238} \cdot t} - 1) + 0.006(e^{\lambda_{235} \cdot t} - 1)]$$

where  $C_{Pb}$ ,  $C_{Th}$ , and  $C_U$  are concentrations of Pb, Th, and U (in ppm) measured in situ in the uraninite;  $\lambda_{232}$ ,  $\lambda_{238}$ , and  $\lambda_{235}$  are the decay constants (in year<sup>-1</sup>) for <sup>232</sup>Th, <sup>238</sup>U, and <sup>235</sup>U respectively; and t is age (in year). All the calculations were done at 2σ level with 95% of confidence considering absolute errors from the standard deviation given on each individual measurement. Then, the chemical age results are plotted with the Isoplot program (Ludwig, 1999) providing an average weighted mean of the more confident age population.

## RESULTS

### ***Geochemical characterization of the magmatic rocks***

Rocks from the four different magmatic cycles have been plotted in the geochemical diagrams commonly used to classify igneous rocks.

The SiO<sub>2</sub>/K<sub>2</sub>O diagram presented in Figure 2.1.3 discriminates rocks with tholeiitic composition from calc-alkaline affinity and shoshonitic. Only four analyses of Paleoproterozoic rocks are available but they reveal that this magmatism was bimodal with two main affinities, basaltic and felsic as suggested by Thiéblemont (2004). Two eclogite samples are in the field of basalts. The two felsic samples have distinct compositions, one plot in the field of low-K rhyolite whereas the other presents a high K-granitic rock close to an adamellite composition. The Leonian magmatic rocks have a wide range of composition from basaltic to extremely felsic and from low to high-K contents, whereas the Liberian ones are more restricted to the medium- to high-K calc-alkaline series with felsic composition generally within the dacite and rhyolite fields. The Paleoproterozoic granites average 73.5 wt% SiO<sub>2</sub> and mostly belong to the high-K calc-alkaline suite except for the syenite sample with lower SiO<sub>2</sub> content (61.3 wt%) and which plots within the ultrapotassic shoshonitic field.

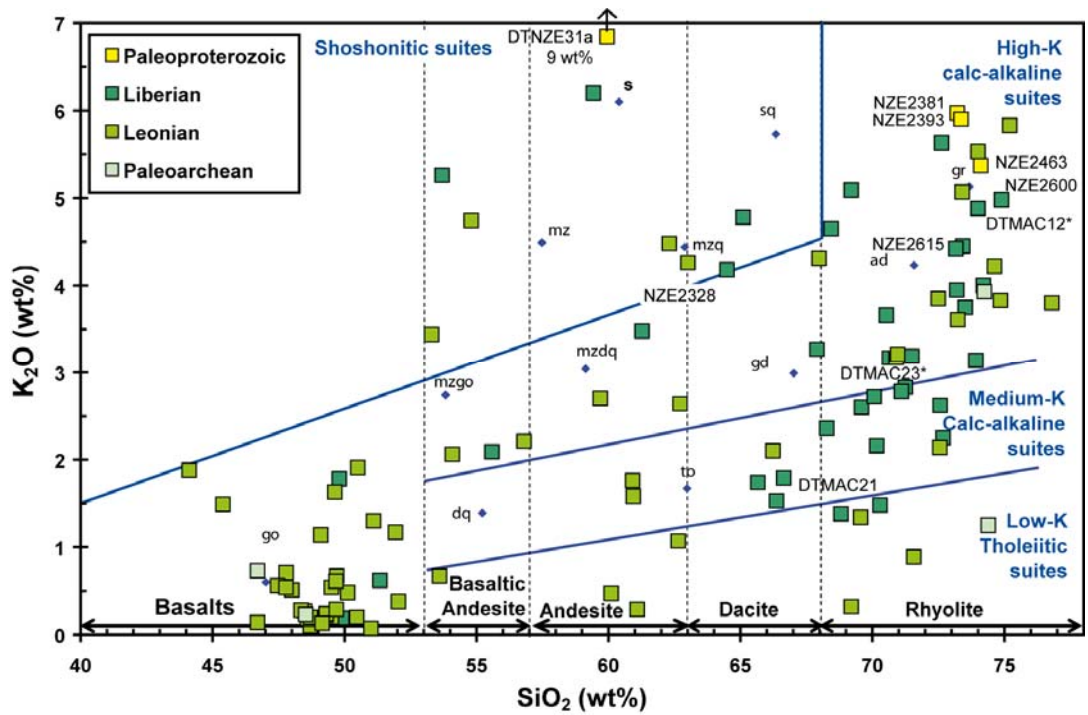


**Figure 2.1.3.** Binary diagram showing the  $K_2O$  vs.  $SiO_2$  contents (wt%) of the Guinean magmatic rocks. The composition limits and fields are from Peccerillo and Taylor (1976) and rock composition references are from Debon and Lefort (1983): go = gabbro; mzgo = monzogabbro; mz = monzonite; mzq = quartz-monzonite; mzdq = quartz monzodiorite; dq = quartz diorite; s = syenite; sq = quartz syenite; to = tonalite; gd = granodiorite; ad = adamellite; gr = granite.

The  $K_2O$  content is generally increasing with magmatic differentiation. This trend is even more pronounced in the  $Na_2O$  and  $K_2O$  diagram (Fig. 2.1.4). The Archean rocks have  $K_2O$  content generally below 5 wt% with soda-rich composition up to 5.5 wt%. The Paleoproterozoic granitoids are highly potassic with  $K_2O > 5$  wt% and up to 9 wt% for the syenite (sample DTNZE31a), with lower  $Na_2O$  content from 2.4 to 3 wt%. The corresponding  $K_2O/Na_2O$  ratios (Table 2.1.1) range between 1.8 and 3.5 for the Paleoproterozoic cycle, much higher than in the older magmatic rocks, in which it is generally below 1, except for some Leonian and Liberian migmatitic gneisses and granitoids with values ranging from 1.5 to 2.

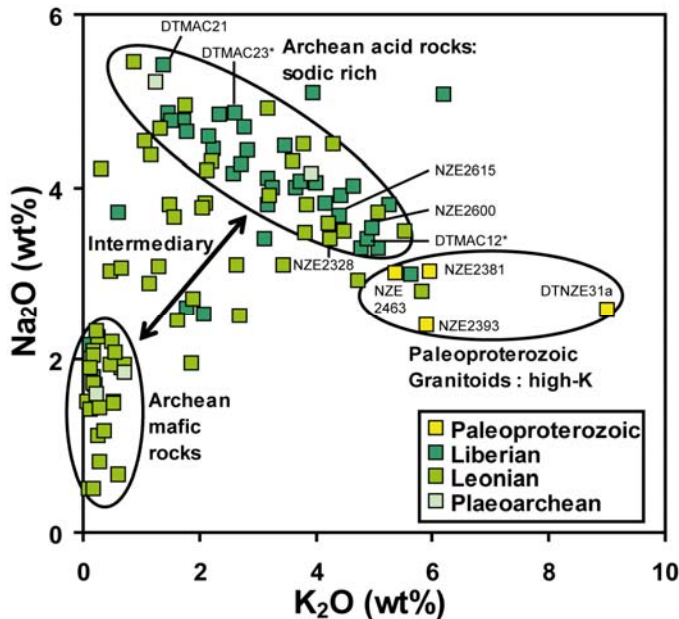


**Figure 2.1.4.** Binary diagram showing the  $K_2O$  vs.  $Na_2O$  contents (wt%) of the Guinean magmatic rocks.

The mineralogical-chemical diagrams of Debon and Lefort (1988) permit to plot whole-rock major elements in relation with the abundances of the main rock forming minerals. In the P-Q diagram (Figure 2.1.5) all the magmatic rocks from south-east Guinea plot in the quartz-saturated field. The Archean ones present highly variable quartz/feldspars proportions (highly variable Q and P parameters). The most sodic samples have the lowest quartz content (Q < 100) and are rich in albite. The rest of magmatic rocks present a progressive enrichment in K-feldspar (increasing P) with a moderate increase in quartz content (Q increase from 150 to 200) which is typical of the intermediate-K rich calc-alkaline series. The Paleoproterozoic granitoids are among the richest in K-feldspar, however the syenite sample is close to the quartz-undersaturated field as expected for a syenite if this sample is of magmatic origin.

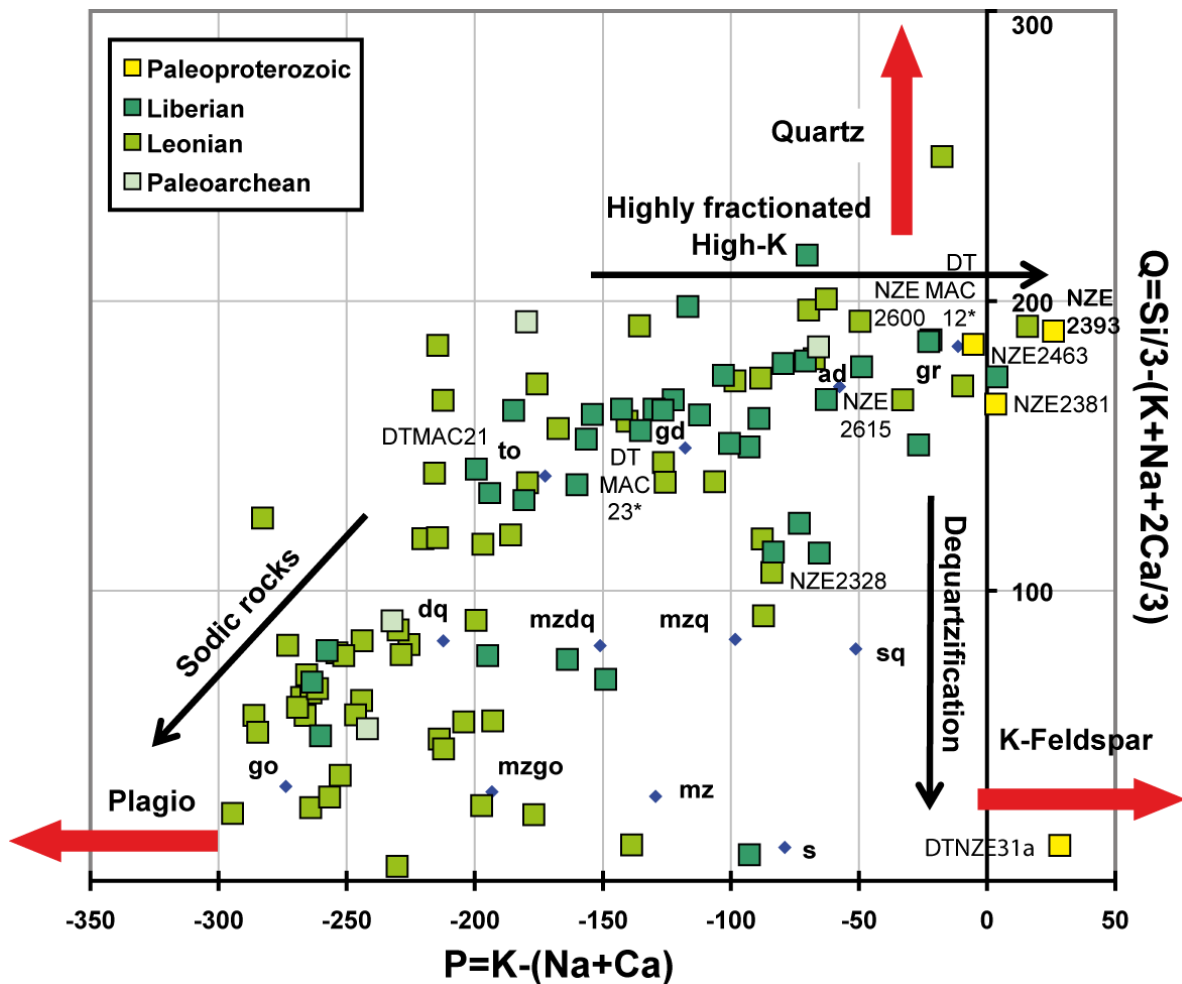


**Figure 2.1.5.** Variation of P versus Q parameters for magmatic rocks from south-east Guinea (diagram from Debon and Lefort, 1988). The Q and P values are calculated in thousands of cations. Rock composition references are indicated: go = gabbro; mzgo = monzogabbro; mz = monzonite; mzq = quartz-monzonite; mzdq = quartz monzodiorite; dq = quartz diorite; s = syenite; sq = quartz syenite; to = tonalite; gd = granodiorite; ad = adamellite; gr = granite.

In the A-B diagram (Figure 2.1.6), the abundance of coloured minerals represented by the B parameter (Fe-Ti oxides, biotite and amphibole) tends to decrease with the increasing peraluminous index (A). Because the loss of ignition (L.O.I.) in the Guinean magmatic rocks ranges from 0 to 1.5 (Appendix 2 - Table A1) and that the most peraluminous terms have L.O.I. between 0.3 and 0.5, the increase of the peraluminous index is not related to alteration but is caused by the progressive magmatic differentiation. The mafic Paleoproterozoic magmatic rocks and most of the Leonian rocks plot in the metaluminous field whereas the felsic Paleoproterozoic rocks and most of the Liberian and Paleoproterozoic samples are slightly peraluminous (closer view in Fig. 2.1.6:  $-10 < A < +55$ ).

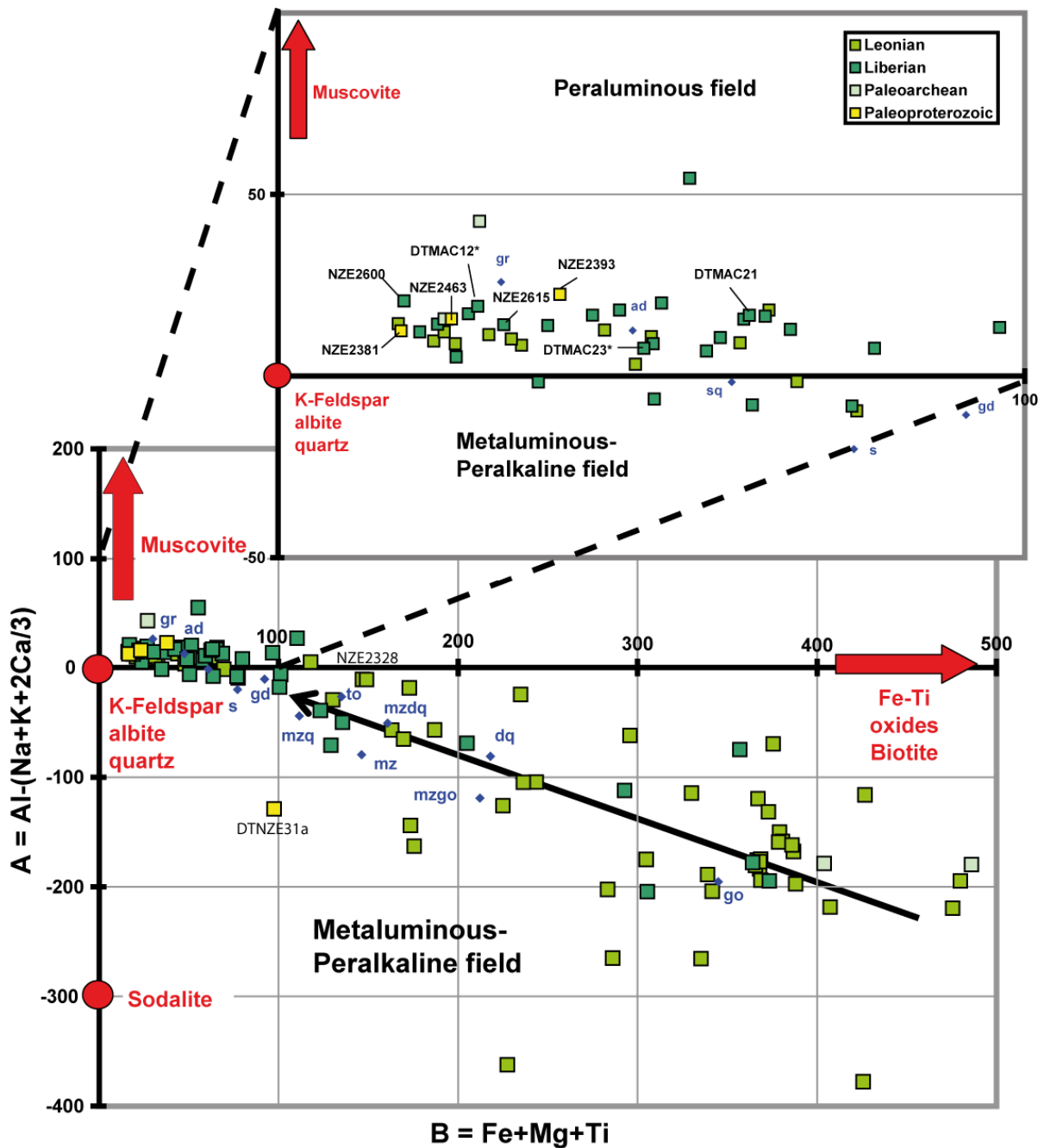
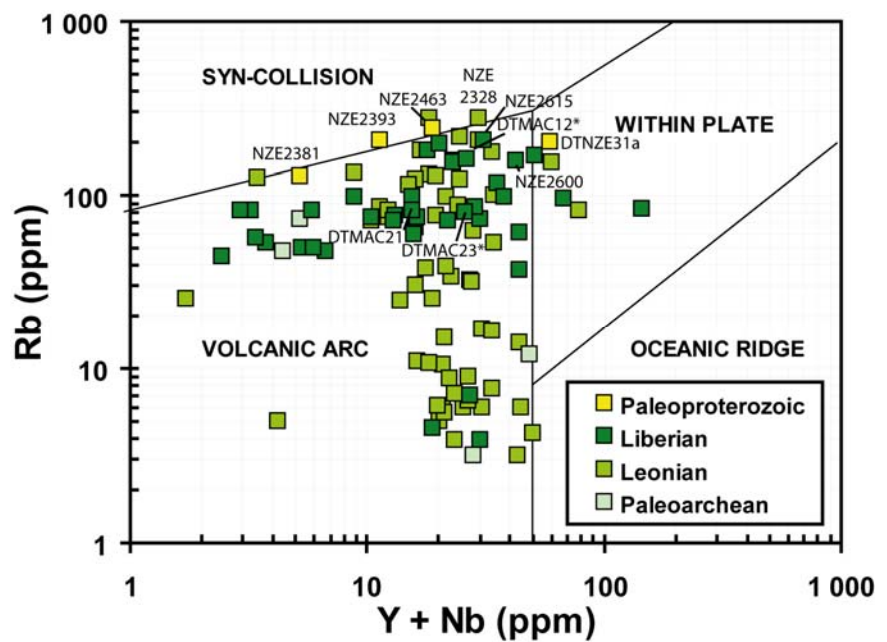


Figure 2.1.6. Variation in the peraluminous index A with the fractionation parameter B (coloration index) for Guinean magmatic rocks (diagram from Debon and Lefort, 1988). The A and B parameters are calculated in thousands of cations.

**Geotectonic settings of the magmatic series**

The abundances in hygromagmaphile elements are generally used as discriminant features to define the geotectonic setting of volcanic rocks (Pearce, 1982 and 1983). The Guinean magmatic rocks plot mainly in convergent tectonic environments in the Rb versus Y+Nb diagram (Fig. 2.1.7). The Archean series are dominantly within the volcanic arc field characterized by  $Y+Nb < 50$  ppm. The Liberian magmas show a remarkable increase in Rb content compared to the older Archean rocks with most of samples ranging between 40 and 200 ppm. The Paleoproterozoic granites are closer to the syn-collision field with 130 to 230 ppm Rb, except for the syenite which plots in the within plate field and is probably associated to a distinct late-kinematic intrusion.



**Figure 2.1.7.** Binary diagram showing Rb versus Y+Nb contents (in ppm) of the Guinean magmatic rocks (diagram from Pearce, 1982).

In the Th/Yb versus Ta/Yb diagram (Fig. 2.1.8), all the compositions define a positive correlation straddling over the boundary between oceanic arc and continental active margin define by the red line ( $Ta/Yb=0.1$ ) which confirm a prevailing convergent orogenic signature. The Leonian magmatic rocks are dominated by tholeiitic series and probably derived from a basaltic protolith. The Liberian magmas are mostly calc-alkaline series with Th/Yb and Ta/Yb ratios rising up to 350 and 2 respectively. This trend corresponds to increasing fractionation and is probably partly related to an increase of a crustal derived component.

This corroborates the genetic model defined by Thieblemont et al. (2004) suggesting that Liberian granitization and migmatization took place into the ancient Archean basement and Leonian volcanic rocks during continental accretion. The late Eburnean orogeny led to emplacement of younger diapiric plutons in upper crustal levels by reworking of the Archean rocks.

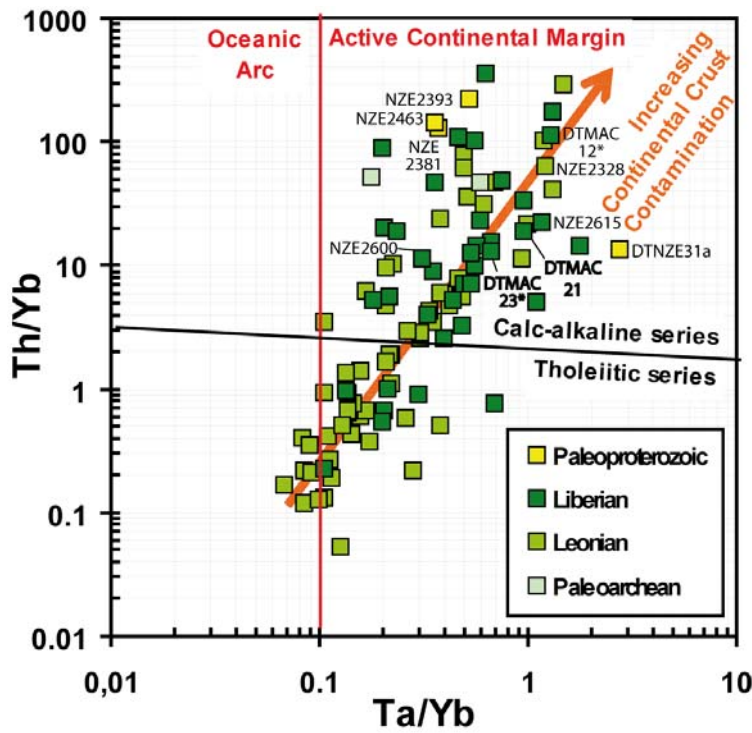


Figure 2.1.8. Variation of Th/Yb ratio with Ta/Yb ratio for Guinean magmatic rocks (diagram from Pearce, 1983).

**Radioelement contents of the magmatic rocks**

Within each magmatic cycle of the Guinean samples, the highest U contents are recorded within the most peraluminous rocks with  $A/CNK > 1$  and  $A/NK > 1$  (Table 2.1.1 and Fig. 2.1.9). The global trend clearly shows that U abundances increase progressively from the older metaluminous rocks to the younger peraluminous high K calc-alkaline granites.

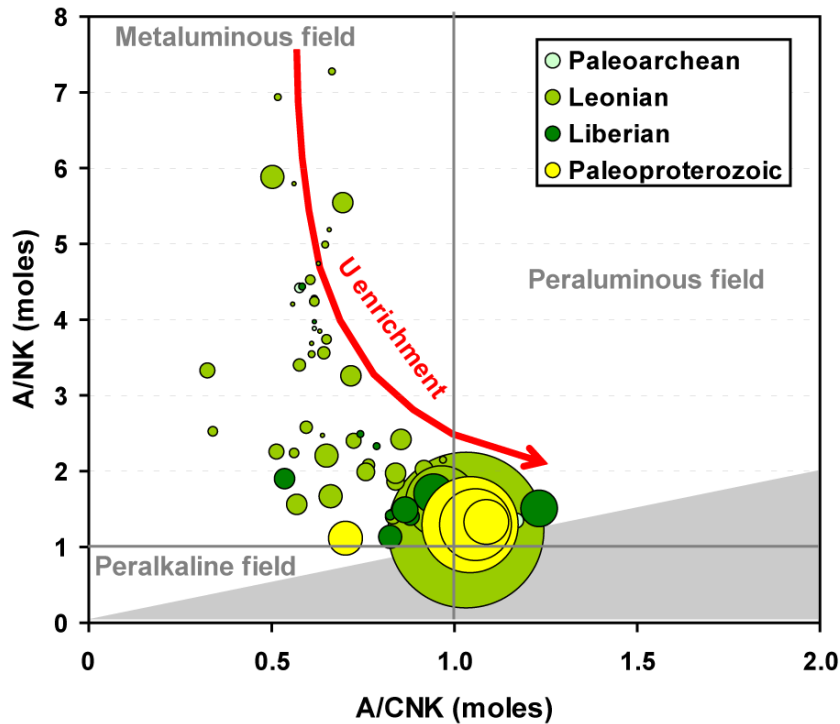


Figure 2.1.9. A/NK vs. A/CNK diagram of the magmatic rocks from south-east Guinea (data from Table 2.1.1). Colour of circles refer to the age of the magmatic cycle and the size is proportional of the U content.

The U vs. Th content binary diagram (Fig. 2.1.10) show two separate groups corresponding to the Paleoproterozoic rocks, one with low U and Th concentrations (0.14 ppm U and 0.38 ppm Th) for the most mafic material to 0.96 ppm U and 14.33 ppm Th in the felsic rocks ( $Th/U = 2.1-2.3$ ). In the Leonian rocks, the radioelement contents increase notably and range from 0.1 ppm U and 0.7 ppm Th in the mafic rocks to 57 ppm U and 68.23 ppm Th in migmatitic gneisses and granites ( $0.8 < Th/U < 51$ ). The Liberian rocks have generally lower U contents (0.1 to 9.8 ppm U) but higher Th concentrations (0.1 to 102.8 ppm Th,  $0.7 < Th/U < 120$ ), the highest contents occurring in the granites, granodiorites, tonalites and adamellites. The most felsic Paleoproterozoic granitoids have U contents between 2.98 and 22.15 ppm and Th contents between 18.4 and 94.8 ppm ( $Th/U = 0.83-18.8$ ).

The Th/U ratios of the Guinean magmatic rocks range between 0.8 and 120 but most of the analyses plot generally higher than the average continental crust ( $Th/U > 4$ ). This suggests that the radioelements are probably distributed mostly within Th-rich phases as monazite group minerals. Samples that have a Th/U ratio below 1 are very rare and correspond to the field of uraninite crystallization (Cuney and Friedrich, 1987). Only one sample collected for this study has such a low ratio namely the Eburnean granite NZE2381. The highest Th/U ratios may reflect either uranium leaching, especially if uraninite was initially present because of its easy leachability at the surface by oxidized meteoric fluids, or melting of a high Th/U source, such as granulites.

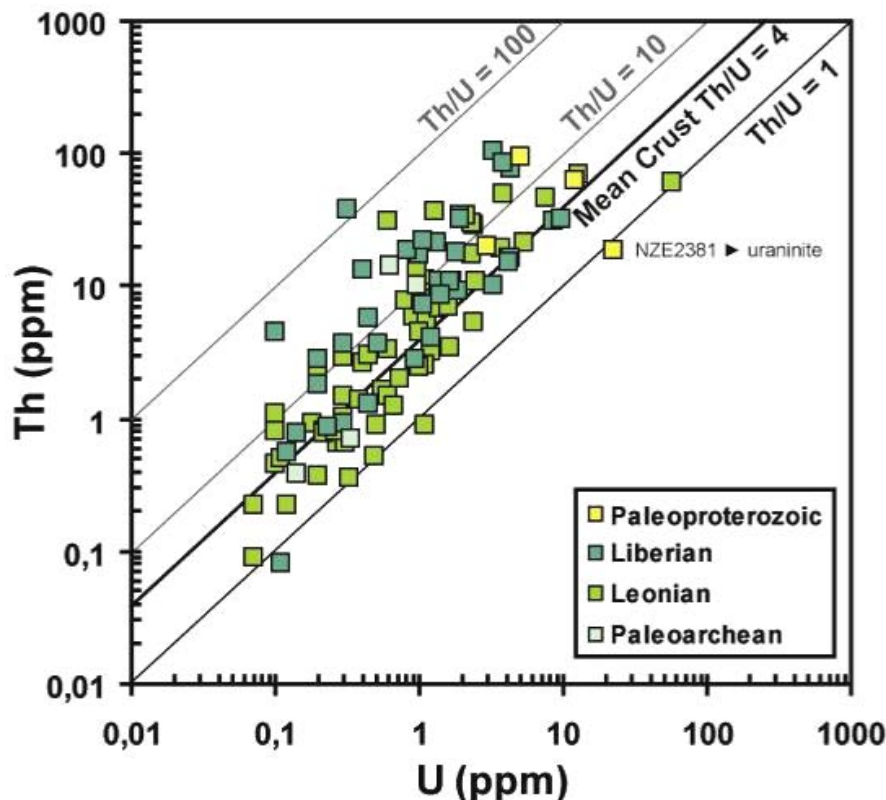
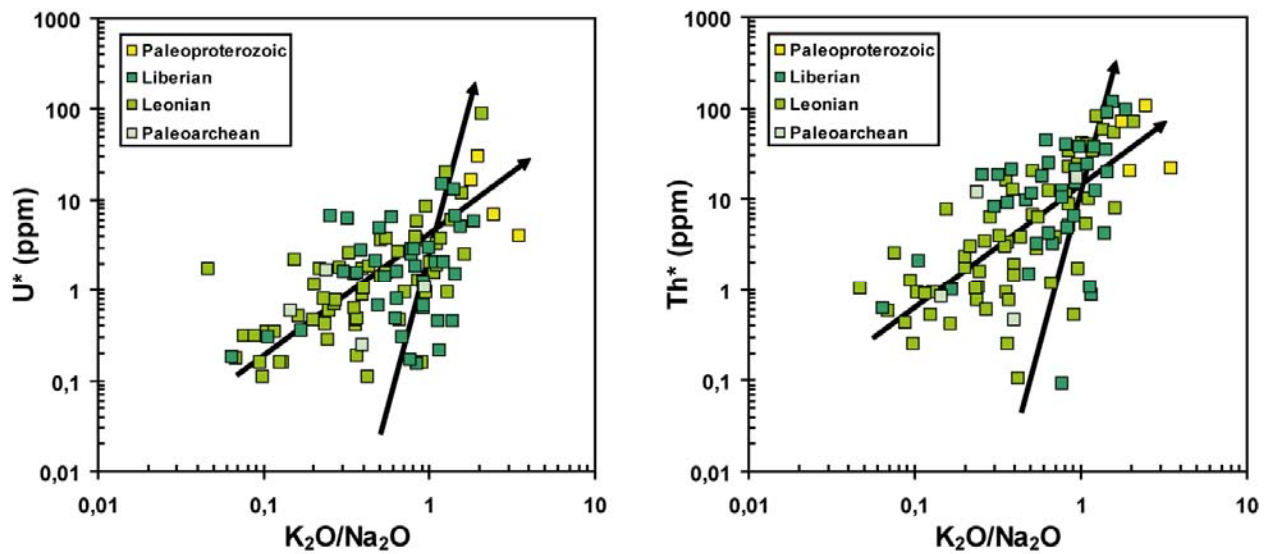


Figure 2.1.10. Th-U variations in the magmatic rocks from south-east Guinea (data from Table 2.1.1).

The lowest U and Th original contents of the Guinean magmatic rocks have been calculated using the present U and Th concentrations of the rocks corrected from the radioactive decay ( $U^*$  and  $Th^*$  in Table 2.1.1). Compared to the  $K_2O/Na_2O$  ratio in Figure 2.1.11,  $U^*$  and  $Th^*$  concentrations in Leonian magmatic rocks are progressively increasing with potassium enrichment of the rocks from 0.1 to 90 ppm U and from 0.7 to 118 ppm Th. This suggests a gradual U and Th enrichment with magmatic fractionation. This evolution is not followed by the Liberian rocks which plot along a sub-vertical trend associated to a remarkably increase in U and Th with almost unchanged  $K_2O/Na_2O$  ratio indicating that at least one other process influences the radioelement contents.



**Figure 2.1.11.**  $Th^*$  and  $U^*$  variations versus  $K_2O/Na_2O$  ratio for the Guinean magmatic rocks (data from Table 2.1.1).  $Th^*$  and  $U^*$  contents (in ppm) are corrected from the radioactive decay.

### **Rare earth element distribution**

The chondrite-normalized REE abundances of the most U- and Th-enriched samples from the Leonian, Liberian and Paleoproterozoic cycle selected for the mineralogical study are presented in Figure 2.1.12 (REE data in Table 2.1.3).

The Leonian and Liberian samples are characterized by a global fractionation pattern similar to that of the average upper continental crust from Taylor and McLennan (1985). They are characterized by higher LREE than HREE abundances corresponding to globally highly fractionated REE patterns with  $[La/Sm]_N = 1.61-3.58$  and  $[Gd/Yb]_N = 1.37-7.27$  generally representative of Archean TTGs (Martin et al., 2005). The Leonian orthogneiss has a weak negative Eu anomaly ( $Eu/Eu^* = 0.73$ ). The Eu anomaly is generally more pronounced in the Liberian granitoids ( $Eu/Eu^* = 0.22-0.85$ ) suggesting stronger plagioclase fractionation in the melts.

The 4 Eburnean samples are characterized by strong fractionated REE patterns with  $[La/Sm]_N = 1.05-3.08$  and  $[Gd/Yb]_N = 6.42-11.96$ , low contents in HREE and a small or even missing negative Eu anomaly. Sample NZE2381 is, however, more enriched in LREE and show the same trend than Closepet-type granites (Martin et al., 2005) which are formed by interaction between a metasomatised mantle magma and products from a low degree of partial melting of the continental crust (Moyen et al., 1997). Sample NZE2393 show the same parallel fractionation trend but is more depleted in REE. The most REE-enriched sample is the syenite DTNZE31a\* with  $\Sigma REE = 614$  ppm. This sample has also distinct anomalous concentrations in Ba = 6248 ppm, Sr = 1798 ppm and Nb = 33.15 ppm (Nb/Ta = 8) that suggest it originates from a different type of magmatism, alkaline or peralkaline.

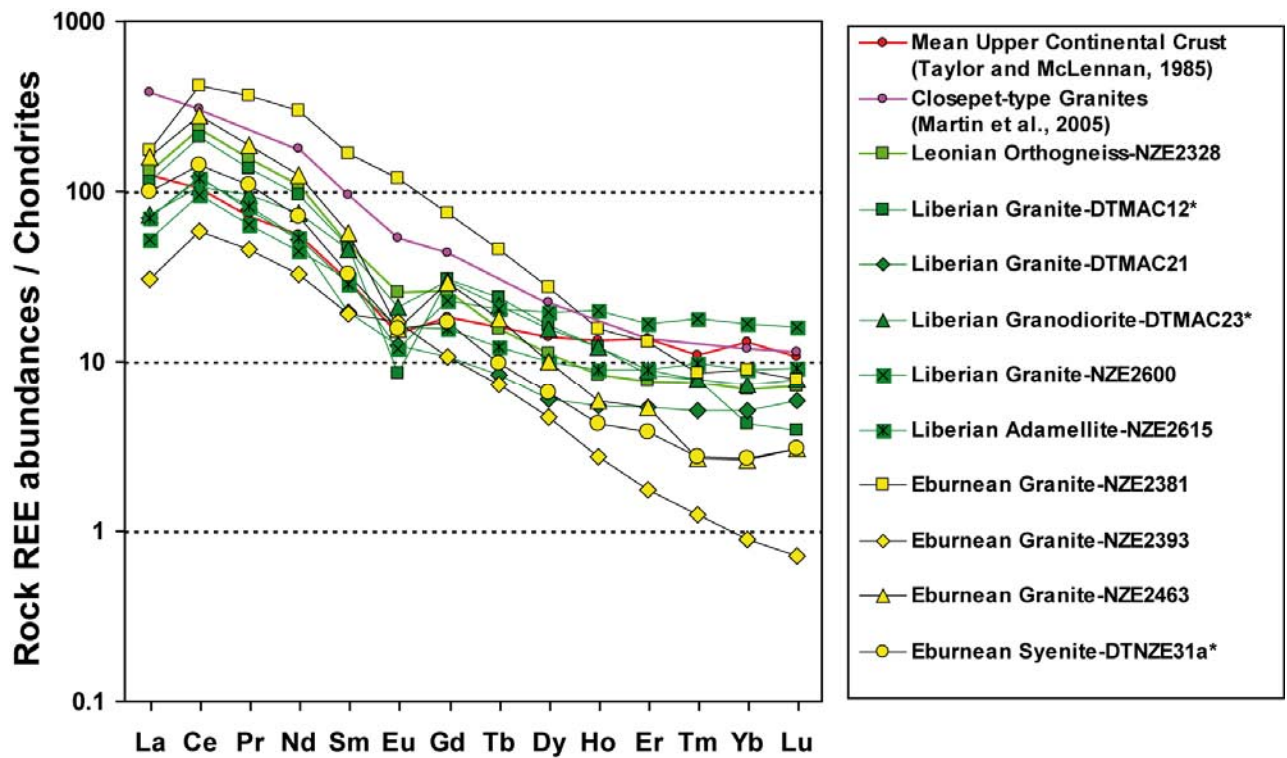


**Figure 2.1.12.** Chondrite-normalized REE spectra of the U-Th-rich samples collected from south-east Guinea. The REE abundances (in ppm) were normalized to the chondrite values C1 from Evensen et al. (1978). The REE distribution of the average upper continental crust from Taylor and McLennan (1985) is given as reference (in red).

### ***Petrographic characteristics***

#### ***- Leonian sample (NZE2328)***

The Leonian orthogneiss is composed mainly of perthitic K-feldspar, quartz and biotite. Quartz is deformed displaying undulous extinction and lobate contacts with neighbouring crystals (Fig. **2.1.13-A**). Formation of myrmekite is observed locally at the edge of the K-feldspar phenocrysts suggesting sub-solidus exsolutions (Fig. **2.1.13-B**). Biotite is partly altered to chlorite and hosts titanite, zircon and monazite rimmed by epidote (Fig. **2.1.13 C to F**). Apatite is disseminated within quartz and feldspar crystals (Fig. **2.1.13-D**). Abundant iron and titanium oxides represent up to 10% of the rock forming minerals which corroborate the high B parameter (=149, Fig. **2.1.6**). Iron oxides occur as large patches and minor titanomagnetite occurs as euhedral grains with a typical hexahedral cross section. Ilmenite is present as very fine lamellae network within the magnetite (Fig. **2.1.13-G**). Hematite has been observed as coating on some of the titanomagnetite suggesting that it is an alteration product of these grains, probably associated to later oxidant fluid circulation (Fig. **2.1.13-H**).

#### ***- Liberian samples (DTMAC12\*, DTMAC21, DTMAC23\*, NZE2600 and NZE2615)***

The Liberian granitoids are composed of both plagioclase and alkali-feldspar phenocrysts, quartz and biotite with the latter being the dominant mafic mineral. Feldspar and quartz show tectonic deformation with deformed twinning and undulous extinction (Fig. **2.1.14 A and B**). Typical polygonal granoblastic textures of quartz with triple junctions also occur. The adamellite sample NZE2615 from the Tounkarata batholith is the most deformed sample with shear bands defined by elongated polycrystalline biotite, epidote and hornblende crystals (Fig. **2.1.14-C**). Chloritization of biotite is very common (Fig. **2.1.14 D and E**) but pervasive sericitization and epidotization of feldspar seems more developed in samples from the Macenta batholith (Fig. **2.1.14-B**). Accessory minerals are mostly zircon and monazite (Fig. **2.1.14-F**), minor apatite (Fig. **2.1.14-G**) and rarely titanite only observed in sample DTMAC23\*. Ilmenite and iron oxides form large aggregates (Fig. **2.1.14-F**) but are less abundant than in the Leonian Gneiss. Hematite is widespread in samples from the Macenta batholith and generally concentrates around zircon and monazite grains (Fig. **2.1.14-H**).

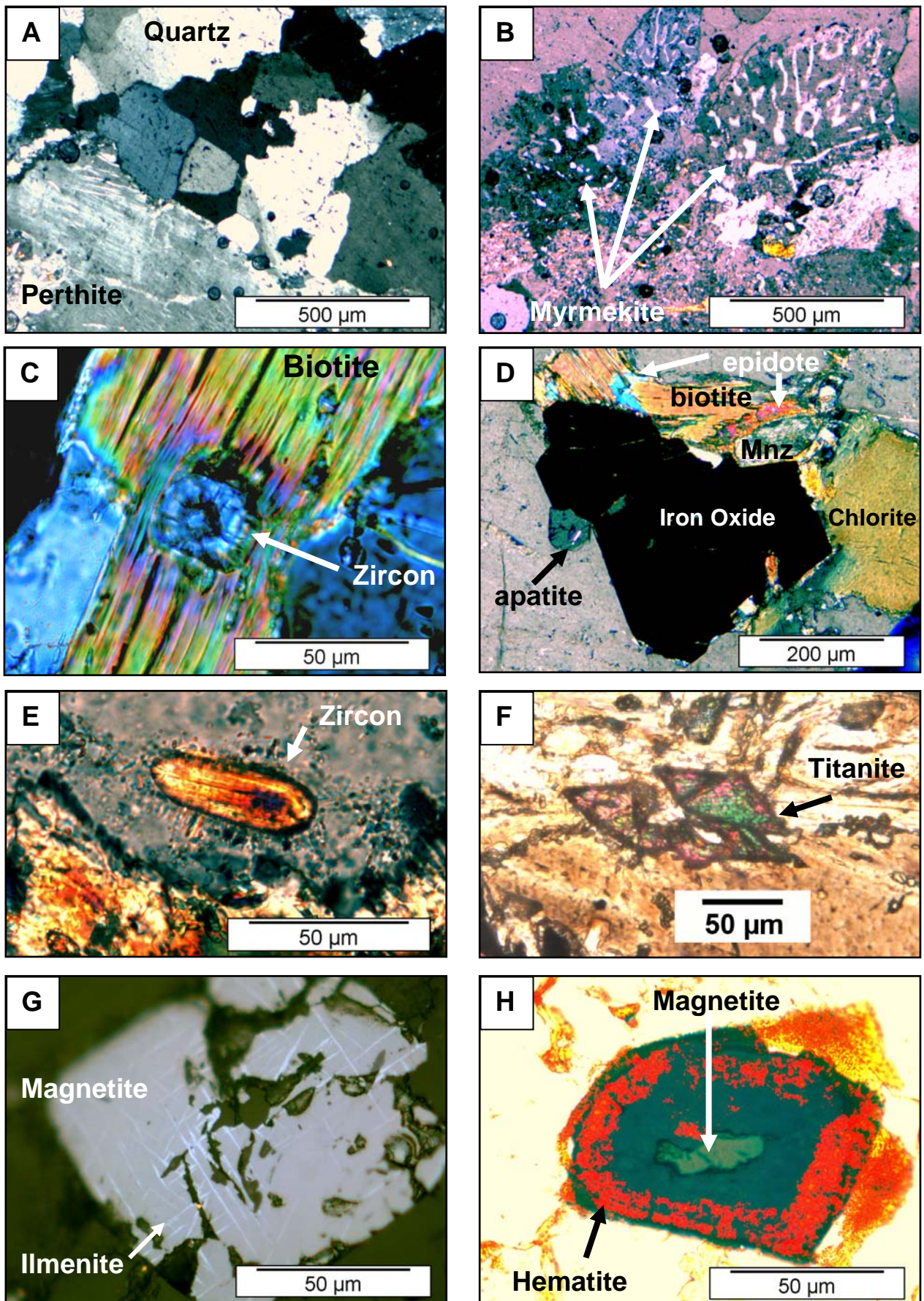


**Figure 2.1.13.** Photomicrographs of Leonian orthogneiss NZE2328: cross nicols transmitted light **A** - perthitic feldspar and quartz with lobate contacts, **B** - myrmekite exsolution at the border of a feldspar, **C** - zoned zircon within biotite, **D** - Monazite rimmed by epidote, **E** - elongated zircon, **F** - titanite with typical wedge-shape and high polarization colours; reflected light **G** - euhedral magnetite crystal with ilmenite lamellae; natural transmitted light **H** - residual magnetite crystal surrounded by hematite.

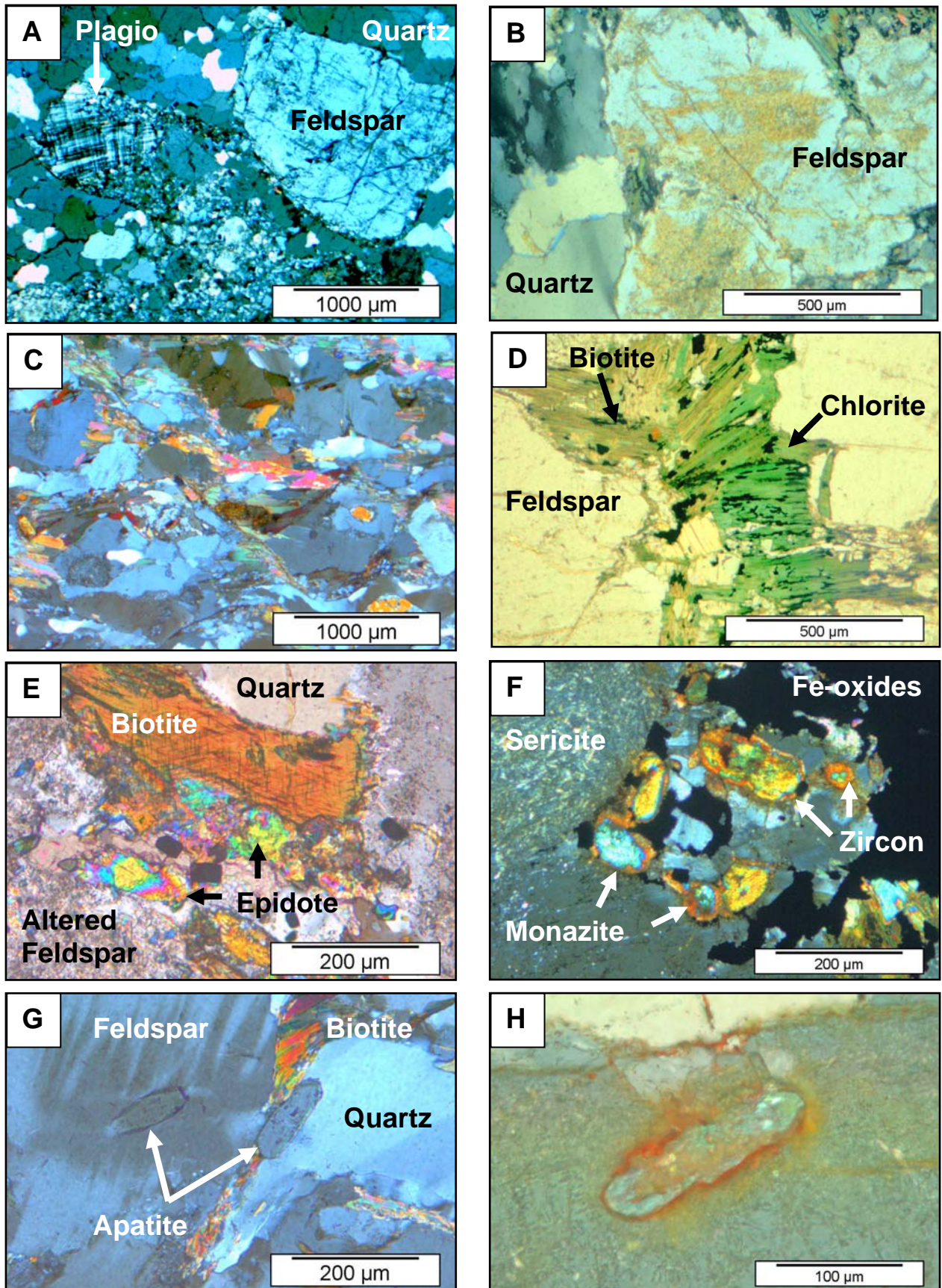


**Figure 2.1.14.** Photomicrographs of Liberian granitoids: crossed nicols transmitted light **A**- deformed twinning plagioclase and fractured feldspar with polycrystalline quartz (NZE2600), **B**- sericitized feldspar and quartz with undulous extinction (DTMAC12\*), **C**- biotite and epidote outlining the schistosity and following curvature of deformed quartz lamellae (NZE2615); natural transmitted light **D**- biotite altered to chlorite (DTMAC12\*); crossed nicols transmitted light **E**- epidotization of biotite and altered feldspar (DTMAC23\*), **F**- monazite and zircon aggregates (DTMAC12\*), **G**- apatite (DTMAC12\*); reflected light: **H**- reddish internal reflection around zircon due to hematite (DTMAC12\*).

*- Paleoproterozoic samples (NZE2381, NZE2393, NZE2463 and DTNZE31a)*

The Eburnean granites (NZE2381, NZE2393, NZE2463) consist mainly of feldspars phenocrysts, quartz and biotite (Fig. **2.1.15 A** and **B**). The dominant feldspar phenocrysts are largely represented by microcline and perthite with only minor and smaller crystals of plagioclase. Quartz is also strongly deformed displaying undulous extinction, lobate contacts and sometimes recrystallized borders. Accessory minerals are mainly apatite, zircon and rare monazite (Fig. **2.1.15 B** and **C**). However, sample NZE2381 shows the presence of abundant sulfides (pyrite and chalcopyrite) filling dissolution cavities (boxworks) generally together with secondary carbonates and hematite with colomorph textures. More rarely, the boxworks show a central residual cubic opaque phase corresponding to altered uraninite (characterized in the following section) (Fig. **2.1.15-D**).

The mineralogy of the Eburnean syenite (DTNZE31a) is dominated by green hornblende, coarse titanite crystals, K-feldspar and epidote (Fig. **2.1.15 E** and **F**). The absence of plagioclase is characteristic of hyper-solvus crystallization conditions typical of alkaline A-type granites (Best, 2003). This syenite is consequently formed from a distinct process and is genetically unrelated to the other Eburnean magmatic rocks as suggested by its bulk rock composition (shoshonitic suite, low REE contents). Quartz is only interstitial and microcrystals display dissolution-recrystallization textures at their margin. Accessories are dominated by iron oxides and apatite generally included in the hornblende (Fig. **2.1.15 E** and **G**). Disseminated euhedral pyrite crystals, up to 200  $\mu\text{m}$  wide (Fig. **2.1.15-H**), have also been noticed.

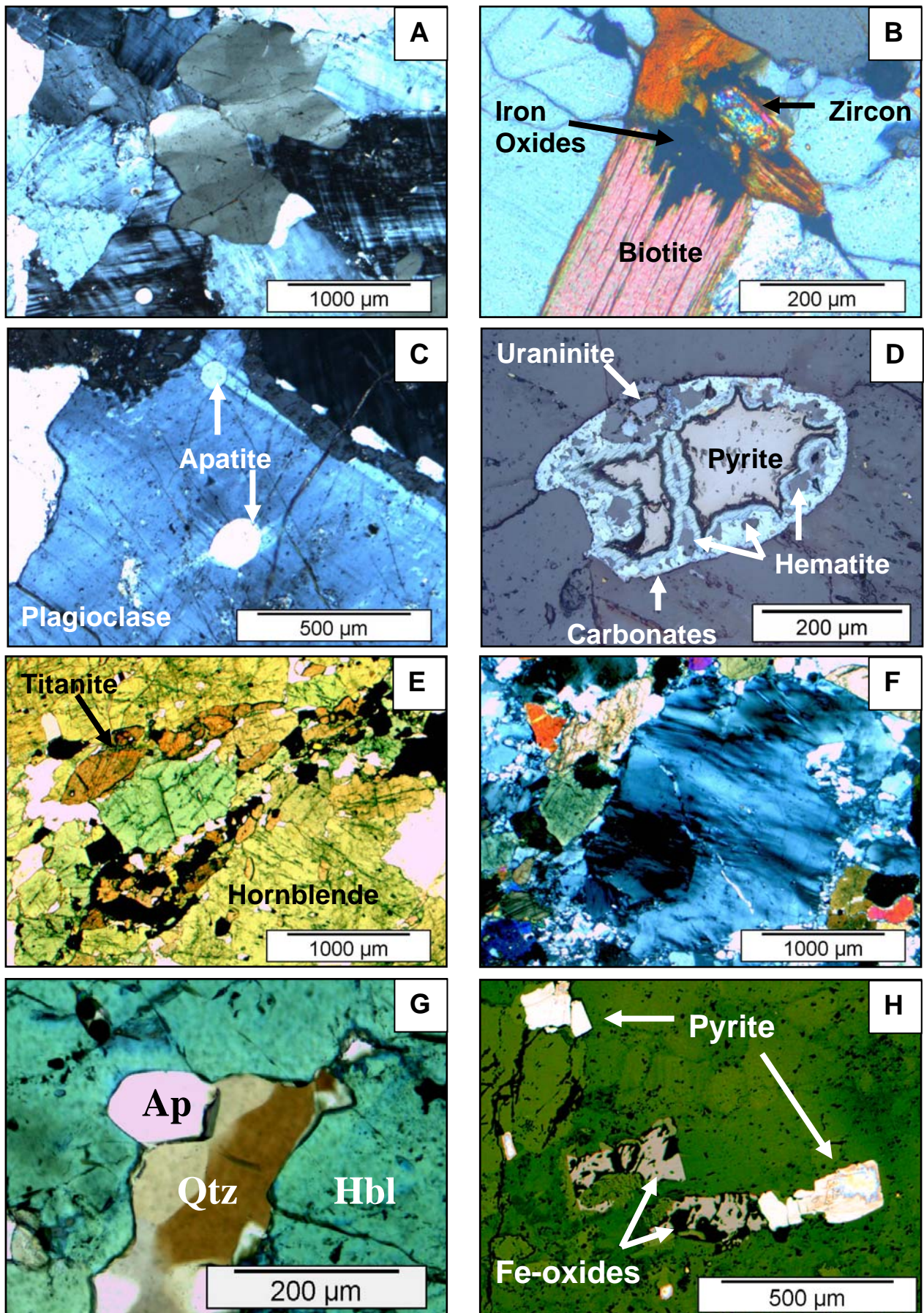


**Figure 2.1.15.** Photomicrographs of Paleoproterozoic samples: crossed nicols transmitted light **A**- quartz with wavy extinction surrounded by K-feldspar phenocrysts (*NZE2381*), **B**- zircon associated with iron oxides within biotite (*NZE2393*), **C**- apatite crystals within plagioclase (*NZE2381*); reflected light **D**- residual euhedral uraninite surrounded by carbonate, hematite and pyrite (*NZE2381*); transmitted light: **E**- brown titanite crystals with green hornblende (*DTNZE31a*); crossed nicols transmitted light: **F**- perthitic K-feldspar surrounded by hornblende (green) and epidote (orange to violet) (*DTNZE31a*), **G**- apatite in typical hexagonal cross section between hornblende and polycrystalline quartz (*DTNZE 31a*); reflected light **H**- Cubes of pyrite and iron oxides (*DTNZE31a*).

**Characterization of U- and Th-bearing minerals**

**Refractory minerals**

The Guinean felsic rocks contain the classical suite of accessories generally found in granites which consist mainly of monazite, apatite, zircon and titanite. The fact that the accessory minerals mainly occur as inclusions within feldspar, quartz or biotite phenocrysts indicates that these accessories are magmatic in origin and form early during crystallization. The typical average uranium and thorium concentrations in these minerals are given in Table 2.1.5.

**Table 2.1.5.** Typical U and Th abundances in accessory minerals (modified from Robb et al., 1990; data after Wedepohl, 1969)

<i>Mineral</i>	<i>General Formula</i>	<i>U (ppm)</i>	<i>Th (ppm)</i>	<i>Th/U</i>
Apatite	(Ca <sub>5</sub> (PO <sub>4</sub> ) <sub>3</sub> (OH,F,Cl))	65 (10-100)	70 (15-250)	1
Titanite	CaTiSiO <sub>5</sub>	280 (10-700)	510 (100-1.000)	1.7
Zircon	ZrSiO <sub>4</sub>	1.330 (100-6.000)	650 (100-1.000)	0.4
Monazite	(LREE,Th,U)PO <sub>4</sub>	3.000 (500-3.000)	125.000 (2.000-200.000)	> 25

Zircon and monazite represent generally the most enriched refractory minerals and usually the solubility of such minerals in fluids are low (Cuney and Friedrich, 1987). However, zircon and monazite in BSE-SEM images generally show complex internal textures with large variations of average atomic number indicative of chemical heterogeneities. Zircon crystals are commonly euhedral and are 10 to 50 µm large and up to 200 µm long (Fig. 2.1.16). They always display well developed concentric zoning associated to progressive magmatic growth. Zircon is variably affected by metamictization with radiative microcracks facilitating probably introduction of water and alteration (darker grey area). Monazite exhibits subhedral to sub-rounded shapes, is 30 to 100 µm in diameter, and shows extremely variable degree of alteration ranging from homogeneous pristine grains with primary uranothorianite inclusions to porous material and dissolution textures with residual crystals of thorite (Fig. 2.1.17).

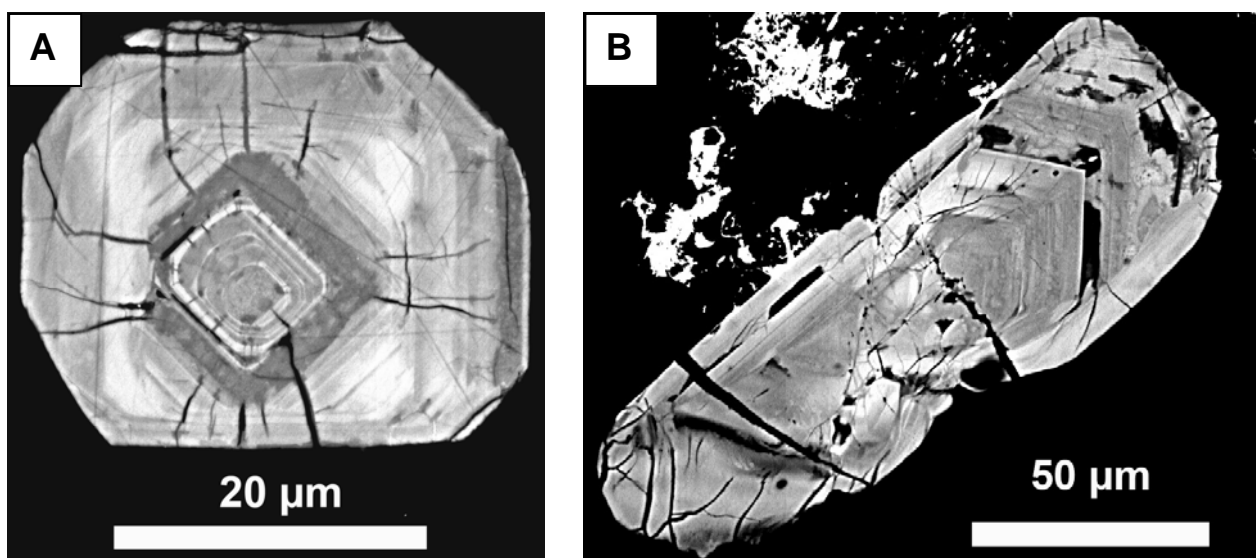


**Figure 2.1.16.** BSE-SEM images of zoned zircon **A** - from Leonian gneiss (NZE2328) showing distinctive average atomic number zones and radial fractures and **B** - from a Liberian granite (DTMAC12\*).

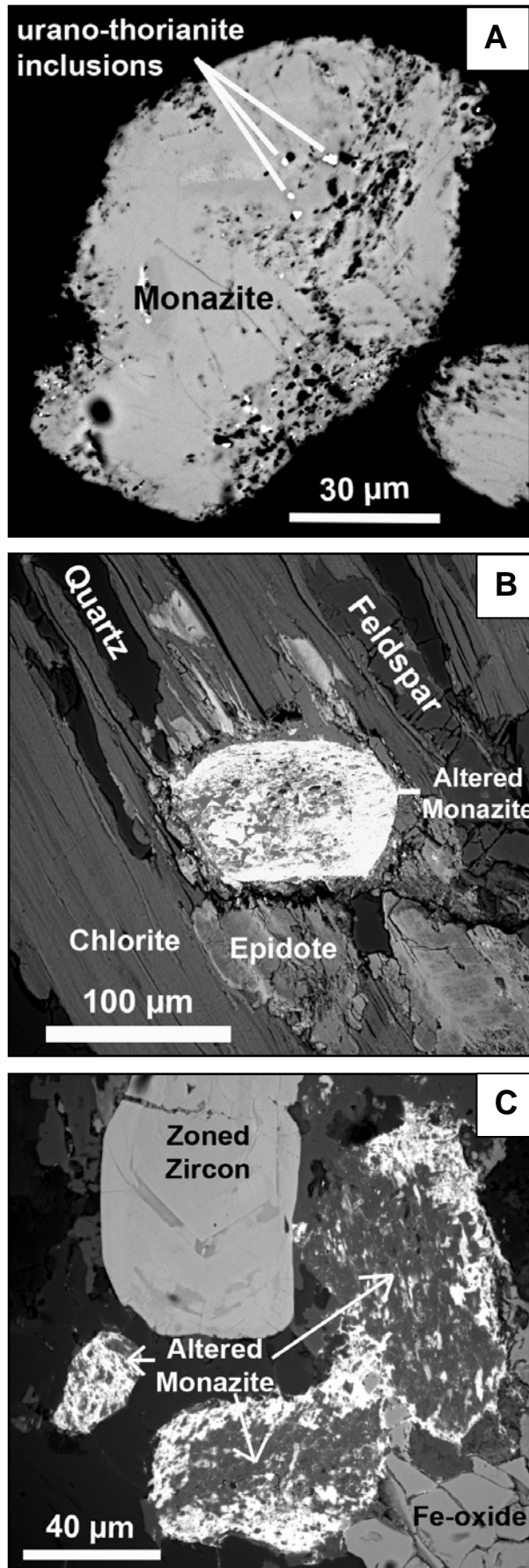


**Figure 2.1.17.** BSE-SEM images of different monazite grains from the Liberian Macenta batholith (DTMAC12\*) and showing various alteration stages presented in increasing order: **A** - relatively pristine monazite with urano-thorianite inclusions, **B** - porous monazite surrounded by a radiation damage rim and **C** - completely altered monazite with huttonite newly formed crystals (light grey).

The average compositions of 42 electron-microprobe analyses of zircon are presented in Table 2.1.6. Zircon from Leonian, Liberian and Eburnean granites show equivalent chemical composition with Zr + Hf + Si oxides representing ~ 95 % of the analytical totals. However, in the darker zones of the BSE-SEM images that correspond to lighter average atomic numbers, mostly calcium (up to 3.38 wt% CaO) and iron (up to 1.6 wt% FeO) enrichments with minor amounts of aluminium (up to 1.75 wt% Al<sub>2</sub>O<sub>3</sub> but generally less than 1 wt%), uranium (up to 1.78 wt% UO<sub>2</sub> but mostly less than 0.5 wt%), thorium (up to 4.12 wt% ThO<sub>2</sub> but mainly below 1wt%), and occasionally phosphorus, titanium and yttrium (< 0.5 wt%) are detected.

**Table 2.1.6.** Representative electron-microprobe analyses of zircon in magmatic rocks

<i>Sample</i>	<i>Leonian Gneiss NZE2328</i>	<i>Liberian Granite DTMAC12*</i>	<i>Eburnean Granite NZE2393</i>
EMPA	14	14	14
ZrO <sub>2</sub>	59.21 ± 4.97	61.18 ± 1.59	59.66 ± 3.96
HfO <sub>2</sub>	1.21 ± 0.22	1.36 ± 0.32	1.43 ± 0.27
SiO <sub>2</sub>	30.86 ± 1.12	31.13 ± 0.55	31.95 ± 0.43
Al <sub>2</sub> O <sub>3</sub>	0.42 ± 0.52	0.26 ± 0.14	0.69 ± 0.56
P <sub>2</sub> O <sub>5</sub>	<D.L.	0.17 ± 0.13	<D.L.
CaO	1.45 ± 0.96	1.63 ± 0.70	1.87 ± 1.07
FeO	1.25 ± 0.35	0.83 ± 0.52	0.74 ± 0.35
TiO <sub>2</sub>	0.07 ± 0.12	<D.L.	<D.L.
Y <sub>2</sub> O <sub>3</sub>	0.30 ± 0.67	<D.L.	<D.L.
PbO	<D.L.	<D.L.	<D.L.
ThO <sub>2</sub>	0.41 ± 1.10	0.17 ± 0.27	0.11 ± 0.15
UO <sub>2</sub>	0.20 ± 0.21	0.21 ± 0.11	0.36 ± 0.33
La <sub>2</sub> O <sub>3</sub>	<D.L.	<D.L.	<D.L.
Dy <sub>2</sub> O <sub>3</sub>	<D.L.	<D.L.	<D.L.
Er <sub>2</sub> O <sub>3</sub>	<D.L.	<D.L.	<D.L.
Yb <sub>2</sub> O <sub>3</sub>	<D.L.	<D.L.	<D.L.
<b>Total</b>	<b>94.23 ± 3.29</b>	<b>97.34 ± 0.87</b>	<b>97.19 ± 2.51</b>

*Notes:* Calculated mean ± standard derivative; <D.L. = below detection limits (Zr = 0.20 wt%; Hf = 0.08 wt%; Si = 0.06 wt%; Al = 0.04 wt%; P = 0.07 wt%; Ca = 0.06 wt%; Fe = 0.14 wt%; Ti = 0.04 wt%; Y = 0.08 wt%; Pb = 0.15 wt%; Th = 0.09 wt%; U = 0.11 wt%; La = 0.14 wt%; Dy = 0.17 wt%; Er = 0.24 wt%; Yb = 0.21 wt%).

In Figure 2.1.18 a negative correlation is obtained between abundances in Zr, Hf and Si and substituting elements: Al, P, Y, Ca, Fe, U and Th almost perfectly plotting on a line with a slope ~1.22 ( $R^2 = 0.98$ ). Introduction of iron is probably related to late alteration or weathering linked to the pervasive hematization shown by the petrographic observations. The negative correlation between U+Th and Zr contents is inferred to the zirconium replacement by radioelements in the crystal lattice during magmatic crystallization. This correlation demonstrate that cationic exchanges are mainly represented by  $2Zr^{4+} \leftrightarrow 2Ca^{2+} + (U,Th)^{4+}$  facilitated because of the close ionic radii of calcium, radioelements and zirconium (1.12 Å for Ca<sup>2+</sup>, 1 Å for U<sup>4+</sup>, 1.05 Å for Th<sup>4+</sup> and 0.84 Å for Zr<sup>4+</sup>). The sum of uranium and thorium contents in zircon remains however low, below 1 at% of the mineral (or 1.5 wt%) and thus, zircon does not contribute significantly

in the radioelement abundances of the whole-rock budget. For example the most U-enriched zircons hosting 3600 ppm U are in Eburnean granite sample NZE2393 which contains 223 ppm Zr. Considering that zircon ( $ZrSiO_4$ ) has only 50% of Zr, the total U budget hosted in zircon grains of the granite can be calculated as follow:  $[(223 \times 10^{-6}) \times 2] \times (3600 \times 10^{-6}) = 1.61$  ppm U. Additionally, the bulk composition of the rock has 5.05 ppm U, zircon contributes to only 32% of total U content in the rock. The same method of calculation gives only 11% of the total U for Liberian granite DTMAC12\* and 10% for Leonien gneiss NZE2328. U and Th are therefore evidently hosted by the other dominant refractory minerals, monazite.

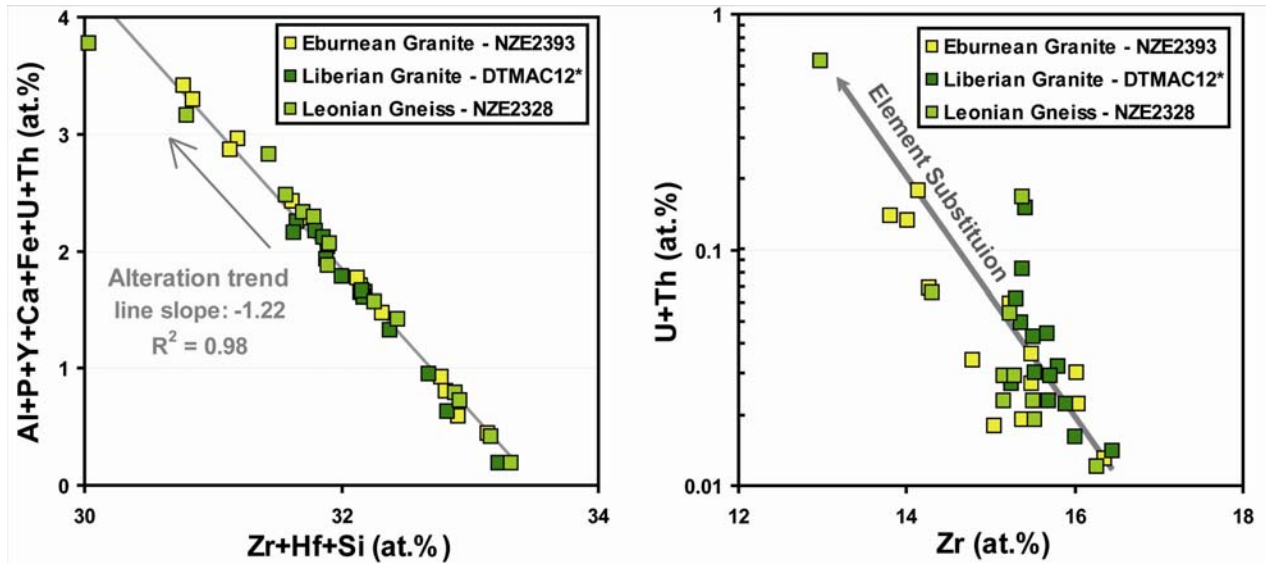


**Figure 2.1.18.** Variations in the major element content composing zircon (Zr+Hf+Si) with minor element content (Al+P+Y+Ca+Fe+U+Th) in atomic percent and increasing radioelement content (U+Th) substitute to Zr.

Samples with the highest Th contents in the whole-rock geochemical analyses (Table 2.1.3) have higher monazite accumulations: the Leonian Gneiss NZE2328 (69.23 ppm Th and Th/U = 5.34), the Liberian granite DTMAC12\* (76.80 ppm Th and Th/U = 17.86) and the Eburnean granite NZE2393 (94.80 ppm Th and Th/U = 18.77).

In the Liberian granite DTMAC12\*, monazite has been observed with various degree of alteration (Fig. 2.1.17). Average chemical compositions of the different phases are presented in Table 2.1.7. This type of alteration has been observed also in the Leonien gneiss NZE2328 but no remaining monazite grains could be found due to their replacement by allanite (Table 2.1.8). Mineralogical and chemical analyses enable to distinguish three stages of monazite evolution:

(i) the primary magmatic stage is related to pristine monazite with high  $P_2O_5$  (24.7-28.2 wt%), LREE ( $\Sigma = 50.3$ -55.3 wt%) and  $ThO_2$  (8.6-15.6 wt%) contents and low concentrations in  $SiO_2$  (1.2-4 wt%),  $Y_2O_3$  (0.86-2.67 wt%), CaO (0.5-1.3 wt%), PbO (1.05-1.44 wt%) and  $UO_2$  (0.22-0.40 wt%). Urano-thorianite inclusions consisting mostly of 68.9 wt%  $ThO_2$ , 7.4 wt%

PbO, 6.9 wt% UO<sub>2</sub>, moderate concentrations of LREE ( $\Sigma = 6.67$  wt%) and P<sub>2</sub>O<sub>5</sub> (3.15 wt%) where probably incorporated during the growths of the crystal.

**Table 2.1.7.** Representative electron-microprobe analyses of the monazite group minerals from the Liberian granite DTMAC12\*

Sample	Liberian Granite DTMAC12*					
	Monazite 1	Monazite 2	Monazite 3	Average Monazite	Uranothorianite inclusion	Huttonitic Monazite
EMPA	5	5	6	16	1	2
Al <sub>2</sub> O <sub>3</sub>	<D.L.	<D.L.	<D.L.	<D.L.	0.11	1.15 ± 0.01
SiO <sub>2</sub>	1.33 ± 0.08	1.55 ± 0.09	2.16 ± 1.07	1.71 ± 0.72	0.42	16.42 ± 1.74
P <sub>2</sub> O <sub>5</sub>	28.05 ± 0.13	27.89 ± 0.23	26.78 ± 1.40	27.52 ± 1.01	3.15	6.96 ± 1.56
CaO	1.25 ± 0.04	1.02 ± 0.13	0.92 ± 0.33	1.06 ± 0.25	0.64	3.02 ± 2.18
TiO <sub>2</sub>	<D.L.	<D.L.	<D.L.	<D.L.	<D.L.	0.73 ± 0.17
MnO	<D.L.	<D.L.	<D.L.	<D.L.	<D.L.	<D.L.
FeO	<D.L.	<D.L.	<D.L.	<D.L.	<D.L.	1.00 ± 0.40
Y <sub>2</sub> O <sub>3</sub>	2.53 ± 0.12	1.87 ± 0.35	1.85 ± 0.79	2.07 ± 0.59	0.73	5.85 ± 1.47
ZrO <sub>2</sub>	<D.L.	<D.L.	<D.L.	<D.L.	<D.L.	2.15 ± 0.02
La <sub>2</sub> O <sub>3</sub>	14.34 ± 0.14	14.89 ± 0.77	14.24 ± 0.31	14.47 ± 0.53	1.70	0.64 ± 0.38
Ce <sub>2</sub> O <sub>3</sub>	25.85 ± 0.22	26.64 ± 1.07	25.96 ± 0.68	26.14 ± 0.77	3.37	2.02 ± 0.29
Pr <sub>2</sub> O <sub>3</sub>	2.18 ± 0.02	2.17 ± 0.05	2.14 ± 0.05	2.16 ± 0.04	0.37	0.28 ± 0.05
Nd <sub>2</sub> O <sub>3</sub>	7.48 ± 0.02	7.59 ± 0.13	7.78 ± 0.10	7.63 ± 0.16	0.98	1.45 ± 0.06
SmO	1.33 ± 0.04	1.29 ± 0.18	1.40 ± 0.05	1.34 ± 0.11	0.25	0.71 ± 0.09
ThO <sub>2</sub>	9.74 ± 0.10	9.81 ± 0.75	11.44 ± 2.47	10.40 ± 1.70	68.87	48.51 ± 0.54
UO <sub>2</sub>	0.33 ± 0.02	0.30 ± 0.05	0.32 ± 0.05	0.32 ± 0.04	6.92	1.00 ± 0.03
PbO	1.30 ± 0.07	1.30 ± 0.14	1.23 ± 0.16	1.27 ± 0.13	7.40	<D.L.
Total	95.72 ± 0.11	96.36 ± 0.49	96.24 ± 0.70	96.11 ± 0.56	94.94	91.89 ± 2.21
End-member molecules (in mole fractions)						
Monazite-Ce [CePO <sub>4</sub> ]	0.834 ± 0.003	0.844 ± 0.015	0.832 ± 0.012	0.837 ± 0.012		0.304 ± 0.094
Huttonite [ThSiO <sub>4</sub> ]	0.055 ± 0.003	0.055 ± 0.004	0.088 ± 0.040	0.071 ± 0.027		0.531 ± 0.013
Brabantite [CaTh(PO <sub>4</sub> ) <sub>2</sub> ]	0.110 ± 0.003	0.091 ± 0.013	0.080 ± 0.031	0.093 ± 0.023		0.165 ± 0.107

**Notes:** Calculated mean ± standard derivative; <D.L. = below detection limits (Al = 0.05 wt%; Si = 0.05 wt%; P = 0.05 wt%; Ca = 0.05 wt%; Ti = 0.04 wt%; Mn = 0.15 wt%; Fe = 0.13 wt%; Y = 0.11 wt%; Zr = 0.21 wt%; La = 0.24 wt%; Ce = 0.27 wt%; Pr = 0.14 wt%; Nd = 0.17 wt%; Sm = 0.14 wt%; Th = 0.10 wt%; U = 0.09 wt%; Pb = 0.31 wt%).

(ii) the second stage is interpreted as the transformation of monazite into huttonite. The pseudomorphic replacement of monazite grains (Fig. 2.1.17-C) shows higher average atomic numbers that correspond to extreme decreases in P<sub>2</sub>O<sub>5</sub> (5.9-8.1 wt%) and LREE ( $\Sigma = 4.7-5.5$  wt%) than values of the pristine monazite. However, ghost-like minerals display much higher contents in SiO<sub>2</sub> (15.2-17.7 wt%), CaO (1.5-4.6 wt%), Y<sub>2</sub>O<sub>3</sub> (4.8-6.9 wt%), ThO<sub>2</sub> (48.1-48.9 wt%) and UO<sub>2</sub> (0.98-1.02 wt%), traces of Ti, Fe and Zr and disappearance of Pb. Finally, lower analytical totals could be linked to water incorporation. Hydration of the monazite together with P and REE leaching are common features observed during metamictization of monazite (Cuney and Mathieu, 2000; Hecht and Cuney, 2000). It is generally associated to leaching of U and Pb in the fluids whereas insoluble Th forms thorite. Uranium seems to remain in the crystal lattice and reconcentrates locally. The variations in the monazite chemical composition have been represented in the ternary system of the end-member molecules huttonite, monazite-(Ce) and brabantite (Fig. 2.1.19). The pristine monazite grains are part of the “common” monazite-(Ce)

end-member whereas the alteration products have an intermediate composition between the three end-member molecules, mainly monazite-(Ce) and huttonite with a lower contribution of brabantite. This solid solution is known as cheralite (Bowie and Horne, 1953) or huttonitic monazite (Förster, 1998). This monazite transformation is accompanied by relative U, Th and Si enrichments and leaching of LREE and P.

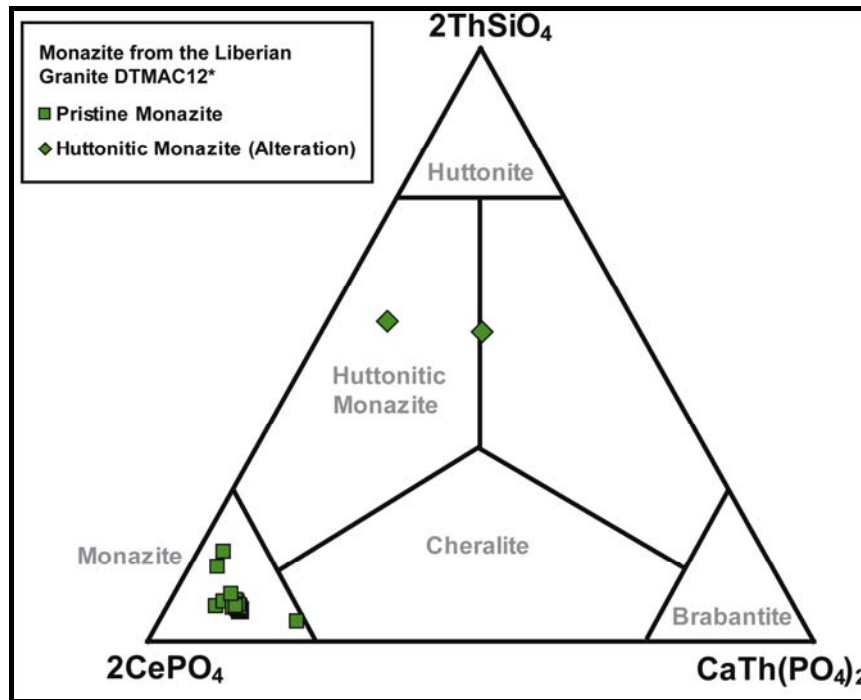


**Figure 2.1.19.** Distribution of monazite compositions from the Liberian granite DTMAC12\* represented in the ternary system of the end-member molecules (diagram from Bowie and Horne, 1953 and Förster, 1998).

(iii) a third stage associated to alteration of monazite by calcic-fluids and to the newformation of epidote and allanite. Monazite grains in Leonian and Liberian rocks are mainly hosted in biotite and are frequently surrounded by authigenic epidote ranging 10 to 100  $\mu\text{m}$  wide aureoles (Fig. 2.1.13-D, 2.1.14-E, 2.1.17-B). BSE imaging and EDS analyses reveal that aureoles are partly composed of allanite forming agglomerated small elongated crystals in contact with monazite (Fig. 2.1.20). Also, fibrous crystals of allanite are sometime developed from monazite along the cleavage of surrounding biotite crystals. Small prismatic euhedral apatite of few microns large are often closely associated to altered monazite adjacent or within epidote-allanite aureoles and are inferred to secondary crystallization of phosphate associated to P leaching from monazite. The inner part of monazite shows very complex internal heterogeneities in BSE-SEM images corresponding to replacement by mosaic of small allanite crystals. The chemical analyses of monazite from the Leonian gneiss (Table 2.1.8) also show highly variable Y ( $\text{Y}_2\text{O}_3 = 0.2\text{-}3.1$  wt%), REE ( $\Sigma\text{REE} = 5.3\text{-}10.6$  wt%) and Th ( $\text{ThO}_2 = 1\text{-}3.1$  wt%) concentrations. Uranium concentration in allanite is below the detection limit ( $< 0.07$  wt%). The low totals of the analyses indicate a strong hydration of the crystals. The new formation of allanite at the expend of

monazite in these granites indicates that calcium-bearing fluids are responsible of this alteration. Monazite is not stable in equilibrium with melts or fluids with high Ca-activity (Cuney and Friedrich, 1987). Authigenic epidote wrapping the altered monazite grains and allanite observed as replacement phases within the residual minerals or as elongated crystals filling the surrounded biotite's cleavage have crystallized from the reaction between the calcic fluids and the LREE mobilized from the altered monazite-(Ce).

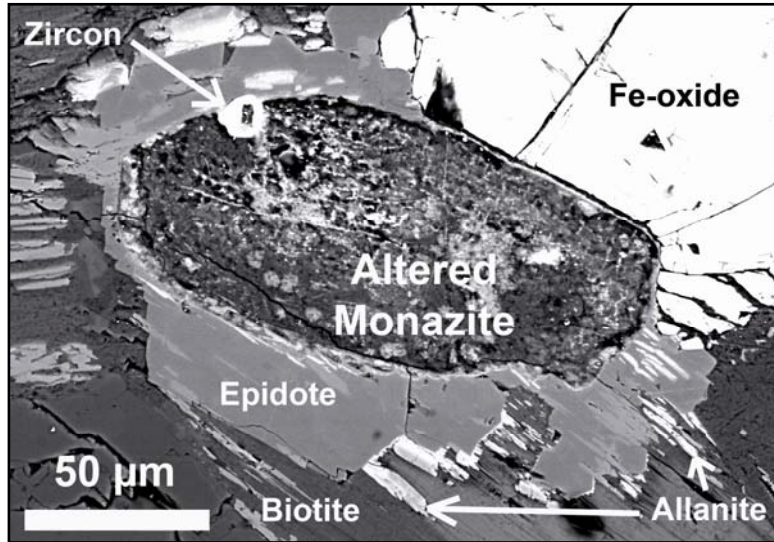


**Figure 2.1.20.** BSE-SEM image of an altered monazite grain surrounded by an epidote aureole in the Leonian gneiss (sample NZE2328). Note the radial fractures in Fe-oxides and the fibrous allanite crystals developed from monazite and elongated along the biotite's cleavage.

**Table 2.1.8.** Representative electron-microprobe analyses of alteration material within monazite from the Leonian gneiss NZE2328.

<i>Sample</i>	<i>Leonian Gneiss NZE2328</i>
<i>3 monazite grains replaced by allanite</i>	
EMPA	14
Al <sub>2</sub> O <sub>3</sub>	11.57 ± 1.58
SiO <sub>2</sub>	34.50 ± 3.54
P <sub>2</sub> O <sub>5</sub>	0.24 ± 0.08
CaO	11.93 ± 2.77
TiO <sub>2</sub>	0.77 ± 0.16
MnO	0.29 ± 0.10
FeO	13.32 ± 1.60
Y <sub>2</sub> O <sub>3</sub>	0.59 ± 0.72
ZrO <sub>2</sub>	0.73 ± 0.26
La <sub>2</sub> O <sub>3</sub>	2.67 ± 2.03
Ce <sub>2</sub> O <sub>3</sub>	3.61 ± 0.89
Pr <sub>2</sub> O <sub>3</sub>	0.54 ± 0.32
Nd <sub>2</sub> O <sub>3</sub>	1.98 ± 1.34
SmO	0.37 ± 0.29
Gd <sub>2</sub> O <sub>3</sub>	0.23 ± 0.31
ThO <sub>2</sub>	1.80 ± 0.59
UO <sub>2</sub>	<D.L.
PbO	0.63 ± 0.17
<b>Total</b>	<b>85.82 ± 3.36</b>

*Notes:* Calculated mean ± standard derivative; <D.L. = below detection limits (Al = 0.05 wt%; Si = 0.04 wt% ; P = 0.04 wt%; Ca = 0.06 wt%; Ti = 0.03 wt% ; Mn = 0.10 wt% ; Fe = 0.09 wt%; Y = 0.09 wt%; Zr = 0.14 wt% ; La = 0.19 wt% ; Ce = 0.14 wt% ; Pr = 0.10 wt% ; Nd = 0.12 wt% ; Sm = 0.11 wt% ; Gd = 0.19 wt% ; Th = 0.05 wt%; U = 0.07 wt% ; Pb = 0.22 wt%).

*Uranium oxides*

In the Eburnean high-K calc-alkaline granite NZE2381, a distinct U-Th bearing accessory mineral paragenesis has been observed. The granite is very felsic ( $B = 16.5$ ) with low Ca-content and is slightly peraluminous ( $A/CNK=1.04$ ). The U concentration is elevated (22.2 ppm) for relatively low REE ( $\Sigma REE=85$  ppm) and Th (18.4 ppm) contents, conferring a low Th/U ratio of 0.8 to the rock. Monazite and zircon are rare ( $Zr = 34$  ppm) but uraninite is present. Some of the uraninite grains are partly to totally dissolved and can be typically identified from the remaining boxworks with preservation of cubic cavities and surrounding damage ring (Fig. 2.1.21-A). Boxworks are generally replaced by secondary carbonates, hematite, pyrite and chalcopyrite in paragenetic order. Only two euhedral grains of 30-40  $\mu m$  wide are preserved (Fig. 2.1.21 B and C).

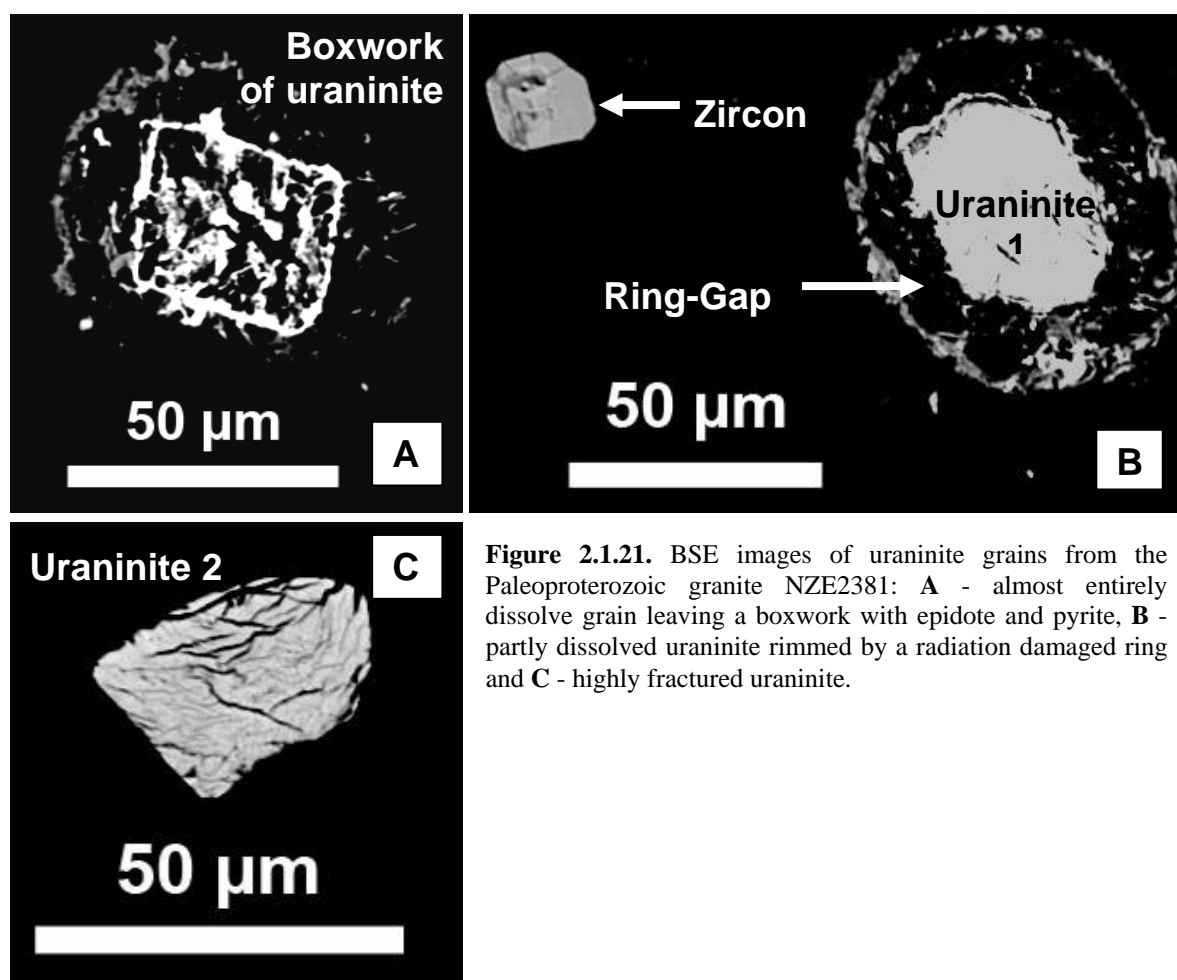


**Figure 2.1.21.** BSE images of uraninite grains from the Paleoproterozoic granite NZE2381: **A** - almost entirely dissolve grain leaving a boxwork with epidote and pyrite, **B** - partly dissolved uraninite rimmed by a radiation damaged ring and **C** - highly fractured uraninite.

The analytical totals vary from 83.27 to 96.40 wt%, with uranium content ranging from 59.63 to 69.07 wt%  $UO_2$  (Table 2.1.9). The low totals reflect the hydration of the mineral. The Pb and Th contents are elevated and vary from 14.64 to 18.15 wt%  $PbO$  and from 3.11 to 6.59 wt%  $ThO_2$ . The  $Y_2O_3$  contents are close to 1 wt%, and CaO content half a percent.  $SiO_2$ ,  $K_2O$ ,  $SO_2$ ,  $TiO_2$  and FeO contents are always below 1 wt%.

**Table 2.1.9.** Representative electron-microprobe analyses of uraninite in the Paleoproterozoic granite NZE2381 and calculated chemical ages.

Uraninite grain EMPA spot	1						2			Average (9)
	#1	#2	#3	#4	#5	#6	#1	#2	#3	
Na <sub>2</sub> O	<D.L.	<D.L.	<D.L.	<D.L.	<D.L.	<D.L.	<D.L.	<D.L.	<D.L.	<D.L.
MgO	<D.L.	<D.L.	<D.L.	<D.L.	<D.L.	<D.L.	<D.L.	<D.L.	<D.L.	<D.L.
Al <sub>2</sub> O <sub>3</sub>	<D.L.	<D.L.	<D.L.	<D.L.	<D.L.	<D.L.	<D.L.	<D.L.	<D.L.	<D.L.
SiO <sub>2</sub>	0.49	0.82	<D.L.	0.51	0.51	2.24	0.39	0.66	0.22	0.66 ± 0.63
P <sub>2</sub> O <sub>5</sub>	<D.L.	0.22	<D.L.							
SO <sub>2</sub>	0.35	0.39	0.74	0.56	0.45	0.72	0.67	0.89	0.51	0.59 ± 0.18
K <sub>2</sub> O	0.21	0.19	<D.L.	<D.L.	0.24	<D.L.	0.18	<D.L.	0.19	0.18 ± 0.03
CaO	0.54	0.68	0.47	0.27	0.31	0.47	0.58	0.38	0.41	0.46 ± 0.13
TiO <sub>2</sub>	0.51	0.73	<D.L.	<D.L.	<D.L.	0.16	<D.L.	<D.L.	<D.L.	0.17 ± 0.27
V <sub>2</sub> O <sub>3</sub>	<D.L.	<D.L.	<D.L.	<D.L.	<D.L.	<D.L.	<D.L.	<D.L.	<D.L.	<D.L.
MnO	<D.L.	<D.L.	<D.L.	<D.L.	<D.L.	<D.L.	<D.L.	<D.L.	<D.L.	<D.L.
FeO	0.38	0.59	<D.L.	0.50	<D.L.	1.80	<D.L.	0.51	0.41	0.54 ± 0.49
Y <sub>2</sub> O <sub>3</sub>	0.88	0.86	0.99	0.59	0.76	0.73	0.64	0.79	0.80	0.78 ± 0.12
ZrO <sub>2</sub>	<D.L.	<D.L.	<D.L.	<D.L.	<D.L.	<D.L.	<D.L.	<D.L.	<D.L.	<D.L.
MoO <sub>3</sub>	<D.L.	<D.L.	<D.L.	<D.L.	<D.L.	<D.L.	<D.L.	<D.L.	<D.L.	<D.L.
La <sub>2</sub> O <sub>3</sub>	<D.L.	<D.L.	<D.L.	<D.L.	<D.L.	<D.L.	<D.L.	<D.L.	<D.L.	<D.L.
Ce <sub>2</sub> O <sub>3</sub>	<D.L.	<D.L.	<D.L.	<D.L.	<D.L.	<D.L.	<D.L.	<D.L.	<D.L.	<D.L.
PbO	14.64	16.47	16.82	18.15	17.25	17.94	17.03	16.85	15.19	16.70 ± 1.16
ThO <sub>2</sub>	6.59	6.30	5.24	3.59	3.53	5.06	4.15	3.11	5.44	4.78 ± 1.25
UO <sub>2</sub>	61.67	68.88	69.07	65.62	66.23	62.22	60.27	59.63	63.85	64.16 ± 3.51
Total	86.72	96.40	93.87	90.12	89.81	91.93	84.34	83.27	87.18	89.29 ± 4.35
Chemical age ± error	680±25	1495±42	1524±44	1702±49	1620±46	1750±49	1726±47	1732±47	1491±40	

**Notes:** Average = Calculated mean ± standard derivative; <D.L. = below detection limits (Na = 0.20 wt%; Mg = 0.08 wt%; Al = 0.06 wt%; Si = 0.04 wt%; P = 0.07 wt%; S = 0.06 wt%; K = 0.14 wt%; Ca = 0.04 wt%; Ti = 0.08 wt%; V = 0.15 wt%; Mn = 0.09 wt%; Fe = 0.11 wt%; Y = 0.14 wt%; Zr = 0.17 wt%; Mo = 0.24 wt%; La = 0.21 wt%; Ce = 0.17 wt%; Pb = 0.24 wt%; Th = 0.21 wt%; U = 0.21 wt%); Pb/U calculated from the Pb and U contents in atomic percent; chemical age calculated from Pb/U ratio and error from the standard derivative (method of Cocherie and Albarède, 2001).

Pb/U ratios of the uraninites range from 0.29 to 0.35. Corresponding chemical ages are between 680 and 1750 Ma for uraninite 1 and from 1491 Ma to 1732 Ma for grain 2 (Table 2.1.9). In Figure 2.1.22, 9 chemical ages are grouped and define a mean at  $1671 \pm 95$  Ma. Only one data gives a younger age at  $680 \pm 25$  Ma. However, the mean square of weighted deviates parameter (MSWD) considering the best age population (N=8) is 6.3 and the high  $2\sigma$  variation of the mean ( $\pm 95$  Ma) show that chemical ages are not referring to one event. The chemical ages are younger than the crystallization age of the granite at 2.1-2.0 Ga (Lahondère et al., 1999a-b; Thiéblemont et al., 1999a) due to lead diffusion outside of the uraninite structure. The data being relatively grouped, the chemical age may reflect a Mesoproterozoic thermal event.

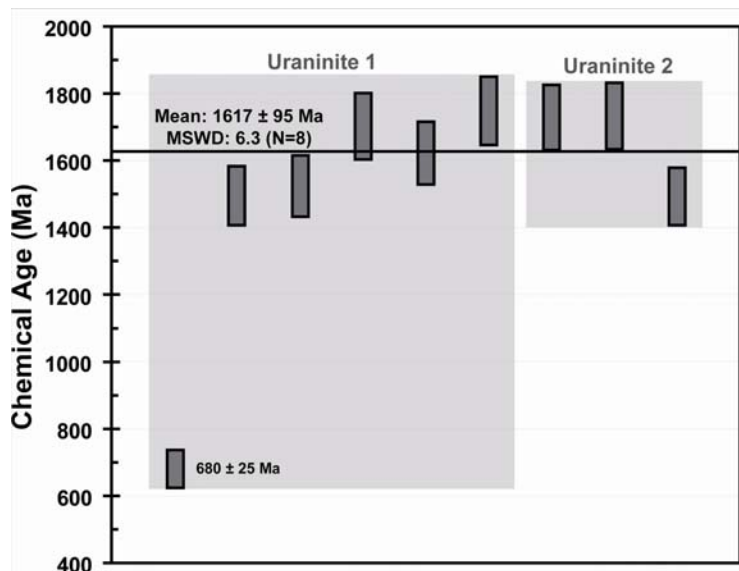


**Figure 2.1.22.** Distribution of the chemical age dating in uraninite from the Eburnean granite NZE2381.

## DISCUSSION AND CONCLUSIONS

### *Provenance and geochemical characteristics of the magmatic suites*

The magmatic rocks from southeast Guinea aged between 3.5 and 2.0 Ga are characterized by different bulk chemical compositions which show that they are issued from various natures of protolithes and involving different melting processes associated to crustal evolution through the geological time.

The old tholeiitic volcanites > 2.9 Ga represented by Paleoproterozoic eclogites and the Leonian mafic to ultra-mafic rocks represent the mantle derived relics of the volcanic activity which has formed the oceanic crust in Early Archean time (Thiéblemont, 2004). These volcanic rocks are poor in quartz ( $Q < 100$ ), have low  $K_2O/Na_2O$  ratios ( $< 1$ ), are highly mafic ( $B > 200$ ), and metaluminous ( $-400 < A < -100$ ).

Beside oceanic arc magmatism, the Archean Kénéma-Man continental nucleus is formed by melt of the subducting slab with mantle wedge interaction producing the Leonian TTG-type magmas (Thiéblemont et al., 2001; Thiéblemont, 2004). The first melts between 3.5 and 2.95 Ga have mainly intermediate to acid compositions with low to medium-K calc-alkaline typology. They are rich in quartz ( $100 < Q < 200$ ) and plagioclase ( $P < -150$ ) and are metaluminous ( $-150 < A < 0$  and  $0.5 < A/CNK < 1$ ). However, some Paleoproterozoic and Leonian felsic rocks that have slightly peraluminous compositions indicate the early incorporation of older continental crust ( $> 3.5$  Ga). The Archean continental crust grow from continuous subduction with incorporation of older TTGs in the magmas, producing more felsic plutonic rocks as the studied orthogneiss sample NZE2328 with medium to high-K calc-alkaline typology ( $K_2O/Na_2O \geq 1$  and  $-100 < P < 50$ ) and becoming slightly peraluminous ( $A > 0$  and  $A/CNK > 1$ ).

The Liberian granitoids (2.9-2.8 Ga) forming the Tounkarata and Macenta batholiths represent a more differentiated Archean magmatism with slightly peraluminous composition ( $-10 < A < +55$ ) and high-K calc-alkaline typology. The strong enrichment in incompatible elements compared to the Leonian rocks (up to 10 ppm U and 100 ppm Th) cannot be explained by a simple crustal differentiation (Fig. 2.1.11). Thiéblemont (2004) suggested that granulitization could be at the origin of the Liberian granitoids, probably associated to a major heating event at the base of the continental lithosphere which was involved by an asthenospheric mantle plume or the lower crust delamination.

The Paleoproterozoic granites were emplaced within various Leonian and Liberian Archean rocks during a period of crustal accretion between 2.3 to 2.05 Ga (Thiéblemont et al., 2004). The

Eburnean Orogeny is more developed to the east of Guinea, in the Paleoproterozoic domain covering partly the Ivory Coast and Burkina Faso (Vidal et al., 2009). In the studied Kénéma-Man domain, Guinean Eburnean granites are enriched in incompatible elements: Rb = 130-230 ppm, Th = 18-95 ppm, U = 5-22 ppm and  $\Sigma$ REE = 85-379 ppm. They have a typical high-K calc-alkaline affinity ( $K_2O/Na_2O > 5$ ) with slightly peraluminous composition. Sample NZE2381 hosting uraninite displays chondrite-normalized REE pattern similar to the Closepet-type granites (Martin et al., 2005) resulting from the mixture between a metasomatised mantellic magma and the low degree of partial melting of the continental crust (Moyen et al., 1997). The Eburnean syenite has a distinct metaluminous and shoshonitic composition enriched in Ba, Sr, Nb and REE corresponding to an alkaline post-orogenic magmatism. The Eburnean Orogeny induced slight partial melting of older Archean lithologies and the parental rock compositions give the various affinities to the resultant melts.

### ***The primary uranium and thorium distribution***

The composition of the Guinean magmatic rocks evolved clearly with the magmatic differentiation showing the progressive enrichment in U and Th with increasing silica, potassium contents and aluminosity index (A/CNK) (Fig. 2.1.9 and 2.1.11).

The Archean granitoids are generally poorer in U and Th relatively to the present continental crust but in the most felsic terms of each magmatic cycles, in the weakly peraluminous rocks ( $1 < A/CNK < 1.3$ ), U and Th may reach some tens of ppm. The Th/U ratios are always higher than 2 and these elements are therefore dominantly located within refractory minerals as monazite-(Ce) with uranothorianite inclusions, zircon, apatite or titanite. The increasing incompatible element concentrations and Th/Yb and Ta/Yb ratios (Fig. 2.1.7) are thought to be related to increasing continental crust contamination although reflecting the increasing volume of crust formed.

The high-K Eburnean granitoids formed by partial melting of the Leonian and Liberian TTGs hosts the most abundant U and Th concentrations. Granite NZE 2381 has up to 22 ppm U with a Th/U ratio below 1 permitting the crystallization of uraninite with moderate Th contents (3.11 to 6.59 wt%  $ThO_2$ ) attesting of its magmatic origin (Cuney and Friedrich, 1987). This uranium oxide occurrence shows that the TTGs can be considered as pre-enriched source rocks for the next generation of magmas. However, the degree of partial melting is probably of major importance in this case for the radioelement fractionation. Low partial melting at low temperature ( $\sim 600^\circ C$ ) access to segregate the incompatible elements in the melt but higher

temperature would drown them in more volumetric melt (Cuney and Kyser, 2008). The presence of uraninite within the Paleoproterozoic granites which derive from Archean rocks with relatively low U and Th contents requires low degree of partial melting.

The large diversity of the Guinean magmatic rocks have widely variable radioelement concentrations that are influenced by three main factors:

(1) the composition of the source rock(s) more or less enriched in U and Th:

- for the Paleoarchean and Leonian rocks involving a basaltic protolithe, mantle interaction pre-enriched by melt of the subducted slab, and progressive rise of the crustal contamination;
- for the Liberian granitoids forming the Tounkarata and Macenta batholiths, granulitization of ancient Archean rocks and enriched asthenospheric mantle interaction;
- for the Paleoproterozoic granitic rocks by anatexis of the older Archean rocks during the ultimate cratonization Eburnean event;

(2) the rate of partial melting (high rate would dilute U in a larger volume of magma), and

(3) the degree of fractional crystallization.

### ***Alteration of accessories and its role in radioelement mobility***

The petrographic and SEM observations have shown that the Guinean granitoids have undergone post-magmatic alteration in relation with Ca-bearing fluid circulation.

All the Guinean magmatic rocks studied, from Leonian to Eburnean, present calcic alteration but to variable degree. Secondary Ca-bearing minerals is mostly observed in plagioclase with preferential sericitization of Ca-rich cores which is the only in situ source of Ca with hornblende, in biotite with epidotization, as replacement of monazite by allanite and epidote, or as carbonates filling the uraninite boxworks. The Ca-rich paragenetic sequence with primary calcic-plagioclase and hornblende and secondary sericite, epidote and carbonates, is supported by the very high whole-rock calcium contents (Table 2.1.3) giving: 3.64% CaO for the Leonian gneiss NZE2328, the Liberian granites DTMAC21 and DTMAC23\* host respectively 3.03% and 2.40% CaO, the Paleoproterozoic granites host 1.24-1.45% CaO and up to 4.47% in the Eburnean syenite DTNZE31a.

The calcium enrichment is also recognizable at the micron-meter scale within minerals with the cationic exchange in zircon ( $2\text{Zr}^{4+} \leftrightarrow 2\text{Ca}^{2+} + (\text{U,Th})^{4+}$ ) and the breakdown of monazite with its progressive transformation into huttonitic monazite and replacement by epidote and allanite. The calcium enrichment in the zircon grains seems to be associated with the radioelement contents

and is inferred to magmatic enrichment during primary crystallization. However, monazite breakdown is a relatively common feature in felsic granites altered by metasomatic fluids carrying calcium (Poitrasson et al., 1996; Finger et al., 1998; Broska and Siman, 1998; Broska, 2003) and is generally associated with the reaction between biotite, anorthite and monazite liberating the necessary Fe, Ca, Al, Si, LREE and P for new formation of apatite+epidote+allanite coronas. Considering the mineralogy and the geological setting of the Guinean granites, the source of Ca can be in situ from the alteration of hornblende and plagioclase or external from the metasomatism of greenstone belts (volcanic or sedimentary bedrock lithologies) in which granites are emplaced.

Alteration of uraninite by calcic fluids in the Paleoproterozoic granite NZE2381 is obvious with up to 0.68 wt% CaO in the better preserved grains and sometimes a total dissolution (boxworks) occurring with replacement by hematite, carbonates and pyrite. The uranium must have been remobilised out from the granite either from hydrothermal alteration or surface weathering. Similar calcic metasomatism associated to secondary U mineralization has been observed in Senegal in calc-alkaline and syenitic intrusions within the Birrimian metasediments (Mouthier, 1988). Calc-alkaline magmatism in Senegal occurred during the Eburnean Orogen approximately at the same time than in Guinea ca. 2.05-1.97 Ga during an intracratonic rifting event upon a subducting oceanic crust (Bassot and Caen-Vachette, 1984; Bassot, 1987). The Saraya Batholith provides a good example of U concentrations relevant of superimposed deuteric and hydrothermal alterations (Mouthier, 1988): pervasive chloritization, local greisenization, albitization, sericitization of feldspar and finally carbonatization. U mineralization occurs as leucoxene and micrograins of uraninite (without Th) along cleavage of chloritized biotite and coffinite associated with hematite, pyrite and carbonate filling dissolution cavities. This last mineralization stage is associated to the same paragenetic sequence (hematite-carbonates-pyrite) replacing uraninite in the Eburnean Guinean granite. The calcic fluid circulation in Saraya is inferred to interaction of the cooling magma with the surrounding sedimentary host rocks. In the Guinean granite, the alteration process is less developed and no albitization has been observed which suggest that the order and degree of alterations are very important for the U mobilization and re-concentrations. Thus, the lower alteration degree also permits the preservation of some primary uraninite crystals of magmatic origin in the Guinean Eburnean Granite which are totally absent in the Saraya batholith.

Timing of the late Ca metasomatism in the Guinean rocks cannot be well constrained by the U-Th-Pb chemical dating of the last preserved uraninite crystals because of the radiogenic lead loss yielding mainly Mesoproterozoic ages ~1.6 Ga. Hydrothermalism and uranium mobilization

occurred at least after 2.0 Ga (age of the youngest Eburnean altered rocks), and more detailed geochronology is required to better constrain the age of this event. The last generation of uraninite-bearing high-K calc-alkaline series formed in Paleoproterozoic time in south-east Guinea seems to represent the best source from the Kénéma-Man domain for possible uranium ore deposition in the region.

## ACKNOWLEDGEMENTS

BRGM is sincerely thanked for providing the geochemical data and samples that allowed this research. Funding for the mineralogical analyses has been provided by AREVA. Authors acknowledge most particularly Alain Kohler and Johan Ravaux from the SCMEM for their technical support with SEM and EMP instruments.

## REFERENCES

- Bassot, J. P., 1987, Le complexe volcano-plutonique calco-alkalin de la rivière Daléma (Est Sénégal) : discussion de sa signification géodynamique dans le cadre de l'orogénie éburnéenne (Protérozoïque inférieur), *Journal of African Earth Sciences*, Vol. 6, No. 4, p. 505-519.
- Bassot, J. P. and Caen-Vachette, M., 1984, Données géochronologiques et géochimiques nouvelles sur les granitoïdes de l'Est Sénégal : implications sur l'histoire géologique du Birrimien de cette région, In: J. Klerkx and J. Michot (eds.), *Géologie Africaine*, Tervuren.
- Bering, D., Brinckmann, J., Camara, N., Diawara, M., Gast, L. and Kieita, S., 1998, Evaluation de l'Inventaire des Ressources Minérales de Guinée, *Coopération Technique République de Guinée – République Fédérale d'Allemagne*, Projet 94.2025.8, BRG, Hannover, 109 p.
- Best, M. G., 2003, *Igneous and metamorphic petrology*, Second edition, Blackwell Publishing, 729 p.
- Billa, M., Feybesse, J. L., Bronner, G., Lerouge, C., Milési, J. P., Traoré, S., Diaby, S., 1999, Les formations à quartzites rubanés ferrugineux des Monts Nimba et du Simandou : des unités empilées tectoniquement, sur un « soubassement » plutonique Archéen (craton de Kénéma-Man), lors de l'orogène éburnéen, *Comptes Rendus de l'Académie des Sciences*, Paris 296, p. 149-151.
- Boher, M., Abouchami, W., Michard, A., Albarède, F. and Arndt, F., 1992, Crustal Growth in West Africa at ca. 2.1 Ga, *J. Geophys. Res.* 97, p. 345-369.
- Bowles, J. F. W., 1990, Age dating of individual grains of uraninite in rocks from electron microprobe analyses, *Chemical Geology* 83, p. 47-53.
- Bowie, S. H. U. and Horne, J. E. T., 1953, Cheralite, a new mineral of the monazite group, *Mineral. Mag.* 30, p. 93-99.
- Bronner, G., Roussel, J., Trompette, R. and Clauer, N., 1980, Genesis and geodynamic evolution of the Taoudeni Cratonic Basin (Upper Precambrian and Paleozoic), western Africa, *Dynamics of Plate Interiors*, *Geodynamics Series*, Vol. 1, p. 81-90.

- Broska, I., 2003, REE accessory minerals in the felsic silicic rocks of the Westcarpathians: their distribution, composition and stability; *Acta Mineralogica-Petrographica*, Abstract Series 1, Szeged., p. 15.
- Broska, I. and Siman, P., 1998, The breakdown of monazite in the West-Carpathian Veporic orthogneisses and Tatric granites; *Geol. Carpath.*, 49, p. 161-167.
- Cocherie, A. and Albarède, F., 2001, An improved U-Th-Pb age calculation for electron microprobe dating of monazite, *Geochimica et Cosmochimica Acta*, Vol. 65, p. 4509-4522.
- Condie, K. C., 2004, Supercontinents and superplume events: distinguishing signals in the geologic record, *Physics of the Earth and Planetary Interiors* 146, p. 319-332.
- Condie, K. C., 2001, *Mantle Plumes and Their Record in Earth History*, Cambridge, New York, 320 p.
- Condie, K. C., 2000, Episodic continental growth models: afterthoughts and extensions, *Tectonophysics* 322, p. 153-162.
- Cuney, M. and Kyser, K., 2008, Recent and not-so-recent developments in uranium deposits and implications for exploration, *Mineralogical Association of Canada, Short Course Series Vol. 39*, Quebec city, R. Raeside Series Editor, 257 p.
- Cuney, M. and Mathieu, R., 2000, Extreme Light Rare Earth Element mobilization by diagenetic fluids in the geological environment of the Oklo natural reactor zones, Franceville basin, Gabon; *Geology*, Vol. 28, No. 8, p. 743-746.
- Cuney, M. and Friedrich, M., 1987, Physicochemical and crystal-chemical controls on accessory mineral paragenesis in granitoids: implications for uranium metallogenesis, *Bulletin de mineralogie* 110, p. 235-247.
- Debon, F. and Le Fort, P., 1988, A cationic classification of common plutonic rocks and their magmatic associations: principles, method, applications, *Bulletin de Minéralogie* 111, p. 493-510.
- Debon, F. and Le Fort, P., 1983, A chemical–mineralogical classification of common plutonic rocks and associations, *Transactions of the Royal Society of Edinburgh, Earth Sciences* 73, p. 135-149.
- Deckart, K., Féraud, G., Bertrand, H., 1997, Age of Jurassic continental tholeiites of French Guyana, Surinam and Guinea: implications for the initial opening of the Central Atlantic Ocean, *Earth Planet Sci. Lett.* 150, p. 205-220.
- Egal, E., Thiéblemont, D., Lahondère, D., Guerrot, C., Adi Costea, C., Iliescu, D., Delor, C., Goujou, J.-C., Lafon, J. M., Tegye, M., Diaby, S. and Kolie, P., 2002, Late Eburnean granitization and tectonics along the western and northwestern margin of the Archean Kénéma–Man domain (Guinea. West African Craton), *Precambrian Research* 117, p. 57-84.
- Evensen, N. M., Hamilton, P.J., and O'Nions, R. K., 1978, Rare-earth abundances in chondritic meteorites, *Geochimica et Cosmochimica Acta*, Vol. 42, p. 1199-1212.
- Finger, F., Broska, I., Roberts, M. P. and Schermaier, A., 1998, Replacement of primary monazite by apatite-allanite-epidote coronas in an amphibolite facies granite gneiss from the eastern Alps, *American Mineralogist*, Vol. 83, p. 248–258.
- Förster, H.-J., 1998, The chemical composition of REE-Y-Th-U-rich accessory minerals in peraluminous granites of the Erzgebirge-Fichtelgebirge region, Germany; Part I: The monazite-(Ce)-brabantite solid solution series, *American Mineralogist* 83, p. 259-272.

- Goujou, J. C., Thiéblemont, D., Delor, C., Cocherie, A., Lacomme, A., Lafon, J. M., Tegye, M., Théveniaut, H., Sall, H., Souaré, S., Touré, J., Bah, M., Baldé, A. and Sané, H., 1999a, BRGM, DNRGH, Notice explicative de la Carte géologique de la Guinée à 1/200.000; Feuille No. 30. Macenta-Conakry (GIN): Ministère des Mines, de la Géologie et de l'Environnement, 22 p.
- Goujou, J. C., Sall, H., Souaré, S., Touré, J., Thiéblemont, D., Delor, C., Barry, Y., Vidal, M., Théveniaut, H. and Pierre, D., 1999b, Carte géologique de la Guinée à 1/200.000; Feuille No. 30, Macenta-Conakry (GIN): Ministère des Mines, de la Géologie et de l'Environnement.
- Hecht, L. and Cuney, M., 2000, Hydrothermal alteration of monazite in the Precambrian basement of the Athabasca basin: implications for the genesis of unconformity related deposits; *Mineralium Deposita*, Vol. 35, p. 791-795.
- Katja, D., 1996, Etude du magmatisme associé au rifting de l'Atlantique Central et Sud: Géochronologie  $^{40}\text{Ar}/^{39}\text{Ar}$  et géochimie sur les intrusions jurassiques de Guinée et Guyane française/Suriname, et crétacés du Brésil, Unpublished Ph. D. Thesis, Nice University. France, 256 p.
- Lahondère, D., Lacomme, A., Le-Berre, P., Illiescu, D., Guerrot, C., Cocherie, A., Diabaté, B., Gaye, F., Thiéblemont, D., Minthé, D. and Feybesse, J.L., 1999a, BRGM, DNRGH, Notice explicative de la Carte géologique de la Guinée à 1/200.000, Feuille No. 27-28, Damaro-Odienné, Conakry (GIN) : Ministère des Mines, de la Géologie et de l'Environnement, 22 p.
- Lahondère, D., Illiescu, D., Bah, M., Baldé, A., Barry, Y., Diabaté, B., Gaye, F., Minthé, D., Sané, H. and Théblemont, D., 1999b, BRGM, DNRGH, Carte géologique de la Guinée à 1/200.000, Feuille No. 27-28, Damaro-Odienné, Conakry (GIN) : Ministère des Mines, de la Géologie et de l'Environnement.
- Ludwig, K. R., 1999, Isoplot/Ex version 2.00 – A geochronological toolkit for Microsoft Excel, Berkeley Geochronology Center, Special Publication No. 2.
- Maniar P. D., Piccoli P. M., 1989, Tectonic discrimination of granitoids, *Geological Society of American Bulletin*, vol. 101, p. 635-643.
- Martin, H., 1999, Adakitic magmas: modern analogues of Archean Granitoids, *Lithos* 46, p. 411-429.
- Martin, H., 2005, Genesis and Evolution of the Primitive Earth Continental Crust, In: M. Gargaud et al. (Ed.), *Lectures in Astrobiology*, Springer-Verlag Berlin Heidelberg, Vol. I, p. 113-163.
- Martin, H., Smithies, R. H., Rapp, R., Moyen, J. F. and Champion, D., 2005, An overview of adakite, tonalite-trondjemite-granodiorite (TTG), and sanukitoid: relationships and some implications for crustal evolution, *Lithos* 79, p. 1-24.
- Mouthier, B., 1988, L'épisyénite albitisée uranifère à matière carbonée de Saraya (Sénégal): un exemple de superposition de deux altérations hydrothermales, *Comptes rendus de l'Académie des sciences. Série 2*, vol. 307, No. 7, p. 761-764.
- Moyen, J.-F., Mertin, H. and Jayananda, M., 1997, Origin of the late-Archean granite of Closepet, South India: information from geochemical modeling of trace element behaviour, *Comptes Rendus de l'Académie des Sciences de Paris, Sciences de la terre et des planètes*, No. 325, p. 659-664.
- Obermüller, A. and Roques, M., 1946, Discordance de la Série antécambrienne du Simandou sur les Gneiss de la Guinée (A. O. F.) *Comptes Rendus de l'Académie des Sciences, Paris*, 223, p. 1163-1164.

- Pearce, J. A., 1983, Role of sub-continental lithosphere in magma genesis at active continental margins, *In: Hawkesworth, C.J. and Norry M.J. (Eds), Continental Basalts and Mantle Xenoliths, Shiva, Chesire, p. 203-249.*
- Pearce, J. A., 1982, Trace elements characteristics of lavas from destructive plate boundaries, *In: Thorpe, R.S. (Ed.), Andesites, John Wiley and Sons, London, p. 525-548.*
- Peccerillo, A. and Taylor, S. R., 1976, Geochemistry of Eocene calc-alkaline volcanic rocks from the Kastamonu area, Northern Turkey, *Contributions to Mineralogy and Petrology* 58, p. 63-81.
- Poitrasson, F., Chenery, S., Bland, D. J., 1996, Contrasted monazite hydrothermal alteration mechanisms and their geochemical implications, *Earth Planet. Sci. Lett.* 145, p. 79-96.
- Pommier, A., Cocherie, A. and Legendre, O., 2002, EPMA Dating User's manual: Age calculation from electron probe microanalyser measurements of U-Th-Pb, BRGM, 9 p.
- Robb, L. J., Meyer, F. M., Ferraz, M. F. and Drennan, G. R., 1990, The distribution of the radioelements in Archean granites of the Kaapvaal Craton, with implications for the source of uranium in the Witwatersrand Basin, *South African Journal of Geology*, Vol. 93, part 1, p. 5-40.
- Shand, S. J., 1947, *Eruptive Rocks: Their Genesis, Composition, Classification, and their Relation to Ore-deposits*, 3rd ed. New York, John Wiley, p. 1-488.
- Taylor, S. R. and McLennan, S. M., 1985, *The continental crust: composition and evolution*, Backwell, Oxford, UK., 312 p.
- Thiéblemont, D., 2004, *Genèse de la croûte continentale en Afrique de l'Ouest à l'Archéen : une approche «régionale et systématique»*, Mémoire d'Habilitation à Diriger des Recherches, BRGM, 149 p.
- Thiéblemont, D., Goujou, J. C., Egal, E., Cocherie, A., Delor, C., Lafon, J. M. and Fanning, C. M., 2004, Archean evolution of the Leo Rise and its Eburnean reworking, *Journal of African Earth Sciences* 39, p. 97-104.
- Thiéblemont, D., Delor, C., Cocherie, A., Lafon, J.M., Goujou, J.C., Baldé, A., Bah, M., Sané, H. and Fanning, C.M., 2001, A 3.5 Ga granite-gneiss basement in Guinea: further evidence for early Archean accretion within the West African Craton, *Precambrian Research* 108, p. 179-194.
- Thiéblemont, D., Goujou, J. C., Delor, C., Cocherie, A., Lafon, J. M., Tegye, M., Théveniaut, H., Lacomme, A., Bah, M., Baldé, A., Sané, H., Sall, H., Souaré, S. and Touré, J., 1999a, BRGM, DNRGH, Notice explicative de la Carte géologique de la Guinée à 1/200.000; Feuille No. 34-33, N'Zérékoré-Tinsou, Conakry (GIN): Ministère des Mines, de la Géologie et de l'Environnement, 31 p.
- Thiéblemont, D., Goujou, J. C., Bah, M., Baldé, A., Sané, H., Sall, H., Souaré, S., Touré, J., Delor, C., Vidal, M., Pierre, D. and Théveniaut, H. 1999b, Carte géologique de la Guinée à 1/200.000 ; Feuille No. 34-33, N'Zérékoré-Tinsou, Conakry (GIN): Ministère des Mines, de la Géologie et de l'Environnement.
- Vidal, M., Gumiaux, C., Cagnard, F., Pouclet, A., Ouattara, G. and Pichon, M., 2009, Evolution of a Paleoproterozoic "weak type" orogeny in the West African Craton (Ivory Coast), *Tectonophysics*, Vol. 477, Issues 3-4, p. 145-159.
- Wedepohl, K. H., 1969, *Handbook of geochemistry*; New York., Springer-Verlag, Vol. I, 442 p.

## PARTIE 2.2

### U, Th and REE mobility during Ca-metasomatism of Archean K-rich granites from the Pilbara Craton, Western Australia

I. Duhamel<sup>1</sup>, M. Cuney<sup>1</sup> and M. J. Van Kranendonk<sup>2</sup>

<sup>1</sup>*G2R, Nancy-Université, CNRS, CREGU, Boulevard des Aiguillettes BP 239, 54506, Vandœuvre-lès-Nancy, France*

<sup>2</sup>*Geological Survey of Western Australia, 100 Plain St., East Perth, WA 6004, Australia*

---

#### Abstract

The process involved in the emergence of high-K granites from the older TTG-composition crust in Mesoarchean time remain poorly understood although these potassic rocks are generally enriched in incompatible elements and represent the potential source of uranium accumulation in the quartz pebble conglomerates. This work investigate the processes involved in the radioelement concentrations in the late-Archean potassic granites (2850-2830 Ma) from the north-eastern part of the Pilbara Craton in western Australia. This study provides a detailed geochemical and mineralogical characterization of the granites to access to a better understanding of the uranium concentration and fractionation in the Archean crust.

Late-Archean potassic granites also known as the Slit Rock Supersuite, have high  $K_2O/Na_2O$  ratios ( $1.30 \pm 0.25$ ) and moderate A/CNK values ( $1.04 \pm 0.04$ ) corresponding to slightly peraluminous composition. They are enriched in U, Th and LREE with high REE fractionation patterns and Eu anomaly.

The primary mineral paragenesis is mainly microcline, plagioclase, quartz and biotite, minor ilmenite, and accessory zircon, xenotime and monazite. Ferro-columbite has been observed in one occurrence of granite. Rocks have been submitted to high grade amphibolite metamorphism with formation of ferri-tschermakitic hornblende and garnet, and a retrograde metamorphism to the green schist facies with retromorphic muscovite and biotite retromorphosed to chlorite. Intensive metasomatism of the rocks resulting from hydrothermal fluid circulation during retrometamorphism has created a mineral assemblage partly replacing the primary paragenesis: myrmekite patches replace microcline, epidote replaces plagioclase and chlorite, garnet displays calcic rims, and apatite, titanite, fluorite and pumpellyite are newly formed. The metamictization of zircon and hydrothermal alteration of monazite induce the leaching of uranium, thorium and REE's out from their crystalline structure. Finally metasomatism results in the radioelement reconcentration and the neof ormation of thorite, Y-REE and Th-rich fluorocarbonate and pyrochlore-group minerals replacing the core of primary columbite. Considering the secondary mineral paragenesis, the metasomatic fluids were apparently rich in Ca and F.

---

#### Keywords

Western Australia, Pilbara Craton, Archean, K-rich granites, Ca-metasomatism, accessory mineral alteration, REE, uranium, thorium

## INTRODUCTION

Although tonalite-trondhjemite-granodiorite series (TTGs) represent the most important volumes of Archean rocks on the Earth surface (Martin, 1986, 1994), they tend to disappear in Paleoproterozoic time and are replaced by more differentiated K-rich rocks as sanukitoids or Closepet-type granites. The mechanisms leading to the evolution of the continental crust at the Archean-Paleoproterozoic transition are still poorly understood. Authors postulates in a major geodynamic change associated with the decrease in heat production of the Earth influencing the mechanism of plate tectonic (Martin and Moyen, 2002; Martin et al., 2005). The Archean plate tectonics was characterized by very small plates of basaltic or komatiitic composition which rapid melting in subducting slabs at low depths ( $P < 10$  kbar) produced the first felsic continental rocks, the tonalite-trondhjemite-granodiorite complexes (TTGs) made of Na-rich lithologies (López et al., 2006 and reference therein). The progressive cooling of the Earth induced an increase in the dip of the subducting slabs and conduced to the partial melting of basaltic and TTG rocks at higher depths ( $P > 10$  kbar) with possible interaction of the overlying mantle wedge (Smithies et al., 2003).

The post-Archean juvenile continental crust is dominated by K-rich igneous rocks enriched in incompatible elements as uranium and thorium. The origin and emplacement of the fertile K-granites is controversial because different sources and processes can be involved in their formation. The various models proposed imply alkaline metasomatism of ancient tonalites (Condie et al., 1986), melting of a basic magma pre-enriched by fractional crystallization and mixed with partial melting of continental crust (Moyen et al., 1997), partial melting of older tonalitic gneisses in a subduction or post-subduction environment (Moyen et al., 2003) linked probably to intense crustal reworking with increasing crust thickness (Champion and Smithies, 2004) or interaction between ascendant TTG magmas and hydrous mantle-derived igneous lithologies known as sanukitoids, with both magnesian and potassium enrichment (Jayananda et al., 2000; Martin et al., 2005; López et al., 2005).

The Pilbara Craton in north-western Australia provide a good example to study the emergence of the first K-rich granites because it represents one of the best preserved and best exposure of Paleoarchean to Mesoarchean granite and greenstone terranes (Smithies et al., 2009). Moreover, the radiometric signature of the high-K granites observed by gamma-ray spectrometry from airborne survey (Minty et al., 2008) are generally characterized by high equivalent K, U and Th

signatures. The major radiometric anomalies are known to be due to radioactive decay products of uranium in the surficial geochemistry and are probably related to the mineralogy of the rocks.

Moreover, some detrital uraninite, pyrite and siderite grains have been discovered in the Archean fluvial siliciclastic sediments of the Pilbara Craton deposited ca. 3.25-2.75 Ga (Rasmussen and Buick, 1999). Uraninite grains are associated to bitumen nodules in sandstones of various sedimentary units and at several stratigraphic levels constituting strong similarities with the Witwatersrand deposits in South Africa (Buick et al., 1998): in the Fortescue Group (~2.75 Ga) and the Lalla Rookh Formation (~3.0 Ga) and in the deltaic sediments of the Mosquito Creek Formation (~3.25 Ga). The high-K calc-alkaline granites from the Split-Rock Supersuite (2850-2830 Ma) represent therefore a potential source for the youngest placer-type deposits from the Fortescue Group and should be better studied.

In this contribution, whole-rock geochemistry and a detailed mineralogical study of the potassic granites from the Split rock Supersuite are provided to characterize their magmatic and hydrothermal fractionation, to identify the nature of the U-bearing mineral paragenesis and the processes involved in the uranium enrichment.

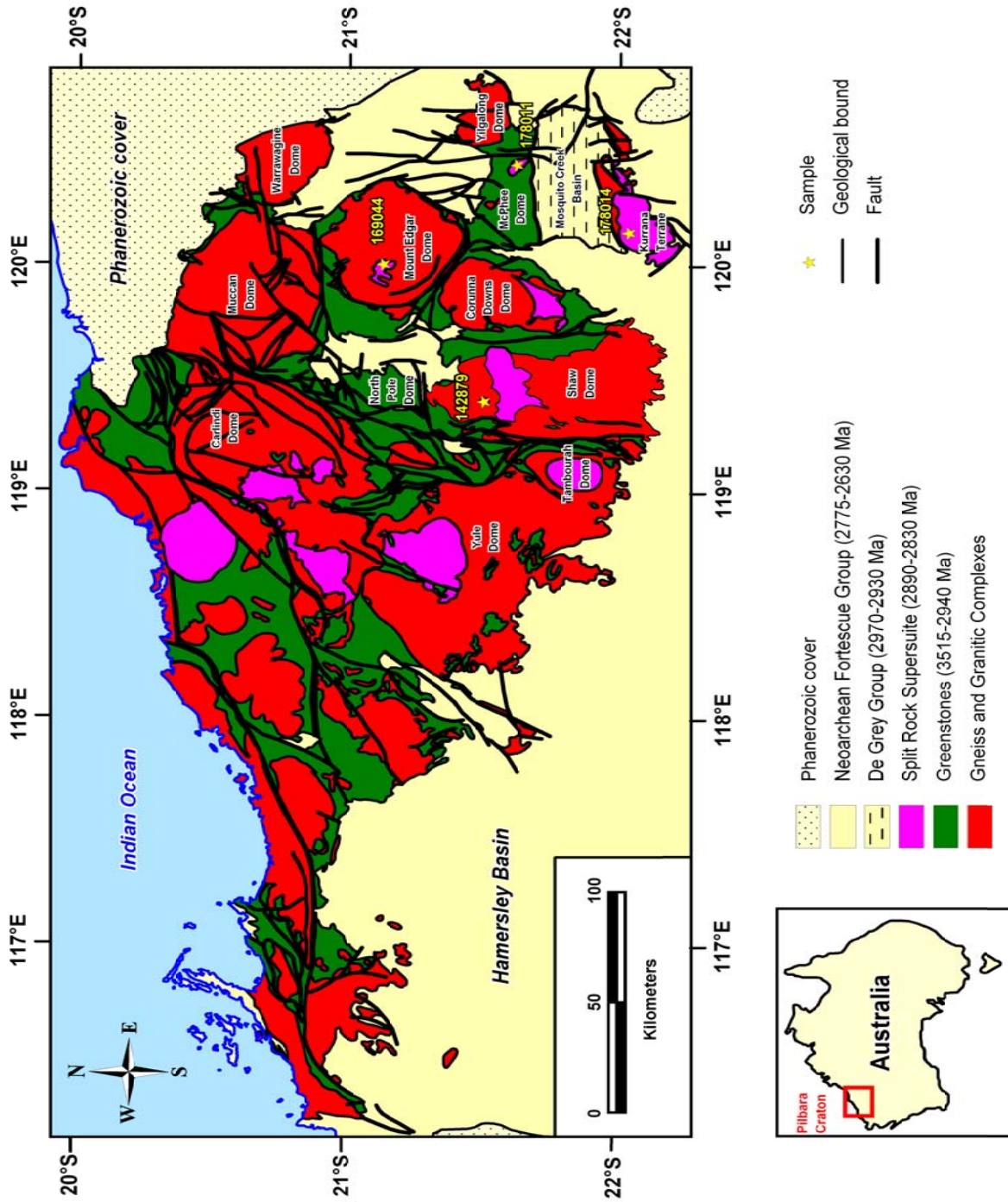


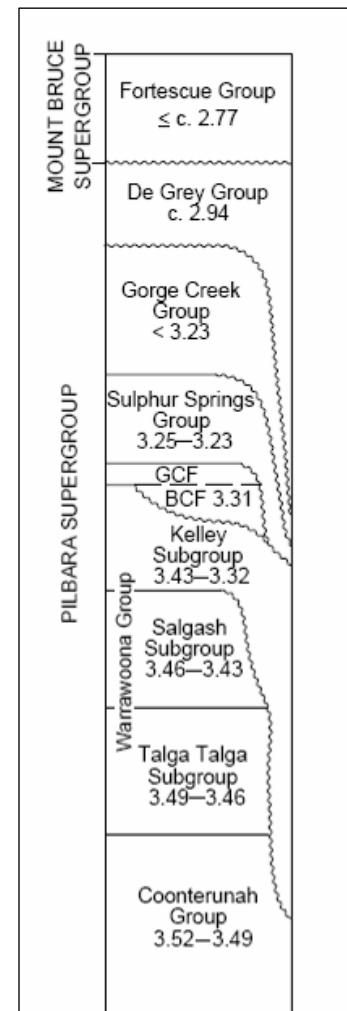
**Figure 2.2.1** Geological map of the Pilbara Craton showing the Archean granite-greenstone terranes and the location of samples (modified from Hickman, 1983).

## GEOLOGICAL SETTING

The Pilbara Craton, located in north-western Australia (Fig. 2.2.1), is represented by North Pilbara Terrane composed of granite and greenstone rocks very well preserved and presenting good exposures, limited to the south by the Neoproterozoic Hamersley Basin, and to the north by a Phanerozoic cover. The North Pilbara Terrane forms a typical dome and basin structural pattern with pluri-kilometric granitoid complex domes separated by synclinal greenstone belts intensely faulted and deformed along northeastern major structures. The batholiths are composed of approximately 70 % of sodic tonalite-trondhjemite-granodiorite rocks (TTGs) and minor younger granitoids referred as the Split Rock Supersuite and comprising highly fractionated monzogranites and syenite pegmatites (Van Kranendonk et al., 2004).

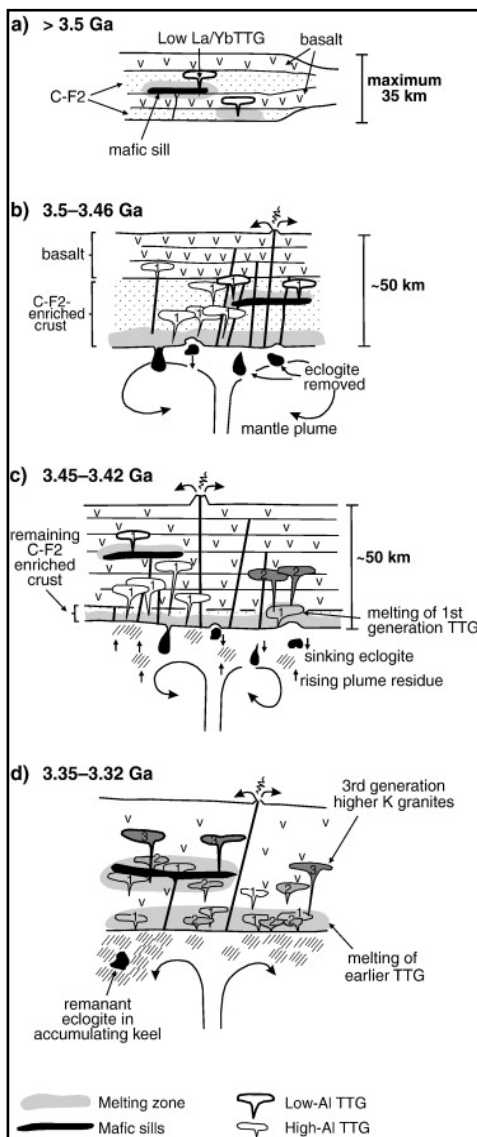
The greenstone belts are composed of metamorphosed volcanic and sedimentary rocks separated by major unconformities and subdivided into the following units presented in stratigraphic order (Fig. 2.2.2; Hickman, 1983; Buick et al., 1995; Van Kranendonk et al., 2002, 2004 and 2005): the Coonterunah Group ca. 3515 Ma (mafic and felsic volcanic rocks), the Warrawoona Group which deposition starts at ca. 3490 Ma (mainly mafic to ultra-mafic rocks with minor felsic volcanics, chert and stromatolite carbonates) and ends with the Wyman Formation ca. 3325-3315 Ma (ryholitic volcanic rocks), the Sulphur Springs Group ca. 3240 Ma (basalt and ryholite), the Gorge Creek Group ca. 3240-2950 Ma (mostly epiclastic sediments: shale, sandstones and conglomerates with minor chert and banded iron formations) and at the top the De Grey Group ca. 2930 Ma (mainly turbiditic rocks with minor sandstones and mafic volcanics) forming the Mosquito Creek Basin in the southeast.

**Figure 2.2.2.** Generalised stratigraphic column of the Pilbara Supergroup (after Van Kranendonk et al., 2004). Numbers represent ages in Ga. BCF: Budjan Creek Formation; GCF: Golden Cockatoo Formation. Wiggly lines are unconformities.



The greenstone belts are supposed to represent the remnants of a rift basin succession (3515-2930 Ma) emplaced in the older TTGs (Van Kranendonk et al., 2002; Hickman, 2004). The major dome and basin deformation pattern would be caused by the “diapirism” of the TTGs ca. 3300-3315 Ma penetrating vertically by gravity-driven tectonism in the denser mafic volcanic sequence (Hickman, 1981, 1984; Collins, 1989; Hickman and Van Kranendonk, 2004; Van Kranendonk et al., 2004) or by horizontal shortening along Alpine-type thrusts (Bickle et al., 1980 and 1985; Van Haafte and White, 1998).

The intrusion of K-rich monzogranite and syenogranite, the Split Rock Supersuite, emplaced lately in both TTGs and greenstone rocks. These K-granites are associated with major northeast faults which are related to major regional NW-SE horizontal compression or shortening (Belwett, 2002) and to two major tectono-thermal events, from 2950 to 2930 Ma and from 2850 to 2830 Ma (Van Kranendonk et al., 2002). They are considered as post-tectonic and some of these late intrusive bodies host rare metal Sn-Ta-Li mineralization (Sweetapple and Collins, 2002; Van Kranendonk et al., 2004).



The model proposed for the crustal evolution in the Pilbara Craton to explain the emergence of differentiated magmas is presented in Figure 2.2.3 (Smithies et al., 2009). Three magmatic cycles are distinguished from their geochemical affinity and are associated to the degree of crustal reworking, mantle interaction and somehow to the various types of parental magmas.

**Figure 2.2.3.** Schematic diagram showing various stages in the development of Paleoproterozoic crust of the Pilbara Craton (after Smithies et al., 2009). Numbers in plutons represent various generations (i.e. 1 = basaltic source, 2 = source includes 1st generation TTG etc).

The first generation of TTGs, between 3.5 and 3.46 Ga, are characterized by low-Al content and are thought to be formed by infracrustal melting of a basaltic source (Smithies et al., 2009). Geochemistry of the first TTGs is characterized by variable silica content (62-70% SiO<sub>2</sub>), is sodium-rich (medium-K), LREE-enriched, HREE- and Y- depleted with weak to no Eu anomalies and Sr-undepleted composition (Bickle et al., 1993). Their bulk composition requires a basaltic source pre-enriched in K, LILE, Th and REE, probably inherited from a mantle source by recycling the crustal material (slab melt after Smithies et al., 2009) or in response to thickening of a pre-existing crust older than 3.5 Ga with mantle plume ascension (Barley and Pickard, 1999).

The second generation of TTGs aged ca. 3.45-3.42 Ga, also named transitional TTGs, are the result of a pure melting of the pre-enriched continental crust (Champion and Smithies, 2001 and 2004). They are characterized by higher Al concentrations, high silica content (65-75% SiO<sub>2</sub>), more potassic compositions, HREE-undepleted with slight Eu anomalies and Sr-depleted.

The more chemically evolved magmas are the high-K granites appearing at ca. 3.35-3.32 Ga that represent products of episodic partial melting of the high-Al TTGs and typically correspond to I-type granites (Champion and Smithies, 2001). They are characterized by high K<sub>2</sub>O/Na<sub>2</sub>O and Rb/Sr ratios, high HREE and Y contents and large negative Eu anomalies. The last generation of magma evolution emplaced from 2890 to 2850 Ma, indeed 800 Ma after the initial crust formation (Cassidy et al., 2006). It is postulated that that this late highly differentiated potassic magmatism results from an orogenic collapse following the thickening period generating TTGs.

Finally, the Late Archean Fortescue Group (2775-2630 Ma), representing the basal part of the Hamersley Basin, unconformably overlays the granites and greenstones from the basement (Bolhar and Van Kranendonk, 2007). The Fortescue Group is considered as a platform succession of flood basalt with interbedded calcareous sandstones, stromatolites and banded iron formations. This late sedimentary sequence occur as patchy occurrences upon the granite-greenstone terrane suggesting that the Hamersley Basin probably extended much more to the north than presently observed and probably has reached a thickness of up to 6 kilometres.

All the rocks of the North Pilbara Terrane were affected by low grade metamorphism to the greenschist facies except for the eastern domain where Mount Edgar and Shaw batholiths have reached the amphibolite facies (Wijbrans and McDougall, 1987).

## SAMPLE DESCRIPTION

This study focused on the youngest granitoids, the Split Rock Supersuite which is widely distributed throughout the Pilbara Craton and emplaced between 2850 and 2830 Ma. Samples were collected during regional mapping by the geologists of the Geological Survey of Western Australia in the northeast Pilbara (see location in Fig. 2.2.1). Samples have been collected both in drill cores (142879 and 169044) and from surface outcrops (178011 and 178014). Samples 142879 and 169044 are granitoids intruding the central parts of the Shaw and Mount Edgar Domes, respectively. Sample 142879 is from the Spear Hill monzogranite dated by SHRIMP on zircon at  $2851 \pm 2$  Ma (Nelson, 1998). Sample 169044 is from the Moolyella Suite, named successively granite by De Laeter and Blockley (1972), adamellite by Hickman and Lipple (1975) and biotite monzogranite by Sims and Carson (2001). Moolyella Suite has been dated using Rb/Sr isotopes at  $2613 \pm 93$  Ma (De Laeter and Blockley, 1972) while Rb-Sr whole rock isochron yield an age of  $2804 \pm 62$  Ma (Collins and Gray, 1990). Samples 178011 and 178044 are located more south-easterly, intruding the greenstone belt of the Mc Phee Dome and the granite-gneisses of the Kurrana Terrane respectively. They are separated from each other by the Mosquito Creek Basin apparently in fault contact with its basement (Fig. 2.2.1) and which maximum deposition as been dated at  $2972 +14/-37$  Ma by SHRIMP on detrital zircon grains (Bagas et al., 2008).

Macroscopically, they are medium to coarse grained granites composed of plagioclase, microcline, quartz, biotite, chlorite, muscovite and more rarely hornblende (178011) and garnet (169044). Sample 178011 seems to be less K-rich than the other leucocratic granites because of the apparent lower abundance of pink feldspar (Fig. 2.2.4). The apparent absence of foliation suggests a low deformation constraint. The bulk radiometry of samples measured with a SPP2 scintillometer is close to the background, between 100 and 120 counts per second.

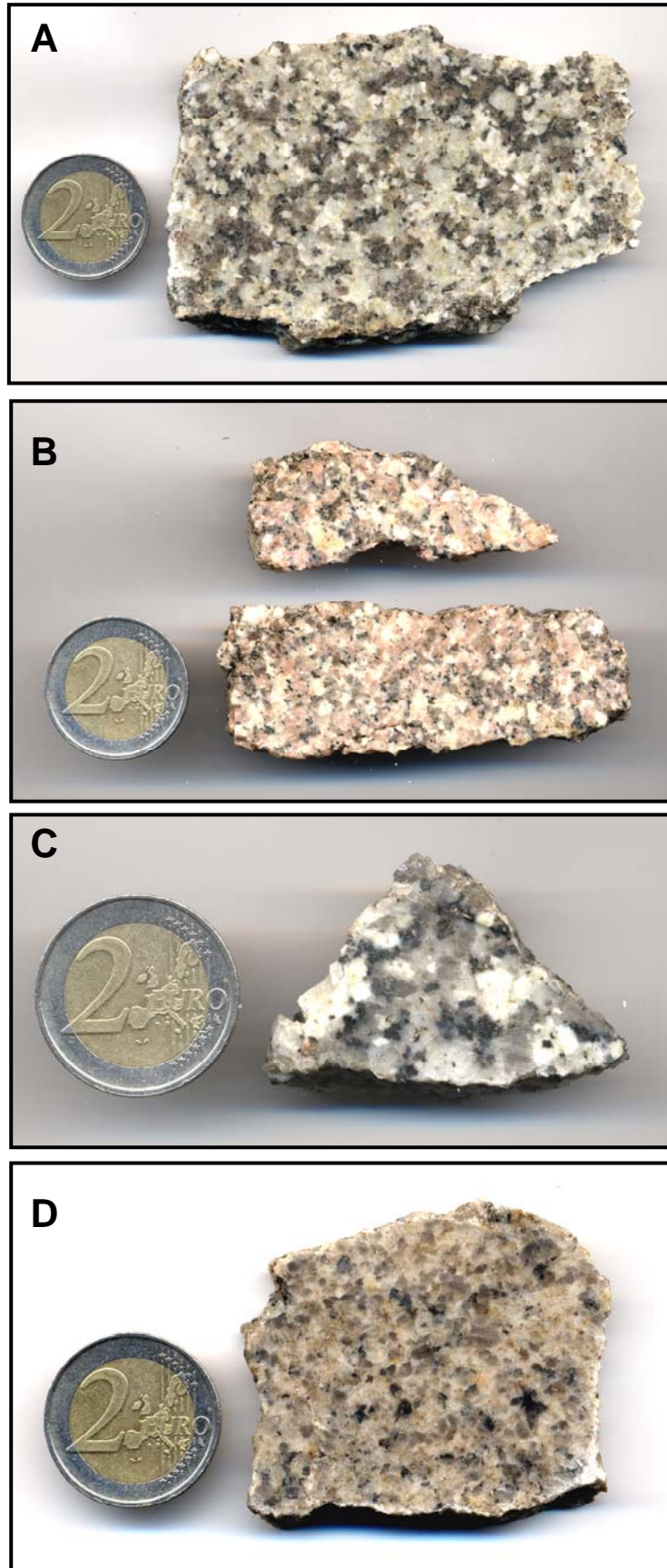


**Figure 2.2.4.** Granitic samples from the Pilbara Craton: **A-** 142879 Spear Hill Monzogranite (core sample of the Shaw Granitic Complex), **B-** 169044 Moolyella Monzogranite (core sample of the Mount Edgar Granitic Complex), **C-** 178011 Cooke Creek Monzogranite (hand sampling) and **D-** 178014 Bonney Downs Monzogranite (hand sampling). The coin used as scale is approximately 2.6 cm wide.

## ANALYTICAL PROCEDURE

The four selected samples were separated in two pieces, half of the rock was crushed for whole-rock geochemistry and the other half part was soared, polished and transformed into thin sections for the petrographic study.

Four whole-rock samples have been analyzed at the SARM laboratory (CRPG, CNRS, Nancy, France) using the Carignan et al. (2001) methodology and standards. Major elements were determined using ICP-AES and the trace elements using ICP-MS. Results obtained on the four granites were compared to the whole-rock composition of the Split Rock Supersuite compiled from the Australian Government Survey Organisation (AGSO) and the Geological Survey of Western Australia (GSWA) database (OZCHEM). This represents 60 additional chemical analyses of ~2.85 Ga granites from the Moolyella, Numbana, Shaw, Minnamonica and Cooglegong batholiths located within the North Pilbara Granite-Greenstone Terrane (data in Appendix 2 – Table A2). Various rock classification schemes are then used to characterize the complex nature of the granites but also to describe their mineralogy and chemical composition variations that are involved in their formation and weathering. The average composition of reference rocks have been reported in the diagrams: gb = gabbro; mgb = monzogabbro; mz = monzonite; mzdq = quartz monzodiorite; dq = quartz diorite; s = syenite; sq = quartz syenite; to = tonalite; gd = granodiorite; ad = adamellite; gr = granite (data from Debon and Le Fort, 1983). Igneous rocks are classified according to their aluminous index ( $A/CNK = (Al_2O_3/102) / [(2CaO/56) + (Na_2O/62) + (K_2O/94)]$  in moles; Shand, 1947) and the peralkaline series are discriminated with the parameter ( $Al < [K+N]$ ), from the metaluminous ones ( $Al > [K+N]$ ) and with the parameter ( $Al < [K+Na+2Ca]$ ) from the peraluminous ones ( $Al > [K+Na+2Ca]$ ). The aluminous index  $A/CNK$  is represented versus the reverse of the alppaitic index [ $A/NK = (Al_2O_3/102) / ((Na_2O/62) + (K_2O/94))$ ] calculated in molar fraction (Minard and Piccoli, 1989). The mineralogical-chemical diagrams proposed by Debon and Le Fort (1988) permit to decipher magmatic fractionation and alteration trends of the granites comparing 1) the quartz content [ $Q = Si/3 - (Na+K+2Ca/3)$ ] relatively to the proportion of K-feldspar and Na-Ca bearing minerals [ $P = K - (Na+Ca)$ ] and 2) the peraluminous index [ $A = Al - (Na+K+2Ca)$  representing the amount of aluminium in the rock diminished by the amount of Al present in the feldspars] versus the differentiation index [ $B = Fe + Mg + Ti$  representing the amount of femic minerals and titanium oxides]. The binary diagrams (Th vs. U and Th vs. La) permit to characterize the fractionation of the element and their possible leaching or enrichment during alteration processes.

The mineralogical study has been performed using both optical microscopy in transmitted and reflected light and scanning electron microscopy (SEM) coupled with an energy dispersive spectrometer (EDS) allowing semi-qualitative measurements of major mineral components. Imagery in backscattered mode and analyses were conducted at the SCMEM laboratory using a HITACHI FEG S4800 SEM and a Noran Vantage EDS to identify the different mineral phases, the internal textures, zoning and the chemical heterogeneities.

The chemical composition of selected minerals was measured at the SCMEM laboratory using the electron microprobes (EMP) CAMECA SX50 and SX100 equipped with wavelength dispersive spectrometers (WDS). Operating conditions were an accelerating voltage of 15 kV, a beam current of 10 nA with acquisition times ranging between 5 and 30 s to measure chemical composition within a 2  $\mu\text{m}$  diameter spot.

The calculation procedure to obtain the composition in atoms per formula unit (apfu) for minerals include to normalized the data on the sum of oxygen ions corresponding to the ideal formula. The structural formula were calculated on the basis of 23 oxygens for hornblende, 14 oxygens for chlorite (half formula), 12.5 oxygens for epidote, 12 oxygens for garnet and pumpellyite, 6 oxygens for columbite and 5 oxygens for titanite. In some cases, when the cation sum surpassed the theoretical value (for example 12 cations in columbite), the  $\text{Fe}^{2+}$  is partly converted in  $\text{Fe}^{3+}$  to complete the other cationic sites of the crystal structure. Then, the data were plotted in binary, ternary or quadrilateral diagrams to characterize the mineral solid solutions and to evidence fractionation trends.

The  $\text{Al}^{\text{IV}}$  content in the tetrahedral site of chlorites is thermo-dependent and the following empirical formula defined by Cathelineau (1988) permit to estimate the temperature of its formation:  $T (^{\circ}\text{C}) = -61.92 + 321.98 \text{Al}^{\text{IV}}$  (in apfu).

In the specific case of Tschermak Ca-rich hornblende which ideal formula is  $[\text{Ca}_2(\text{Mg,Fe})_3\text{Al}^{\text{VI}}_2\text{Si}_6\text{Al}^{\text{IV}}_2\text{-O}_{22}(\text{OH})_2]$ , the mineral composition can be used as a geobarometer. An empirical correlation exists between the total Al content of the mineral and the pressure of the crystallization of the mineral. The linear correlation was firstly define by Hammarstrom and Zen (1986) and successively revised by Hollister et al. (1987), Johnson and Rutherford (1989) and Schmidt (1992) with different experimental calibrations. The different equations are given in Table 2.2.1 where Al is the aluminium content of the mineral (in apfu) and P the pressure (in kilobars: kbar). Figure 2.2.5 summarised the linear relations from which the range of pressures obtained for the various EMPA spots in our hornblende have been calculated.

**Table 2.2.1.** Relation between pressure (P in kbar) and the total Al content of hornblende ( $Al=Al^{IV}+Al^{VI}$  in apfu) for melt temperature between approximately 600-800°C

<i>Reference</i>	<i>Equation</i>
Hammarstrom & Zen 86	$P = -3.92 + 5.03 Al$
Hollister et al. 87	$P = 5.64 Al - 4.76$
Johnson & Rutherford 89	$P = 4.23 Al - 3.46$ (T ~ 760 °C)
Schmidt 92	$P = -3.01 + 4.76 Al$ (T ~ 675 °C)

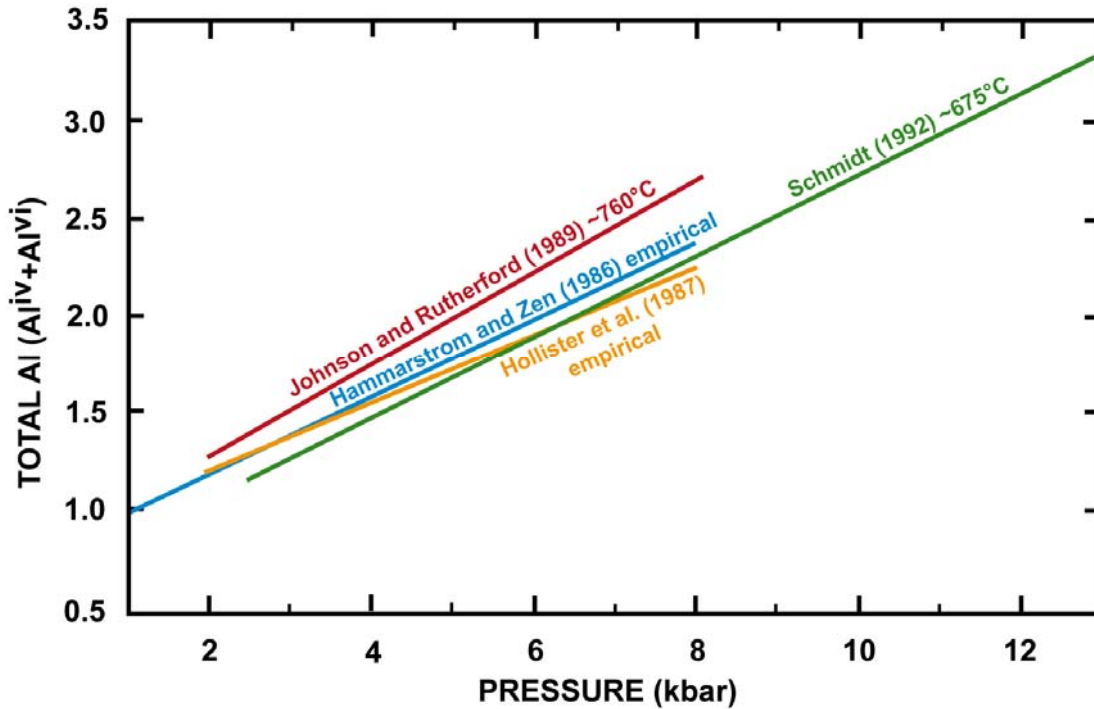


**Figure 2.2.5.** Hornblende geobarometer relations (modified from Anderson and Smith, 1995).

## WHOLE-ROCK GEOCHEMISTRY

Whole-rock major and trace element composition of the four granites analysed in this study are presented in Table 2.2.2 and other analyses compiled from the OZCHEM database are presented in Appendix 2 (Table A2) with the average value for all the granitoids of the Split Rock Supersuite.

Granitoids of the Split Rock Supersuite have high silica (mean/64 analyses:  $74.09 \pm 1.61$  wt%  $SiO_2$ ) and potassium contents (mean:  $4.76 \pm 0.60$  wt%  $K_2O$ ) and moderate sodium (mean:  $3.74 \pm 0.39$  wt%  $Na_2O$ ) and calcium contents (mean:  $0.92 \pm 0.30$  wt%  $CaO$ ). The mean  $K_2O/Na_2O$  ratio of the 64 analyses from the Split Rock Supersuite is  $1.30 \pm 0.25$ .

**Table 2.2.2.** Whole-rock geochemical composition of the granitoids sampled from the Split Rock Supersuite

<i>Sample</i>	<i>142879</i>	<i>169044</i>	<i>178011</i>	<i>178014</i>
SiO <sub>2</sub> (%)	74.30	76.42	69.15	72.47
Al <sub>2</sub> O <sub>3</sub>	13.36	13.61	13.99	13.62
Fe <sub>2</sub> O <sub>3</sub>	1.46	0.88	3.65	1.57
MnO	0.03	0.06	0.06	0.03
MgO	0.19	0.05	0.55	0.29
CaO	0.96	0.21	1.79	0.84
Na <sub>2</sub> O	3.65	4.23	3.75	3.41
K <sub>2</sub> O	4.80	4.39	4.38	5.43
TiO <sub>2</sub>	0.15	0.04	0.48	0.21
P <sub>2</sub> O <sub>5</sub>	0.03	< L.D.	0.11	0.06
LOI	0.64	0.53	0.77	0.72
Total	99.58	100.41	98.68	98.65
As (ppm)	< L.D.	< L.D.	1.85	1.52
Ba	418	22.61	502	505
Be	5.37	4.57	4.15	3.09
Bi	0.17	47.72	0.22	0.41
Cd	< L.D.	< L.D.	0.19	< L.D.
Co	1.54	0.48	5.36	1.75
Cr	11.61	9.00	11.44	11.05
Cs	10.3	20.56	19.59	7.93
Cu	< L.D.	109	6.61	5.12
Ga	23.54	30.89	23.61	21.04
Ge	1.33	1.98	1.31	1.16
Hf	4.90	2.35	5.54	4.89
In	< L.D.	< L.D.	< L.D.	< L.D.
Mo	< L.D.	1.22	0.66	< L.D.
Nb	27.9	38.1	18.7	17.91
Ni	5.93	5.29	7.15	5.88
Pb	47.09	34.08	34.09	36.47
Rb	385	560	361	328
Sb	< L.D.	< L.D.	< L.D.	< L.D.
Sn	7.43	21.8	11.6	8.20
Sr	74.44	7.12	96.6	71.53
Ta	4.32	12.94	3.05	2.7
Th	43.19	11.65	29.94	32.58
U	17.82	6.23	7.52	7.54
V	7.45	1.37	22.58	10.74
W	0.72	1.36	0.44	< L.D.
Y	33.86	39.36	33.1	31.51
Zn	50.14	28.53	75.92	48.02
Zr	142	37.78	195	164
Th/U	2.42	1.89	3.98	4.32
La (ppm)	45.09	11.89	38.25	51.83
Ce	88.08	25.74	77.39	105.7
Pr	9.51	3.27	8.63	11.56
Nd	32.17	11.8	30.35	39.31
Sm	6.5	4.01	5.93	7.40
Eu	0.42	0.05	0.96	0.51
Gd	5.42	4.19	5.10	5.85
Tb	0.92	0.88	0.84	0.90
Dy	5.40	5.73	5.05	5.15
Ho	1.05	1.12	1.02	1.01
Er	3.10	3.36	3.09	2.90
Tm	0.49	0.59	0.50	0.44
Yb	3.28	4.21	3.47	3.01
Lu	0.50	0.62	0.54	0.45
ΣREE (ppm)	202	77.5	181	236
[La/Sm] <sub>N</sub>	1.67	0.72	1.56	1.69
[Gd/Yb] <sub>N</sub>	1.34	0.80	1.19	1.57
Eu/Eu* = Eu <sub>N</sub> /√(Gd <sub>N</sub> ×Sm <sub>N</sub> )	0.22	0.04	0.53	0.24
A/CNK = Al/(Na+K+2Ca)	1.03	1.12	0.99	1.05
Q = Si/3-(K+Na+2Ca/3)	181.4	191.9	148.5	167.0
P = K-(Na+Ca)	-32.7	-46.9	-59.8	-9.2
A = Al-(K+Na+2Ca)	8.1	29.5	-3.7	11.9
B = Fe+Ti+Mg	25.0	12.7	65.5	29.5

**Notes:** [X]<sub>N</sub> = normalized to chondrites; A/CNK index calculated in moles whereas Q, P, A and B parameters are calculated in thousands of cations.

All the granitoids are part of the high-K calc-alkaline series with composition ranging between adamellite and granite (Fig. 2.2.6). Only sample 178011 intruding the greenstone rocks of the McPhee Dome is close to the adamellite composition whereas the three other samples have granitic compositions with relatively higher silica and slightly higher potassium contents.

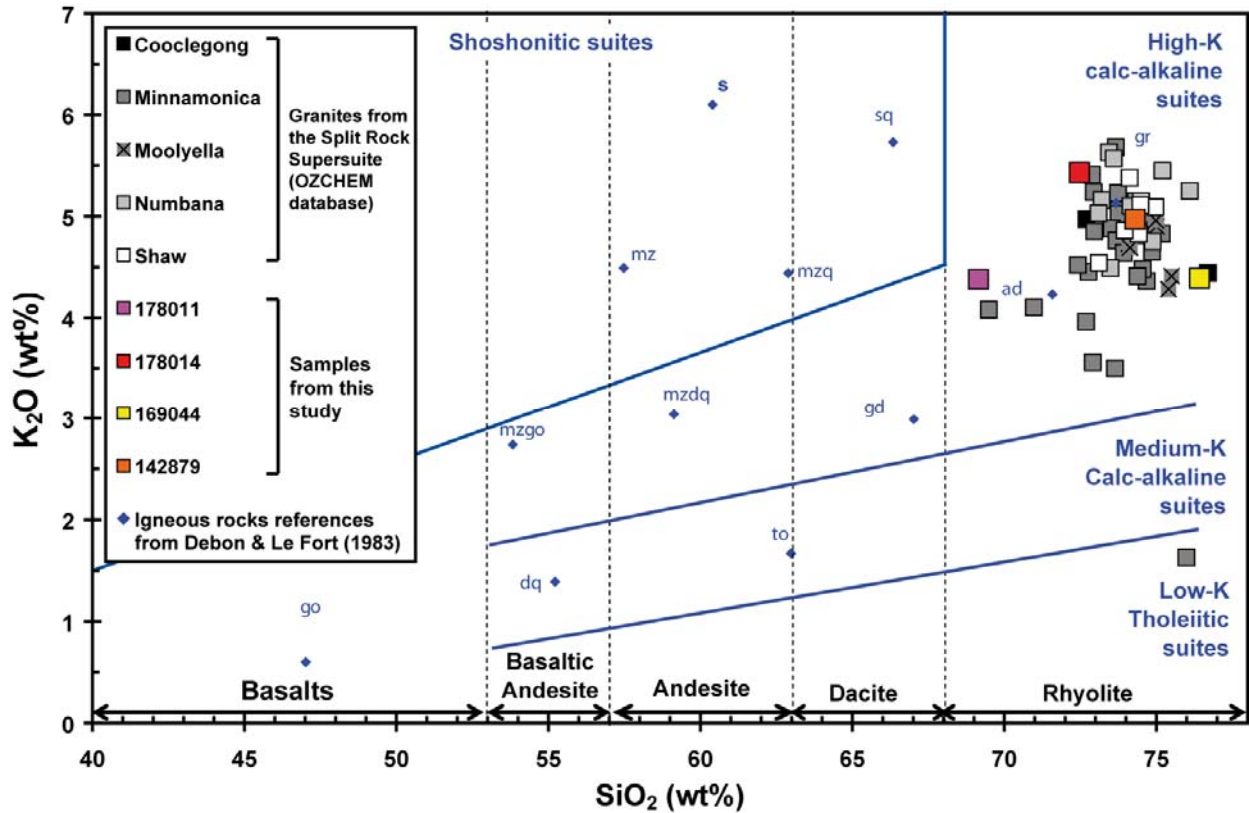


**Figure 2.2.6.** Binary diagram showing the  $K_2O$  vs.  $SiO_2$  contents (wt%) of the Split Rock Supersuite from the Pilbara Craton. The composition limits and fields are from Peccerillo and Taylor (1976) and rock composition references are from Debon and Le Fort (1983): go = gabbro; mzgo = monzogabbro; mz = monzonite; mzq = quartz-monzonite; mzdq = quartz monzodiorite; dq = quartz diorite; s = syenite; sq = quartz syenite; to = tonalite; gd = granodiorite; ad = adamellite; gr = granite.

They are metaluminous to slightly peraluminous  $0.88 < A/CNK < 1.12$  (mean:  $1.04 \pm 0.04$ ) with an A/NK index between 0.99 and 1.33 (mean:  $1.19 \pm 0.06$ ). The Split Rock Supersuite is generally slightly peraluminous with  $A/CNK > 1$  (Fig. 2.2.7) and a few exceptions are the granitoids from the Shaw batholith and sample 178011 which plot in the metaluminous field.

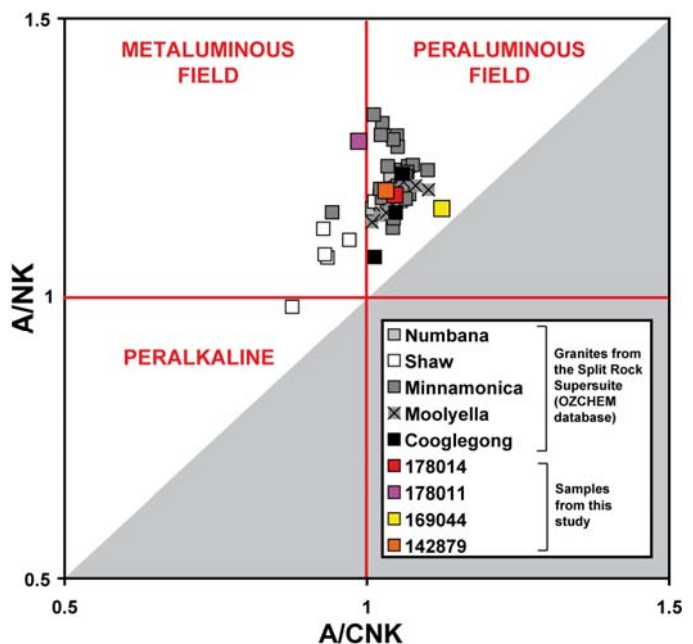


**Figure 2.2.7.** A/NK versus A/CNK diagram (Maniardi and Piccoli, 1989).

The granitoids show mostly invariant high Q parameter  $\sim 180$  (Fig. 2.2.8). The main chemical variation corresponds to the relative abundance of plagioclase and K-feldspar. The highly negative P values at nearby a constant Q parameter are probably representative of the albite predominance compare to the K-feldspar proportion as in sample 178011 which was already suggested by the macroscopic observations.

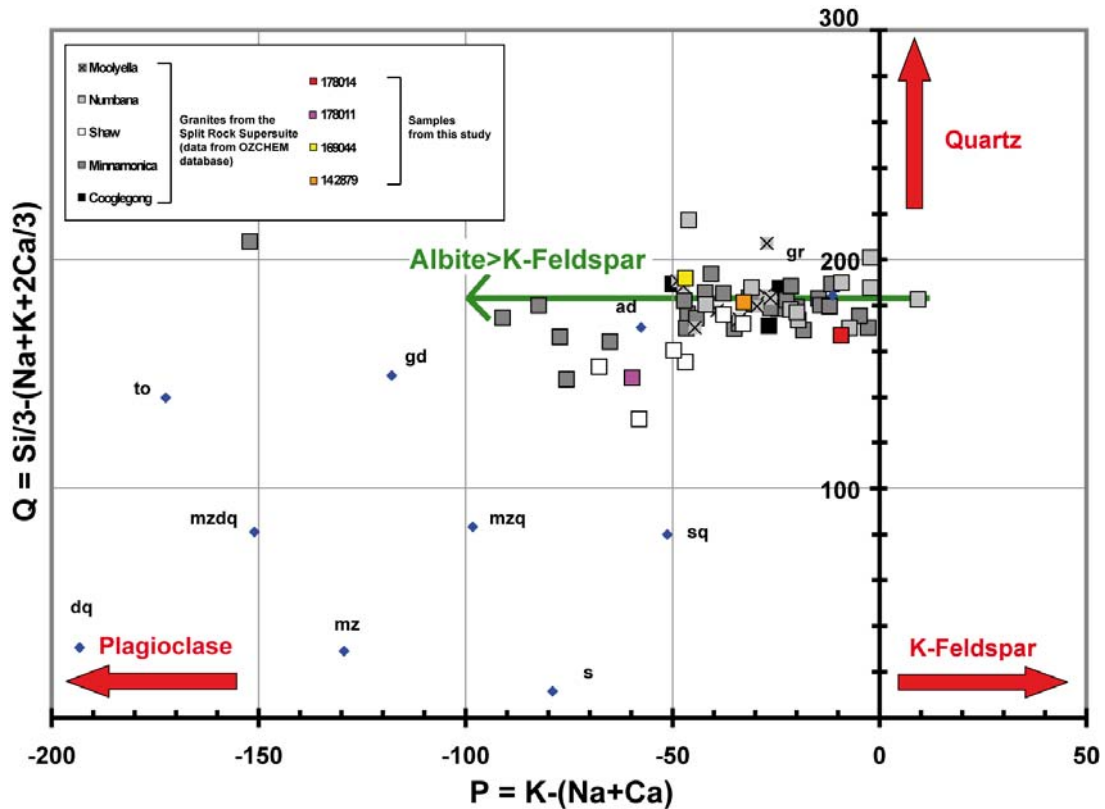


**Figure 2.2.8.** Q-P chemical-mineralogical diagram of Debon and Le Fort (1988) representing variations of the proportions of quartz relative to plagioclase and K-feldspar for the granitoids of the Split Rock Supersuite from the Eastern Pilbara Terrane.

The general low mafic mineral content of the Slip Rock Supersuite ( $B < 66$ ) indicates that most of these rocks correspond to leucogranites (Fig. 2.2.9). However, the few samples that plot in the metaluminous field, those from the Shaw batholith and sample 178011 ( $A = -3.7$ ), are the most femic samples with a maximum for 178011 ( $B = 65.5$ ) and thus are the less fractionated. This specific composition corresponds mineralogically to the presence of abundant biotite, Fe-Ti oxides and predominance of plagioclase. The lowest values of the peraluminous index of some of the rocks correspond to the formation of Al-free and Ca-bearing minerals (178011: 1.79 wt% CaO). In comparison, the granite 169044 is the most fractionated of samples with highest silica content, lowest femic mineral and Ca contents and the most peraluminous ( $A = 30$ ). This is in accordance with its high Ta (12.94 ppm), Rb (560 ppm), Cs (20.56 ppm), Bi (47.72 ppm) and Sn (21.8 ppm) contents and its low Th (11.65 ppm), Zr (37.78 ppm) and  $\Sigma\text{REE}$  (77.5 ppm) contents, these last elements having a low solubility in peraluminous low temperature melts (Cuney and Friedrich, 1987).

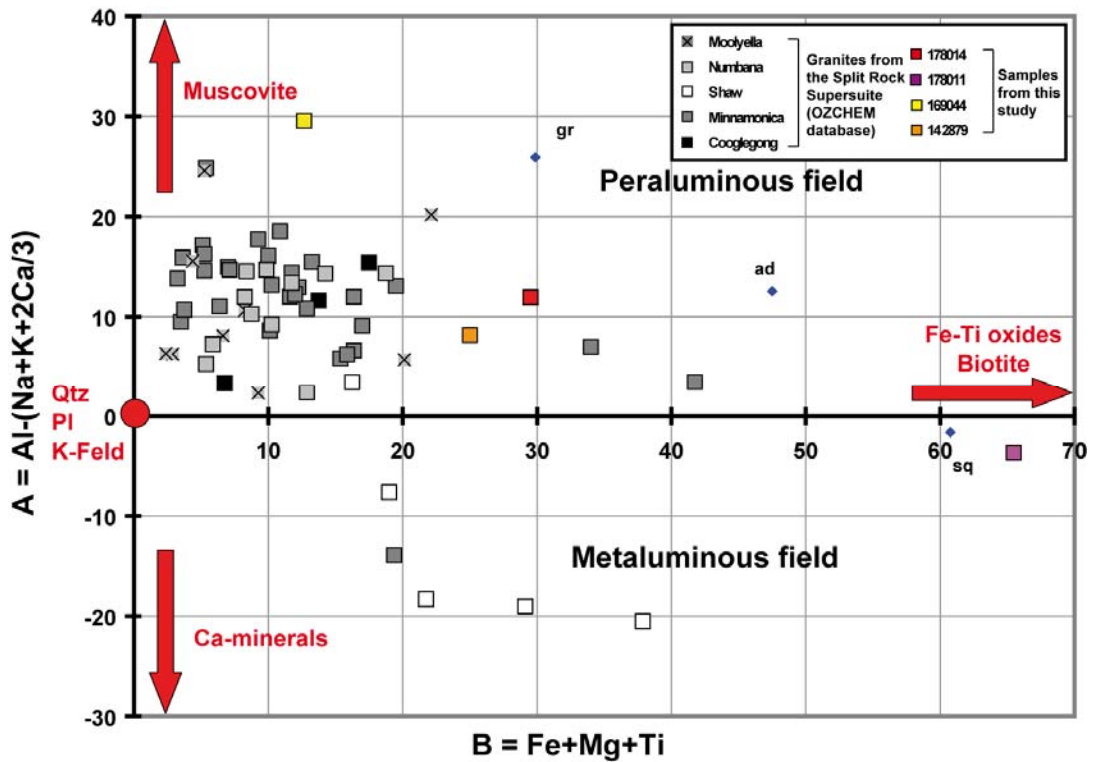


**Figure 2.2.9.** A-B chemical-mineralogical diagram of Debon and Le Fort (1988) representing the variations of the peraluminous index (A) versus a differentiation index (B) for the granitoids of the Eastern Pilabara Terrane.

The chondrite-normalized rare earth elements (REE) patterns for the four granitoids are shown in Figure 2.2.10. Samples 142879, 178011 and 178014 show a global distribution similar to that of the average continental upper crust (Taylor and McLennan, 1985) with fractionated REE patterns and a distinct La and Eu depletion. Leucogranite 169044 has lower LREE contents, a flat pattern and a much stronger negative Eu anomaly ( $Eu/Eu^*=0.04$ ) compared to the 3 other rocks. This rock probably derive from the extreme fractionation of a high-K calc-alkaline magma at shallow crustal level because it typically displays more moderate Th, Zr and REE enrichment, these elements being less soluble in peraluminous melts (Cuney and Kyser, 2008).

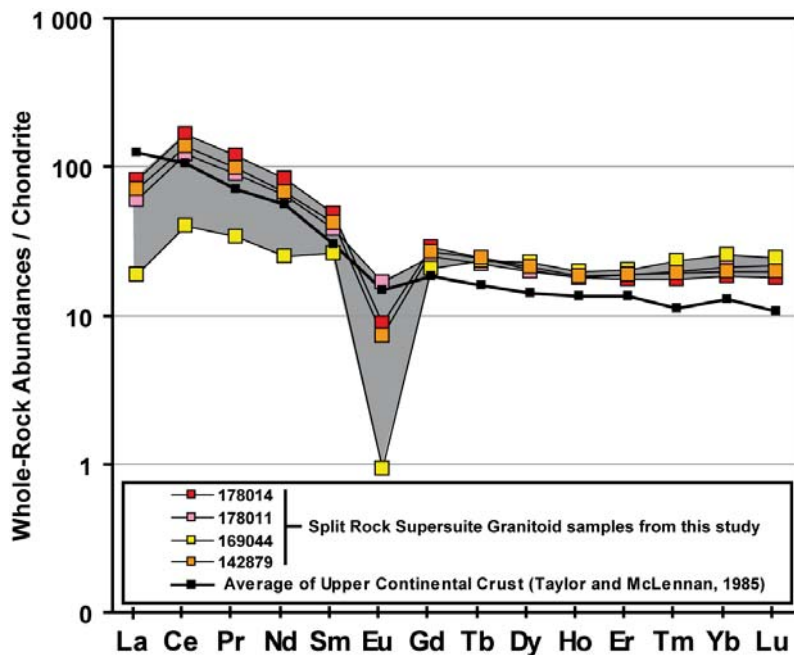


**Figure 2.2.10.** Chondrite-normalized spectra of whole-rock REE abundances in the Split Rock Supersuite granitoids sampled in this study compare to the average upper continental crust composition (Taylor and McLennan, 1985). The REE abundances (in ppm) were normalized to the chondrite values C1 from Evensen et al. (1978).

The granites are variably enriched in Th (9-65.40 ppm) and U (2.10-25.10 ppm) comparatively to the average concentrations of the upper continental crust (2.8 ppm U and 10.7 ppm Th, Taylor and McLennan, 1985). The whole-rock Th/U ratios range between 10.52 and 1.13 (Fig. 2.2.11): granitoids with  $Th/U > 4$  have U and Th mostly incorporated in monazite whereas samples closer to the mean leucogranite Th/U ratio (1) must contain other U-bearing minerals. Peralkaline to peraluminous melts define normally a correlation between Th and U about 4 along the average crustal ratio with the magmatic fractionation (Cuney and Kyser, 2008). Granitoids from the Split Rock Supersuite define a trend with a strong U-enrichment and a moderate Th increase (red arrow). This behaviour is observed in some high-K calc-alkaline series which are slightly peraluminous and are formed at moderate temperature of the source-magmas. This trend reflects the effect of magmatic and late- to post-magmatic processes related to U-enrichment with fluid fractionation.

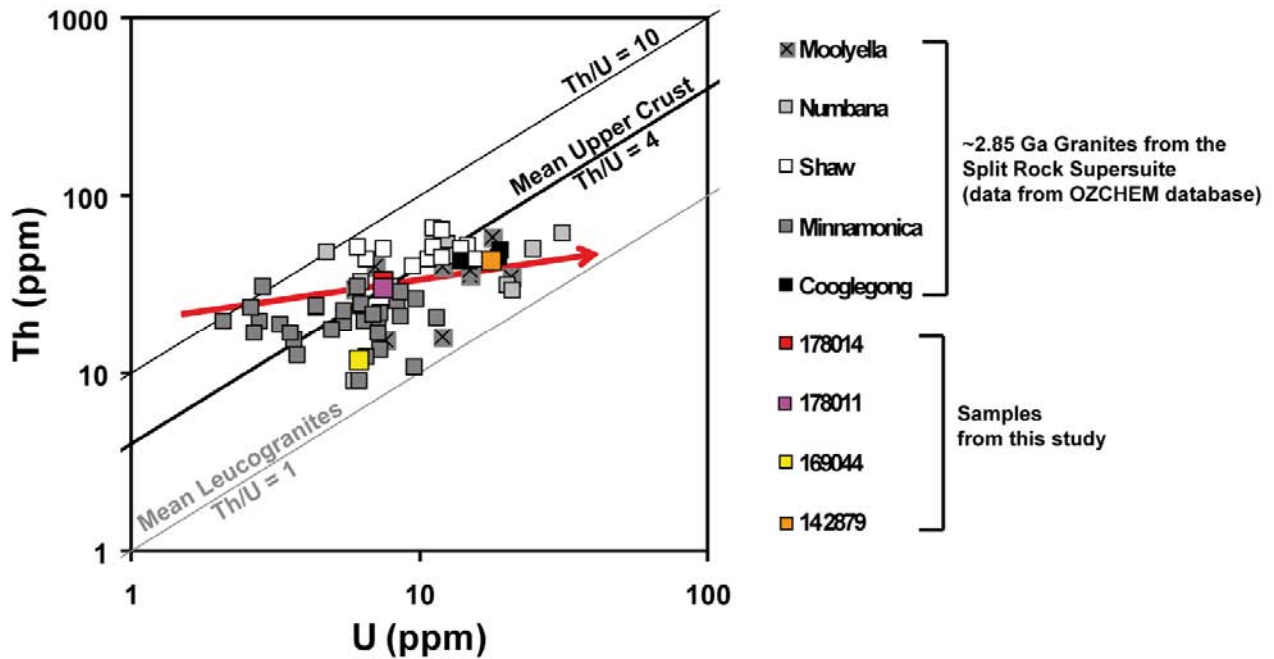


**Figure 2.2.11.** Binary diagram showing whole-rock Th vs. U contents (in ppm) of the Split Rock Supersuite granitoids from the East Pilbara Terrane. The red arrow in the diagram indicates the limited Th enrichment associated with high U enrichment.

## MINERALOGY

### Primary magmatic phases

#### Feldspar

In the 4 studied samples, plagioclase is the first phase to crystallise as well tabular albitic plagioclase ranging up to 500  $\mu\text{m}$  wide and 2 mm long, followed by crystallization of large euhedral centimetre-scale K-feldspar phenocrysts represented mostly by microcline and minor sanidine and orthoclase (Fig. 2.2.12). Myrmekite patches also appear to replace microcline occasionally (Fig. 2.2.13). As noticed by bulk geochemistry and macroscopic observations, adamellite sample 178011 hosts more abundant albitic plagioclase than the three other granites.

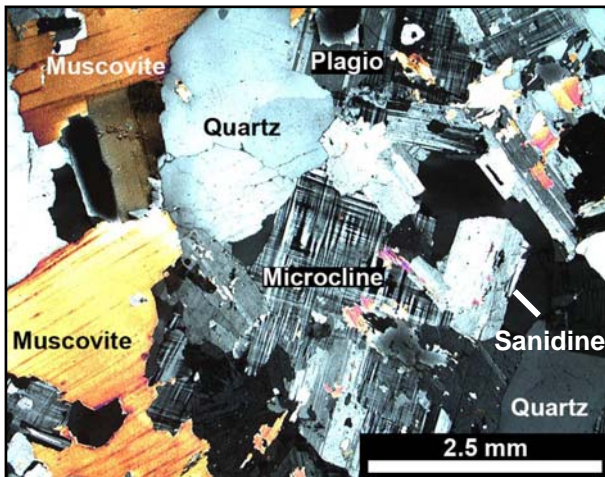


**Figure 2.2.12.** Polarized transmitted light image of the well preserved primary magmatic assemblage of quartz, feldspar and muscovite phenocrysts (*sample 169044*).

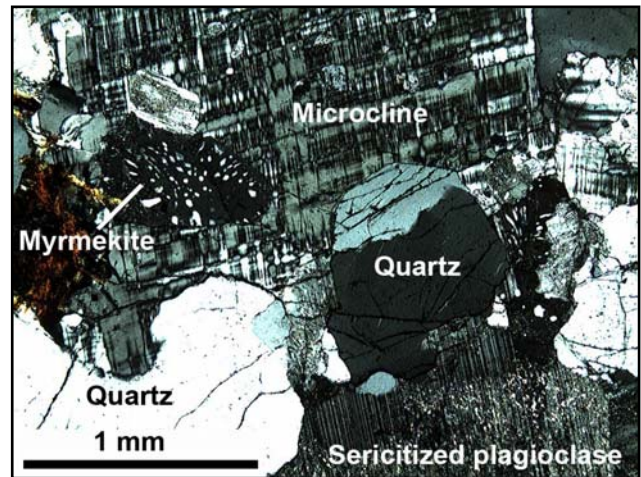


**Figure 2.2.13.** Myrmekite in microcline (the plaid twinning) observed in polarized transmitted light (*sample 142879*).

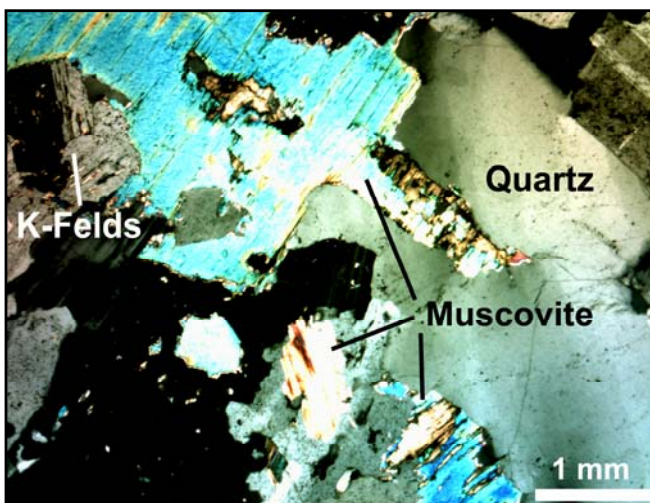


**Figure 2.2.14.** Quartz with rolling extinction, feldspar and muscovite partly replaced by chlorite observed in polarized transmitted light (*sample 169044*).

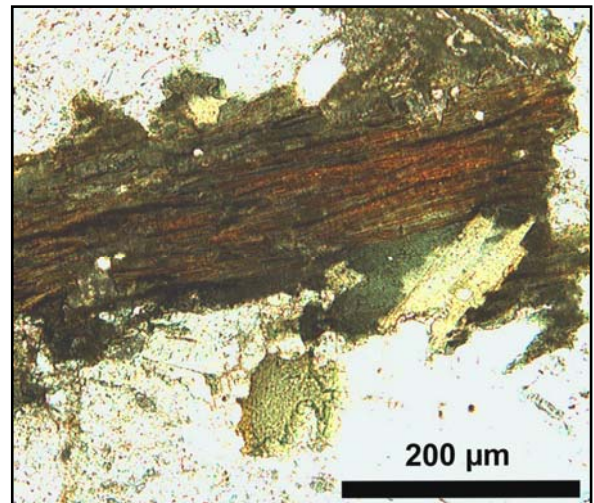


**Figure 2.2.15.** Biotite partly altered to chlorite observed in natural transmitted light (*sample 178014*).

Quartz

Quartz is less abundant, displays irregular shape and occupies interstitial space between feldspar grains (Fig. 2.2.12). Undulous extinction in quartz is common (Fig. 2.2.14) and indicates the occurrence of a slight tectonic deformation after the granite emplacement but no granulation is visible.

Micas

Biotite is present as large monocrystals with no predominant orientation or deformation but only later chloritization (Fig. 2.2.15). Biotite is more abundant in the metaluminous sample 178011 than in samples 142879 and 178014, slightly more fractionated with intermediary compositions and lower B parameters (Fig. 2.2.9). Leucogranite 169044, which is characterized by the lowest B and highest A parameters, is a two mica granite and hosts large phenocrysts of muscovite occurring between K-feldspar and quartz crystals (Fig. 2.2.12 and 2.2.14).

Titanite I

Primary titanite has been observed in the metaluminous granite 178011 as coarse phenocrysts of one centimetre large with a typical double wedge or diamond shape (Fig. 2.2.16). Presence of titanite could explain part of the much higher B parameter calculated for this sample, part of its metaluminous character as well as its higher Ca content (1.79 % CaO) compare to other granitoids (<1% CaO). Titanite from sample 178011 (Table 2.2.3) shows significant amounts of fluorine, aluminium and iron that should correlate to the ideal formula  $\text{CaTiSiO}_5$ . This composition probably reflects alteration by hydrothermal fluids bearing F and Fe, responsible of the cavity dissolution observed.

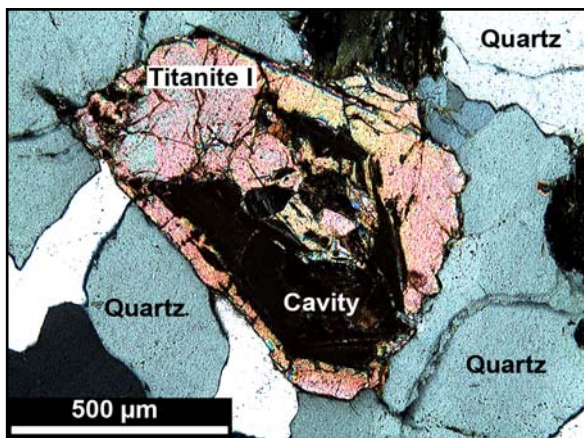


**Figure 2.2.16.** Titanite (stage I) observed in polarized transmitted light (*sample 178011*).

**Table 2.2.3.** EMPA results (in wt%) of titanite minerals from sample 178011

<i>Sample 178011</i>	<i>Titanite Stage I</i>	<i>Titanite Stage II</i>	<i>Average Titanite</i>
EMPA	(15)	(4)	(19)
Na <sub>2</sub> O	<D.L.	<D.L.	<D.L.
Al <sub>2</sub> O <sub>3</sub>	3.05 ± 0.20	4.87 ± 1.26	3.43 ± 0.94
SiO <sub>2</sub>	30.26 ± 0.27	30.87 ± 1.09	30.39 ± 0.57
K <sub>2</sub> O	<D.L.	<D.L.	<D.L.
CaO	26.38 ± 0.63	27.92 ± 0.84	26.70 ± 0.92
TiO <sub>2</sub>	32.14 ± 0.54	30.31 ± 1.34	31.75 ± 1.05
Cr <sub>2</sub> O <sub>3</sub>	<D.L.	<D.L.	<D.L.
FeO	2.22 ± 0.27	1.44 ± 0.38	2.06 ± 0.44
MgO	<D.L.	<D.L.	<D.L.
MnO	<D.L.	<D.L.	<D.L.
F	1.70 ± 0.16	2.06 ± 0.38	1.78 ± 0.26
Total	95.98 ± 1.17	97.69 ± 1.51	96.34 ± 1.40
Structural formula based on 5 oxygen atoms			
Ca	0.97 ± 0.02	1.01 ± 0.05	0.98 ± 0.03
Ti	0.83 ± 0.01	0.77 ± 0.04	0.82 ± 0.03
Si	1.04 ± 0.01	1.04 ± 0.02	1.04 ± 0.01
Fe	0.06 ± 0.01	0.04 ± 0.01	0.06 ± 0.01
Al	0.12 ± 0.01	0.19 ± 0.05	0.14 ± 0.04
Σ cations	3.03 ± 0.01	3.06 ± 0.02	3.03 ± 0.02

*Notes:* <D.L. = below detection limits (Al = 0.05 wt%; Si = 0.05 wt%; Ca = 0.06 wt%; K = 0.06 wt%, Na = 0.10 wt%; Ti = 0.07 wt%; Fe = 0.15 wt%; Mg = 0.05 wt%; Mn = 0.16 wt%; Cr = 0.09; F = 0.57 wt%).

Hornblende

Euhedral phenocrysts of amphibole also characterize the metaluminous sample 178011 in accordance with its less fractionated composition and its high bulk calcium content. They are up to 500  $\mu\text{m}$  wide and pleochroic in the brown (Fig. 2.2.17-A). The BSE picture provides a relatively homogeneous internal texture with common ilmenite inclusions (Fig. 2.2.17-B). This observation is concordant to the low standard deviation of the EMP analysis average (10 analyses widespread in one crystal, Table 2.2.4). They are mainly ferric iron and calcium rich with small amounts of magnesium, manganese, titanium, potassium and sodium. The calculation of their structural formula (ideally as  $\text{A}_{2-3}\text{B}_5\text{T}_8\text{O}_{22}(\text{OH})_2$  with T-site occupied by Si and  $\text{Al}^{\text{IV}}$ , B-site by  $\text{Al}^{\text{VI}}$ ,  $\text{Fe}^{3+}$ , Mg, Ti and Mn, and A-site by Ca, K and Na after Deer et al., 1963) revealed that they are part of the ferri-tschermakitic hornblende family with  $\text{Si} = 6.25$  apfu and  $\text{Mg}/(\text{Mg}+\text{Fe}^{2+}) = 1$ .

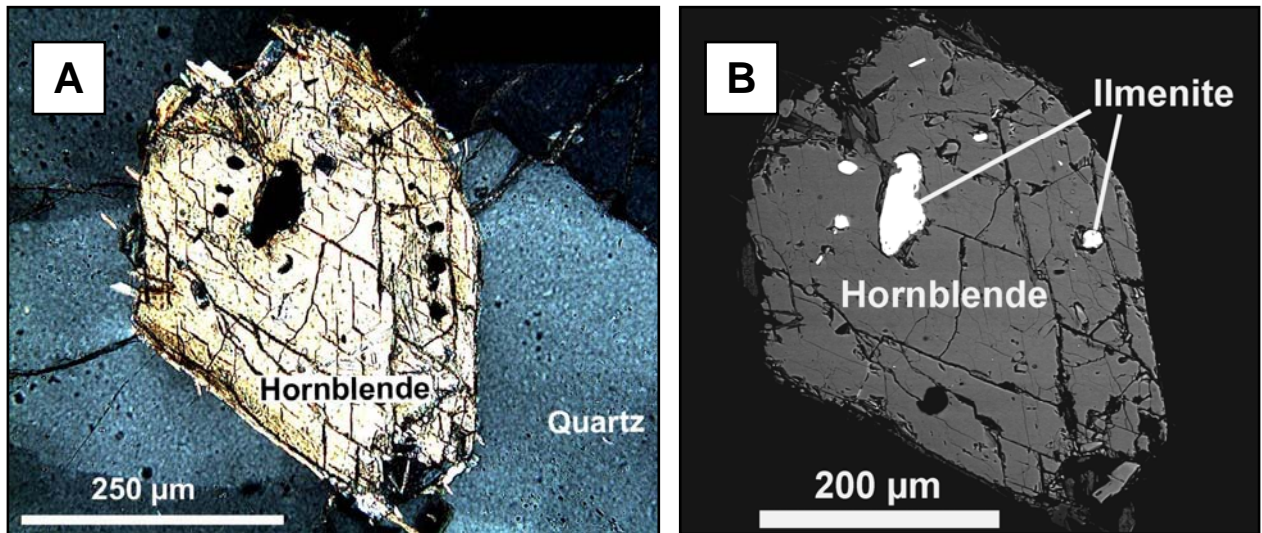


**Figure 2.2.17.** Hornblende A- in polarized transmitted light and B- in BSE mode (*sample 178011*) showing ilmenite inclusions and the typical crossing cleavage.

**Table 2.2.4.** EMPA results (in wt%) of hornblende in sample 178011

Mineral Classification	Ca-Amphibole Group, ferri-tschermakitic hornblende		
Analysis (10)	Average $\pm \sigma$	Structural formula based on 23 oxygen atoms	
$\text{SiO}_2$	$41.06 \pm 0.50$	Si	$6.25 \pm 0.07$
$\text{TiO}_2$	$1.65 \pm 0.16$	$\text{Al}^{\text{IV}}$	$1.56 \pm 0.04$
$\text{Al}_2\text{O}_3$	$8.69 \pm 0.25$	Total T site	$7.80 \pm 0.04$
$\text{Cr}_2\text{O}_3$	$0.01 \pm 0.02$	$\text{Al}^{\text{VI}}$	$0.00 \pm 0.00$
$\text{FeO}^*$	$0.00 \pm 0.00$	Cr	$0.00 \pm 0.00$
$\text{Fe}_2\text{O}_3^*$	$27.43 \pm 0.62$	Ti	$0.19 \pm 0.02$
MnO	$0.70 \pm 0.08$	$\text{Fe}^{2+}$	$0.00 \pm 0.00$
MgO	$4.16 \pm 0.10$	$\text{Fe}^{3+}$	$3.14 \pm 0.06$
CaO	$10.71 \pm 0.21$	Mn	$0.09 \pm 0.01$
$\text{Na}_2\text{O}$	$1.24 \pm 0.13$	Mg	$0.94 \pm 0.03$
$\text{K}_2\text{O}$	$1.28 \pm 0.08$	Total B site	$4.36 \pm 0.07$
$\text{H}_2\text{O}^{**}$	$1.97 \pm 0.01$	Ca	$1.74 \pm 0.03$
Total	$98.89 \pm 0.76$	Na	$0.37 \pm 0.04$
		K	$0.25 \pm 0.02$
		Total A site	$2.36 \pm 0.03$
		Total	$14.52 \pm 0.04$

\*  $\text{Fe}_2\text{O}_3$  ( $\text{Fe}^{2+}$ ) vs  $\text{FeO}$  ( $\text{Fe}^{3+}$ ) contents recalculated to not exceed 13 in B site

\*\*  $\text{H}_2\text{O}$  calculated from ideal formula with 22 O and 2 OH

The mineral assemblage (Fds+Qtz+Bt+Ilm+Ttn+Hbn) of the granite and the composition of hornblende permit to use the Al-in-hornblende geobarometers (Hammarstrom and Zen, 1986; Hollister et al., 1987; Johnson and Rutherford, 1989; Schmidt, 1992) yielding pressure in the range between 2.7 and 4.6 kbar. Although the pressure value calculation is not accurate for temperature exceeding 800°C and is also dependent of the oxygen fugacity (Anderson and Smith, 1995), this estimation suggests that the hornblende has crystallized from a magma at relatively high pressure rising possibly up to 4.6 kbar which corresponds to relatively deep crustal level at ~15 km depth.

#### Fe & Ti oxides

Fe-Ti oxides are extremely abundant phases. They are widespread in all the studied granite samples but however, they are more abundant in the metaluminous adamellite 178011. Ilmenite is the most common although the BSE images show a complex internal texture with exsolutions of rutile (Fig. 2.2.18). Ilmenite is represented mainly by prismatic crystals up to 40 µm wide disseminated in altered biotite (chlorite). Ilmenite also occurs as xenomorphic phase within fractures of some early magmatic minerals as in hornblende (Fig. 2.2.17).

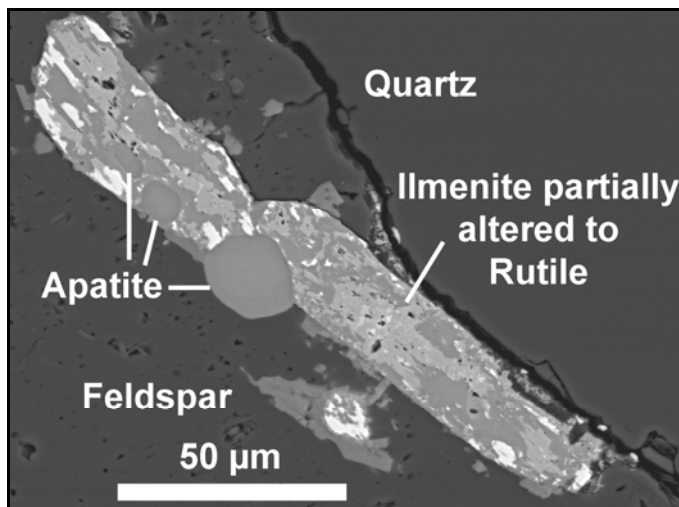


**Figure 2.2.18.** BSE image of apatite crystals occurring in Fe-Ti oxide (*sample 178014*).

#### Garnet

Garnets only occur in the peraluminous leucogranite 169044 as 1 to 1.5 centimetres wide crystals interstitial between quartz, feldspar and muscovite, and are characterized by a pale brown to reddish colour in natural transmitted light (Fig. 2.2.19). They are fragmented in numerous sub-grains separated by fractures filled with chlorite and epidote. The sub-grains show a distinct darker rim surrounding a fairly homogeneous core in BSE images (Fig. 2.2.20) which corresponds to a sharp decrease of the average atomic number reflecting an increase in calcium content (Table 2.2.5).

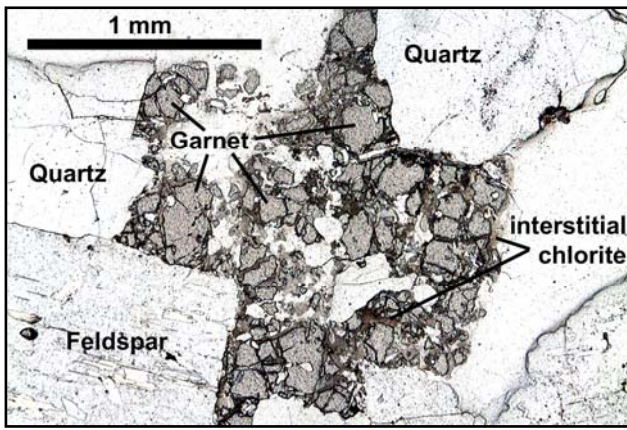


**Figure 2.2.19.** Fragmented garnet phenocryst in natural transmitted light (*sample 169044*)

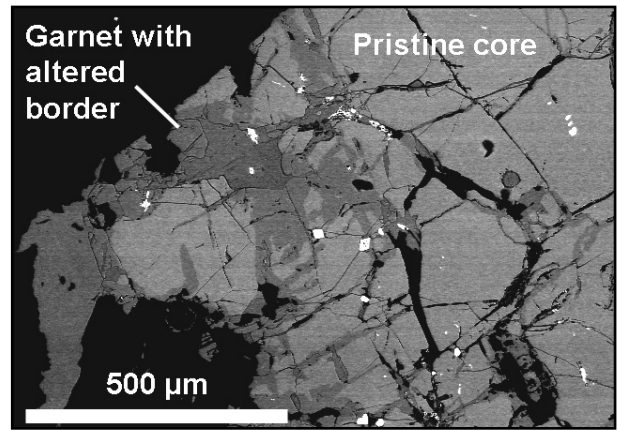


**Figure 2.2.20.** BSE image of a garnet showing a darker zoning at the edge of the crystal and along microcracks (*sample 169044*)

The core of garnets has a spessartite-almandine composition whereas the rim shows an increase in the grossular end-member compound (Fig. 2.2.21). The core is mainly composed of manganese, iron, aluminium and silicium whereas the rim is highly enriched in calcium (up to + 10 wt% of CaO). This increase in Ca is correlated with the decrease in the Mn and Fe contents whereas the Al and Si concentrations do not change significantly. A slight decrease in the analytical totals (0.5-1 wt%) is also noticed in the rim and could be related to hydration of the edge of the mineral (hydrogrossular which is a typical hydrothermal mineral with formula  $[Ca_3Al_2(SiO_4)_{3-x}(OH)_{4x}]$ ). Therefore, the calcic rim of garnets is interpreted as an alteration rim probably corresponding to diffusion of Ca, Mn and Fe elements between the garnet and the minerals in its close environment (epidote and chlorite).

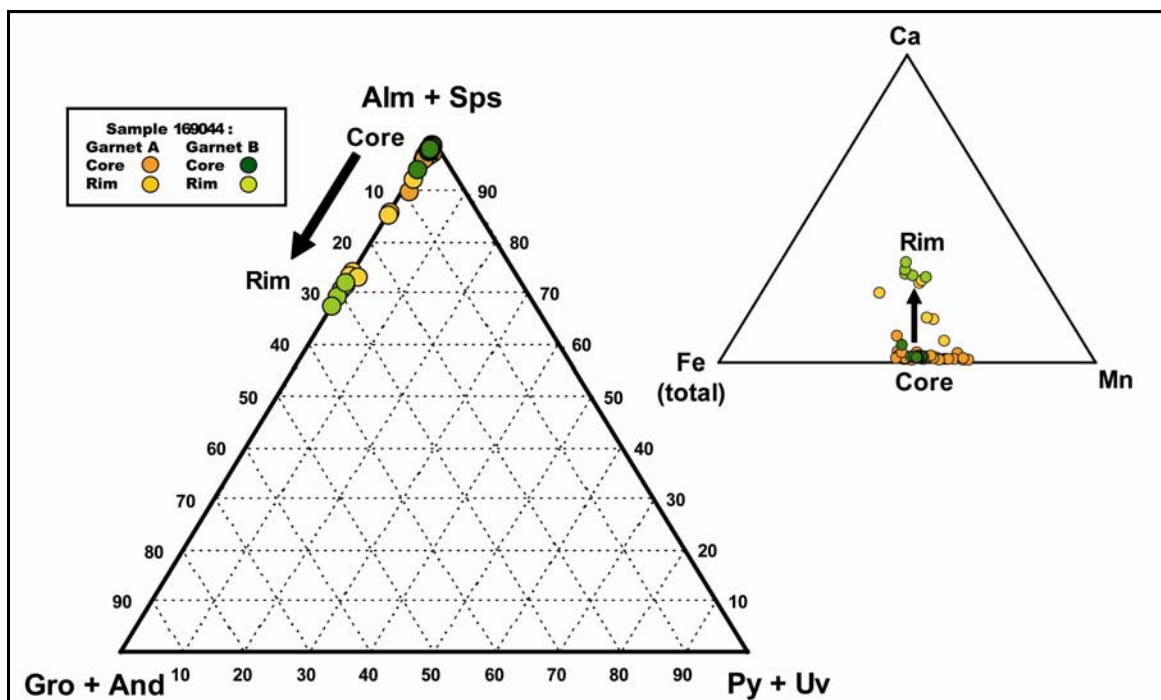


**Figure 2.2.21.** Ternary diagrams representative of the end member molecules (Alm = Almandine; Sps = Spessartite; Gro = Grossular; And = Andradite; Py = Pyrope; Uv = Uvarovite) and the Fe, Mn and Ca contents in two phenocrysts of garnet (*sample 169044*).

**Table 2.2.5.** Average composition of garnets in a late-orogenic Archean granite (sample 169044) from the the Pilbara craton, Australia.

Garnet	169044-A		169044-B		Average	
	Core	Rim	Core	Rim	Core	Rim
EMPA measurements	(15)	(5)	(64)	(6)	(79)	(11)
SiO <sub>2</sub>	36.01 ± 0.43	36.70 ± 0.45	36.25 ± 0.40	36.35 ± 2.03	36.20 ± 0.41	36.51 ± 1.48
TiO <sub>2</sub>	0.09 ± 0.04	< D.L.	0.17 ± 0.10	0.09 ± 0.09	0.15 ± 0.09	0.07 ± 0.07
Al <sub>2</sub> O <sub>3</sub>	19.51 ± 0.82	19.52 ± 0.74	20.70 ± 0.21	21.19 ± 0.62	20.47 ± 0.61	20.43 ± 1.08
Cr <sub>2</sub> O <sub>3</sub>	< D.L.					
Y <sub>2</sub> O <sub>3</sub>	< D.L.					
Fe <sub>2</sub> O <sub>3</sub> *	0.57 ± 0.61	0.43 ± 0.39	0.34 ± 0.58	1.06 ± 2.56	0.38 ± 0.58	0.77 ± 1.86
FeO	19.60 ± 0.58	14.72 ± 0.91	19.10 ± 2.03	15.19 ± 0.74	19.20 ± 1.85	14.97 ± 0.82
MnO	22.09 ± 0.96	15.88 ± 1.28	22.72 ± 2.21	19.13 ± 3.45	22.60 ± 2.05	17.65 ± 3.08
MgO	0.11 ± 0.02	< D.L.	0.12 ± 0.05	0.11 ± 0.11	0.12 ± 0.05	0.07 ± 0.09
CaO	0.64 ± 0.34	10.19 ± 0.64	0.58 ± 0.35	6.33 ± 2.75	0.59 ± 0.35	8.08 ± 2.83
Σ oxides (wt%)	98.66 ± 1.58	97.50 ± 1.77	100.0 ± 0.80	99.48 ± 1.43	99.75 ± 1.12	98.58 ± 1.83
Atomic contents normalized to 12 oxygen atoms and 8 cations per formula unit						
Si	3.02 ± 0.04	3.03 ± 0.03	2.98 ± 0.03	2.96 ± 0.13	2.99 ± 0.03	2.99 ± 0.10
Al <sup>iv</sup>	0.01 ± 0.01	0.00 ± 0.00	0.02 ± 0.02	0.05 ± 0.12	0.02 ± 0.02	0.03 ± 0.09
Al <sup>vi</sup>	1.92 ± 0.05	1.90 ± 0.04	1.99 ± 0.03	1.98 ± 0.04	1.98 ± 0.04	1.95 ± 0.06
Ti	0.01 ± 0.00	0.00 ± 0.00	0.01 ± 0.01	0.01 ± 0.01	0.01 ± 0.01	0.00 ± 0.00
Fe <sup>3+</sup>	0.04 ± 0.04	0.03 ± 0.02	0.02 ± 0.04	0.07 ± 0.16	0.02 ± 0.04	0.05 ± 0.12
Fe <sup>2+</sup>	1.37 ± 0.05	1.02 ± 0.06	1.32 ± 0.14	1.03 ± 0.05	1.33 ± 0.13	1.03 ± 0.05
Mn	1.57 ± 0.06	1.11 ± 0.09	1.58 ± 0.15	1.32 ± 0.23	1.58 ± 0.14	1.22 ± 0.20
Mg	0.01 ± 0.00	0.00 ± 0.00	0.01 ± 0.01	0.01 ± 0.01	0.01 ± 0.01	0.01 ± 0.01
Ca	0.06 ± 0.03	0.90 ± 0.06	0.05 ± 0.03	0.55 ± 0.24	0.05 ± 0.03	0.71 ± 0.25
Σ cations	8.00 ± 0.01	8.00 ± 0.00	7.99 ± 0.01	7.98 ± 0.03	7.99 ± 0.01	7.99 ± 0.02
End member molecules						
Pyrope	0.46 ± 0.10	0.11 ± 0.10	0.48 ± 0.21	0.48 ± 0.50	0.48 ± 0.19	0.31 ± 0.41
Almandine	45.59 ± 1.35	33.52 ± 1.80	44.36 ± 4.74	35.48 ± 1.94	44.60 ± 4.32	34.59 ± 2.05
Spessartite	52.03 ± 2.09	36.65 ± 3.10	53.43 ± 5.08	45.11 ± 7.51	53.17 ± 4.69	41.26 ± 7.18
Andradite	1.80 ± 1.91	1.35 ± 1.19	1.03 ± 1.73	2.89 ± 7.02	1.18 ± 1.78	2.19 ± 5.08
Uvarovite	0.00 ± 0.00	0.01 ± 0.02	0.00 ± 0.01	0.00 ± 0.00	0.00 ± 0.01	0.00 ± 0.01
Grossular	0.11 ± 2.41	28.37 ± 2.41	0.68 ± 1.75	16.04 ± 8.41	0.57 ± 1.89	21.64 ± 8.90
Σ	100.0	100.0	100.0	100.0	100.0	100.0

Notes: Measurements are realised using an electronic microprobe CAMECA SX100; <D.L.: below detection limits (Si = 0.05 wt%; Ti = 0.04 wt%; Al = 0.06 wt%; Cr = 0.05 wt%; Y = 0.23 wt%; Fe = 0.20 wt%; Mn = 0.22 wt%; Mg = 0.05 wt%; Ca = 0.07 wt%); \* Fe<sub>2</sub>O<sub>3</sub> calculated to eliminate excess cations over 8. The rim of garnet fragments is distinct from the core by a decrease of brightness in BSE mode (SEM) and corresponds to a decrease in the average atomic number consecutive to the substitution of Fe and Mn by Ca (lighter element).

Columbite

Columbite has also been observed in the peraluminous granite 169044 which is the richest sample in tantalum and niobium with 12.94 ppm Ta and 38.1 ppm Nb, respectively (Nb/Ta ~ 2.94; Table 2.2.2). Columbite occurs as a euhedral cubic crystal showing a complex internal zoning in BSE mode image (Fig. 2.2.22). The core is represented by a darker grey amorphous material rimmed by a better crystallized mineral phase with domains presenting variable average atomic number. A composition profile has been realized by EMP across the crystal to study the element distribution along the zonation pattern. The average chemical composition of both domains is given in Table 2.2.6.

**Table 2.2.6.** EMPA results (in wt%) of columbite in sample 169044

<i>Sample 169044B</i>	<i>Average Pristine Columbite (margin)</i>	<i>Average Metamict Material (core)</i>
EMPA	(104)	(29)
Na <sub>2</sub> O	<D.L.	0.78 ± 0.13
CaO	<D.L.	1.98 ± 0.20
Al <sub>2</sub> O <sub>3</sub>	<D.L.	0.76 ± 0.07
P <sub>2</sub> O <sub>5</sub>	<D.L.	<D.L.
K <sub>2</sub> O	<D.L.	0.29 ± 0.07
SiO <sub>2</sub>	<D.L.	13.51 ± 1.53
FeO	12.17 ± 0.83	1.29 ± 0.36
MnO	7.49 ± 0.78	<D.L.
MgO	<D.L.	0.10 ± 0.03
TiO <sub>2</sub>	1.74 ± 0.33	8.08 ± 0.76
Nb <sub>2</sub> O <sub>5</sub>	56.93 ± 3.67	8.54 ± 0.88
Ta <sub>2</sub> O <sub>5</sub>	19.03 ± 3.13	17.70 ± 2.21
SnO <sub>2</sub>	<D.L.	<D.L.
WO <sub>3</sub>	<D.L.	1.46 ± 0.37
PbO	0.23 ± 0.06	12.03 ± 1.42
ThO <sub>2</sub>	<D.L.	2.15 ± 0.38
UO <sub>2</sub>	<D.L.	9.65 ± 0.94
Sb <sub>2</sub> O <sub>3</sub>	<D.L.	<D.L.
Bi <sub>2</sub> O <sub>3</sub>	<D.L.	1.08 ± 0.24
Sc <sub>2</sub> O <sub>3</sub>	0.10 ± 0.03	<D.L.
Y <sub>2</sub> O <sub>3</sub>	0.29 ± 0.13	0.34 ± 0.54
ZrO <sub>2</sub>	<D.L.	1.29 ± 1.09
F	<D.L.	<D.L.
Total	98.70 ± 1.80	78.93 ± 5.79
Structural Formula calculated with 6 oxygen atoms		
Fe	0.63 ± 0.04	
Mn	0.39 ± 0.04	
ΣA site	1.02 ± 0.03	
Ti	0.08 ± 0.02	
Nb	1.58 ± 0.07	
Ta	0.32 ± 0.06	
Sc	0.01 ± 0.00	
Y	0.01 ± 0.00	
ΣB site	2.00 ± 0.02	
Total	3.02 ± 0.02	
Mn/(Mn+Fe)	0.38 ± 0.04	
Ta/(Ta+Nb)	0.17 ± 0.03	

Notes: <D.L.: below detection limits (Na = 0.08 wt%; Ca = 0.09 wt%; Al = 0.05 wt%; P = 0.06 wt%; K = 0.09 wt%; Si = 0.07 wt%; Fe = 0.14 wt%; Mn = 0.13 wt%; Mg = 0.06 wt%; Ti = 0.06 wt%; Nb = 0.47 wt%; Ta = 0.24 wt%; Sn = 0.14 wt%; W = 0.44 wt%; Pb = 0.16 wt%; Th = 0.29 wt%; U = 0.15 wt%; Sb = 0.19 wt%; Bi = 0.56 wt%; Sc = 0.05 wt%; Y = 0.21 wt%; Zr = 0.27 wt%; F = 0.12 wt%).

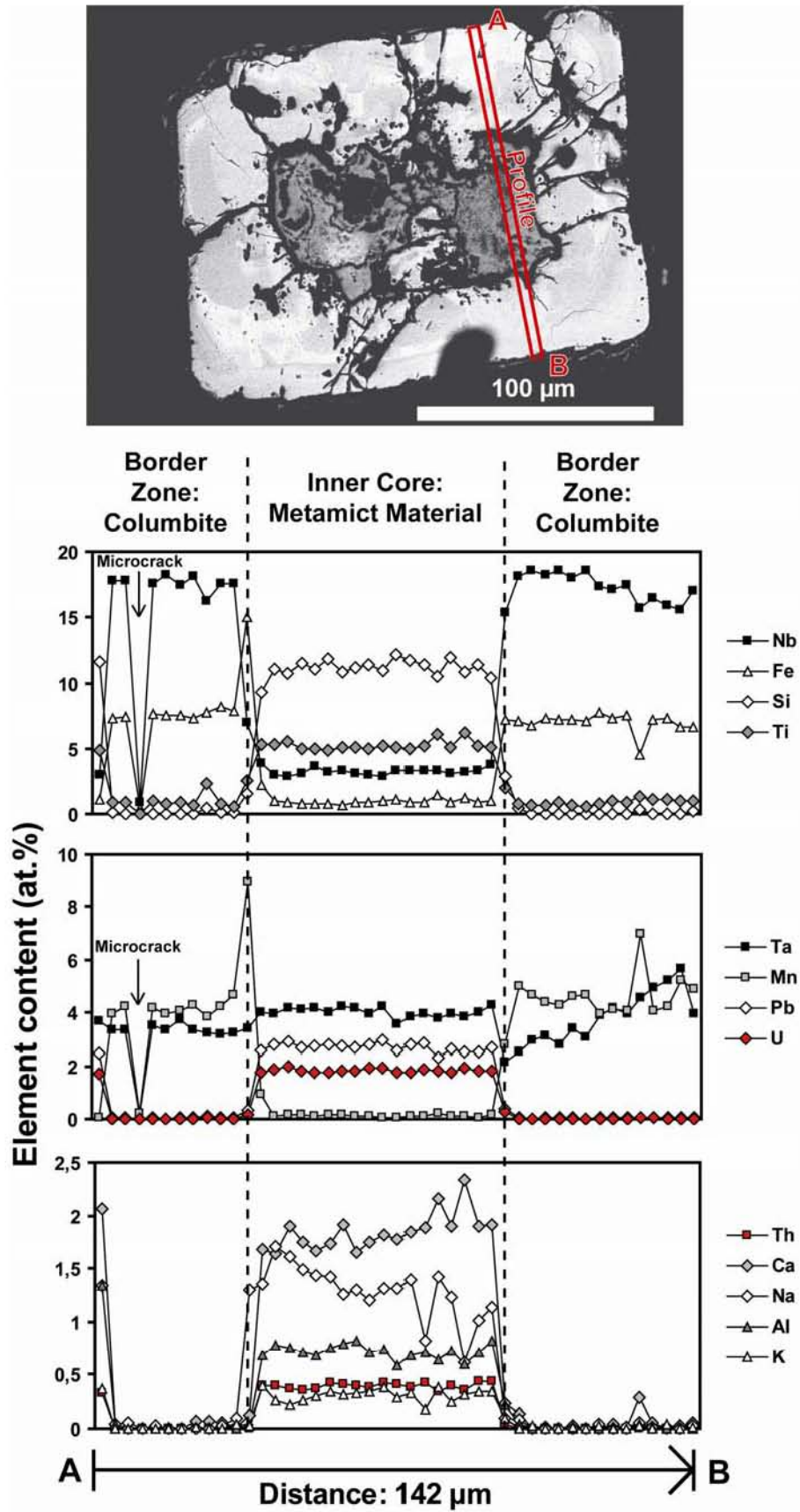


**Figure 2.2.22.** BSE image showing the complex texture and composition heterogeneities in a columbite crystal (sample 169044). Chemical profile through the grain was realized by electron microprobe analysis along the A-B line approximately each 3.5 µm.

The composition of the columbite rim in the columbite-tantalite quadrilateral (Fig. 2.2.23) plot in the field of ferro-columbite ( $\text{FeNb}_2\text{O}_6$ ) which generally characterized the metaluminous alkali granites (Abdalla et al., 1998). It is mostly composed of niobium ( $1.58 \pm 0.07$  apfu), tantalum ( $0.32 \pm 0.06$  apfu), iron ( $0.63 \pm 0.04$  apfu) and manganese ( $0.39 \pm 0.04$  apfu) giving  $\text{Ta}/(\text{Ta}+\text{Nb})$  ranging between 0.13 and 0.27 and  $\text{Mn}/(\text{Mn}+\text{Fe})$  ratio between 0.32 and 0.54. The small variations of the columbite chemical composition are essentially related to the Nb-Ta substitution occurring during progressive fractional crystallization (Černý et al., 1986). Titanium can reach high concentrations from 1.08 to 3.31 wt%  $\text{TiO}_2$  (average  $1.74 \pm 0.33$  wt%) which is not uncommon in columbite-tantalite group minerals (Van Lichtervelde et al., 2007). Small amounts of scandium, yttrium and lead have also been detected but they are always under the weight percent of oxides all together. Ferro-columbite is generally associated to primary magmatic paragenetic sequence of early formed and petalite-free fractionated granitoids as the Separation Rapids pluton in Canada (Tindle and Breaks, 1998). The occurrence of both garnet and columbite is normally extremely rare in highly fractionated granites (Linnen and Cuney, 2005) which remain possible in the Split Rock Supersuite because this slightly peraluminous granite sample probably derives from the fractionation of metaluminous melts.

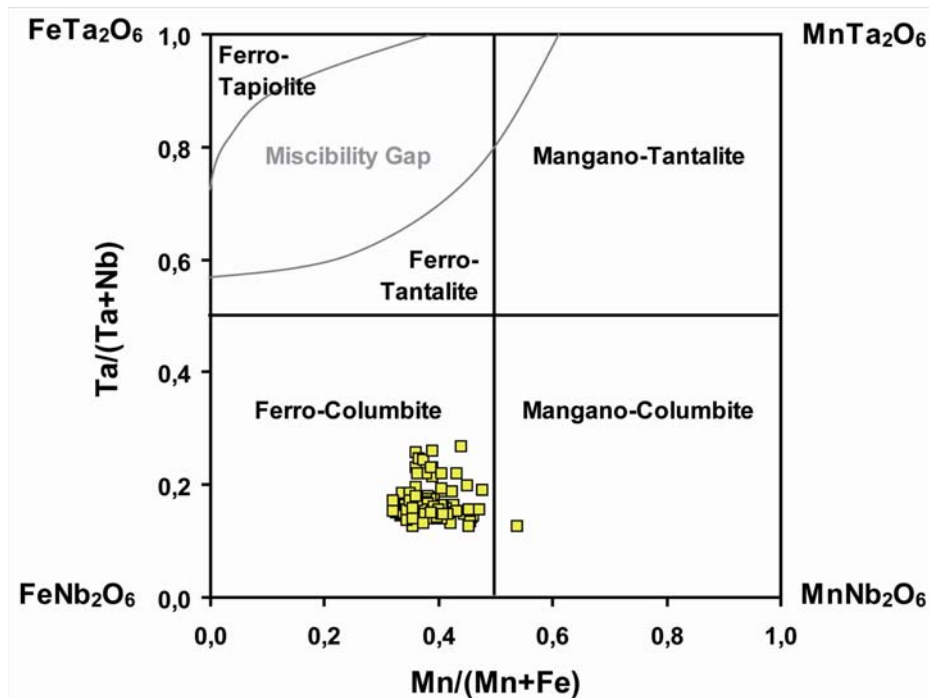


**Figure 2.2.23.** Columbite-Tantalite quadrilateral representing binary plot of  $\text{Mn}/(\text{Mn}+\text{Fe})$  against  $\text{Ta}/(\text{Ta}+\text{Nb})$  in atom per formula unit (apfu) for the pristine columbite observed in sample 169044.

The composition of the amorphous material from the inner part does not fit with any stoichiometric mineral composition which suggests that this is a composite phase. The inner core is mainly composed of tantalum ( $17.70 \pm 2.21$  wt%  $\text{Ta}_2\text{O}_5$ ) in proportions higher than niobium

( $8.54 \pm 0.88$  wt%  $\text{Nb}_2\text{O}_5$ ), uranium ( $9.65 \pm 0.94$  wt%  $\text{UO}_2$ ), lead ( $12.03 \pm 1.42$  wt%  $\text{PbO}$ ), silicium ( $13.51 \pm 1.53$  wt%  $\text{SiO}_2$ ), titanium ( $8.08 \pm 0.76$  wt%  $\text{TiO}_2$ ), and thorium (2.15 wt%) with extremely low analytical totals ( $78.93 \pm 5.79$  wt%) suggesting strong metamictization and hydration. Significant calcium ( $1.98 \pm 0.20$  wt%  $\text{CaO}$ ), zirconium ( $1.29 \pm 1.09$  wt%  $\text{ZrO}_2$ ) and yttrium ( $0.34 \pm 0.54$  wt%  $\text{Y}_2\text{O}_3$ ) contents are also present.

The global composition corresponds to a mixture between pyrochlore group minerals such as plumbo-pyrochlore  $[(\text{Pb},\text{Y},\text{U},\text{Ca})_{2-x}\text{Nb}_2\text{O}_6(\text{OH})]$ , betafite  $[(\text{U},\text{Ca})_2(\text{Ti},\text{Nb},\text{Ta})_2\text{O}_6(\text{OH})]$  and possibly other complex mineral phases. The very high  $\text{Pb}/(\text{U}+\text{Th})$  ratio suggests that the mineral may have lost uranium if all the lead is radiogenic.

### Zircon, Xenotime and Monazite

Primary zircon and monazite grains occur sporadically in all the samples, sometimes included in quartz and feldspar but more often within micas and are easily recognizable because of the pleochroic halo surrounding them and corresponding to radiation damage (Fig. 2.2.24). They range from 10 to 100  $\mu\text{m}$  wide, are generally euhedral and can be overgrown by secondary epidote and titanite.

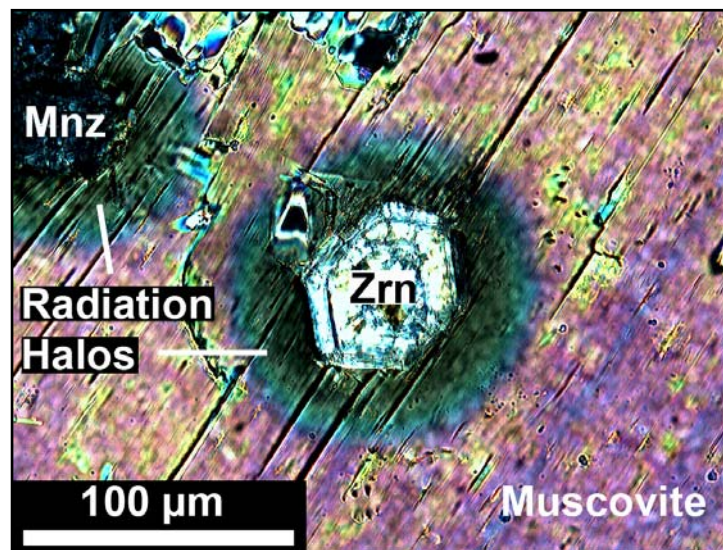


**Figure 2.2.24.** Zircon and monazite grains in polarised transmitted light showing a radiation damage halo in the surrounding muscovite (sample 178011).

Zircon is more abundant than monazite. Crystals often display a well developed grow zoning but generally they are altered and metamict as shown by the decrease of the average atomic number in the BSE pictures (Fig. 2.2.25 and 2.2.26). Zircon may become metamict as a result of alpha-recoil from the radioelement decay (Cuney and Friedrich, 1987). Some of the grains also show partial dissolution with complex internal textures adjoining secondary fluorocarbonates (Fig. 2.2.27) which suggest later fluid alteration.

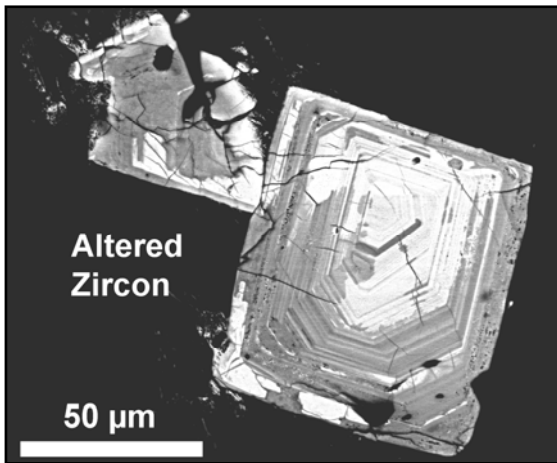


**Figure 2.2.25.** Euhedral zircons showing the crystal grow zoning and altered areas (darker grey) in BSE mode (*sample 178014*).

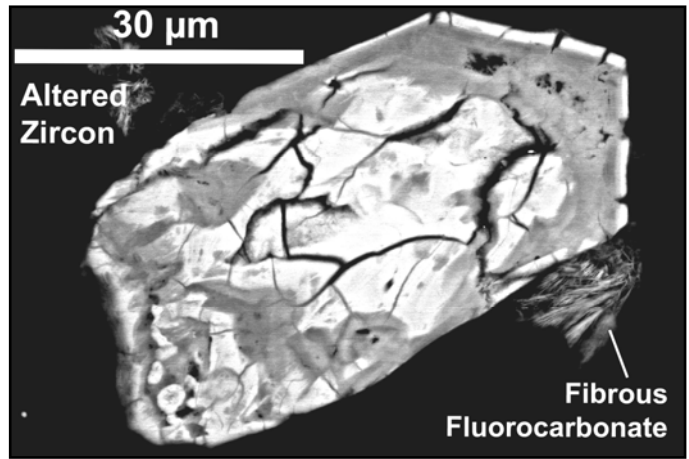


**Figure 2.2.26.** Euhedral zircon with a complex heterogeneous texture in BSE mode associated to metamictization (*sample 169044*).

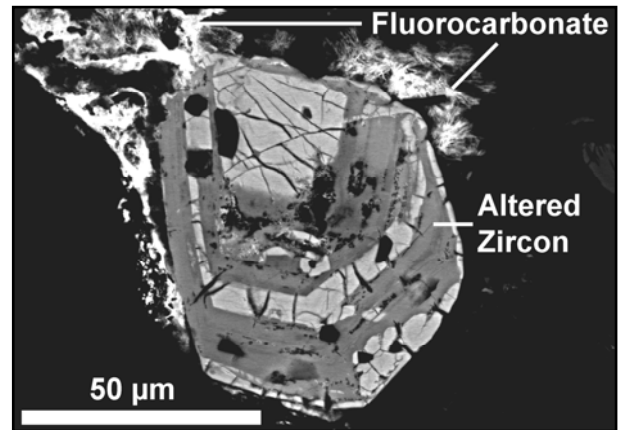
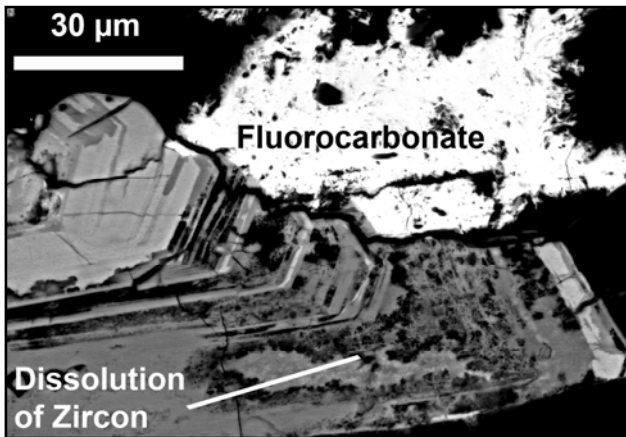


**Figure 2.2.27.** Fractured and altered zircon surrounded by fluorocarbonate in BSE mode (*sample 142879*).

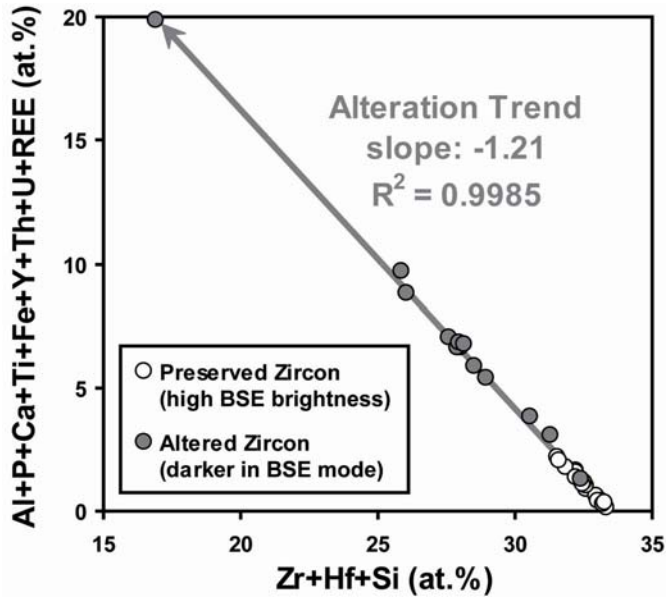
The altered domains have been separated from non altered zircon for the average results presented in Table 2.2.7. The composition of the best preserved domains in zircon is consistent in all the granites with  $31.65 \pm 0.97$  wt%  $\text{SiO}_2$ ,  $61.61 \pm 3.14$  wt%  $\text{ZrO}_2$ ,  $2.61 \pm 0.99$  wt%  $\text{HfO}_2$ , and high analytical totals ( $98.38 \pm 2.19$  wt%). Other elements (Al, P, Ca, Ti, Fe, Y, La, Th, U, Pb and REE) are generally close or below the instrumental detection limits. The altered areas appearing darker in the BSE images show a decrease in the major components  $\text{SiO}_2$  (- 6 wt%),  $\text{ZrO}_2$  (- 20 wt%),  $\text{HfO}_2$  (- 1 wt%) and in the analytical totals (- 11 wt%) whereas the contents in  $\text{Al}_2\text{O}_3$  (+ 1.5 wt%),  $\text{Y}_2\text{O}_3$  (+ 5 wt%) and  $\text{CaO}$  (+ 3 wt%) increase. The concentrations in P, Ti, Fe, Th, U and REE also increase slightly but only locally in some analytical spots. The maximum Th and U contents measured in zircon are respectively of 2.55 wt%  $\text{ThO}_2$  and 0.64 wt%  $\text{UO}_2$ .

Table 2.2.7. EMPA results (in wt%) of zircons from the late K-rich granites sampled in the East Pilbara Terrane

Sample	142879			169044			178011			178014			Average		
	High	Low	EMPA												
Al <sub>2</sub> O <sub>3</sub>	0.16 ± 0.21	2.16 ± 0.36	12	0.30 ± 0.16	1.09 ± 0.03	2	0.14 ± 0.22	0.80 ± 0.47	3	0.19 ± 0.04	2.34 ± 0.69	3	0.20 ± 0.19	1.72 ± 0.78	13
SiO <sub>2</sub>	32.03 ± 0.96	22.59 ± 2.37		31.00 ± 0.77	26.40 ± 1.06		32.12 ± 0.78	32.24 ± 0.46		30.80 ± 0.36	24.00 ± 2.44		31.65 ± 0.97	25.50 ± 3.93	
P <sub>2</sub> O <sub>5</sub>	<D.L.	2.05 ± 4.58		0.31 ± 0.28	0.26 ± 0.05		<D.L.	<D.L.		0.28 ± 0.05	0.39 ± 0.02		0.11 ± 0.20	0.92 ± 2.81	
CaO	0.39 ± 0.45	5.38 ± 7.56		0.40 ± 0.24	1.05 ± 0.19		0.37 ± 0.37	2.51 ± 1.34		1.03 ± 0.20	2.19 ± 0.07		0.45 ± 0.40	3.32 ± 4.74	
TiO <sub>2</sub>	0.18 ± 0.16	1.11 ± 0.82		<D.L.	0.51 ± 0.09		<D.L.	<D.L.		<D.L.	1.11 ± 0.04		<D.L.	0.77 ± 0.68	
FeO	0.38 ± 0.26	0.99 ± 0.58		0.71 ± 0.40	1.01 ± 0.37		0.44 ± 0.06	1.05 ± 0.30		0.48 ± 0.04	3.16 ± 2.83		0.49 ± 0.30	1.51 ± 1.53	
Y <sub>2</sub> O <sub>3</sub>	0.19 ± 0.33	7.16 ± 0.82		0.97 ± 0.60	8.29 ± 0.15		<D.L.	0.46 ± 0.47		0.19 ± 0.16	5.36 ± 1.28		0.38 ± 0.53	5.37 ± 3.05	
ZrO <sub>2</sub>	62.18 ± 2.18	38.22 ± 9.25		58.77 ± 3.63	41.43 ± 4.00		64.69 ± 2.48	54.85 ± 7.01		62.36 ± 0.81	40.55 ± 3.42		61.61 ± 3.14	43.09 ± 9.30	
La <sub>2</sub> O <sub>3</sub>	<D.L.	0.39 ± 0.27		<D.L.	<D.L.		<D.L.	<D.L.		<D.L.	0.27 ± 0.06		<D.L.	0.22 ± 0.23	
ThO <sub>2</sub>	0.08 ± 0.13	1.09 ± 1.25		<D.L.	0.30 ± 0.01		<D.L.	<D.L.		0.06 ± 0.01	0.49 ± 0.12		<D.L.	0.59 ± 0.85	
UO <sub>2</sub>	0.11 ± 0.09	0.30 ± 0.13		0.40 ± 0.28	0.12 ± 0.04		0.06 ± 0.04	0.34 ± 0.23		0.08 ± 0.00	0.23 ± 0.03		0.18 ± 0.20	0.26 ± 0.14	
PbO	<D.L.	<D.L.		0.32 ± 0.26	<D.L.		<D.L.	<D.L.		<D.L.	<D.L.		<D.L.	<D.L.	
HfO <sub>2</sub>	2.75 ± 1.02	1.35 ± 0.59		3.27 ± 0.56	3.24 ± 0.38		1.61 ± 0.13	1.80 ± 0.55		1.42 ± 0.08	1.16 ± 0.12		2.61 ± 0.99	1.70 ± 0.84	
Dy <sub>2</sub> O <sub>3</sub>	0.09 ± 0.07	0.97 ± 0.11		<D.L.	0.77 ± 0.05		<D.L.	<D.L.		<D.L.	0.89 ± 0.03		0.11 ± 0.11	0.73 ± 0.34	
Er <sub>2</sub> O <sub>3</sub>	<D.L.	0.85 ± 0.16		<D.L.	0.92 ± 0.32		<D.L.	<D.L.		<D.L.	0.68 ± 0.02		<D.L.	0.66 ± 0.34	
Yb <sub>2</sub> O <sub>3</sub>	<D.L.	1.03 ± 0.15		0.37 ± 0.26	1.39 ± 0.20		<D.L.	<D.L.		<D.L.	0.86 ± 0.01		0.18 ± 0.20	0.85 ± 0.43	
Total	98.82 ± 2.09	85.69 ± 5.26		97.32 ± 2.34	86.82 ± 4.13		99.76 ± 2.19	93.66 ± 4.10		97.12 ± 1.29	83.69 ± 7.67		98.38 ± 2.19	87.24 ± 6.14	

Notes: The high and low average atomic number areas observed in BSE mode represent "pristine" and altered zircon areas respectively; EMPA = number of electron microprobe analysis used for the averages; <D.L. = below detection limits (Al = 0.06 wt%; Si = 0.06 wt%; P = 0.08 wt%; Ca = 0.07 wt%; Ti = 0.04 wt%; Fe = 0.14 wt%; Y = 0.09 wt%; Zr = 0.22 wt%; La = 0.18 wt%; Th = 0.05 wt%; U = 0.05 wt%; Pb = 0.06 wt%; Hf = 0.09 wt%; Dy = 0.19 wt%; Er = 0.34 wt%; Yb = 0.30 wt%).

The chemical composition variations between pristine and altered zircon areas are presented in Figure 2.2.28. The element substitutions occurring with the altered domains do not compensate totally the loss of the major components (Hf+Zr+Si), the slope of the alteration trend being -1.21. Thus, hydration of the zircon probably occurs as well as element leaching out from the crystal lattice together with metamictization.



**Figure 2.2.28.** Binary diagram showing the element substitutions occurring during alteration of zircon with the decreasing average atomic number in BSE mode. Sum of the element contents increasing in the alteration zones (Al+P+Ca+Ti+Fe+Y+Th+U+REE) versus the element contents decreasing (Zr+Hf+Si) are given in atomic percent (at.%).

In sample 178014, some rare monazite grains are preserved showing only a few dissolution cavities (Fig. 2.2.29), but in other samples monazite crystals are completely altered leaving only a residual boxwork filled by fluorocarbonate and subsequent phospho-thorite (Fig. 2.2.30). The dissolution features seem to be more important in monazite than in zircon. The textural features observed in BSE images indicate that monazite seems to be the most altered mineral generally displaying internal dissolution damages rather than zircon only partly altered at the edge of grains or along fractures.

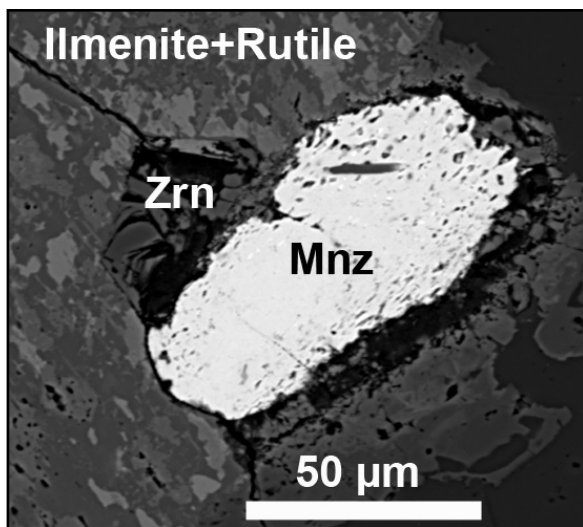


**Figure 2.2.29.** Monazite (Mnz) in BSE mode showing porosity at the edge of the grain corresponding to dissolution cavities and surrounding zircon (Zrn) and ilmenite-rutile association (sample 178014).

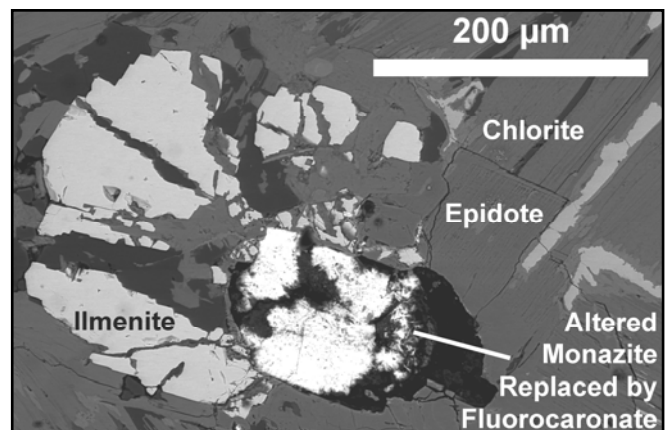


**Figure 2.2.30.** BSE image of an altered monazite completely replaced by fluorocarbonate (sample 142879). Secondary ilmenite and epidote surround the cavity.

The average composition of some preserved monazite grains is presented in Table 2.2.8. The LREE content of monazite is  $\Sigma\text{LREE}=\text{La}_2\text{O}_3+\text{Ce}_2\text{O}_3+\text{Pr}_2\text{O}_3+\text{Nd}_2\text{O}_3$ :  $\sim 56.53$  wt%) with phosphorous content averaging  $27.25 \pm 0.87$  wt%  $\text{P}_2\text{O}_5$ . The maximal amounts of thorium and uranium are respectively of 6.60 wt%  $\text{ThO}_2$  (average 4.82 wt%) and 0.13 wt%  $\text{UO}_2$  (average close to the detection limit). Small contents in silicium, calcium and yttrium are also noticed and are probably incorporated for natural charge balance to neutralize the disequilibrium created by substitutions of the REE trivalent ions by tetravalent  $\text{U}^{4+}$  and  $\text{Th}^{4+}$ .

**Table 2.2.8.** EMPA results (in wt%) of monazite from sample 178014

<i>Monazite Composition</i>	<i>178014</i>
Analyses (7)	Average $\pm$ $\sigma$
$\text{Al}_2\text{O}_3$	<D.L.
$\text{SiO}_2$	$1.92 \pm 0.59$
$\text{P}_2\text{O}_5$	$27.25 \pm 0.87$
$\text{CaO}$	$0.73 \pm 0.39$
$\text{TiO}_2$	$0.08 \pm 0.09$
$\text{MnO}$	<D.L.
$\text{FeO}$	<D.L.
$\text{Y}_2\text{O}_3$	$1.00 \pm 0.28$
$\text{ZrO}_2$	$0.28 \pm 0.06$
$\text{La}_2\text{O}_3$	$14.33 \pm 0.43$
$\text{Ce}_2\text{O}_3$	$28.42 \pm 0.82$
$\text{Pr}_2\text{O}_3$	$2.61 \pm 0.14$
$\text{Nd}_2\text{O}_3$	$11.17 \pm 0.62$
$\text{SmO}$	$1.58 \pm 0.23$
$\text{Gd}_2\text{O}_3$	$0.87 \pm 0.18$
$\text{ThO}_2$	$4.82 \pm 1.01$
$\text{UO}_2$	$0.09 \pm 0.02$
$\text{PbO}$	$0.49 \pm 0.18$
Total	$95.64 \pm 1.00$

Notes: <D.L. = below detection limits (Al = 0.09 wt%; Si = 0.05 wt%; P = 0.05 wt%; Ca = 0.07 wt%; Ti = 0.04 wt%, Mn = 0.16 wt%; Fe = 0.15 wt%; Y = 0.13 wt%; Zr = 0.20 wt%; La = 0.17 wt%; Ce = 0.20 wt%; Pr = 0.15 wt%; Nd = 0.20 wt%; Sm = 0.15 wt%; Gd = 0.26 wt%; Th = 0.04 wt%; U = 0.04 wt%; Pb = 0.14 wt%).

Xenotime has been observed once in the peraluminous leucogranite 169044. It occurs as euhedral crystals of 20-30  $\mu\text{m}$  large closely associated to zircon with very small ( $\sim 1$ -2  $\mu\text{m}$ ) inclusions of uranothorite (Fig. 2.2.31). Xenotime is mostly composed of yttrium ( $45.47 \pm 1.17$  wt%  $\text{Y}_2\text{O}_3$ ), phosphorous ( $31.75 \pm 0.30$  wt%  $\text{P}_2\text{O}_5$ ) and MREE ( $0.62 \pm 0.11$  wt%  $\text{Sm}_2\text{O}_3$  and  $4.40 \pm 0.18$  wt%  $\text{Gd}_2\text{O}_3$ ) with notable amount of Ca (Table 2.2.9). Locally Th and U contents are upon the detection limits (up to 0.14 wt%  $\text{ThO}_2$  and 0.44 wt%  $\text{UO}_2$ ). Phosphothorite and uranothorite inclusions in monazite and xenotime respectively are too small to the size of the analytical spot.

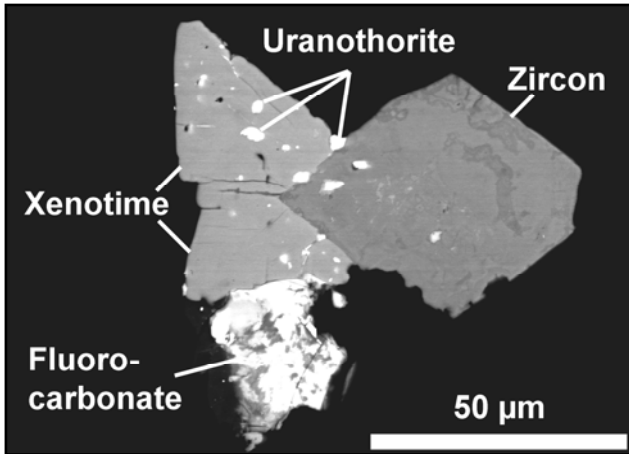


**Figure 2.2.31.** Euhedral zircon and xenotime crystals in BSE mode showing small inclusions of uranothorite and secondary fluorocarbonate adjacent to the assemblage (sample 169044).

**Table 2.2.9.** EMPA results (in wt%) of xenotime from sample 169044

<i>Xenotime Composition</i>	<i>169044</i>
Analysis (5)	Average $\pm$ $\sigma$
Al <sub>2</sub> O <sub>3</sub>	<D.L.
SiO <sub>2</sub>	<D.L.
P <sub>2</sub> O <sub>5</sub>	31.75 $\pm$ 0.30
CaO	0.78 $\pm$ 1.64
TiO <sub>2</sub>	<D.L.
MnO	<D.L.
FeO	<D.L.
Y <sub>2</sub> O <sub>3</sub>	45.47 $\pm$ 1.17
ZrO <sub>2</sub>	<D.L.
La <sub>2</sub> O <sub>3</sub>	<D.L.
Ce <sub>2</sub> O <sub>3</sub>	<D.L.
Pr <sub>2</sub> O <sub>3</sub>	<D.L.
Nd <sub>2</sub> O <sub>3</sub>	<D.L.
SmO	0.62 $\pm$ 0.11
Gd <sub>2</sub> O <sub>3</sub>	4.40 $\pm$ 0.18
ThO <sub>2</sub>	0.09 $\pm$ 0.05
UO <sub>2</sub>	0.18 $\pm$ 0.15
PbO	<D.L.
<b>Total</b>	<b>83.61 <math>\pm</math> 0.71</b>

*Notes:* <D.L. = below detection limits (Al = 0.09 wt%; Si = 0.05 wt%; P = 0.06 wt%; Ca = 0.07 wt%; Ti = 0.04 wt%, Mn = 0.10 wt%; Fe = 0.11 wt%; Y = 0.10 wt%; Zr = 0.30 wt%; La = 0.15 wt%; Ce = 0.16 wt%; Pr = 0.12 wt%; Nd = 0.17 wt%; Sm = 0.13 wt%; Gd = 0.23 wt%; Th = 0.04 wt%; U = 0.04 wt%; Pb = 0.15 wt%).

### **Secondary paragenetic minerals associated to late- or post-magmatic fluid circulation**

#### Alteration of feldspar

Sample 169044 collected from the Mount Edgar batholith seems to be the best preserved (Fig. 2.2.12) compare to the three other granitoids which show intense alteration of feldspar. Plagioclase is generally the most altered phase and are clouded by epidote and sericite microcrystals whereas K-feldspar are less affected (Fig. 2.2.32).

Plagioclase dissolution is a common feature observed in hydrothermally altered granites that generally affects preferentially the Ca-rich core of the crystals and is accompanied by Ca-release with Al and Si re-precipitation into spread tetrahedrons of phyllosilicates, mainly epidote, sericite, muscovite and chlorite.

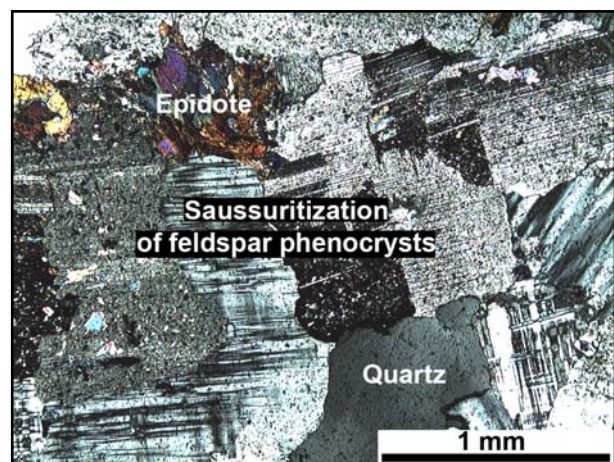


**Figure 2.2.32.** Saussuritization of the feldspar phenocrysts partly to totally replace by finely grained micas and epidote, observed in polarized transmitted light (sample 142879).

Chloritization

Chloritization is pervasive in all the studied granitoids and affect generally biotite crystals transformed partly to totally into green chlorite (Fig. 2.2.15) or forming the edge of garnet corroded surfaces (Fig. 2.2.14). The composition of the chlorites from three samples is presented in Table 2.2.10. Their average simplified structural formula is  $[(Mg_xFe_{4-x}Al^{VI}_{1.5})(Al^{IV}Si_3)O_{10}(OH)_8]$  with  $0.2 < x < 1.5$ . The chlorites are relatively poor in magnesium ( $m = 1.09 \pm 0.44$  apfu) with high Fe/(Fe+Mg) ratios  $> 0.60$ . In the classification of Hey (1954), they mostly plot in the composition field of pycnochlorite (Fig. 2.2.33). However, the chlorite from the leucogranite 169044 is richer in iron with a Fe/(Fe+Mg) ratio rising up to 0.94 and plots in the field of daphnite. Using the geothermometer defined by the tetrahedral aluminium occupancy (Cathelineau and Nieva, 1985; Cathelineau, 1988), the temperatures of crystallization of the different chlorite species range between 212°C and 358°C.

**Table 2.2.10.** Representative average chemical compositions of chlorite (EMPA results in wt%  $\pm$  standard derivative)

Sample EMPA	142879 (15)	169044 (5)	178014 (10)	Average (30)
Al <sub>2</sub> O <sub>3</sub>	19.81 $\pm$ 0.61	19.92 $\pm$ 0.33	17.55 $\pm$ 0.52	19.07 $\pm$ 1.22
SiO <sub>2</sub>	24.67 $\pm$ 0.75	22.72 $\pm$ 0.31	27.20 $\pm$ 0.47	25.19 $\pm$ 1.71
TiO <sub>2</sub>	0.12 $\pm$ 0.10	<D.L.	0.20 $\pm$ 0.19	0.13 $\pm$ 0.14
Cr <sub>2</sub> O <sub>3</sub>	<D.L.	<D.L.	<D.L.	<D.L.
FeO	31.46 $\pm$ 0.92	31.67 $\pm$ 0.50	28.05 $\pm$ 0.72	31.36 $\pm$ 3.36
MgO	6.17 $\pm$ 0.28	1.36 $\pm$ 0.05	9.14 $\pm$ 0.52	6.35 $\pm$ 2.67
MnO	0.83 $\pm$ 0.10	2.16 $\pm$ 0.13	0.65 $\pm$ 0.11	0.99 $\pm$ 0.55
Na <sub>2</sub> O	<D.L.	<D.L.	<D.L.	<D.L.
K <sub>2</sub> O	0.07 $\pm$ 0.16	<D.L.	0.12 $\pm$ 0.04	0.08 $\pm$ 0.12
CaO	<D.L.	<D.L.	0.10 $\pm$ 0.07	<D.L.
F	<D.L.	<D.L.	<D.L.	<D.L.
Total	83.17 $\pm$ 0.72	83.93 $\pm$ 0.45	83.05 $\pm$ 1.05	83.26 $\pm$ 0.85
Structure calculation based on 14 oxygen atoms (half formula)				
Si	2.86 $\pm$ 0.08	2.74 $\pm$ 0.03	3.08 $\pm$ 0.05	2.91 $\pm$ 0.14
Ti	0.01 $\pm$ 0.01	0.01 $\pm$ 0.00	0.02 $\pm$ 0.02	0.01 $\pm$ 0.01
Al <sup>IV</sup>	1.14 $\pm$ 0.08	1.26 $\pm$ 0.03	0.92 $\pm$ 0.05	1.09 $\pm$ 0.14
Al <sup>VI</sup>	1.56 $\pm$ 0.03	1.57 $\pm$ 0.02	1.43 $\pm$ 0.04	1.52 $\pm$ 0.07
Fe <sub>total</sub>	3.05 $\pm$ 0.09	3.80 $\pm$ 0.05	2.66 $\pm$ 0.07	3.04 $\pm$ 0.39
Mg	1.06 $\pm$ 0.05	0.24 $\pm$ 0.01	1.54 $\pm$ 0.07	1.09 $\pm$ 0.44
Mn	0.08 $\pm$ 0.01	0.22 $\pm$ 0.01	0.06 $\pm$ 0.01	0.10 $\pm$ 0.06
I.C.	0.02 $\pm$ 0.03	0.00 $\pm$ 0.00	0.05 $\pm$ 0.02	0.03 $\pm$ 0.03
Fe/(Fe+Mg)	0.74 $\pm$ 0.01	0.94 $\pm$ 0.00	0.63 $\pm$ 0.01	0.74 $\pm$ 0.10
Temperature range (Cathelineau, 1988)	266-332°C	329-358°C	212-251°C	212-358°C

Notes: EMPA = values in parentheses refer to number of analyses used to calculate the mean; <D.L. = below detection limits (Na = 0.10 wt%; Al = 0.05 wt%; Si = 0.06 wt%; K = 0.06 wt%; Ca = 0.05 wt%; Ti = 0.06 wt%; Cr = 0.08 wt% ; Fe = 0.17 wt%; Mg = 0.05 wt%; Mn = 0.15 wt%; F = 0.72 wt%); I.C. = the interlayer charge.

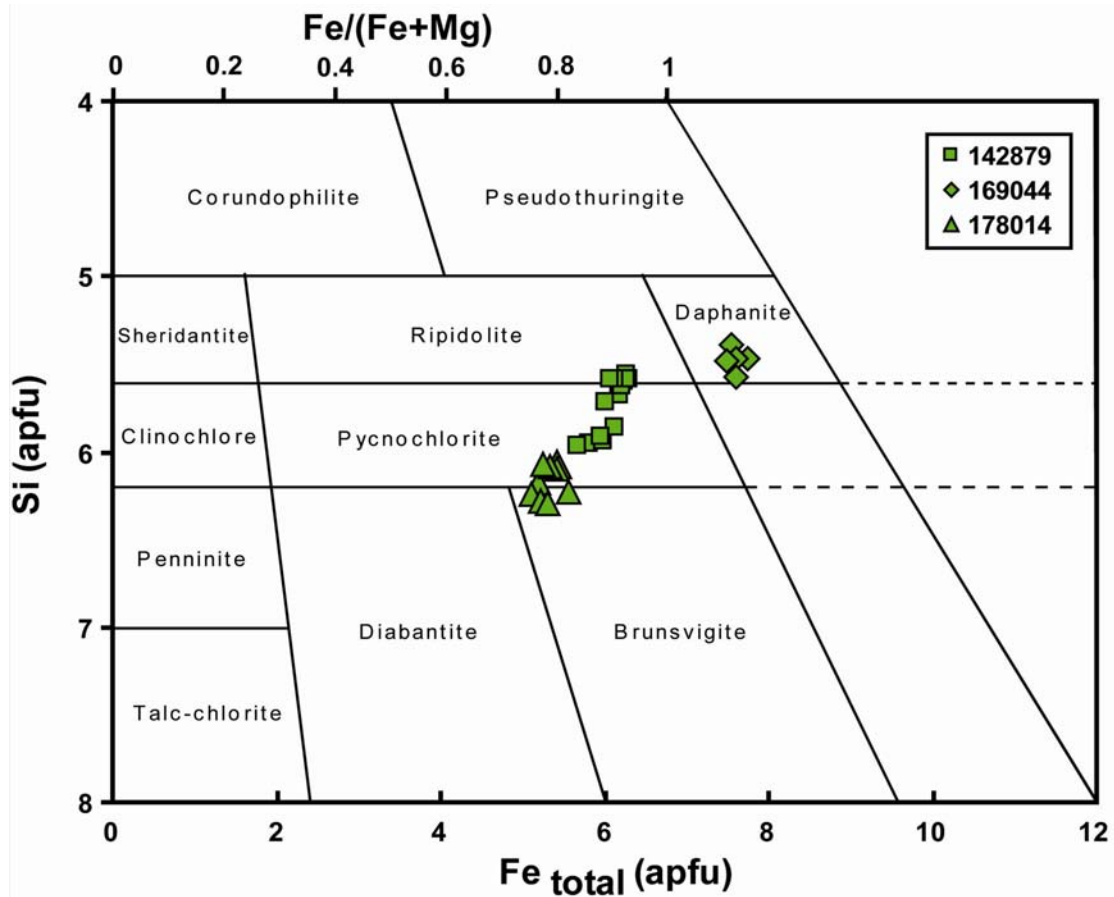


Figure 2.2.33. Classification of chlorite crystals after Hey (1954).

LREE-Fluorocarbonates

The textural features show clearly that the fluorocarbonates are alteration products of monazite, zircon and xenotime (Fig. 2.2.27, 2.2.30 and 2.2.31). They mostly occur as masses of fine-grained needles in the mineral interspaces or as replacement of monazite in dissolution cavities (Fig. 2.2.34 and 2.2.35).

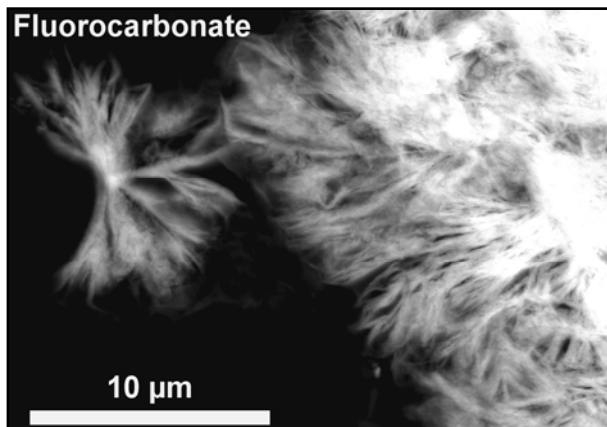


Figure 2.2.34. Fluorocarbonate within a cavity of altered monazite observed in BSE mode (sample 142879).

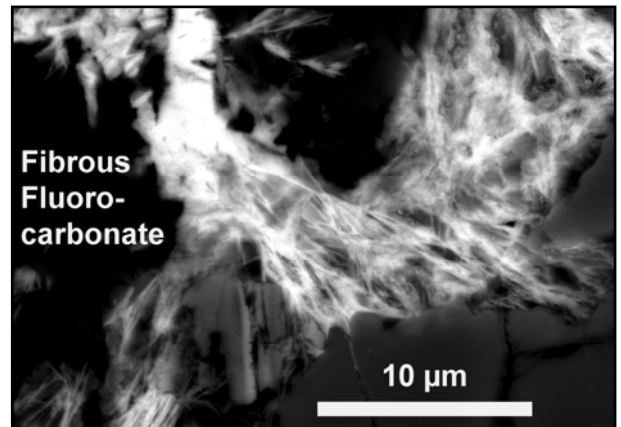


Figure 2.2.35. BSE image of fibrous fluorocarbonate developed in intergrain space (sample 178014).

The fluorocarbonate composition reflects the characteristic of the altered mineral and the chemistry of the fluids from which they are formed (Table 2.2.11). These epigenetic phases are principally enriched in LREE ( $\text{La}_2\text{O}_3+\text{Ce}_2\text{O}_3+\text{Pr}_2\text{O}_3+\text{Nd}_2\text{O}_3 \sim 48.76$  wt%), calcium ( $9.91 \pm 1.92$  wt% CaO) and fluorine ( $3.96 \pm 0.40$  wt% F) and lower amounts of MREE ( $\text{Sm}_2\text{O}_3+\text{Gd}_2\text{O}_3 \sim 2.51$  wt%). They show highly variable amounts in thorium, yttrium, silicium, iron and phosphorous ranging between 0.60-10.67 wt%  $\text{ThO}_2$ , <0.26-5.03 wt%  $\text{Y}_2\text{O}_3$ , 0.51-7.11 wt%  $\text{SiO}_2$ , 0.22-4.37 wt% FeO and 0.10-3.80 wt%  $\text{P}_2\text{O}_5$ . Their high Th contents may represent an indication of their derivation from the alteration of monazite. The maximum uranium content is 0.44 wt%  $\text{UO}_2$  but is generally below the detection limit of the microprobe (<0.11 wt%) as the HREE, potassium, sodium and magnesium concentrations.

**Table 2.2.11.** EMPA results (in wt%) of REE-fluorocarbonate

<i>Sample</i>	<i>142879</i>	<i>178011</i>	<i>178014</i>	<i>Average</i>
EMPA	(21)	(4)	(8)	(33)
$\text{Al}_2\text{O}_3$	$0.39 \pm 0.17$	$0.50 \pm 0.26$	$0.51 \pm 0.41$	$0.37 \pm 0.27$
$\text{SiO}_2$	$1.92 \pm 0.85$	$3.07 \pm 2.85$	$1.62 \pm 1.28$	$1.98 \pm 1.32$
$\text{P}_2\text{O}_5$	$0.21 \pm 0.07$	$0.19 \pm 0.06$	$0.74 \pm 1.24$	$0.33 \pm 0.63$
CaO	$10.11 \pm 0.99$	$12.90 \pm 1.84$	$7.87 \pm 1.61$	$9.91 \pm 1.92$
$\text{K}_2\text{O}$	<D.L.	<D.L.	<D.L.	<D.L.
$\text{Na}_2\text{O}$	<D.L.	<D.L.	<D.L.	<D.L.
FeO	$1.61 \pm 0.63$	$0.32 \pm 0.10$	$2.14 \pm 1.17$	$1.58 \pm 0.91$
MgO	<D.L.	<D.L.	<D.L.	<D.L.
$\text{Y}_2\text{O}_3$	$4.14 \pm 0.44$	$1.03 \pm 0.57$	$1.23 \pm 0.54$	$3.06 \pm 1.53$
$\text{La}_2\text{O}_3$	$14.08 \pm 0.94$	$18.86 \pm 1.53$	$23.59 \pm 3.54$	$16.97 \pm 4.52$
$\text{Ce}_2\text{O}_3$	$22.37 \pm 1.70$	$29.21 \pm 2.59$	$26.30 \pm 3.44$	$24.15 \pm 3.39$
$\text{Pr}_2\text{O}_3$	$1.77 \pm 0.30$	$1.97 \pm 0.09$	$2.05 \pm 0.30$	$1.86 \pm 0.30$
$\text{Nd}_2\text{O}_3$	$5.49 \pm 0.72$	$5.49 \pm 0.71$	$6.70 \pm 0.89$	$5.78 \pm 0.91$
SmO	$1.79 \pm 0.25$	$1.20 \pm 0.26$	$1.39 \pm 0.20$	$1.62 \pm 0.33$
$\text{Gd}_2\text{O}_3$	$1.09 \pm 0.18$	$0.57 \pm 0.17$	$0.53 \pm 0.24$	$0.89 \pm 0.33$
$\text{Yb}_2\text{O}_3$	<D.L.	<D.L.	<D.L.	<D.L.
$\text{ThO}_2$	$8.93 \pm 1.36$	$2.80 \pm 1.58$	$2.66 \pm 2.07$	$6.66 \pm 3.40$
$\text{UO}_2$	$0.31 \pm 0.05$	<D.L.	$0.24 \pm 0.04$	$0.27 \pm 0.09$
PbO	$0.47 \pm 0.23$	$0.39 \pm 0.25$	$0.58 \pm 0.36$	$0.49 \pm 0.27$
F	$3.88 \pm 0.33$	$4.35 \pm 0.47$	$3.96 \pm 0.45$	$3.96 \pm 0.40$
<b>Total</b>	<b><math>78.57 \pm 1.34</math></b>	<b><math>83.04 \pm 1.97</math></b>	<b><math>82.31 \pm 3.76</math></b>	<b><math>80.02 \pm 2.90</math></b>

Notes: <D.L. = below detection limits (Al = 0.08 wt%; Si = 0.06 wt%; P = 0.04 wt%; Ca = 0.08 wt%; K = 0.06 wt%, Na = 0.05 wt%; Fe = 0.16 wt%; Mg = 0.09 wt%; Y = 0.26 wt%; La = 0.10 wt%; Ce = 0.20 wt%; Pr = 0.12 wt%; Nd = 0.46 wt%; Sm = 0.34 wt%; Gd = 0.44 wt%; Yb = 0.33 wt%; Th = 0.13 wt%; U = 0.11 wt%; Pb = 0.24 wt%; F = 0.05 wt%).

Epidotization

Authigenic epidote is widespread in the granitoids as patchy alteration minerals in the vicinity of plagioclase laths (Fig. 2.2.32) or as large overgrowths around monazite (Fig. 2.2.30) giving rise to pleochroic halos in transmitted light. It mainly occurs or in association with chlorite, titanite and opaque minerals (Fig. 2.2.36). The chemical composition of epidote measured by EMPA is given in Table 2.2.12 and respect globally the following stoichiometric formula  $\text{Ca}_2\text{FeAl}_2(\text{SiO}_4)_3(\text{OH})$  which corresponds to the iron-rich clinzoizite epidote-type (Bonazzi and Menchetti, 1995).

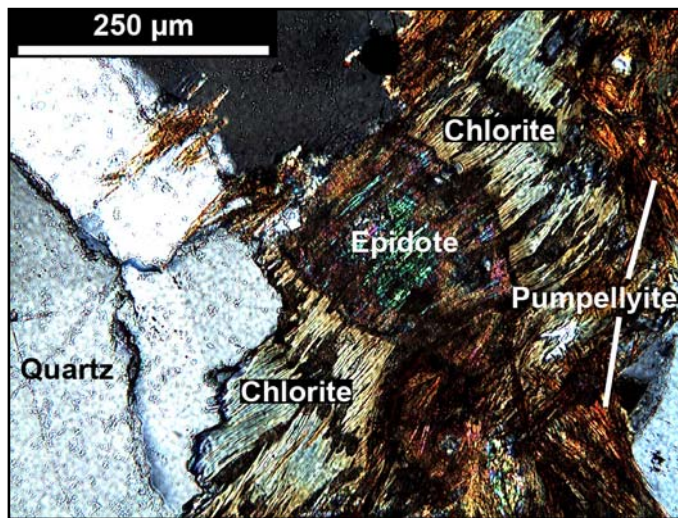


Figure 2.2.36. Epidote and later pumpellyite associated to chlorite in polarized transmitted light (sample 142879).

Table 2.2.12. EMPA results (in wt%) of epidote

Sample	142879	178011	178014	Average
EMPA	(8)	(9)	(3)	(20)
Na <sub>2</sub> O	<D.L.	<D.L.	<D.L.	<D.L.
Al <sub>2</sub> O <sub>3</sub>	20.19 ± 0.92	22.49 ± 0.62	21.32 ± 0.12	21.39 ± 1.29
SiO <sub>2</sub>	36.93 ± 0.79	37.47 ± 0.35	37.45 ± 0.23	37.25 ± 0.60
K <sub>2</sub> O	<D.L.	<D.L.	<D.L.	<D.L.
CaO	21.09 ± 1.39	22.42 ± 0.42	22.21 ± 0.21	21.86 ± 1.10
TiO <sub>2</sub>	0.15 ± 0.30	<D.L.	<D.L.	0.10 ± 0.19
FeO	12.81 ± 1.25	10.91 ± 0.86	11.84 ± 0.24	11.81 ± 1.30
MgO	0.14 ± 0.31	<D.L.	<D.L.	<D.L.
MnO	<D.L.	<D.L.	<D.L.	<D.L.
Cr <sub>2</sub> O <sub>3</sub>	<D.L.	<D.L.	<D.L.	<D.L.
F	<D.L.	0.17 ± 0.05	0.10 ± 0.05	<D.L.
Total	91.74 ± 3.07	93.70 ± 1.28	93.25 ± 0.37	92.85 ± 2.25
Structural formula based on 12.5 oxygen atoms				
Ca	1.90 ± 0.10	1.97 ± 0.02	1.96 ± 0.01	1.94 ± 0.07
Fe	0.90 ± 0.07	0.75 ± 0.06	0.82 ± 0.02	0.82 ± 0.09
Al	2.00 ± 0.04	2.17 ± 0.06	2.07 ± 0.01	2.09 ± 0.09
Si	3.10 ± 0.04	3.07 ± 0.02	3.09 ± 0.00	3.08 ± 0.03
Σ cations	7.90 ± 0.07	7.95 ± 0.01	7.94 ± 0.01	7.93 ± 0.05

Notes: <D.L. = below detection limits (Al = 0.05 wt%; Si = 0.05 wt%; Ca = 0.06 wt%; K = 0.06 wt%, Na = 0.09 wt%; Ti = 0.06 wt%; Fe = 0.17 wt%; Mg = 0.05 wt%; Mn = 0.16 wt%; Cr = 0.09; F = 0.49 wt%).

Apatite

Numerous small apatite crystals are widespread in the granites and are generally present in elongated assemblage of rounded to hexagonal grains from 5 to 20  $\mu\text{m}$  in diameter (Fig. 2.2.18). Normally, apatite in granites crystallizes during early magmatic stage with zircon and monazite but in the Split Rock samples they occur associated to epidotization preferentially around the monazite aureole and crystallize secondary to titanite I, chlorite and epidote (Fig. 2.2.37). This phenomenon is obviously related to alteration of monazite by some calcic-fluids leaching P out from the crystal lattice which precipitates into secondary apatite.

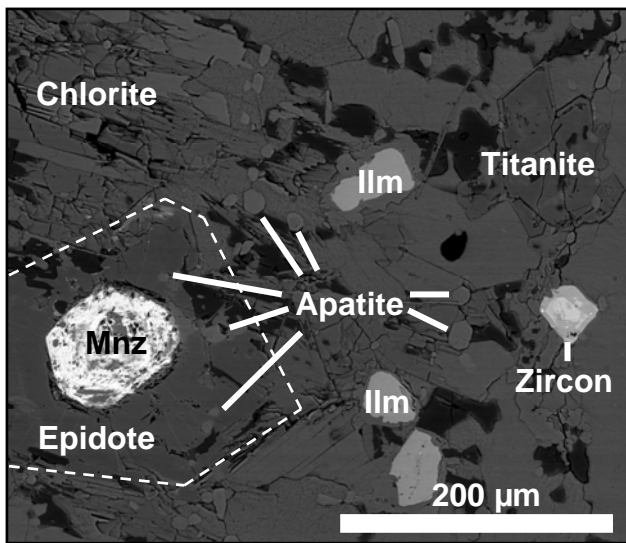


**Figure 2.2.37.** BSE image showing primary magmatic ilmenite, titanite I, zircon and altered monazite replaced to REE-fluorocarbonates (white) surrounded by epidote aureole and disseminated apatite crystallization (*sample 178011*).

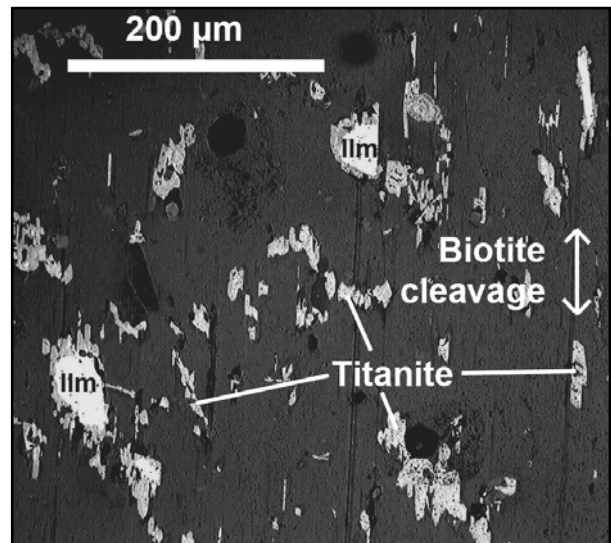


**Figure 2.2.38.** Titanite (stage II) overgrowing on ilmenite (Ilm) in reflected light (*sample 178011*). Note the development of crystals along the biotite cleavage.

Titanite II

Secondary growths of titanite have been observed in the four granitoid samples. They occur as small crystals along cleavage plane of chloritized biotite and as corona around opaque minerals (Fig. 2.2.38). They always form a ring of automorphous crystals around ilmenite. The elongated shape along the cleavage planes of the host-crystal indicates a certain reaction between ilmenite and some fluid circulating along cleavage. Composition of titanite formed during this second crystallization stage is slightly more enriched in Ca, Al and F than the primary stage (Table 2.2.3) indicating that this reaction occurs with Ca- and F-bearing fluids. Titanite II is considered to represent the result of crystallization from an inward diffusion of Ca from fluid percolation in cleavage and the outward diffusion of Ti from the ilmenite (Janardan et al., 1973).

Fluorite

Some euhedral fluorite crystals have been observed in the peraluminous leucogranite 169044. Fluorite ( $\text{CaF}_2$ ) occurs also as overgrowth on ilmenite along the muscovite and chlorite cleavage (Fig. 2.2.39), which also indicates that the late hydrothermal fluid phase must have been Ca-rich but also fluorine-rich. Fluorite shows a purple colour in natural transmitted light and grows as well as coarse cubic crystals up to 300  $\mu\text{m}$  large. Rare galena inclusions within the fluorite have also been observed in BSE image (Fig. 2.2.40).

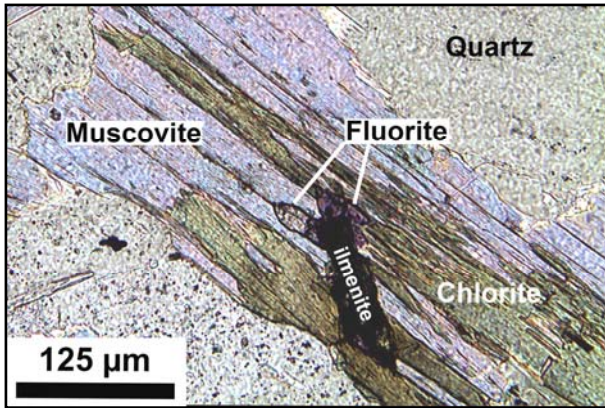


**Figure 2.2.39.** Fluorite overgrowing on ilmenite along muscovite-chlorite cleavage planes in natural polarised light (*sample 169044*).

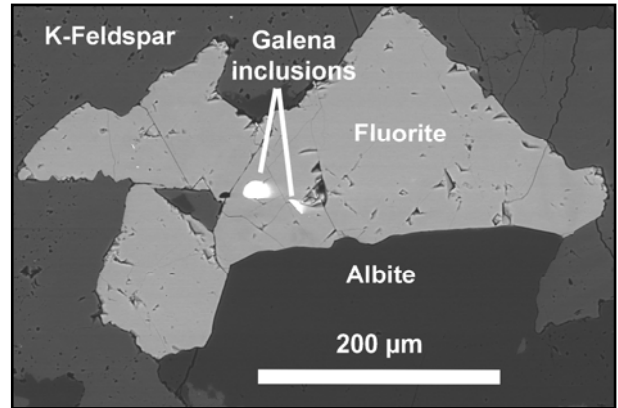


**Figure 2.2.40.** BSE image of pseudocubic fluorite crystals between two feldspar phenocrysts (*sample 169044*).

Pumpellyite

Clusters of finely fibrous crystals with asterisk shape have been observed at the boundary of micas in samples 142879 and 178011 and seem to be related to the last alteration episode superimposed to all other stages (Fig. 2.2.36, 2.2.41 and 2.2.42).

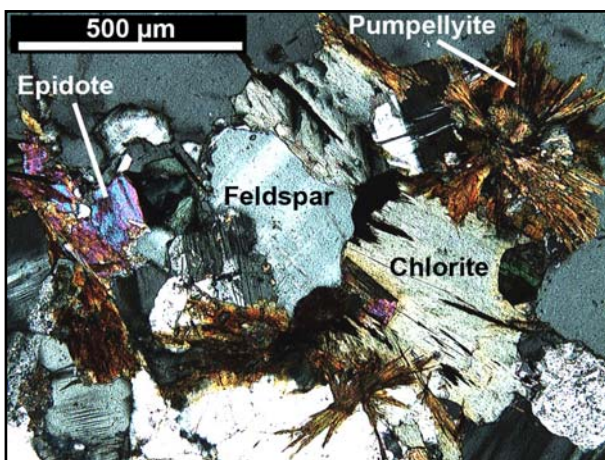


**Figure 2.2.41.** amygdaloid pumpellyite superimposed to chlorite and epidote between quartz and feldspar phenocrysts in polarised transmitted light (*sample 142879*).

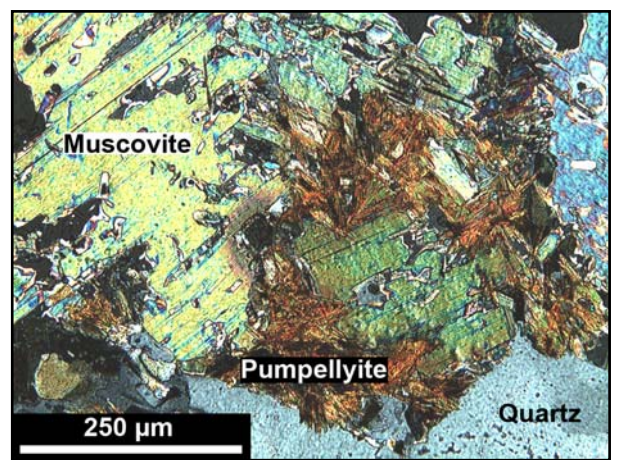


**Figure 2.2.42.** Pumpellyite affecting a muscovite phenocryst (*sample 178011*).

Pumpellyite (Table 2.2.13) is a hydrous silicate of calcium and aluminium with the following formula  $\text{Ca}_2(\text{Fe,Mg,Mn})\text{Al}_2[(\text{OH})_2 \text{SiO}_4 \text{Si}_2\text{O}_7]\text{H}_2\text{O}$ . The red to brownish colour of the crystals observed in the Pilbara granites is rare, pumpellyite generally being pale green to bluish-green, and is characteristic of the iron-rich pumpellyite. Pumpellyite is generally stable with prehnite between 250°C and 380°C and at pressures acceding 2 kbar (Liou, 1971) in agreement with the temperature range determined previously from the chlorite geothermometer.

**Table 2.2.13.** EMPA results (in wt%) of pumpellyite in sample 142879

<i>Sample 142879</i> EMPA	Average $\pm \sigma$ (4)
SiO <sub>2</sub>	37.42 $\pm$ 0.48
TiO <sub>2</sub>	<D.L.
Al <sub>2</sub> O <sub>3</sub>	21.04 $\pm$ 0.61
Cr <sub>2</sub> O <sub>3</sub>	<D.L.
FeO	13.11 $\pm$ 0.81
MnO	0.27 $\pm$ 0.12
MgO	0.10 $\pm$ 0.13
CaO	21.71 $\pm$ 0.90
Na <sub>2</sub> O	<D.L.
K <sub>2</sub> O	<D.L.
F	<D.L.
Total	93.88 $\pm$ 0.92
Structural formula based on 12 oxygen atoms	
Si	2.95 $\pm$ 0.02
Al	1.96 $\pm$ 0.04
Fe	0.87 $\pm$ 0.05
Mn	0.02 $\pm$ 0.01
Mg	0.01 $\pm$ 0.01
Ca	1.83 $\pm$ 0.06
$\Sigma$ cations	7.63 $\pm$ 0.02

*Notes:* <D.L. = below detection limits (Al = 0.05 wt%; Si = 0.05 wt%; Ca = 0.06 wt%; K = 0.06 wt%, Na = 0.08 wt%; Ti = 0.06 wt%; Fe = 0.16 wt%; Mg = 0.05 wt%; Mn = 0.13 wt%; Cr = 0.08; F = 0.48 wt%).

**SYNTHESIS OF THE PARAGENETIC SEQUENCE**

The following paragenetic sequence presented in Figure 2.2.43 has been deduced from the petrographic and SEM observations:

<i>Mineral</i>	<i>Primary Magmatic Stage</i>			<i>Ca-metasomatism and associated alteration</i>
	<b>Metaluminous granite (178011)</b>	<b>Intermediary granites (142879+178014)</b>	<b>Peraluminous leucogranite (169044)</b>	
Plagioclase				Saussuritization
K-Feldspar				
Hornblende				
Titanite I				
Biotite				
Quartz				
Ilmenite/Rutile				
Zircon				Metamictization
Monazite				Alteration
Xenotime				
Muscovite				from saussuritization of plagioclase
Ferro-Columbite				Metamictization
Pyrochlore-group minerals (as inclusion in Columbite)				
Garnet				
Chlorite				
Epidote				
Thorite				from monazite alteration
Th-REE-Fluorocarbonate				from monazite alteration
Titanite II				
Apatite				
Fluorite				
Pumpellyite				

**Figure 2.2.43.** Mineral paragenesis following the evolution of the high-K granites from the eastern Pilbara Craton

## DISCUSSION

### *Origin of the high-K granites*

The biotite-amphibole granite 178011 is the less differentiated sampled rock because it has a metaluminous composition with  $A/CNK=0.99$  and is the richest in dark minerals mostly biotite, titanite, ilmenite and hornblende ( $B$  parameter = 66). It contains also abundant plagioclase giving the lowest  $P$  parameter (-60). Its primary mineral assemblage (quartz + plagioclase > K-feldspar + biotite + titanite + hornblende + Fe-Ti minerals) and its geochemical characteristics corresponds to a ferro-potassic calc-alkaline adamellite and would correspond to an A2 type granite in the classification of Eby (1992). Even if it is the less fractionated sample, this granite is already significantly enriched in incompatible elements compare to TTG-type granitoids with 30 ppm Th, 3 ppm Ta, 7.5 ppm U and 180 ppm  $\Sigma$ REE. The source melt of this metaluminous rock derives probably from a mixing between partial melting of sub-continental lithospheric mantle and contamination by crustal material as proposed by Smithies et al. (2009; Fig. 2.2.3). This model is supported by the relatively high pressure calculated by Al-in hornblende geobarometer and implying that granitoid 178011 emplaced at a deep crustal level.

Samples 142879 and 178014 are more felsic than granite 178011 and have a weakly peraluminous composition ( $8 < A < 12$ ) and are leucocratic ( $25 < B < 30$ ) with higher  $K_2O$  contents and a smaller proportion of biotite, titanite and plagioclase compare to K-feldspar. These samples also correspond to ferro-potassic calc-alkaline granites but are probably associated to a greater contribution of crustal components and would correspond to A2 type granites, transitional to A1 according to the classification of Eby (1992).

The garnet-muscovite peraluminous leucogranite 169044 is the most fractionated granite from the studied samples of the Split Rock Supersuite. It has the lowest  $B$  parameter (13) and is more peraluminous ( $A = 30$ ). This sample has also to the lowest enrichment in large ion and/or highly charged elements (Th, Zr, REE), but it is the richest in Ta, Rb, Sn, Nb, Bi, and has a strong negative Eu anomaly indicating an extreme fractionation of plagioclase. The presence of peraluminous minerals as muscovite and garnet and its geochemical signature may reflect the melting of sediments or the extreme fractional crystallization from a calc-alkaline magma with assimilation of peraluminous component of the crust, or partial melting of Al-TTGs at high supracrustal level as suggested by Smithies et al. (2009).

### ***Metamorphism and Ca-Metasomatism***

Three stages of crystallization have been recognized in the mineralogic assemblage: 1) an early stage corresponding to high temperature crystallization of magmatic minerals, 2) a late magmatic hydrothermal stage with the crystallization of hydrogrossular and part of the muscovite, and 3) a purely hydrothermal stage with chloritization of biotite, muscovitization of the feldspars associated with Ca-metasomatism with the new formation of epidote, titanite II, fluorite, alteration of monazite to uranothorite and Th-REE fluorocarbonates and pumpellyite.

The temperature and pressure conditions would have been 2.7-4.6 kbar (Al-in hornblende geobarometer) for temperature of 700-800°C during the magmatic stage, approximately between 500-600°C (stability field of hydrogrossular) during the magmatic-hydrothermal stage and then 350-250°C for the hydrothermal Ca-metasomatic stage. This last stage is probably related to convective fluid circulations created during the exhumation of the granite bodies with introduction of calcium from enclosing greenstone belts rich in mafic material.

### ***U, Th and REE mobilization and concentration***

Uranium, thorium and REE bearing minerals from the magmatic paragenetic sequence are zircon, monazite and titanite for the ferro-potassic calc-alkaline granites and adamellite, and zircon, monazite and more rarely xenotime for the peraluminous leucogranite. The initial content of uranium and thorium in the granites is mostly dependant of the magmatic source composition, of the degree of partial melting and of the fractional crystallization (Cuney and Friedrich, 1987). The late magmatic and hydrothermal circulation of fluids rich in Ca and F combined with metamictization of U-Th-rich accessory minerals has led to the remobilization of uranium and REE. The Ca- and F-rich fluids responsible of this alteration are known to increase the mobility of REE and Th from accessory minerals in granites (Agangi et al., 2009). The intense alteration of monazite into uranothorite and REE-fluorocarbonate may have liberated some uranium potentially transported by the hydrothermal fluid circulation and conducting to local re-concentrations as already established during monazite alteration in other conditions in the Precambrian crystalline basement under the Athabasca Basin in Canada (Hecht and Cuney, 2000).

## CONCLUSION

The magmatism represented by the latest granite intrusion of the Pilbara Craton represented by the Split Rock Supersuite provides a strong evidence for the existence of a highly fractionated magmatism in the continental crust prior to 2.85 Ga. These high-K granites have a bulk chemistry and mineralogy characteristic of post-collisional magmatism and can be classified as A-type granites emplaced at various crustal levels. This late-Archean magmatic suite is enriched in incompatible elements as REE, Y, U, Th and Nb that crystallize in the accessory minerals with abundances depending of the melt composition, the degree of partial melting and fractional crystallization. The most fractionated leucogranite studied from this suite is slightly peraluminous, has low Th/U ratio (1.89) and formed at moderate temperature which supposes a low degree of partial melting. This extreme fractionation may have attempt the preferential field of uraninite crystallization generally occurring for Th/U close to 1 or below. However, no uraninite has been observed and if it has crystallized, it can have been altered by the intense Ca-metasomatism evidenced in the four areas sampled almost hundred kilometres from each others (Fig. 2.2.1). During cooling and exhumation of the granite bodies, hydrothermal fluids have interacted with calcium-rich lithologies (metasediments or greenstone assemblages) present in the inliers around the TTG domes and has generated intense Ca-metasomatism in the granites and alteration of the primary mineral assemblage. Refractory minerals, mostly monazite and zircon, have undergone intense alteration with mobilization of the REE and radioelements which have been redeposited *in situ* mostly as Y-REE-Th-enriched fluorocarbonate and thorium silico-phosphate (phosphothorite and uranothorite). A more representative and exhaustive sampling is necessary to better evaluate the uranium potential of the Split Rock Supersuite. Because occurrences of detrital uraninite in sandstones from the Fortescue Group have been discovered in the Pilbara Craton, the Split Rock Supersuite granites represent preferential source-rocks for uraninite crystallization in comparison to the low-grade TTGs and we strongly recommend to further investigate possible U mineralization in this younger magmatic cycle focussing on less altered Archean leucogranites.

## REFERENCES

- Agangi, G., Kamenetski, V., McPhie, J., Allen, S.R. and Chambefort, I., 2009, Mobility of lithophile trace elements during the late magmatic stage in the felsic Gawler Range Volcanics, South Australia, Goldschmidt Conferences, *Geochimica et Cosmochimica Acta*, Volume 73, Issue 13, Supplement 1, p. A15.
- Anderson, L. J. and Smith, D. R., 1995, The effects of temperature and  $fO_2$  on the Al-in-hornblende barometer *American Mineralogist*, Vol. 80, p. 549-559.
- Bagas, L., Bierlein, F. P., Bodorkos, S. and Nelson, D. R., 2008, Tectonic setting, evolution and orogenic gold potential of the late Mesoarchean Mosquito Creek Basin, North Pilbara Craton, Western Australia; *Precambrian Research*, Vol. 160, Issues 3-4, p. 227-244.
- Barley, M. E. and Pickard, A. L., 1999, An extensive, crustally-derived 3325-3310 Ma silicic volcanoplutonic suite in the eastern Pilbara Craton: evidence from the Kelly Belt, McPhee Dome and Corunna Downs Batholith; *Precambrian Research*, Vol. 96, p. 41-62.
- Blewett, R., 2002. Archaean tectonic processes: a case for horizontal shortening in the North Pilbara Granite–Greenstone terrane, Western Australia; *Precambrian Research*, Vol. 113, p. 87-120.
- Bickle, M. J., Bettenay, L. F., Chapman, H. J., Groves, D. I., McNaughton, N. J., Campbell, I. H. and Lacter, J. R., 1993, Origin of the 3500-3300 Ma calc-alkaline rocks in the Pilbara Archaean isotopic and geochemical constraints from the Shaw Batholith, *Precambrian Research*, Vol. 60, p. 117-149.
- Bickle, M. J., Bettenay, L. F., Boulter, C. A., Groves, D. I., Morant, P., 1980, Horizontal tectonic intercalation of an Archaean gneiss belt and greenstones, Pilbara Block, Western Australia, *Geology* 8, p. 525-529.
- Bickle, M. J., Bettenay, L. F., Barley, M.E., Chapman, H. J., Groves D. I., Campbell, I. H. and De Laeter, J. R., 1983, A 3500 Ma plutonic and volcanic calc-alkaline province in the Archaean East Pilbara Block, *Contributions to Mineralogy and Petrology* 84, p. 25-35.
- Bolhar, R. and Van Kranendonk, M. J., 2007, A non-marine depositional setting for the northern Fortescue Group, Pilbara Craton, inferred from trace element geochemistry of stromatolitic carbonates *Precambrian Research* 155, p. 229-250.
- Bonazzi and Menchetti, 1995, Monoclinic members of the epidote group: effects of the  $Al \rightleftharpoons Fe^{3+} \rightleftharpoons Fe^{2+}$  substitution and of the entry of  $REE^{3+}$ , *Mineralogy and Petrology*, Vol. 53, Issue 1-3, p. 133-153.
- Buick, R., Rasmussen, B. and Krapez, B., 1998, Archean Oil: Evidence for extensive hydrocarbon generation and migration 2.5-3.5 Ga, *AAPG Bulletin*, Vol. 82, Issue 1, p. 50-69.
- Buick, R., Thornett, J. R., McNaughton, N. J., Smith, J. B., Barley, M. E. and Savage, M., 1995, Record of emergent continental crust ~3.5 billion years ago in the Pilbara Craton of Australia, *Nature* 375, p. 574-577.
- Carignan J., Hold, P., Mevelle, G. Morel, J. and Yeghichevan, D., 2001, Routine analysis of trace elements in geological samples using flow injection and low pressure on line liquid chromatography coupled to ICP-MS: a study of geochemical reference materials BR, DR-N, UB-N, AN-G and GH, *Geostandards Newsletter* 25, p. 187-198.

- Cassidy, K. F., Champion, D.C. and Smithies, R. H., 2006, Origin of Archean late potassic granites: Evidence from the Yilgarn and Pilbara Cratons, Goldschmidt Conference Abstract, A88.
- Cathelineau, M., 1988, Cation site occupancy in chlorites and illites as a function of temperature., *Clay Minerals*, 23, p. 471-485.
- Cathelineau, M. and Nieva, D., 1985, A chlorite solid solution geothermometer: The Los azufres geothermal system, *Contrib. Mineral. Petrol.* 91, 235-244.
- Černý, P., Goad, B. E., Hawthorne, F. C. and Chapman, R., 1986, Fractionation trends of the Nb- and Ta-bearing oxide minerals in the Greer Lake pegmatitic granite and its pegmatite aureole, southeastern Manitoba, *American Mineralogist* 71, p. 501-517.
- Champion, D. C. and Smithies, R. H., 2004, Archaean granites, *The Ishihara Symposium: Granites and Associated Metallogenesis*, Geoscience Australia, p. 13-17.
- Champion, D. C. and Smithies, R. H., 2001, Archaean granites of the Yilgarn and Pilbara cratons, Western Australia, In: K. F. Cassidy, J. M. Dunphy and M. J. Van Kranendonk (eds.), 4<sup>th</sup> International Archaean Symposium 2002, Extended abstracts, AGSO Geoscience Australia, Record 2001/37, p. 134-136.
- Collins, W.J., 1989. Polydiapirism of the Archaean Mount Edgar Batholith, Pilbara Block, Western Australia, *Precambrian Research* 43, p. 41-62.
- Collins, W. J., Gray, C. M., 1990, Rb–Sr isotopic systematics of an Archaean granite-gneiss terrain: the Mount Edgar batholith, Pilbara Block, Western Australia. *Aust. J. Earth Sci.* 37, p. 9-22.
- Condie, K. C., Bowling, G. P. and Allen, P., 1986, Origin of granites in an Archean high-grade terrane, southern India, *Contribution to Mineralogy and Petrology*, Vol. 92, p. 93-103.
- Cuney, M. and Kyser, K., 2008, Chapter 4: Deposits related to magmatic differentiation, In: Cuney, M. and Kyser, K. (eds.), *Recent and not-so-recent developments in uranium deposits and implications for exploration*; Mineralogical Association of Canada, Short Course Series, Vol. 39, p. 57-77.
- Cuney, M. and Friedrich, M., 1987, Physicochemical and crystal-chemical controls on accessory mineral paragenesis in granitoids: implications for uranium metallogenesis. *Bulletin de Minéralogie* 110, p. 235-247.
- Debon, F. and Le Fort, P., 1988, A cationic classification of common plutonic rocks and their magmatic associations: principles, method, applications, *Bulletin de Minéralogie* 111, p. 493-510.
- Debon, F. and Le Fort, P., 1983, A chemical–mineralogical classification of common plutonic rocks and associations, *Transactions of the Royal Society of Edinburgh, Earth Sciences* 73, p. 135-149.
- Deer, W. A., Howie, R. A. and Zussman, J., 1963, *Rock Forming Minerals*, Vol. 4, London (Longmans).
- De Laeter, J. R. and Blockley, J. G., 1972, Granite ages within the Archaean Pilbara Block, Western Australia, *Geological Society of Australia, Journal* 19 (3), p. 363-370.
- Eby, G. N., 1992, Chemical subdivision of the A-type granitoids: Petrogenetic and tectonic implications, *Geology*, Vol. 20, p. 641-644.
- Evensen, N. M., Hamilton, P.J., and O'Nions, R. K., 1978, Rare-earth abundances in chondritic meteorites, *Geochimica et Cosmochimica Acta* 42, p. 1199-1212.

- Hammarstrom, J. M. and Zen, E.-an., 1986, Aluminum in hornblende: An empirical igneous geobarometer, *American Mineralogist*, 71, p. 1297-1313.
- Hecht, L. and Cuney, M., 2000, Hydrothermal alteration of monazite in the Precambrian crystalline basement of the Athabasca Basin (Saskatchewan, Canada): implications for the formation of unconformity-related uranium deposits, *Mineralium Deposita*, Vol. 35, p. 791-795.
- Hey, M. H., 1954, A new review of the chlorites, *The mineralogical magazine* 30, p. 277-292.
- Hickman, A. H., 2004, Two contrasting granite–greenstone terranes in the Pilbara Craton, Australia: evidence for vertical and horizontal tectonic regimes prior to 2900 Ma, *Precambrian Research* 131, p. 153-172.
- Hickman, A. H., 1983, Geology of the Pilbara Block and its environs, *Geological Survey of Western Australia, Bull.* 127, p. 268.
- Hickman, A. H., 1981, Crustal evolution of the Pilbara Block, In: Glover, J. E. and Groves, D. I. (Eds.), *Archaean Geology, Second International Archaean Symposium, Perth.*, Geological Society of Australia Special Publication 7, p. 57-69.
- Hickman, A. H. and Van Kranendonk, M. J., 2004, Diapiric emplacement of Archaean granitoids, In: *Tempos and Events in Precambrian Time*, 22 p.
- Hickman, A. H. and Lipple, S. L., 1975, Explanatory notes on the Marble Bar 1:250 000 geological sheet, Western Australia; *Geological Survey of Western Australia Record*, 1974/20.
- Hollister, L. S., Grissom, G. C., Peters, E. K., Stowell, H. H., and Sisson, V. R., 1987, Confirmation of the empirical correlation of Al in hornblende with pressure of solidification of calc-alkaline plutons. *American Mineralogist*, 72, p. 231-239.
- Jayananda, M., Moyen, J. F., Martin, H., Peucat, J. J., Auvray, B. and Mahabaleswar, B., 2000, Late Archaean (2550–2520 Ma) juvenile magmatism in the Eastern Dharwar craton, southern India: constraints from geochronology, Nd–Sr isotopes and whole rock geochemistry, *Precambrian Research*, Vol. 99, p. 225-254.
- Janardan Rao, Y., Murthy, I. S. N. and Sree Ramulu, C., 1973, Sphene Coronites from Hyderabad Granites, Andhra Pradesh, India, *Contr. Mineral. and Petrol.* 41, p. 57-60.
- Johnson, M. C., and Rutherford, M. J., 1989, Experimental calibration of the aluminum-in-hornblende geobarometer with application to Long Valley caldera (California), *Geology*, 17, p. 837-841.
- Linnen, R. and Cuney, M., 2005, Granite-Related-Element Deposits and Experimental Constraints on Ta-Nb-W-Sn-Zr-Hf Mineralization, In: Linnen, R. L. and Samson, I. M. (eds.) *Rare-Element Geochemistry and Mineral Deposits*, Geological Association of Canada, GAC Short Course Notes, Vol. 17, p. 45-67.
- Liou, J. G., 1971, Synthesis and stability relations of prehnite,  $\text{Ca}_2\text{Al}_2\text{Si}_3\text{O}_{10}(\text{OH})_8$ , *American Mineralogist*, 56, No. 3 and 4, p. 507-531.
- López, S., Fernández, C. and Castro, A., 2006, Evolution of Archean continental crust: Insights from the experimental study of Archean granitoids, *Current Science*, Vol. 91, No. 5, p. 607-621.
- López, S., Castro, A. and García-Casco, A., 2005, Production of granodiorite melt by interaction between hydrous mafic magma and tonalitic crust: Experimental constraints and implications for the generation of Archean TTG complexes, *Lithos*, Vol. 79, p. 229-250.

- Maniar P. D., Piccoli P. M., 1989, Tectonic discrimination of granitoids, *Geological Society of American Bulletin*, vol. 101, p. 635-643.
- Martin, H., 1986, Effect of steeper Archean geothermal gradient on geochemistry of subduction-zone magma, *Geology* 14, p. 753-756.
- Martin, H., 1994, The Archean grey gneiss and the genesis of continental crust, In: K. C. Condie (Ed.), *Archean Crustal Evolution*, Elsevier, Amsterdam, p. 205–259.
- Martin, H. and Moyen, J.-F., 2002, Secular changes in TTG composition as markers of the progressive cooling of the Earth, *Geology* 30, p. 319-322.
- Martin, H., Smithies, R. H., Rapp, R., Moyen, J.-F. and Champion, D., 2005, An overview of adakite, tonalite–trondhjemitite–granodiorite (TTG), and sanukitoid: relationships and some implications for crustal evolution, *Lithos* 79, p. 1-24.
- Minty, B., Richardson, M. and Wilford, J., 2008, New Radiometric Map of Australia, Australian Government-Geoscience Australia, AusGeo News Issue No. 92 (December 2008), 3 p.
- Moyen, J. F., Martin, H., Jayananda, M. and Auvray, B., 2003, Late Archaean granites : typology based on the Dharwar Craton (India), *Precambrian Research*, Vol. 127, p. 103-123.
- Moyen, J. F., Martin, H. and Jayananda, M., 1997, Origin of the late-Archean granite of Closepet, South India: information from geochemical modelling of trace element behaviour, *Académie des Sciences de Paris, Earth and Planetary Sciences*, Vol. 325, p. 659-664.
- Nelson, D.R., 1998, Compilation of SHRIMP U–Pb zircon geochronology data, 1997; Geological Survey of Western Australia, Record 1998/2, 242 p.
- Peccerillo, A. and Taylor, S. R., 1976, Geochemistry of Eocene calc-alkaline volcanic rocks from the Kastamonu area, Northern Turkey, *Contributions to Mineralogy and Petrology* 58, p. 63-81.
- Rasmussen, B. and Buick, R., 1999, Redox state of the Archean atmosphere: Evidence from detrital heavy minerals in ca. 3250–2750 Ma sandstones from the Pilbara Craton, Australia, *Geological Society of America*, Vol. 27, p. 115-118.
- Schmidt, M.W., 1992, Amphibole composition in tonalite as a function of pressure: An experimental calibration of the Al-in-hornblende barometer, *Contributions to Mineralogy and Petrology*, 110, p. 304-310.
- Shand, S. J., 1947, *Eruptive Rocks: Their Genesis, Composition, Classification, and their Relation to Ore-deposits*, 3rd ed. New York, John Wiley, p. 1-488.
- Sims, J. P. and Carson, L. J., 2001, The Geology of the Mount Edgar and Corunna Downs Igneous Complexes; East Pilbara Craton, Western Australia; AGSO – Geoscience Australia, Record 2001/35.
- Smithies, R. H., Champion, D. C. and Van Kranendonk, M. J., 2009, Formation of Paleoproterozoic continental crust through infracrustal melting of enriched basalt, *Earth and Planetary Science Letters*.
- Smithies, R. H., Champion, D. C., Cassidy, K. F., 2003, Formation of Earth's Early Archean continental crust, *Precambrian Research* 127, p. 89-101.
- Sweetapple, M. T. and Collins, L. F., 2002, Genetic Framework for the Classification and Distribution of Archean Rare Metal Pegmatites in the North Pilbara Craton, Western Australia, *Economic Geology*, Vol. 97, No. 4, p. 873-895.

- Taylor, S. R. and McLennan, S. M., 1985, *The continental crust: composition and evolution*. Backwell, Oxford, UK., 312 p.
- Tindle, A. G. and Breaks, F. W., 1998, Oxide Minerals of the Separation Rapids Rare-Element Granitic Pegmatite-Group, Northwestern Ontario, *The Canadian Mineralogist*, Vol. 36, p. 609-635.
- Van Haafte, W. M. and White, S. H., 1998, Evidence for multiphase deformation in the Archean basal Warrawoona Group in the Marble Bar area, East Pilbara, Western Australia, *Precambrian Research* 88, p. 53-66.
- Van Kranendonk, M.J., Smithies, R.H., Hickman, A.H., Bagas, L., Williams, I.R., Farrell, T.R., 2005, Event stratigraphy applied to 700 m.y. of Archean crustal evolution, Pilbara Craton, Western Australia, *Western Australia Geological Survey, Annu. Rev. 2003-2004*, p. 49-61.
- Van Kranendonk, M. J., Collins, W. J., Hickman, A. and Pawley M. J., 2004, Critical tests of vertical vs. horizontal tectonic models for the Archean East Pilbara Granite-Greenstone Terrane, Pilbara Craton, Western Australia; *Precambrian Research* 131, p.173-211.
- Van Kranendonk, M. J., Hickman, A. H., Smithies, R. H. and Nelson, D. R., 2002, Geology and Tectonic Evolution of the Archean North Pilbara Terrain, Pilbara Craton, Western Australia, *Economic Geology*, vol. 97, p. 695-732.
- Van Lichtervelde, M., Salvi, S. and Beziat, D., 2007, Textural features and chemical evolution in tantalum oxides: magmatic versus hydrothermal origins for Ta mineralization in the Tanco Lower Pegmatite, Manitoba, Canada, *Economic Geology* 102, p. 257-276.
- Wijbrans, J. R. and McDougall, I., 1987, On the metamorphic history of an Archean granitoid greenstone terrane, East Pilbara, Western Australia, using the  $^{40}\text{Ar}/^{39}\text{Ar}$  age spectrum technique, *Earth and planetary science letters*, vol. 84, n°2-3, p. 226-242.

## Partie 2.3

# Geochemical characterization of U-bearing minerals from the Archean TANCO pegmatite, Manitoba, Canada: Magmatic origin and later hydrothermal remobilization

I. Duhamel,<sup>1\*</sup> M. Cuney,<sup>1</sup> and M. Van Lichtenvelde<sup>2</sup>

<sup>1</sup> *Laboratoire de Géologie et de Gestion des Ressources Minérales et Énergétiques (G2R), Nancy-Université, CNRS, CREGU, Boulevard des Aiguillettes B.P. 239 F-54506 Vandœuvre lès Nancy, France*

<sup>2</sup> *Bundesanstalt für Geowissenschaften und Rohstoffe, Stilleweg 2, 30665 Hannover, Germany*

---

### Abstract

Mineralogical and geochemical characteristics of uranium-bearing phases in an Archean pegmatite are described for the first time, taking the Tanco rare element pegmatite from south-eastern Manitoba as an example. Such a characterization is a major importance to understand the beginning of the uranium fractionation during magmatic crystallization in the early crust and the later alteration processes.

Euhedral uraninite and uranmicrolite crystals are the main U-bearing minerals observed associated with columbite-tantalite group minerals, wadginite and cassiterite. Textural (SEM) and in situ chemical investigations (EMP) in uraninite have shown that a later fluid-circulation induced internal substitution of radiogenic elements by Ca, Si, P and Fe, with the partly dissolution of the most altered crystals and the redeposition of secondary U, Th and Pb phases in microcracks and porosity of the rock. However, the original geochemical characteristics in the less altered uraninite crystals present moderate ThO<sub>2</sub> (3.36 wt%) and CaO (2.66 wt%) contents typical of strongly peraluminous leucocratic granites and enrichments in MnO (1.30 wt%), P<sub>2</sub>O<sub>5</sub> (1.15 wt%) and alkalis (0.47 wt% Na<sub>2</sub>O and 0.23 wt% K<sub>2</sub>O) distinctive of highly fractionated high phosphorous rare element pegmatites.

REE patterns of uraninite, determined by secondary ion mass spectrometry (SIMS), are globally weakly fractionated ( $\Sigma\text{HREE}/\Sigma\text{LREE} \sim 0.30$ ) with a significant europium anomaly. This signature is typical of uraninite crystallizing from a magma. However, compared to other occurrences, REE abundances are significantly lower (maximum 10<sup>2</sup> times chondritic abundances:  $\Sigma\text{REE} \sim 229.2$  ppm) reflecting the strong REE depletion characteristic of highly fractionated low temperature highly peraluminous magmas.

Pb-Pb and U-Pb isotopic age determinations (SIMS) reveals three main age groups circa 650, 900 and 1150 Ma, with the older age at  $1250 \pm 30$  Ma, much younger than the 2.64 Ga age determined previously by Baadsgaard and Černý (1993) and attesting the existence of younger thermal/hydrothermal events strongly resetting the U-Pb isotopic system in these minerals.

---

### Key words

Tanco, Bernic Lake, Ontario, Canada, Archean, peraluminous pegmatite, uraninite, uranmicrolite.

## INTRODUCTION

The Tanco pegmatite in south-eastern Manitoba is well-known for its exceptional world-class tantalum deposit. Its mineralogy and petrogenesis have been intensely studied since the past three decades (summarised in Černý, 2005) but have focused mainly on the Ta mineralization and some other associated rare elements (Li, Rb, Cs). Although the presence of uraninite has been noticed during previous microscopic observations (Černý and Siivola, 1980; Černý et al., 1996; Stilling, 1998), no specific study has been carried out on uranium oxides. Uranium, together with Th, REE and others, is one of the most incompatible elements because of its large ionic radius combined with a high charge. The most abundant felsic rocks during Archean correspond to rocks of tonalite-trondhjemite-granodiorite (TTG) composition which only reach a few ppm uranium (Martin, 2005).

The processes that control the first U enrichments in the Archean rocks during early crust forming are poorly understood. The main reason is because the U-rich Archean granitoids are rare, and no detailed geochemical characterization of U and Th bearing minerals has been done in these rocks. Uraninite bearing ones are still more scarce and no detailed geochemical characterization of this mineral has been performed in Archean granitoids.

Understanding the processes leading to the formation of the first granitoids sufficiently enriched in uranium to be able to crystallize uraninite in the most extreme differentiate series is of major importance for constraining the genesis of the uranium mineralization in the Archean (such as the Witwatersrand Basin in South Africa: Robb and Meyer, 1995) to Early Paleoproterozoic (such as the Blind River - Elliot Lake deposits in Huronian formations in Canada: Robinson and Spooner, 1982, Prasad and Roscoe, 1996) quartz pebble conglomerates. The debate is still open, since nearly a century, between the supporters of a uraninite mineralization having a placer (Mellor, 1916) or modified placer origin (Pretorius 1961; Thiel et al., 1979; Minter, 1981) and those defending a purely hydrothermal origin (Barnicoat et al., 1997; Law and Phillips, 2006). The granitoidic sources of the detrital uraninites still remain poorly known (Robb et al., 1990; Frimmel and Minter, 2002).

The present paper gives the first textural, major and trace element and U-Pb isotopic characterization of uraninites and associated U-rich phases from an Archean granitic pegmatite. The Tanco pegmatite, Manitoba, Canada (Stilling et al., 2006) has been selected because of: (i) its Archean age (2.64 Ga, Baadsgaard and Černý, 1993), (ii) its peraluminous character combined with a high degree of fractionation having lead to a uranium enrichment permitting the

crystallization of uraninite (Cuney and Friedrich, 1987), (iii) the possibility to sample it in drill cores and a mine to be able to get the best preserved uraninite crystals, this mineral being easily leached out by oxidizing meteoric waters on outcrops (Friedrich et al., 1987).

More globally this work is a contribution to the understanding of magmatic uranium fractionation during the early stages of the Earth history and to the formation of uranium mineralization hosted by quartz pebble conglomerates, which represent the first uranium deposits which have been formed on Earth.

## GEOLOGICAL SETTING

The Tanco pegmatite is located in south-eastern Manitoba, at approximately 180 kilometres east-northeast of Winnipeg (Fig. 2.3.1). The pegmatite is emplaced at the English River – Winnipeg River boundary which separates the dominantly metasedimentary English River terrane from mainly metaplutonic Winnipeg River terrane. Between the two terranes lies the mafic metavolcanic Bird River subprovince (Breaks, 1991). The boundary zone is a focus for emplacement of peraluminous leucogranites and rare metal pegmatites (Breaks et al., 2003; Smith et al., 2004), including the Tanco field. The partial melting event at the origin of the peraluminous leucogranites has been related to crustal thickening resulting from a continental collision which has occurred in the Western Superior Province (Larbi et al., 1999).

The Tanco pegmatite represents one of the intrusions of the Bernic Lake pegmatite group. It belongs to the petalite-subtype of LCT-type pegmatites according to Černý and Ercit (2005). It corresponds in fact to a highly fractionated, highly peraluminous [ $Al/(Na+K) > 1.15$ ] and high phosphorous rare metal granites after Linnen and Cuney (2005), and Černý et al., (2005). They are typically strongly enriched in Li, Rb, Cs, F, P and Ta with  $Ta > Nb$  and to a lesser extent in U, Tl, Be, B, Ga, Sn and strongly depleted in transition elements and Th, Zr, Y and REE. From U-Pb isotopic dating of tantalite, the pegmatite emplacement has been estimated at  $2640 \pm 7$  Ma (Baadsgaard and Černý, 1993). Černý et al. (1998) propose that the Tanco pegmatite derives from the extreme crystal fractionation of a peraluminous leucogranite parent body assumed to be present under the central portion of the Bernic Lake but which is not outcropping at the surface. The parent peraluminous leucogranite ultimately derive from the partial melting of “fertile” peraluminous upper-crustal rocks, i.e. already relatively enriched in rare elements (Černý, 1992).

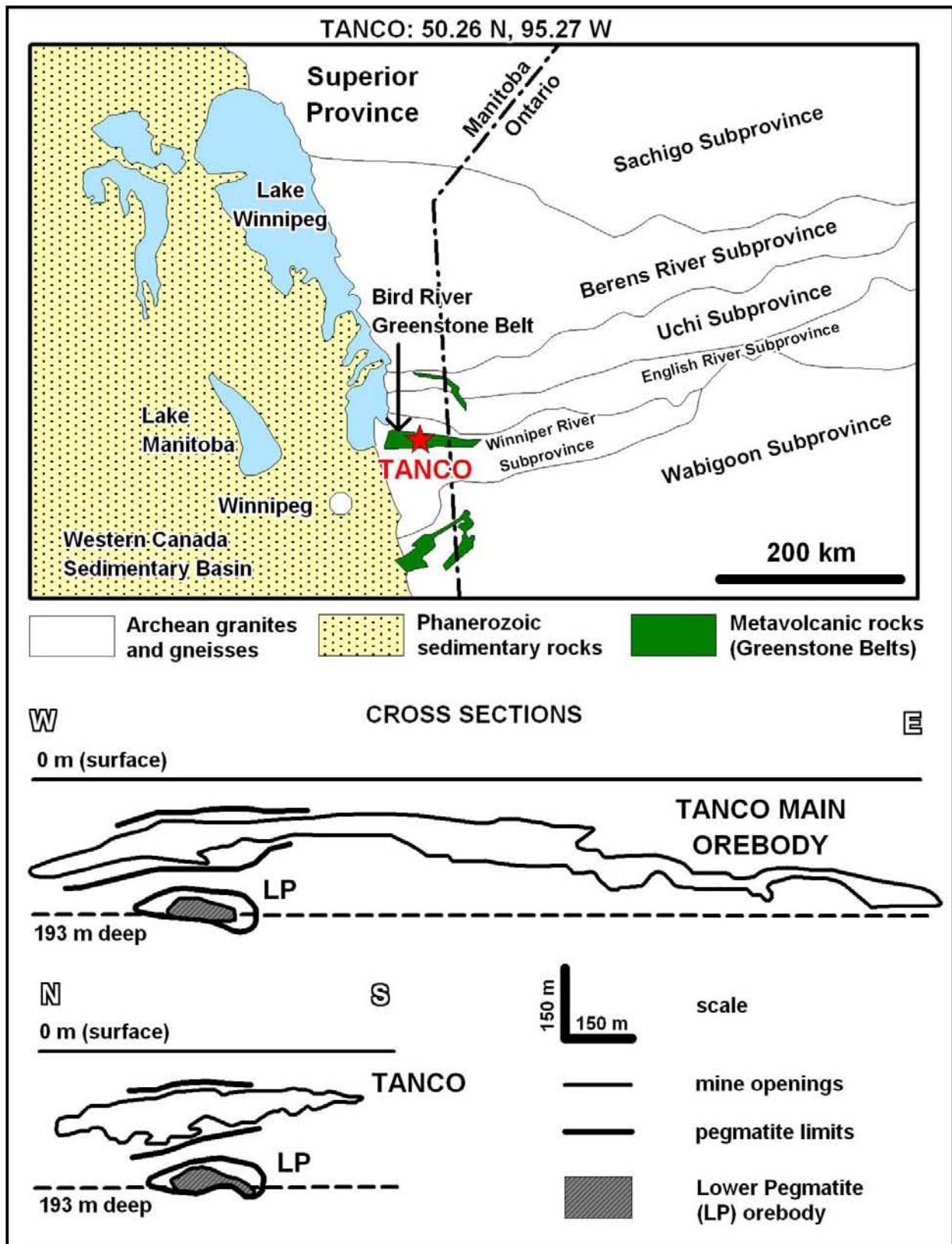


Figure 2.3.1. Location and geological setting of the Tanco pegmatite. East-west and south-north cross sections through the pegmatite showing the Lower Pegmatite (LP) orebody. The limits of the Tanco pegmatite are extrapolated from drill hole information. After Van Lichtervelde et al., 2007, modified.

The main body of the intrusion is sub-horizontal, about 1990m x 1060m x 100m in size elongated and double-plunging east-westernly, and shallowly dipping to the north (Stilling, 1998; see cross-section in Fig. 2.3.1). The internal structure of the pegmatite has been divided into nine zones because of its complex mineralogy: (10) border zone, (20) wall zone, (30) aplitic albite zone, (40) lower intermediate zone, (50) upper intermediate zone, (60) central intermediate zone, (70) quartz zone, (80) pollucite zone and (90) lepidolite zone. The mineral assemblage and texture of each zone are described in detail by Stilling (1998) who observed uraninite in zones (50), (60) and (90) which are the richest in Ta-oxides, and therefore the most fractionated. A bulk uranium content of 55 ppm U has been calculated for the whole pegmatite.

A sub-parallel smaller dyke system, which larger intrusion is referred as the Lower Pegmatite (LP), is located 50 meters below the main body (Fig. 2.3.1). Detailed mineralogy of the LP intrusion (Van Lichtervelde et al., 2007) has shown that the tantalum mineralization has a magmatic origin and that some U-bearing phases are associated with. Therefore the LP body represents a good target for the first textural and geochemical characterization of U-bearing minerals in the Tanco pegmatite and the understanding of uranium fractionation.

## **SAMPLING AND ANALYTICAL METHODS**

Four samples were collected from the Tanco Lower Pegmatite orebody: LP-16 comes from freshly opened underground exposure and samples 2-22, 2-57 and 2-85 are from three different drill-cores, 02-U-26, 01-U-51 and 02-U-01 respectively (see location in Fig. 2.3.2).

The radioactive minerals have been located on polished rock surface using autoradiography to select the best area for making the polished thin sections using MEDEX SD-SPEEDX reactive films placed in contact with during a week.

Then, U-bearing minerals, mostly uraninite  $[U,Pb,Th,REE,\dots]O_{2-x}$  and uranmicrolite  $(U,Ca,Na,\dots)_{2-n}(Ta \gg Nb)_{2-m}O_6(O,OH,F)$  associated with other Nb-Ta minerals and cassiterite  $SnO_2$ , have been identified using a polarizing microscope Olympus BX51 in transmitted and reflected lights and the scanning electron microscope (SEM) HITACHI FEG S4800 from the SCMEM laboratory (University of Nancy, France). Backscattered electron (BSE) imaging mode has been used to identify the variations of composition, the variations of grey deriving from the average atomic number. The Noran Vantage energy dispersive spectrometer (EDS) has allowed obtaining a semi-quantitative composition of the minerals.

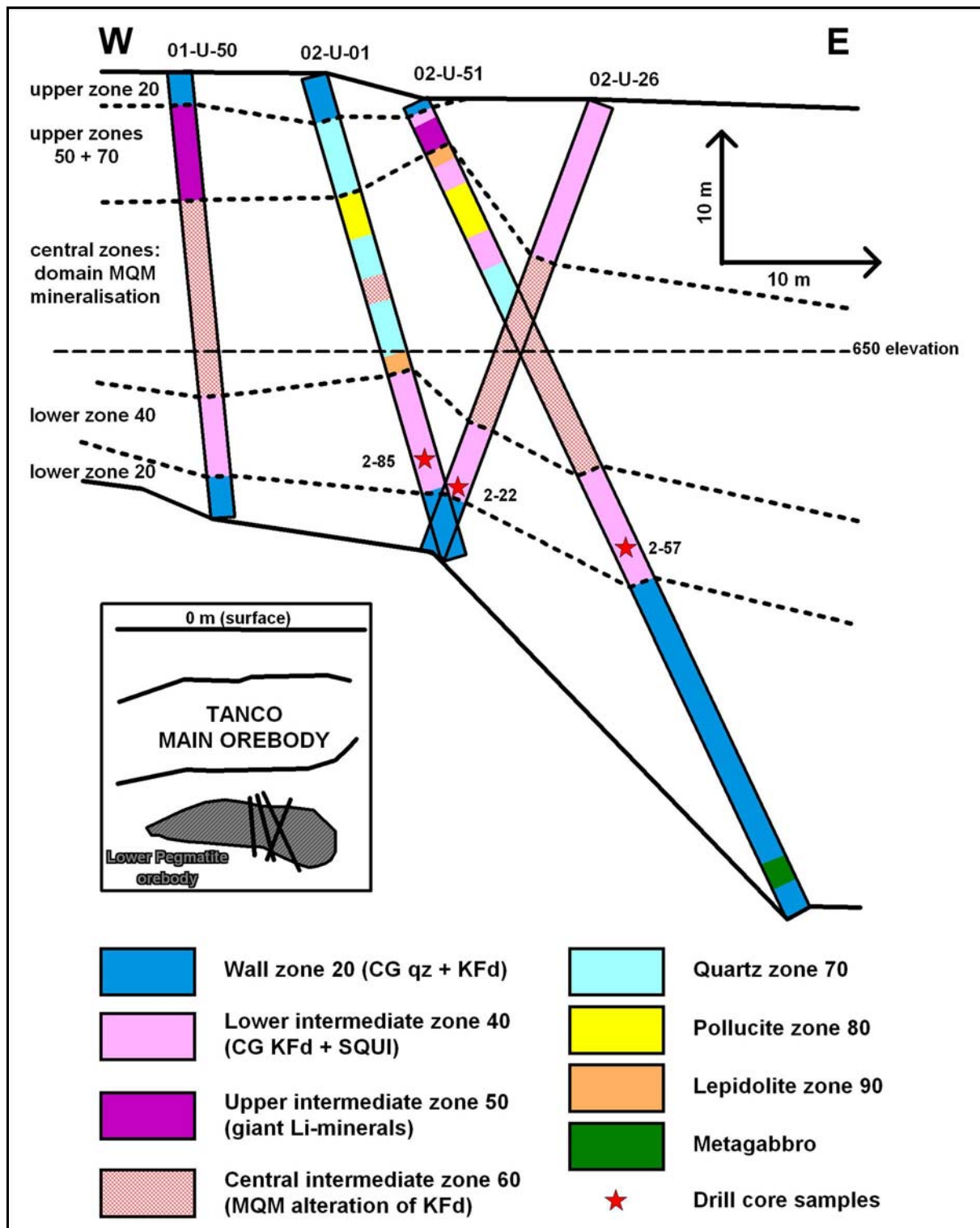


**Figure 2.3.2.** East-west section showing the general geology of the Tanco Lower pegmatite and location of the studied samples. The three samples 2-22, 2-57 and 2-85 are from three drill cores, 02-U-26, 01-U-51 and 02-U-01 respectively. Sample LP-16 was handpicked from the mine opening approximately at level 650 (~160 m depth). Note that the locations of the drill holes are projected onto the section and the holes are not entirely within the east-west plane. CG = coarse grained, qz = quartz, Kfd = K-feldspar, MQM = mica-quartz alteration, SQUI = spodumene-quartz intergrowths. After Van Lichtervelde et al., 2007, modified.

Major element concentrations of the different U-bearing phases and other accessory minerals associated were determined with a CAMECA SX100 electron microprobe (EMP) also from the SCMEM laboratory. Electron microprobe analysis (EMPA) were performed with an accelerating voltage of 15 kV, a beam current of 10 nA, and a 2 µm beam diameter for all elements. Standard calibration, spectrometer crystals, background position and counting times on peaks used for experiments are given in Table 2.3.1.

**Table 2.3.1.** Overview of major element set-up for the CAMECA SX100 electron microprobe including analysed line, calibration standard, and background positions used during integrated analysis of uranium and tantalum bearing minerals

<i>Mineral analysed</i>	<i>Element</i>	<i>Line</i>	<i>Spectrometer crystal</i>	<i>Standard</i>	<i>High background</i>	<i>Low background</i>	<i>Slope</i>	<i>Peak counting time (s)</i>
<i>U-oxides:</i>	Al	Kα	TAP	Albite	800		1.15	20
	Si	Kα	TAP	Orthose	800		1.20	20
	S	Kα	LPET	SrSO <sub>4</sub>	600		1.05	20
	K	Kα	PET	Orthose	600		1.10	10
	Ca	Kα	PET	Wollastonite	700		1.10	10
	V	Kα	LIF	V metal	600		1.05	40
	Fe	Kα	LIF	Hematite	600		1.10	20
	Zr	Lα	TAP	ZrO <sub>2</sub>	700		1.20	20
	Pb	Mα	PET	PbCrO <sub>4</sub>	1700		1.05	50
	U	Mβ	PET	UO <sub>2</sub>	500		1.10	20
	Na	Kα	TAP	Albite	500		1.10	10
	Mg	Kα	TAP	Olivine	1200		1.05	40
	Ti	Kα	LPET	MnTiO <sub>3</sub>	600		1.20	20
	Mo	Lα	LPET	Mo metal	500		1.10	20
	La	Lα	LPET	LaPO <sub>4</sub>	500		1.10	20
	Th	Mα	LPET	ThO <sub>2</sub>	500		1.10	60
	Mn	Kα	LIF	MnTiO <sub>3</sub>	600		1.10	20
	Y	Lα	TAP	YPO <sub>4</sub>	775	-450		20
	Ce	Lα	PET	CePO <sub>4</sub>	500		1.20	20
	P	Kα	TAP	CePO <sub>4</sub>	600		1.15	20
Nd	Lβ	LIF	NdPO <sub>4</sub>	1143	-991		40	
Dy	Lα	LIF	DyRu <sub>2</sub> Ge <sub>2</sub>	450	-500	1.10	40	
<i>Ta-oxides:</i>	F	Kα	PC1	Topaz	2800	-2600		15
	Na	Kα	TAP	Albite	600		1.10	5
	Ca	Kα	PET	Wollastonite	700		1.10	5
	Sc	Kα	LPET	ScNi <sub>2</sub> Si <sub>2</sub>	800		1.10	5
	Ti	Kα	LPET	MnTiO <sub>3</sub>	1000		1.20	5
	Mn	Kα	LIF	MnTiO <sub>3</sub>	600		1.10	15
	Fe	Kα	LIF	Hematite	600		1.10	15
	Mg	Kα	TAP	Olivine	1200		1.15	5
	Ta	Mα	TAP	LiTaO <sub>3</sub>	800		1.20	5
	Y	Lα	TAP	YPO <sub>4</sub>	800		1.20	5
	Zr	Lα	TAP	ZrO <sub>2</sub>	500		1.20	5
	Nb	Lα	PET	LiNbO <sub>3</sub>	600		1.20	5
	Sn	Lα	LPET	SnO <sub>2</sub>	600		1.1	5
	Sb	Lβ	LPET	Sb <sub>2</sub> S <sub>3</sub>	600		1.1	10
	W	Mβ	TAP	WCaO <sub>4</sub>		-800	0.9	10
	Bi	Mα	PET	Bi metal	500	-1200		5
	Th	Mα	PET	ThO <sub>2</sub>	726	-1274		15
	U	Mα	LPET	UO <sub>2</sub>	793	-1447		15
	Pb	Mα	LPET	PbS	1500		1.05	15

*Notes:* TAP – thallium acid phthalate crystal; LPET – large pentaerythriol crystal; PET – large pentaerythriol crystal; LIF – Lif crystal; PC1 – multilayered W-Si crystal; Background positions refer to number of wavelength, expressed as  $\sin \theta \cdot 10^5$ , above and below the peak position or derived by line regression with the slope indicated. Background counting time is equivalent to half of the peak counting time for each element.

EMPA results in weight percent of the oxides are recalculated to obtain the cationic composition of the different Nb-Ta minerals in atoms per formula unit, their structural formula

depending of the number of oxygen atoms considered. The uranmicrolite is part of the pyrochlore group and microlite subgroup which ideal formula is  $A_2B_2O_6(OH,F)$  where the octa-coordinated A site can be filled by Na, Ca, Mn,  $Fe^{2+}$ , Sr, Sb, Cs, Ba, REE, Pb, Bi, Th, U or K, and the hexa-coordinated B site can be filled by Ta, Nb, Ti, Al,  $Fe^{3+}$ , Zr, Sn or W (Hogarth, 1977). The structural formula of uranmicrolite has been calculated with 6 oxygen atoms, the sum of cations in the B site not exciding 2 and F partly associated with the O=F bounds. The columbite-tantalite family minerals correspond to an ideal stoichiometry of  $AB_2O_6$  with Fe and Mn composing mostly the A site and Nb and Ta in the B site (Černý et al., 1986). The structural formula of columbite-tantalite has been calculated also with 6 oxygen atoms. The composition of wodginite group minerals, which ideal formula is  $MnSnTa_2O_8$ , has been recalculated with 32 oxygen atoms and  $Li_2O$ ,  $Fe_2O_3$  and FeO values have been recalculated using the method of Ercit et al. (1992). The content of FeO ( $Fe^{2+}$ ) is partially converted to  $Fe_2O_3$  ( $Fe^{3+}$ ) when the cation sum surpasses the corresponding theoretical value.

EMPA results in uraninite permit to calculate the approximate chemical age using the following equilibrium formula derived from the radioactive decay law (Cocherie and Albarede, 2001 modified from Bowles, 1990):

$$C_{Pb} = C_{Th} \left[ \frac{M_{208Pb}}{M_{232Th}} (e^{\lambda_{232}t} - 1) \right] + C_U \left[ 0.9928 \frac{M_{206Pb}}{M_{238U}} (e^{\lambda_{238}t} - 1) + 0.0072 \frac{M_{207Pb}}{M_{235U}} (e^{\lambda_{235}t} - 1) \right]$$

where  $t$  is the age of mineral crystallisation,  $C_{Pb}$ ,  $C_{Th}$  and  $C_U$  are concentrations (in ppm) converted from the Pb, Th and U contents measured by EMPA in weight percent,  $M_{206Pb}$  (205.97445 g.mol<sup>-1</sup>),  $M_{207Pb}$  (206.97588 g.mol<sup>-1</sup>),  $M_{208Pb}$  (207.97664 g.mol<sup>-1</sup>),  $M_{232Th}$  (232.03805 g.mol<sup>-1</sup>),  $M_{235U}$  (235.04392 g.mol<sup>-1</sup>),  $M_{238U}$  (238.05078 g.mol<sup>-1</sup>) are molar masses, and  $\lambda_{232}$  ( $0.049475 \times 10^{-9} \text{ y}^{-1}$ ),  $\lambda_{238}$  ( $0.155125 \times 10^{-9} \text{ y}^{-1}$ ) and  $\lambda_{235}$  ( $0.98485 \times 10^{-9} \text{ y}^{-1}$ ) are the decay constants of <sup>232</sup>Th, <sup>238</sup>U and <sup>235</sup>U respectively. This relation is used assuming that <sup>235</sup>U, <sup>238</sup>U and <sup>232</sup>Th produce total lead present in the crystal (<sup>207</sup>Pb+<sup>206</sup>Pb+<sup>208</sup>Pb) so Pb is essentially of radiogenic origin and there is no common lead incorporated in the mineral during crystallization.

Finally, in-situ isotopic determinations of uranium, lead, yttrium and the rare earth elements in uraninite were performed by secondary ion mass spectrometry (SIMS) on a CAMECA IMS-3f ion microprobe from the CRPG (CNRS, Nancy, France).

The standard sample for U-Pb isotopic analysis is a uraninite from Katanga in Zambia (Holliger, 1988) dated at  $540 \pm 4 \text{ Ma}$  (Cathelineau et al., 1990). Three single grains of uraninite, two from the sample 2-22 (grains 1 and 2) and one from the sample 2-57 (grain 3) have been

analyzed for U and Pb isotopic compositions. The analytical spots have been chosen in the least altered parts of uranium oxides corresponding to the brighter domains in BSE mode having the highest Pb/U ratios. However, the size of the analytical spots (20 to 30  $\mu\text{m}$  in diameter) exceeds the size of the homogeneous brighter domains. Therefore, the results represent a mixture of domains with variable U contents and Pb/U ratios. Discordia intersections on the Concordia plot were calculated using the ISOPLOT flowsheet of Ludwig (1999) with the Microsoft EXCEL software. Uncertainties in the ages are reported at the  $1\sigma$  level.

Methodology and calibration of SIMS analysis for yttrium and rare earth element determinations are described by Bonhoure et al. (2007). A uraninite from the Mistamisk Valley in Canada (Kish and Cuney, 1981) is used as a standard. REE patterns were normalized to chondrite values (Anders and Grevesse, 1989).

## RESULTS

### ***Mineralogy and composition of U-bearing phases and associated accessory minerals***

#### **Uraninite**

Uraninite is the main uranium-bearing mineral observed in core samples 2-22, 2-57 and 2-85 but is less abundant than uranmicrolite in sample LP-16 after a visual estimation in thin sections. Uraninite develops radiation-damaged rims in muscovite and plagioclase crystals (Fig. 2.3.3-A) and radial fractures in quartz (Fig. 2.3.3-C) corresponding to characteristic features of U and Th-rich minerals (Friedrich et al., 1987). In reflected light, uraninite generally appears as an assemblage of cubic crystals up to 300  $\mu\text{m}$  wide, generally broken into several fragments 50 to 100  $\mu\text{m}$  in size (Fig. 3-B), but also as isolated cubes with internal micro-cracks (Fig. 2.3.3-C). The uraninite shows large variations of reflectivity (Fig. 2.3.3-B). Decrease of reflectivity corresponds to altered or recrystallized uraninite under reducing conditions and its conversion to coffinite mostly (Alexandre and Kyser, 2005) or higher oxidation state and substitution by lighter elements resulting from alteration by later fluid circulation (Cathelineau et al., 1982).

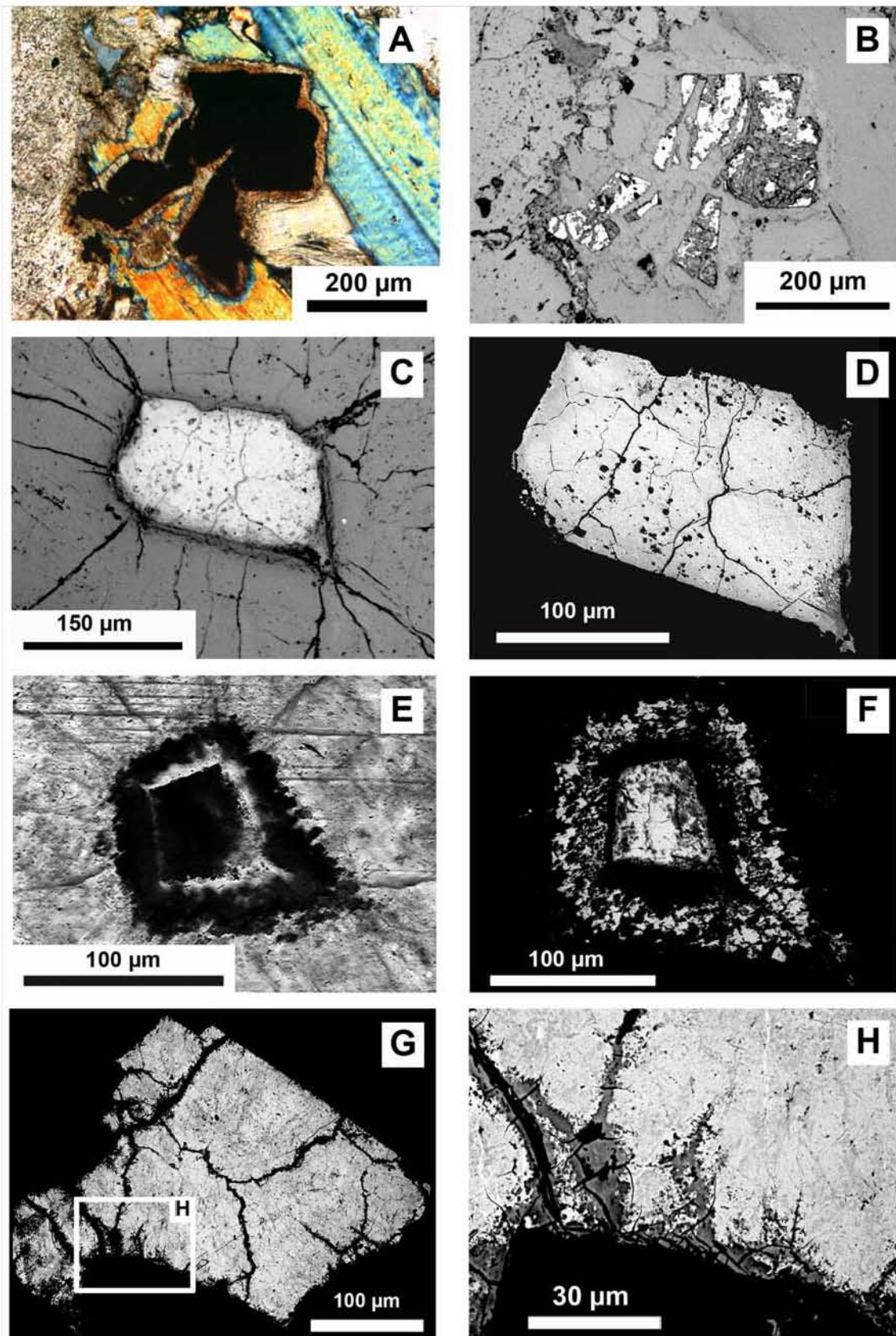


**Figure 2.3.3.** Optical microscopic and SEM images of the euhedral uraninite crystals in the Tanco Lower pegmatite. (A) Uraninite in transmitted light rimmed by a radiation damage halo developed in surrounding micas (sample 2-22). (B) The same crystals in reflected light showing the reflectance variations associated with alteration mainly developed at the margins of the crystals and along cracks. (C) Single grain of uraninite in reflected light surrounded by radial fractures in quartz and (D) in BSE mode (sample 2-57). (E) Dissolution features at the edge of a strongly altered uraninite grain in transmitted light and (F) SEM image in BSE mode (sample 2-85). (G) BSE image of a uraninite splitted by micro-cracks and showing strong internal heterogeneities with variable intensity of grey corresponding to variations in the average atomic number (sample 2-22). The white box outlines the enlarged area presented in (H) showing the heterogeneities down to the micrometer scale and the darker rims that correspond to coffinitization.

The BSE images of uranium oxides (Fig. **2.3.3-D** and **-G**) reveal also heterogeneities in the chemical composition. The brighter zones correspond to higher average atomic number characterized by higher U and Pb contents than the darker zones. The darker grey areas have higher Si, Ca and Fe contents with asymptotic Si energy peak of EDS spectrum occurring at the rims of the uraninite crystals and along micro-cracks (Fig. **2.3.3-H**). The better preserved uraninite crystals with highest average atomic number and the most homogeneous texture in BSE mode are in samples 2-22 and 2-57. Uranium oxides observed in samples LP-16 and 2-85 show the most heterogeneous textures with dissolution features like embayments at the edge of the grains relative to the corrosion of the border of the crystals, dissolution cavities or even boxwork texture with sometimes small residual crystals (Fig. **2.3.3-E** and **-F**).

A total of 45 electron microprobe analysis has been done in three uraninite grains from samples 2-22 and 2-57, the best preserved from alteration which have been used for the following isotopic study. Average EMPA of the Tanco uraninite crystals is given in Table **2.3.2**. Because of the heterogeneity of the minerals at microscopic scale, the brighter and darker zones of the crystals in BSE images are distinguished in the table and the plots. As many uranium oxides, the analytical totals are low, between 94.83 wt% and 86.95 wt% for the brighter and darker parts of the crystals respectively. Lower totals mostly reflect the hydration of the uranium oxides during later alteration episodes.

The brighter areas in BSE images corresponding to heaviest average atomic number are the richest in  $\text{UO}_2$  ( $77.60 \pm 1.45$  wt%) and  $\text{PbO}$  ( $6.78 \pm 1.76$  wt%). They are also characterized by moderate  $\text{ThO}_2$  ( $3.36 \pm 0.94$  wt%) and relatively high  $\text{MnO}$  ( $1.30 \pm 0.50$  wt%),  $\text{P}_2\text{O}_5$  ( $1.15 \pm 0.50$  wt%),  $\text{K}_2\text{O}$  ( $0.23 \pm 0.05$  wt%) and  $\text{CaO}$  ( $2.66 \pm 0.56$  wt%) contents. The amount of  $\text{SiO}_2$  ( $0.35 \pm 0.21$  wt%) and  $\text{FeO}$  ( $0.36 \pm 0.32$  wt% in average but most of time below detection limit) representing elements generally associated with alteration are relatively low. The other elements, Al, Zr, Mo, V, S, Y and REE are always below detection limits except in rare analysed spots in grain 1 of sample 2-22 with few amount of  $\text{Dy}_2\text{O}_3$  ( $0.50 \pm 0.19$  wt%) and in grain 3 of sample 2-57 with small concentrations in S ( $0.06 \pm 0.04$  wt%  $\text{S}_2\text{O}$ ).

The darker zones in BSE mode with the lowest average atomic number are lower in  $\text{UO}_2$  ( $66.26 \pm 4.09$  wt%), show variable contents of  $\text{PbO}$  ( $3.93 \pm 3.83$  wt%) and higher amounts in  $\text{ThO}_2$  ( $5.31 \pm 2.40$  wt%),  $\text{SiO}_2$  ( $1.46 \pm 0.75$  wt%),  $\text{CaO}$  ( $3.21 \pm 0.94$  wt%),  $\text{K}_2\text{O}$  ( $0.41 \pm 0.12$  wt%),  $\text{P}_2\text{O}_5$  ( $2.99 \pm 0.87$  wt%) and  $\text{FeO}$  ( $0.65 \pm 0.25$  wt%). Variations in  $\text{Na}_2\text{O}$  and  $\text{MnO}$  contents are low and seem to not be correlated with the degree of alteration. Traces of Al, S and

in some cases Ti, Mg and Y have also been detected but always below the weight percent of the oxide. Other elements, Zr, Mo, V and REE are still under detection limits.

**Table 2.3.2.** Average chemical compositions of primary uraninite (CAMECA SX100 electron microprobe analysis in wt%)

Sample	2-22		2-22		2-57		Average	
	Uraninite 1		Uraninite 2		Uraninite 3		for uraninite	
Crystal	High	Low	High	Low	High	Low	High	Low
BSE brightness	High	Low	High	Low	High	Low	High	Low
EMPA	(10)	(2)	(13)	(7)	(11)	(2)	(34)	(11)
UO <sub>2</sub>	79.01 ± 1.62	65.16 ± 0.05	77.02 ± 0.81	66.79 ± 4.34	77.00 ± 1.00	62.03 ± 0.00	77.60 ± 1.45	66.26 ± 4.09
PbO	8.34 ± 2.03	1.09 ± 0.16	5.86 ± 1.30	3.74 ± 4.18	6.44 ± 0.90	7.46 ± 0.66	6.78 ± 1.76	3.93 ± 3.83
ThO <sub>2</sub>	2.38 ± 0.52	7.75 ± 0.70	3.38 ± 0.32	4.00 ± 2.02	4.22 ± 0.88	7.42 ± 0.03	3.36 ± 0.94	5.31 ± 2.40
MnO	1.71 ± 0.35	0.95 ± 0.01	1.45 ± 0.34	0.95 ± 0.15	0.75 ± 0.19	<D.L.	1.30 ± 0.50	0.78 ± 0.39
Al <sub>2</sub> O <sub>3</sub>	<D.L.	0.58 ± 0.06	<D.L.	0.70 ± 1.00	<D.L.	0.94 ± 0.00	<D.L.	0.72 ± 0.79
SiO <sub>2</sub>	0.15 ± 0.05	1.77 ± 0.18	0.59 ± 0.08	1.47 ± 0.92	0.26 ± 0.06	1.13 ± 0.06	0.35 ± 0.21	1.46 ± 0.75
K <sub>2</sub> O	0.21 ± 0.03	0.47 ± 0.06	0.22 ± 0.04	0.40 ± 0.15	0.26 ± 0.06	0.42 ± 0.01	0.23 ± 0.05	0.41 ± 0.12
CaO	2.63 ± 0.58	3.78 ± 0.44	2.40 ± 0.63	3.49 ± 0.65	2.99 ± 0.16	1.67 ± 0.25	2.66 ± 0.56	3.21 ± 0.94
Na <sub>2</sub> O	0.20 ± 0.04	0.69 ± 0.27	<D.L.	0.42 ± 0.10	1.14 ± 0.39	<D.L.	0.47 ± 0.52	0.40 ± 0.23
P <sub>2</sub> O <sub>5</sub>	0.59 ± 0.14	2.03 ± 0.22	1.07 ± 0.12	2.88 ± 0.58	1.77 ± 0.16	4.33 ± 0.05	1.15 ± 0.50	2.99 ± 0.87
FeO	<D.L.	0.87 ± 0.16	0.69 ± 0.27	0.70 ± 0.17	<D.L.	<D.L.	0.36 ± 0.32	0.65 ± 0.25
MgO	<D.L.	0.08 ± 0.00	<D.L.	0.11 ± 0.06	<D.L.	<D.L.	<D.L.	0.09 ± 0.06
TiO <sub>2</sub>	<D.L.	0.13 ± 0.03	<D.L.	<D.L.	<D.L.	<D.L.	<D.L.	<D.L.
V <sub>2</sub> O <sub>3</sub>	<D.L.	<D.L.						
ZrO <sub>2</sub>	<D.L.	<D.L.						
MoO <sub>3</sub>	<D.L.	<D.L.						
SO <sub>2</sub>	<D.L.	0.13 ± 0.03	<D.L.	0.20 ± 0.19	0.06 ± 0.04	<D.L.	0.03 ± 0.03	0.16 ± 0.16
Y <sub>2</sub> O <sub>3</sub>	<D.L.	0.14 ± 0.07	<D.L.	<D.L.	<D.L.	<D.L.	<D.L.	<D.L.
La <sub>2</sub> O <sub>3</sub>	<D.L.	<D.L.						
Ce <sub>2</sub> O <sub>3</sub>	<D.L.	<D.L.						
Nd <sub>2</sub> O <sub>3</sub>	<D.L.	<D.L.						
Dy <sub>2</sub> O <sub>3</sub>	0.50 ± 0.19	<D.L.	<D.L.	<D.L.	<D.L.	<D.L.	<D.L.	<D.L.
<i>Total</i>	96.11 ± 0.67	86.18 ± 0.69	93.51 ± 1.25	87.48 ± 2.91	95.24 ± 1.02	85.88 ± 0.27	94.83 ± 1.50	86.95 ± 2.38

**Notes:** The relative BSE brightness is given as indicative of the average atomic number variations in the crystal: High brightness corresponds to well preserve uraninite parts and Low brightness is associated with a decrease in the average atomic number because of enrichment in lighter elements. **Abbreviations:** <D.L. = below Detection Limit (U = 0.57 wt%, Pb = 0.25 wt%, Th = 0.11 wt%, Mn = 0.20 wt%, Al = 0.05 wt%, Si = 0.06 wt%, K = 0.10 wt%, Ca = 0.11 wt%, Na = 0.10 wt%, P = 0.06 wt%, Fe = 0.20 wt%, Mg = 0.04 wt%, Ti = 0.05 wt%, V = 0.15 wt%, Zr = 0.18 wt%, Mo = 0.12 wt%, S = 0.03 wt%, Y = 0.13 wt%, La = 0.13 wt%, Ce = 0.29 wt%, Nd = 0.52 wt%, Dy = 0.39 wt%).

The average Pb/U ratio in the Tanco uraninites is 0.10 (± 0.04) corresponding to a large range of chemical ages between 41 and 1227 Ma (Fig. 2.3.4). In the best preserved parts of the Tanco uraninites, lead content is still extremely variable ranging from 3.73 to 13.99 wt% PbO with a mean at 6.78 wt%. Such lead concentrations are much lower than the ones expected for an Archean uraninite and the expected amount of lead corresponding to a chemical age of 2.64 Ga (U-Pb isotopic age in tantalite of the Tanco pegmatite, Baadsgaard and Černý, 1993) should be around 29.57 wt% PbO (after the correlation PbO concentration versus time established in Fig. 2.3.4 high right).

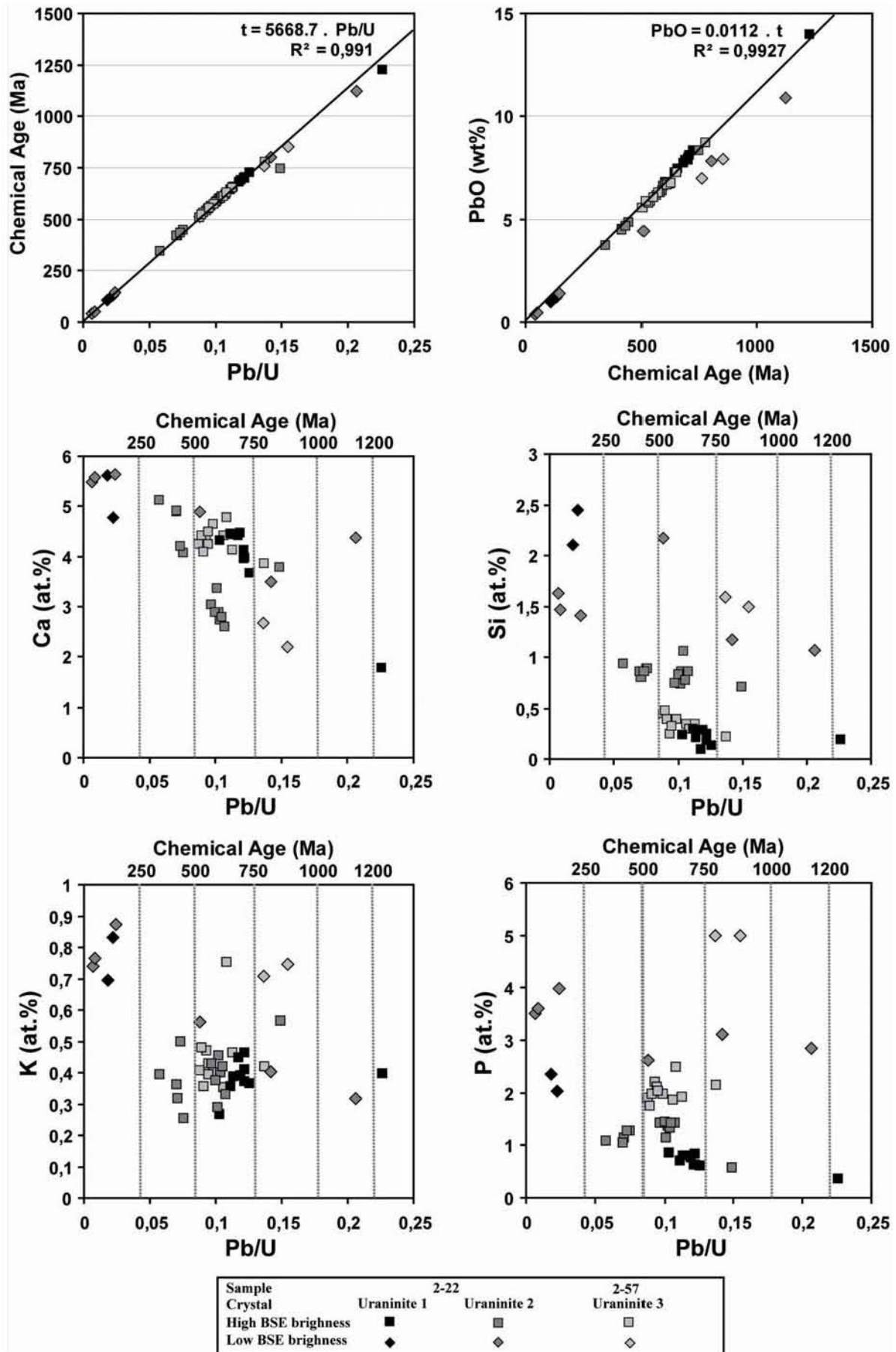
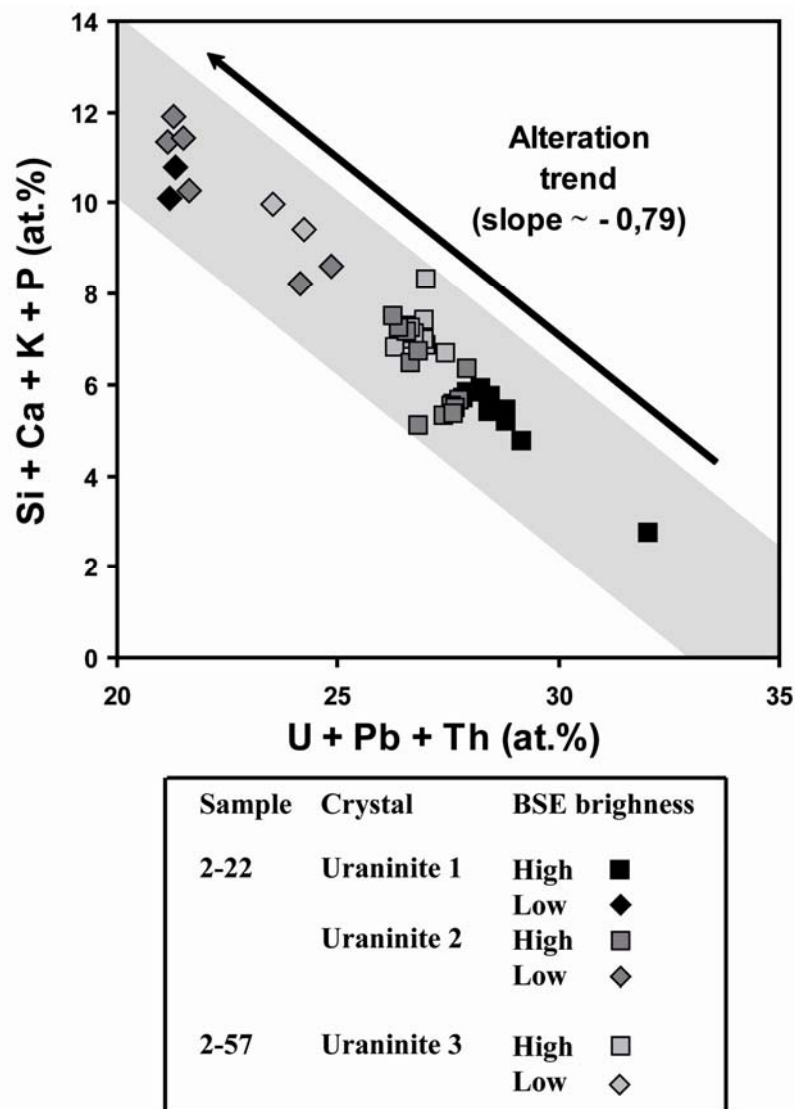


Figure 2.3.4. Binary diagrams illustrating the various chemical compositions of the different BSE brightness parts in the less altered uraninite crystals from samples 2-22 and 2-57 versus the Pb/U ratios and correspondent calculation of U-Pb-Th chemical ages.

Therefore the low lead values of these samples indicate a strong lead loss. The correlative diagrams of the major element variations with Pb/U ratio and the calculated chemical age isochrones (Fig. 2.3.4) show the progressive leaching of U and Pb outside the uraninite crystal with the decreasing of BSE brightness and their replacement by Ca, Si, K and P. The best correlation is with the Ca cation which shows the more significant exchange reaction with a trend clearly inversely proportional to the Pb/U ratio.

The cumulated element variation diagram (Fig. 2.3.5) shows a well linear negative correlation with a slope ( $\sim -0.79$ ) lower than  $-1$  indicating that the loss of radioelements (U+Pb+Th) in uraninite is not completely compensated by the gain in lighter elements. The difference probably corresponds to hydration of the mineral considering the decrease of EMP analytical totals concordant with the decreasing average atomic number and the U and Pb loss.



**Figure 2.3.5.** Variations of U + Pb contents relatively to Si + Ca + K + P (in atom percent) in the brighter and darker grey zones of the uraninite crystals in BSE images. The shaded square and the arrow represent the alteration trend showing the substitution of U and Pb mainly by Si, Ca, K and P during alteration.

**Secondary U-bearing phases**

A second stage of uranium bearing phases has been noticed in BSE mode nearby the primary uraninite grains and their compositions are presented in Table 2.3.3. An uraniferous material characterized by a lower average atomic number in BSE imagery than the primary uraninite occurs as few micrometer thick ribbons with a colloform texture deposited on the walls of the micro-porosity of the sample 2-22 (Fig. 2.3.6-A). Its U and Si contents are highly variable with respectively  $62.88 \pm 15.09$  wt%  $\text{UO}_2$ ,  $8.70 \pm 7.39$  wt%  $\text{SiO}_2$  in average for two spots analysed and separated by few microns. It contains also  $\text{Al}_2\text{O}_3$  ( $4.16 \pm 1.69$  wt%),  $\text{CaO}$  ( $3.85 \pm 0.66$  wt%),  $\text{P}_2\text{O}_5$  ( $3.86 \pm 2.17$  wt%) and minor amounts of  $\text{FeO}$  ( $1.32 \pm 0.43$  wt%),  $\text{PbO}$  ( $0.77 \pm 0.10$  wt%),  $\text{MnO}$  ( $0.75 \pm 0.25$  wt%),  $\text{MgO}$  ( $0.28 \pm 0.06$  wt%) and  $\text{K}_2\text{O}$  ( $0.55 \pm 0.02$  wt%). Na, Y and S contents are close to the detection limits and Th, Ti, V, Zr, Mo and REE remain undetected. Its low EMP analytical totals ( $88.79 \pm 2.40$  wt%) suggests that it is a re-crystallised and hydrated U-Si rich phase. This composition remains not conform to the ideal stoichiometry of the common uraninite alteration products as coffinite, uranophane, becquerelite, etc (Finch and Ewing, 1992). It probably represents a mixture of secondary uraninite and other uranyl minerals of variable composition. Its very low average Pb/U ratio (0.015) corresponds to young chemical ages, 72 and 120 Ma.

**Table 2.3.3.** Average chemical compositions of secondary U-bearing phases occurring in the vicinity of the primary uraninite (CAMECA SX100 electron microprobe analysis in wt%)

Phase	Secondary U-Si phase	Secondary Th-P-Si phase
Sample	2-22	2-22
EMPA	(2)	(2)
$\text{UO}_2$	$62.88 \pm 15.09$	$1.09 \pm 0.19$
$\text{PbO}$	$0.77 \pm 0.10$	$0.33 \pm 0.05$
$\text{ThO}_2$	<D.L.	$60.67 \pm 2.39$
$\text{MnO}$	$0.75 \pm 0.25$	$0.81 \pm 0.24$
$\text{Al}_2\text{O}_3$	$4.16 \pm 1.69$	$0.27 \pm 0.27$
$\text{SiO}_2$	$8.70 \pm 7.39$	$10.45 \pm 0.44$
$\text{K}_2\text{O}$	$0.55 \pm 0.02$	<D.L.
$\text{CaO}$	$3.85 \pm 0.66$	$6.19 \pm 0.17$
$\text{Na}_2\text{O}$	$0.21 \pm 0.12$	<D.L.
$\text{P}_2\text{O}_5$	$3.86 \pm 2.17$	$11.23 \pm 0.39$
$\text{FeO}$	$1.32 \pm 0.43$	$1.25 \pm 1.42$
$\text{MgO}$	$0.28 \pm 0.06$	$0.08 \pm 0.07$
$\text{TiO}_2$	<D.L.	<D.L.
$\text{V}_2\text{O}_5$	<D.L.	<D.L.
$\text{ZrO}_2$	<D.L.	<D.L.
$\text{MoO}_3$	<D.L.	<D.L.
$\text{SO}_2$	$0.17 \pm 0.07$	$0.23 \pm 0.06$
$\text{Y}_2\text{O}_3$	$0.66 \pm 0.81$	$2.01 \pm 0.06$
$\text{La}_2\text{O}_3$	<D.L.	<D.L.
$\text{Ce}_2\text{O}_3$	<D.L.	<D.L.
$\text{Nd}_2\text{O}_3$	<D.L.	<D.L.
$\text{Dy}_2\text{O}_3$	<D.L.	<D.L.
<b>Total</b>	<b><math>88.79 \pm 2.40</math></b>	<b><math>95.43 \pm 2.07</math></b>

**Abbreviations:** <D.L. = below Detection Limit (see Table 2 for D.L. values relative to each element).

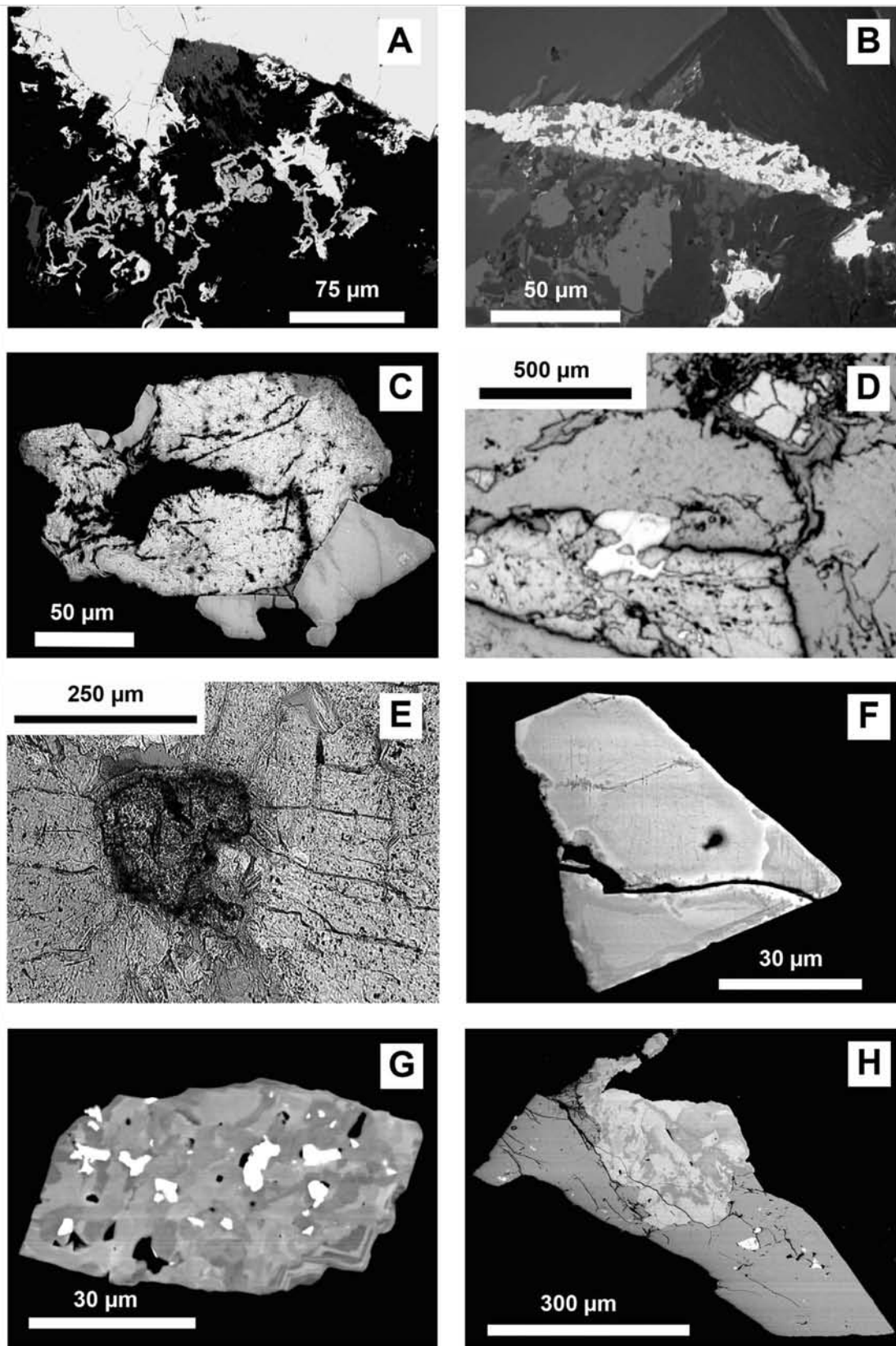


**Figure 2.3.6.** Optical microscopic and SEM images of the accessory minerals associated to the paragenesis of uraninite crystals in the Tanco pegmatite. **(A)** BSE image of colloform U-Si phase (grey strings to the right half of the picture) surrounding a uraninite grain (brighter zones to the left) in sample 2-22. The ribbons seem to line cavities and fractures in the rock. **(B)** BSE image of secondary Th-rich phosphor-silicate filling a fracture (elongated bright phase in centre) and small galena crystals (bright at the bottom right) in muscovite and plagioclase (darker greys at the half left and right respectively) in sample 2-22. **(C)** BSE image of euhedral uranmicrolite grains (grey crystals at the bottom left and up right) intergrown with an altered uraninite crystal (centre) in sample LP-16. **(D)** Uraninite in reflected light (light grey crystal up right) fracturing quartz in the vicinity of a euhedral cassiterite (at the bottom left) interfingered with a columbite-tantalite (highest reflectance) in sample 2-22. **(E)** Uranmicrolite crystal in transmitted light inducing radiation damage within plagioclase in sample LP-16. **(F)** BSE image of an isolated uranmicrolite showing digressive brightness at the edge of the mineral in sample LP-16. **(G)** Columbite-tantalite in BSE mode showing complex internal zoning relevant of Ta-Nb and Fe-Mn substitutions in sample 2-57. **(H)** BSE image of columbite-tantalite with variable chemical composition within a euhedral cassiterite (homogeneous darker grey) in sample 2-85.

Secondary crystallization of galena (PbS) and Th-rich phospho-silicate phases within micro-cracks nearby the primary uraninite has also been noticed in samples 2-22 and 2-85 (Fig. **2.3.6-B**). The Th-P-Si phase is composed mainly of ThO<sub>2</sub> ( $60.67 \pm 2.39$  wt%), SiO<sub>2</sub> ( $10.45 \pm 0.44$  wt%), P<sub>2</sub>O<sub>5</sub> ( $11.23 \pm 0.39$  wt%), CaO ( $6.19 \pm 0.17$  wt%) and lesser amounts of UO<sub>2</sub> ( $1.09 \pm 0.19$  wt%), PbO ( $0.33 \pm 0.05$  wt%), Y<sub>2</sub>O<sub>3</sub> ( $2.01 \pm 0.06$  wt%) and MnO ( $0.81 \pm 0.24$  wt%). Low concentrations of Al, Fe, Mg and S are occasionally detected but the other elements K, Na, REE, Mo, Ti, Zr and V are still under detection limits. The average Pb/U ratio of this phase is 0.37 and corresponds to chemical ages of 114 and 132 Ma for the two analysed spots.

### *Nb-Ta minerals*

Euhedral uranmicrolite crystals have been observed as isolated grains or in close paragenetic association with primary uraninite crystals in sample LP-16. As uraninite grains, uranmicrolite crystals are optically easily recognizable by radiation damage features as fractures or surrounding degradation halo occurring in neighbor minerals (Fig. **2.3.6-E**). The uranmicrolite can be intimately intergrown with the primary uraninite (Fig. **2.3.6-C**) suggesting that these two U-bearing phases are crystallizing at nearly the same time. The uranmicrolite grains are relatively well preserved compare to the altered primary uraninite that presents internal dissolution features and they often display sharp contacts with it.

The EMPA results, 86 analysis summarised in Table **2.3.4**, show that uranmicrolite is mostly composed of tantalum, averaging  $67.13 \pm 2.35$  wt% Ta<sub>2</sub>O<sub>5</sub> with a constant Ta/(Nb+Ta) ratio at 0.94, calcium, with  $7.43 \pm 1.80$  wt% CaO in average, and uranium concentrations varying from 6.94 to 9.29 wt% UO<sub>2</sub> and  $8.15 \pm 0.43$  wt% in average. It also contains minor amounts of sodium ( $2.39 \pm 1.45$  wt% Na<sub>2</sub>O), niobium ( $2.63 \pm 0.57$  wt% Nb<sub>2</sub>O<sub>5</sub>), lead ( $2.57 \pm 1.19$  wt% PbO), antimony ( $2.23 \pm 1.70$  wt% Sb<sub>2</sub>O<sub>3</sub>), and fluorine ( $1.94 \pm 0.54$  wt% F and  $0.82 \pm 0.23$  wt% O=F). The other elements, Fe, Mn, Ti, Sn and W, have contents below 1 wt% or are always under detection limits (Th, Mg, Bi, Sc, Y and Zr).

**Table 2.3.4.** Average chemical compositions of uranmicrolite (CAMECA SX100 electron microprobe analysis in wt%)

<i>Crystal</i> EMPA	<i>LP16 #1</i> (9)	<i>LP16 #2</i> (21)	<i>LP16 #3</i> (12)	<i>LP16 #4</i> (6)	<i>LP16 #5</i> (14)	<i>LP16 #6</i> (5)	<i>LP16 #7</i> (4)	<i>LP16 #8</i> (15)	<i>Average</i> (86)
Na <sub>2</sub> O	0.47 ± 0.20	2.67 ± 1.10	0.72 ± 0.17	1.66 ± 1.14	4.18 ± 0.35	3.74 ± 0.30	3.62 ± 0.38	2.35 ± 1.01	2.39 ± 1.45
CaO	7.97 ± 1.82	8.50 ± 2.58	7.23 ± 1.07	6.69 ± 1.29	7.48 ± 0.55	8.12 ± 0.31	7.55 ± 0.80	5.73 ± 1.00	7.43 ± 1.80
FeO	0.62 ± 0.63	0.39 ± 0.46	0.31 ± 0.53	0.32 ± 0.30	<D.L.	<D.L.	<D.L.	<D.L.	0.25 ± 0.41
MnO	0.36 ± 0.20	0.44 ± 0.16	<D.L.	0.43 ± 0.21	0.44 ± 0.11	0.33 ± 0.11	0.42 ± 0.18	0.44 ± 0.09	0.39 ± 0.17
TiO <sub>2</sub>	0.14 ± 0.10	0.11 ± 0.04	<D.L.	0.16 ± 0.03	0.11 ± 0.03	0.17 ± 0.05	0.50 ± 0.04	0.17 ± 0.05	0.14 ± 0.10
Nb <sub>2</sub> O <sub>5</sub>	2.26 ± 0.48	2.36 ± 0.44	2.25 ± 0.31	2.36 ± 0.37	2.82 ± 0.34	2.82 ± 0.30	2.33 ± 0.30	3.49 ± 0.29	2.63 ± 0.57
Ta <sub>2</sub> O <sub>5</sub>	66.82 ± 2.15	65.71 ± 2.09	68.10 ± 2.54	70.05 ± 1.04	66.71 ± 0.69	64.12 ± 0.84	65.25 ± 0.86	69.23 ± 1.35	67.13 ± 2.35
SnO <sub>2</sub>	0.54 ± 0.23	1.03 ± 0.69	1.18 ± 0.49	1.13 ± 0.45	0.87 ± 0.15	0.70 ± 0.21	1.49 ± 0.91	0.87 ± 0.32	0.95 ± 0.51
WO <sub>3</sub>	0.56 ± 0.27	0.69 ± 0.17	0.69 ± 0.17	0.68 ± 0.17	0.59 ± 0.19	0.63 ± 0.24	0.71 ± 0.19	0.73 ± 0.15	0.67 ± 0.19
PbO	1.41 ± 0.37	1.82 ± 0.40	2.29 ± 0.65	2.11 ± 0.35	2.91 ± 0.49	1.58 ± 0.28	4.08 ± 1.62	4.36 ± 0.83	2.57 ± 1.19
UO <sub>2</sub>	8.03 ± 0.56	8.35 ± 0.41	8.17 ± 0.30	7.39 ± 0.20	8.52 ± 0.19	8.07 ± 0.16	7.84 ± 0.36	8.02 ± 0.27	8.15 ± 0.43
Sb <sub>2</sub> O <sub>3</sub>	4.88 ± 1.27	2.95 ± 0.90	2.52 ± 1.23	1.13 ± 0.99	1.41 ± 0.33	4.27 ± 0.45	1.80 ± 1.52	0.03 ± 0.06	2.23 ± 1.70
F	1.76 ± 0.57	1.86 ± 0.73	2.25 ± 0.59	1.96 ± 0.36	2.20 ± 0.14	2.10 ± 0.15	1.93 ± 0.47	1.61 ± 0.36	1.94 ± 0.54
O=F	0.74 ± 0.24	0.78 ± 0.31	0.95 ± 0.25	0.82 ± 0.15	0.92 ± 0.06	0.88 ± 0.06	0.81 ± 0.20	0.68 ± 0.15	0.82 ± 0.23
<i>Total</i>	95.28 ± 1.00	96.23 ± 1.99	95.11 ± 0.65	95.35 ± 1.29	97.46 ± 0.82	96.07 ± 0.68	96.86 ± 1.01	96.57 ± 0.83	96.19 ± 1.44

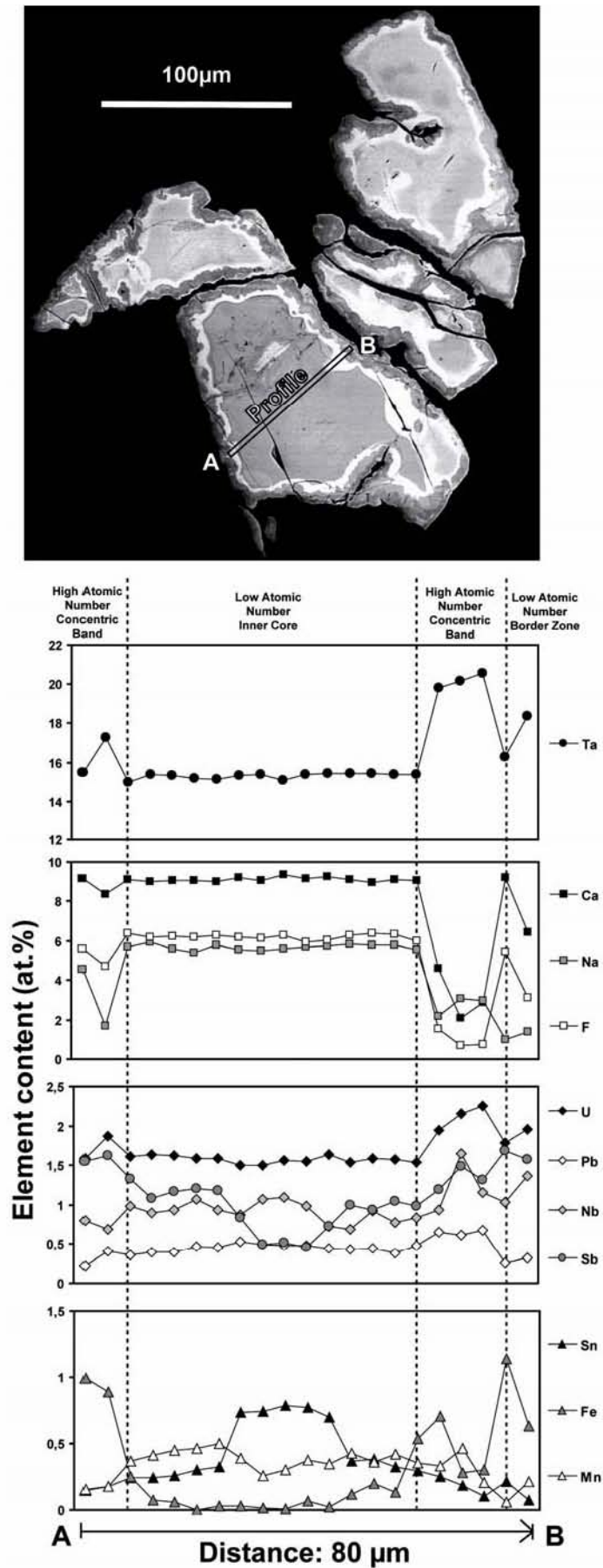
  

Structural Formula calculated with 6 oxygen atoms									
Na	0.08 ± 0.04	0.46 ± 0.18	0.13 ± 0.03	0.29 ± 0.19	0.72 ± 0.06	0.64 ± 0.05	0.63 ± 0.06	0.41 ± 0.17	0.41 ± 0.25
Ca	0.77 ± 0.17	0.80 ± 0.23	0.71 ± 0.10	0.65 ± 0.12	0.71 ± 0.05	0.77 ± 0.03	0.72 ± 0.07	0.56 ± 0.09	0.71 ± 0.16
Fe	0.05 ± 0.05	0.03 ± 0.03	0.02 ± 0.04	0.02 ± 0.02	0.00 ± 0.00	0.01 ± 0.01	0.00 ± 0.00	0.00 ± 0.00	0.02 ± 0.03
Mn	0.03 ± 0.01	0.03 ± 0.01	0.01 ± 0.00	0.03 ± 0.02	0.03 ± 0.01	0.02 ± 0.01	0.03 ± 0.01	0.03 ± 0.01	0.03 ± 0.01
Pb	0.03 ± 0.01	0.04 ± 0.01	0.06 ± 0.02	0.05 ± 0.01	0.07 ± 0.01	0.04 ± 0.01	0.10 ± 0.04	0.11 ± 0.02	0.06 ± 0.03
U	0.16 ± 0.01	0.17 ± 0.01	0.17 ± 0.01	0.15 ± 0.01	0.17 ± 0.00	0.16 ± 0.00	0.16 ± 0.01	0.16 ± 0.01	0.16 ± 0.01
Sb	0.18 ± 0.05	0.11 ± 0.03	0.10 ± 0.05	0.04 ± 0.04	0.05 ± 0.01	0.16 ± 0.02	0.07 ± 0.06	0.00 ± 0.00	0.08 ± 0.06
$\Sigma$ Cations in A site	1.32 ± 0.15	1.65 ± 0.34	1.20 ± 0.16	1.24 ± 0.26	1.75 ± 0.04	1.81 ± 0.04	1.71 ± 0.07	1.28 ± 0.21	1.49 ± 0.31
Ti	0.01 ± 0.01	0.01 ± 0.00	0.01 ± 0.01	0.01 ± 0.00	0.01 ± 0.00	0.01 ± 0.00	0.03 ± 0.00	0.01 ± 0.00	0.01 ± 0.01
Nb	0.09 ± 0.02	0.10 ± 0.02	0.09 ± 0.01	0.10 ± 0.02	0.11 ± 0.01	0.11 ± 0.01	0.09 ± 0.01	0.14 ± 0.01	0.11 ± 0.02
Ta	1.65 ± 0.06	1.59 ± 0.10	1.71 ± 0.07	1.73 ± 0.06	1.60 ± 0.02	1.55 ± 0.02	1.58 ± 0.01	1.71 ± 0.06	1.64 ± 0.09
Sn	0.02 ± 0.01	0.04 ± 0.02	0.04 ± 0.02	0.04 ± 0.02	0.03 ± 0.01	0.02 ± 0.01	0.05 ± 0.03	0.03 ± 0.01	0.03 ± 0.02
W	0.01 ± 0.01	0.02 ± 0.00	0.02 ± 0.00	0.02 ± 0.00	0.01 ± 0.00	0.01 ± 0.01	0.02 ± 0.00	0.02 ± 0.00	0.02 ± 0.00
$\Sigma$ Cations in B site	1.79 ± 0.06	1.75 ± 0.10	1.86 ± 0.07	1.90 ± 0.07	1.77 ± 0.01	1.71 ± 0.02	1.78 ± 0.03	1.91 ± 0.05	1.81 ± 0.09
$\Sigma$ Cations	3.11 ± 0.09	3.40 ± 0.24	3.07 ± 0.09	3.14 ± 0.19	3.52 ± 0.04	3.52 ± 0.03	3.49 ± 0.05	3.19 ± 0.16	3.30 ± 0.23
F	0.50 ± 0.16	0.52 ± 0.20	0.66 ± 0.17	0.56 ± 0.11	0.61 ± 0.04	0.59 ± 0.04	0.54 ± 0.13	0.46 ± 0.10	0.55 ± 0.15
Mn/(Mn+Fe)	0.46 ± 0.27	0.64 ± 0.31	0.55 ± 0.28	0.66 ± 0.26	0.95 ± 0.07	0.77 ± 0.24	0.86 ± 0.13	0.90 ± 0.08	0.72 ± 0.28
Ta/(Ta+Nb)	0.95 ± 0.01	0.94 ± 0.01	0.95 ± 0.01	0.95 ± 0.01	0.93 ± 0.01	0.93 ± 0.01	0.94 ± 0.01	0.92 ± 0.01	0.94 ± 0.01

*Notes:* Th, Mg, Bi, Sc, Y and Zr contents are note given because they are always below detection limits. *Abbreviations:* <D.L. = below Detection Limit (Na = 0.09 wt%, Ca = 0.12 wt%, Fe = 0.15 wt%, Mn = 0.15 wt%, Ti = 0.07 wt%, Nb = 0.49 wt%, Ta = 0.30 wt%, Sn = 0.16 wt%, W = 0.39 wt%, Pb = 0.18 wt%, U = 0.18 wt%, Sb = 0.23 wt%, F = 0.10 wt%, Th = 0.27 wt%, Mg = 0.06 wt%, Bi = 0.53 wt%, Sc = 0.07 wt%, Y = 0.31 wt%, Zr = 0.31 wt%).

Some uranmicrolite crystals show however a complex internal zoning in BSE images. A decrease of brightness is commonly observed along fractures and at the rim of crystals (Fig. **2.3.6-C** and **-F**) suggesting that uranmicrolite have also been submitted to a chemical disorder revealed by a decrease in the average atomic number at the surface exposure.

This alteration texture is even more pronounced in some grains that show an internal banding texture of different grey intensities following with a bowl-shape frame the border of broken crystal fragments (Fig. **2.3.7**). The compositional profile consisting of 21 EMPA realised through this grain shows that banding in uranmicrolite is related to variations in relative abundances of the major elements, Ta, Ca, Na and F mostly, but also in some minor elements. The core of the grain is relatively homogeneous except for the Sb content that seems to increase progressively toward the edge of the crystal whereas Sn decrease, but these two element variations are rather independent from the BSE banding. The brighter bands are relevant to higher Ta, U, Pb, Sb and Fe contents and a decrease in Ca, Na, F and Mn contents. The darker grey band at the edge of the grain is depleted in Ca, Na and F compare to the core. These changes are associated to a decrease of the A-site occupancy with 1.84 cations per formula unit in average in the inner core to 1.24 and 1.32 respectively in the brighter and the darker bands. The chemical variations are accompanied either by a progressive decrease in analytical totals of EMPA, from 97.24 wt% in average in the inner core, to 94.96 wt% in the brighter band and finally 92.35 wt% in the darker border zone. This probably reflects the progressive incorporation of H<sub>2</sub>O in the crystal structure. The Ta/(Ta+Nb) ratio is relatively constant circa 0.94 but the Mn/(Mn+Fe) ratio vary from the maximal value of 1 (0.82 in average) in the core, to 0.33 in average in the brighter band, and finally a minimum of 0.05 at the edge of the grain. This is relevant of the incorporation of Fe in the crystal structure substitute to the Mn element in the border zone. This texture is clearly associated with an alteration front process. It seems that some corrosive fluid penetrates in fragments and concentrates Ta, U, Pb and Sb elements by diffusion to the centre of minerals providing an enriched brighter concentric band, and leaving a darker grey border leached in Ca, Na and F whereas some Fe is incorporated.



**Figure 2.3.7.** BSE image of a broken uranmicrolite crystal showing a complex internal zoning (sample LP-16) and plots of the EMP analysis results across the chemical profile drawn in the picture showing variations in major and trace elements (in atom percent).

In the three other samples (2-22, 2-57 and 2-85), no uranmicrolite has been observed but primary uraninite is generally located in the vicinity of two other Nb-Ta phases, columbite-tantalite and wodginite. Columbite-tantalite group minerals are the most abundant Nb-Ta phase and occur as intergrowth, overgrowth, or small disseminated inclusions in coarse euhedral cassiterite grains (Fig. 2.3.6-D and -H), as well as isolated prismatic crystals (Fig. 2.3.6-G). Rare wodginite has been observed as few micron wide irregular phases in columbite-tantalite minerals associated with cassiterite. This mineral association often exhibits complex internal patterns of different brightness in BSE images but no reaction corona has been observed at the edge of the grains as for uranmicrolite. The most common internal pattern of columbite-tantalite corresponds to irregular darker grey zones, associated to a decrease in Mn and Ta contents whereas Fe and Nb increase. The average composition of columbite-tantalite (214 EMP analyses in Table 2.3.5) is dominated by tantalum ( $48.54 \pm 3.04$  wt%  $Ta_2O_5$ ), niobium ( $27.09 \pm 2.76$  wt%  $Nb_2O_5$ ) and manganese ( $12.59 \pm 1.67$  wt%  $MnO$ ) with some minor amounts of Ti ( $2.90 \pm 0.74$  wt%  $TiO_2$ ), Fe (total as  $Fe^{2+}$  averaging  $2.87 \pm 1.43$  wt%  $FeO$ ), Sn ( $1.17 \pm 0.96$  wt%  $SnO_2$ ) and Sc ( $0.52 \pm 0.11$  wt%  $Sc_2O_3$ ). All the other elements analysed are under detection limits. Results from each sample are reported in the four-pole quadrilateral diagram representing the end-member species in Figure 2.3.8. The columbite-tantalite group minerals observed in the four lower Tanco pegmatite samples show Mn/(Mn+Fe) ratio ranging between 0.65 and 0.98 and Ta/(Ta+Nb) ratio ranging between 0.40 and 0.69 that correspond to the Mn-rich end-members, circa the limit between the fields of mangano-columbite and mangano-tantalite. Indeed, it is well established that columbite-tantalite evolves by fractional crystallization and that composition variations are due to Mn-Fe and Ta-Nb substitutions (Černý et al., 1986).

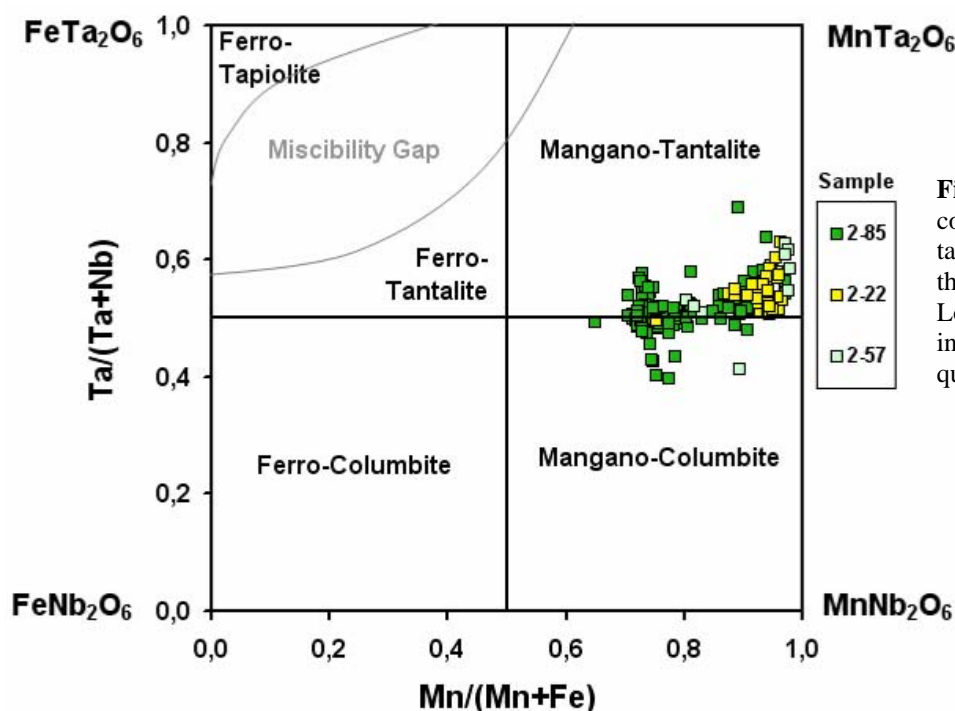


**Figure 2.3.8.** Chemical compositions of columbite-tantalite minerals from the three samples of the Tanco Lower Pegmatite represented in the typical end-member quadrilateral.

**Table 2.3.5.** Average chemical compositions of columbite-tantalite group minerals (CAMECA SX100 electron microprobe analysis in wt%)

<i>Sample</i>	2-22	2-57	2-85	<i>Average</i>
EMPA	(48)	(9)	(157)	(214)
Na <sub>2</sub> O	<D.L.	<D.L.	<D.L.	<D.L.
CaO	<D.L.	<D.L.	<D.L.	<D.L.
FeO	1.07 ± 0.55	1.42 ± 1.25	3.50 ± 1.05	2.87 ± 1.43
MnO	14.62 ± 0.64	14.52 ± 1.18	11.87 ± 1.26	12.59 ± 1.67
MgO	<D.L.	<D.L.	<D.L.	<D.L.
TiO <sub>2</sub>	2.25 ± 0.29	1.81 ± 0.47	3.16 ± 0.67	2.90 ± 0.74
Nb <sub>2</sub> O <sub>5</sub>	25.46 ± 1.87	26.23 ± 4.91	27.63 ± 2.64	27.09 ± 2.76
Ta <sub>2</sub> O <sub>5</sub>	50.27 ± 1.93	53.10 ± 5.18	47.75 ± 2.71	48.54 ± 3.04
SnO <sub>2</sub>	0.62 ± 0.10	0.49 ± 0.18	1.38 ± 1.05	1.17 ± 0.96
PbO	0.22 ± 0.09	0.21 ± 0.07	0.24 ± 0.16	0.23 ± 0.15
ThO <sub>2</sub>	<D.L.	<D.L.	<D.L.	<D.L.
UO <sub>2</sub>	<D.L.	<D.L.	<D.L.	<D.L.
Sb <sub>2</sub> O <sub>3</sub>	<D.L.	<D.L.	<D.L.	<D.L.
Bi <sub>2</sub> O <sub>3</sub>	<D.L.	<D.L.	<D.L.	<D.L.
Sc <sub>2</sub> O <sub>3</sub>	0.58 ± 0.13	0.45 ± 0.15	0.50 ± 0.09	0.52 ± 0.11
Y <sub>2</sub> O <sub>3</sub>	<D.L.	<D.L.	<D.L.	<D.L.
ZrO <sub>2</sub>	<D.L.	<D.L.	<D.L.	<D.L.
F	<D.L.	<D.L.	<D.L.	<D.L.
<i>Total</i>	95.52 ± 0.77	98.56 ± 0.86	96.62 ± 3.05	96.46 ± 2.71
<i>Structural Formula calculated with 6 oxygen atoms</i>				
Fe	0.07 ± 0.03	0.08 ± 0.07	0.21 ± 0.06	0.07 ± 0.03
Mn	0.91 ± 0.04	0.89 ± 0.08	0.72 ± 0.07	0.91 ± 0.04
<i>Σ Cations in A site</i>	0.98 ± 0.02	0.97 ± 0.01	0.93 ± 0.04	0.98 ± 0.02
Ti	0.13 ± 0.02	0.10 ± 0.03	0.17 ± 0.04	0.13 ± 0.02
Nb	0.85 ± 0.05	0.85 ± 0.13	0.89 ± 0.07	0.85 ± 0.05
Ta	1.01 ± 0.05	1.04 ± 0.13	0.93 ± 0.05	1.01 ± 0.05
Sn	0.02 ± 0.00	0.01 ± 0.01	0.04 ± 0.03	0.02 ± 0.00
Sc	0.04 ± 0.01	0.03 ± 0.01	0.03 ± 0.01	0.04 ± 0.01
<i>Σ Cations in B site</i>	2.04 ± 0.01	2.04 ± 0.01	2.07 ± 0.02	2.04 ± 0.01
<i>Σ Cations</i>	3.02 ± 0.01	3.01 ± 0.01	3.00 ± 0.03	3.02 ± 0.01
Mn/(Mn+Fe)	0.93 ± 0.03	0.91 ± 0.08	0.77 ± 0.07	0.93 ± 0.03
Ta/(Ta+Nb)	0.54 ± 0.03	0.55 ± 0.07	0.51 ± 0.03	0.54 ± 0.03

**Abbreviations:** <D.L. = below Detection Limit (Na = 0.09 wt%, Ca = 0.10 wt%, Fe = 0.15 wt%, Mn = 0.15 wt%, Ti = 0.06 wt%, Mg = 0.06 wt%, Nb = 0.51 wt%, Ta = 0.25 wt%, Sn = 0.16 wt%, Pb = 0.18 wt%, U = 0.18 wt%, Sb = 0.22 wt%, F = 0.12 wt%, Th = 0.41 wt%, Mg = 0.06 wt%, Bi = 0.55 wt%, Sc = 0.06 wt%, Y = 0.25 wt%, Zr = 0.30 wt%).

The wodginite group minerals (14 analyses in Table 2.3.6) is mainly composed of tantalum ( $61.95 \pm 1.79$  wt% Ta<sub>2</sub>O<sub>5</sub>), tin ( $10.77 \pm 1.22$  wt% SnO<sub>2</sub>), manganese ( $9.03 \pm 2.60$  wt% MnO), niobium ( $6.78 \pm 0.85$  wt% Nb<sub>2</sub>O<sub>5</sub>) and titan ( $4.63 \pm 0.71$  wt% TiO<sub>2</sub>), a variable iron content ( $2.17 \pm 2.53$  wt% Fe<sub>2</sub>O and  $0.60 \pm 0.28$  wt% Fe<sub>2</sub>O<sub>3</sub>) and a minor amount of Sc ( $0.46 \pm 0.12$  wt% Sc<sub>2</sub>O<sub>3</sub>).

**Table 2.3.6.** Average chemical compositions of wodginite group minerals (CAMECA SX100 electron microprobe analysis in wt%)

Sample	2-22	2-57	Average
EMPA	(5)	(9)	(14)
Li <sub>2</sub> O	0.01 ± 0.01	0.03 ± 0.03	0.02 ± 0.03
FeO	1.53 ± 0.72	2.52 ± 3.12	2.17 ± 2.53
MnO	9.90 ± 0.66	8.55 ± 3.16	9.03 ± 2.60
Fe <sub>2</sub> O <sub>3</sub>	0.43 ± 0.29	0.70 ± 0.23	0.60 ± 0.28
TiO <sub>2</sub>	5.18 ± 0.61	4.33 ± 0.59	4.63 ± 0.71
Nb <sub>2</sub> O <sub>5</sub>	7.16 ± 0.83	6.56 ± 0.82	6.78 ± 0.85
Ta <sub>2</sub> O <sub>5</sub>	61.24 ± 1.40	62.35 ± 1.93	61.95 ± 1.79
SnO <sub>2</sub>	10.69 ± 0.80	10.82 ± 1.45	10.77 ± 1.22
PbO	<D.L.	<D.L.	<D.L.
ThO <sub>2</sub>	<D.L.	<D.L.	<D.L.
UO <sub>2</sub>	<D.L.	<D.L.	<D.L.
Sc <sub>2</sub> O <sub>3</sub>	0.54 ± 0.11	0.42 ± 0.10	0.46 ± 0.12
Sb <sub>2</sub> O <sub>3</sub>	<D.L.	<D.L.	<D.L.
Bi <sub>2</sub> O <sub>3</sub>	<D.L.	<D.L.	<D.L.
<i>Total</i>	96.69 ± 0.38	96.34 ± 1.53	96.47 ± 1.23
Structural Formula calculated with 32 oxygen atoms			
Li	0.01 ± 0.01	0.05 ± 0.06	0.03 ± 0.05
Mn	3.49 ± 0.23	3.06 ± 1.12	3.21 ± 0.91
Fe <sup>2+</sup>	0.53 ± 0.25	0.90 ± 1.12	0.77 ± 0.91
<i>Σ Cations in A site</i>	4.03 ± 0.04	4.01 ± 0.02	4.01 ± 0.03
Fe <sup>3+</sup>	0.13 ± 0.09	0.22 ± 0.08	0.19 ± 0.09
Ti	1.62 ± 0.19	1.37 ± 0.16	1.46 ± 0.20
Sn	1.77 ± 0.13	1.82 ± 0.25	1.81 ± 0.21
Ta (B)	0.28 ± 0.10	0.42 ± 0.15	0.37 ± 0.15
Sc	0.19 ± 0.04	0.15 ± 0.04	0.17 ± 0.04
<i>Σ Cations in B site</i>	4.00 ± 0.00	4.00 ± 0.00	4.00 ± 0.00
Nb	1.35 ± 0.15	1.25 ± 0.14	1.29 ± 0.15
Ta (C)	6.65 ± 0.15	6.75 ± 0.14	6.71 ± 0.15
<i>Σ Cations in C site</i>	8.00 ± 0.00	8.00 ± 0.00	8.00 ± 0.00
<i>Σ Cations</i>	16.03 ± 0.04	16.00 ± 0.02	16.01 ± 0.03
Mn/(Mn+Fe)	0.84 ± 0.06	0.73 ± 0.27	0.77 ± 0.22
Ta/(Ta+Nb)	0.84 ± 0.02	0.85 ± 0.02	0.85 ± 0.02

*Notes:* Li<sub>2</sub>O and Fe<sub>2</sub>O<sub>3</sub> are calculated by the method of Ercit et al. (1992).

*Abbreviations:* <D.L. = below Detection Limit (Na = 0.09 wt%, Ca = 0.11 wt%, Fe = 0.15 wt%, Mn = 0.15 wt%, Ti = 0.07 wt%, Mg = 0.06 wt%, Nb = 0.51 wt%, Ta = 0.28 wt%, Sn = 0.17 wt%, Pb = 0.18 wt%, U = 0.25 wt%, Sb = 0.23 wt%, Th = 0.37 wt%, Mg = 0.06 wt%, Bi = 0.54 wt%, Sc = 0.06 wt%, Y = 0.28 wt%, Zr = 0.29 wt%).

Cassiterite always occurs with the Nb-Ta mineral association. It is present as dark brown elongated prisms in transmitted light, up to 1 mm long with a high relief (Fig. 2.3.6-D). No internal zoning of the cassiterite has been observed in the BSE images (Fig. 2.3.6-H). However, the EMPA (23 analyses summarized in Table 2.3.7) revealed a highly variable tantalum content ( $3.53 \pm 2.92$  wt% Ta<sub>2</sub>O<sub>5</sub> in average but values ranging from under detection limit to 13.18 wt% Ta<sub>2</sub>O<sub>5</sub>) balanced by the tin content ( $93.36 \pm 4.10$  wt% SnO<sub>2</sub>). The calcium content is low and stable ( $0.41 \pm 0.06$  wt% CaO) and sometime iron or magnesium traces are detected but all other elements analysed are under detection limits. Because of the Ta content in cassiterite and its close relation with Nb-Ta minerals interfingered, overgrowing or as disseminated inclusions, it is obvious that the system saturation in Ta during cassiterite crystallization evolved with time.

**Table 2.3.7.** Average chemical compositions of cassiterite (CAMECA SX100 electron microprobe analysis in wt%)

Sample	2-22	2-57	Average
EMPA	(9)	(14)	(23)
Na <sub>2</sub> O	<D.L.	<D.L.	<D.L.
CaO	$0.41 \pm 0.06$	$0.41 \pm 0.06$	$0.41 \pm 0.06$
FeO	<D.L.	$0.66 \pm 0.27$	$0.43 \pm 0.36$
MnO	<D.L.	<D.L.	<D.L.
MgO	$0.14 \pm 0.04$	<D.L.	<D.L.
TiO <sub>2</sub>	<D.L.	<D.L.	<D.L.
Nb <sub>2</sub> O <sub>5</sub>	<D.L.	<D.L.	<D.L.
Ta <sub>2</sub> O <sub>5</sub>	$1.26 \pm 0.34$	$5.00 \pm 2.92$	$3.53 \pm 2.92$
SnO <sub>2</sub>	$96.78 \pm 0.91$	$91.15 \pm 3.81$	$93.36 \pm 4.10$
PbO	<D.L.	<D.L.	<D.L.
ThO <sub>2</sub>	<D.L.	<D.L.	<D.L.
UO <sub>2</sub>	<D.L.	<D.L.	<D.L.
Sb <sub>2</sub> O <sub>3</sub>	<D.L.	<D.L.	<D.L.
Bi <sub>2</sub> O <sub>3</sub>	<D.L.	<D.L.	<D.L.
Sc <sub>2</sub> O <sub>3</sub>	<D.L.	<D.L.	<D.L.
Y <sub>2</sub> O <sub>3</sub>	<D.L.	<D.L.	<D.L.
ZrO <sub>2</sub>	<D.L.	<D.L.	<D.L.
<i>Total</i>	$98.90 \pm 0.98$	$98.27 \pm 1.31$	$98.52 \pm 1.21$

**Abbreviations:** <D.L. = below Detection Limit (Na = 0.11 wt%, Ca = 0.12 wt%, FeO = 0.15 wt%, MnO = 0.15 wt%, MgO = 0.08 wt%, Ti = 0.12 wt%, Nb = 0.40 wt%, Ta = 0.29 wt%, Sn = 0.21 wt%, Pb = 0.14 wt%, Th = 0.22 wt%, U = 0.53 wt%, Sb = 0.29 wt%, Bi = 0.45 wt%, Sc = 0.06 wt%, Y = 0.27 wt%, Zr = 0.24 wt%).

**Isotopic dating of uraninite**

**Pb-Pb ages**

The fifteen calculated  $^{207}\text{Pb}/^{206}\text{Pb}$  ages of the three best preserved single grains of uraninite from samples 2-22 and 2-57 spread from 620 to 1160 Ma (Table 2.3.8) providing a large spectrum of ages in the histogram representing the age repartition (Fig. 2.3.9). The two uraninite grains from sample 2-22 yielded mean ages of  $668 \pm 41$  Ma and  $899 \pm 76$  Ma. The analyses of the third crystal from sample 2-57 are more scattered (770 to 1160 Ma) and give a mean age of  $1037 \pm 190$  Ma with the oldest  $^{207}\text{Pb}/^{206}\text{Pb}$  age circa  $1159 \pm 7$  Ma. These results indicate that several episodes of lead diffusion happened through time since uraninite crystallisation. The relative probability curve of age repartition indicates three dominant  $^{207}\text{Pb}/^{206}\text{Pb}$  age groups circa 650 Ma, 900 Ma and 1150 Ma.

**Table 2.3.8.** Ion probe U-Pb results for three uraninite grains from the Tanco Lower Pegmatite

Sample Crystal Spot number	$\frac{^{204}\text{Pb}}{^{206}\text{Pb}}$	$\frac{^{207}\text{Pb}}{^{206}\text{Pb}}$	$\frac{^{208}\text{Pb}}{^{206}\text{Pb}}$	$\frac{^{207}\text{Pb}}{^{206}\text{Pb}}$ Age (Ma)	$\frac{^{206}\text{Pb}}{^{238}\text{U}}$ Age (Ma)
<i>Sample 222</i>					
Uraninite 1					
1-1	0.00005 (0)	0.0721 (42)	0.0176 (152)	$972 \pm 9$	$814 \pm 15$
1-2	0.00003 (0)	0.0689 (34)	0.0116 (109)	$884 \pm 7$	$665 \pm 10$
1-3	0.00004 (0)	0.0693 (42)	0.0160 (124)	$890 \pm 9$	$559 \pm 7$
1-4	0.00005 (0)	0.0683 (42)	0.0138 (107)	$855 \pm 9$	$622 \pm 9$
<i>Sample 222</i>					
Uraninite 2					
2-1	0.00003 (0)	0.0641 (29)	0.0161 (51)	$733 \pm 6$	$711 \pm 10$
2-2	0.00003 (0)	0.0611 (28)	0.0155 (56)	$629 \pm 6$	$698 \pm 9$
2-3	0.00002 (0)	0.0612 (29)	0.0153 (55)	$635 \pm 6$	$727 \pm 9$
2-4	0.00003 (0)	0.0623 (32)	0.0159 (54)	$673 \pm 7$	$712 \pm 12$
2-5	0.00003 (0)	0.0624 (28)	0.0173 (59)	$675 \pm 6$	$693 \pm 11$
2-6	0.00003 (0)	0.0620 (29)	0.0173 (62)	$658 \pm 8$	$620 \pm 9$
<i>Sample 257</i>					
Uraninite 3					
3-1	0.00001 (0)	0.0699 (28)	0.0152 (55)	$926 \pm 6$	$919 \pm 15$
3-2	0.00001 (0)	0.0650 (28)	0.0190 (47)	$774 \pm 6$	$837 \pm 12$
3-3	0.00012 (0.1)	0.0775 (25)	0.0226 (51)	$1\ 093 \pm 5$	$883 \pm 13$
3-4	0.00002 (0)	0.0777 (18)	0.0188 (51)	$1\ 136 \pm 4$	$921 \pm 12$
3-5	0.00001 (0)	0.0785 (38)	0.0154 (43)	$1\ 159 \pm 7$	$914 \pm 13$

*Notes:* numbers in brackets indicate errors ( $1\sigma \cdot 10^{-4}$ ),  $^{207}\text{Pb}/^{206}\text{Pb}$  ages are corrected for common Pb which is extremely low.

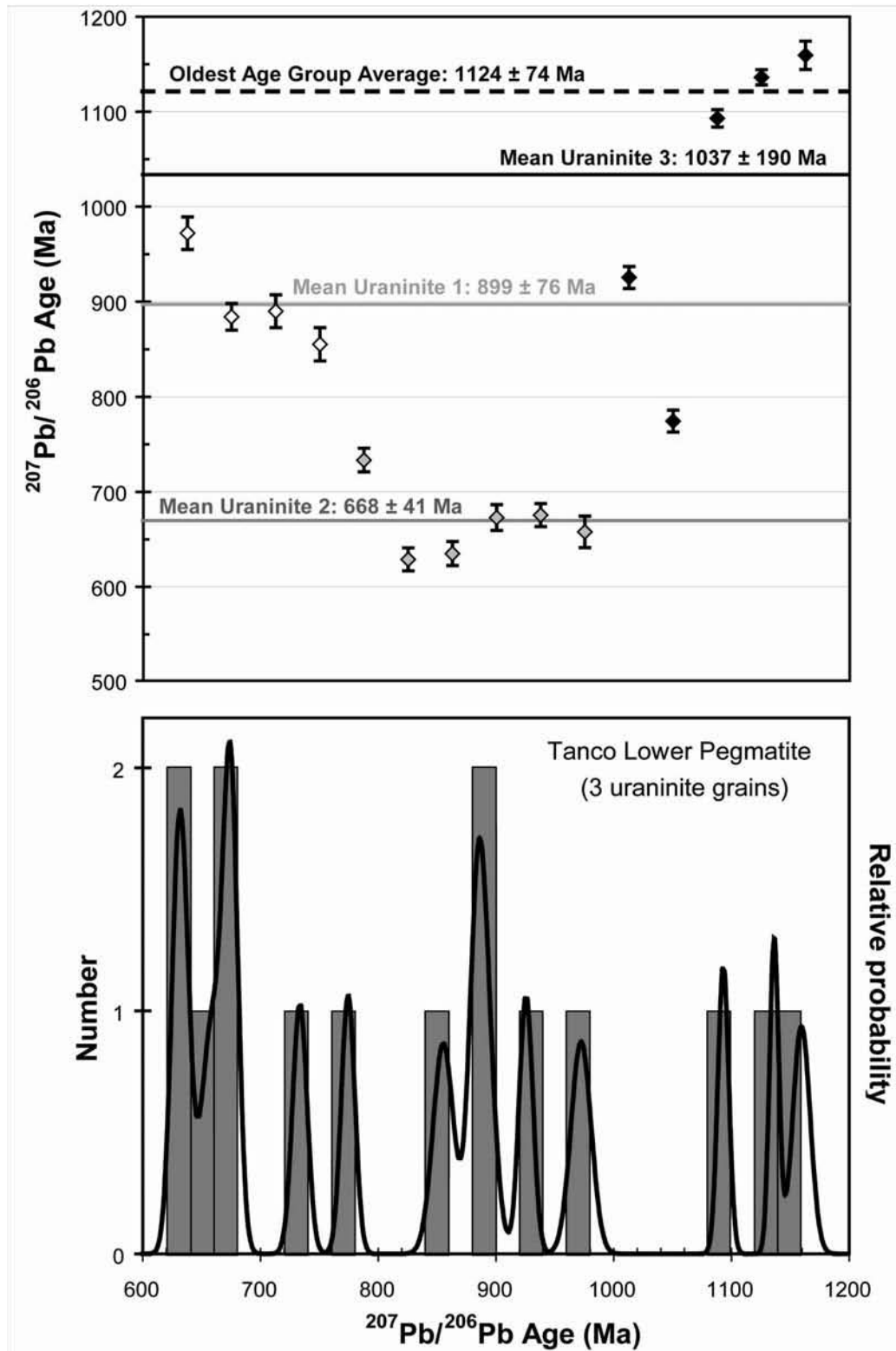


**Figure 2.3.9.** Distribution of  $^{207}\text{Pb}/^{206}\text{Pb}$  ages in three uraninite grains from the Tanco Lower Pegmatite: grain 1 (white symbols) and grain 2 (grey symbols) from sample 222 and grain 3 (black symbols) from sample 257. Error bars are  $2\sigma$  and calculated age average for each grain was also reported as straight lines. The histogram shows the combined relative probability plots with the  $^{207}\text{Pb}/^{206}\text{Pb}$  age distribution.

U-Pb ages

The isotopic U-Pb compositions of the Tanco uraninites (Table 2.3.8) have been plotted in a Concordia diagram (Fig. 10). All the data plot well below the Concordia curve thus indicating an important radiogenic lead loss since uraninite crystallization. Three of the better grouped U-Pb isotopic compositions of each analyzed uraninite grain tend to define distinct Discordia with the following upper intercepts  $729 \pm 40$ ,  $1195 \pm 75$  and  $1250 \pm 30$  Ma, and lower intercepts at  $76 \pm 13$ ,  $192 \pm 31$  and  $119 \pm 24$  Ma respectively. As the  $^{207}\text{Pb}/^{206}\text{Pb}$  ages, the U-Pb ages clearly reflect the resetting of uraninite isotopic composition by recent thermal or hydrothermal events with new formation of secondary uraniferous phases as the uranyl minerals and Th-rich phosphor-silicates observed. The wide range of isotopic compositions and the MSWD (mean square of weighted deviates) values greater than 1 (Fig. 2.3.10) are relevant of the difficulty to separate well preserved uraninite areas (high BSE brightness) and altered coffinitized areas (lower BSE brightness). Therefore, the apparent U-Pb ages found by the Concordia-Discordia method are not representative of distinct single events but more probably result of a mixing between heterogeneities of the crystals and record the opening of the isotopic system occurring later after pegmatite emplacement.

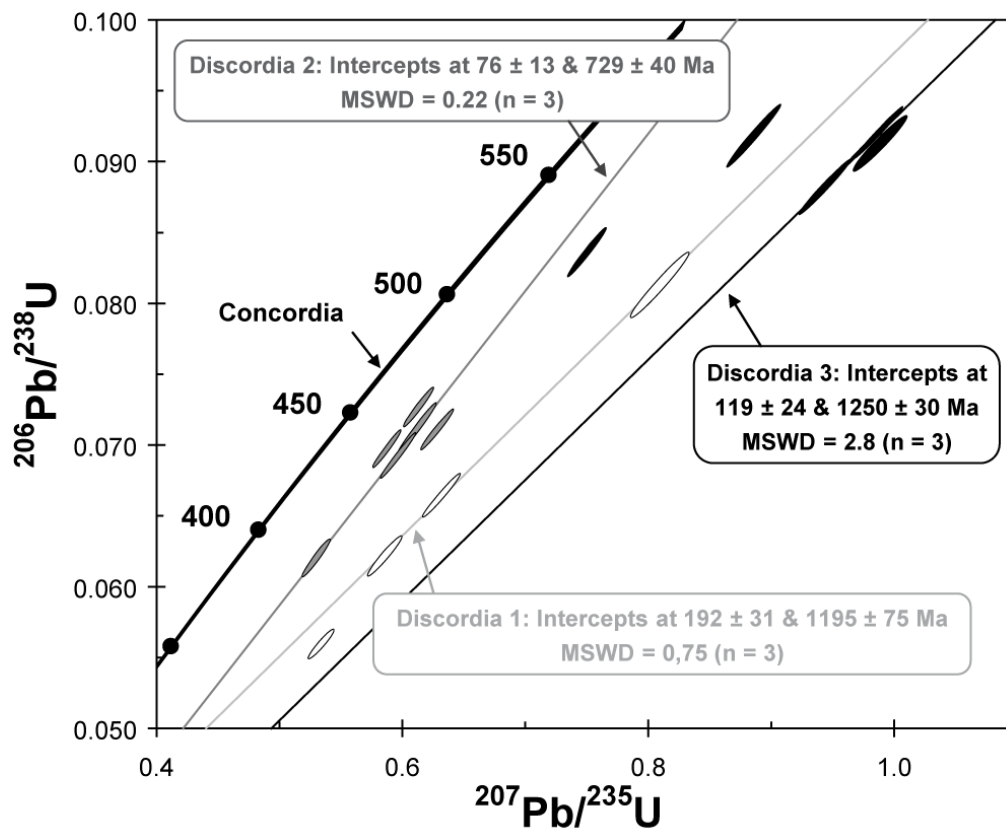


**Figure 2.3.10.** Concordia diagram with the U-Pb isotopic of three uraninite crystals from the Tanco Lower Pegmatite (Table 2.3.8). Error ellipses for each analytical point are plotted in white for uraninite 1, grey symbols for uraninite 2 and black for uraninite 3. Calculated Discordia lines for each uraninite grain were calculated using the software of Ludwig (1999).

**Y and REE abundances in uraninite**

The yttrium (Y) and rare earth elements (REE) are part of the large-ion lithophile elements (LILE) and the high field-strength elements (HFSE) with high ionic charge and radius as U and Th. These highly incompatible elements concentrate in the liquid during partial melting but they are also the first to enter in the crystal structure in the cooling magma. Therefore, their abundances and distribution in magmatic minerals are relevant of the melt particularities from which the pegmatite derived and provide also an accurate geochemical tool to characterize the processes involved in the mineral formation.

Y and REE concentrations have been obtained on uraninite 2 (sample 2-22) using the ion microprobe CAMECA IMS-3f. The SIMS results are presented in Table 2.3.9 and compared to the abundances measured by Bonhoure (2007) in magmatic uraninites from the Rössing alaskite (Namibia) and the Otish Mounts pegmatite (Québec, Canada) using exactly the same analytical procedure and instrument. The element concentrations are quite constant in the three different spot analysed (Fig. 2.3.11) and Y and REE abundances seem to be less dependant of the heterogeneities within the crystal than the previous U-Pb isotopic measurements. This suggests that Y and REE are less soluble during uraninite alteration and quite immobile, thus providing the accurate of this geochemical tool.

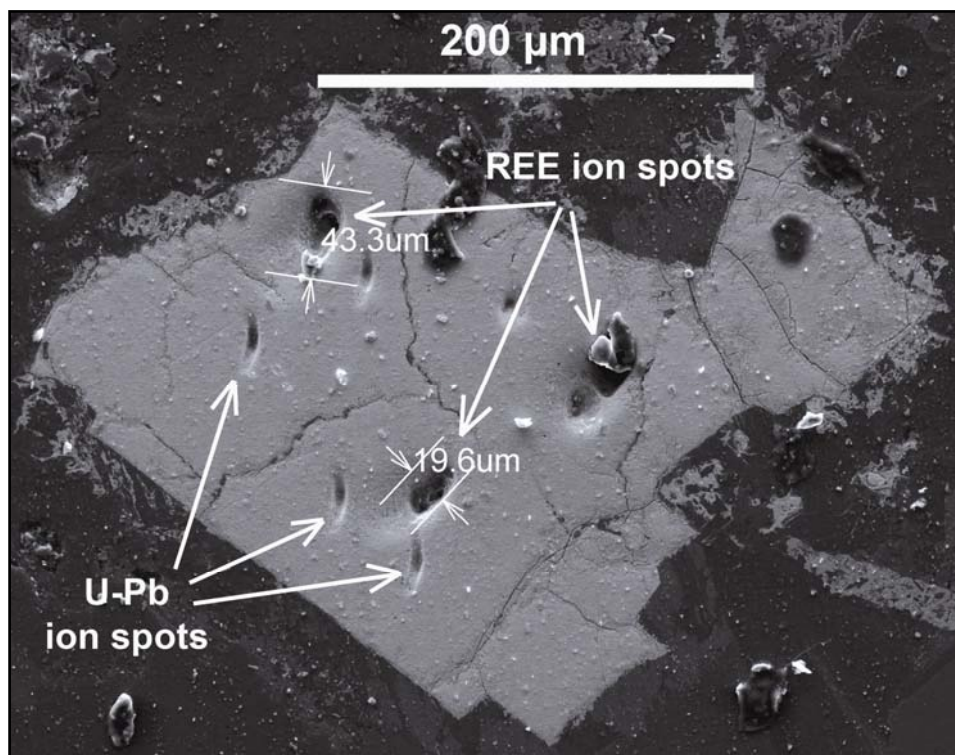


**Figure 2.3.11.** Secondary electron imaging of the different ion spots in uraninite 2 (sample 2-22) analysed by SIMS (ion probe CAMECA IMS-3f).

**Table 2.3.9.** SIMS determinations of Y and REE contents (ppm) in the Tanco uraninites (this study) compare to other uranium oxides from pegmatoids of the Rössing ore showing and the Otish Mounts (from Bonhoure, 2007)

Sample	N°	Y	La	Ce	Pr	Nd	Sm	Eu	Gd*	Tb	Dy	Ho	Er	Tm	Yb*	Lu	ΣREE	ΣLREE	ΣHREE	ΣHREE/ΣLREE
<b>Tanco</b>	1	292.5	10.34	42.18	8.08	40.23	23.92	3.89	24.51	3.84	21.01	3.32	8.63	0.85	4.60	0.53	195.9	128.7	38.93	0.30
	2	346.9	10.68	56.10	10.93	53.22	28.65	4.88	29.54	4.65	24.97	4.36	10.93	1.17	6.15	0.66	246.9	164.5	48.25	0.29
	3	387.5	11.99	55.45	10.76	51.31	27.26	4.47	30.34	5.04	26.02	4.28	10.80	1.06	5.53	0.59	244.9	161.2	48.27	0.30
<b>Average</b>		<b>342.3</b>	<b>11.00</b>	<b>51.24</b>	<b>9.92</b>	<b>48.25</b>	<b>26.61</b>	<b>4.41</b>	<b>28.13</b>	<b>4.51</b>	<b>24.00</b>	<b>3.99</b>	<b>10.12</b>	<b>1.03</b>	<b>5.43</b>	<b>0.59</b>	<b>229.2</b>	<b>151.5</b>	<b>45.15</b>	<b>0.30</b>
<b>Otish</b>	OA2	1	26 058	183.1	1 240.2	221.8	1 281.9	47.22	1 761.0	365.5	2 079.3	482.2	908.1	126.6	533.7	32.51	10 254	3 965.1	4 162.4	1.05
	2	24 913	338.7	1 935.1	314.9	1 653.6	1 133.7	84.19	2 047.7	427.2	2 306.3	529.9	1 057.4	143.5	585.1	30.93	12 588	5 460.1	4 653.1	0.85
	OA5	1	19 079	568.2	2 488.1	372.6	1 753.0	958.5	72.49	1 781.4	375.1	1 820.6	421.3	835.2	111.5	455.5	24.30	12 038	6 213.0	3 668.3
	2	22 601	385.9	2 041.4	352.5	1 922.8	1 245.1	71.16	2 338.3	494.0	2 737.3	634.7	1 201.9	162.6	665.8	35.82	14 289	6 018.8	5 438.2	0.90
<b>Average</b>		<b>23 162</b>	<b>369.0</b>	<b>1 926.2</b>	<b>315.4</b>	<b>1 652.8</b>	<b>1 082.0</b>	<b>68.76</b>	<b>1 982.1</b>	<b>415.5</b>	<b>2 235.9</b>	<b>517.0</b>	<b>1 000.6</b>	<b>136.0</b>	<b>560.0</b>	<b>30.89</b>	<b>12 292</b>	<b>5 414.2</b>	<b>4 480.5</b>	<b>0.85</b>
<b>Rössing</b>	1	61 702	319.9	4 301.3	517.5	2 717.8	1 505.5	93.68	2 439.5	489.9	3 795.6	769.4	2 401.2	397.9	1 581.5	73.49	21 404	9 455.6	9 019.0	0.95
	2	68 134	268.3	3 908.7	494.2	2 643.3	1 540.9	88.33	2 669.6	549.3	4 258.9	889.5	2 851.8	446.0	1 769.6	81.45	22 460	8 943.5	10 297	1.15
	3	110 383	801.5	9 506.1	430.0	1 444.1	1 885.1	85.76	4 057.1	891.1	7 651.7	1 155.5	5 605.8	1 025.8	4 256.5	243.0	39 039	14 153	19 938	1.41
	4	45 505	270.0	3 580.8	428.6	2 659.3	1 386.4	75.19	1 986.7	379.2	3 143.8	694.4	1 903.0	317.7	1 254.0	56.07	18 135	8 400.2	7 368.8	0.88
<b>Average</b>		<b>71 431</b>	<b>414.9</b>	<b>5 324.2</b>	<b>467.6</b>	<b>2 366.1</b>	<b>1 579.5</b>	<b>85.74</b>	<b>2 788.2</b>	<b>577.3</b>	<b>4 712.5</b>	<b>877.2</b>	<b>3 190.5</b>	<b>546.8</b>	<b>2 215.4</b>	<b>113.5</b>	<b>25 259</b>	<b>10 238</b>	<b>11 656</b>	<b>1.10</b>

\* Gd and Yb are calculated from Sm-Tb and Tm-Lu concentrations respectively because of analytical interferences forbidding their accurate measurements.  
 ΣLREE = La+Ce+Pr+Nd+Sm+Eu and ΣHREE = Dy+Ho+Er+Tm+Yb+Lu

The Y and REE contents of the Tanco uraninite (average Y = 342.3 ppm and  $\Sigma\text{REE} = 229.2$  ppm) are much lower than in the other pegmatitic occurrences (average for Rössing: Y = 71 431 ppm and  $\Sigma\text{REE} = 25\,259$  ppm; average for Otish Mounts: Y = 23 162 ppm and  $\Sigma\text{REE} = 12\,292$  ppm). This is well exposed by the chondrite-normalized REE patterns in Figure 2.3.12. The Tanco REE abundances reach only a maximum of  $10^2$  times the chondrites whereas the Rössing and Otish Mounts uraninite concentrations are from  $10^3$  to more than  $10^4$  times the chondrites. The Tanco REE patterns are as a whole weakly fractionated with a relatively flat shape ( $\Sigma\text{HREE}/\Sigma\text{LREE} = 0.30$ ) in comparison of the regular bell-shape pattern centered on Eu of the two other magmatic occurrences (Rössing:  $\Sigma\text{HREE}/\Sigma\text{LREE} = 1.10$  and Otish Mounts:  $\Sigma\text{HREE}/\Sigma\text{LREE} = 0.85$ ). However, beside the lower REE contents of the Tanco uraninite that give a smoother pattern, the global profile is the same as the Otish Mounts with a moderate negative Eu anomaly and decreasing abundances of the heavy REE.

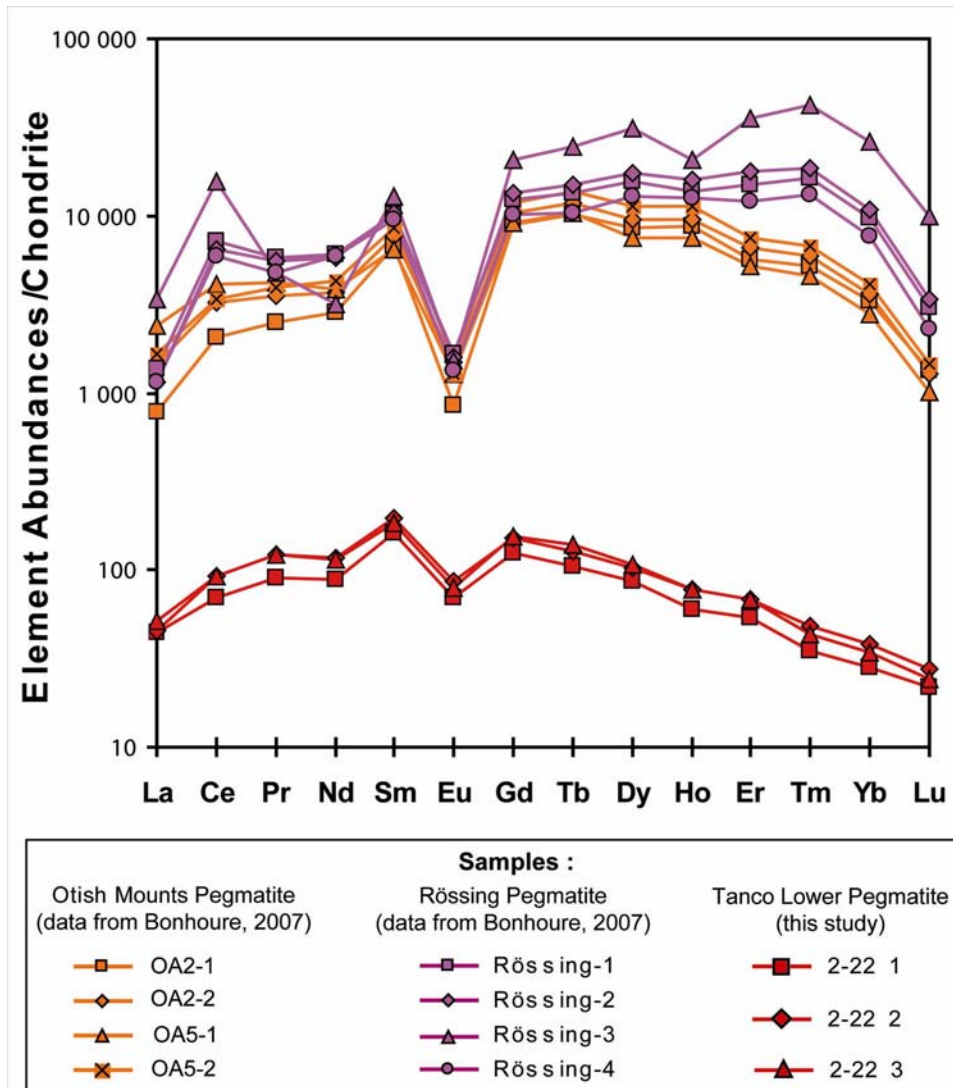


**Figure 2.3.12.** Chondrite-normalized REE abundances in uraninite from the Tanco pegmatite (this study), the Rössing deposit and the Otish Mounts pegmatite (data after Bonhoure, 2007).

## INTERPRETATION

### ***Magmatic origin of primary uranium mineralization***

The paragenetic sequence of primary uranium bearing minerals in the Tanco pegmatite is composed of uraninite, uranmicrolite, mangano-columbite-tantalite, wodginite and cassiterite. All these minerals occur as euhedral crystals in the groundmass composed of quartz, feldspar and muscovite phenocrysts.

The magmatic origin of the Tanco uraninite is sustained by its occurrence with the Nb-Ta minerals. The origin and paragenetic sequence of the different Ta-oxides in the Tanco pegmatite have been previously characterized by Van Lichtenvelde et al. (2007) who distinguished three stages of Ta-oxide crystallization based on mineral assemblage, textures and compositions. The facies 1 with columbite-tantalite + wodginite + rare microlite is recognized as the primary sequence or early magmatic. The facies 2 is the late primary sequence with tantalite + wodginite + microlite and corresponds to a later crystallized melt but it is still magmatic in origin. Finally, the facies 3 with rare wodginite + microlite + ferrotapolite is considered as a replacement stage by metamictization. The paragenetic sequence observed in our samples clearly corresponds to the facies 2 mineral association. Moreover, the restricted field composition obtained for mangano-columbite-tantalite (Fig. 2.3.8) with distinctive high Ta/(Ta+Nb) and Mn/(Mn+Fe) ratios corresponds to the composition of Nb-Ta minerals occurring in facies 2 defined by Van Lichtenvelde et al. (2007). The increase in the Ta and Mn contents with the evolution of the pegmatite crystallization from later melt residue could be explained by the higher degree of fractionation of the source magma. The crystallization of uraninite occurs therefore in the more differentiated melts.

The Tanco best preserved uraninite domains, displaying the highest average atomic number and Pb/U ratio, are considered to be representative of the elementary substitutions happening during primary crystallization from the source magma and their chemical composition is characteristic of the melt composition. They have moderate ThO<sub>2</sub> and CaO contents typical of magmatic uraninite crystallizing from strongly peraluminous leucocratic granites as the Bauvoir leucogranite in the French Massif Central (Kosakevitch, 1976; Cuney and Friedrich, 1987). The relatively high MnO, P<sub>2</sub>O<sub>5</sub> and K<sub>2</sub>O contents reflect the specific chemical characteristics of highly fractionated high phosphorous rare element pegmatites or granites (Černý et al, 2005).

Moreover, the REE patterns of the Tanco uraninite, relatively flat with low fractionation between light and heavy REE and centered on a negative Eu anomaly, is characteristic of magmatic crystallization. The negative Eu anomaly is attributed to the early europium fractionation in plagioclase before uraninite formation in the cooling magma during the progressive fractional crystallization. The lower Y and REE abundances in the Tanco uraninite compared to the Rössing and Otish Mounts occurrences reflect the depletion of incompatible elements in low temperature peraluminous melts (Cuney and Kyser, 2008) that are more differentiated than the two other pegmatites.

Considering the petrographic observations (crystal forms, textures and mineral paragenesis) and the chemical composition of the different accessory minerals, it is obvious that primary euhedral crystals of uraninite and uranmicrolite are magmatic minerals and that uranium mineralization in the Tanco pegmatite crystallized from the more differentiated residual melt before the complete solidification of the magma.

### ***Evidence of post-magmatic alteration and its chemical effects***

The Archean Tanco pegmatite was previously considered to be a well preserved and unweathered primary ore body for tantalum mineralization. However, even if the samples analysed in this study were collected in fresh exposure and drill holes in the Lower Tanco Pegmatite ore body circa 193 metres deep from the surface, this research have shown that both primary uranium bearing minerals, uraninite and uranmicrolite, are strongly affected by post-magmatic alteration.

Petrographic and SEM observations of uraninite have evidenced lower reflectance and decreasing average atomic number domains in all samples, even the dissolution of the grains with cavities, embayment textures and boxworks in samples 2-85 and LP-16. The uranmicrolite crystals as well have shown often a distinct alteration pattern at the edge of the grains and in some case a corroded corona with distinct chemical composition ribbons consecutive to the metamictization acting at the surface exposure. Nevertheless, it has been noticed that the uranmicrolite crystals in the vicinity of partly dissolved uraninite are generally better preserved. The dissemble degree of alteration between primary uraninite and uranmicrolite could be explain by the higher solubility of uranium in oxidizing fluids relatively to tantalum.

In the best preserved uraninite crystals (samples 2-22 and 2-57), the internal chemical composition variations suggest that uraninite crystals have also experienced a recrystallization.

The domains with decreasing reflectance and BSE brightness associated to a lower average atomic number are assumed to correspond to the altered areas. The decreasing average atomic number is associated to the leaching of the uranium and the radiogenic lead out from the crystal structure whereas lighter elements (Ca, Si, P, K) are incorporated but do not totally compensate the depletion (Fig. 5). The main variation is represented by a negative concordance between the Pb/U ratio and the increasing Ca content (Fig. 4) probably because calcium has the closest ionic radius to that of uranium (1.06 Å for Ca and 1.05 Å for U) and commonly replaces it in the crystal lattice during hydrothermal alteration whereas lead (1.37 Å) is rapidly leached out (Alexandre and Kyser, 2005).

As a consequence, the large range of low chemical ages and the discordant isotopic results represent ages of alteration event(s) rather than the primary crystallization age. However, the large range of ages obtained cannot represent a unique event of the U-Pb isotopic system resetting and no geological interpretation can be advanced.

### ***Redeposition***

The occurrences of secondary uranium bearing minerals, the mixture of secondary uraninite with uranyl minerals and Th-rich phospho-silicates, as well as the presence of galena beside the altered primary uraninite, suggest that the radiogenic elements remobilized outside from the magmatic uraninite crystals after later alteration event(s) have re-precipitated just a few millimetres from the primary mineralization. Their textures, as thick ribbons in the walls of micro-pores and as fillings of micro-fractures, permit to assume the happening of a fluid circulation through the open-space of the rock after the first U-stage mineral crystallization. The porosity of the rock must have served as pathways for fluid circulation. The greater alteration rate observed in samples 2-85 and LP-16 may have resulted either from a higher permeability of the rock or/and, considering their location in the Lower Tanco Pegmatite body (Fig. 2), the fluid circulation may have been canalized in the central part of the pegmatite body with less interaction to the walls. The chemical composition of the secondary uranyl minerals and Th-P-Si phases suggests that those fluids brought significant concentrations in Ca, Si, P, Fe and small concentrations in Y and S.

## CONCLUSION

This study provides a full petrographic description and chemical composition of uraniferous minerals of the Tanco pegmatite and its related paragenetic mineral assemblage. The main U-bearing mineral, uraninite, occurs in quartz, plagioclase and muscovite phenocrysts with coeval uranmicrolite, mangano-columbite-tantalite, wodginite and cassiterite suggesting an early (magmatic stage) crystallization. Uraninite textural heterogeneities and the young U-Pb isotopic ages show that the Tanco pegmatite present significant subsolidus alteration, either hydrothermal or meteoric, despite the preservation of the columbite-tantalite oxides. Because sampling was done in drill-cores, uraninite alteration is attributed to hydrothermal alteration rather than weathering. Uranium is partly redistributed at the margins of uraninite, along cracks and grain boundaries with replacement by late uraniferous phases. These heterogeneous uraninite grains have undergone chemical alterations conducting to radiogenic lead loss and disequilibrium of Pb-Pb and U-Pb isotopic systems with composite age patterns scattered between 550 and 1160 Ma. This large fractionation of U might have occurred during late metasomatic hydrothermal processes since at least  $1250 \pm 30$  Ma, the oldest age obtained by Concordia-Discordia calculation method, and the isotopic system has been open until recently according to the youngest age obtained  $76 \pm 13$  Ma. Therefore, the age of primary crystallization of uraninite cannot be reached by common geochronological methods.

Nevertheless, some major element contents in uraninite as Th, Mn and REE, give a clear magmatic signature. The thorium and rare earth element abundances and distribution in uraninite may be considered as a pertinent indicator for the formational mode of these minerals. The textural, paragenetic, and geochemical features of the uraninite leave no doubt either about their magmatic origin. Consequently, the age of uraninite crystallization should be considered as contemporaneous with the age of early magmatic phases (Ta-oxides), but occurs after plagioclase crystallization because of the negative Eu anomaly in the REE patterns relevant of an earlier fractionation from the cooling magma.

## ACKNOWLEDGMENTS

We thank Alain Kohler, Johann Ravaux and Sandrine Mathieu from the SCMEM (Nancy-Université, France) for the help provided with SEM-EDS and EMPA. We are grateful to Michel Champenois, Denis Mangin and Etienne Deloule from the CRPG (CNRS, Vandœuvre lès

Nancy, France) for their help with the CAMECA IMS-3f instrument and for assistance with U-Pb dating calculation. This work was supported by grants from AREVA and CREGU.

## REFERENCES

- Alexandre, P. and Kyser, T.K., 2005, Effects of cationic substitutions and alteration in uraninite, and implications for the dating of uranium deposits; *The Canadian Mineralogist* 43, p. 1005-1017.
- Anders, E. and Grevesse, N., 1989, Abundances of the elements: Meteoritic and solar; *Geochimica and Cosmochimica Acta* 57, p. 197-214.
- Baadsgaard, H. and Černý, P., 1993, Winnipeg River pegmatite populations, southeastern Manitoba (abstr.): GAC-MAC Program with Abstracts 18, A5.
- Barnicoat, A.C., Henderson, I.H.C., Knipe, R.J., Yardley, B.W.D., Napier, R.W., Fox, N.P.C., Kenyon, A.K., Muntingh, D.J., Strydom, D., Winkler, K.S., Lawrence, S.R. and Cornford, C., 1997, Hydrothermal gold mineralization in the Witwatersrand basin; *Nature* 386, p. 820-824.
- Bonhoure, J., 2007, Géochimie des éléments de terres rares et du plomb dans les oxydes d'uranium naturels ; Doc. Univ. Nancy, France.
- Bonhoure, J., Kister, P., Cuney, M. and Deloule, E., 2007, Methodology for Rare Earth Element Determinations of Uranium Oxides by Ion Microprobe; *Geostandards and Geoanalytical Research* 31, p. 209-225.
- Bowles, J.F.W., 1990, Age dating of individual grains of uraninite in rocks from electron microprobe analyses; *Chemical Geology* 83, 47-53.
- Breaks, F.W., 1991, English River subprovince. In: *Geology of Ontario* (eds. P.C. Thurston, H.R. Williams, R.H. Sutcliffe and G.M. Stott) Ontario Geological Survey, Special Vol. 4, Part 1, p. 239-277.
- Breaks, F.W., Selway, J.B. and Tindle, A.G., 2003, Fertile peraluminous granites and related rare-element mineralization in pegmatites, Superior Province, northwest and northeast Ontario; *Operation Treasure Hunt: Ontario Geological Survey, Open File Report 6099*, 179 p.
- Cathelineau, M., Boiron, M.-C., Holliger, P. and Poty, B., 1990, Metallogenesis of the French part of the Variscan orogen. Part II: Time-space relationship between U, Au and Sn-W ore deposition and geodynamic events-mineralogical and U-Pb data; *Tectonophysics* 177, p. 59-79.
- Cathelineau, M., Cuney, M., Leroy, J., Lhote, F., Nguyen, C.T., Pagel, M. et Poty, B., 1982, Caractères minéralogiques des pechblendes de la province hercynienne d'Europe. Comparaison avec les oxydes d'uranium du Protérozoïque de différents gisements d'Amérique du Nord, d'Afrique et d'Australie; In: *Vein type and similar uranium deposits in rocks younger than Proterozoic*, Proc. Symp. Lisbon, 1979, IAEA, p. 159-177.
- Černý, P., 2005, The Tanco rare-element pegmatite deposit, Manitoba: regional context, internal anatomy, and global comparisons; In: *Rare-element geochemistry and mineral deposits*, Geological Association of Canada Short Course Notes 17, p. 127-158.

- Černý, P., 1992, Geochemical and petrogenetic features of mineralization in rare-element granitic pegmatites in the light of current research; *Applied Geochemistry* 7, Issue 5, p. 393-416.
- Černý, P. and Ercit, T.S., 2005, The classification of granitic pegmatites revisited; *Canadian Mineralogist* 43, p. 2005-2026.
- Černý, P. and Siivola, J., 1980, The Tanco pegmatite at Bernic Lake, Manitoba. XII, Hafnian zircon; *Canadian Mineralogist* 18, p. 313-321.
- Černý, P., Blevin, P.L., Cuney, M. and London, D., 2005, Granite-Related Ore Deposits; *Society of Economic Geologists, 100<sup>th</sup> Anniversary 2005*, p. 337-370.
- Černý, P., Ercit, T.S. and Vanstone, P.J., 1998, Mineralogy and petrology of the Tanco rare-element pegmatite deposit, south-eastern Manitoba; *International Mineralogical Association, 17<sup>th</sup> General Meeting Toronto, Field Trip Guidebook B6*.
- Černý, P., Ercit, T.S. and Vanstone, P.J., 1996, Petrology and mineralization of the Tanco rare-element pegmatite, Southeastern Manitoba, *Field Trip Guidebook A3, Geological Association of Canada/Mineralogical Association of Canada Annual Meeting, Winnipeg, Canada*, 63 p.
- Černý, P., Goad, B.E., Hawthorne, F.C., and Chapman, R., 1986, Fractionation trends of the Nb- and Ta-bearing oxide minerals in the Greer Lake pegmatitic granite and its pegmatite aureole, southeastern Manitoba; *American Mineralogist* 71, p. 501-517.
- Cocherie, A. and Albarede, F., 2001, An improved U-Th-Pb age calculation for electron microprobe dating of monazite, *Geochimica et Cosmochimica Acta*, Vol. 65, p. 4509-4522.
- Cuney, M. and Friedrich, M., 1987, Physicochemical and crystal-chemical controls on accessory mineral paragenesis in granitoids: implications for uranium metallogenesis; *Bulletin de Minéralogie* 110, p. 235-247.
- Cuney, M. and Kyser, K., 2008, Hydrothermal uranium deposits related to igneous rocks, Chapter 7. In: *Recent and not-so-recent developments in uranium deposits and implications for exploration* (eds. M. Cuney and K. Kyser), *Short Course Series vol. 39, Mineralogical Association of Canada*, p. 117-160.
- Ercit, T.S., Černý, P., Hawthorne, F.C. and McCammon, C.A., 1992, The wodginite group. II. Crystal chemistry; *Canadian Mineralogist* 30, p. 613-631.
- Finch, R.J. and Ewing, R.C., 1992, The corrosion of uraninite under oxidizing conditions. *Journal of Nuclear Materials* 190, p. 133-156.
- Friedrich, M.H., Cuney, M. and Poty, B., 1987, Uranium Geochemistry in Peraluminous Leucogranites; *Uranium* 3, p. 353-385.
- Frimmel, H.E. and Minter, W.E.L., 2002, Recent Developments Concerning the Geological History and Genesis of the Witwatersrand Gold Deposits, South Africa; *Society of Economic Geologists Special Publication* 9, p. 17-45.
- Hogarth, D.D., 1977, Classification and nomenclature of the pyrochlore group; *American Mineralogist* 62, p. 403-410.
- Holliger, P., 1988, Ages U-Pb définis in situ sur oxydes d'uranium à l'analyseur ionique: méthodologie et conséquences géochimiques ; *Comptes rendus de l'Académie des Sciences de Paris* 307, p. 367-373.
- Kish, L. and Cuney, M., 1981, Uraninite-albite veins from Mistamisk Valley of the Labrador Through, Quebec; *Mineralogical Magazine* 44, p. 471-483.

- Kosakevitch, A., 1976, Evolution de la minéralisation Li, Ta, Nb dans la coupole granitique de Bauvoir (Massif d'Echassières, Allier), Rapport interne BRGM, 82 p.
- Larbi, Y., Stevenson, R., Breaks, F., Machado, N. and Gariépy, C., 1999, Age and isotopic composition of late Archean leucogranites: implications for continental collision in the western Superior Province; *Canadian Journal of Earth Sciences* 36, p. 495-510.
- Law, J.D.M. and Phillips, G.N., 2006, Witwatersrand gold-pyrite-uraninite deposits do not support a reducing Archean atmosphere. In: *Evolution of Early Earth's atmosphere, hydrosphere, and biosphere* (eds. S.E. Kesler and H. Ohmoto); Geological Society of America Memoir 198, p. 121-141.
- Linnen, R.L. and Cuney, M., 2005, Granite-related rare-element deposits and experimental constraints on Ta-Nb-W-Sn-Zr-Hf mineralization; In: *Rare-Element Geochemistry and Mineral Deposits* (eds. R.L. Linnen and I.M. Samson I.M.) Mineralogical Association of Canada, Short Course Notes 17, p. 45-67.
- Ludwig, K.R., 1999, Isoplot/ex version 2.10. A geochronological toolkit for Microsoft Excel; Special Publication n°1a, Berkeley Geochronological Center.
- Martin, H., 2005, Genesis and Evolution of the Primitive Earth Continental Crust. In: *Lectures in Astrobiology, Advances in Astrobiology and Biogeophysics Book Series* (eds. M. Gargaud et al.), Springer Berlin, Vol. I, p. 113-163.
- Mellor, E.T., 1916, The conglomerates of the Witwatersrand; *Trans. Inst. Min. Met.* 25, p. 226-348.
- Minter, W.E.L., 1981, The distribution and sedimentary arrangement of carbon in South African Proterozoic placer deposits; In: *Genesis of uranium- and gold-bearing Precambrian quartz-pebble conglomerates* (ed. C.F. Armstrong), U.S. Geol Surv Prof Paper 1161-P, P1-P4.
- Prasad, N. and Roscoe, S.M., 1996, Evidence of anoxic to oxic atmospheric change during 2.45-2.22 Ga from lower and upper sub-Huronian paleosols, Canada, *Catena* 27, p. 105-121.
- Pretorius, D.A., 1961, The nature of the Witwatersrand gold-uranium deposits; In: *Handbook of stratabound and stratiform ore deposits* (ed. K.H. Wolf), Elsevier, Amsterdam, p. 29-88.
- Robb, L.J. and Meyer, F.M., 1995, The Witwatersrand Basin, South Africa: Geological framework and mineralization processes; *Ore Geology Reviews* 10, p. 67-94.
- Robb, L.J., Davis, D.W. and Kamo, S.L., 1990, U-Pb ages on single detrital zircon grains from the Witwatersrand Basin, South Africa: constraints on the age of sedimentation and on the evolution of granites adjacent to the basin; *The Journal of Geology* 98, p. 311-328.
- Robinson, A. and Spooner, E.T.C., 1982, Source of detrital components of uraniferous conglomerates, Quike ore zone, Elliot Lake, Ontario, Canada; *Nature* 299, p. 622-624.
- Smith, S.R., Foster, G.L., Romer, R.L., Tindle, A.G., Kelley, S.P., Noble, S.R., Horstwood, M. and Breaks, F.W., 2004, U-Pb columbite-tantalite chronology of rare-element pegmatites using TIMS and Laser Ablation-Multi Collector-ICP-MS: Contributions to Mineralogy and Petrology 147, p. 549-564.
- Stilling, A., 1998, Bulk composition of the Tanco pegmatite at Bernic Lake, Manitoba, Canada. M.Sc. Thesis, Department of Geological Sciences, University of Manitoba, Winnipeg (MB- Canada), 75 p.
- Stilling, A., Černý, P. and Vanstone, P.J., 2006, The Tanco pegmatite at Bernic Lake, Manitoba. XVI. Zonal and bulk compositions and their petrogenetic significance; *Canadian Mineralogist* 44 (3), p. 599-623.

- Thiel, K., Saager, R. and Muff, R., 1979, Distribution of uranium in early Precambrian gold-bearing conglomerates of the Kaapvaal Craton, South Africa: a review of a case study for the application of fission track micromapping of uranium, *Min Sci Eng* 11, p. 225-245.
- Van Lichtervelde, M., Salvi, S. and Beziat, D., 2007, Textural features and chemical evolution in tantalum oxides: magmatic versus hydrothermal origins for Ta mineralization in the Tanco Lower Pegmatite, Manitoba, Canada; *Economic Geology* 102, p. 257-276.

## Partie 2.4

### Uranium occurrences associated to partial melting and metasomatism in Precambrian granitoids from the Baltic Shield

Isabelle Duhamel, Michel Cuney, Anne-Sylvie André-Mayer<sup>1</sup> and Leonid Serov<sup>2</sup>

<sup>1</sup>*G2R, Nancy-Université, CNRS, CREGU, Boulevard des Aiguillettes BP 239, 54506, Vandœuvre-lès-Nancy, France*

<sup>2</sup>*VSEGEI, A.P. Karpinsky Russian Geological Research Institute, Russian Federation*

---

#### Abstract

This work presents the results of geochemistry, petrography, in situ chemical composition of minerals and U-Pb geochronology in 5 different intrusive granitoids from two major Archean provinces of the Baltic Shield: Mustalampi and Huhtilampi granitoids from Karelia and Dikoe, Skalnøe, Polyarnøe ore showings from Kola. The granitoids dated from 2.7 to 1.85 Ga intrude typical Archean metavolcanic and aluminous metasedimentary rocks and occur along major regional NW trending structures resulting from multi-generation of rifting events. The peraluminous granitoids are mainly composed of quartz, feldspar and biotite and formed by migmatization and partial melting of biotite-rich gneisses. U mineralization occurs mainly as primary uraninite rich in Th, Y and REE crystallizing in biotite selvages with monazite or zircon. The U-Pb isotopic dating of primary uraninite in Mustalampi and Polyarnøe pegmatites yields highly discordant results because of U and Pb losses generally linked to fluid circulation along the ancient weakness zones (faults, limbs of folds, shearing zones) and locally associated to Na-metasomatism. Primary uraninite is sometimes totally dissolved leaving boxworks and lateral secondary deposition of hexavalent-U products (coffinite, pitchblende without Th, kasolite, uranophane, bequerellite) in fractures and intergrain spaces.

This study emphasizes the role of a pre-enriched protholith and a low degree of partial melting both involved in the genesis of the first U enrichment in Archean time within the Baltic Shield. It also highlights the importance of metasomatism and fluid circulation for the mobility of radioelements and reconcentration processes.

---

#### Key words

Baltic Shield, Karelia, Kola, Precambrian, S-type granites, magmatic uraninite, metasomatism and uranium remobilization

## INTRODUCTION

Precambrian uranium occurrences in igneous rocks are extremely rare and thus poorly studied, however they are of great interest to understand the first step of U fractionation at the beginning of the continental crust formation and represent the source rocks of U deposits in Archean to Paleoproterozoic quartz pebble conglomerates. Uranium occurrences are known in the Karelian and Kola crustal megablocks from the Baltic Shield. Some anomalous radioactive Archean granite-gneiss plutons have been identified 40 years ago in the Puruvesi region of the Karelian Province. They host quartz-biotite pegmatites with uraninite yielding U-Pb ages ca. 2.4 Ga. Intrusive-type U occurrences are also known in the northeastern part of the Kola Peninsula in the Litsa region in Russia within disseminated pegmatite bodies formed in Archean time ca. 2.75-2.65 Ga (Dikoe and Skalnoe) or during Paleoproterozoic ca. 2.2-1.85 Ga (Polyarnoe). The older ones are known as potassic metasomatite emplaced in aluminium-rich garnet and two-mica paragneisses whereas the youngest pegmatites are issued from partial melting and hosted in peraluminous sillimanite-biotite migmatitic gneisses (Cuney and Kyser, 2008). The various processes involved in the formation of the ore are characterized by a specific mineralogical assemblage. Whole-rock geochemistry, petrographical study, mineral chemical composition and textural features have been analysed in this work in an attempt to characterize the specificities of the different type of uranium occurrences encountered in the Archean granitoids of the Baltic Shield.

## GEOLOGICAL SETTING OF THE BALTIC SHIELD

The Baltic (also named Fennoscandian) Shield located in northeastern Europe is divided into 5 lithotectonic provinces: Svecofennian, Sveconorwegian, Karelian, Belomorian and Kola, the age of terranes decreasing from east to west (Martin, 1985). The older Archean crust is represented by the Karelian, Kola and Belomorian Provinces separated by major Paleoproterozoic thrust faults (Fig. 2.4.1; Gaál and Gorbatshev, 1987; Bogdanova and Bibikova, 1993). This block architecture supposedly derived from the break-up of the supercontinent Kenorland into several micro-continents that reassembled all together during Paleoproterozoic (Williams et al., 1991).

The Karelian province is the largest block exceeding 200,000 km<sup>2</sup> and represents a typical granite-greenstone terrain. It is composed of narrow northerly trending greenstone belts consisting in interlayered metasediments and metavolcanic rocks intruded by granodiorite and monzogranite plutons. The geochronological work provided in the Karelian rocks yields up to

3.1 Ga ages corresponding to remnant of the Saamian substratum (Gaál and Gorbatshev, 1987) but the majority of rocks is dated mainly ca. 2.7 Ga corresponding to greenstone rocks and monzogranites intrusions formed during the Lopian Orogeny (2.9-2.6 Ga) in tectonic environments resembling rifts and island arcs (Nironen, 1997). This episode coincides with the peak of metamorphism affecting most of the Karelian Province under upper amphibolite facies to granulite facies conditions (Käpyaho et al., 2007). The uplift of the Karelian Archean block has conducted to the deposition of clastic and mafic volcanic rocks forming the various greenstone belts. This Archean block was probably close to Greenland during Kenorland supercontinent assemblage in Neoproterozoic at 2.8-2.5 Ga (Daly et al., 2006; Mertanen et al., 2006; Höltta et al., 2008) but experienced multiple rifting events between 2.45 and 2.1 Ga that finally conducted to a major break-up between Laurentia and Baltica continents in the western margin of Karelia ca. 2.1-2.05 Ga (Lahtinen et al., 2005 and 2008) and involved probably an eastern shortening associated to collision with the Kola block at ca. 1.97-1.95 Ga (Lahtinen et al., 2009).

The Kola Province occupies the northern part of the eastern Baltic Shield and is divided into two main units, the Murmansk domain composed of high grade orthogneisses and migmatites and the Central Kola domain comprising gneisses of tonalite to granodiorite composition, aluminous metasedimentary rocks and banded iron formations. These two units are separated by the narrow 2.7 Ga Kolmozero-Voronya greenstone belt composed of metavolcanic and metasedimentary rocks emplaced in a major shear zone. The Kola rocks have been affected by the ~ 2.9-2.6 Ga Lopian orogeny and the oldest isotopic age found is in the Murmansk orthogneiss at ca. 2.96 Ga (Sm/Nd from Timmerman and Daly, 1995).

The Belomorian belt located between the Karelian and Kola blocks represents metasediments, metabasalts and metaplutonic rocks intensely reworked during the Svecofennian Orogeny ca. 1.9-1.8 Ga (Bibikova et al., 1999 and 2001). The Belomorian belt forms a thick elongated tectonic pile of imbricated nappes folded, metamorphosed and obducted southwestwards over the eastern margin of the Karelian Province. This belt corresponds to the collision suture between Kola and Karelian blocks induced by the activation of the Paleoproterozoic/Archean margin southwest of the Karelian block. The collision resulted in lithospheric thickening along thrust faults, subsequent delamination of the thickened lithosphere and underplating of a hot mantle plume resulting in granitoid magmatism (Nironen, 1997). The Belomorian rocks are intruded by late granites composed by tonalite, granodiorite and calc-alkaline compositions representing the mixture between mantle magma and remelted arc complex material.

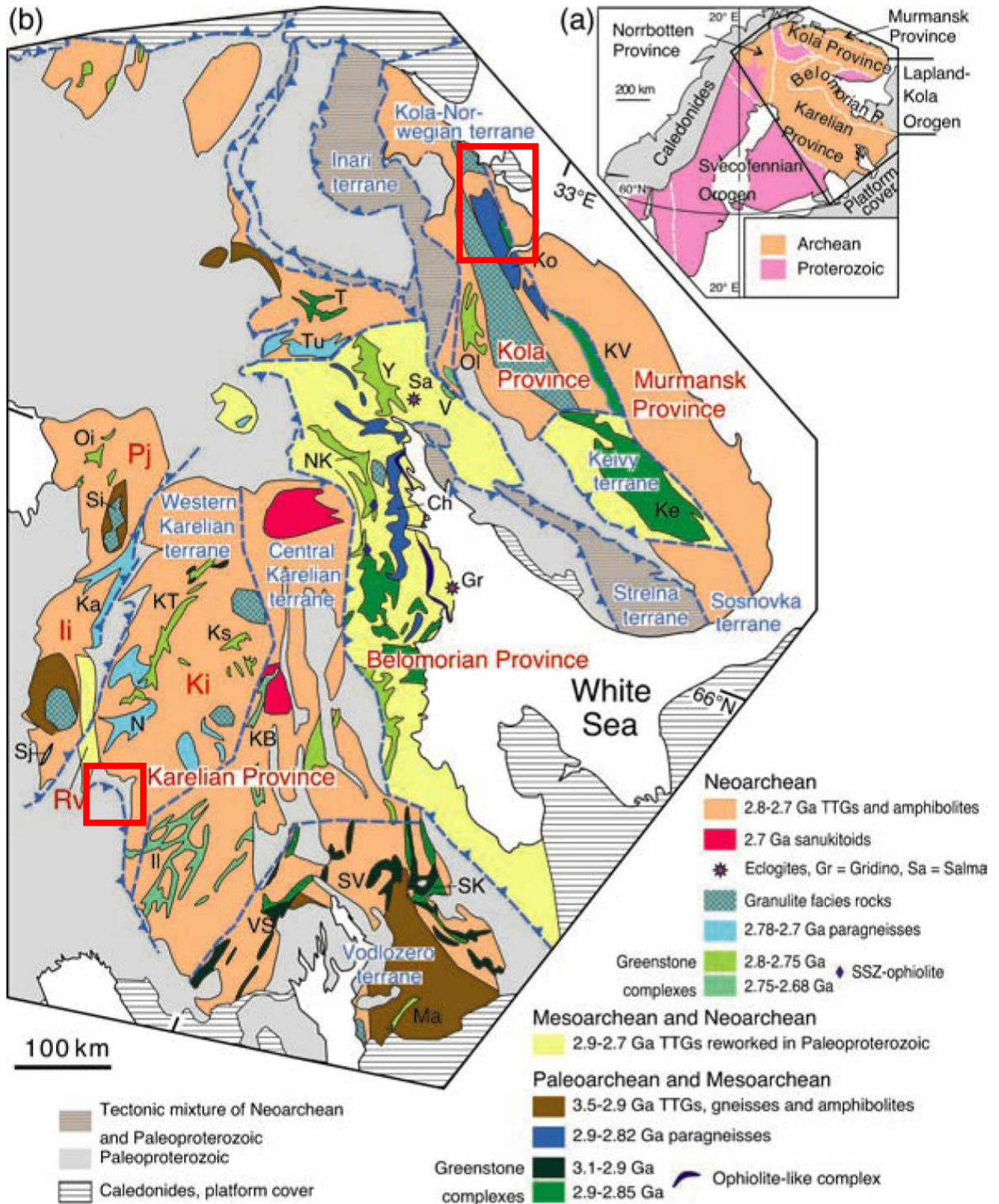


**Figure 2.4.1.** Sketch map of the Archean crust in the Baltic Shield (after Hölttä et al., 2008) showing the location of the studied areas (red squares): (a) Principal tectonic units of the Baltic shield; (b) Geological representation of the main Archean terranes, and greenstone, schist and paragneiss belts: Ch = Chupa; Il = Ilomantsi; KB = Khedozero-Bolshezero; Ke = Keivy; Ko = Kola; Ks = Kostomuksha; KT = Kuhmo-Suomussalmi-Tipasjärvi; KV = Kolmozero-Voronya; Ma = Matkalahta; N = Nurmes; NK = North Karelian; Ol = Olenegorsky; Oi = Oijärvi; SK = Sumozero-Kenozero; SV = South Vyzozero; Tu = Tuntsa; T = Tulppio; V = Voche-Lambina; VS = Vedlozero-Segozero; Y = Yena. Complexes of the Western Karelian terrane: Ii = Iisalmi; Ki = Kianta; Pj = Pudasjärvi; Rv = Rautavaara; Sj = Siilinjärvi carbonatite; Si = Siurua gneiss.

## METHODOLOGY

Sixteen samples have been collected from drill cores and surface outcrops in the Precambrian basement rocks from the Baltic Shield during two field trips: 8 samples from Finland in the radioactive Karelian Archean granites of the Puruvesi region (Caillat et al., 2006) and 8 samples from intrusive-type U occurrences of the Kola Peninsula in Russia (Kister et al., 2007). The best radioactive rocks in surface outcrops have been chosen using a SPP $\gamma$  scintillometer and the most radiogenic areas of samples were selected for making the polished thin sections using autoradiography with MEDEX SD-SPEEDX reactive films placed in contact with the rock during a week.

The mineralogical study has been performed at the G2R laboratory (Géologie et Gestion des Ressources Minérales et Energétiques, Nancy University, France) on 25 polished thin sections using a polarizing microscope Olympus BX51 in transmitted and reflected lights.

Whole-rock samples have been analyzed at the SARM laboratory (CRPG, CNRS, Nancy, France) using the Carignan et al. (2001) methodology and standards. The geochemistry of 3 samples from the Finish granitoids (9375-2, 9375-3 and 9375-4) has not been characterized because of the too small amounts of material left after the thin section preparation. Major elements of the 13 other samples were determined using ICP-AES and the trace elements using ICP-MS. Geochemical results will be discussed using AB and QP chemical-mineralogical diagrams of Debon and Lefort (1988). The parameters Q [=  $\text{Si}/3 - (\text{K} + \text{Na} + 2\text{Ca}/3)$ ], P [=  $\text{K} - (\text{Na} + \text{Ca})$ ], A [=  $\text{Al} - (\text{K} + \text{Na} + 2\text{Ca})$ ] and B [=  $\text{Fe} + \text{Ti} + \text{Mg}$ ] are calculated in thousands of cations from the major element contents. The average composition of reference rocks have been reported in the diagrams: gb = gabbro; mgb = monzogabbro; mz = monzonite; mzdq = quartz monzodiorite; dq = quartz diorite; s = syenite; sq = quartz syenite; to = tonalite; gd = granodiorite; ad = adamellite; gr = granite (data from Debon and Le Fort, 1983). The aluminosity index A/CNK [=  $(\text{Al}_2\text{O}_3/102)/((\text{CaO}/56) + (\text{Na}_2\text{O}/62) + (\text{K}_2\text{O}/94))$ ] and the peralkaline index A/NK [=  $(\text{Al}_2\text{O}_3/102)/((\text{Na}_2\text{O}/62) + (\text{K}_2\text{O}/94))$ ] are calculated in molar fraction (Shand, 1947; Maniar and Piccoli, 1989). The rock sample REE concentrations are normalized to the chondrite values from Anders and Grevesse (1989) and plotted as comparative REE patterns. The binary diagram Th vs. U (in part per million) permit to characterize the fractionation of the element and their possible leaching or enrichment during alteration processes.

Identification and chemical composition of uranium-bearing minerals were undertaken at the SCMEM laboratory (Service Commun de Microscopie et de Microanalyses, Nancy University, France) on the polished thin section samples coated with carbon. Scanning electron

microscopy (SEM: HITACHI FEG S4800) coupled with an energy dispersive spectrometer (EDS: Noran Vantage) have been used for semi-qualitative measurements of major mineral components. Imagery in backscattered mode was used to study the internal textures and the chemical heterogeneities whereas the secondary electron images access to appreciate the relief of samples for the observation of dissolution cavities. The chemical composition of selected minerals was measured using the electron microprobes (EMP) CAMECA SX50 and SX100 equipped with wavelength dispersive spectrometers (WDS). Operating conditions were an accelerating voltage of 20 kV for monazite and 15 kV for all other minerals (zircon, xenotime, apatite, uranorthorite, U oxides and hexavalent alteration products), a beam current of 10 nA with acquisition times ranging between 5 and 30 s to measure chemical composition within a 2  $\mu\text{m}$  diameter spot. To allow comparison between the different radiogenic grains, EMP analytical results in weight percent (wt.%) have been recalculate for the plots in atomic percent (at.%). Chemical dating of Th and U bearing minerals have been provided by the EMP analytical results using the CHIME method developed by Susuki and Adachi (1991) and commonly used for high spatial resolution age determination in monazite and zircon grains. The equations for age computation and the statistical method are described in detail in Susuki and Adachi (1991), Montel et al. (1996) and Cocherie and Albarede (2001). The chemical ages have been determined with decay constants  $\lambda(^{238}\text{U}) = 0.155125 \times 10^{-9} \text{ y}^{-1}$ ,  $\lambda(^{235}\text{U}) = 0.98485 \times 10^{-9} \text{ y}^{-1}$ ,  $\lambda(^{232}\text{Th}) = 0.049475 \times 10^{-9} \text{ y}^{-1}$  and assuming that the initial Pb in the mineral is zero, Pb content actually present is of radiogenic origin and there is no common lead incorporated in the mineral after its crystallization.

Ion microprobe analyses by secondary ion mass spectrometry (SIMS) of U and Pb isotopes for the dating of uraninite as well as their yttrium (Y) and rare earth element (REE) contents were measured at the CRPG (CNRS, Nancy, France) using a CAMECA IMS-3f instrument. A beam of negatively charged oxygen atoms is focused on to the gold-coated surface of the polished samples. Ions sputtered from a spot size between 20  $\mu\text{m}$  to 50  $\mu\text{m}$  of the uraninite grain are accelerated by an electrical field and separated magnetically into the different atom species by the mass spectrometers. The precise isotopic composition is quantified using specific standards, uraninite from Zambia dated at  $540 \pm 4 \text{ Ma}$  (Holliger, 1988; Cathelineau et al., 1990) for U and Pb isotope measurements and uraninite from the Mistamisk Valley in Canada (Kish and Cuney, 1981) for Y and REE measurements using the method defined by Bonhoure et al. (2007). The  $^{206}\text{Pb}/^{238}\text{U}$  and  $^{207}\text{Pb}/^{235}\text{U}$  ratios of uraninite grains from Karelia and Kola were plotted in a Concordia diagram using the ISOPLOT flowsheet of Ludwig (1999) with the Microsoft EXCEL software. The discordia line intersections were calculated in order to define the lowermost MSWD (mean square weighted deviation) value. The isotopic ages are given with

uncertainties at the  $1\sigma$  level. The REE abundances are normalized to chondrite values (Anders and Grevesse, 1989) and results are compared to the REE patterns of magmatic uraninites from the Rössing Alaskite in Namibia (Bonhoure, 2007).

## KARELIAN ARCHEAN BASEMENT ROCKS

Several Archean-Lower Proterozoic granite-gneiss domes from the Puruvesi region, in northeastern Finland, display strong radioactive anomalies and were investigated for their uranium potential (Caillat et al., 2006). Granitoids from the Mustalampi and Hutilampi areas were collected in the Janisjarvi fault zone corresponding to NW-SE striking faults at the margin between the NE Archean Karelian block and the SW Svecofennian Raahe-Ladoga domain (Fig. 2.4.2). The Janisjarvi fault zone defines the contact between Archean granite-gneiss basement rocks also called the Pre-svecokarelidic Basement Complex and the younger Karelian formations.

Archean granite-gneisses are composed of ~3.0-2.8 Ga metavolcanic and metasedimentary rocks predominantly amphibolites, mica schists and quartz-feldspar gneisses, and younger granodiorite and granite plutons emplaced about 2.6-2.8 Ga ago (zircon and titanite U-Pb analysis; Wetherill et al., 1962; Kouvo and Tilton, 1966; Tilton and Grünefelder, 1968; Nykänen, 1968). Basement in this region are broken into several blocks that trend mainly NW separated by fault zones used as channels by metagabbro and metadiabase dykes during multi-generation of rifting events between 2.45 and 1.98 Ga (Kohonen, 1995; Iljina and Hanski, 2005; Vuollo and Huhma, 2005).

The Karelian formations unconformably overlying the Basement Complex is divided into a lower sequence, the ~2.1-2.3 Ga Jatulian metasediments composed of arkose with local conglomerates, dolomitic carbonates and quartzite sediments interbedded with metabasalts, and an upper sequence forming the ~1.8-2.1 Ga Kalevian Group mainly composed of metaturbidites and mica schists (Pekkarinen, 1979). The Karelian formations were metamorphosed to the greenschist facies, faulted and folded into a NW to NNW oriented synclinorium during the compressional Svecofennian Orogeny and intruded by syn-tectonic Vespian granitic plutons about 1.8-1.95 Ga ago (Nironen, 1997). The Jatulian sedimentary sequence covering the Archean basement hosts U and Th anomalies within quartz-pebble conglomerates that suggest a local fertile source (Shurilov et al., 2007; Shurilov, 2008; chapter 3 – part 3) and caught our interest on this area for our study of Archean U sources.

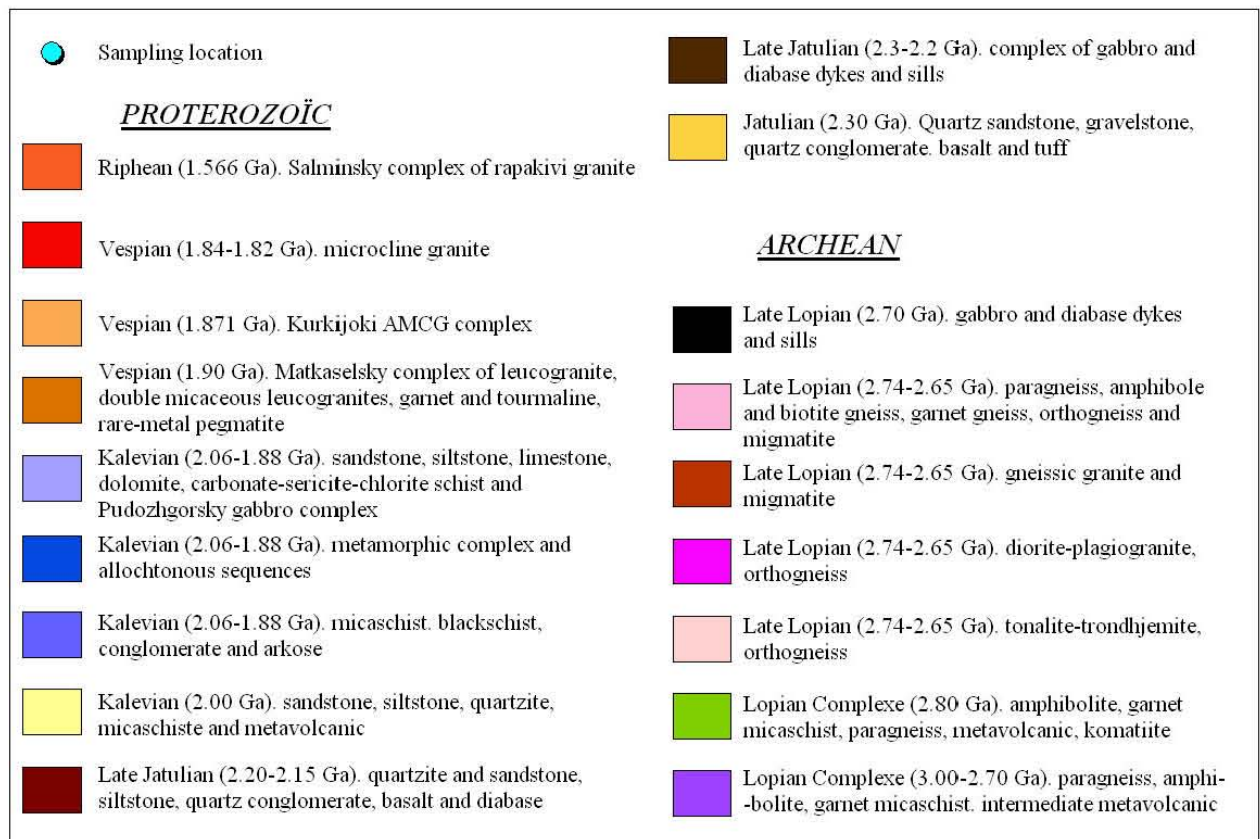
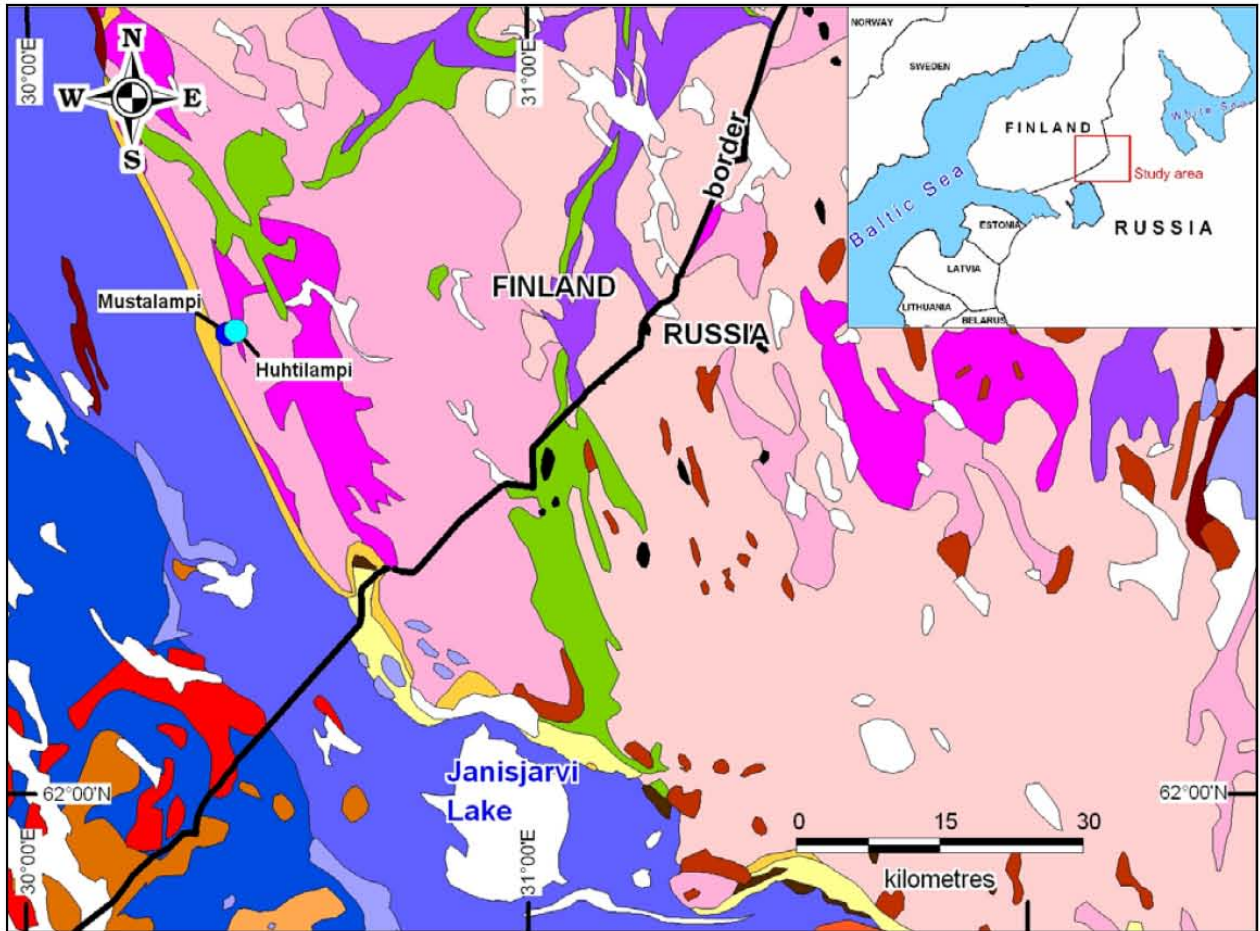


Figure 2.4.2. Geological map of the southeast Karelia at the boundary between Finland and Russia elaborated from the data of the Geological Survey of Finland.

**Mustalampi area (samples 9375-1 to -6)**

The Mustalampi area comprises Late Archean quartz-biotite pegmatite containing 2340 Ma uraninite and thorite (U-Pb dating from Pekkarinen, 1979). Samples were selected from a core in drill hole M52-4241-R324 realised by GTK (Geological Survey of Finland) in the 1970's. Two samples of pegmatite were collected between 45.5 and 46.75 m depth (Table 2.4.1). Enclosing Archean rocks, amphibolite on top and biotite-rich gneisses underneath, were also sampled for an estimation of the average U content.

**Table 2.4.1.** Mustalampi samples from drill hole M52-4241-R324

Sample	Depth interval (m)		Lithology	Rock radioactivity (cps)
9375-1	35.80	36.20	Black amphibolite	40-65
9375-2	45.50	45.60	Pegmatite (Quartz+Feldspar+Biotite)	60-85
9375-3	46.60	46.75	Pegmatite (Quartz+Feldspar+Biotite)	60-85
9375-4	52.60	52.75	Biotite-rich granite-gneiss (Quartz+Plagioclase+Sulfides)	120-150
9375-5	70.75	71.00	Biotite-rich gneiss with quartzofeldspathic blasts	60-110
9375-6	87.10	87.55	Biotite-rich gneiss with quartzofeldspathic blasts	45-60

*Notes:* Radioactivity measured with a scintillometer SPP2 in count per second (cps).

The Archean amphibolite 9375-1 is macroscopically black coloured and fine grained (Fig. 2.4.3). It is composed mainly of polygonal amphibole crystals from 300 µm to 1 mm wide with a granoblastic texture and minor plagioclase, biotite, titanite and quartz which suggest a mafic protolith (Fig. 2.4.4 and 2.4.5). It is obvious consistent with the whole-rock geochemical results (Table 2.4.2) showing a basaltic composition (Fig. 2.4.6) in the metaluminous field ( $A/CNK = 0.61$  and  $A/NK = 2.24$ ) with low silica (<50 wt%  $SiO_2$ ), high contents in calcium (8.71 wt% CaO), magnesium (6.66 wt% MgO) and iron (14.78 wt%  $Fe_2O_{3t}$ ) and low contents in Zr (55.18 ppm), Th (0.76 ppm), U (0.32 ppm) and REE ( $\Sigma = 35$  ppm). The abundance in femic minerals (hornblende, biotite and titanite) and moreover calcium-rich ones induces a high B parameter (362.86) whereas P (-209.4) and A (-167.82) values are very low.

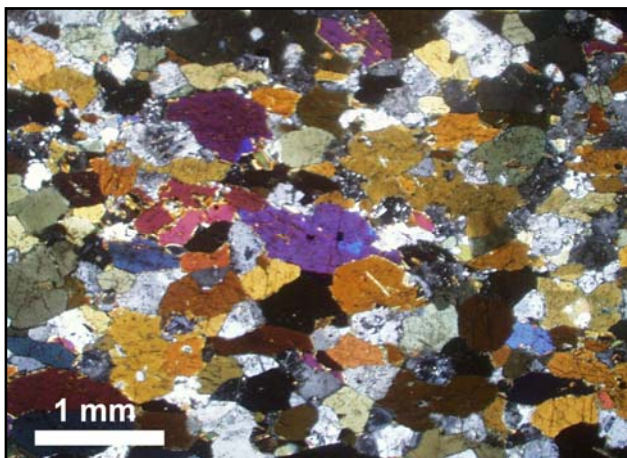


**Figure 2.4.4.** Granoblastic texture in Archean amphibolite (sample 9375-1, crossed nicols transmitted light).

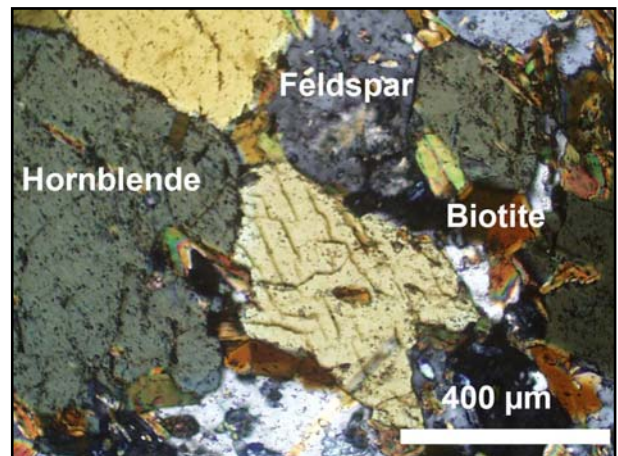
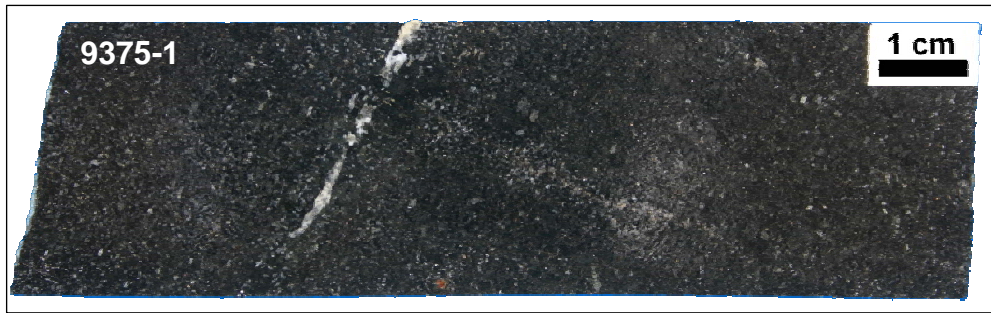


**Figure 2.4.5.** Hornblende, feldspar and biotite within Archean amphibolite (sample 9375-1, crossed nicols transmitted light).

Archean amphibolite



Archean pegmatites



Archean biotite-rich gneisses

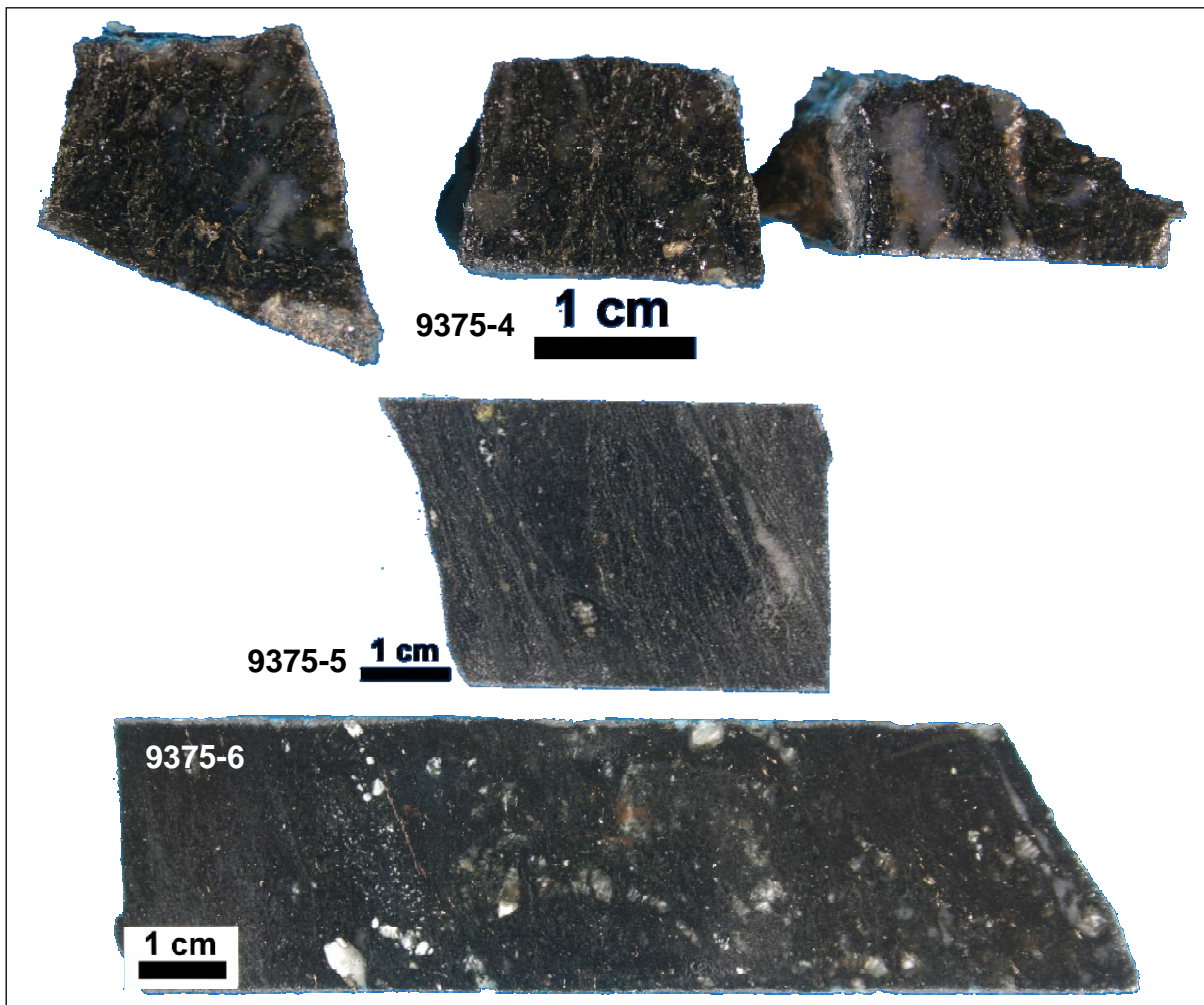


Figure 2.4.3. Macroscopic pictures of the various Archean lithologies sampled in the Mustalampi area

## Chapitre 2 : Sources Magmatiques Archéennes de l'Uranium

**Table 2.4.2.** Chemical composition of Archean rocks collected from the Puruvesi region (Karelian Province)

Location Sample Lithology	Mustalampi area			Huhtilampi area	
	9375-1 Black amphibolite	9375-5 Biotite-rich gneiss	9375-6 Biotite-rich gneiss	9375-16 K-rich granite	9375-17 K-rich granite
SiO <sub>2</sub> (wt%)	49.63	64.75	64.44	73.09	74.82
Al <sub>2</sub> O <sub>3</sub>	13.19	10.96	15.02	13.91	13.89
Fe <sub>2</sub> O <sub>3</sub> total	14.78	9.86	7.99	1.62	0.56
MnO	0.36	0.08	0.13	0.02	0.01
MgO	6.66	6.07	3.26	0.46	0.21
CaO	8.71	0.75	1.97	0.61	0.31
Na <sub>2</sub> O	2.63	1.49	3.83	3.34	3.17
K <sub>2</sub> O	1.45	2.35	1.27	6.30	6.72
TiO <sub>2</sub>	0.93	1.07	0.58	0.21	0.08
P <sub>2</sub> O <sub>5</sub>	0.09	0.11	0.12	0.08	0.02
LOI	0.65	2.24	2.00	0.67	0.48
Total	99.07	99.74	100.61	100.29	100.26
As (ppm)	< D.L.	< D.L.	< D.L.	< D.L.	< D.L.
Ba	283.20	464.60	716.10	1063.00	989.80
Be	0.64	1.10	1.93	0.95	1.00
Bi	0.47	0.35	0.24	< D.L.	< D.L.
Cd	0.25	0.72	0.60	0.23	0.17
Co	58.11	22.56	22.69	1.84	0.75
Cr	42.95	289.60	162.00	4.93	4.34
Cs	1.33	2.86	1.32	1.52	2.15
Cu	53.99	66.05	28.61	14.95	< D.L.
Ga	16.46	23.40	20.47	17.51	17.12
Ge	1.79	1.68	1.54	0.89	0.97
Hf	1.54	18.08	3.52	8.00	6.84
In	0.07	< D.L.	< D.L.	< D.L.	< D.L.
Mo	0.43	55.60	1.57	< D.L.	< D.L.
Nb	1.90	25.26	6.21	5.49	2.22
Ni	72.74	116.70	69.89	3.23	< D.L.
Pb	36.75	126.32	278.66	29.99	31.85
Rb	72.80	116.70	62.28	179.40	203.40
Sb	< D.L.	< D.L.	< D.L.	< D.L.	< D.L.
Sn	0.95	1.42	0.67	1.61	0.84
Sr	142.40	47.01	248.30	203.40	202.20
Ta	0.14	2.14	0.62	1.00	0.39
Th	0.76	510.70	8.69	72.59	112.80
U	0.32	241.60	3.16	8.14	6.27
V	311.20	157.70	111.00	13.63	5.43
W	0.67	2.54	0.69	0.27	0.18
Y	24.30	16.37	12.84	8.21	14.95
Zn	229.70	140.00	518.70	23.10	11.61
Zr	55.18	724.10	139.10	259.60	200.00
La (ppm)	3.02	15.49	26.27	122.70	201.30
Ce	7.92	44.41	54.89	235.40	377.00
Pr	1.22	5.15	6.45	21.76	35.76
Nd	6.34	21.23	24.32	62.20	105.70
Sm	2.16	4.79	4.60	6.25	11.18
Eu	0.77	1.71	1.14	0.90	1.16
Gd	2.83	3.95	3.45	3.18	5.71
Tb	0.53	0.51	0.46	0.35	0.71
Dy	3.67	2.64	2.41	1.57	3.29
Ho	0.81	0.50	0.44	0.25	0.52
Er	2.47	1.45	1.22	0.80	1.49
Tm	0.40	0.22	0.19	0.12	0.20
Yb	2.72	1.61	1.26	0.83	1.25
Lu	0.44	0.31	0.20	0.13	0.17
ΣREE	35.30	103.98	127.29	456.43	745.43
[Ce/Yb] <sub>N</sub>	0.75	7.13	11.28	73.76	78.00
Eu/Eu*	0.95	1.20	0.87	0.62	0.44
[Gd/Yb] <sub>N</sub>	0.84	1.98	2.21	3.12	3.69
P = K-(Na+Ca)	-209.40	-11.18	-131.57	15.46	35.38
Q = Si/3-(K+Na+2Ca/3)	56.32	252.67	183.99	157.02	166.57
B = Fe+Ti+Mg	362.86	288.36	188.59	34.41	13.30
A = Al-(K+Na+2Ca)	-167.82	90.45	73.99	9.50	16.31
A/CNK	0.61	1.72	1.33	1.04	1.06
A/NK	2.24	2.19	1.96	1.13	1.11
K <sub>2</sub> O/Na <sub>2</sub> O	0.55	1.58	0.33	1.89	2.12
Th/U	2.36	2.11	2.75	8.92	18.00

Notes: Geochemical analysis performed by the SARM laboratory (CRPG, CNRS, Nancy, France); Major elements are determined by ICP-AES and trace elements by ICP-MS; <D.L. = below detection limits; [X]<sub>N</sub> = normalized to chondrites; A/CNK and A/NK indexes calculated in moles; Q, P, A and B parameters calculated in thousands of cations.

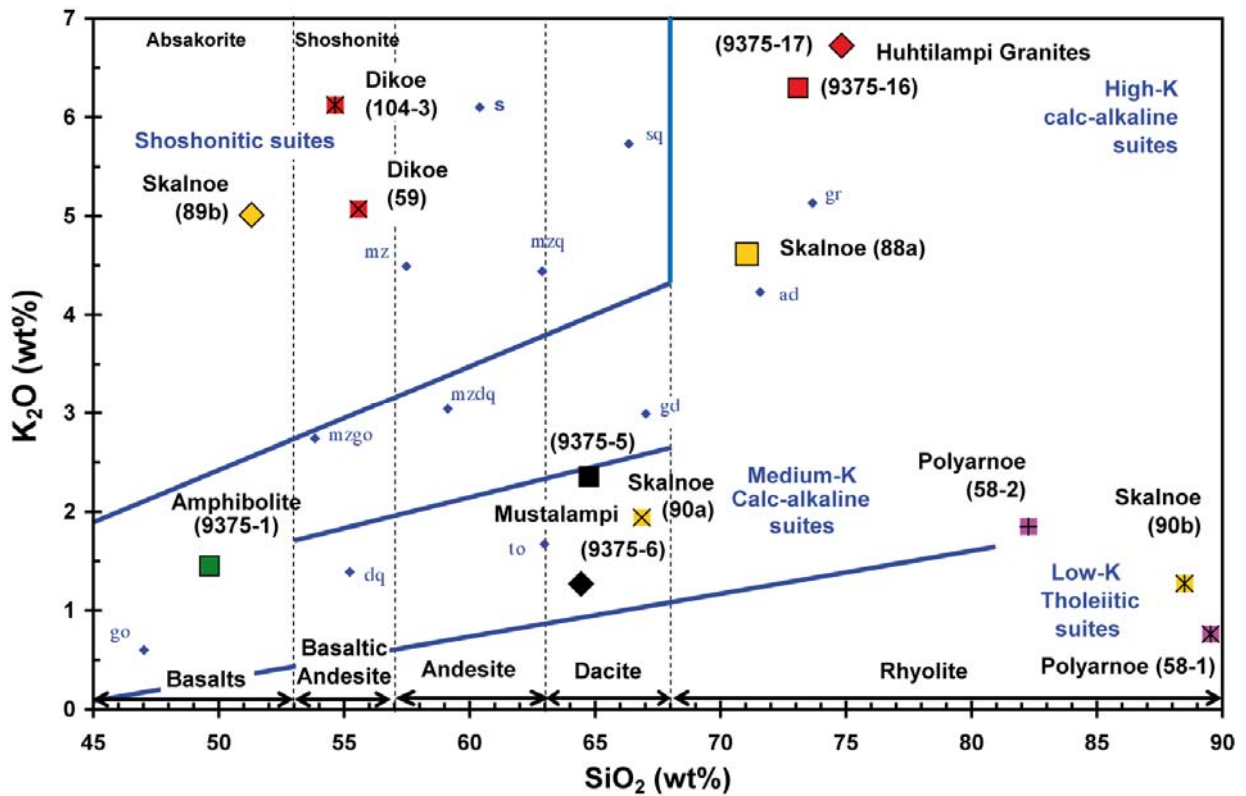


**Figure 2.4.6** Binary diagram showing the  $K_2O$  vs.  $SiO_2$  contents (wt%) of the Baltic Shield basement rocks. The composition limits and fields are from Peccerillo and Taylor (1976) and rock composition references are from Debon and Lefort (1983): go = gabbro; mzgo = monzogabbro; mz = monzonite; mzq = quartz-monzonite; mzdq = quartz monzodiorite; dq = quartz diorite; s = syenite; sq = quartz syenite; to = tonalite; gd = granodiorite; ad = adamellite; gr = granite.

The Mustalampi biotite-rich gneisses (9375-4 to -6) are macroscopically black coloured with quartz-feldspar blasts elongated along foliation plans (Fig. 2.4.3). At the microscopic scale, it appear that rocks are dominated by biotite melanosome bands around 500  $\mu m$  wide interlayered with fine grained quartz, feldspar and less biotitic bands representing mesosome discontinuous layers. Foliation is defined by alignment of biotite elongated crystals. Occasionally feldspar porphyroblasts ranging 2 to 5 mm wide occur in the mesosome bands and show a ductile deformation related to shear zones (Fig. 2.4.7).

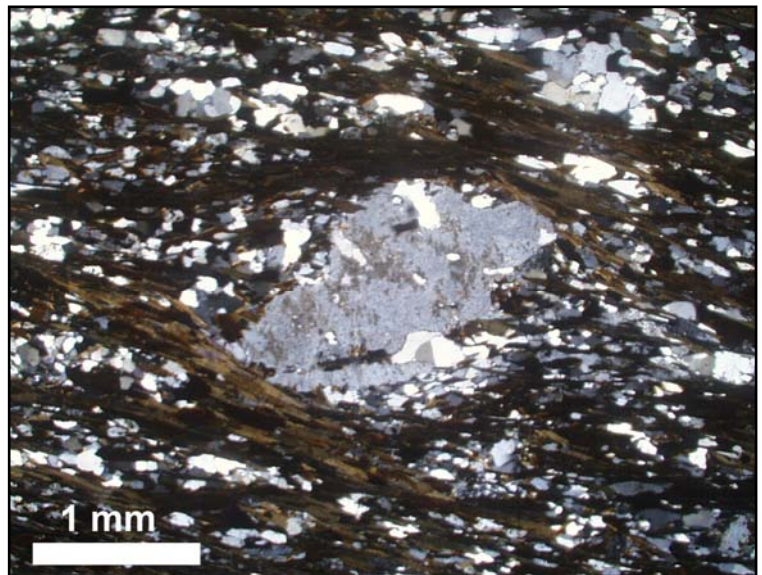


**Figure 2.4.7.** Feldspar porphyroblast (center) indicating a dextral sense of shearing with the schistosity defined by biotite elongation (sample 9375-5, crossed polarized light).

Gneisses range in composition from tonalitic to granodioritic dacite and plot in the field of medium calc-alkaline suites (Fig. 2.4.6). They are peraluminous ( $A/CNK = 1.33-1.72$  and  $A/NK = 1.96-2.19$ ), mainly composed of silica and aluminium ( $SiO_2+Al_2O_3 \sim 75-80$  wt%) with high iron and magnesium contents ( $Fe_2O_3+MgO \sim 11-16$  wt%) associated to the abundance in biotite that gives a high B parameter (188.59-288.36). Wide variations in the P parameter between gneisses indicate variable feldspar proportions dominated by sodic plagioclase in sample 9375-6 ( $P=-131.57$  and  $K_2O/Na_2O=0.33$ ) whereas K-feldspar is more abundant in sample 9375-5 ( $P=-11.18$  and  $K_2O/Na_2O=1.58$ ). Gneisses have slightly fractionated REE patterns compare to the flat pattern of mafic sample 9375-1 (Fig. 2.4.8). They are more enriched in LREE ( $[Ce/Yb]_N=7.13-11.28$ ), depleted in HREE and are characterized by none to slightly positive Eu anomalies ( $Eu/Eu^*=0.87-1.20$ ) suggesting feldspar accumulation.

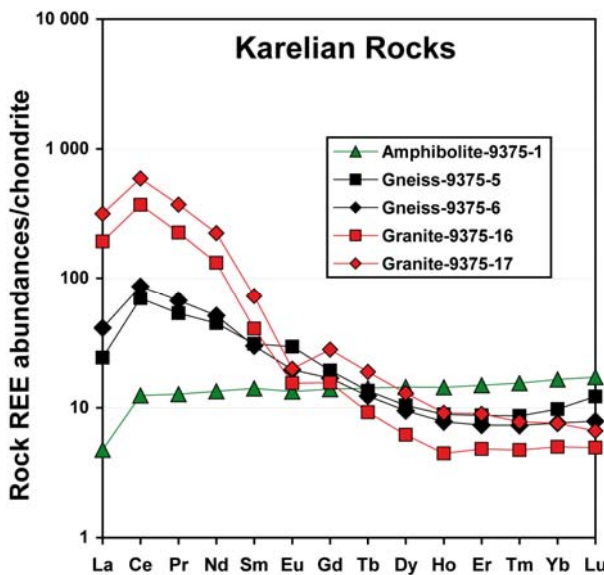


Figure 2.4.8. Chondrite-normalized REE patterns of the Karelain basement rocks.

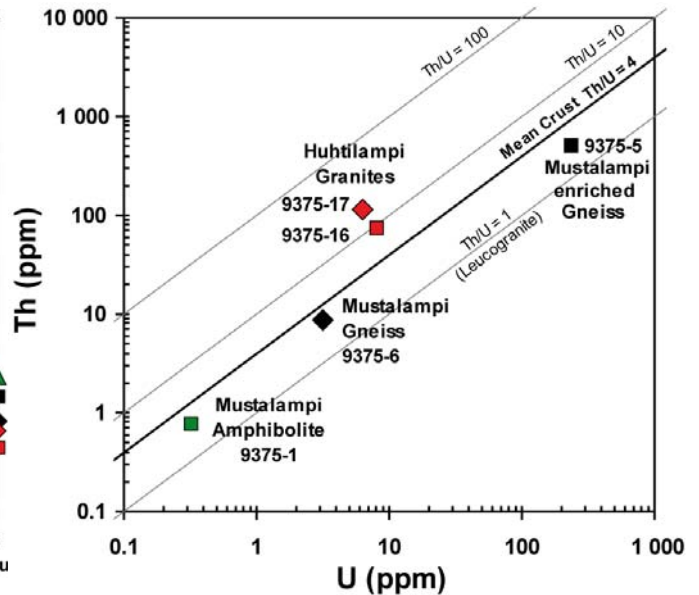
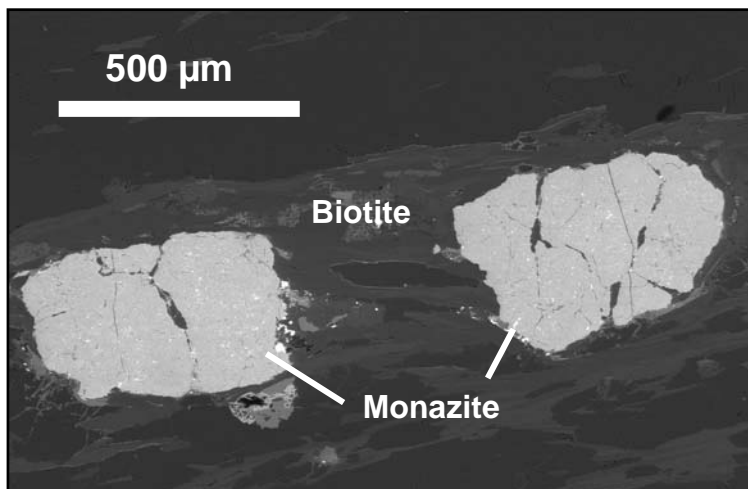


Figure 2.4.9. Th vs. U contents (ppm) of the Karelain basement rocks.

The trace elements show also large concentration variations between samples (Table 2.4.2): in chalcophile and siderophile elements ( $Ni = 70-117$  ppm,  $Cr = 162-290$  ppm,  $Co = 22.56-22.69$  ppm,  $Cu = 28.6-66$  ppm) as well as in lithophile elements ( $Rb = 62-117$  ppm,  $Ba = 465-716$  ppm,  $Th = 8.7-510.7$  ppm,  $U = 3.16-241.6$  ppm,  $Pb = 126-279$  ppm,  $Nb = 6.21-25.26$  ppm,  $Sr = 47-248$  ppm,  $Zr = 139-724$  ppm). Sample 9375-5 is the richest in different trace elements. The Th (510.7 ppm) and U (241.6 ppm) enrichment of this K-rich gneiss is unusually high considering the present average upper continental crust (2.8 ppm U and 10.7 ppm Th after Taylor and McLennan, 1985). Considering that uraninite crystallization preferentially occurs at Th/U close or below 1 (Cuney and Friedrich, 1987), those gneisses with Th/U ranging 2.11 to 2.75 (Fig. 2.4.9) have lower chance to crystallize abundant uraninite. This is confirmed by the microscopic observations by SEM showing that monazite is the main accessory phase hosting the

radioelements in gneisses with rare zircon, both occurring within biotite, and no observed uraninite (Fig. 2.4.10 and 2.4.11). Pyrite and molybdenite elongated crystals occurring along biotite cleavages have also been observed but seem to be secondary in origin as vein-like aggregates or impregnations (Fig. 2.4.12). Monazite is present as subhedral 200-500  $\mu\text{m}$  wide crystals with a porous internal texture in backscattered electron images and dust of white micron-scale cubes (Fig. 2.4.13). White cubes within altered monazite have been identified by EMP analyses as uranothorite crystals (Table 2.4.3). Uraniothorite can occur as alteration products of monazite or as primary inclusions trapped during the crystal growth. In this case, uranothorite is mainly composed of silica (17.1-23.7 wt%  $\text{SiO}_2$ ), thorium (33.5-50.5 wt%  $\text{ThO}_2$ ), uranium (8.6-25.3 wt%  $\text{UO}_2$ ) and lead (0.15-5.97 wt%  $\text{PbO}$ ). Traces of LREE have been detected (0.6-1.9 wt%  $\text{La}_2\text{O}_3$ , 2-3.9 wt%  $\text{Ce}_2\text{O}_3$ , 0.2-2.3 wt%  $\text{Nd}_2\text{O}_3$ ) as well as high concentrations for some analytical spots in iron (0.5-12.6 wt%  $\text{FeO}$ ), sulphur (0.5-10.9 wt%  $\text{SO}_2$ ) and molybdenum (0-0.5 wt%  $\text{MoO}_3$ ) which suggest that uranothorite crystallized from the alteration of monazite during late hydrothermal event(s) coeval with the deposition of pyrite and molybdenite by metal-bearing fluids. This is corroborated by the young chemical ages calculated from the U-Th-Pb contents and yielding a large panel of results from 31 to 1374 Ma. Metamictization of monazite can also cause lead loss and yield to younger ages.



**Figure 2.4.10** BSE-SEM image of two monazite crystals within biotite (sample 9375-5).

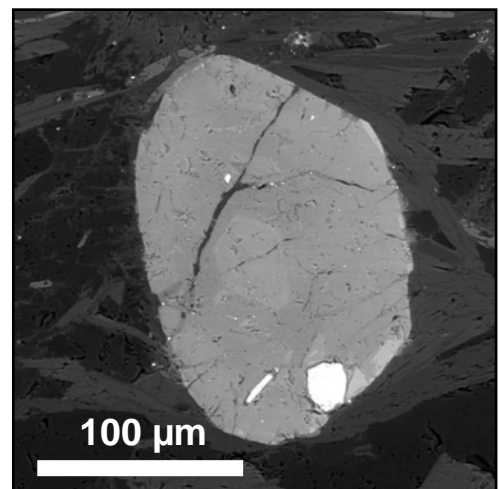


**Figure 2.4.11** BSE-SEM image of zoned zircon grain within biotite (sample 9375-5).

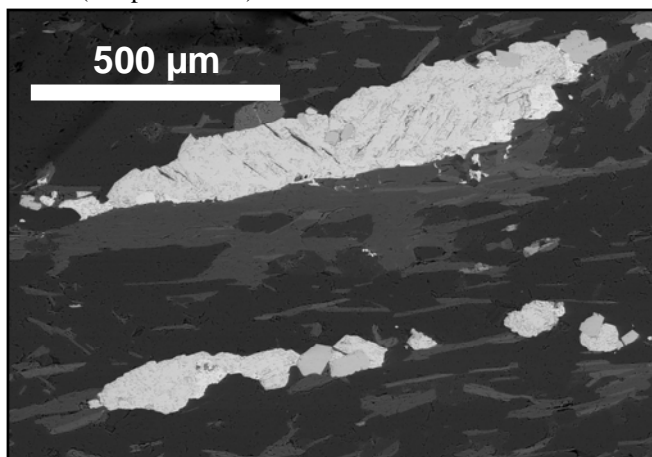


**Figure 2.4.12** BSE-SEM image of pyrite and molybdenite vein-like deposition (light grey) along biotite (sample 9375-5).

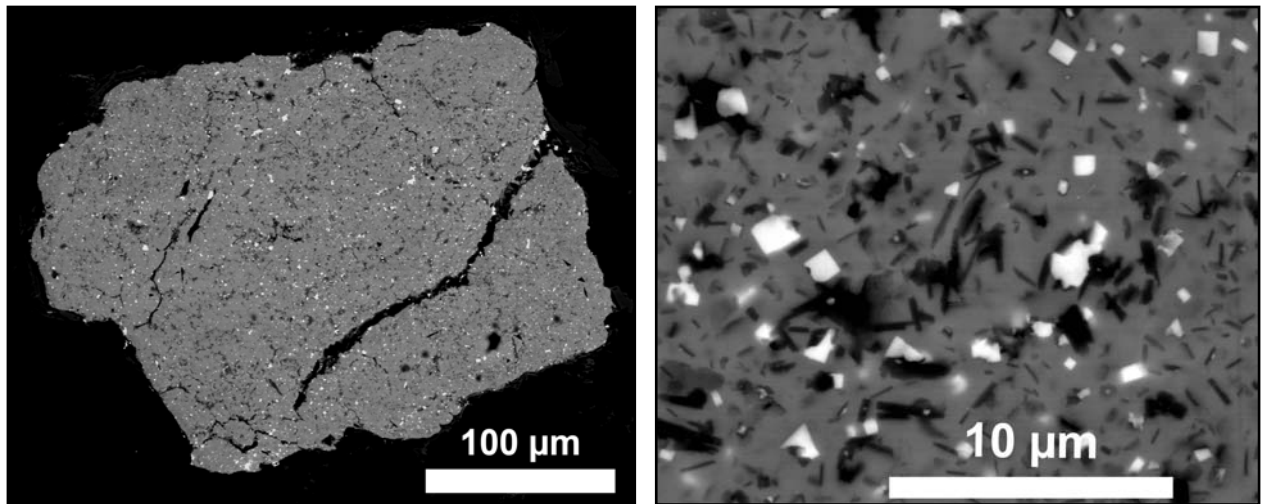


**Figure 2.4.13** BSE-SEM image of a monazite crystal (left) and detail textural features in the same grain (right) showing white cubes of uranothorite (sample 9375-5).

**Table 2.4.3** Average chemical composition of uranothorite hosted in the Mustalampi Archean pegmatite 9375-2 and biotite-rich gneiss 9375-5.

Sample	9375-2	9375-5	Average
Rock type	Quartz-Biotite Pegmatite	Biotite-rich Gneiss	Uranothorite
EMPA	Mean±σ (N=22)	Mean±σ (N=35)	Mean±σ (N=57)
Na <sub>2</sub> O	<D.L.	<D.L.	<D.L.
MgO	<D.L.	<D.L.	<D.L.
Al <sub>2</sub> O <sub>3</sub>	1.19 ± 0.14	1.36 ± 0.37	1.29 ± 0.31
SiO <sub>2</sub>	19.85 ± 1.08	20.22 ± 1.75	20.08 ± 1.52
P <sub>2</sub> O <sub>5</sub>	0.31 ± 0.08	0.28 ± 0.08	0.29 ± 0.08
SO <sub>2</sub>	3.81 ± 2.35	4.31 ± 2.89	4.12 ± 2.69
K <sub>2</sub> O	<D.L.	<D.L.	<D.L.
CaO	1.01 ± 0.11	0.58 ± 0.16	0.75 ± 0.26
TiO <sub>2</sub>	0.09 ± 0.06	0.07 ± 0.04	0.08 ± 0.05
V <sub>2</sub> O <sub>3</sub>	<D.L.	<D.L.	<D.L.
MnO	<D.L.	<D.L.	<D.L.
FeO	3.69 ± 2.63	4.50 ± 2.97	4.19 ± 2.85
Y <sub>2</sub> O <sub>3</sub>	0.33 ± 0.08	0.70 ± 0.28	0.56 ± 0.29
MoO <sub>3</sub>	<D.L.	0.20 ± 0.15	<D.L.
La <sub>2</sub> O <sub>3</sub>	1.19 ± 0.18	1.04 ± 0.35	<D.L.
Ce <sub>2</sub> O <sub>3</sub>	2.45 ± 0.33	3.07 ± 0.43	2.83 ± 0.49
Nd <sub>2</sub> O <sub>3</sub>	1.15 ± 0.26	1.19 ± 0.54	1.17 ± 0.45
Dy <sub>2</sub> O <sub>3</sub>	<D.L.	<D.L.	<D.L.
Ta <sub>2</sub> O <sub>5</sub>	<D.L.	<D.L.	<D.L.
PbO	0.99 ± 0.78	1.60 ± 1.49	1.36 ± 1.29
ThO <sub>2</sub>	42.81 ± 3.90	38.63 ± 3.15	40.25 ± 3.99
UO <sub>2</sub>	13.82 ± 2.09	16.43 ± 3.45	15.42 ± 3.24
<b>Total</b>	<b>93.04 ± 2.72</b>	<b>94.45 ± 2.24</b>	<b>93.91 ± 2.51</b>

**Notes:** “<D.L.”=below detection limit (Na=0.09wt%; Mg=0.03wt%; Al=0.05wt%; Si=0.06wt%; P=0.05wt%; S=0.03wt%; K=0.10wt%; Ca=0.07wt%; Ti=0.04wt%; V=0.14wt%; Mn=0.20wt%; Fe=0.20wt%; Y=0.11wt%; Mo=0.12wt%; La=0.12wt%; Ce=0.28wt%; Nd=0.52wt%; Dy=0.56wt%; Ta=0.20wt%; Pb=0.25wt%; Th=0.16wt%; U=0.54wt%).

The Mustalampi pegmatites (9375-2 and 9375-3, Fig. 2.4.3) intruding the older biotite-rich gneisses and hosting uraninite mineralization are characterized by a two-mica granitic mineralogy. Centimetre-scale biotite selvages containing millimetric crystals with no preferential orientation separate coarse feldspathic material dominated by K-feldspar and less abundant plagioclase (Fig. 2.4.14). Biotite selvages probably correspond to restitic segregations during the partial melting. Feldspars are weakly foliated, sericitized with local development of short tabular

muscovite crystals interfingering with small amount of xenomorphic elongated quartz patches. Pegmatites are crossed by millimetric veins cutting the general foliation direction and composed of massive polycrystalline quartz with undulous extinction (Fig. 2.4.15). Quartz veins are supposedly controlled by fracture displacement related to rising of the granitic domes during the Svecofennian orogeny ~1800 Ma ago and associated to local metasomatic granitization (Pekkarinen, 1979). Recrystallization of quartz from the margin of the pegmatite is locally observed over tens of microns which suggest that the rock was solidified at the time of displacement.

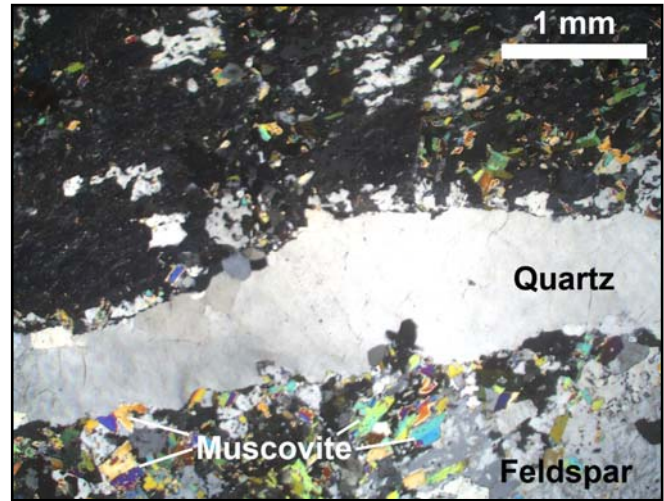
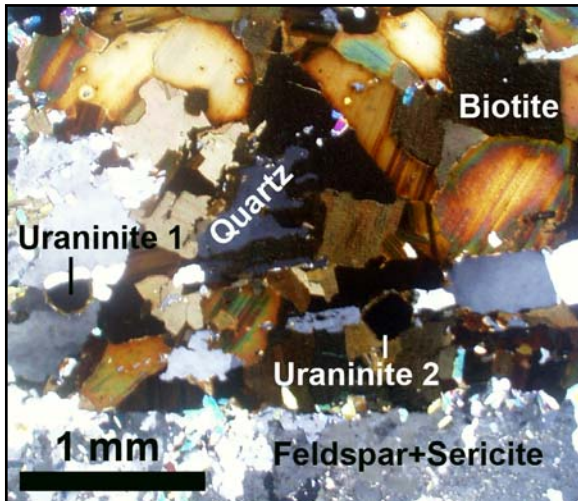


**Figure 2.4.14.** Biotite, sericitized feldspar and quartz pegmatite containing two isolated uraninite grains (sample 9375-3, crossed nicols transmitted light). **Figure 2.4.15.** Quartz vein cutting the two-mica pegmatite (sample 9375-3, crossed nicols transmitted light).

Accessories identified by SEM-EDS analyses in the pegmatite are represented by apatite (Fig. 2.4.16), monazite with uranothorite inclusions (Fig. 2.4.17), uraninite (Fig. 2.4.18) and secondary anatase encountered as a hydrothermal alteration product deposited on biotite lamellae and filling porosity (Fig. 2.4.19).

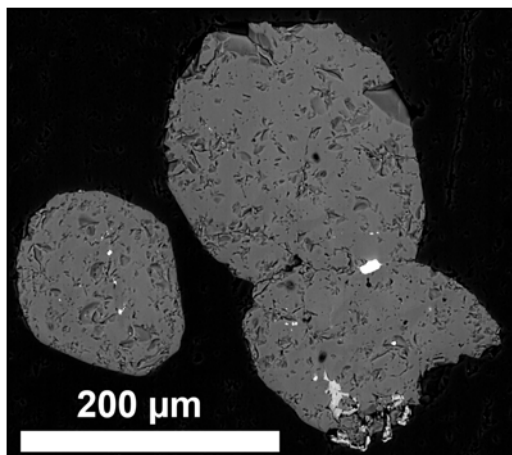


**Figure 2.4.16.** BSE-SEM image of three apatite grains displaying typical hexagonal shape (sample 9375-2).

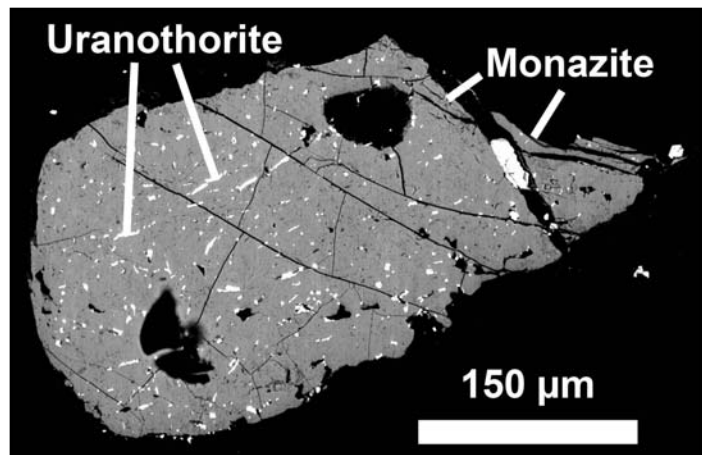


**Figure 2.4.17.** BSE-SEM image of a monazite fractured grain showing uranothorite inclusions (white) and internal porosity (sample 9375-2).

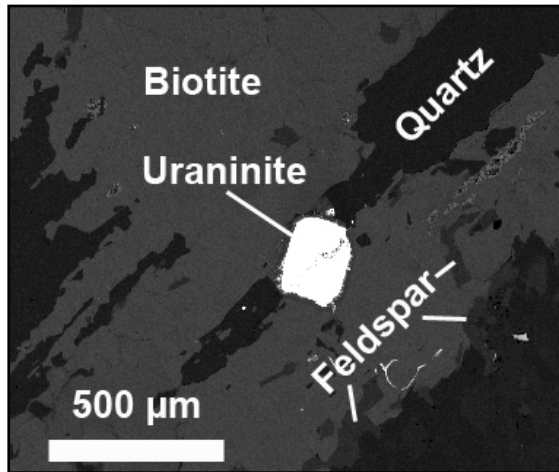


**Figure 2.4.18.** BSE-SEM image of cubic uraninite crystal in biotite selvage and elongated quartz (sample 9375-3).

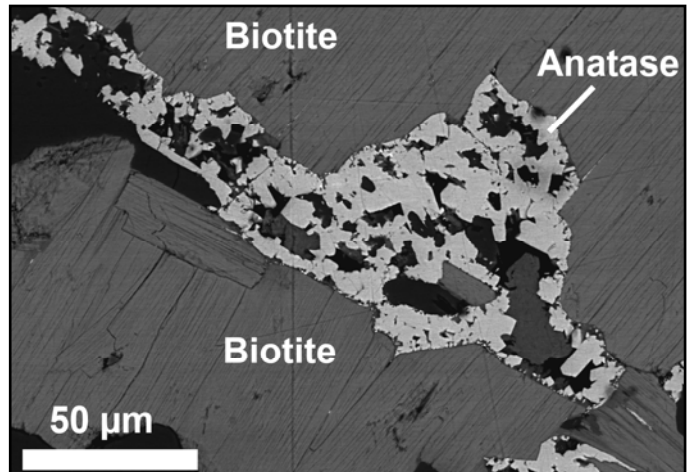


**Figure 2.4.19.** BSE-SEM image of small anatase crystal aggregates lining pore space on the surface of biotite lamellae (sample 9375-3).

Apatite from sample 9375-2 analysed by EMP (Table 2.4.4) is composed principally of potassium ( $m = 42.54 \pm 0.38$  wt%  $P_2O_5$ ) and calcium ( $m = 57.23 \pm 0.39$  wt%  $CaO$ ) with traces of yttrium ( $m = 0.11 \pm 0.07$  wt%  $Y_2O_3$ ) and silica ( $m = 0.34 \pm 0.09$  wt%  $SiO_2$ ). U and Th contents in apatite are below detection limits of the electron microprobe ( $U < 0.36$  wt% and  $Th < 0.09$  wt%) and therefore apatite does not represent the main radioelement-bearing phase of the rock.

**Table 2.4.4.** Average chemical composition of apatite hosted in the Archean granitoids from Karelia

Sample	9375-2	9375-16	Average
Rock type	Mustalampi Pegmatite	Huhtilampi Granite	Apatite
EMPA	Mean $\pm\sigma$ (N=5)	Mean $\pm\sigma$ (N=5)	Mean $\pm\sigma$ (N=10)
Na <sub>2</sub> O	<D.L.	0.11 $\pm$ 0.06	<D.L.
MgO	<D.L.	<D.L.	<D.L.
Al <sub>2</sub> O <sub>3</sub>	<D.L.	<D.L.	<D.L.
SiO <sub>2</sub>	0.34 $\pm$ 0.09	0.13 $\pm$ 0.09	0.23 $\pm$ 0.14
P <sub>2</sub> O <sub>5</sub>	42.54 $\pm$ 0.38	42.03 $\pm$ 0.44	42.29 $\pm$ 0.47
SO <sub>2</sub>	<D.L.	<D.L.	<D.L.
K <sub>2</sub> O	<D.L.	<D.L.	<D.L.
CaO	57.23 $\pm$ 0.39	54.95 $\pm$ 0.42	56.09 $\pm$ 1.26
TiO <sub>2</sub>	<D.L.	<D.L.	<D.L.
V <sub>2</sub> O <sub>3</sub>	<D.L.	<D.L.	<D.L.
MnO	<D.L.	<D.L.	<D.L.
FeO	<D.L.	<D.L.	<D.L.
Y <sub>2</sub> O <sub>3</sub>	0.11 $\pm$ 0.07	<D.L.	<D.L.
MoO <sub>3</sub>	<D.L.	<D.L.	<D.L.
La <sub>2</sub> O <sub>3</sub>	<D.L.	<D.L.	<D.L.
Ce <sub>2</sub> O <sub>3</sub>	<D.L.	<D.L.	<D.L.
Nd <sub>2</sub> O <sub>3</sub>	<D.L.	<D.L.	<D.L.
Dy <sub>2</sub> O <sub>3</sub>	<D.L.	<D.L.	<D.L.
Ta <sub>2</sub> O <sub>5</sub>	<D.L.	<D.L.	<D.L.
PbO	<D.L.	<D.L.	<D.L.
ThO <sub>2</sub>	<D.L.	<D.L.	<D.L.
UO <sub>2</sub>	<D.L.	<D.L.	<D.L.
Total	101.18 $\pm$ 0.52	97.76 $\pm$ 0.56	99.47 $\pm$ 1.87

*Notes:* “<D.L.”=below detection limit (Na=0.07wt%; Mg=0.03wt%; Al=0.03wt%; Si=0.04wt%; P=0.04wt%; S=0.03wt%; K=0.07wt%; Ca=0.07wt%; Ti=0.03wt%; V=0.12wt%; Mn=0.15wt%; Fe=0.14wt%; Y=0.09wt%; Mo=0.09wt%; La=0.09wt%; Ce=0.20wt%; Nd=0.36wt%; Dy=0.45wt%; Ta=0.13wt%; Pb=0.22wt%; Th=0.09wt%; U=0.36wt%).

Uranothorite from the same sample displays an equivalent average composition to the uranothorite enclosed in the monazite in the Th and U enriched biotite-gneiss (Table 2.4.3). The various grain composition analysed by EMP ranges from 17.35 to 21.59 wt% SiO<sub>2</sub>, 34.66 to 50.47 wt% ThO<sub>2</sub>, 8.63 to 17.37 wt% UO<sub>2</sub> and 0.26 to 4.16 wt% PbO with small amounts of LREE (0.94-1.52 wt% La<sub>2</sub>O<sub>3</sub>, 2-3.15 wt% Ce<sub>2</sub>O<sub>3</sub>, 0.68-1.66 wt% Nd<sub>2</sub>O<sub>3</sub>) and highly variable concentrations in iron (0.52-8.67 wt% FeO) and sulphur (0.82-9.1 wt% SO<sub>2</sub>). The chemical ages calculated from the U-Th-Pb contents are ranging from 73 to 1102 Ma which corroborates either the late hydrothermal alteration origin or the lead loss during general metamictization of all U-Th silicate minerals.

Uraninite observed in sample 9375-3 is in direct association with the primary mineral assemblage represented by biotite, feldspar and quartz (Fig. 2.4.14 and 2.4.18). Backscattered electron imaging (Fig. 2.4.20) shows strong alteration features with abundant zones with lower average atomic number (dark grey) and fractures filled with galena (white). EMP analyses were made both in dark grey areas considered as alteration zones with less U, Th and Pb contents and in the more pristine areas corresponding to zones with higher average atomic number (Table 2.4.5). The lighter and darker zones of the crystals have also been distinguished in the plots (Fig. 2.4.21) to show the main element composition variations in uraninite with increasing alteration. The pristine uraninite areas (lighter in BSE mode) have high initial contents in U ranging from 60.26 to 70.68 wt% UO<sub>2</sub> ( $m = 65.70 \pm 2.07$  wt%), thorium ranging from 7.36 to 11.79 wt% ThO<sub>2</sub> ( $m = 9.71 \pm 0.97$  wt%) and lead ranging from 6.27 to 21.38 wt% PbO ( $m = 13.02 \pm 3.39$  wt%). The U-Th-Pb chemical ages calculated for this composition range yield between 1055 and 2216 Ma for uraninite A, between 1073 and 2126 Ma for grain B and between 1290 to 2495 Ma for grain C. Small amounts of calcium (from 0.17 to 3.20 wt% CaO), manganese (up to 1.76 wt% MnO), yttrium (from 0.32 to 1.48 wt% Y<sub>2</sub>O<sub>3</sub>) and LREE (up to 0.77 wt% Ce<sub>2</sub>O<sub>3</sub> and 1.25 wt% Nd<sub>2</sub>O<sub>3</sub>) have also been detected. The element associated with the alteration is mainly Si with a drastic increasing trend of almost up to 18 at% Si in the most altered areas corresponding to concentrations reaching up to 20.29 wt% SiO<sub>2</sub> close to the coffinite composition. The analytical totals in the darker grey zones are low, between 84.03 wt% and 96.83 wt% ( $m = 90.12 \pm 3.26$  wt%) mostly reflecting the hydration of the uranium oxides with coffinitization. The metasomatic-hydrothermal alteration is also accompanied by increase of the aluminium, iron and sulfur contents with up to 1.55 wt% Al<sub>2</sub>O<sub>3</sub>, 2.47 wt% FeO and 6.07 wt% SO<sub>2</sub> whereas the major element contents decrease down to minimal values of 1.18 wt% PbO and 30.95 wt% UO<sub>2</sub> reflecting some lead and uranium leaching. The yttrium and LREE contents seem stable with alteration and still rise up to 2.03 wt% Y<sub>2</sub>O<sub>3</sub>, 1.18 wt% Ce<sub>2</sub>O<sub>3</sub> and 1.26 wt% Nd<sub>2</sub>O<sub>3</sub> in the darker areas which suggests that the alteration process was developed at relatively low temperature.

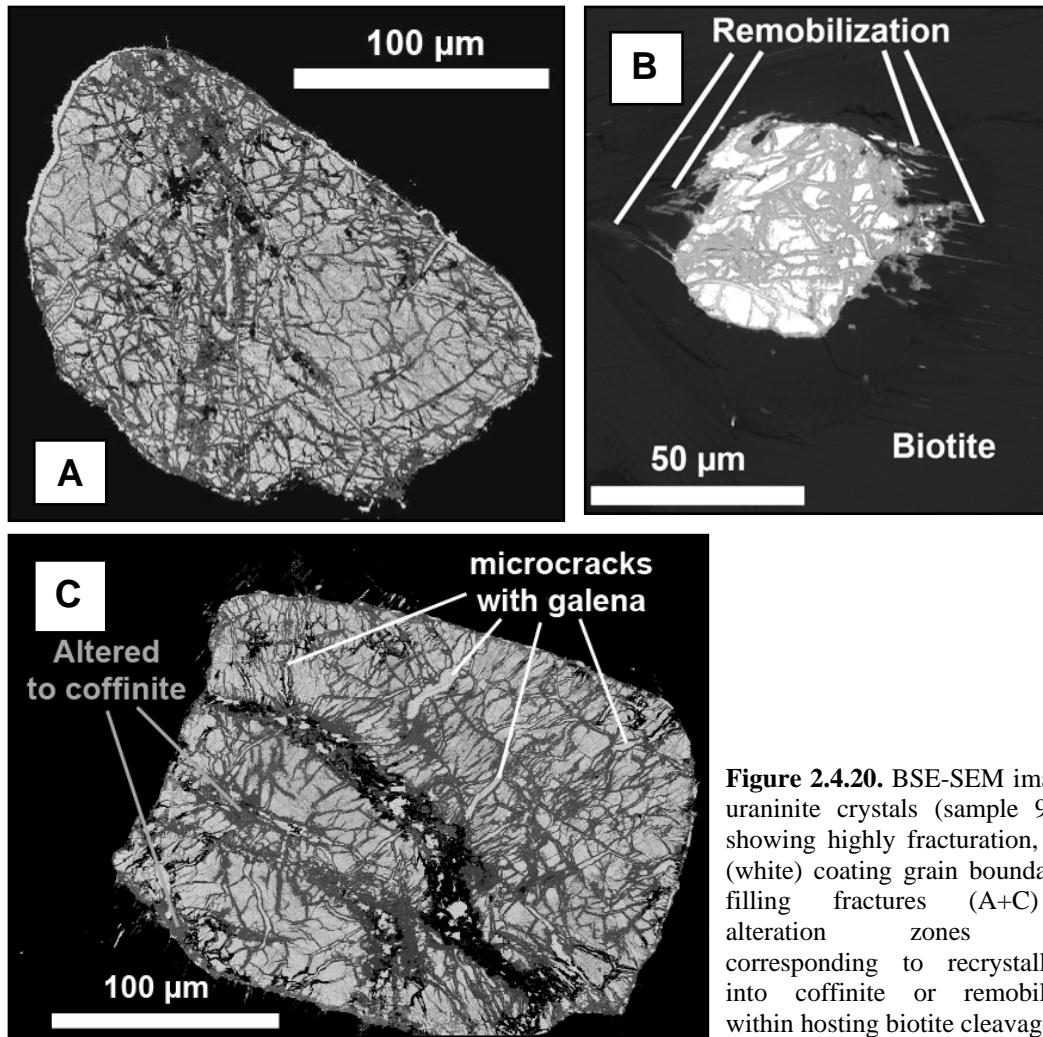


**Figure 2.4.20.** BSE-SEM images of uraninite crystals (sample 9375-3) showing highly fracturation, galena (white) coating grain boundary and filling fractures (A+C) and alteration zones (grey) corresponding to recrystallization into coffinite or remobilization within hosting biotite cleavage (B).

**Table 2.4.5.** Average chemical composition (in weight percent) of uraninite crystals hosted in the Archean pegmatite 9375-3 from the Mustalampi area in Karelia (A, B and C refer to 3 separate grains shown in Fig. 2.4.20).

Sample Uraninite Phase	Quartz-Biotite Pegmatite 9375-3							
	A		B		C		Average	
EMPA	Pristine (high BSE) Mean±σ (N=36)	Altered (low BSE) Mean±σ (N=14)	Pristine (high BSE) Mean±σ (N=10)	Altered (low BSE) Mean±σ (N=10)	Pristine (high BSE) Mean±σ (N=34)	Altered (low BSE) Mean±σ (N=13)	Pristine (high BSE) Mean±σ (N=80)	Altered (low BSE) Mean±σ (N=37)
Al <sub>2</sub> O <sub>3</sub>	<D.L.	0.86 ± 0.28	<D.L.	1.08 ± 0.17	<D.L.	0.99 ± 0.32	0.07 ± 0.09	0.96 ± 0.28
SiO <sub>2</sub>	1.20 ± 1.32	16.68 ± 3.72	1.23 ± 1.23	16.57 ± 1.69	1.66 ± 1.59	11.82 ± 3.49	1.40 ± 1.43	14.94 ± 3.90
P <sub>2</sub> O <sub>5</sub>	<D.L.	<D.L.	<D.L.	<D.L.	<D.L.	<D.L.	<D.L.	<D.L.
K <sub>2</sub> O	0.16 ± 0.04	0.12 ± 0.03	0.15 ± 0.05	0.17 ± 0.07	0.16 ± 0.04	0.21 ± 0.08	0.16 ± 0.04	0.17 ± 0.07
Na <sub>2</sub> O	<D.L.	<D.L.	<D.L.	<D.L.	<D.L.	<D.L.	<D.L.	<D.L.
CaO	1.37 ± 0.91	1.02 ± 0.17	1.28 ± 0.82	0.90 ± 0.11	1.33 ± 0.43	1.16 ± 0.33	1.34 ± 0.72	1.04 ± 0.25
SO <sub>2</sub>	0.77 ± 0.49	1.54 ± 1.65	1.14 ± 0.95	1.79 ± 0.76	0.79 ± 0.52	1.37 ± 1.31	0.82 ± 0.58	1.55 ± 1.31
TiO <sub>2</sub>	<D.L.	0.35 ± 0.26	<D.L.	0.27 ± 0.08	<D.L.	0.15 ± 0.06	<D.L.	0.26 ± 0.19
V <sub>2</sub> O <sub>3</sub>	<D.L.	<D.L.	<D.L.	<D.L.	<D.L.	<D.L.	<D.L.	<D.L.
FeO	0.53 ± 0.20	0.40 ± 0.62	1.02 ± 0.37	0.55 ± 0.26	0.56 ± 0.17	0.46 ± 0.34	0.61 ± 0.27	0.46 ± 0.45
MgO	<D.L.	<D.L.	<D.L.	<D.L.	<D.L.	<D.L.	<D.L.	<D.L.
MnO	0.46 ± 0.25	<D.L.	0.82 ± 0.52	<D.L.	0.50 ± 0.21	<D.L.	0.53 ± 0.30	<D.L.
MoO <sub>3</sub>	<D.L.	<D.L.	<D.L.	<D.L.	<D.L.	<D.L.	<D.L.	<D.L.
Ta <sub>2</sub> O <sub>5</sub>	<D.L.	<D.L.	<D.L.	<D.L.	<D.L.	<D.L.	<D.L.	<D.L.
Y <sub>2</sub> O <sub>3</sub>	0.90 ± 0.24	1.10 ± 0.26	0.74 ± 0.28	1.12 ± 0.14	1.08 ± 0.28	0.86 ± 0.57	0.96 ± 0.29	1.02 ± 0.39
La <sub>2</sub> O <sub>3</sub>	<D.L.	<D.L.	<D.L.	<D.L.	<D.L.	<D.L.	<D.L.	<D.L.
Ce <sub>2</sub> O <sub>3</sub>	0.32 ± 0.18	0.68 ± 0.25	0.35 ± 0.22	1.01 ± 0.15	<D.L.	0.28 ± 0.12	0.26 ± 0.19	0.63 ± 0.35
Nd <sub>2</sub> O <sub>3</sub>	0.61 ± 0.25	0.72 ± 0.21	<D.L.	0.86 ± 0.24	<D.L.	<D.L.	<D.L.	0.62 ± 0.32
Dy <sub>2</sub> O <sub>3</sub>	<D.L.	<D.L.	<D.L.	<D.L.	<D.L.	<D.L.	<D.L.	<D.L.
PbO	13.08 ± 3.96	6.78 ± 5.57	12.66 ± 3.95	6.60 ± 1.51	13.06 ± 2.55	10.75 ± 6.22	13.02 ± 3.39	8.13 ± 5.34
ThO <sub>2</sub>	10.00 ± 1.03	10.35 ± 3.41	10.26 ± 0.74	7.93 ± 1.30	9.23 ± 0.74	11.04 ± 6.12	9.71 ± 0.97	9.94 ± 4.33
UO <sub>2</sub>	65.87 ± 1.70	49.27 ± 7.13	65.22 ± 2.20	49.36 ± 4.15	65.66 ± 2.41	50.59 ± 9.43	65.70 ± 2.07	49.75 ± 7.26
<b>Total</b>	95.68 ± 1.24	90.53 ± 3.58	95.92 ± 1.96	88.92 ± 3.06	95.10 ± 1.54	90.59 ± 3.06	95.46 ± 1.49	90.12 ± 3.26

**Notes:** "high BSE"= bright in BSE images; "low BSE"=dark grey; "<D.L."=below detection limit (Al=0.06wt%; Si=0.05wt%; P=0.06wt%; K=0.08wt%; Na=0.12wt%; Ca=0.06wt%; S=0.07wt%; Ti=0.07wt%; V=0.09wt%; Fe=0.14wt%; Mg=0.04wt%; Mn=0.16wt%; Mo=0.18wt%; Y=0.12wt%; La=0.22wt%; Ce=0.23wt%; Nd=0.52wt%; Dy=0.59wt%; Ta=0.21wt%; Pb=0.19wt%; Th=0.15wt%; U=0.38wt%).

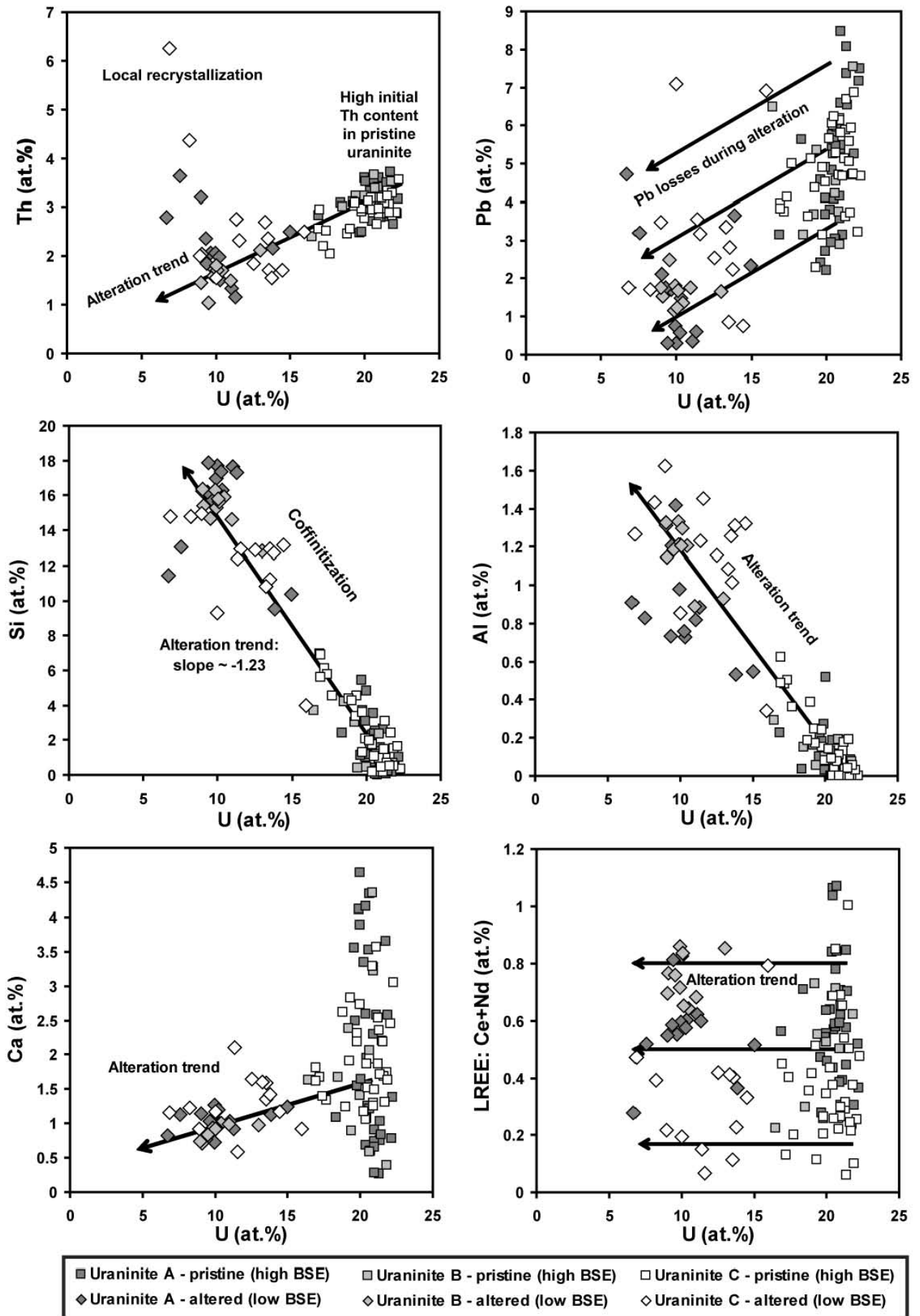


**Figure 2.4.21.** Binary diagrams Th, Pb, Si, Al, Ca and LREE vs. U (in atomic percent) illustrating the variations of the chemical composition in uraninite crystals from the Mustalampi pegmatite 9375-3 with alteration (A, B and C refer to the grains shown in Fig. 2.4.20).

Chemical ages calculated for the 117 EMP analytical spots realized in the 3 uraninite grains are plotted in Fig. 2.4.22 and yield a broadly Gaussian repartition with a peak centred around 1500-1600 Ma that may correspond to a rough age approximation for the hydrothermal event that led to the coffinitization of uraninite. Only a few points have retained an Archean age.

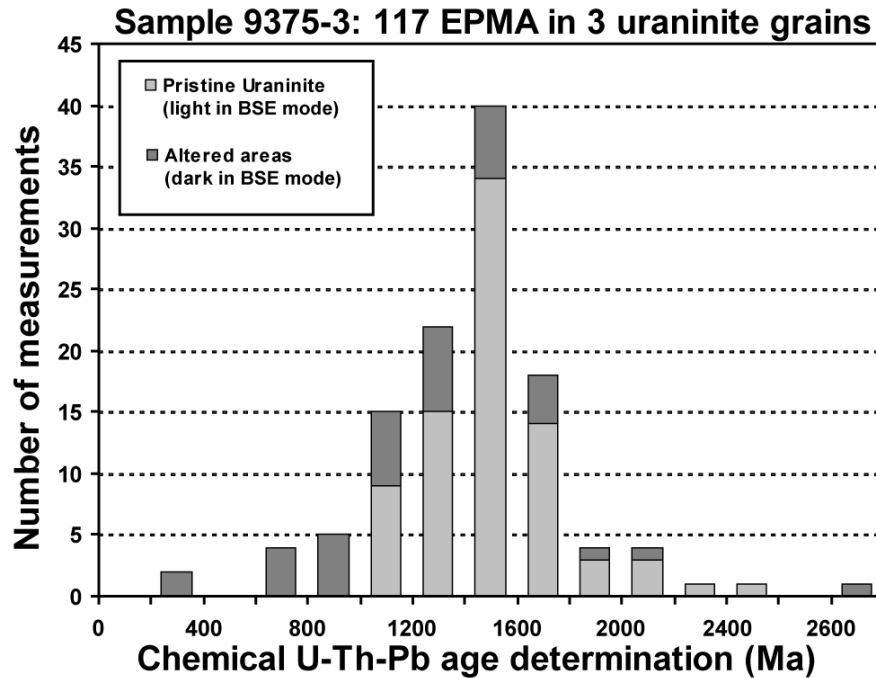


**Figure 2.4.22.** Histogram showing the repartition of chemical U-Th-Pb ages determined from 117 EMPA in uraninite grains from the Mustalampi pegmatite (sample 9375-3).

Isotopic U-Pb analyses (SIMS) in the less altered parts of the two uraninite crystals A and C have been also done. The 5 analytical spots have been chosen in areas without galena veinlets but however it was impossible to separate uniquely the lighter areas observed in BSE images and the results presented in Table 2.4.6 represent a mixture of coffinitized areas (dark grey) with pristine uraninite. Therefore, we have not obtained the age of deposition of the pristine uraninite but an intermediate age between that of the pristine uraninite and the altered part.

**Table 2.4.6.** Ion probe U-Pb results for 2 uraninite grains from the Mustalampi pegmatite 9375-3

Sample	$\frac{^{204}\text{Pb}}{^{206}\text{Pb}}$	$\frac{^{207}\text{Pb}}{^{206}\text{Pb}}$	$\frac{^{208}\text{Pb}}{^{206}\text{Pb}}$	$\frac{^{207}\text{Pb}}{^{206}\text{Pb}}$	Age (Ma)	$\frac{^{206}\text{Pb}}{^{238}\text{U}}$	Age (Ma)
<b>Uraninite Crystal</b>							
Spot number							
<b>9375-3</b>							
<b>Grain A</b>							
Spot 1	0.000107 (0)	0.112 (2)	0.039 (6)		1854 ± 3		1232 ± 55
Spot 2	0.000121 (0)	0.124 (1)	0.043 (5)		2027 ± 2		1419 ± 63
Spot 3	0.000124 (0)	0.125 (2)	0.043 (6)		2046 ± 3		1710 ± 76
<b>Grain C</b>							
Spot 4	0.000311 (1)	0.138 (2)	0.054 (8)		2214 ± 3		1550 ± 69
Spot 5	0.000213 (1)	0.148 (2)	0.050 (8)		2338 ± 2		1689 ± 75

**Notes:** numbers in brackets indicate errors ( $1\sigma \cdot 10^{-5}$  for  $^{204}\text{Pb}/^{206}\text{Pb}$ ,  $1\sigma \cdot 10^{-3}$  for  $^{207}\text{Pb}/^{206}\text{Pb}$  and  $^{208}\text{Pb}/^{206}\text{Pb}$ ),  $^{207}\text{Pb}/^{206}\text{Pb}$  ages are corrected from the common Pb.

All the points are highly discordant, indicating a strong radiogenic lead loss. When taking into account the maximum error deviation, the  $^{206}\text{Pb}/^{238}\text{U}$  ages calculated range from 1177 to 1786 Ma in grain A and from 1481 to 1764 Ma in grain C. The U-Pb isotopic composition plots in the Concordia diagram show a highly discordant distribution (Fig. 2.4.23). An upper intercept has been obtained at  $2030 \pm 5$  Ma for the two analytical spots aligned in the plot for grain A but the MSWD value is remarkably high (19) and thus this age cannot be considered.

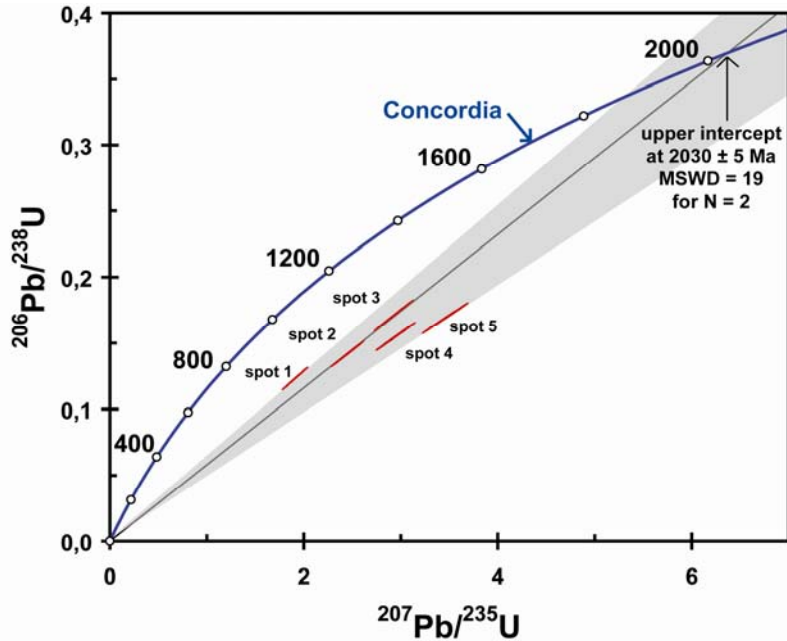


**Figure 2.4.23.** Concordia diagram for the five isotopic measurements realized in 2 uraninite grains from the Mustalampi pegmatite (sample 9375-3). The  $2\sigma$  error ellipse for each analytical spot is represented in red. The grey zone represents the large panel of intercepts possibilities with the scattered results. The black line corresponds to the Discordia obtained with spots 2 and 3 for the same grain. The upper intercept of the Discordia calculated using the isoplot software (Ludwig, 1999) is at  $2030 \pm 5$  Ma.

The  $^{207}\text{Pb}/^{206}\text{Pb}$  ages calculated range from 1.85 to 2.05 Ga in grain A and from 2.21 to 2.33 Ga in grain C (Table 2.4.6 and Fig. 2.4.24). Considering the SEM observations, uraninite has suffered undoubtedly radiogenic lead loss partly redeposited in galena veinlets and coating grains. Therefore, the oldest apparent age obtained in grain C rising  $2338 \pm 2$  Ma is considered as the minimal age of uraninite. This result is very close to the  $^{207}\text{Pb}/^{206}\text{Pb}$  age at  $2322 \pm 15$  Ma previously obtained by Kouvo from the Geological Survey of Finland (reported in Pekkarinen, 1979) in uraninite from a mineralized quartz vein intruding the Kiihtelysvaara mica gneiss approximately 0.5 km southwest of the Mustalampi sampling area. The uraninite studied in this previous work was a subeuhedral cubic crystal surrounded by molybdenite scales as observed in our gneiss samples. Uraninite was considered as epigenetic in origin considering its occurrence within late quartz veins. Here, uraninite is considered to be magmatic in origin because of its relation with the primary mineral assemblage and also because of its high Th content that was certainly incorporated during high temperature melting processes. Therefore, the age of primary crystallization is older than  $2322 \pm 15$  Ma, thus probably of Archean age, and all the younger apparent ages calculated from the U-Pb or Pb-Pb measurements in this study represents recrystallization ages (coffinitization) with U and Pb losses.

The large variation in U-Th-Pb chemical ages and the partly reset U-Pb isotopic system are interpreted as reflecting intermediate ages between the Archean crystallization of uraninite during magma cooling, the age of the peak regional metamorphism about 1800 Ma ago during the Svecofennian Orogeny and finally episodic and subsidiary later hydrothermal remobilization event(s).

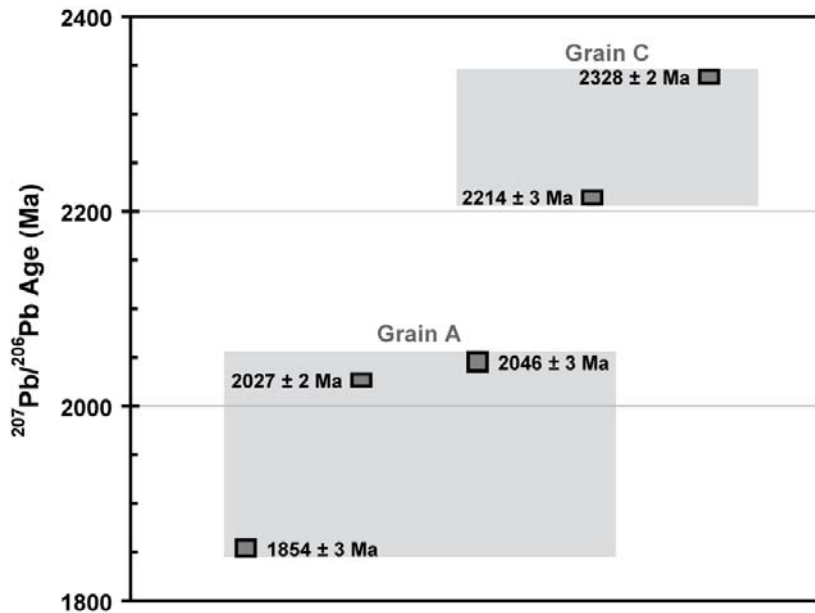


**Figure 2.4.24.** Distribution of  $^{207}\text{Pb}/^{206}\text{Pb}$  ages (Ma) measured in 2 uraninite grains from the Mustalampi pegmatite (sample 9375-3 from Karelia, Finland). The darker grey bars represent  $2\sigma$  errors.

Y and REE concentrations in uraninite grains have also been measured by SIMS. The results are presented in Table 2.4.7 in comparison with the abundances measured by Bonhoure (2007) in the magmatic uraninites from the Rössing alaskite (Namibia) using the same analytical procedure. Spots 1 and 2 have been measured in grain A and spot 3 in grain C respectively. Y and REE abundances incorporated in the Mustalampi uraninites are high: 1.7 wt% Y (1.48-1.9 wt%) and  $\Sigma\text{REE} \sim 1.6$  wt% (1-2.35 wt%) but their average contents are lower than in the Rössing alaskite uraninites ( $m = 7.1$  wt% Y and  $\Sigma\text{REE} \sim 2.5$  wt%). The chondrite-normalized REE distribution patterns (Fig. 2.4.25) display the characteristic shape of uraninite from a magmatic origin (Bonhoure, 2007) with concentrations between  $10^3$  and  $10^4$  times the chondrites and a slightly negative Eu anomaly ( $0.30 < \text{Eu}/\text{Eu}^* < 0.84$ ) corresponding to fractionation during the early plagioclase crystallization in the magma. The REE patterns of uraninite of the Mustalampi biotite-rich pegmatites reflects the composition of the magma from which it derives, which was probably less fractionated than for the leucocrate Rössing alaskite characterized by stronger negative Eu anomaly ( $0.09 < \text{Eu}/\text{Eu}^* < 0.15$ ). Weak Eu anomaly is generally a characteristic feature observed in the Archean rocks (Condie et al., 1985; Gao and Wedepohl, 1995) that probably represent sources of the Mustalampi pegmatites.

**Table 2.4.7.** SIMS determinations of Y and REE contents (ppm) in the uraninite from pegmatites of the Baltic Shield (this study) compare to the chemistry of uraninite from the Rössing alaskite in Namibia (Bonhoure, 2007)

Sample	N°	Y	La	Ce	Pr	Nd	Sm	Eu	Gd*	Tb	Dy	Ho	Er	Tm	Yb*	Lu	$\Sigma$ REE	[La/Sm] <sub>N</sub>	[Gd/Yb] <sub>N</sub>	Eu/Eu*	
<i>Magmatic uraninites from the Polyarnoe pegmatite in the Kola Peninsula (Russia) – this study</i>																					
52-2/2	1	27 593	2 329	9 285	1 271	7 131	2 334	395	2 722	466	2 177	292	1 203	272	1 432	155	31 464	0.63	1.57	0.48	
	2	22 690	779	2 778	580	4 259	2 696	168	2 976	492	2 639	334	985	101	556	65	19 406	0.18	4.43	0.18	
	3	16 324	835	5 325	858	4 201	1 433	203	1 592	264	1 396	188	612	89	687	116	17 797	0.37	1.91	0.41	
<b>Average</b>		<b>22 202</b>	<b>1 314</b>	<b>5 796</b>	<b>903</b>	<b>5 197</b>	<b>2 154</b>	<b>255</b>	<b>2 430</b>	<b>407</b>	<b>2 070</b>	<b>271</b>	<b>933</b>	<b>154</b>	<b>892</b>	<b>112</b>	<b>22 889</b>	<b>0.39</b>	<b>2.64</b>	<b>0.35</b>	
<i>Magmatic uraninites from the Mustalampi pegmatite in Karelia (Finland) – this study</i>																					
9375-3	1	14 841	217	1 581	345	2 214	1 205	141	1 469	258	1 545	292	831	96	490	50	10 734	0.13	0.95	0.30	
	2	16 531	301	1 898	393	2 292	1 364	453	1 711	306	1 884	357	1 027	133	642	58	12 818	0.15	0.86	0.84	
	3	18 981	865	4 470	911	5 436	2 472	412	2 763	460	2 703	504	1 421	153	801	86	23 455	0.21	1.19	0.40	
<b>Average</b>		<b>16 784</b>	<b>461</b>	<b>2 649</b>	<b>550</b>	<b>3 314</b>	<b>1 680</b>	<b>335</b>	<b>1 981</b>	<b>341</b>	<b>2 044</b>	<b>384</b>	<b>1 093</b>	<b>127</b>	<b>644</b>	<b>65</b>	<b>15 669</b>	<b>0.16</b>	<b>1.00</b>	<b>0.51</b>	
<i>Magmatic uraninites from the Rössing Alaskite (Namibia) – data from Bonhoure (2007)</i>																					
Rössing	1	61 702	320	4 301	518	2 718	1 505	94	2 440	490	3 796	769	2 401	398	1 582	73	21 404	0.13	1.27	0.15	
	2	68 134	268	3 909	494	2 643	1 541	88	2 670	549	4 259	889	2 852	446	1 770	81	22 460	0.11	1.25	0.13	
	3	110 383	802	9 506	430	1 444	1 885	86	4 057	891	7 652	1 155	5 606	1 026	4 257	243	39 039	0.27	0.79	0.09	
	4	45 505	270	3 581	429	2 659	1 386	75	1 987	379	3 144	694	1 903	318	1 254	56	18 135	0.12	1.31	0.14	
<b>Average</b>		<b>71 431</b>	<b>415</b>	<b>5 324</b>	<b>468</b>	<b>2 366</b>	<b>1 579</b>	<b>86</b>	<b>2 788</b>	<b>577</b>	<b>4 712</b>	<b>877</b>	<b>3 190</b>	<b>547</b>	<b>2 215</b>	<b>114</b>	<b>25 259</b>	<b>0.16</b>	<b>1.15</b>	<b>0.13</b>	

\* Gd and Yb are calculated from Sm-Tb and Tm-Lu concentrations respectively because of analytical interferences forbidding their accurate measurements:  $Gd^* = Sm + 2/3Tb$  and  $Yb^* = (Tm + Lu)/2$   
 $[X]_N =$  normalized to chondrite values:  $F_{Eu/Er}^* = F_{Eu}/(F_{Sm} \cdot Gd \cdot Y)$

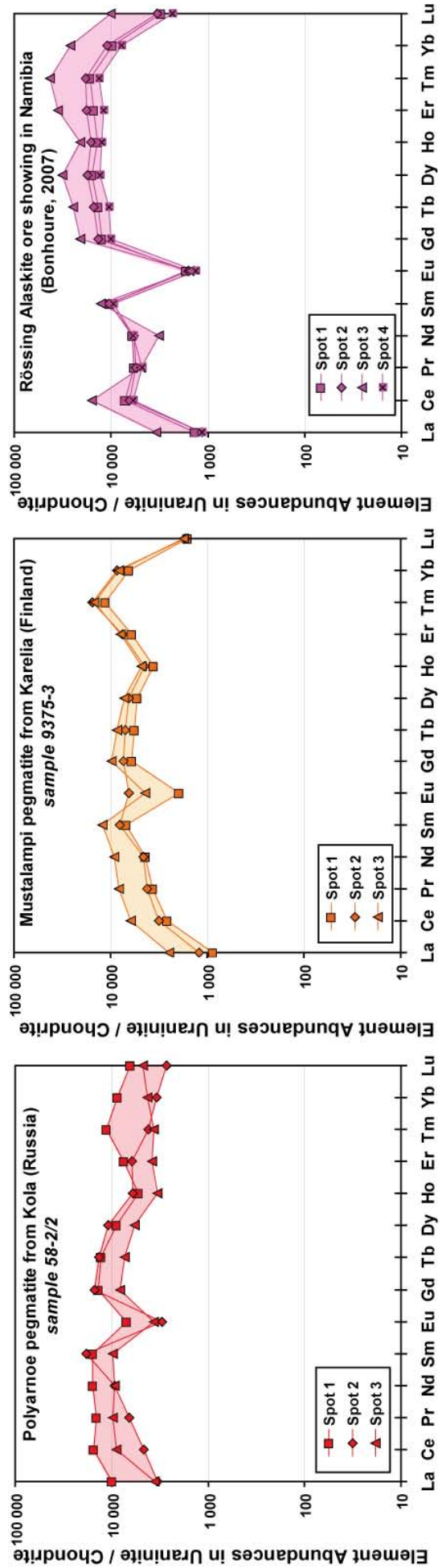


**Figure 2.4.25.** Chondrite-normalized spectra of REE abundances in magmatic uraninites from S-type granitoids (data from Table 2.4.7).

**Huhtilampi granite (samples 9375-16 and 9375-17)**

The Huhtilampi granitic batholith was emplaced at about 2.6 Ga ago (zircon U-Pb analysis, Wetherill et al., 1962). The batholith is elongated north-westerly parallel to the Janisjarvi fault zone (Fig. 2.4.2). It has been sampled its western edge close to its contact with the Paleoproterozoic Karelian sedimentary formations. The Archean granite shows a high radioactive background between 300 to up to 500 cps measured with a gamma scintillometer (Caillat et al., 2006). The two samples collected from outcrops are medium grained, isotropic and characterized by a strong red coloration (Fig. 2.4.26).



**Figure 2.4.26.** Huhtilampi granite samples characterized by a red coloration (scale bar = 1 cm).

Microscopically, the Huhtilampi granite is principally composed of feldspar, quartz and minor biotite with a granoblastic texture (Fig. 2.4.27). Both samples have a quite similar whole-rock geochemistry (Table 2.4.2). They plot in the field of high-K calc-alkaline granites with high silica (73.09-74.82 wt% SiO<sub>2</sub>) and potassium (6.3-6.72 wt% K<sub>2</sub>O) contents (Fig. 2.4.6). They are slightly peraluminous with A/CNK = 1.4-1.6 and A/NK = 1.11-1.13. The mineralogical composition of the granite is dominated by K-feldspar, mainly microcline, and minor plagioclase (Fig. 2.4.28) in accordance with their high K<sub>2</sub>O/Na<sub>2</sub>O ratios comprised between 1.89 and 2.12 and positive P parameters (15.46 and 35.38; Fig. 2.4.33). K-feldspar, from 1 to 3 mm wide, often exhibits finely dispersed sericite and muscovite crystals and late carbonates (Fig. 2.4.29). Quartz is usually of small grain-size not exceeding 1 mm with undulous extinction and shows occasionally ternary junctions between grains. Biotite is regularly distributed in the rock and represents the most abundant dark coloured mineral with minor titanite and hematite. Biotite is commonly altered to chlorite and sometimes is associated to opaque mineral accumulation, aggregates of idiomorphic cubes of pyrite (Fig. 2.4.30). Femic minerals and white micas issued from the feldspar alteration are less abundant than in the Mustalampi gneisses giving lower A and B parameters, A = 9.5-16.31 and B = 13.30- 34.41 (Fig. 2.4.34).

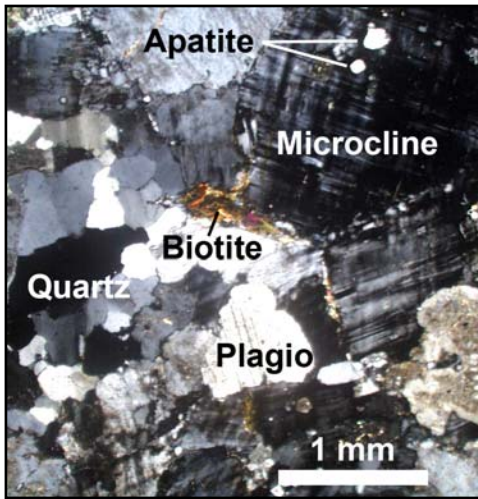


**Figure 2.4.27.** Granoblastic texture of quartz and feldspar with minor interstitial biotite (sample 9375-17, crossed polarized transmitted light).

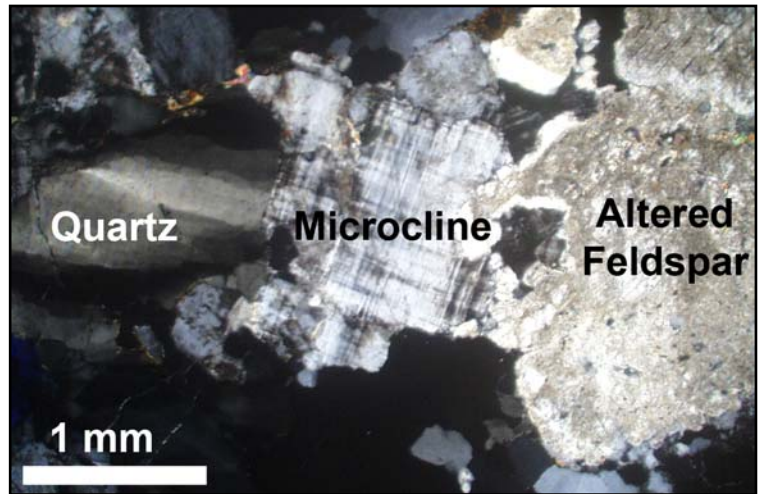


**Figure 2.4.28.** Quartz with undulous extinction and feldspar xenomorphic grains with recrystallized borders (sample 9375-17, crossed polarized transmitted light).

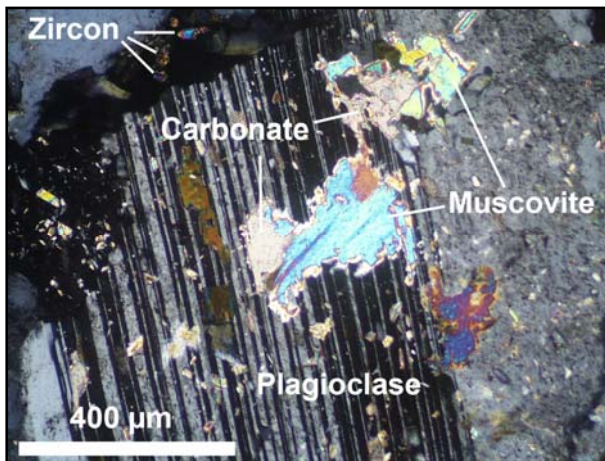


**Figure 2.4.29.** Plagioclase altered to sericite and muscovite with late carbonate minerals (sample 9375-16, crossed polarized transmitted light).

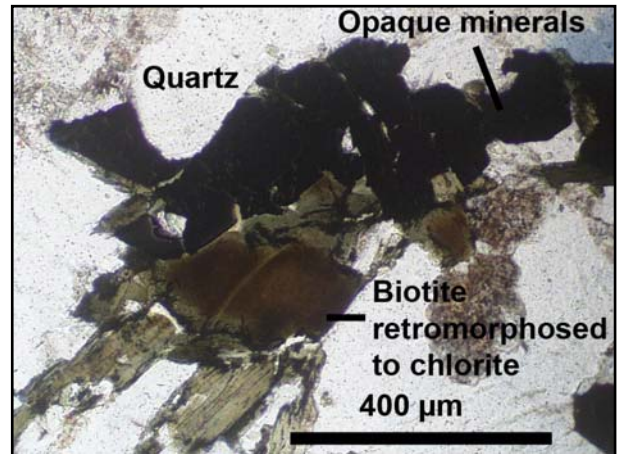


**Figure 2.4.30.** Biotite altered to chlorite and associated with pyrite (opaque) and disseminated hematite giving a reddish coloration (sample 9375-16, natural transmitted light).

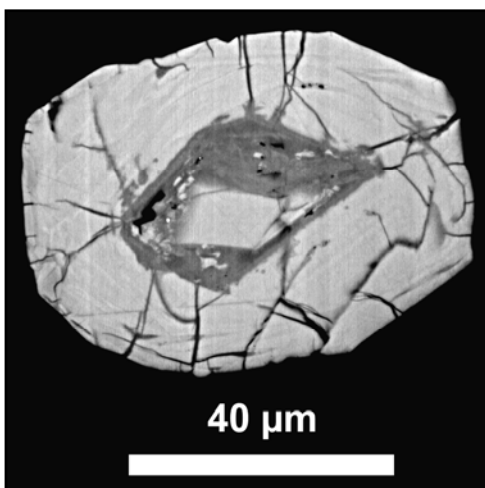


**Figure 2.4.31.** BSE-SEM image of a zircon grain (sample 9375-16).

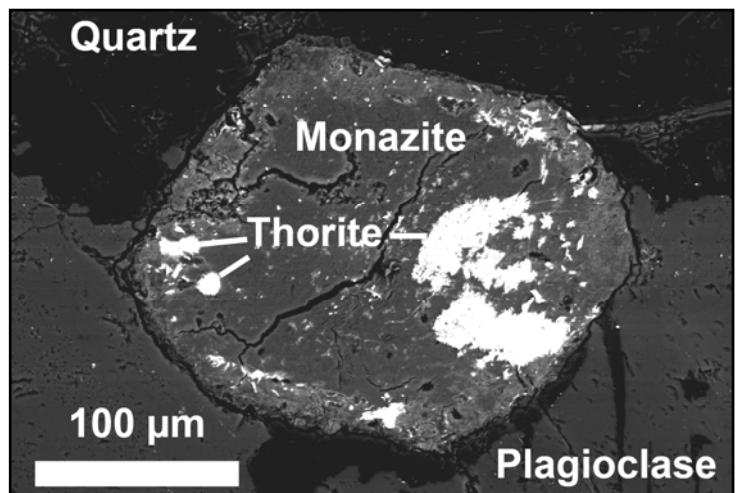


**Figure 2.4.32.** BSE-SEM image of monazite with thorite inclusions (sample 9375-17).

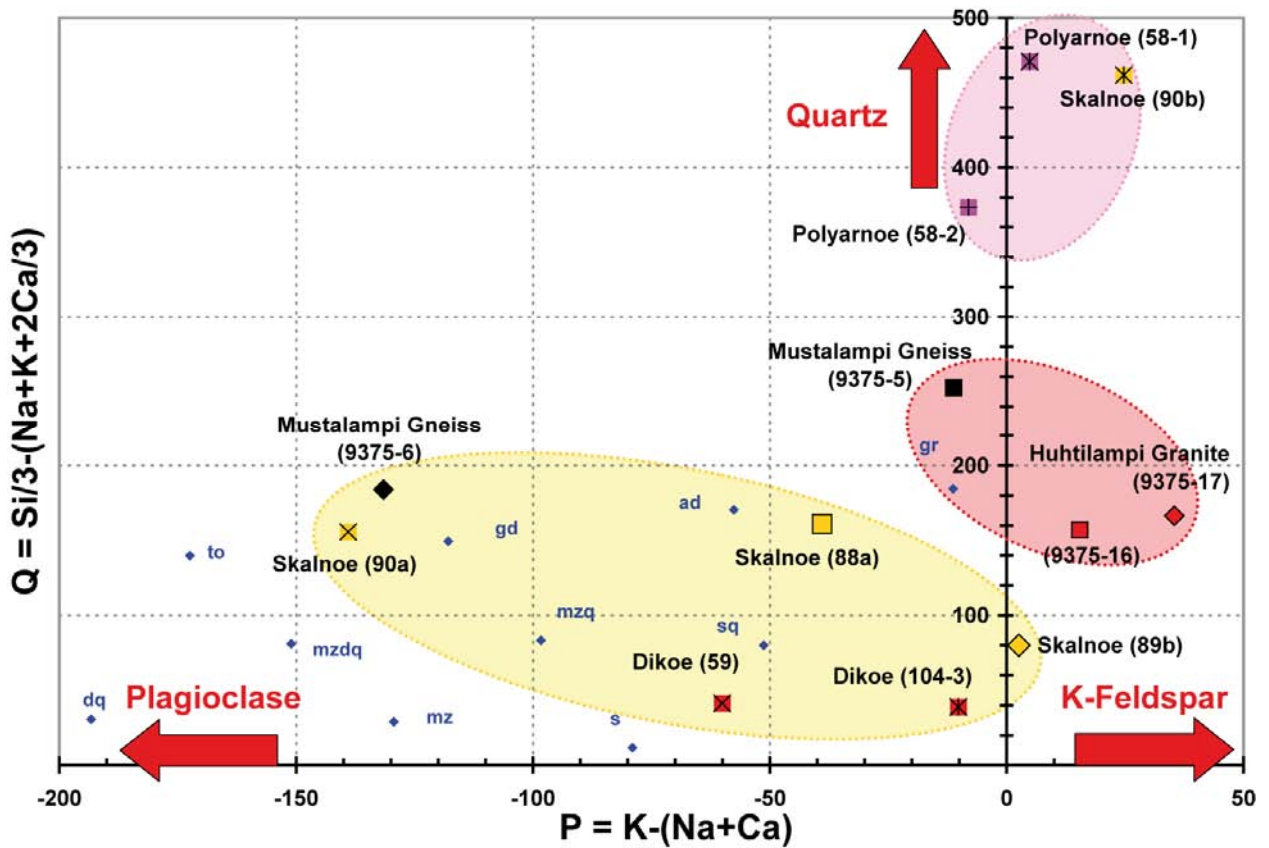


Figure 2.4.33. Variation of P versus Q parameters for Kola and Karelia basement rocks from the Baltic Shield (diagram from Debon and Lefort, 1988). The Q and P values are calculated in thousands of cations. Rock composition references are indicated: mz = monzonite; mzq = quartz-monzonite; mzdq = quartz monzodiorite; dq = quartz diorite; s = syenite; sq = quartz syenite; to = tonalite; gd = granodiorite; ad = adamellite; gr = granite.

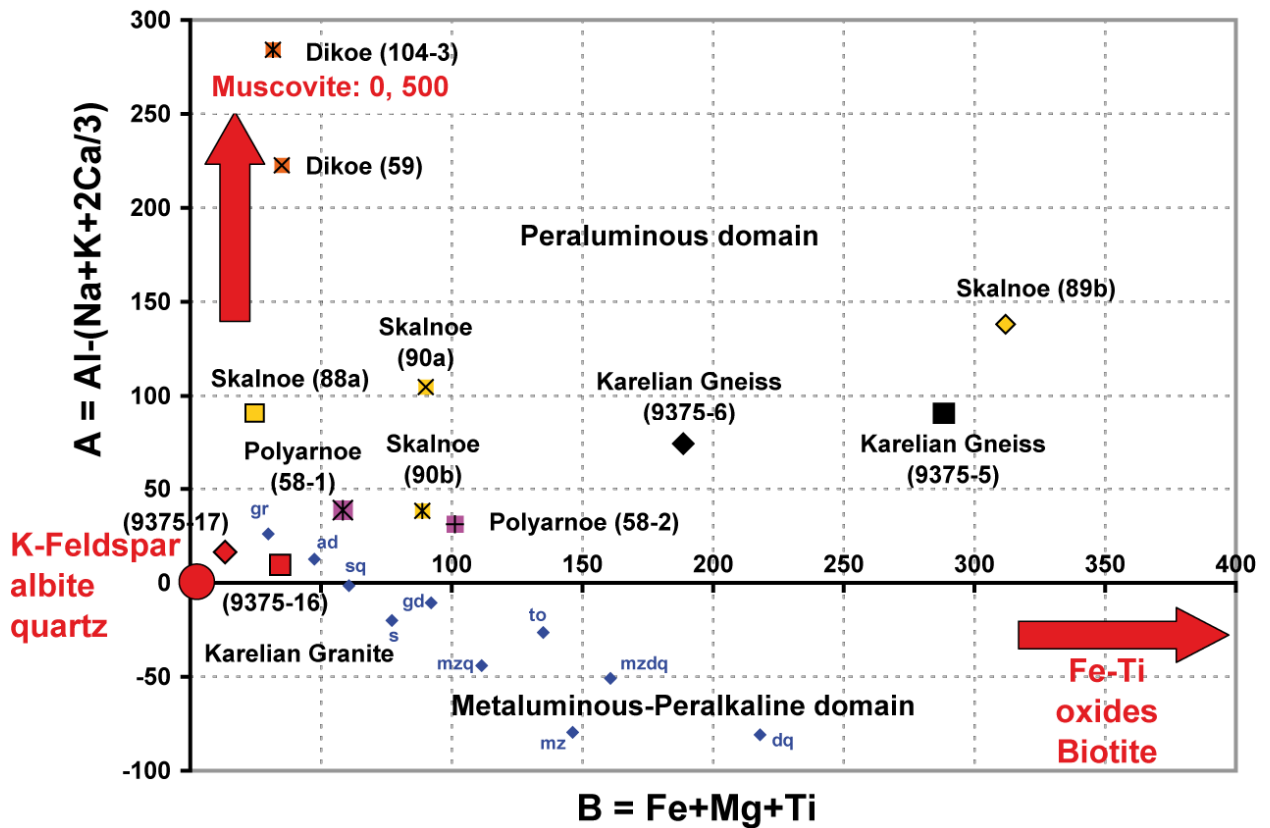


Figure 2.4.34. Variation in the peraluminous index A with the fractionation parameter B (coloration index) for Kola and Karelia basement rocks (diagram from Debon and Lefort, 1988). The A and B parameters are calculated in thousands of cations.

The Huhtilampi highly potassic granites are remarkably rich in Ba (989.8-1063 ppm), Rb (179.4-203.4 ppm), Sr (202.2-203.4 ppm) and REE ( $\Sigma = 456.43-745.43$  ppm). They display more fractionated REE patterns than the Mustalampi gneisses (Fig. **2.4.8**) with stronger enrichment in LREE ( $[\text{Ce}/\text{Yb}]_{\text{N}} = 73.76-78$ ), lower depletion in HREE ( $[\text{Gd}/\text{Yb}]_{\text{N}} = 3.12-3.69$ ), a sigmoidal shape and a stronger negative Eu anomaly ( $\text{Eu}/\text{Eu}^* = 0.44-0.62$ ). The more fractionated REE pattern compared to the older enclosing rocks (amphibolite and biotite-rich gneisses) reflects the higher fractionation of the magma from which they derive.

The Huhtilampi granites are slightly enriched in U (6.27-8.14 ppm) and especially in Th (72.59-112.8 ppm) compare to the mean crust (Fig. **2.4.9**) giving high Th/U ratios (8.92-18) suggesting that most of radioelements are within accessory minerals as monazite. This is confirmed by the petrographic and SEM observations showing that both samples host minor amounts of apatite (Fig. **2.4.27**) and zircon (Fig. **2.4.31**), but abundant monazite (Fig. **2.4.32**) disseminated within quartz and feldspars. The apatite composition analysed by EMP (Table **2.4.4**) is that of classical apatite ( $m = 54.95 \pm 0.42$  wt% CaO and  $42.03 \pm 0.44$  wt%  $\text{P}_2\text{O}_5$ ) with U and Th concentrations under detection limits ( $\text{U} < 0.36$  wt% and  $\text{Th} < 0.09$  wt%). The zircons are well zoned in BSE imaging (Fig. **2.4.31**). The darker grey zone in the core of the zircon grain and the radial fracturation are caused by metamictization of the crystals. On the other hand, hydrothermal alteration has partially altered monazite crystals with the leaching of P and REE, leaving a residual mineral with higher average atomic number (Fig. **2.4.32**) filling only partially the dissolution cavities (Fig. **2.4.35**). EDS analyses revealed the residual minerals are a mixture between thorite and allanite (LREE and Si mainly with minor Th, Ca, Mg and Fe).

## INTRUSIVE-TYPE U OCCURRENCES FROM THE LITSA AREA IN THE KOLA PROVINCE

The Litsa area located in northeastern Kola Peninsula contains various types of U occurrences within intrusive rocks, migmatized metasediments, mafic dykes or veins crosscutting gneisses (Fig. 2.4.36), estimated all together at 102,000 tU at an average grade of 0.01 %U and up to 3% (IAEA data after Afanasieva, 2006 and Afanasieva et al., 2007). The U occurrences studied in this section are intrusive-type from Dikoe, Skalnoe and Polyarnoe ore showings located in the Central Kola terrane near the boundary separating the Murmansk and Kola blocks, two structural units of the Archean Baltic Shield. Archean metamorphic rocks in this region comprise mainly peraluminous gneisses and schists from the Kola Suite oriented along northwestern lineation corresponding to pluri-kilometric folds separate by a limb distance of 3 to 4 km (Savitskii et al., 1995). The age of the Kola Suite long time considered Neoproterozoic remains ambiguous because of recent whole-rock Sm-Nd dating in the metamorphic host-rocks and uraninite Pb-Pb age dating yielding Paleoproterozoic ages (Daly et al., 2006). However, it is constrained by the late Litsa granodiorite and granite intrusions forming the NE-SW striking batholiths (in red on the map Fig. 2.4.36) dated at 1.77-1.76 Ga (Vetrin et al., 2006). Uranium-bearing pegmatoid granites are injected in strongly deformed biotite, garnet-biotite and two-mica gneisses of the Tundra series. Intrusions are vein-like or lenticular bodies along fault-related systems or follow boudinage zones along the axial plans or steep-dipping limbs of the regional anticlines.

Samples of uraninite-bearing pegmatites from the Litsa area were collected in outcrops during field trip excursion in July 2007 (Kister et al., 2007). The outcrop location and a brief sample description are given in Table 2.4.8.

**Table 2.4.8.** Location of outcrops sampled during field trip 2007 in the Litsa area, Kola Peninsula (Russia)

<i>U occurrence</i>	<i>WGS84 coordinates</i>		<i>Sample</i>	<i>Rock-type</i>
	<i>Latitude</i>	<i>Longitude</i>		
Dikoe	32.3784	69.3097	59	Leucocratic pegmatite with muscovite- rich shearing
			104-3	Leucocratic pegmatite with muscovite- rich shearing
Skalnoe	31.63785	69.5865	88a	Leucocratic pegmatite with muscovite- rich shearing
			89b	Biotite-rich gneiss
			90a	Fractured quartz-feldspar-biotite pegmatite
			90b	Fractured quartz-feldspar-biotite pegmatite
Polyarnoe	31.18064	69.46264	58-1	Quartz-feldspar-biotite gneiss
			58-2	Quartz-feldspar-biotite gneiss

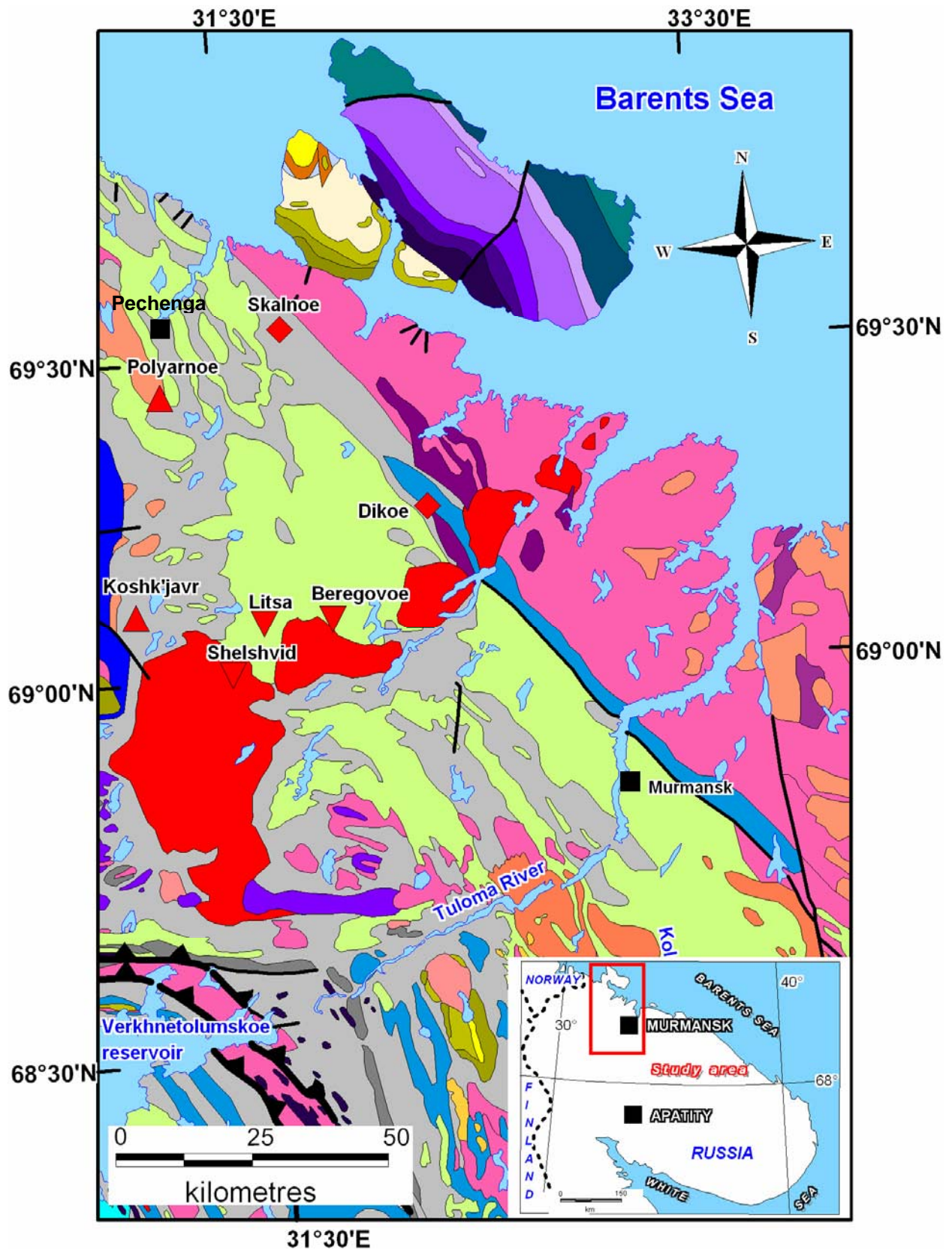


**Figure 2.4.36.** Geological map and location of the uranium occurrences from the Litsa region in northeastern Kola Peninsula, Russia (modified from Afanasieva et al., 2007).

<b>LITHOLOGICAL LEGEND</b>	
	Fault
	Overlapping fault
	Arkose and polymict sandstones, siltstone, mudstone
	Quartz, arkose and polymict sandstones, siltstone with phosphorite
	Dolomite, marl, siltstone
	Arkose and polymict sandstones, siltstone with phosphorite lenses
	Arkose and polymict sandstones, siltstone, variegated mudstone
	Quartz and arkose sandstones, siltstone / dolomite, limestone, siltstone, mudstone
	Intercalation of phyllite, sandstone and siltstone, carbonate rocks lenses
	Intercalation of phyllite, sandstone and siltstone
	Polymict conglomerate, sandstones
	Polymict and arkose sandstones, siltstone with conglomerate lenses
	Polymict and arkose sandstones, siltstone
	Polymict conglomerate
	Granodiorite, granite / leucogranite
	Picrite and diabase porphyries, tuff / rhyolite, dacite, tuff
	Charnockite, granite / monzodiorite, granite / alkaline granite, syenite
	Leucogranite, granodiorite
	Enderbite, granite, granodiorite, monzodiorite
	Diorite, granodiorite, plagiogranite
	Micaceous, garnet-micaceous paragneiss and schiste
	Harzburgite / troctolite, gabbro
	Acid and medium metavolcanics / Hastingsite gneiss
	Basic metavolcanics, metakomatite / medium acid, and basic metavolcanics / conglomerate, metapsammite, basic and acide metavolcanics, quartzite
	Micaceous and garnet-micaceous paragneiss and schist, conglomerate, quartzite
	Granodiorite, tonalite, plagiogranite / enderbite
	Micaceous and garnet-micaceous gneisses with kyanite and / or sillimanite
	Gneiss, amphibolite, calciphyre
	Gneiss, amphibolite, ferruginous quartzite
	Gneiss, amphibolite with ferruginous quartzite deposit
	Biotite, amphibole- and pyroxene-biotite gneisses, migmatite, tonalite gneiss, granodiorite gneiss, amphibolite
	Ore showings in albite-hydromica-chlorite metasomatite
	Ore showings in quartz-feldspar metasomatite and pegmatite
	Ore showings in pegmatoid granite and quartz-plagioclase-orthoclase metasomatite

**Archean Dikoe metasomatites**

The Dikoe ore showing is located between Murmansk and Pechenga, (Fig. 2.4.36). Hundreds of elongated and plurimetric radioactive granitoid bodies are distributed along two strikes oriented NW-SE parallel to the major regional fault boundary and extend over 1 x 5 km and 1.5 x 6 km long areas (Kister et al., 2007). The ore has been discovered by airborne survey in 1961 and explored in the 70's but granitoids which grade from 8.5 ppm to 0.2 wt% U remain uneconomic because of the dispersion of the mineralization. The uranium ore is represented by uraninite associated with molybdenite in quartz-feldspar-biotite granitoid bodies with lenticular or vein forms intruding biotite and two-mica gneisses belonging to the Late Archean Tundra Suite. Previous U-Pb isotopic dating on uraninite has established the age of uranium mineralization at  $2730 \pm 30$  Ma (Savitskii et al., 1995) and biotites from the host-rock yield  $2750 \pm 50$  Ma with the K-Ar method (Afanasieva et al., 2007). The Dikoe samples (59 and 104-3) were taken from leucocratic granite through which numerous muscovite-rich shear plans are developed (Fig. 2.4.37). Euhedral grains of tourmaline are very common in the muscovite-rich shear zones, ranging up to 1-2 mm long and black-coloured macroscopically (Fig. 2.4.38). Previous geochronological work on tourmaline in muscovite granites from the same tectonic zone (Kolmozero-Voronya) yielded isotopic Pb-Pb age at  $2520 \pm 70$  Ma confirming their post-magmatic crystallization (Kudryashov, 1999 and Kudryashov et al., 2003).



**Figure 2.4.37.** Outcrop picture (104) of the Dikoe Archean leucogranite cross cut by anastomosing muscovite-bearing fractures (dark shearing zones).

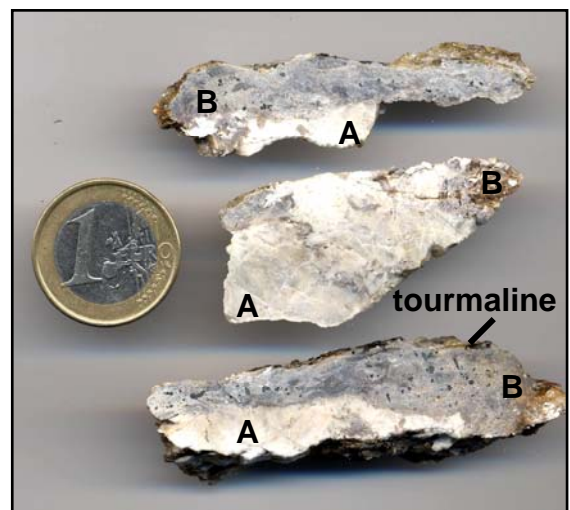
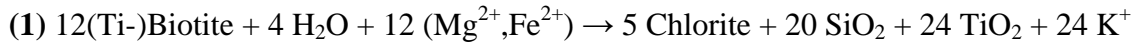


**Figure 2.4.38.** Macroscopic image of different rock pieces of the Dikoe samples (104-3) showing leucocrate quartz-feldspar pegmatite (A) in contact with muscovite shear zone (B) containing disseminated black tourmaline crystals.

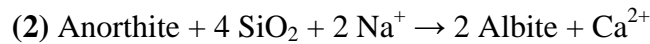
Sample 59 is composed of fine-grained quartz, albite and orthoclase with abundant biotite grains oriented along the general rock foliation. Biotite is elongated parallel to the shear plans and altered into muscovite (Fig. 2.4.39). In the centimetre-scale shear zones, only a few quartz grains remain between the coarse-grained muscovite. Sample 104-3 has a typical muscovite-quartz-

tourmaline greisen-like composition. It is mainly composed of fine-grained muscovite in a lepidoblastic texture almost totally replacing chloritized biotite.

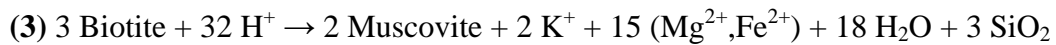
The early chloritization of biotite has probably released Ti-oxides, according to the following reaction (1) and has recrystallized into abundant fine acicular rutile crystals (Fig. 2.4.40).



Alteration of primary plagioclase has been observed locally with development of secondary albite and disseminated dust of sericite (Fig. 2.4.41). Quartz is restricted to patches between micas which suggest dequartzification according to albitization in reaction (2) that is frequently associated with K- and Na-metasomatism (Cathelineau, 1986).



Then muscovitization of biotite, as in reaction (3), has provided Mg and Fe that contributed to the final tourmaline crystallization.



Tourmaline observed in the Dikoe leucogranite displays blue to green colour under the microscope in transmitted light with a zoned hexagonal section (Fig. 2.4.42) with age of cristallization estimated by Pb-Pb isotopic dating at  $2520 \pm 70$  Ma (Kudryashov et al., 2003).

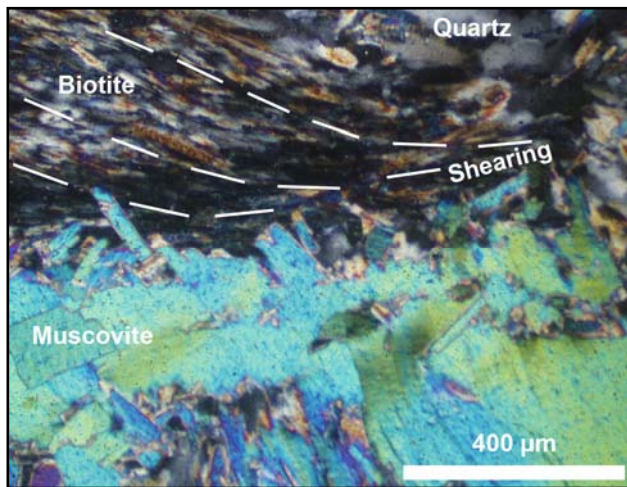


**Figure 2.4.39.** Shear zone showing biotite muscovitization and disappearance of quartz (sample 59, crossed polarized transmitted light).

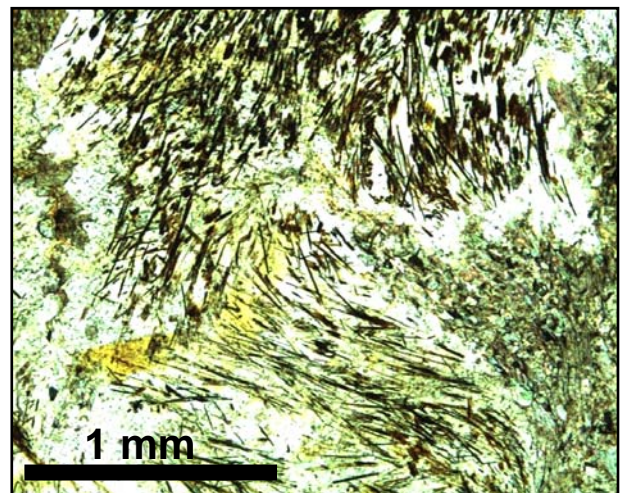


**Figure 2.4.40.** Acicular brown rutile needles issued from the chloritization of biotite (sample 104-3, natural transmitted light).

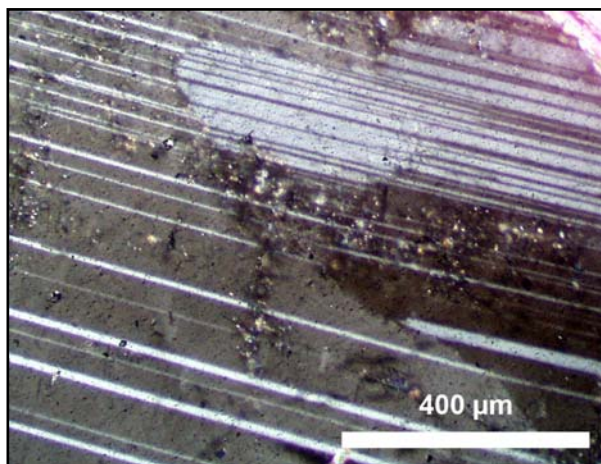


**Figure 2.4.41.** Progressive development of albitization (right) in a plagioclase with local sericite dust (sample 59, crossed polarized transmitted light).

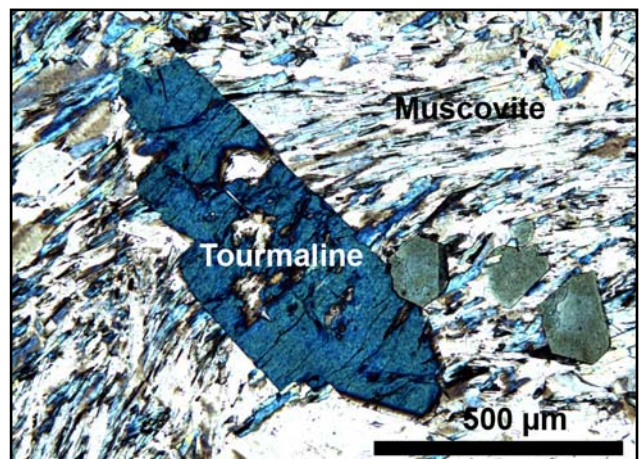


**Figure 2.4.42.** Green to bluish tourmaline crystals within muscovite-rich shear zone (sample 104-3, crossed polarized transmitted light).

The geochemistry of the Dikoe samples (Table 2.4.9) is characterized by a peraluminous composition ( $A/CNK = 1.74-1.98$  and  $A/NK = 2.09-2.28$ ) and plot in the field of ultra-potassic shoshonitic suites (Fig. 2.4.6). The high A parameters (222.68 and 284.02) correspond to the elevated muscovite content and low Q (38.88 and 41.31) and B (31.58 and 35) parameters reflect the low quartz and biotite contents respectively (Fig. 2.4.33 and 2.4.34). The relatively lower P parameter in sample 59 (-60.08) compare to sample 104-3 (-10.22) is probably due to the abundance of anorthite, only slightly albitized (Fig. 2.4.42), which is corroborated by its high Ca and Na contents (1.44 wt% CaO and 4.41 wt% Na<sub>2</sub>O).

Chondrite-normalized REE patterns of Dikoe samples (Fig. 2.4.43) are highly enriched in REE with  $10^2$  to  $10^3$  times chondrite values and display a general flat shape because of both LREE and HREE enrichment ( $[Ce/Yb]_N = 6.87-7.39$  and  $[Gd/Yb]_N = 2.76-2.96$ ). Negative Eu anomaly is well pronounced ( $Eu/Eu^* = 0.14$ ) corresponding to early plagioclase fractionation in the source melt. Accessories are represented partly by apatite, zircon and xenotime (Fig. 2.4.44), the last one explaining the high HREE and Y contents (367 and 508 ppm).

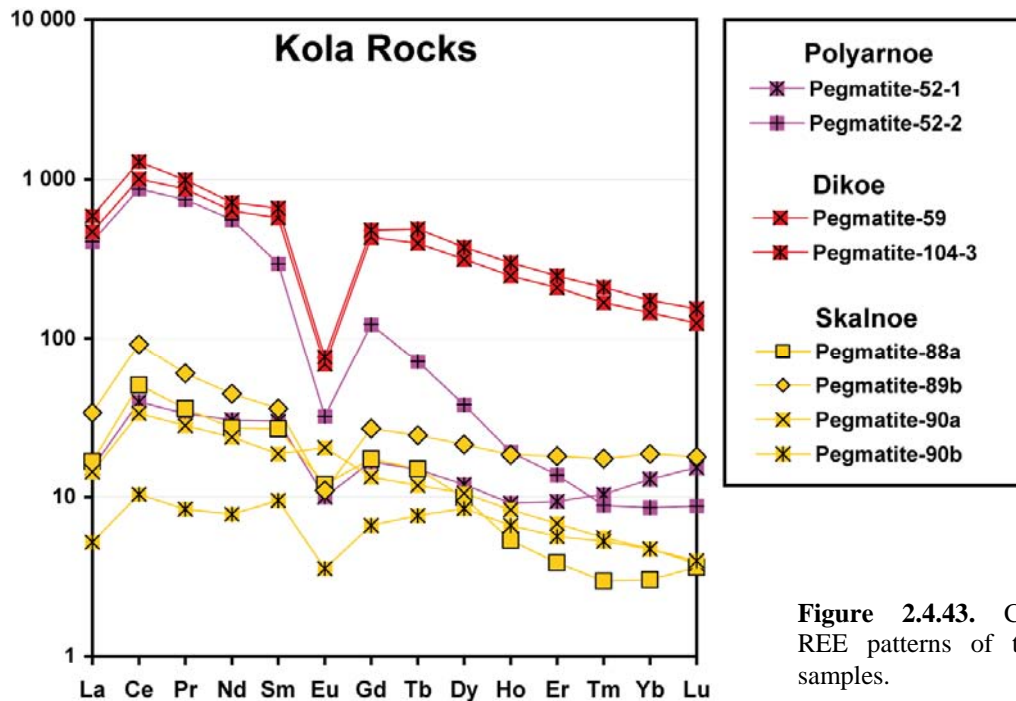


Figure 2.4.43. Chondrite-normalized REE patterns of the Kola pegmatite samples.

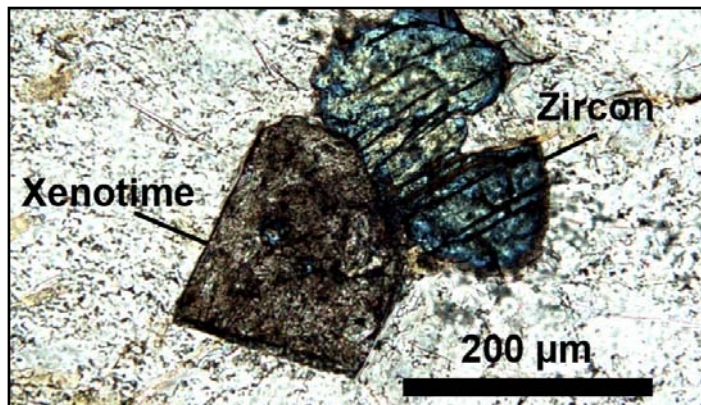


Figure 2.4.44. Zircon and xenotime preserved crystals within the muscovite-rich shear zone (sample 104-3, crossed polarized transmitted light).

## Chapitre 2 : Sources Magmatiques Archéennes de l'Uranium

**Table 2.4.9.** Chemical composition of individual pegmatite samples from the uranium occurrences Polyarnoe, Dikoe and Skalnoe in the Kola Peninsula (Russia)

Occurrence	Polyarnoe		Dikoe		Quartz-feldspar-biotite metasomatite with muscovite	Skalnoe		Lithology
	Quartz-feldspar-biotite gneisses	58-2	Quartz-feldspar-biotite metasomatite with muscovite	104-3		Biotite-rich gneiss	90a	
Sample	58-1	58-2	59	104-3	88a	89b	90a	90b
SiO <sub>2</sub> (wt%)	89.53	82.27	55.57	54.63	71.05	51.31	66.86	88.49
Al <sub>2</sub> O <sub>3</sub>	3.55	6.52	26.72	29.24	16.87	18.64	17.52	3.45
Fe <sub>2</sub> O <sub>3</sub> total	2.16	4.12	1.67	1.55	0.88	14.52	3.49	3.34
MnO	0.02	0.01	0.02	0.01	0.01	0.07	0.02	0.02
MgO	1.07	1.66	0.48	0.42	0.49	4.79	1.66	1.65
CaO	0.20	0.56	1.44	1.06	0.29	0.95	0.99	< L.D.
Na <sub>2</sub> O	0.24	1.16	4.41	3.77	4.09	2.70	5.04	0.07
K <sub>2</sub> O	0.76	1.85	5.07	6.12	4.61	5.01	1.94	1.27
TiO <sub>2</sub>	0.37	0.66	0.17	0.15	0.11	0.85	0.39	0.45
P <sub>2</sub> O <sub>5</sub>	0.02	0.11	0.19	0.20	0.10	0.14	0.07	0.05
LOI	1.04	0.94	2.79	3.21	1.20	2.01	2.23	0.80
Total	98.96	99.87	98.53	100.36	99.71	100.98	100.23	99.60
As (ppm)	< D.L.	< D.L.	< D.L.	< D.L.	1.54	< D.L.	< D.L.	< D.L.
Ba	141,00	388,00	704,00	897,90	1929,00	473,00	351,90	134,40
Be	0,37	0,21	1,56	<D.L.	<D.L.	1,67	<D.L.	<D.L.
Bi	0,18	<D.L.	0,23	0,25	0,16	0,43	<D.L.	0,13
Cd	1,04	0,46	<D.L.	0,17	0,21	0,38	0,45	0,63
Co	6,81	14,70	2,86	2,21	1,53	21,84	9,69	10,60
Cr	101,00	89,80	19,80	6,72	33,07	137,10	116,60	205,10
Cs	1,05	2,34	4,43	4,04	<D.L.	6,39	2,15	2,63
Cu	23,70	60,40	4,10	<D.L.	7,45	5,90	19,03	20,29
Ga	9,20	18,70	54,70	59,80	23,72	29,58	24,75	11,04
Ge	0,80	1,83	2,41	2,89	1,18	2,51	1,10	0,98
Hf	39,50	19,90	4,18	5,17	5,64	10,48	4,67	7,77
In	<D.L.	<D.L.	<D.L.	<D.L.	<D.L.	<D.L.	<D.L.	<D.L.
Mo	138,00	6,24	9,09	22,99	3,61	1,43	120,60	175,70
Nb	6,09	16,80	10,70	7,56	2,30	20,30	6,53	8,80
Ni	25,50	21,20	8,80	6,22	13,74	72,20	38,82	40,01
Pb	400,00	288,00	888,00	1014,50	33,23	40,71	407,19	348,64
Rb	36,20	118,00	157,00	174,50	69,53	143,60	83,72	67,61
Sb	<D.L.	<D.L.	<D.L.	<D.L.	<D.L.	<D.L.	0,21	<D.L.
Sn	0,40	1,64	5,34	5,23	1,03	2,22	2,11	1,80
Sr	20,10	107,00	273,00	237,00	172,10	126,00	282,90	5,02
Ta	0,30	0,92	0,62	0,49	0,25	1,72	0,52	0,73
Th	188,00	389,00	356,00	390,30	49,79	28,96	28,66	53,45
U	597,00	299,00	2288,00	2495,00	38,67	59,32	500,10	610,60
V	55,90	65,20	15,50	15,47	33,38	99,40	92,80	100,50
W	0,28	0,26	2,90	3,26	1,63	2,27	3,78	2,91
Y	12,20	27,40	367,00	508,70	8,54	31,90	12,30	7,12
Zn	33,30	82,40	19,00	19,25	13,78	87,97	83,34	90,80
Zr	1195,00	562,00	112,00	134,50	172,80	334,70	163,50	256,20
La (ppm)	9,72	259,00	298,00	375,10	10,67	21,65	9,18	3,31
Ce	25,30	553,00	640,00	819,30	32,34	58,64	21,42	6,65
Pr	3,22	71,90	83,70	95,11	3,46	5,79	2,71	0,81
Nd	14,50	265,00	300,00	337,90	12,91	21,08	11,27	3,70
Sm	4,60	45,50	87,80	101,30	4,14	5,54	2,88	1,47
Eu	0,58	1,87	3,96	4,43	0,70	0,64	1,18	0,21
Gd	3,42	25,10	88,20	97,95	3,55	5,50	2,74	1,35
Tb	0,56	2,67	14,80	18,30	0,56	0,92	0,44	0,29
Dy	3,06	9,66	80,20	95,23	2,52	5,43	2,68	2,16
Ho	0,52	1,09	14,00	16,97	0,30	1,04	0,47	0,38
Er	1,56	2,28	34,70	41,01	0,64	3,00	1,13	0,94
Tm	0,27	0,23	4,30	5,38	0,08	0,45	0,14	0,14
Yb	2,14	1,42	24,10	28,68	0,50	3,08	0,78	0,78
Lu	0,39	0,22	3,18	3,91	0,09	0,45	0,10	0,10
ΣREE	69,83	1238,94	1676,94	2040,57	72,46	133,20	57,13	22,27
[Ce/Yb] <sub>N</sub>	3,06	100,79	6,87	7,39	16,77	4,93	7,08	2,20
Eu/Eu*	0,45	0,17	0,14	0,14	0,56	0,35	1,29	0,45
[Gd/Yb] <sub>N</sub>	1,29	14,28	2,96	2,76	5,74	1,44	2,82	1,40
P = K-(Na+Ca)	4,86	-8,05	-60,08	-10,22	-38,94	2,56	-139,02	24,70
Q = Si/3-(K+Na+2Ca/3)	470,89	373,42	41,31	38,88	160,99	79,90	155,64	461,92
B = Fe+Ti+Mg	58,38	101,25	35,00	31,58	24,68	311,90	90,08	88,73
A = Al-(K+Na+2Ca)	38,59	31,14	222,68	284,02	90,48	138,08	104,57	38,25
A/CNK	2,24	1,32	1,74	1,98	1,38	1,61	1,44	2,30
A/NK	2,91	1,67	2,09	2,28	1,44	1,89	1,68	2,30
K <sub>2</sub> O/Na <sub>2</sub> O	3,17	1,59	1,15	1,62	1,13	1,85	0,38	17,20
Th/U	0,31	1,30	0,16	0,16	1,29	0,49	0,06	0,09

Notes: Geochemical analysis performed by the SARM laboratory (CRPG, CNRS, Nancy, France); Major elements are determined by ICP-AES and trace elements by ICP-MS; <D.L. = below detection limits; [X]<sub>N</sub> = normalized to chondrites; A/CNK and A/NK indexes calculated in moles; Q, P, A and B parameters calculated in thousands of cations.

Zircon composition (Table 2.4.10) show only small variations in the major element contents,  $63.35 \pm 2.76$  wt%  $ZrO_2$ ,  $30.18 \pm 3.78$  wt%  $SiO_2$  and  $1.53 \pm 0.34$  wt%  $HfO_2$ , which decrease are mostly balanced by local increase in the Ca content and a slight increase in Fe, P and Al. Occasionally some analytical spots reach higher U contents with up to 0.71 wt%  $UO_2$  ( $m = 0.30 \pm 0.23$  wt%) but generally U, Th and Pb contents are below detection limits.

**Table 2.4.10.** Average chemical composition of zircon from the different U-occurrences Dikoe, Skalnoe and Polyarnoe, Kola Peninsula.

Ore	Dikoe	Skalnoe	Polyarnoe
Sample	104-3	90a	58-2
Nb zircon grains	3	5	24
EMPA	8	15	240
	Mean $\pm$ $\sigma$	Mean $\pm$ $\sigma$	Mean $\pm$ $\sigma$
$ZrO_2$	$63.35 \pm 2.76$	$62.30 \pm 3.80$	$51.56 \pm 5.23$
$HfO_2$	$1.53 \pm 0.34$	$1.40 \pm 0.22$	$1.45 \pm 0.20$
$SiO_2$	$30.18 \pm 3.78$	$31.17 \pm 2.15$	$28.88 \pm 1.81$
$Al_2O_3$	$0.28 \pm 0.30$	$0.34 \pm 0.39$	$0.75 \pm 0.33$
$P_2O_5$	$0.23 \pm 0.25$	<D.L.	<D.L.
CaO	$1.24 \pm 0.99$	$0.87 \pm 0.79$	$2.82 \pm 1.01$
FeO	$0.29 \pm 0.12$	$0.51 \pm 0.30$	$1.11 \pm 0.65$
$TiO_2$	<D.L.	<D.L.	$0.09 \pm 0.16$
$Y_2O_3$	<D.L.	<D.L.	<D.L.
$La_2O_3$	<D.L.	<D.L.	<D.L.
$Dy_2O_3$	<D.L.	<D.L.	<D.L.
$Er_2O_3$	<D.L.	<D.L.	<D.L.
$Yb_2O_3$	<D.L.	<D.L.	<D.L.
PbO	<D.L.	<D.L.	$1.21 \pm 3.18$
$ThO_2$	<D.L.	<D.L.	<D.L.
$UO_2$	$0.30 \pm 0.23$	$0.16 \pm 0.18$	$1.38 \pm 1.45$
Total	$97.65 \pm 3.43$	$97.02 \pm 3.89$	$89.56 \pm 3.61$

**Notes:** "<D.L."=below detection limit ( $Zr=0.20$ wt% ;  $Hf=0.08$ wt% ;  $Si=0.06$ wt% ;  $Al=0.05$ wt% ;  $P=0.07$ wt% ;  $Ca=0.06$ wt% ;  $Fe=0.13$ wt% ;  $Ti=0.04$ wt% ;  $Y=0.08$ wt% ;  $La=0.14$ wt% ;  $Dy=0.16$ wt% ;  $Er=0.24$ wt% ;  $Yb=0.21$ wt% ;  $Pb=0.13$ wt% ;  $Th=0.08$ wt% ;  $U=0.10$ wt%).

However, the Dikoe samples provide the highest U (2288-2495 ppm) and Th (356-390.3 ppm) contents observed in the Kola samples with very low Th/U ratios (0.16; Fig. 2.4.45) which suggest that radioelements are not only located in those refractory minerals and reflect a specific U enrichment with crystallization of uranium oxides.

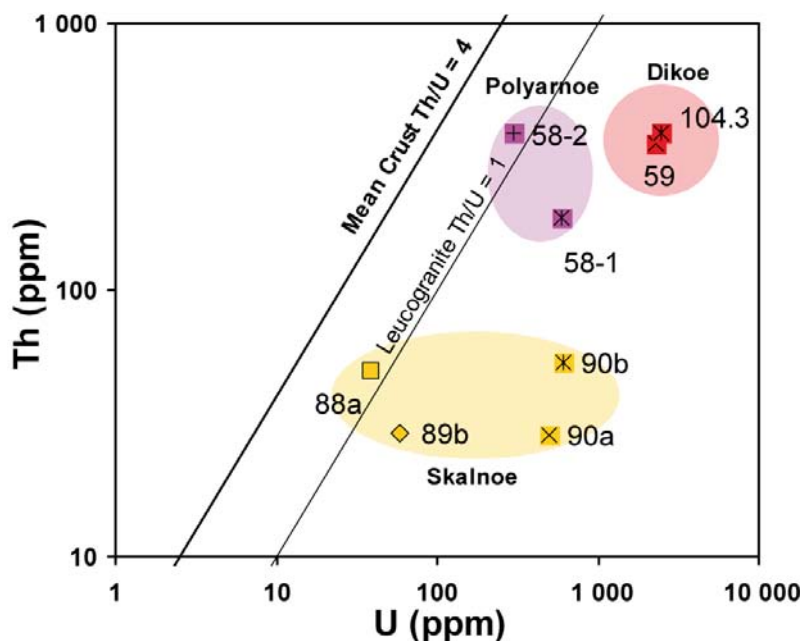


**Fig. 2.4.45.** U versus Th contents (ppm) in individual pegmatite samples from the uranium occurrences Dikoe, Skalnoe and Polyarnoe. Th/U ratios of the mean crust and leucogranites are also represented.

Euhedral uraninite included in monazite (Fig. 2.4.46) and as isolated aggregates (Fig. 2.4.47) are highly altered and partly recrystallized as hexavalent-U minerals, a mixture between kasolite  $[\text{Pb}(\text{UO}_2)\text{SiO}_4 \cdot \text{H}_2\text{O}]$ , uranophane  $[\text{Ca}(\text{UO}_2)_2(\text{SiO}_3\text{OH})_2 \cdot 5\text{H}_2\text{O}]$  and bequerellite  $[\text{Ca}(\text{UO}_2)_6\text{O}_4(\text{OH})_6 \cdot 8\text{H}_2\text{O}]$ .

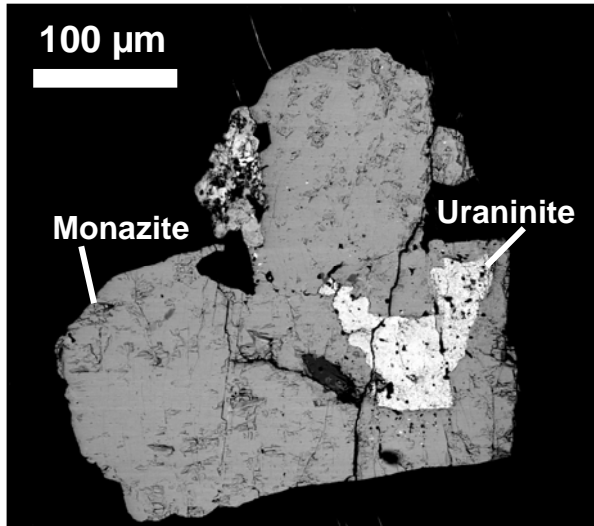


**Fig. 2.4.46.** BSE-SEM image of a primary monazite grain with cubic uraninite inclusions.

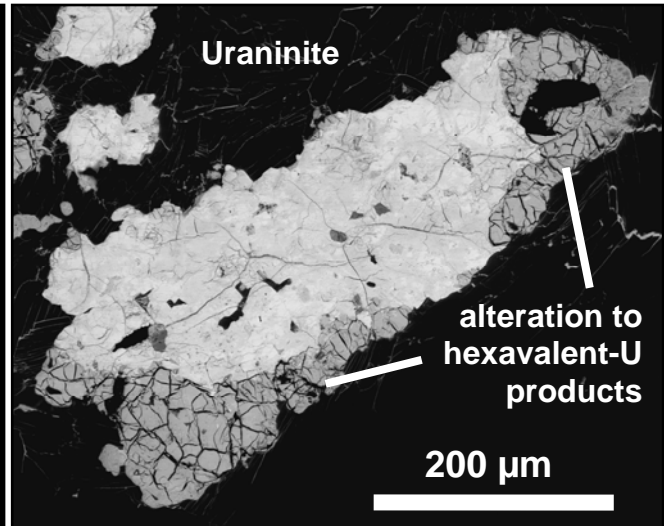


**Fig. 2.4.47.** BSE-SEM image of isolated Th-rich uraninite (white) altered to hexavalent-U mineralization (darker material with microcracks).

The uraninite (Table 2.4.11) has between 57.26 and 77.04 wt%  $\text{UO}_2$  ( $m = 68.86 \pm 4.89$  wt%) and 1.50 to 6.22 wt%  $\text{ThO}_2$  ( $m = 3.64 \pm 1.30$  wt%). The high Th content of uraninite confirms its magmatic origin. The variable contents in lead for these grains ranging from 1.17 to 15.02 wt%  $\text{PbO}$  yield a wide range of U-Th-Pb chemical ages comprised between 134 and 1634 Ma, younger than the previous isotopic U-Pb dating uraninite at  $2730 \pm 30$  Ma (Savitskii et al., 1995). The very high concentrations in silica (2.64-14.71 wt%  $\text{SiO}_2$ ) and calcium (2.49-5.84 wt%  $\text{CaO}$ ) are relevant of a strong alteration by Ca-rich fluids which could derived from the break-down of calcic plagioclase during alteration. Traces of yttrium and sometimes LREE have also been detected with up to 1.21 wt%  $\text{Y}_2\text{O}_3$  and 0.63 wt%  $\text{Ce}_2\text{O}_3$ .

Monazite grains (Table 2.4.12) have high U (0.27-2.35 wt%  $\text{UO}_2$ ), Th (7.33-10.99 wt%  $\text{ThO}_2$ ), Y (1.31-3.85 wt%  $\text{Y}_2\text{O}_3$ ) and REE ( $\Sigma\text{REE} \sim 45$  wt%) contents with traces of Ca (1.45-2.98 wt%  $\text{CaO}$ ) and Si (0.18-1.37 wt%  $\text{SiO}_2$ ). Chemical ages of monazite range between 1597 and 2756 Ma with a peak at 2450 Ma (Fig. 2.4.48). These results are in accordance with the previous Archean isotopic U-Pb ages of primary uraninite and also record the later alteration event(s) affecting the primary mineral assemblage and U mineralization.

**Table 2.4.11.** Average chemical composition of uraninite hosted in the Archean Dikoe metasomatized leucogranite (sample 104-3).

<i>Sample</i>	<i>104-3</i>
<i>Rock type</i>	<i>Dikoe Metasomatite</i>
<i>EMPA</i>	<i>Mean±σ (N=16)</i>
Na <sub>2</sub> O	<D.L.
MgO	<D.L.
Al <sub>2</sub> O <sub>3</sub>	<D.L.
SiO <sub>2</sub>	6.96 ± 4.37
P <sub>2</sub> O <sub>5</sub>	<D.L.
SO <sub>2</sub>	<D.L.
K <sub>2</sub> O	0.34 ± 0.12
CaO	3.53 ± 0.95
TiO <sub>2</sub>	<D.L.
V <sub>2</sub> O <sub>3</sub>	<D.L.
MnO	<D.L.
FeO	0.22 ± 0.13
Y <sub>2</sub> O <sub>3</sub>	0.41 ± 0.30
MoO <sub>3</sub>	<D.L.
La <sub>2</sub> O <sub>3</sub>	<D.L.
Ce <sub>2</sub> O <sub>3</sub>	<D.L.
Nd <sub>2</sub> O <sub>3</sub>	<D.L.
Dy <sub>2</sub> O <sub>3</sub>	<D.L.
PbO	4.67 ± 3.69
ThO <sub>2</sub>	3.64 ± 1.30
UO <sub>2</sub>	68.86 ± 4.89
<b>Total</b>	<b>89.44 ± 3.03</b>

*Notes:* “<D.L.”=below detection limit (Na=0.11wt%; Mg=0.03wt%; Al=0.06wt%; Si=0.04wt%; P=0.06wt%; S=0.06wt%; K=0.08wt%; Ca=0.06wt%; Ti=0.06wt%; V=0.09wt%; Mn=0.14wt%; Fe=0.13wt%; Y=0.12wt%; Mo=0.17wt%; La=0.21wt%; Ce=0.22wt%; Nd=0.48wt%; Dy=0.56wt%; Pb=0.19wt%; Th=0.14wt%; U=0.41wt%).

**Table 2.4.12.** Average chemical composition of monazite in the Archean Dikoe metasomatized leucogranite (sample 104-3).

<i>Sample</i>	<i>104-3</i>
<i>Rock type</i>	<i>Dikoe Metasomatite</i>
<i>EMPA</i>	<i>Mean±σ (N=36)</i>
Al <sub>2</sub> O <sub>3</sub>	<D.L.
SiO <sub>2</sub>	0.43 ± 0.29
P <sub>2</sub> O <sub>5</sub>	29.58 ± 0.53
CaO	2.52 ± 0.38
TiO <sub>2</sub>	<D.L.
MnO	<D.L.
FeO	<D.L.
Y <sub>2</sub> O <sub>3</sub>	3.04 ± 0.55
La <sub>2</sub> O <sub>3</sub>	10.30 ± 0.65
Ce <sub>2</sub> O <sub>3</sub>	22.44 ± 1.03
Pr <sub>2</sub> O <sub>3</sub>	2.17 ± 0.12
Nd <sub>2</sub> O <sub>3</sub>	8.60 ± 0.37
Sm <sub>2</sub> O <sub>3</sub>	2.39 ± 0.10
Gd <sub>2</sub> O <sub>3</sub>	2.23 ± 0.17
ThO <sub>2</sub>	9.48 ± 0.65
UO <sub>2</sub>	1.59 ± 0.51
PbO	1.76 ± 0.36
<b>Total</b>	<b>96.57 ± 0.64</b>

*Notes:* “<D.L.”=below detection limit (Al=0.07wt%; Si=0.05wt%; P=0.06wt%; Ca=0.07wt%; Ti=0.04wt%; Mn=0.17wt%; Fe=0.14wt%; Y=0.11wt%; La=0.24wt%; Ce=0.20wt%; Pr=0.14wt%; Nd=0.17wt%; Sm=0.15wt%; Gd=0.25wt%; Th=0.07wt%; U=0.09wt%; Pb=0.31wt%).

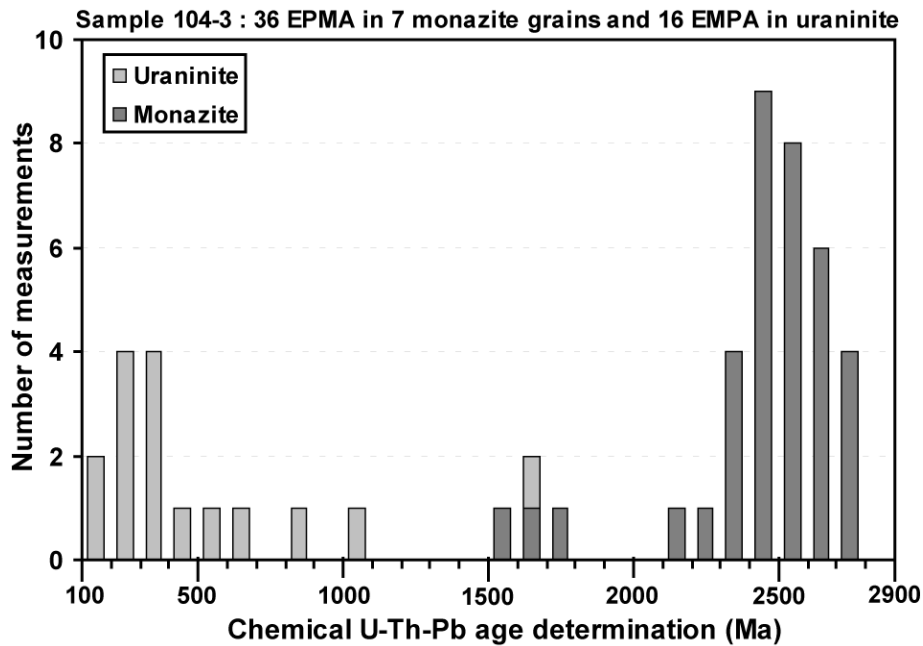


**Figure 2.4.48.** Histogram showing the repartition of chemical U-Th-Pb ages determined from EMPA measurements in uraninite and monazite grains from the Dikoe metasomatite (sample 104-3).

**Archean Skalnøe ore showing**

The Skalnøe occurrence is located 20 km west of Pechenga and 40 km northwest from the Dikøe ore (Fig. 2.4.36) all occurring in the Kolmosero-Voronya tectonic zone (Fig. 2.4.1). Skalnøe ore showing consists of quartz-feldspar granitoid vein-like bodies injected into gneisses along NW faults sometimes discordant and displaying a sharp contact with the host-rock (Kister et al., 2007). The U mineralization has been dated from 2650 to 2280 Ma (Afanasieva et al., 2007) which potentially indicates an Archean primary ore associated with a Paleoproterozoic U remobilization. Rock samples were collected from three different outcrops representing the various lithologies encountered in this area.

Outcrop 88 represents one of the intrusive quartz-feldspar granitoids strongly deformed and very similar to the Dikøe ore previously described but presenting here silicified borders with muscovite-rich shear zones (Fig. 2.4.49).

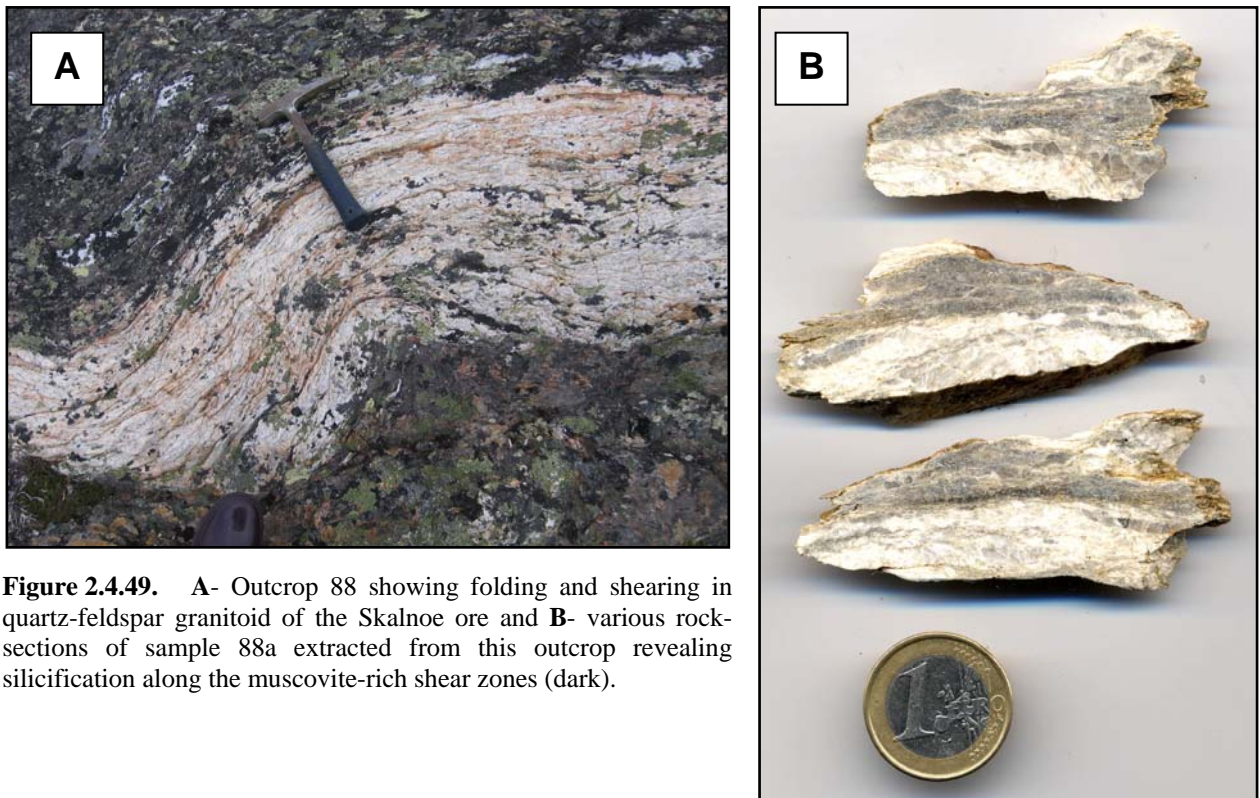


**Figure 2.4.49.** A- Outcrop 88 showing folding and shearing in quartz-feldspar granitoid of the Skalnøe ore and B- various rock-sections of sample 88a extracted from this outcrop revealing silicification along the muscovite-rich shear zones (dark).

Geochemistry of sample 88a (Table 2.4.9) reveals a composition intermediate between adamellite and granite and plotting in the field of high-K calc-alkaline suites with 4.61 wt% K<sub>2</sub>O (Fig. 2.4.6). The silica content is slightly higher than at Dikøe with a Q parameter of 160.99 corresponding microscopically to intense silicification with abundant recrystallization of microgranular quartz (Fig. 2.4.50). The negative P parameter (-38.94) reflects the slight albitization of K-feldspar (Fig. 2.4.51). The sample is also peraluminous (A/CNK = 1.38; A/NK = 1.44; A = 90.48) with low B parameter (24.68) reflecting the muscovitization of disseminated biotite.

Chondrite-normalized REE pattern (Fig. 2.4.43) shows a strong fractionation with HREE depletion ( $[Ce/Yb]_N = 16.77$  and  $[Gd/Yb]_N = 5.74$ ), relatively low REE contents ( $\Sigma REE = 72.46$  ppm) compare to the Dikoe metasomatites and a less pronounced Eu anomaly ( $Eu/Eu^* = 0.56$ ). Contents in Ba (1929 ppm), U (38.67 ppm) and Th (49.79 ppm) are elevated reflecting local accumulation of monazite and apatite, but no uraninite has been observed despite the low Th/U ratio (1.29) and the U enrichment compared to the mean crust (Fig. 2.4.45).

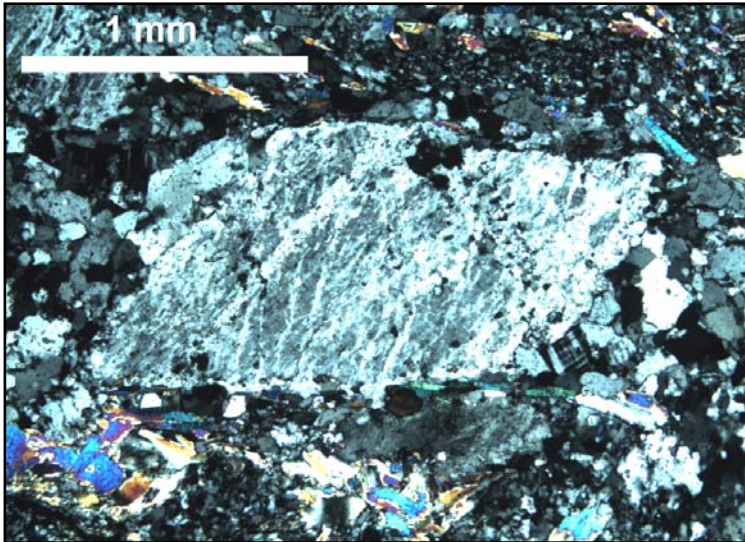


**Figure 2.4.50.** Perthitic feldspar with a sigmoidal shape surrounded by microgranular quartz and muscovite clusters (sample 88a; crossed nicols).

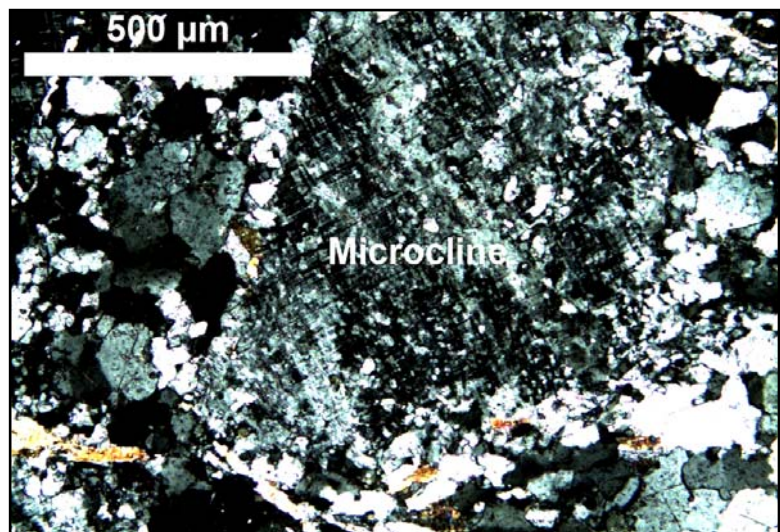


**Figure 2.4.51.** Albitized microcline crystal surrounded by orthoclase and recrystallized patches of quartz (sample 88a; crossed nicols).

Outcrop 89 presents sharp contact between Archean mylonitic paragneiss and the incipient development of quartz-feldspar leucosome as a vein-like intrusion with boudinage deformation (Fig. 2.4.52). Sample 89b corresponds to the melanocratic mylonitic gneiss is macroscopically melanocrate with brecciated and recrystallized quartz-feldspar eyes (Fig. 2.4.53). Sample 89b represents a restite layer rich in biotite trapped between the migmatized gneiss and quartzofeldspathic mobilisates. Microscopically, the gneiss is characterized by a nematoblastic texture defined by very abundant biotite elongated crystals partly recrystallized to chlorite and muscovite (Fig. 2.4.54). The predominance of biotite and its muscovitization give both high B (311.90) and A (138.08) parameters (Fig. 2.4.34) with high contents in  $Al_2O_3$  (18.64 wt%),

$\text{Fe}_2\text{O}_{3t}$  (14.52 wt%) and  $\text{MgO}$  (4.79 wt%) (Table 2.4.9). The restite plots in the field of shoshonitic series (Fig. 2.4.6) with a highly potassic composition (5.01 wt%  $\text{K}_2\text{O}$ ), but this is due to its biotite enrichment, for a very low quartz content (51.31 wt%  $\text{SiO}_2$ ). No albitization has been observed in this sample and accessory minerals are restricted to disseminated titanite and zircon which could explain respectively the high contents in 0.95 wt%  $\text{CaO}$  and 0.85 wt%  $\text{TiO}_2$ , and the low fractionation between LREE and HREE ( $[\text{Ce}/\text{Yb}]_N = 4.93$ ) in the chondrite-normalized pattern (Fig. 2.4.43). The restite has also high U (59.32 ppm) and Th (28.96 ppm) contents with a low Th/U ratio (0.49) below leucogranite (Fig. 2.4.45) but no uraninite has been observed in this sample.



**Figure 2.4.52.** Outcrop 89 at Skalnøe showing the sharp contact between vein-like intrusion of quartz-feldspar granitoid (right) and the darker fine grained mylonitic gneisses (left) where coarse grained biotite restite occur.



**Figure 2.4.53.** Picture of a rock-section from the migmatitized paragneiss at Skalnøe (sample 89b).

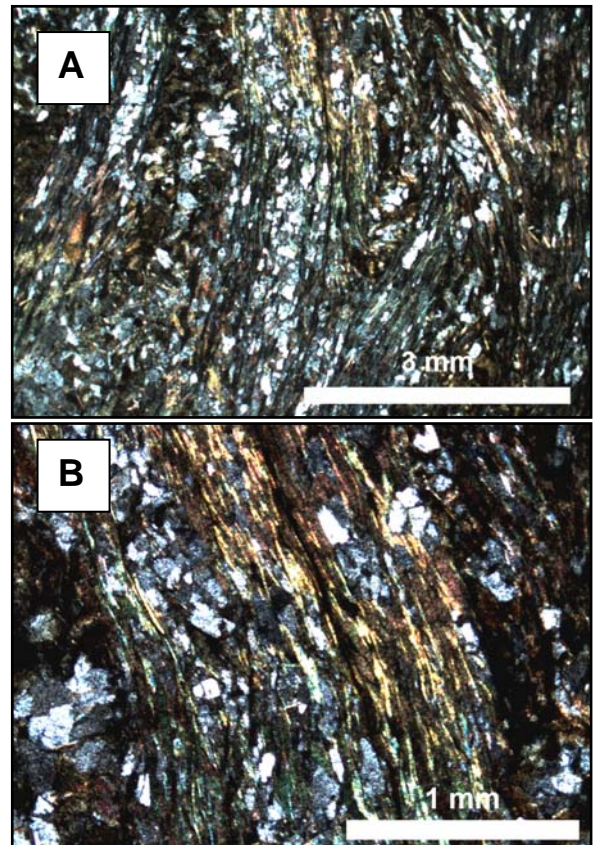


**Figure 2.4.54.** Migmatitic gneiss at Skalnøe (sample 89b, crossed nicols): **A**- nematoblastic texture of biotite and **B**- a closer view showing muscovitization of biotite and recrystallized feldspar and quartz grains with ternary junctions.

The pegmatite dyke intruding the gneisses in outcrop 90 is composed of quartz-feldspar cataclasite with biotite selvages (Fig. 2.4.55). Sample 90a plots in the field of medium-K calc-alkaline suites whereas sample 90b has a much higher SiO<sub>2</sub> content (Fig. 2.4.6). This difference is remarkable in the P-Q diagram (Fig. 2.4.33) with a much higher Q parameter for 90b (461.92) associated microscopically to intense silicification and very abundant quartz recrystallized in wide polycrystalline patches with undulous extinction and ternary junction points in transmitted light (Fig. 2.4.56-A). On the other side, sample 90a exhibits lower Q (155.64) and P (-139.02) parameters associated to relatively lower amounts of quartz but still abundant (Fig. 2.4.56-B) and accumulation of plagioclase in the restite (Fig. 2.4.56-C) which conduce to a slightly positive Eu anomaly of the REE pattern (Fig. 2.4.43; Eu/Eu\* = 1.29). Biotite selvages corresponding to restitic segregations during extraction of the melt are more abundant in sample 90a and show intense alteration to chlorite and muscovite (Fig. 2.4.56-C and -D) that yield to an increase of the A value (Fig. 2.4.34; 38.25 for 90b and 104.57 for 90a). Both samples display strong U enrichment (500.1-610.6 ppm) compared to Th contents (28.66-53.45 ppm) resulting in very low Th/U ratios (0.06-0.09) which should correspond to the presence of uraninite (Fig. 2.4.45). Small millimetric cubic boxworks in biotite have been observed macroscopically with yellow products indicating the alteration of the primary uranium oxides into hexavalent U-minerals.

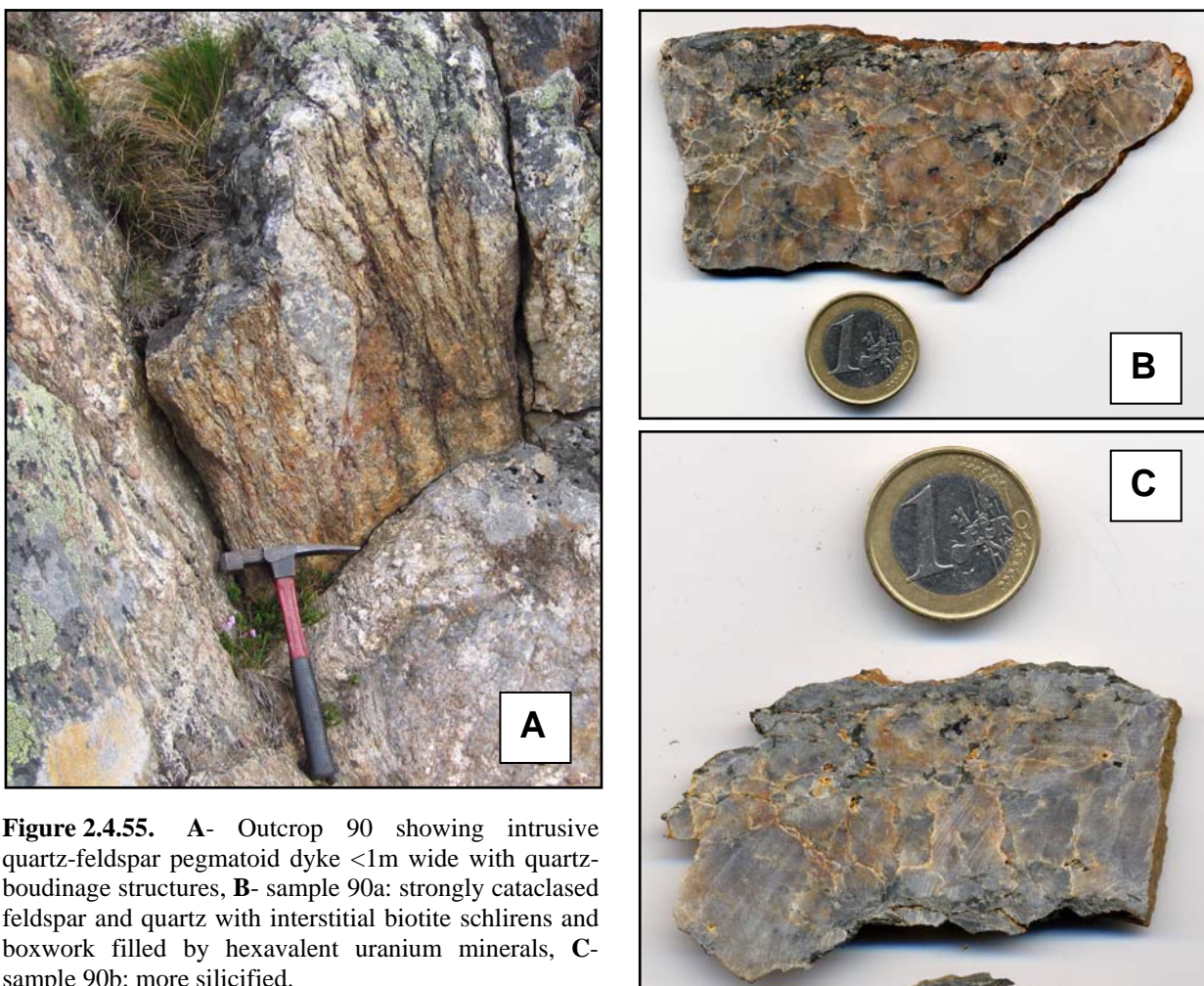


**Figure 2.4.55.** A- Outcrop 90 showing intrusive quartz-feldspar pegmatoid dyke <1m wide with quartz-boudinage structures, B- sample 90a: strongly cataclased feldspar and quartz with interstitial biotite schlirens and boxwork filled by hexavalent uranium minerals, C- sample 90b: more silicified.

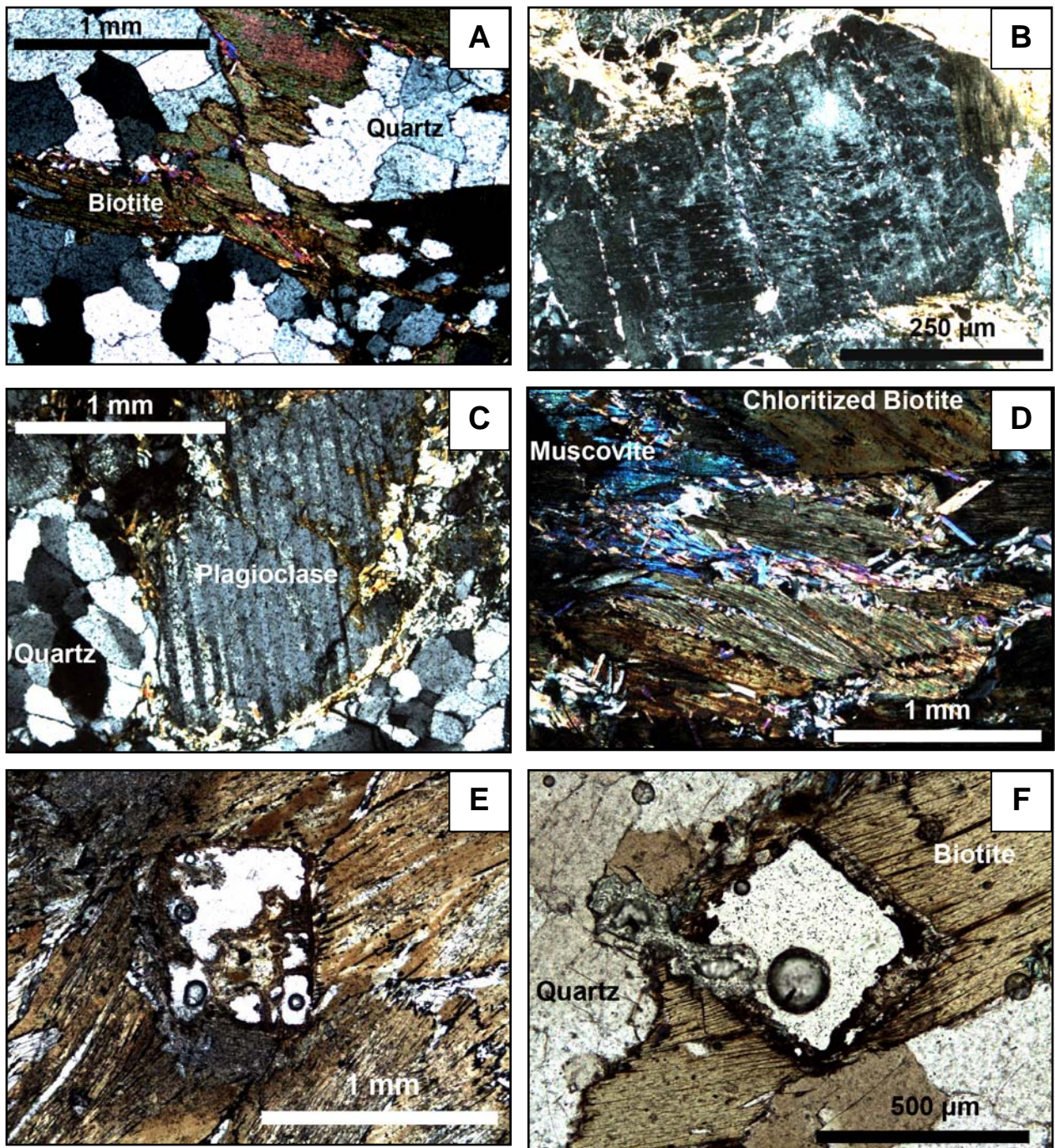


**Figure 2.4.56.** Photomicrographs of Skalnøe pegmatites showing **A-** quartz recrystallization and altered biotite (90b, crossed nicols), **B-** pethitic feldspar (90a, crossed nicols), **C-** plagioclase enclosed in the biotite-rich restite (90a, crossed nicols), **D-** muscovitization of chloritized biotite (90a, crossed nicols), **E-** cubic boxwork in biotite selvage (90a, transmitted light), **F-** boxwork surrounded by a pleochroic halo in biotite (90b, transmitted light).

Microscopically, no preserved primary uraninite has been observed in the thin sections but the cubic dissolution cavities (~ 500 µm large) in biotite with characteristic destruction rims due to alpha radiations (Fig. 2.4.56-E and -F). SEM observations revealed sometimes that the cavities and fractures are coated by secondary pitchblende with small galena cubes and a mixture of iron oxides (hematite or goethite) and ferrimolybdate (Fig. 2.4.57-B). The absence of thorium in the pitchblende (Th below detection limit < 0.15 wt%; Table 2.4.13) confirms its late hydrothermal origin. The U-Th-Pb chemical dating of pitchblende yields wide range of ages between 214 and

1081 Ma meaning around 866 Ma. Ferrimolybdenite is probably responsible of the yellow coloration observed macroscopically and results from the alteration of primary molybdenite preserved locally (Fig. 2.4.57-A). Zircon grains are also disseminated in the pegmatites (Table 2.4.10). The uranium content in Skalnøe zircons reach up to 0.73 wt% UO<sub>2</sub> but in most of them U, Th and Pb contents are below detection limits.

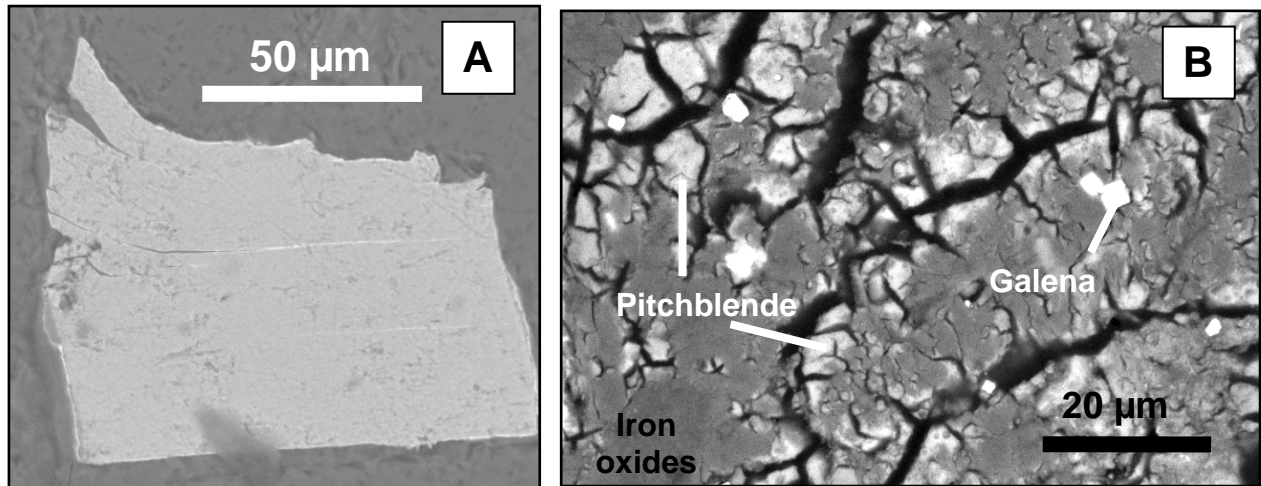


**Figure 2.4.57.** BSE-SEM images of **A-** primary molybdenite and **B-** secondary U-mineralization represented by pitchblende coating microcracks mixed with iron oxides and euhedral cubes of galena (sample 90a).

**Table 2.4.13.** Average chemical composition (in wt%) of pitchblende hosted in the Archean Skalnøe intrusive pegmatites (sample 90a).

<i>Skalnøe ore showing (sample 90a)</i>	
Pitchblende recrystallization	Mean ± σ
EMPA measurements	50
Al <sub>2</sub> O <sub>3</sub>	<D.L.
SiO <sub>2</sub>	1.06 ± 1.90
P <sub>2</sub> O <sub>5</sub>	<D.L.
Na <sub>2</sub> O	0.20 ± 0.09
CaO	1.73 ± 0.80
K <sub>2</sub> O	0.29 ± 0.24
SO <sub>2</sub>	<D.L.
FeO	0.19 ± 0.11
MgO	0.09 ± 0.14
TiO <sub>2</sub>	0.19 ± 0.12
MoO <sub>3</sub>	<D.L.
ZrO <sub>2</sub>	<D.L.
V <sub>2</sub> O <sub>3</sub>	<D.L.
MnO	<D.L.
Y <sub>2</sub> O <sub>3</sub>	0.28 ± 0.09
La <sub>2</sub> O <sub>3</sub>	<D.L.
Ce <sub>2</sub> O <sub>3</sub>	<D.L.
Nd <sub>2</sub> O <sub>3</sub>	<D.L.
Dy <sub>2</sub> O <sub>3</sub>	<D.L.
PbO	10.25 ± 2.17
ThO <sub>2</sub>	<D.L.
UO <sub>2</sub>	81.31 ± 3.39
<b>Total</b>	<b>96.37 ± 1.77</b>

**Notes:** “<D.L.”=below detection limit (Al=0.07wt%; Si=0.05wt%; P=0.06wt%; Ca=0.06wt%; Na=0.12wt%; K=0.08wt%; S=0.07wt%; Fe=0.14wt%; Mg=0.04wt%; Ti=0.07wt%; Mo=0.18wt%; Zr=0.14wt%; V=0.10wt%; Mn=0.15wt%; Y=0.13wt%; La=0.22wt%; Ce=0.23wt%; Nd=0.51wt%; Dy=0.59wt%; Pb=0.20wt%; Th=0.15wt%; U=0.42wt%).

***Paleoproterozoic Polyarnoe pegmatites***

The Polyarnoe occurrence is located 15 km south of Pechenga (Fig. 2.4.36). Few meters thick pegmatoid vein-like bodies intrude migmatitized biotite-quartz-feldspar gneisses along a NNW direction nearly concordant to the gneissic foliation (Fig. 2.4.58). Savitskii et al. (1995) and Afanasieva et al. (2007) have estimated pegmatoid ages around 2.2 Ga by Rb-Sr and U/Pb isotopic geochronology and described the ore as albitized-chloritized metasomatites. However, the two samples studied in this work show no sign of albitization of feldspar or even chloritization in biotite. Microscopically, biotite is well preserved as selvages with various crystal orientations with abundant accumulation of zircon grains and opaque minerals (Fig. 2.4.59-A). Feldspar is represented both by primary microcline and plagioclase with disseminated sericite alteration. Quartz is largely predominant, medium to coarse grained (Fig. 2.4.59-B), which corroborates the whole-rock composition of both samples 58-1 and 58-2 with very high silica contents (82.27-89.53 wt% SiO<sub>2</sub>), associated to silicification with elevated Q parameters (373.42-470.89) and plotting in the field of low-K granitic suites close to the composition of the silicified Skalnøe pegmatite 90b (Fig. 2.4.6 and 2.4.33). However, samples have distinct REE patterns (Fig. 2.4.43): both show HREE depletion and negative Eu anomalies but sample 58-2 is much more fractionated with strong LREE enrichment ( $[Ce/Yb]_N = 100.79$ ) that was not explain petrographically because of the absence of monazite. Accessories are dominated by zircon ranging 50 to 150 µm wide with disseminated micron-scale uranothorite inclusions and abundant uraninite from 50 to 200 µm large crystals intergrown with zircon in biotite selvages (Fig. 2.4.60). The crystallization of uraninite and uranothorite supports the low whole-rock Th/U ratios (0.31-1.30) and the high U (299-597 ppm) and Th (188-389 ppm) contents.



**Fig. 2.4.58.** Polyarnoe granitoid dyke intruding biotite-quartz-feldspar gneiss.

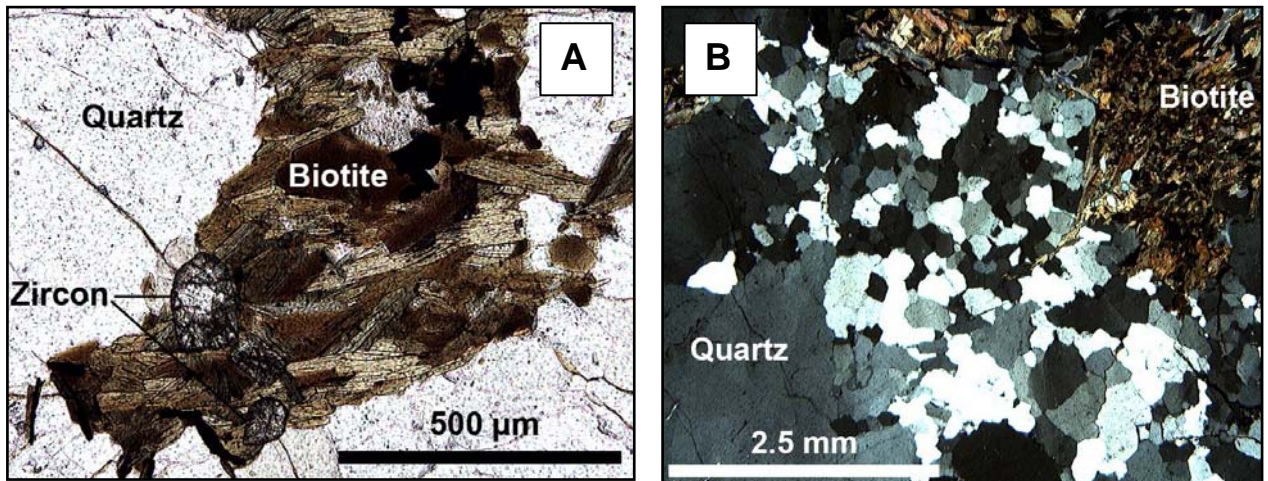


**Figure 2.4.59.** A- Biotite selvage with zircon and opaque minerals (transmitted light) and B- quartz and biotite (crossed nicols) in Polyarnoe pegmatite (sample 58-1).

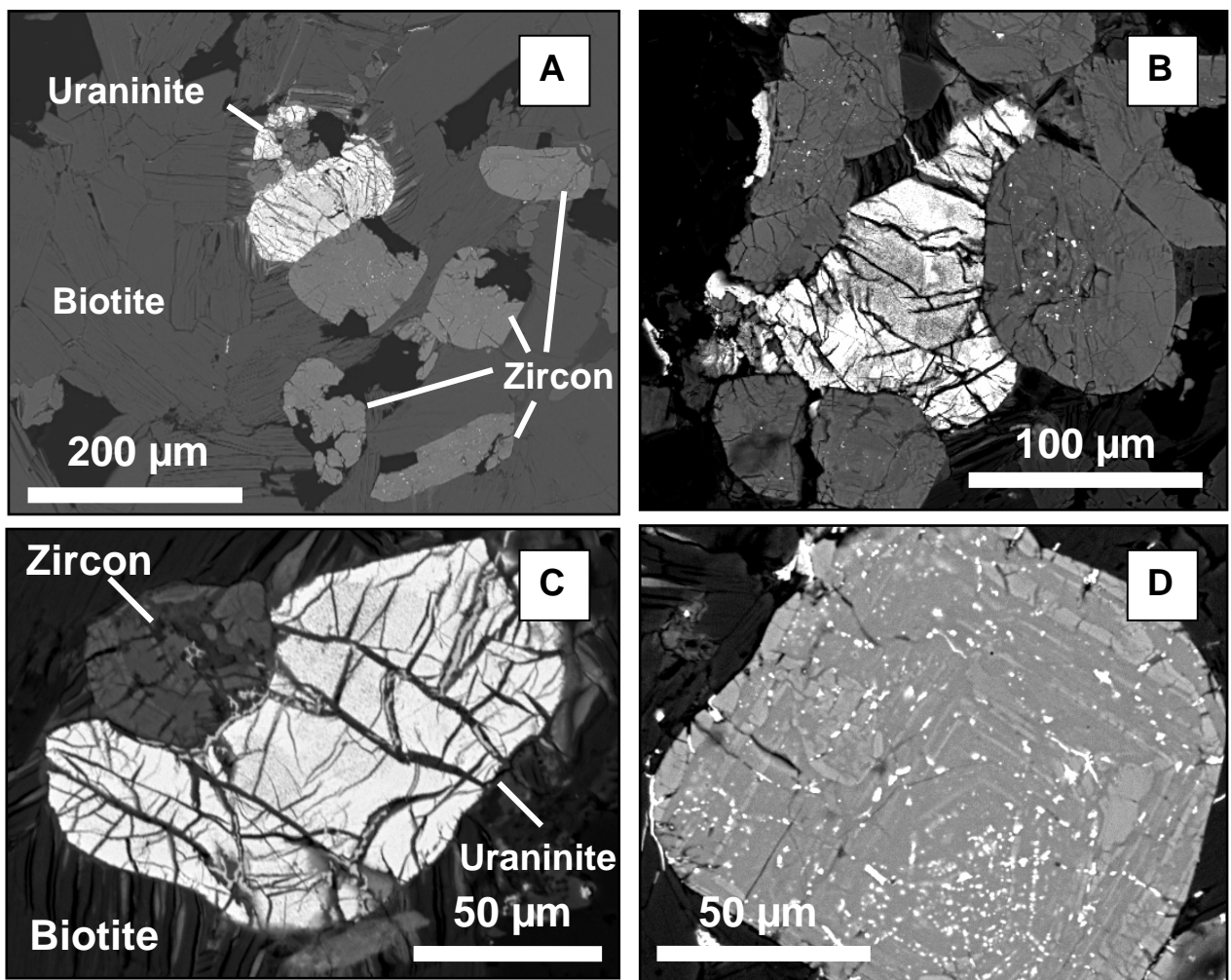


**Figure 2.4.60.** SEM-BSE images of various zircon and uraninite grains in biotite selvages of the Polyarnoe pegmatite (sample 58-2) showing intergrow relation (A-B-C) and small uraninite inclusions in zircon (D).

Zircon grains display strong average atomic number variations in BSE mode that characterized metamictization rather than primary growth zoning during magmatic crystallization. Polyarnoe zircon composition (Table 2.4.10) is compared to zircon from Dikoe and Skalnøe occurrences (Fig. 2.4.61). The composition variations are mainly due to decrease in major elements Zr, Hf and Si with a parallel increase in Ca, Fe, U and Pb contents with up to 8 at% of substitutions corresponding mainly to the presence of radiogenic lead. Metamictization results in the volumic expansion and fracturing of the crystals, facilitating the diffusion of Ca and Fe-rich fluids.

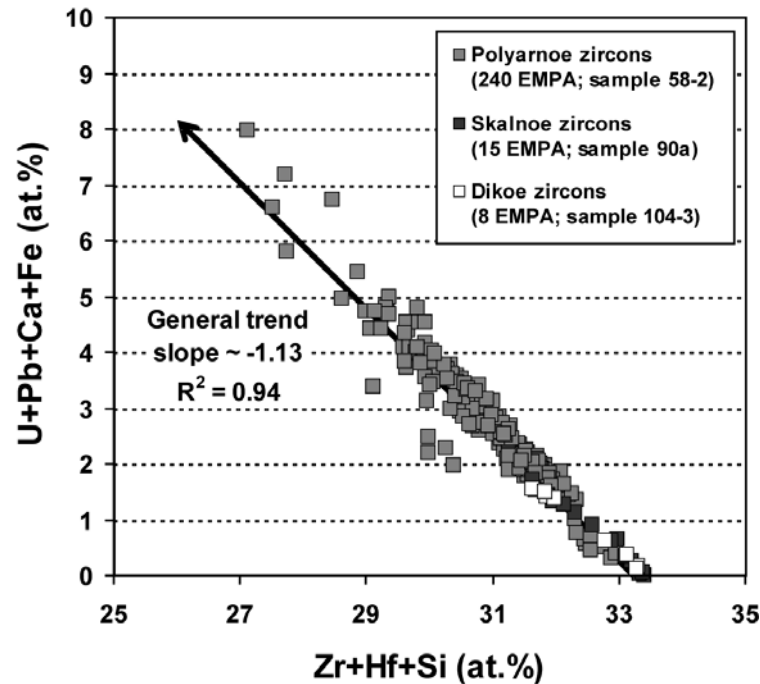


**Figure 2.4.61.** Binary diagram showing element substitutions Zr+Hf+Si vs. U+Pb+Ca+Fe (in atomic %) in zircon from the Polyarnoe pegmatite (sample 58-2)

Uraninite composition is also quite variable (Table 2.4.14): with between 53.35 and 75.63 wt% UO<sub>2</sub>, from 5.05 to 20.66 wt% PbO and between 6.05 and 11.48 wt% ThO<sub>2</sub>. The U-Th-Pb chemical ages obtained range from 485 to 1828 Ma. Y and REE (up to 1.88 wt% Y<sub>2</sub>O<sub>3</sub>, 1.04wt% Ce<sub>2</sub>O<sub>3</sub>, 2.07 wt% Nd<sub>2</sub>O<sub>3</sub> and 0.85 wt% Dy<sub>2</sub>O<sub>3</sub>) are also present in elevated contents. High contents in Si, Ca, Fe and S in some analytical spots (up to 1.59 wt% SiO<sub>2</sub>, 3.07 wt% CaO, 2.43 wt% FeO and 2.06 wt% SO<sub>2</sub>) are related to local alteration of uraninite and coincide with decreasing analytical totals caused by hydration of the mineral.

**Table 2.4.14.** Average chemical composition of uraninite (in weight percent) from the Polyarmoe ore showing (sample 58-2).

Polyarmoe ore showing (sample 58-2)		Average									
Uraninite grain	#1	#2	#3	#4	#5	#6	#7	#8	#9	#10	Mean ± σ
EPMA measurements	7	1	5	3	8	8	10	8	15	12	77
Al <sub>2</sub> O <sub>3</sub>	<D.L.	<D.L.	<D.L.	<D.L.	<D.L.	<D.L.	<D.L.	<D.L.	<D.L.	<D.L.	<D.L.
SiO <sub>2</sub>	0.23	<D.L.	<D.L.	<D.L.	<D.L.	<D.L.	0.18	0.17	0.12	0.20	0.16 ± 0.27
P <sub>2</sub> O <sub>5</sub>	<D.L.	<D.L.	<D.L.	<D.L.	<D.L.	<D.L.	<D.L.	<D.L.	<D.L.	<D.L.	<D.L.
Na <sub>2</sub> O	0.15	0.29	0.31	<D.L.	<D.L.	<D.L.	<D.L.	0.20	0.23	0.15	0.17 ± 0.11
CaO	1.10	1.89	0.63	0.48	0.57	0.65	1.77	0.48	0.67	1.10	0.89 ± 0.74
K <sub>2</sub> O	0.19	0.34	0.26	0.21	0.21	0.21	0.20	0.21	0.21	0.21	0.21 ± 0.05
SO <sub>2</sub>	1.17	0.74	1.11	1.40	1.46	1.17	0.50	0.63	0.84	0.63	0.91 ± 0.52
FeO	0.32	0.40	0.86	0.82	0.27	0.43	0.53	0.36	0.55	0.56	0.49 ± 0.39
MgO	<D.L.	<D.L.	<D.L.	<D.L.	<D.L.	<D.L.	<D.L.	<D.L.	<D.L.	<D.L.	<D.L.
TiO <sub>2</sub>	<D.L.	<D.L.	<D.L.	<D.L.	<D.L.	<D.L.	0.10	0.11	<D.L.	<D.L.	<D.L.
MoO <sub>3</sub>	<D.L.	<D.L.	<D.L.	<D.L.	<D.L.	<D.L.	<D.L.	<D.L.	<D.L.	<D.L.	<D.L.
ZrO <sub>2</sub>	<D.L.	<D.L.	<D.L.	<D.L.	<D.L.	<D.L.	<D.L.	<D.L.	<D.L.	<D.L.	<D.L.
V <sub>2</sub> O <sub>5</sub>	<D.L.	<D.L.	<D.L.	<D.L.	<D.L.	<D.L.	<D.L.	<D.L.	<D.L.	<D.L.	<D.L.
MnO	<D.L.	<D.L.	<D.L.	<D.L.	<D.L.	<D.L.	<D.L.	<D.L.	<D.L.	<D.L.	<D.L.
Ta <sub>2</sub> O <sub>5</sub>	<D.L.	<D.L.	<D.L.	<D.L.	<D.L.	<D.L.	<D.L.	<D.L.	<D.L.	<D.L.	<D.L.
Y <sub>2</sub> O <sub>3</sub>	1.33	1.20	0.95	1.14	0.83	1.75	1.08	0.87	0.84	1.18	1.09 ± 0.48
La <sub>2</sub> O <sub>3</sub>	<D.L.	<D.L.	<D.L.	<D.L.	<D.L.	<D.L.	<D.L.	<D.L.	<D.L.	<D.L.	<D.L.
Ce <sub>2</sub> O <sub>3</sub>	<D.L.	0.53	0.10	<D.L.	<D.L.	0.84	0.40	<D.L.	<D.L.	0.37	<D.L.
Nd <sub>2</sub> O <sub>3</sub>	0.88	0.98	0.47	0.50	0.57	1.37	1.02	0.36	0.51	0.88	0.75 ± 0.49
Dy <sub>2</sub> O <sub>3</sub>	<D.L.	<D.L.	<D.L.	<D.L.	<D.L.	<D.L.	<D.L.	<D.L.	<D.L.	<D.L.	<D.L.
PbO	12.05	11.34	14.63	13.73	16.65	14.50	10.44	11.59	11.24	12.08	12.60 ± 3.39
ThO <sub>2</sub>	8.60	9.00	8.92	7.85	7.85	8.72	8.32	7.19	7.09	8.60	8.05 ± 1.20
UO <sub>2</sub>	68.98	68.85	66.00	70.14	67.38	64.50	67.18	70.50	72.19	68.30	68.64 ± 3.46
Total	95.76	95.88	95.13	97.06	96.69	94.89	92.37	93.06	94.98	94.77	94.73 ± 2.54

Notes: “<D.L.”=below detection limit (Al=0.05wt%; Si=0.06wt%; P=0.06wt%; Na=0.11wt%; Ca=0.08wt%; K=0.11wt%; S=0.05wt%; Fe=0.21wt%; Mg=0.04wt%; Ti=0.05wt%; Mo=0.12wt%; Zr=0.23wt%; V=0.15wt%; Mn=0.21wt%; Y=0.12wt%; La=0.11wt%; Ce=0.29wt%; Nd=0.55wt%; Dy=0.64wt%; Ta=0.19wt%; Pb=0.25wt%; Th=0.14wt%; U=0.58wt%).

The isotopic dating (SIMS) of two uraninite grains by ion probe (Table 2.4.15) yields a wide range of  $^{207}\text{Pb}$ - $^{206}\text{Pb}$  ages from 2015 to 2130 Ma approximately (Fig. 2.4.62):  $2019 \pm 3$  Ma and  $2066 \pm 5$  Ma for grain 1 and  $2115 \pm 5$  Ma and  $2122 \pm 9$  Ma for grain 2. The U-Pb ratios have been plotted in a Concordia diagram and the four measurements are reliable in a single discordia line with low MSWD (0.94) giving a lower intercept at  $196 \pm 9$  Ma and  $2174 \pm 5$  Ma for the upper intercept (Fig. 2.4.63). This last age is concordant with the previous isotopic dating giving  $\sim 2.2$  Ga (Savitskii et al., 1995 and Afanasieva et al., 2007) and precedently interpreted as the age of the pegmatite rock.

Nevertheless, the mineralogical assemblage and the textural relationship between zircon and uraninite suggest that both minerals are magmatic. The high Th, Y and REE contents of Polyarnoe uraninite also indicate a primary origin. The REE patterns of three uraninite grains (Table 2.4.7 and Fig. 2.4.25) are characteristic of early fractionation of Eu by the plagioclase during melt crystallization ( $\text{Eu}/\text{Eu}^* = 0.18\text{-}0.48$ ) and of the very high REE contents in the magma during crystallization of uranium oxides ( $\Sigma\text{REE} \sim 1.78\text{-}3.15$  wt%). This signature is typical of magmatic uraninites from pegmatoids deriving from partial melting of U-pre-enriched metasediments as for the Rössing deposit in alaskites from Namibia (Cuney and Kyser, 2008). Therefore, the age determined by the upper intercept at  $2174 \pm 5$  Ma is considered by authors as the minimal age for primary U mineralization and subsequent Pb loss during alteration event(s) have partly reset the isotopic U-Pb system.

**Table 2.4.15.** Ion probe U-Pb results for 2 uraninite grains from the Polyarnoe ore showing

Sample	$\frac{^{204}\text{Pb}}{^{206}\text{Pb}}$	$\frac{^{207}\text{Pb}}{^{206}\text{Pb}}$	$\frac{^{208}\text{Pb}}{^{206}\text{Pb}}$	$\frac{^{207}\text{Pb}}{^{206}\text{Pb}}$	Age (Ma)	$\frac{^{206}\text{Pb}}{^{238}\text{U}}$	Age (Ma)
<b>Uraninite</b>							
<b>Crystal</b>							
<b>Spot number</b>							
<i>Polyarnoe: 58-2</i>							
<b>Grain 1</b>							
Spot 1	0.000000 (1)	0.125 (2)	0.041 (6)		$2019 \pm 3$		$1585 \pm 14$
Spot 2	0.000014 (1)	0.128 (3)	0.041 (7)		$2066 \pm 5$		$1917 \pm 17$
<b>Grain 2</b>							
Spot 3	0.000000 (1)	0.132 (6)	0.034 (10)		$2122 \pm 9$		$2826 \pm 25$
Spot 4	0.000000 (1)	0.132 (3)	0.037 (12)		$2115 \pm 5$		$2423 \pm 23$

**Notes:** numbers in brackets indicate errors ( $1\sigma \cdot 10^{-5}$  for  $^{204}\text{Pb}/^{206}\text{Pb}$ ,  $1\sigma \cdot 10^{-3}$  for  $^{207}\text{Pb}/^{206}\text{Pb}$  and  $^{208}\text{Pb}/^{206}\text{Pb}$ ),  $^{207}\text{Pb}/^{206}\text{Pb}$  ages are corrected from the common Pb.

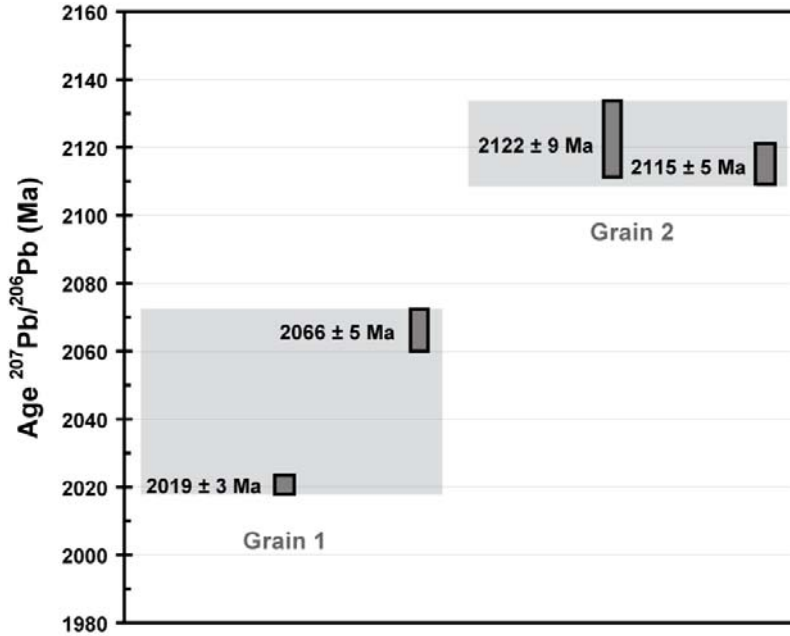


**Figure 2.4.62.** Distribution of  $^{207}\text{Pb}/^{206}\text{Pb}$  ages (Ma) measured in 2 uraninite grains of the Polyarnoe pegmatite (sample 58-2). The darker grey bars represent  $2\sigma$  errors.

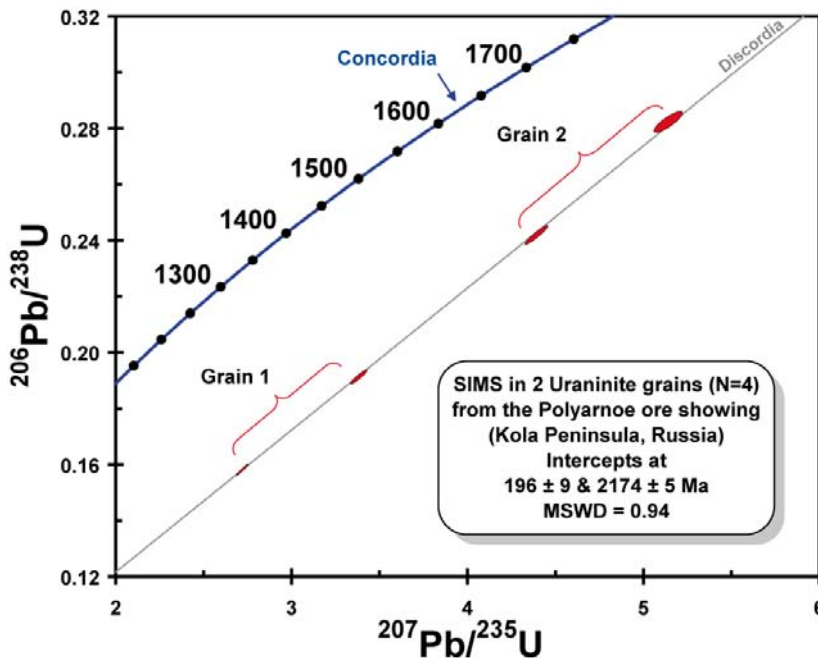


**Figure 2.4.63.** Concordia diagram for the two uraninite grains from Polyarnoe (sample 58-2). The error ellipse for each analytical measurement is represented in red. The intercepts of the Discordia line with the Concordia curve were calculated using the isoplot software (Ludwig, 1999).

## CONCLUSIONS

The intrusive-type U occurrences of the Baltic Shield are represented by uraninite in biotite-quartz-feldspar pegmatoids issued from the partial melting of migmatized Archean biotite-rich gneisses. In terms of geochemistry, the gneisses are peraluminous with low to medium-K contents and derived from metavolcanic and metasedimentary rocks. The pegmatoid composition varies widely in silica and alkali contents because of the variable proportions in quartz, feldspar and two micas (biotite / secondary muscovite). The highly variable contents in major and trace elements of these pegmatoids are linked mainly to primary magmatic processes that influence directly the mineral assemblage. It reflects the diverse nature of the source material being melt, the degree of partial melting, the ratio between restite and extracted magma and the complex equilibrium reactions that may occur with the host-rock during emplacement (Cuney and Kyser, 2008). The magmatic processes related to migmatization of Archean gneisses start during Late Archean (~2.7-2.6 Ga) until Early Paleoproterozoic with emplacement of structural domes during partial melting with emplacement of the Mustalampi pegmatites in Karelia at the edge of the Huhtilampi granite batholith in amphibolite and biotite-rich gneisses and the Litsa ore showings in Kola occurring in faults and fold limbs in migmatized paragneisses. The tectonic structures and timing correspond to a period of rifting that supposedly started under the influence of a mantle plume related to the break-up of the Kenorland supercontinent at the end of Archean era (Daly et al., 2001 and 2006). The U-rich pegmatoids are emplaced as vein-like or lenticular bodies generally concordant to the host-rock foliation and at the scale of outcrop or thin section they often show brittle-ductile features as boudinage and granoblastic polygonal recrystallization textures.

The main U-mineralization is represented by uraninite concentrated into biotite rich-selvages with other accessories dominated by monazite and zircon with minor apatite and xenotime. The chemical signature of uraninite characterized by very high contents in Th ( $\text{ThO}_2$  ranging 7.76-11.79 wt% in Mustalampi grains / 1.5-6.22 wt% in Dikoe crystals/ 6.05-11.48 wt% in Polyarnoe uraninite), Y (up to 1.88 wt%  $\text{Y}_2\text{O}_3$ ) and REE ( $\Sigma\text{REE}$  1.07-3.15 wt%) supporting a magmatic origin. Uranium probably preferentially concentrated in the restite undmixed material with other incompatible and high field strength elements. U-Pb isotopic and U-Th-Pb chemical dating provided in this work indicate a multistage alteration event(s) with strong Pb loss both in Karelia and Kola occurrences. Secondary U mineralization differs between both areas: in Karelia, the alteration is hydrothermal with coffinitization of uraninite and replacement of altered monazite by allanite and uranothorite with pyrite and molybdenite deposition; in Kola, the alteration is due to oxidizing meteoric fluids with primary uraninite altered to hexavalent

uranium minerals (kasolite, uranophane and bequerellite) or totally dissolved leaving cubic boxwork and new crystallization of pitchblende without Th. Metasomatism of the Kola pegmatoids is associated to successive alterations: chloritization, albitization, muscovitization and finally tourmalinization at ~2.52 Ga in shear zones.

The U-mineralization in the pegmatoids of the Baltic Shield is interpreted as associated to partial melting of metasediments with local late metasomatism and could be compared to the metallogenic model of the Rössing deposit in Namibia (Cuney 1981, 1982). The Rössing uraniferous alaskite granites are emplaced as dykes or lenses along foliation of high-grade migmatitic paragneisses in a similar geological setting. The Rössing uraninites have comparable composition ranging 3.3-8 wt% ThO<sub>2</sub>, 1.6-7.14 wt% Y<sub>2</sub>O<sub>3</sub> and 2.3 wt% REE (Cuney and Kyser, 2008). Moreover, both Mustalampi uraninites from Karelia and Polyarnoe uraninites from Kola have chondrite-normalized REE patterns corresponding to the signature of uraninite from the Rössing alaskite (Bonhoure, 2007). The Rössing ore is strongly affected by late hydrothermal fluid circulation that reconcentrates the U mineralization. In the Archean Baltic Shield, the distribution of pegmatitic bodies and U mineralization is much more scattered than at Rössing and the average grade is also generally too low to be considered of economic importance. Nevertheless, Archean paragneisses provide fertile protoliths for subsequent remelting processes in migmatites and the resulting uraninite-bearing granitoids are good sources for sedimentary U accumulations or in paleoplacer-type deposits.

## ACKNOWLEDGEMENTS

The authors are grateful to AREVA for the financial support and to the VSEGEI for scientific work exchanges and field trip assistance. The author thanks Alain Kohler, Johann Ravaux and Sandrine Mathieu for their assistance with the SEM and EMP at the SCMEM laboratory. Michel Champenois and Denis Mangin are also grateful for their support with the ion microprobe instrument at the CRPG-CNRS.

## REFERENCES

- Afanasieva, E., Lipner, A. A. and Serov, L., 2007, Kola field trip report 2007, VSEGEI internal report, 34 p.
- Afanasieva, E., 2006, Kola field trip report 2006, VSEGEI internal report, 36 p.
- Anders E. and Grevesse N., 1989, Abundances of the elements: Meteoritic and solar. *Geochimica and Cosmochimica Acta* 57, 197-214.
- Bibikova, E., Skiöld, T., Bogdanova, S., Gorbatshev, R. and Slabunov, A., 2001, Titanite-rutile thermochronometry across the boundary between the Archean Craton in Karelia and the Belomorian Mobile Belt, eastern Baltic Shield, *Precambrian Research*, vol. 105, p. 315-330.
- Bibikova, E. V., Bogdanova, S., Claesson, S. and Skiold, T., 1999, NORDSIM Ages on Provenance and Metamorphic Zircon Material in Belomorian Metasediments of the Baltic Shield, *Journal of Conference Abstracts*, Vol. 4, No. 1, Symposium A08, Early Evolution of the Continental Crust.
- Bogdanova, S. V. and Bibikova, E. V., 1993, The 'Saamian' of the Belomorian Mobile Belt: new geochronological constraints, In: Gorbatshev, R. (Ed.), *The Baltic Shield, Precambrian Research*, vol. 64, p. 131-152.
- Bonhoure, J., 2007, *Géochimie des éléments de terres rares et du plomb dans les oxydes d'uranium naturels*, Doc. Univ. Nancy, France.
- Bonhoure, J., Kister, P., Cuney, M. and Deloule, E., 2007, Methodology for Rare Earth Element Determinations of Uranium Oxides by Ion Microprobe, *Geostandards and Geoanalytical Research* 31, p. 209-225.
- Caillat, C., Kister, P. and Chemillac, R., 2006, *Compte Rendu de Mission: Puruvesi (Finland) – Northern Ladoga (Russia) Field Trip 26.09.06-04.10.06*, Internal Report AREVA NC/BUM/DEX/PN 06-FIN-CRM-03, 41 p.
- Carignan J., Hold, P., Mevelle, G. Morel, J. and Yeghichevan, D., 2001, Routine analysis of trace elements in geological samples using flow injection and low pressure on line liquid chromatography coupled to ICP-MS: a study of geochemical reference materials BR, DR-N, UB-N, AN-G and GH, *Geostandards Newsletter* 25, p. 187-198.
- Cathelineau, M., 1986, The hydrothermal alkali metasomatism, Effects on Granitic rocks: Quartz dissolution and related subsolidus changes; *Journal of Petrology*, Vol. 27, No. 4, p. 945-965.
- Cathelineau, M., Boiron, M.-C., Holliger, P. and Poty, B., 1990, Metallogensis of the French part of the Variscan orogen; Part II: Time-space relationship between U, Au and Sn-W ore deposition and geodynamic events-mineralogical and U-Pb data, *Tectonophysics* 177, p. 59-79.
- Cocherie, A. and Albarède, F., 2001, An improved U-Th-Pb age calculation for electron microprobe dating of monazite, *Geochimica et Cosmochimica Acta*, Vol. 65, p. 4509-4522.
- Condie, K. C., Bowling, G. P. and Allen, P., 1985, Missing Eu anomaly and Archean high-grade granites, *Geology*, Vol. 13, No. 9, p. 633-636.
- Cuney, M., 1981, *Comportement de l'uranium et du thorium au cours du métamorphisme, Rôle de l'anatexis dans la genèse des magmas riches en radioéléments*, Doctoral thesis, INPL, Nancy, France, 511 p.

- Cuney, M., 1982, Processus de concentration de l'uranium et du thorium au cours de la fusion partielle et de la cristallisation des magmas granitiques, In: Les méthodes de prospection de l'uranium, OCDE (ed.), Paris, p. 277-292.
- Cuney, M. and Friedrich, M., 1987, Physicochemical and crystal-chemical controls on accessory mineral paragenesis in granitoids: implications for uranium metallogenesis; *Bulletin de Minéralogie* 110, p. 235-247.
- Cuney, M. and Kyser, K., 2008, Deposits related to Partial Melting, In: M. Cuney and K. Kyser (eds.) Recent and not-so-recent developments in uranium deposits and implications for exploration, Short Course Series Vol. 39, Mineralogical Association of Canada, p. 79-95.
- Daly, J. S., Balagansky, V. V., Timmerman, M. J., Whitehouse, M. J., de Jong, K., Guise, P., Bogdanova, S., Gorbatshev, R. and Bridgwater, D., 2001, Ion microprobe U-Pb zircon geochronology and isotopic evidence for trans-crustal suture in the Lapland-Kola Orogen, northern Fennoscandian Shield, *Precambrian Research* 105, p. 289-314.
- Daly, J. S., Balagansky, V. V., Timmerman, M. J. and Whitehouse, M. J., 2006, The Lapland-Kola Orogen: Palaeoproterozoic collision and accretion of the northern Fennoscandian lithosphere, In: Gee, D. G. and Stephenson, R. (eds.), *European Lithosphere Dynamics*, Geological Society, London Memoir, Vol. 32, p. 579-598.
- Debon, F. and Le Fort, P., 1988, A cationic classification of common plutonic rocks and their magmatic associations: principles, method, applications, *Bulletin de Minéralogie* 111, p. 493-510.
- Debon, F. and Le Fort, P., 1983, A chemical–mineralogical classification of common plutonic rocks and associations, *Transactions of the Royal Society of Edinburgh, Earth Sciences* 73, p. 135-149.
- Gaál, G., Gorbatshev, R., 1987, An outline of the Precambrian evolution of the Baltic Shield, In: Gaffl, G., Gorbatshev, R. (Eds.) *Precambrian Geology and Evolution of the Central Baltic Shield*, *Precambrian Res.* 35, p. 15-52.
- Gao, S. and Wedepohl, K. H., 1995, The negative Eu anomaly in Archean sedimentary rocks: Implications for decomposition, age and importance of their granitic sources, *Earth and Planetary Science Letters*, Vol. 133, Issues 1-2, p. 81-94 .
- Holliger, P., 1988, Ages U-Pb définis in situ sur oxydes d'uranium à l'analyseur ionique: méthodologie et conséquences géochimiques, *Comptes rendus de l'Académie des Sciences de Paris* 307, p. 367-373.
- Hölttä, P., Balagansky, V., Garde, A. A., Mertanen, S., Peltonen, P., Slabunov, A., Sorjonen-Ward, P. and Whitehouse, M., 2008, Archean of Greenland and Fennoscandia, *Episodes*, Vol. 31, No. 1, p. 13-19.
- Iljina, M. and Hanski, E., 2005, Layered mafic intrusions of the Tornio-Näränkäväära belt, In: Lehtinen, M., Nurmi, P. A., Rämö, O. T. (eds.), *The Precambrian Geology of Finland – Key to the Evolution of the Fennoscandian Shield*, *Developments in Precambrian Geology* 14, Elsevier Science B. V., Amsterdam.
- Käpyaho, A., Hölttä, P. and Whitehouse, M., 2007, U-Pb zircon geochronology of selected Neoproterozoic migmatites in eastern Finland: *Bulletin of the Geological Society of Finland*, Vol. 79 (1), p. 95-115.
- Kish, L. and Cuney, M., 1981, Uraninite-albite veins from Mistamisk Valley of the Labrador Through, Quebec. *Mineralogical Magazine* 44, 471-483.

- Kohonen, J., 1995, From continental rifting to collisional crustal shortening – Paleoproterozoic Kaleva metasediments of the Höytiäinen area in North Karelia, Finland, Geological Survey of Finland, Bulletin 380.
- Kouvo, O. and Tilton, G. R., 1966, Mineral Ages from the Finnish Precambrian, *The Journal of Geology*, Vol. 74, No. 4, p. 421-442.
- Kudryashov, N., 1999, Archean Kolmozero-Voronja Greenstone Belt: U-Pb Zircon and Sphene Data; *Journal of Conference Abstracts*, Vol. 4, No. 1, Symposium A08, Early Evolution of the Continental Crust.
- Kudryashov, N., Gavrilenko, B., Apanasevich, E., 2003, Geochronology of the Archaean Kolmozero-Voron'ya Greenstone Belt: U-Pb dating of zircon, titanite, tourmaline and tantalite (Kola Region, North-Eastern Baltic Shield), EGS - AGU - EUG Joint Assembly, *Geophysical Research Abstracts*, Vol. 5, Abstract #398.
- Kister, P., Cuney, M. and André-Mayer, A.-S., 2007, U potential of the Litsa area in the Kola Peninsula (Russia), Field Work Report July 2006-2007, *Compte rendu de mission AREVA BUM/DEX RM 07/234*, 81 p.
- Lahtinen, R., Korja, A., Nironen, M. and Heikkinen, P., 2009, Palaeoproterozoic accretionary processes in Fennoscandia; In: Cawood, P.A., Kröner, A. (Eds.), *Earth Accretionary Systems in Space and Time*, The Geological Society, London, Spec. Publ. 318, p. 237-256.
- Lahtinen, R., Garde, A. A. and Melezhik, V. A., 2008, Paleoproterozoic evolution of Fennoscandia and Greenland, *Episodes* 31, p. 20-28.
- Lahtinen, R., Korja, A. and Nironen, M., 2005, Palaeoproterozoic tectonic evolution of the Fennoscandian Shield; In: Lehtinen, M., Nurmi, P.A., Rämö, O.T. (Eds.), *The Precambrian Bedrock of Finland-Key to the Evolution of the Fennoscandian Shield*. Elsevier Science B.V., p. 418-532.
- Lehtinen, M., Nurmi, P. A. and Rämö, T., 2005, Precambrian geology of Finland: key to the evolution of the Fennoscandian shield, C. K. Condie Editor Series, Elsevier, *Development in Precambrian Geology* Vol. 14, 736 p.
- Ludwig, K.R., 1999, Isoplot/Ex version 2.00 – A geochronological toolkit for Microsoft Excel, Berkeley Geochronology Center, Special Publication No. 2.
- Maniar P. D., Piccoli P. M., 1989, Tectonic discrimination of granitoids, *Geological Society of American Bulletin*, vol. 101, p. 635-643.
- Martin, H., 1985, Nature, origine et evolution d'un segment de croûte continentale archéenne : contraintes chimiques et isotopiques, exemple de la Finlande orientale ; *Mémoires et Documents du Centre Armoricaïn d'Etude Structurale des Socles (CAESS) N° 1*, Université de Rennes II (France), 324 p.
- Mertanen, S., Vuollo, J. I., Huhma, H., Arestova, N. A. And Kovalenko, A., 2006, Early Paleoproterozoic-Archaean dykes and gneisses in Russian Karelia of the Fennoscandia Shield – New paleomagnetic, isotopic age and geochemical investigations, *Precambrian Research*, Vol. 144, p. 239-260.
- Montel, J. M., Foret, S., Veschambre, M., Nicollet, Ch. And Provost, A., 1996, Electron microprobe dating of monazite; *Chemical Geology*, Vol. 131, p. 37-53.
- Nironen, M., 1997, The Svecofennian Orogen: a tectonic model, *Precambrian Research* 86, p. 21-44.
- Nykänen, O., 1968, Kaalioperäkartan selitys, 4232-4234 Tohmajärvi, English summary: Explanation to the map rocks, *Geological map of Finland 1:100 000*, 68 p.

- Peccerillo, A. and Taylor, S. R., 1976, Geochemistry of Eocene calc-alkaline volcanic rocks from the Kastamonu area, Northern Turkey, *Contributions to Mineralogy and Petrology* 58, p. 63-81.
- Pekkarinen, L., 1979, The Karelian formations and their depositional basement in the Kiihtelysvaara-Värtsilä area, East Finland. *Geological Survey of Finland Bulletin* 301, 141 p.
- Riihiaho, M. A. and Holmes, 1998, P. K., Summary Report for the Mustalampi Claim (5926/2), Finsearch Oy internal report, 6 p.
- Savitskii, A. V., Gromov, A. Yu., Mel'nikov, E. K. and Sharikov, P. I., 1995, Uranium ore mineralization of the Litsk District in the Kola Peninsula (Russia), *Geo. Ore Deposits*, 37, p. 351-362.
- Shand, S. J., 1947, *Eruptive Rocks: Their Genesis, Composition, Classification, and their Relation to Ore-deposits*, 3rd ed. New York, John Wiley, p. 1-488.
- Shurilov, A.V., 2008, Métallogenèse de l'uranium dans la région de Ladoga (Karélie, Russie), thèse pour l'obtention du diplôme de doctorat de l'Université Henry Poincaré, Nancy, France, 463 p.
- Shurilov, A.V., Cuney, M. and Polekhovsky, Yu.S., 2007, Evolution of uranium enrichment in the Ladoga region (Russia), 9th biennial SGA meeting, 20th-23rd august 2007, Dublin, Session 17a, 4 p.
- Suzuki, K. and Adachi, M., 1991, Precambrian provenance and Silurian metamorphism of the Tsunosawa paragneiss in the South Kitakami terrane, Northeast Japan, revealed by the chemical Th-U-total Pb-isochron ages of monazite, zircon and xenotime; *Geochemical Journal*, Vol. 25, p. 357-376.
- Tilton, G. R. and Grünefelder, M. H., 1968, Sphene: Uranium-lead ages, *Science* 159, p. 1458-1461.
- Timmerman, M. J. and Daly, J. S., 1995, Sm-Nd evidence for late Archaean crust formation in the Lapland-Kola Mobile Belt, Kola Peninsula, Russia and Norway; *Precambrian Research* 72, p. 97-107.
- Vetrin, V. R., Berezhnaya, N. G. and Rodionov, N. V., 2006, Petrology of Postorogenic Granitoids of the Northern Baltic Shield, *Doklady Earth Sciences*, 2006, Vol. 411A, No. 9, p. 1476-1479.
- Vuollo, J.I. and Huhma, H., 2005, Palaeoproterozoic mafic dykes in NE Finland. In: Lehtinen, M., Nurmi, P.A. and Rämö, O.T. (eds.), *Precambrian Geology of Finland*, Elsevier. B.V. Amsterdam, p. 195-236.
- Wetherill, G. W., Kouvo, O., Tilton, G. R. and Cast, P. W., 1962, Age measurement on rocks from the Finnish Precambrian, *Journal of Geology*, Vol. 70, No. 1, p. 74-88.
- Williams, H., Hoffman, P. F., Lewry, J. F., Monger, J. W. H. and Rivers, T., 1991, Anatomy of North America: thematic geological portrayals of the continent, *Tectonophysics*, vol. 187, Issue 1-3, p. 117-134.

## **SYNTHESE ET DISCUSSION SUR LES SOURCES MAGMATIQUES ARCHEENNES DE L'URANIUM**

### ***Granitoïdes du Craton de Kénéma-Man en Guinée***

Les granitoïdes archéens de Guinée sont essentiellement peralcalins et métalumineux. Ils se sont formés par différenciation magmatique progressive lors de la fusion partielle d'une croûte océanique dans un contexte d'accrétion crustale au dessus d'une zone de subduction (Thiéblemont et al., 2001). Les premiers magmas qui se mettent en place dans les ceintures de roches métavolcaniques sont des TTG sodiques pauvres en U, riches en minéraux métalumineux (amphibole très abondante, pyroxène non observé dans nos échantillons), ferromagnésiens et titanifères (biotite, magnétite, ilménite et sphène). Les TTG sont repris lors de fusions épisodiques au Léonien (3.05-2.95 Ga) et au Libérien (2.85-2.7 Ga) qui produisent des magmas d'affinité calco-alkaline de plus en plus enrichis en éléments incompatibles (U, Th, K, REE) et suivent un axe de corrélation positif entre l'indice de peraluminosité A et de différenciation B (Fig. 2.A). Ces lignées magmatiques correspondent à des granitoïdes de type I (Cuney and Kyser, 2008). L'uranium dans ces granitoïdes est essentiellement présent dans les phases minérales réfractaires, principalement le zircon et la monazite. Les minéraux accessoires peuvent libérer leurs radioéléments lorsqu'ils deviennent métamictes (zircon) ou s'ils sont intensément altérés par des fluides hydrothermaux (monazite) formant des phases secondaires comme les huttonites, les thorites ou des épidotes enrichies (allanite). Seuls les derniers termes les plus différenciés ( $B < 50$ ), les plus potassiques ( $K_2O > 5\text{wt}\%$ ) et qui entrent dans le domaine peralumineux ( $0 < A < 50$ ) sont capables de cristalliser de l'uraninite. C'est le cas des produits de fusion partielle d'un évènement magmatique tardif au Paléoprotérozoïque (échantillon Eburnéen NZE2381 d'âge ~2.1 Ga), dont la concentration en uranium, bien que faible (de l'ordre d'une vingtaine de ppm seulement), est suffisante pour voir la cristallisation d'uraninite magmatique caractérisée par des teneurs en thorium comprises entre 3.11 wt% et 6.59 wt% ThO<sub>2</sub> (Fig. 2.B). Cependant les quantités d'uranium ne permettent pas de former des concentrations économiques.

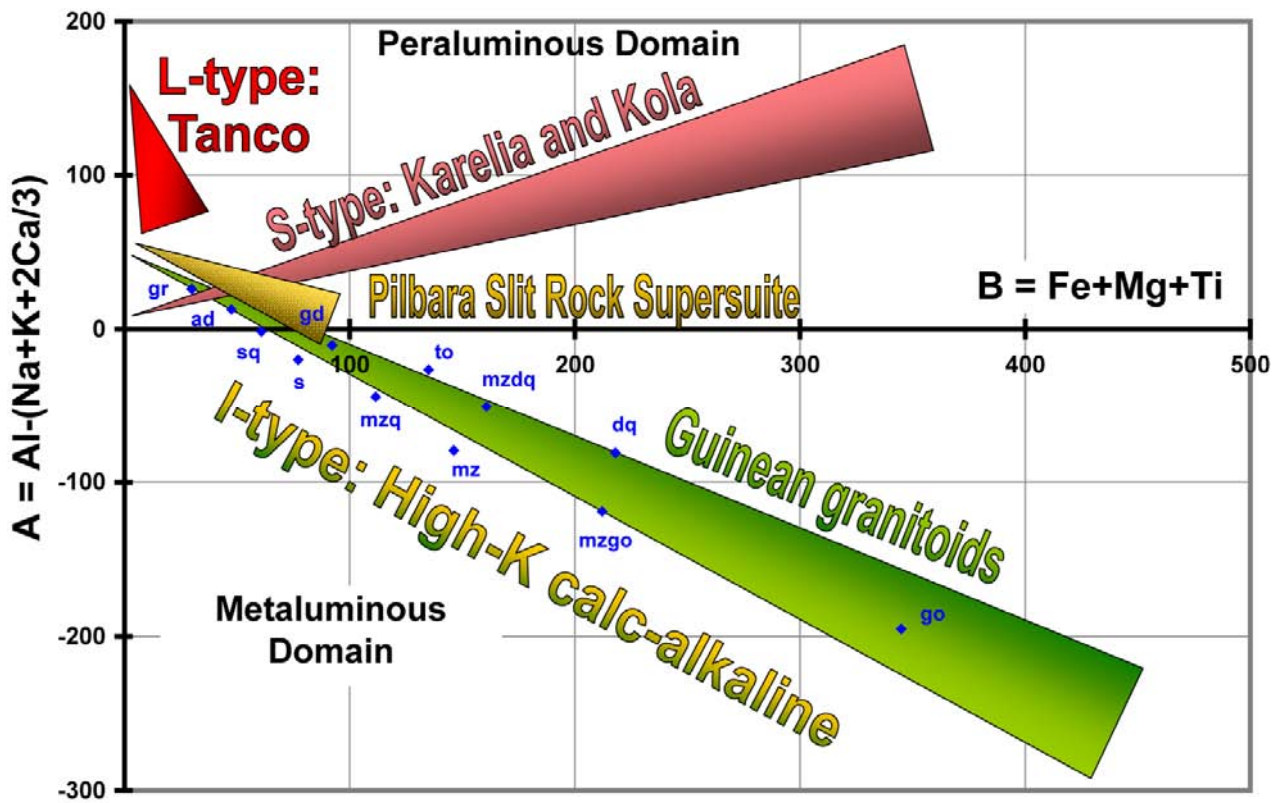


**Figure 2-A.** Diagramme binaire de synthèse montrant l'évolution des lignes magmatiques étudiées en fonction de l'indice de peraluminosité (A) et de l'indice de différenciation (B) d'après Debon and Lefort (1988). Les compositions de référence des roches (d'après Debon et Lefort, 1983) sont données à titre indicatif : go = gabbro; mzgo = monzogabbro; mz = monzonite; mzq = quartz-monzonite; mzdq = quartz monzodiorite; dq = quartz diorite; s = syénite; sq = quartz syénite; to = tonalite; gd = granodiorite; ad = adamellite; gr = granite.

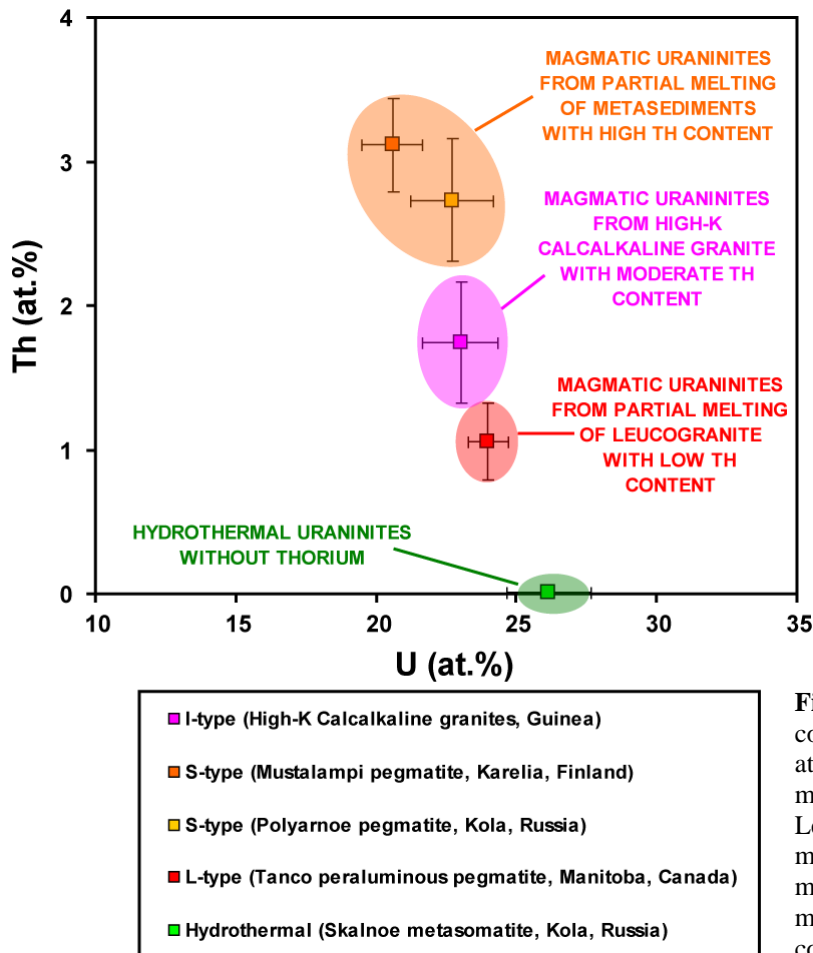


**Figure 2-B.** Diagramme binaire des concentrations Th vs. U (en pourcentage atomique) des uraninites dans les roches magmatiques étudiées dans ce chapitre. Les carrés de couleur représentent les moyennes mesurées lors des microanalyses quantitatives à la microsonde électronique et les barres correspondent aux écart-types.

### ***Granitoïdes du Craton de Pilbara en Australie***

Les granites potassiques calco-alcalins peralumineux du craton de Pilbara en Australie sont issues du même type de lignée magmatique que les granitoïdes de Guinée (type I d'après Champion and Smithies, 2001 et 2004). Ces granites dérivent du fractionnement par fusion partielle des grands dômes de TTG séparés par des ceintures de roches vertes. Ces granites potassiques de la Split Rock Supersuite dériveraient des TTG riches en aluminium issus d'une première fusion du matériel crustal. Ils représentent les termes les plus différenciés. Les mêmes phases réfractaires que dans le craton Ouest Africain sont présentes : zircon, monazite, sphène et biotite accompagnés de grenat de type almandin, d'amphibole calcique (hornblende) et de ferro-colombite. Cependant, aucune uraninite n'a été observée et ce probablement à cause de l'échantillonnage trop restreint. Cette étude a cependant montré que des fluides métasomatiques calciques et riches en fluor libérés très certainement lors de la mise en place des batholithes dans les ceintures de roches vertes ont permis de lessiver les minéraux magmatiques primaires pour former de nouvelles phases secondaires telles que des fluorocarbonates de terres rares légères ou des phases complexes à Nb-Ta-Ti enrichies en U et Th (mélange de phases de la famille des pyrochlores).

### ***Pegmatite leucocrate à métaux rares de Tanco, Manitoba, Canada***

Les granites peralumineux encore plus fortement fractionnés comme la pegmatite de Tanco au Canada sont capables de cristalliser des phases magmatiques uranifères telles que l'uranmicrolite et l'uraninite. Ces granites dit de type L pour leucogranites (Cuney and Kyser, 2008) sont riches en muscovite ( $50 < A < 150$ ) et contiennent très peu de minéraux fémiqes ( $B < 50$ ) comme les granites de Beauvoir en France (Cuney et al., 1992 ; Fig. 2-A). Ils sont formés par un très faible taux de fusion partielle (moins de 30%) à des températures de fusion relativement basses ( $\sim 600^{\circ}\text{C}$ ) du matériel supracrustal (Černý, 1991; Cuney and Kyser, 2008). Ces roches sont beaucoup plus leucocrates et sont marquées par la présence de minéraux riches en éléments incompatibles et métaux rares, cassitérite, lépidolite et oxydes de tantale plus évolué comme mangano-tantalite et wodginite. Les uraninites magmatiques enregistrent les caractéristiques du magma dans lequel elles se sont formées et sont dans ce cas assez pauvres en thorium ( $3.36 \pm 0.94 \text{ wt\% ThO}_2$  ; Fig. 2-B) ainsi qu'en yttrium ( $Y = 300\text{-}400 \text{ ppm}$ ) et en terres rares ( $\Sigma\text{REE} = 200\text{-}250 \text{ ppm}$ ) avec une forme de spectre normalisé aux chondrites faiblement fractionné ( $\text{LREE/HREE} \sim 0.30$ ) et une anomalie négative en europium ( $\text{Eu/Eu}^* \sim 0.5$ ) qui découle de la cristallisation précoce du plagioclase dans le magma source (Fig. 2-C).

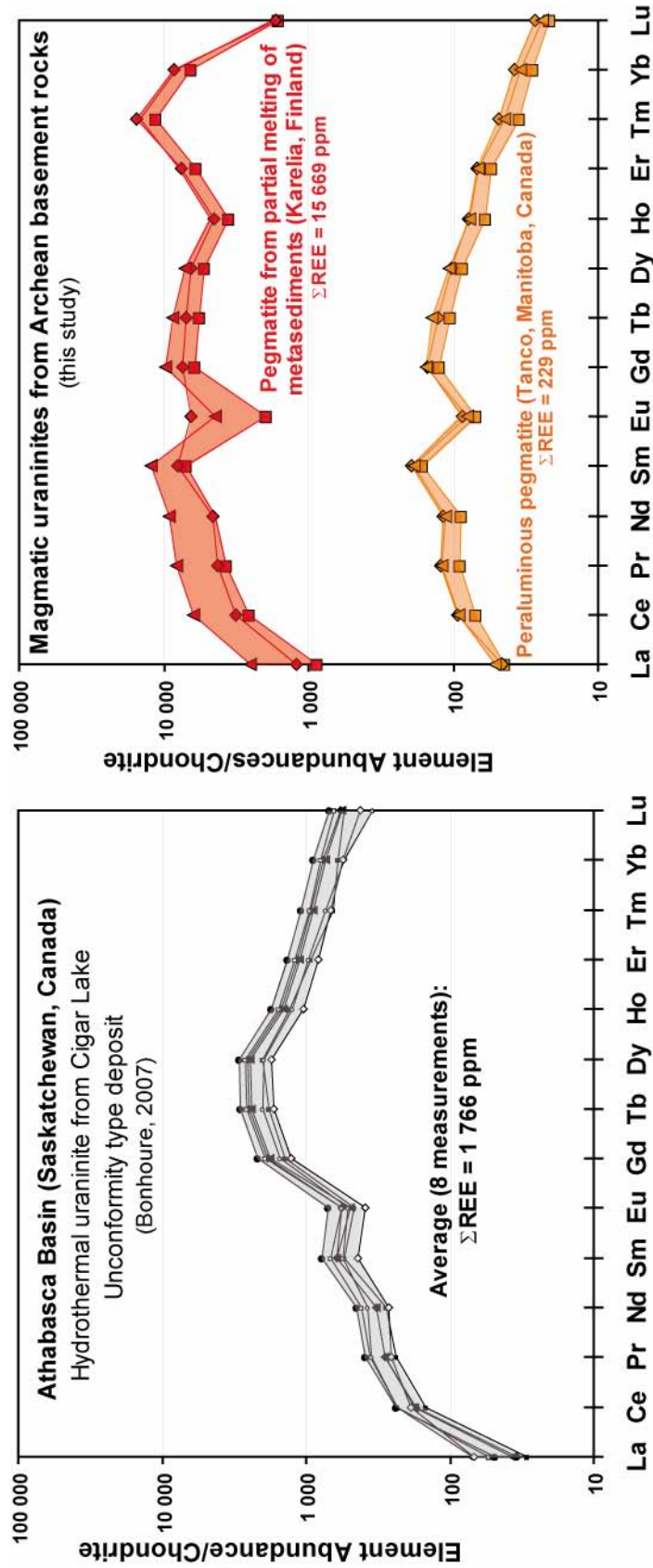


**Figure 2-C.** Comparaison entre les spectres des éléments des Terres Rares normalisés aux chondrites, d'oxydes d'uranium cristallisés par des processus hydrothermaux protérozoïques (données de Bonhoure, 2007) et des uraninites magmatiques cristallisées à hautes températures dans des pegmatites archéennes (cette étude).

***Pegmatites du Bouclier Baltique de la région de Carélie et de la Péninsule de Kola***

Enfin, un dernier type de source encore plus riche en uranium est créé par la fusion de méta-sédiments, les granites de type S. Ces granites sont formés lors d'un fort taux de fusion partiel associés à des températures élevées ( $>800^{\circ}\text{C}$ ). L'uranium enrichi dans les sédiments des ceintures de roches vertes, comme les métapélites par exemple, est fractionné dans le résidu de fusion jusqu'à saturation du système et cristallisation d'uraninite. Les uraninites formées dans les granites de type S du Bouclier Baltique sont toujours associées aux schlierens de biotite et ont une signature chimique bien distincte de celles des granites de type I : elles sont très riches en thorium ( $\text{ThO}_2 = 7.76\text{-}11.79 \text{ wt\%}$  pour les uraninites de la pegmatite de Mustalampi en Carélie et  $6.05\text{-}11.48 \text{ wt\%}$  pour les uraninites de Polyarnoe de la péninsule de Kola ; Fig. 2-B), en yttrium ( $\text{Y} = 1.7 \text{ à } 2.2 \text{ wt\%}$ ) et peuvent incorporer entre  $1.6$  et  $2.5 \text{ wt\%}$   $\Sigma\text{REE}$ . La forme du spectre normalisé aux chondrites reste similaire à celui des autres uraninites magmatiques avec un faible fractionnement entre LREE et HREE et une anomalie négative en europium ( $\text{Eu}/\text{Eu}^*$  variable entre  $0.2$  et  $0.8$ ). Cependant, les concentrations étant beaucoup plus importantes, le spectre atteint des valeurs beaucoup plus hautes que pour les uraninites des granites de type L, pouvant atteindre plus de  $10^4$  fois les teneurs en REE des chondrites (Fig. 2-C).

Enfin, toutes ces uraninites magmatiques thorifères ont une signature géochimique très distincte de la composition des uraninites d'origine hydrothermale. En effet, le thorium très peu soluble n'est pas mobilisable par les fluides et les oxydes d'uranium hydrothermaux ont une composition caractérisée par l'absence de Th telles que la pechblende secondaire de la pegmatite de Skalnoe (Fig. 2-B). D'autre part, la pechblende hydrothermale, comme celle issue des gisements U de type discordance du Bassin d'Athabasca au Canada, est beaucoup généralement plus appauvrie en REE que les uraninites magmatiques ( $0.15\text{-}0.23 \text{ wt\%}$  pour les oxydes d'U du gisement de Cigar Lake d'après Bonhoure, 2007), et ont un spectre typique en forme de cloche (Fig. 2-C), centré sur les terres rares intermédiaires avec un maximum mesuré généralement en Dy de l'ordre de  $0.1 \text{ wt\%}$  et des valeurs très basses en LREE  $<100 \text{ ppm}$  (gisements d'Eagle Point et Millennium d'après Mercadier, 2008). Les teneurs en Th et en REE des uraninites sont donc des critères déterminants qui peuvent être utilisés comme témoin du processus de formation des uraninites et du type de magma source dans lequel elles se sont formées.

Cette étude vient de démontrer la présence de multiples types de lignées granitiques archéennes pré-enrichies en uranium qui ont pu constituer des protolithes fertiles ou des sources potentielles. La caractérisation des différents granitoïdes archéens à paléoprotérozoïques vient de montrer que chaque type de roches felsiques se distingue par une minéralogie bien distinctes suivant la nature et la chimie de la roche, qui découlent elles-mêmes de la composition du protolithe, du taux de fusion partiel, du degré de fractionnement magmatique et de la cristallisation fractionnée progressive lors du refroidissement. Afin de représenter une source pour la formation de concentrations d'uranium, un granitoïde doit tout d'abord présenter une teneur en uranium suffisante, plus forte que la moyenne crustale (généralement  $Th/U < 1$ ), et surtout l'uranium doit être facilement mobilisable des minéraux porteurs, ce qui est plus difficile lorsqu'il est présent dans des minéraux réfractaires (monazite et zircon étant les plus courants).

Les uraninites formées dans les granites Archéens de type I (Guinée), L (Tanco) ou S (Carélie et Kola) représentent des sources importantes pour des concentrations ultérieures magmatiques ou sédimentaires. L'uranium des uraninites est en effets fortement soluble et le cristal peut être facilement oxydé contrairement aux minéraux réfractaires. Les hétérogénéités texturales et chimiques observées au sein des uraninites au MEB ou mesurées lors des analyses chimiques et isotopiques in situ (EMPA et SIMS) sont la preuve de la fragilité du minéral, extrêmement sensible aux changements de conditions redox. La composition chimique des uraninites, notamment les teneurs en Th et la signature des terres rares, reste cependant un outil de premier ordre afin de caractériser les processus de formation des concentrations et de retracer la source des gisements.

## Références citées dans la synthèse du Chapitre 2:

- Bonhore, J., 2007, Géochimie des éléments de terres rares et du plomb dans les oxydes d'uranium naturels, Unpub. Ph.D thesis, Univ. Nancy, France, 390 p.
- Champion, D. C. and Smithies, R. H., 2004, Archaean granites, The Ishihara Symposium: Granites and Associated Metallogenesis, Geoscience Australia, p. 13-17.
- Champion, D. C. and Smithies, R. H., 2001, Archaean granites of the Yilgarn and Pilbara cratons, Western Australia, In: K. F. Cassidy, J. M. Dunphy and M. J. Van Kranendonk (eds.), 4<sup>th</sup> International Archaean Symposium 2002, Extended abstracts, AGSO Geoscience Australia, Record 2001/37, p. 134-136.
- Cuney, M. and Kyser, K., 2008, Recent and not-so-recent developments in uranium deposits and implications for exploration, Short Course Series Vol. 39, Mineralogical Association of Canada, 257 p.
- Cuney, M., Marignac, C. and Weisbrod, A., 1992, The Beauvoir topaz-lepidolite albite granite (Massif Central, France): the disseminated magmatic Sn-Li-Ta-Nb-Be mineralization; *Economic Geology*, Vol. 87, No. 7, p. 1766-1794.
- Černý, P., 1991, Fertile granites of Precambrian rare-element pegmatite fields: is geochemistry controlled by tectonic setting or source lithologies? *Precambrian Research*, Vol. 51, Issues 1-4, p. 429-468.
- Debon, F. and Le Fort, P., 1988, A cationic classification of common plutonic rocks and their magmatic associations: principles, method, applications, *Bulletin de Minéralogie* 111, p. 493-510.
- Debon, F. and Le Fort, P., 1983, A chemical–mineralogical classification of common plutonic rocks and associations, *Transactions of the Royal Society of Edinburgh, Earth Sciences* 73, p. 135-149.
- Mercadier, 2008, Conditions de genèse des gisements d'uranium associés aux discordances protérozoïques et localisés dans les socles : Exemple du socle du bassin d'Athabasca (Saskatchewan, Canada), Unpub. Ph.D thesis, INPL, France, 325 p.
- Thiéblemont, D., Delor, C., Cocherie, A., Lafon, J. M., Goujou, J. C., Baldé, A., Bah, M., Sané, H. and Fanning, C.M., 2001, A 3.5 Ga granite-gneiss basement in Guinea: further evidence for early Archean accretion within the West African Craton, *Precambrian Research* 108, p. 179-194.



---

**CHAPITRE 3 :**  
**PALEO-PLACERS URANIFERES**

---



## INTRODUCTION

Les gisements d'uranium associés à des conglomérats à galets de quartz ont contribué à une part importante de la production mondiale d'uranium (11%) et représentent encore une réserve non négligeable (5,5%) compte tenu des ressources connues qui s'amenuisent (données 2007 de l'IAEA). Les deux plus importants gisements exploités sont situés dans le Bassin du Witwatersrand en Afrique du Sud et dans le district d'Elliot Lake au Canada, cependant plusieurs autres occurrences sont connues au Brésil (Jacobina, Quadrilatero Ferrifero), en Australie (Bassin de Hamersley) ou encore en ex-URSS (Krivoy Rog) et appartiennent tous à des boucliers précambriens (Bruneton, 2001). Ces minéralisations uranifères sont restreintes à des dépôts dont l'âge est compris entre 3,1 et 2,2 Ga, à quelques exceptions près dans des conditions de sédimentation bien particulières dans des rivières situées en altitude où l'oxygène se raréfie avec un fort taux d'érosion et un enfouissement rapide (Maynard *et al.*, 1991 ; Maynard, 1992).

Les gisements du Bassin de Witwatersrand sont exploités depuis 1886 principalement pour l'or et dès les années 50 pour l'uranium bien que les teneurs restent faibles 0,015 à 0,03 %U. Les minéralisations exploitées sont situées dans les dépôts conglomératiques pyriteux du Super-Groupe de Witwatersrand (Groupes de West Rand et Central Rand) sous la forme de petits grains arrondis et disséminés d'uraninite dans la matière carbonée d'origine diagénétique. L'origine détritique ou hydrothermale des uraninites est encore largement débattue. D'autre part, les sédiments situés directement sur le socle Archéen sous le Super-Groupe de Witwatersrand et appartenant au Groupe de Dominion sont beaucoup plus riches en uranium et ont été bien moins étudiés du fait des teneurs réduites en or. La première partie de ce chapitre sera donc consacrée à l'étude et à la comparaison de ces dépôts d'un point de vue géochimique et minéralogique.

Les minéralisations du district d'Elliot Lake concentrées dans les chenaux conglomératiques de la Formation de Matinenda (Super-Groupe Huronien) atteignent une teneur de 0,14% U. La minéralogie de ces dépôts diffère du Witwatersrand : l'uranium est présent sous la forme d'uraninite riche en thorium et de brannérite principalement avec très peu d'association uranium-matière carbonée. L'étude minéralogique et les caractéristiques chimiques et isotopiques de ces minéralisations uranifères seront présentées dans la deuxième partie de ce chapitre.

La troisième partie présentera l'étude géochimique et minéralogique des grès et conglomérats Jatuliens déposés il y a 2,1 Ga sur un socle Archéen fertile en uranium (pegmatites

archéennes à uraninite échantillonnées à proximité – chapitre 2/partie 2.4). Ces dépôts présentent des enrichissements en thorium par accumulation de monazites détritiques et se seraient formés dans le même contexte environnemental que les conglomérats précambriens du Witwatersrand et d'Elliot Lake mais cependant après l'oxyatmoversion ~2.4-2.2 Ga (chapitre 1/partie 4). Cette dernière partie permettra d'appréhender l'importance des conditions anoxiques de l'atmosphère primitive pour la formation des gisements d'uranium de type conglomérat à galets de quartz.

### **Références:**

- Bruneton, P., 2001, Géologie de l'uranium, COGEMA BUM/DEX, IPSN-Saclay, Initiation-cycle Combustion 1, 72 p.
- Maynard, J. B., 1992, Chemistry of modern soils as a guide to interpreting Precambrian paleosols, *J. Geol.* 100, p. 279-289.
- Maynard, J. B., Ritger, S. D. and Sutton, S. J., 1991, Chemistry of sands from the modern Indus River and the Archean Witwatersrand basin: Implications for the composition of the Archean atmosphere, *Geology* 19, p. 265-268.

## PARTIE 3.1

# Mineralogy and Geochemistry of uranium mineralization in the Archean quartz-pebble conglomerate deposits of the Witwatersrand Basin, South Africa

Isabelle Duhamel<sup>1</sup>, Michel Cuney<sup>1</sup>, Christoph Gauert<sup>2</sup> and Ulrike Rantzsch<sup>3</sup>

<sup>1</sup> *Laboratoire de Géologie et de Gestion des Ressources Minérales et Energétiques (G2R), Nancy-Université, CNRS, CREGU, Boulevard des Aiguillettes, B.P. 239, F-54506 Vandœuvre-lès-Nancy Cedex (France)*

<sup>2</sup> *University of the Free State, Bloemfontein, Republic of South Africa*

<sup>3</sup> *University of Leipzig, Germany*

---

## Abstract

The mineralogical and geochemical characteristics of quartz pebble conglomerates and uraniferous minerals within the Dominion and Central Rand Groups (namely DG and CRG respectively) were studied in detail to determine the origin (detrital or hydrothermal) and the source of uranium in the Witwatersrand Basin.

The DG reefs are distinguished from the CRG reefs by their higher contents in U, Th, REE and other HFSE. The whole rock composition variations are explainable by the different accessory mineral assemblages observed by optical and SEM microscopy. The heavy mineral paragenesis in the DG reefs is composed of abundant detrital sub-rounded pyrite, uraninite, almandine-family garnet, monazite, zircon, chromite, ilmenite and ferro-tantalite with subsequent hydrothermal recrystallization to colloform pitchblende, microcrystalline (U,Th)-silicates and urano-titanates, and euhedral sulfides. In the CRG reefs, the U mineralization is more scattered and is mainly represented by very fine grained uraninite disseminated within carbonaceous matter seams or nodules with pyrite, gold, zircon, more rarely monazite and secondary galena and (U,Ti)-silicates re-deposited on kerogen after alteration of primary uraninite. The moderate to high Th concentrations measured in various primary uraninite grains from both sedimentary sequences using EMPA are relevant of their formation during high temperature magmatic processes. Moreover, the REE distribution patterns (SIMS) of the DG uraninites are characteristic of the crystallisation in S-type granites.

The textural relationships, the paragenetic sequence and the chemical composition of the primary uraninites from the Witwatersrand Basin indicate a detrital origin with latter hydrothermal recrystallization confirming the modified paleo-placer theory. The source rocks mechanically eroded were issued from the partial melting of pre-enriched Archean supracrustal rocks or metasediments.

---

## Key words

Au-U paleoplacer, Witwatersrand, South Africa, detrital uraninite, hydrothermal remobilization

## Introduction

The Witwatersrand Basin is the largest gold-producing province of the world since its discovery in 1886 and it hosts also the oldest known uranium concentrations exploited as a by product. The basin yielded over 47,000 tonnes of gold between 1886 to 2002 and approximately 172,000 tonnes of uranium between 1952 and 2003 (after the Chamber of Mines of South Africa).

For the past 50 years, the origin of uranium in quartz-pebble conglomerates of the Witwatersrand Basin (South Africa) has been subject to controversy. The detrital origin of uraninite and pyrite is sustained by geochronological data and grains are preserved as placer deposits thanks to the low level of oxygen atmosphere that prevails in Archean time during sedimentation (Minter, 2006). A secondary hydrothermal origin has been strongly debated mostly because of the presence of authigenic pyrite and post-sedimentary U-bearing minerals, pitchblende, brannerite and (U,Th)-silicates that are associated with carbonaceous matter in hydrothermal quartz veins (Nedachi et al., 1998). Moreover, the source rock area is composed of multi-generated granitic rocks reflecting the complex tectonic history of the region which leaves large uncertainties for the source of the possibly detrital mineralization.

This paper presents an original attempt to investigate if U ore has been deposited in the basin by purely sedimentological processes or if it was formed by later hydrothermal processes by defining the geochemical signatures of uraninite and associated minerals. The original scope of this work was to apply geochemistry using a combination of chemical and mineralogical aspects, major and trace element compositions of minerals as well as the determination of uraninite REE patterns characterizing mineral forming processes and signatures of potential sources.

## Geological background

### ***Geodynamic setting***

The Witwatersrand basin is located in the central part of the Kaapvaal craton of southern Africa (Fig. 3.1.1). The fluvial to marine sedimentary sequence that filled the basin, referred as the Witwatersrand Supergroup, has been deposited between approximately 3074 and 2714 Ma (U-Pb zircon ages of volcanic rocks that bracket the Witwatersrand basin after Robb and Meyer, 1995) during pulses of sedimentation associated with continental crust formation (de Wit et al., 1992).

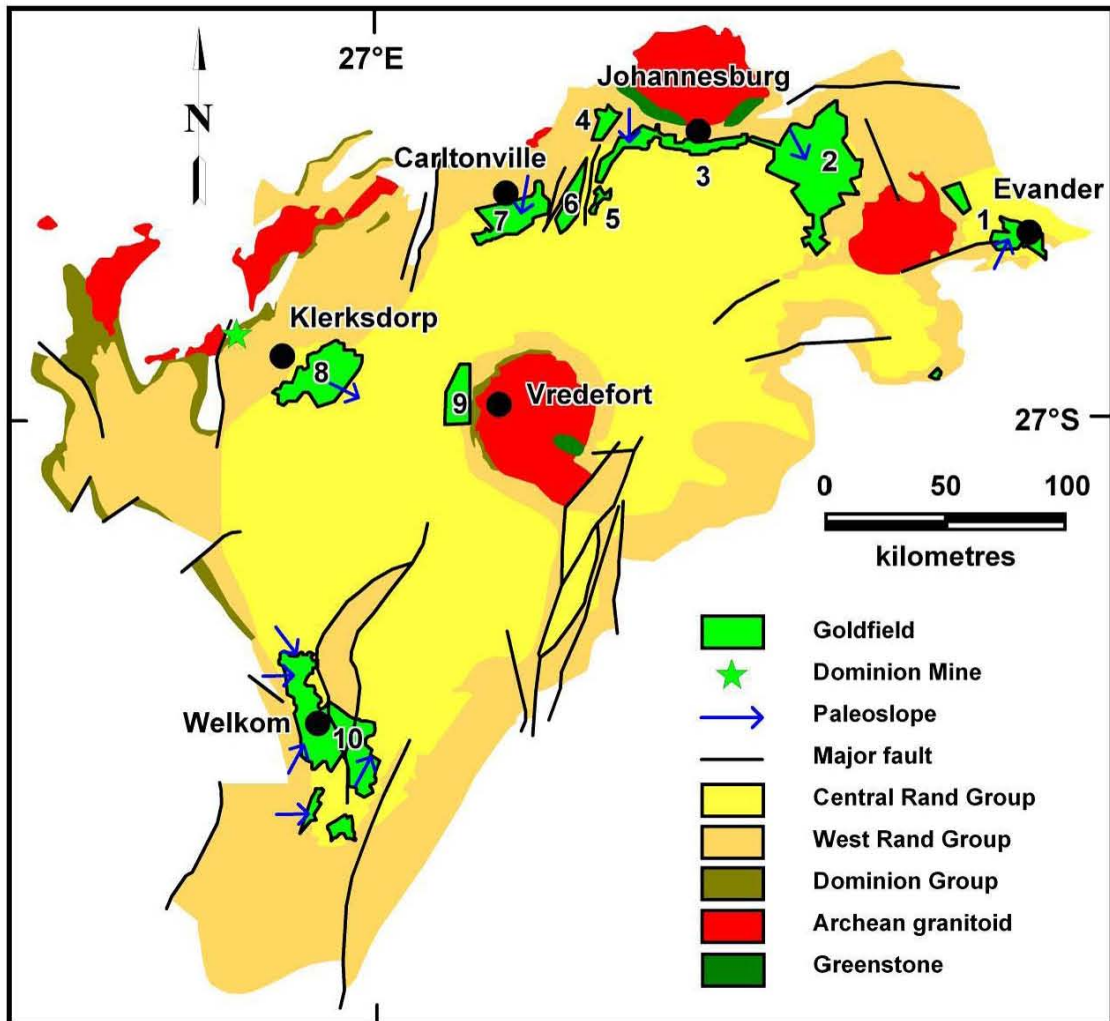
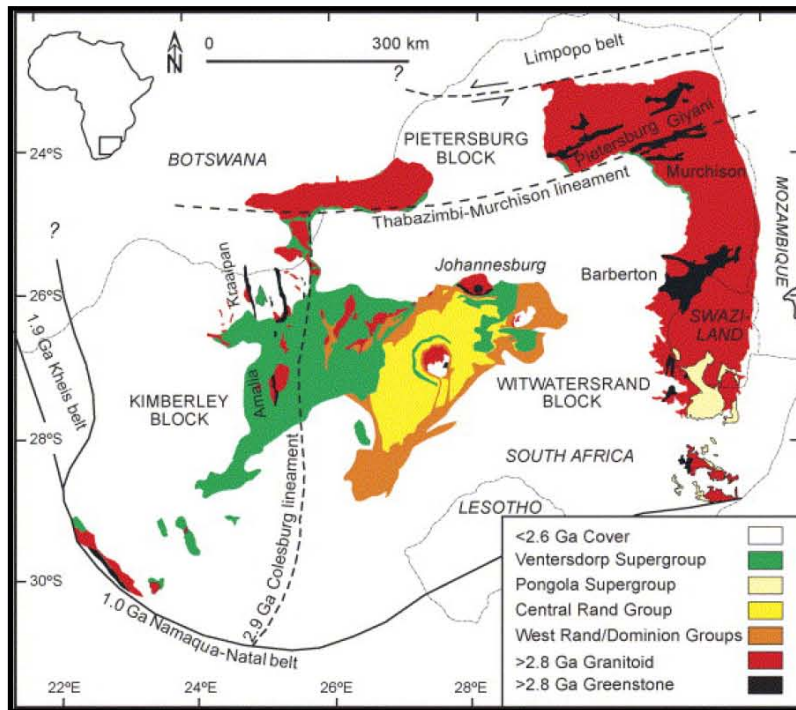


**Figure 3.1.1.** Geological map of the Witwatersrand Basin and surrounding Archean granite-greenstone terranes with location of the principal goldfields: 1- Evander, 2- East Rand, 3- Central Rand, 4- West Rand, 5- South Deep, 6- Western Areas, 7- Carletonville, 8- Klerksdorp, 9- Venterskroon, 10- Welkom) and the Dominion mine where samples were collected for this study (after Frimmel, 2005, modified from Schmitz et al., 2004 and closer view modified from Frimmel and Minter, 1992; Minter and Loen, 1991).

Two geodynamic models for the formation of the basin are currently proposed:

(1) a flexural retro-arc foreland basin fed by the erosion of a rising orogen formed upon the subduction of the Limpopo ocean; the subducting slab was plunging southwards under the Kaapvaal Craton and conduct to the amalgamation of the Zimbabwe Craton inducing ancient fault reactivation thrusting in the basin (Fig. 3.1.2; Robb et al., 1991; Robb and Meyer, 1995; McCourt, 1995; Catuneanu and Biddulph, 2001; Schmitz et al., 2004; Catuneanu, 2004);

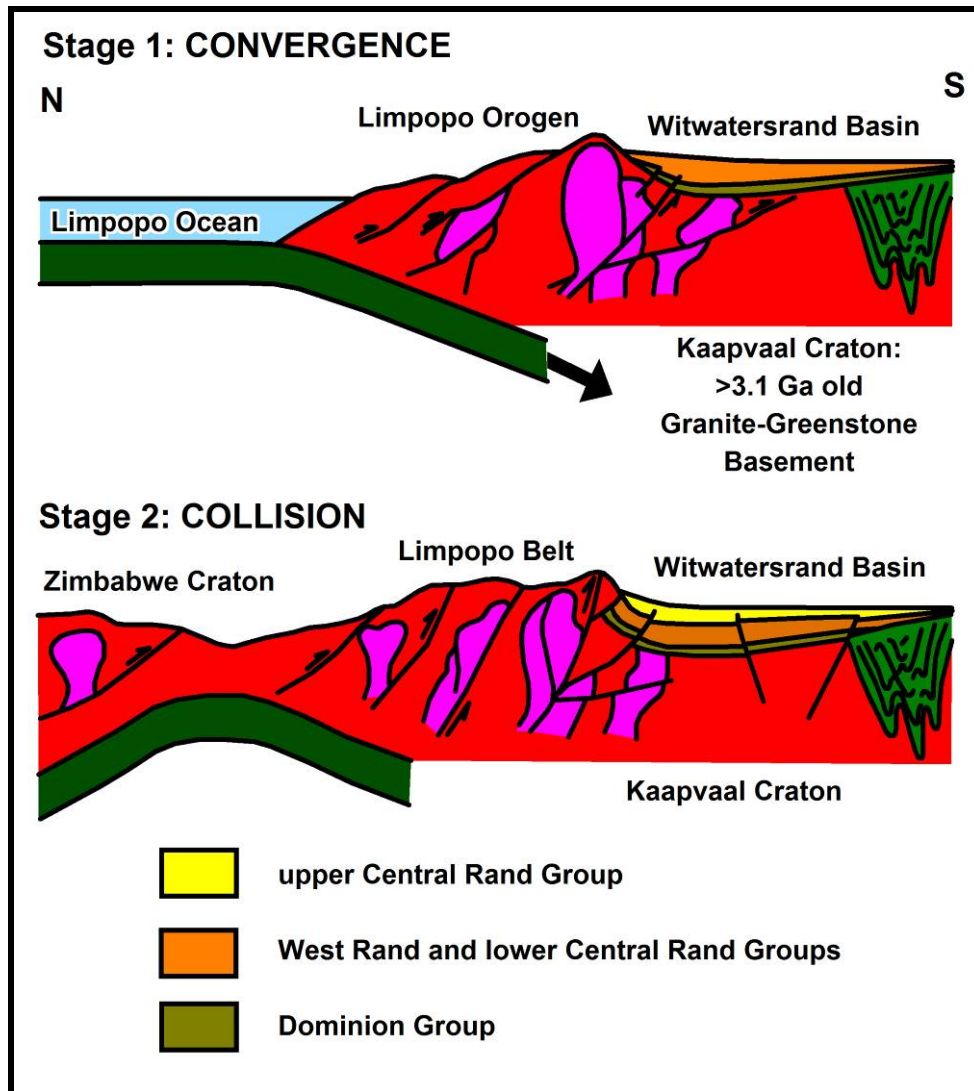


**Figure 3.1.2.** Sketch model of the tectonic setting during the deposition of the Witwatersrand Basin (after Catuneanu and Biddulph, 2001; modified from Robb et al., 1991).

(2) a more recent model suggests a thermal subsiding basin created by a mantle plume beneath the Kaapvaal Craton; the heat anomaly created by underplating produced juvenile oceanic crust at mid-oceanic ridges and accretion at the border of the stable nucleus resulting in composite terrains of greenstones, TTGs (tonalite-trondhjemite-granodiorite) and granites (Fig. 3.1.3; Eriksson et al., 2009).

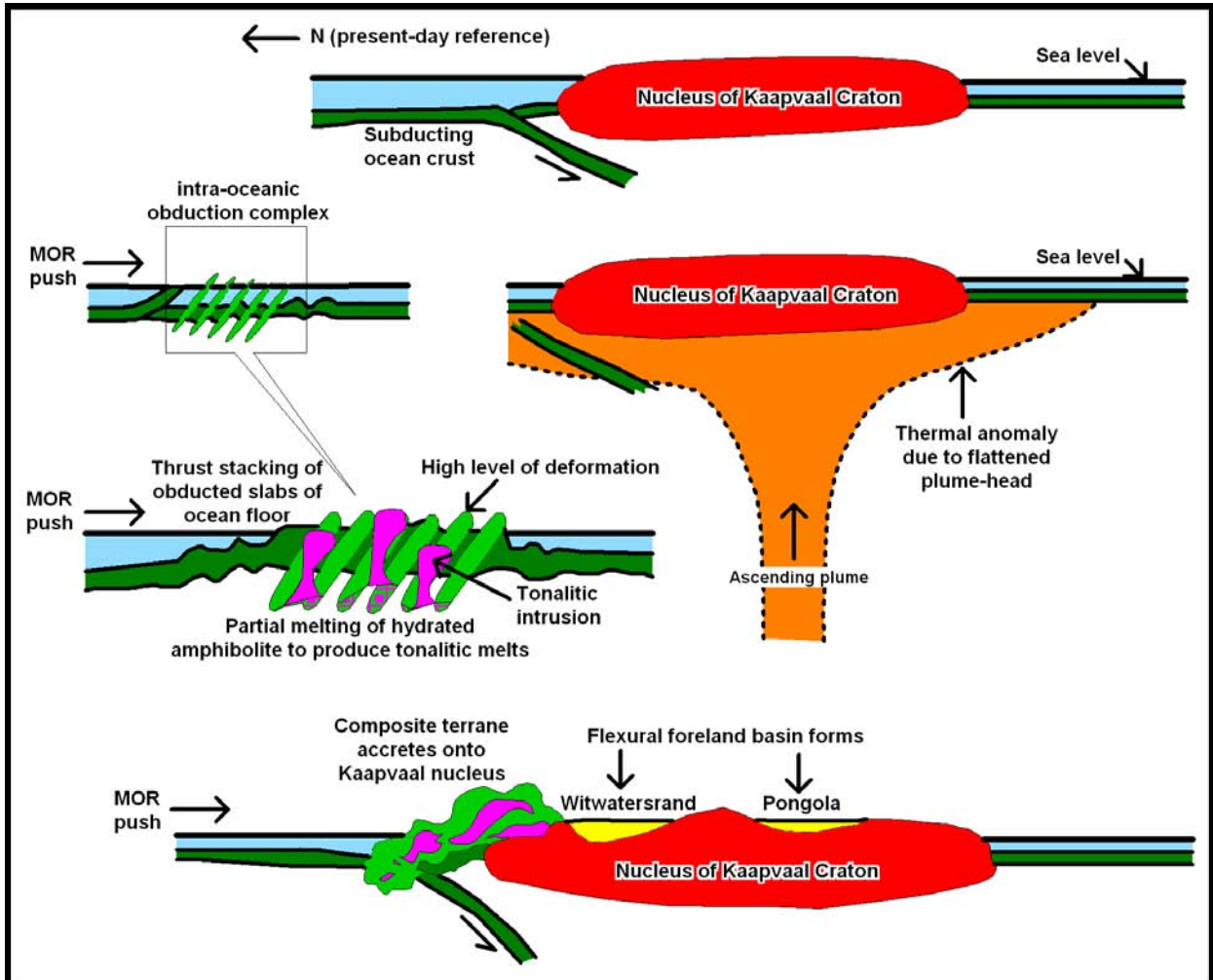


**Figure 3.1.3.** Schematic representation of the postulated model for accretion of intra-oceanic obduction complexes onto the Kaapvaal nucleus related to an underplating mantle superplume (modified from Eriksson et al., 2009). The final stage is the formation of flexural foreland basins respectively in the foredeep (Witwatersrand) and back-bulge (Pangola) zones.

The granite-greenstone rocks, formed during the orogenesis or accretion, depending on the dynamics considered, were eroded and detrital grains were mechanically transported into fluvial paleo-valleys and concentrated via large braided alluvial to deltaic fan systems into the flexural deflection that formed the Witwatersrand Basin.

### ***Sedimentary sequence and mineralization***

The volcanic-sedimentary sequence located at the bottom of the basin (Fig. 3.1.4), the Dominion Group (DG), lies upon the granite-greenstone terranes >3.1 Ga of the Kaapvaal Craton. It was deposited during a continental rift extensional system (Stanistreet and McCarthy, 1991; Frimmel, 2005). This group comprises mainly bimodal volcanic rocks with a siliciclastic sediment member at the base of the sequence, referred to as the Rhenosterspruit Quartzite Formation, has a thickness of 40 to 100 m. This lower member is composed of quartzite with two mineralized conglomerate beds of maximum 2 meters thickness, hosting abundant pyrite and uraninite with low gold grades, referred to as the lower and upper Dominion reefs. The reefs consist of slightly metamorphosed oligomictic quartz pebble conglomerate layers (Kyser and Cuney, 2008). The lower DG reef forms narrow lenses deposited by a braided stream system within paleo-valleys incising into the underlying Archean granitic basement whereas the upper DG reef is laterally more persistent (Button and Tyler 1981). Principal U-ore minerals are rounded uraninite grains associated to heavy minerals such as pyrite, garnet, magnetite, ilmenite, chromite, monazite, zircon, cassiterite and columbite (Hiemstra, 1968; Simpson and Bowles, 1977). These minerals are accumulated in relatively coarse beds on the concave side of channels typical of the point-bar model (Harley and Dixon, 2006). Secondary minerals occur around primary rounded uraninite grains or as alteration products in pseudomorphosed minerals such as pyrrhotite, brannerite, leucocene and galena (Davidson 1957; Ramdohr, 1958; Burger et al., 1962). The age of this first ore sequence is constrained by U-Pb zircon ages of the basement at  $3086 \pm 3$  Ma (Westerdam granite after Robb et al., 1992) and the upper Dominion volcanics at  $3074 \pm 6$  Ma (Armstrong et al., 1991). The DG is followed by a 100 Ma hiatus in the sedimentary record and a major change in the tectonic regime.

The Witwatersrand Supergroup sequence, divided in the lower West Rand Group and upper Central Rand Group, was deposited during a second tectonic period associated with the collapse of the rift system and the development of a foreland basin (Liebenberg, 1955).

The sediments of the West Rand Group, lying unconformably on the Dominion Group, is up to 5150 m thick in the western edge of the basin in the Klerkesdorp Goldfield and thins to the north-east (Frimmel, 2005). The West Rand Group is mostly composed of shales and sandstones with minor conglomerates interlayered with andesitic lavas. U-Pb zircon dating prevails a maximum age of  $2985 \pm 14$  Ma in detrital grains (Kositcin and Krapez, 2004) and a minimum age of  $2914 \pm 8$  Ma in one zircon from the cross-cutting lavas of the Crown Formation

(Armstrong et al., 1991). Only three sub-economic Au-U reefs are present in the Government Subgroup (Frimmel and Minter, 2002).

The uppermost Central Rand Group (CRG) is by far the richest sequence representing the world largest gold deposits hosting either 87% of the all uranium resources of South Africa (Ford, 1993). CRG is mainly composed of sandstones interlayered with gold-bearing quartz pebble conglomerate reefs generally less than 2 meters thick. Ore mineralogy is dominated by complex mineral assemblage between quartz pebbles: pyrite represents 3 to 10% of the ore and is the dominant mineral, pyrrhotite, chalcopyrite, other As, Co and Ni sulfides, gold, chromite, uraninite, brannerite, galena, zircon and ilmenite are the most common heavy minerals occurring in a gangue of chlorite, sericite, pyrophyllite, chloritoid and biotite (Ford, 1993; Safonov and Prokof'ev, 2006 and reference therein). Most of the gold occurs as crystalline grains associated with authigenic minerals such as pyrrhotite and chalcopyrite and only a low proportion of gold occurs as rounded grains or flattened flakes from a detrital origin (Robb and Robb, 1998). A strong correlation exists between pebble size from 4 mm to 10 cm large and gold concentrations occurring generally at the base of channels which suggests that gold distribution was partly controlled by sedimentary processes. In the Kimberley reef, gold, uraninite, pyrite, chromite and zircon are distributed along the point bars of channels and vertically sorted according to their specific gravity (Hirdes, 1978). However, mineralization is also associated to major regional faults and deposits are sometimes tectonically controlled by normal faults, shears and thrust (Kyser and Cuney, 2008). The most uraniferous beds are related to tucholite, a radiogenic carbonaceous material (kerogen/bitumen) with disseminated uraninite grains, conferring a dark colour to the conglomerate horizons. Uraninite has an average size about 100  $\mu\text{m}$  and are generally rounded. Uranium grade ranges from 0.013% to 0.06% U (Brynard and Andreoli, 1988).

The genetic model that is widely accepted to explain the origin of mineralization in the basin is the modified paleo-placer theory (Reimer and Mossman, 1990; Frimmel and Gartz, 1997; Minter, 1976 and 1999; Meyer et al., 1994b; Frimmel and Minter, 2002; Minter, 2006). It proposes that gold and uraninite are respectively detritus of older Archean greenstone belts and granitoids. This model is sustained by 3.05 Ga U-Pb dating of uraninite grains from both Dominion (Rundle and Snelling, 1977) and Witwatersrand conglomerates as well as Re-Os isochron age of 2.99 Ga obtained for rounded pyrite grains associated with the uraninite (Minter, 2006).

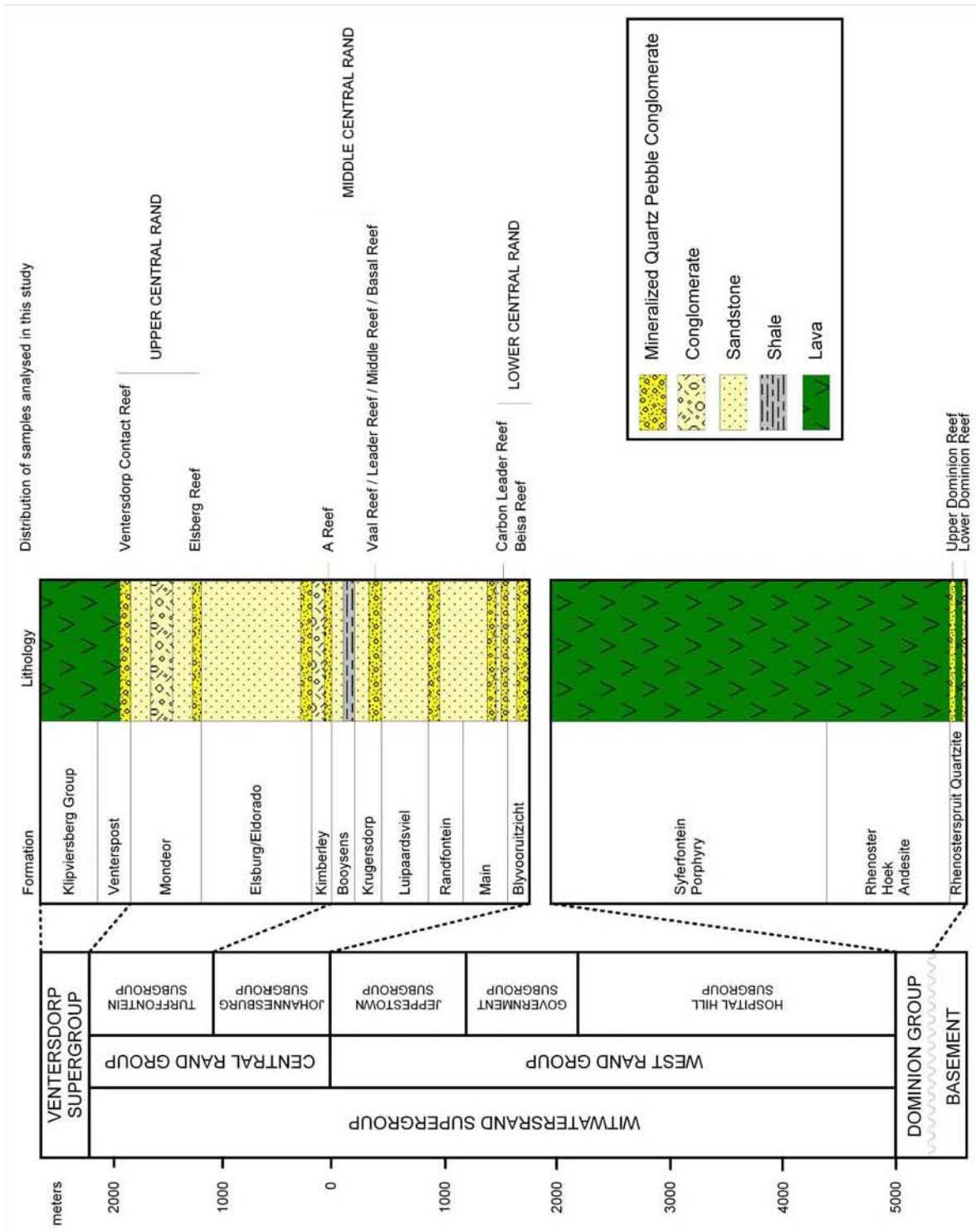


**Figure 3.1.4.** Simplified stratigraphic column for the Dominion Group (after the Uranium One Ltd. data) and Central Rand Group (modified from Frimmel and Minter, 2002) with relative stratigraphic position of the various reefs sampled in this study.

The Witwatersrand Basin sedimentary sequence and hosting deposits are buried below the Ventersdorp volcanics (lower basalts dating at  $2714 \pm 8$  Ma and upper quartz porphyries at  $2709 \pm 4$  Ma after Armstrong et al., 1991) and the subsequent deposition of the Transvaal Basin (2.67-2.1 Ga). They were latterly affected by the thermal effect of the emplacement of the Bushveld Igneous Complex (2050-2025 Ma; Buick et al., 2001) and finally the Vredefort impact event at 2000 Ma (Gibson et al., 1997). The behaviour of the basin after its deposition results in a metamorphism peak reaching approximately 2.5 kb and 350°C (Phillips, 1987; Wallmach and Meyer, 1990; Wallmach et al., 1990).

### ***Assumption on the source of mineralization***

Geochronological data (comparison between U-Pb isotope dating of detrital and magmatic zircons) and the measurements of paleoslope directions in the sedimentary units (c.f. blue arrows in Fig. 3.1.1) are pointing two possible source areas, the granitoid domes of the Hinterland surrounding the basin and the Barberton Mountain Land granite and greenstone terranes approximately 400 kilometres from its north-eastern margin in Swaziland and along the boundary with Mozambique.

The granitoid domes from the Hinterland surrounding the basin are mostly composed of sodic granitoids aged ca. 3.1-3.0 Ga and potassic granitoids aged ca. 2.8 Ga, where numerous U-enriched granitoids have been found (Robb et al., 1990a and 2006):

- the Westerdam batholith north of Klerksdorp dated at  $2810 \pm 200$  Ma (Barton et al., 1986) with sample V53 containing 8.47 ppm U and 5.49 ppm Th providing a Th/U ratio of 0.65 corresponding to the ideal field of uraninite crystallization ( $\text{Th}/\text{U} < 1$ );
- granites from drill holes RAT1, north of Klerksdorp: sample RAT1(1684) with 20.5 ppm U and 6.24 ppm Th ( $\text{Th}/\text{U} = 0.30$ ) and many other samples from the same hole showing low Th/U ratios (0.3-2.5) with crystallization of leucoxene and pitchblende around in propylitic alteration zones;
- the Schweizer-Reneke batholith west of Klerksdorp and aged at  $2870 \pm 70$  Ma (Barton et al., 1986) with low U content (0.95-4.93 ppm) and high concentrations in Th (11.5-23.5 ppm) but maybe caused by leaching of U by alteration (Robb and Meyer, 1985a et b); and adjacent to this pluton, a core sample TKB3(120) enriched in U (33.8 ppm) and Th (26.7 ppm) with low Th/U (0.79);
- the Johannesburg batholith comprising tonalites aged at  $3170 \pm 34$  Ma (Anhaeusser and Burger, 1982) and potassic intrusions at  $3060 \pm 30$  Ma (Barton et al., 1986), where uraninite has been

observed (Hallbauer, 1982) despite low U and Th concentrations with U = 0.19-12.6 ppm, Th = 1.09-17.5 ppm and elevated Th/U ratios;

- granitoid WE1(579.5) collected south-east from the Evander goldfield having U = 23.6 ppm, Th = 16.6 ppm and Th/U = 0.70 and pegmatite ST8(587.5) with U = 33.4 ppm, Th = 51.9 ppm and Th/U = 1.55 hosting uranothorites (Ferraz, 1989);

- and finally sample from a drill hole located west to the Welkom goldfield GH1(6221) with U = 116.1 ppm, Th = 15.55 ppm leading to the lowest Th/U ratio 0.15.

The Barberton Mountain Land domain is composed of multi-generated granitoids associated to the various plutonism episodes between ~3.5 and ~3.1 (Clemens et al., 2006 and reference therein). The older Swazian TTG-type gneisses formed at ca. 3650-3500 Ma (Compston and Kröner, 1988; Kröner et al., 1991), at ca. 3480-3440 and ca. 3250-3220 Ma (Armstrong et al., 1990; de Ronde and de Wit, 1994; Kamo and Davis, 1994). The TTGs are poor in U and Th (Meyer et al., 1986) but later Randian S-type and I-type intrusions aged between 3100 and 2700 Ma are richer in uranium. The Randian intrusions correspond to anatectic potassic plutons, leucogranites and syenites probably associated with partial melting of the older greenstone belts and TTGs and are coeval with the basin sedimentation (Robb et al., 1992; de Wit et al., 1993; Kamo and Davis, 1994; Meyer et al., 1994a). The Randian granites are locally enriched in LILE and HFSE, and are notably anomalous in U with low Th/U ratios as the 3080 Ma S-type Sinceni granite in Swaziland (Trumbull, 1993), the peraluminous GH1 and Westerdam granites (Robb et al., 1990a, b), the 3174 Ma greisenized granites around Hartebeestfontein and the peraluminous 2880 Ma old Schweizer-Reneke granite (Robb and Meyer, 1995). They represent most probable sources of U mineralization within the Witwatersrand basin (Robb and Meyer, 1990; Robb et al., 1992; Robb and Meyer, 1995). However, occurrences of uraninite within the granites are associated to later hydrothermal alteration with greisenization of the rock associated to quartz-muscovite-chlorite-albite-fluorite paragenetic assemblage post-dating the Witwatersrand deposition (Drennan, 1988 ; Robb et al., 1990a). Moreover, uraninite and uranothorite grains in the peraluminous granites are coated in bituminous nodules as observed in the Central Rand Group sequence and are believed to be related to the migration of the Witwatersrand kerogen at ca. 2350 Ma which strengthen the hydrothermal origin of U mineralization for both granitoids and basin (Hallbauer, 1984 ; Klemd and Hallbauer, 1987; Drennan, 1988 ; Robb and Meyer, 1985a et b ; Robb et al., 1994 ; Robb et al., 1995). These hydrothermal modifications have occurred during diagenesis and metamorphism after sedimentation conducting probably to the mobilization and new precipitation of gold, uranium and sulphides in secondary mineral assemblage at ca. 2500, ca.

2300 and ca. 2050 Ma (Robb and Meyer, 1995). Origin and potential sources of U mineralization in the Witwatersrand reefs are still ambiguous.

## Sampling and Macroscopic description

The study area attempts to cover a large part of the Witwatersrand Basin and of its sedimentary column with widespread sampling from the northern West Rand goldfield, the western Dominion mine and Klerksdorp goldfield, to the southern Welkom goldfield (respectively 4, 8 and 10 on the map in Fig. 3.1.1). The lower Dominion Group at the base of the basin and the upper Central Rand Group, the two major uraniferous sedimentary units of the Witwatersrand series, have been sampled (stratigraphic column in Fig. 3.1.4). Drill core samples have been collected in the two lowermost Dominion reefs from the prospect of Uranium One Ltd. at the Dominion mine. Handpicked samples from various reefs of the uppermost Central Rand Group sequence were collected in different underground mine exposures. Samples at the base of the Central Rand Group were collected from the Beisa Reef of the southern Welkom goldfield and from the Carbon Leader Reef of the West Rand goldfield. Samples covering the middle part of the Central Rand Group stratigraphy are from the A Reef and the Vaal Reef collected from the Klerksdorp goldfield as well as from the Leader, the Middle and the Basal Reefs at the base of the Krugersdorp Formation in the Welkom goldfield. Finally, samples covering the uppermost units of the Central Rand Group are from the Elsberg Reef at the base of the Mondeor Formation and the Ventersdorp Contact Reef (VCR) at the top of the sequence; both reefs were sampled at Stilfontein Mine in the Klerksdorp goldfield. This represents a total of 20 samples collected from the Dominion Group (17 in the upper reef and 3 in the lower reef) and 30 samples from the Central Rand Group (20 in the lower part, 5 in the middle and 5 in the upper reefs).

The Witwatersrand conglomerates from both sedimentary sequences are monogenic, composed of matrix-supported sub-angular to well-rounded quartz pebbles. The matrix in the DG reefs is fine to coarse quartzite with disseminated eye-visible heavy minerals as abundant rounded pyrite and pink garnet grains pluri-millimetres wide. The matrix of CRG reefs is also composed of abundant quartz and pyrite grains but mixed within argillaceous material and black carbonaceous matter. Samples were preferentially selected thanks to the determination of their relative radioactivity measured with a SPP2 scintillometer in count per second (cps): from 150 cps in the Dominion quartzite to a maximum of 1200 cps in the Dominion mineralized conglomerates, and from 80-100 cps to a maximum of 6000 cps in the Central Rand reefs. It has been observed that in the DG reefs, the highest radioactivity is correlated with the most pyritic

zones, and that in the CRG reefs the main radioactive areas are associated with linear black beds of carbonaceous matter up to 5 cm large, generally discontinuous laterally and sometimes accompanied by yellowish superficial alteration products (pictures of representative samples in Fig. 3.1.5, 3.1.6 and 3.1.7). Some of the quartz pebbles are made of smoky quartz (dark) probably related to irradiation.

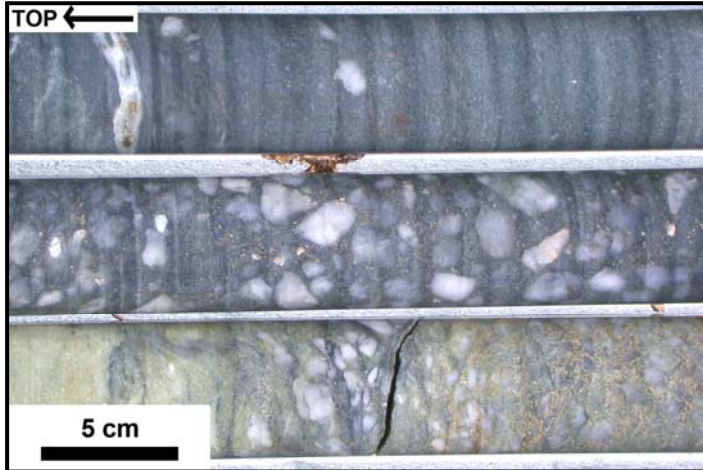


**Figure 3.1.5.** Drill core showing the upper quartzite and conglomerate member succession of the Dominion Group: (up) grey quartzite, (middle) conglomerate with sub-angular to rounded quartz pebbles (down) pale green to yellowish pyritic and sericitic conglomerate.



**Figure 3.1.6.** Sample from the Beisa reef (Welkom Goldfield) at the base of the Central Rand Group. Note the large carbonaceous matter beds following the elongation of the white to black coloured quartz pebbles.



**Figure 3.1.7.** Sample from the Carbon Leader reef (West Rand Goldfield) at the base of the Central Rand Group. Note the discontinuous black beds of carbonaceous matter with yellow alteration products wrapping the quartz pebbles in the conglomeratic level (half bottom of the picture) and following the stratigraphic contact with the upper grey quartzite.

## **Analytical techniques**

### ***Whole-rock geochemistry***

Rock samples collected during fieldwork were separated from their weathered surface exposure or from sulphide veins by sawing when it was necessary to limitate the nugget effect in the whole-rock analyses. Samples were then crushed and powdered to a granulometry below 80  $\mu\text{m}$  using successively a jaw crusher, a roller mill and an agate planetary micro-mill at the G2R laboratory (Géologie et Gestion des Ressources Minérales et Energétiques, University of Nancy, France). The whole-rock geochemical analyses were performed at the SARM laboratory (Service d'Analyse des Roches et des Minéraux, CRPG, CNRS, Nancy): 20 samples from the Dominion Group conglomerates and 12 from the Central Rand Group reefs. Bulk composition was analyzed using inductively coupled plasma spectroscopy techniques, ICP-OES (emission) for major element detection and ICP-MS (mass) for trace elements. The analytical procedure and the international standards used for calibration are fully described by Carignan et al. (2001). The detection limits are low in order to  $1 \text{ ng.g}^{-1}$  and uncertainties on measurements also,  $<1\%$  for Si,  $<2\%$  for Fe,  $<10\%$  for Al,  $<5-10\%$  for Mn, Mg and Ti, below 5% for Th and Rare Earth Elements (REE) and below 8% for U. The loss on ignition (LOI) was generally impossible to evaluate because of the high sulphide content. Further technical data is available on the web-site of the SARM laboratory (<http://helium.crpm.cnrns-nancy.fr/SARM/analyses/roches.html>). Results for whole-rock chemistry are reported as weight percent (wt%) and for trace element and REE data it is reported in parts per million (ppm). The REE patterns are plotted normalized to the chondrite reference of Anders and Grevesse (1989).

### ***Detailed mineralogical studies***

Mineralogical studies were performed at the University of Nancy (France) on a set of approximately 80 polished thin sections representative of the different sampled reefs. Autoradiography of the polished rock surfaces permits to localize rapidly the most radioactive areas where U-bearing minerals are accumulated. Detailed petrographic, textures and assemblage of the minerals were carried out using both polarized microscope Olympus BX51 and scanning electron microscope Hitachi FEG-S4800 (SEM). Semi-quantitative analyses were performed by a coupled energy dispersive spectrometer Noran Vantage with the SEM. They allow element repartition mapping to evaluate the composition variations associated to average atomic number differences in backscattered electron images (BSE). High brightness areas in BSE mode

correspond to heavy atomic weight element concentrations whereas darker domains are associated to lighter element accumulations.

Electron microprobe analyses (EMPA) in the U-bearing minerals and associated accessories (garnet, columbite-tantalite, zircon, monazite) were conducted on CAMECA SX100 and SX50 instruments at the SCMEM laboratory (Nancy University). The elements (Al, Si, S, K, Ca, Fe, Pb, U, Mg, Ti, Th, Mn, Y, P, La, Ce, Pr, Nd, Sm, Gd, Dy, Yb, Nb, Ta, F, W, Sn, Sb) were analysed by wavelength-dispersive spectrometers (WDS) equipped by TAP (thallium acid phthalate), LPET (large pentaerythriol), PET (large pentaerythriol), LIF (Lif) and PC1 (multilayered W-Si) crystals. Calibration of the machine was performed with natural and synthetic standards (topaz, albite, orthose, hematite, wollastonite, garnet, olivine, Mo metal, V metal, Bi metal, SrSO<sub>4</sub>, ZrO<sub>2</sub>, UO<sub>2</sub>, ThO<sub>2</sub>, PbS, PbCrO<sub>4</sub>, MnTiO<sub>3</sub>, LaPO<sub>4</sub>, YPO<sub>4</sub>, CePO<sub>4</sub>, PrPO<sub>4</sub>, NdPO<sub>4</sub>, DyRu<sub>2</sub>Ge<sub>2</sub>, ScNi<sub>2</sub>Si<sub>2</sub>, LiNbO<sub>3</sub>, LiTaO<sub>3</sub>, WCaO<sub>4</sub>, SnO<sub>2</sub>, Sb<sub>2</sub>S<sub>3</sub>). The measurements were performed with a current intensity of 10 nA, an accelerating voltage of 15 kV (U-bearing minerals, columbite-tantalite and garnet) or 20 kV (zircon and monazite) and a beam spot size of 2 µm. The counting times range between 5 to 60 seconds per element, the longer time being used for the trace concentrations. The relative errors on each element measurements are below 1%. To allow comparison between the different minerals, the results given in weight percent (wt.%) have been recalculate for the plots in atomic percent (at.%).

### ***Chemical U-Th-Pb age dating of radiogenic minerals***

The chemical ages of U-bearing minerals for each EMPA were calculated by iteration resolving the following equation derived from the radioactive decay law (modified from Bowles, 1990 after Cocherie and Albarède, 2001):

$$C_{Pb} = C_{Th}[0.897(e^{\lambda_{232} \cdot t} - 1)] + C_U[0.859(e^{\lambda_{238} \cdot t} - 1) + 0.006(e^{\lambda_{235} \cdot t} - 1)]$$

where  $C_{Pb}$ ,  $C_{Th}$ , and  $C_U$  are concentrations of Pb, Th, and U (in ppm) measured in situ in the uraninite;  $\lambda_{232}$  ( $0.049475 \times 10^{-9} \text{ y}^{-1}$ ),  $\lambda_{238}$  ( $0.155125 \times 10^{-9} \text{ y}^{-1}$ ) and  $\lambda_{235}$  ( $0.98485 \times 10^{-9} \text{ y}^{-1}$ ) are the decay constants for <sup>232</sup>Th, <sup>238</sup>U, and <sup>235</sup>U respectively; and t is age (in year). This relation is used assuming that <sup>235</sup>U, <sup>238</sup>U and <sup>232</sup>Th produce the totality of the lead present in the analyzed spot (<sup>207</sup>Pb+<sup>206</sup>Pb+<sup>208</sup>Pb), thus Pb is considered to be entirely of radiogenic origin and there was no common lead incorporated in the mineral during its crystallization. This method is commonly used for monazite dating (Suzuki et al., 1994; Montel et al., 1996; Cocherie and Albarède, 2001, Williams et al., 2007) and uraninite dating (Kempe, 2003; Alexandre and Kyser, 2005). The

chemical age results are finally plotted in histograms with the Isoplot program (Ludwig, 1999) providing a probability curve for the more confident age population and showing the distribution of chemical ages calculated in various grains of the same ore phase.

### ***In situ REE isotope measurements of uraninite***

An analytical procedure has been developed by Bonhoure and co-authors (2007) for the in situ measurement of REE isotope composition of uranium oxides on the CAMECA IMS-3f ion microprobe at the CRPG (CNRS, Nancy, France). This recent technique has been performed in the uraninite grains from two samples of the upper Dominion reef, AO3883 and AO5686. These two conglomerate samples host the better preserved uraninite crystals considering the more homogeneous texture and the higher average atomic number observed by SEM in BSE mode and the higher average U and Pb contents measured by EMP. The thin section areas where the selected grains occur have been transferred into an aluminium ring metallised with gold and placed in the vacuum chamber of the ion microprobe. The instrument uses a beam of ion oxygen atoms well focus on the uraninite grain which vaporizes the material and creates a crater of 30-50  $\mu\text{m}$  large. The different ionized atoms ejected from the surface of the uraninite are accelerated to a potential of 4500 V and directed to a secondary ion mass spectrometer (SIMS). Each analysed spot corresponds to the average of 60 measures of each stable isotope of the rare earths totalizing for each spot a counting time of approximately 2 hours. The standard used as a reference material is an uranium oxide from the Mistamisk Valley in Canada (Kish and Cuney, 1981). Two mass molecular interferences cannot be resolved with the elements Gd and Yb, their abundances are thus calculated using their proximal element abundances as follow:  $\text{Gd}^* = \text{Sm} + 2/3\text{Tb}$  and  $\text{Yb}^* = (\text{Tm} + \text{Lu})/2$ . The REE abundances are then normalized to chondrite values of Anders and Grevesse (1989) and plot in a spidergram. Considering the spatial resolution of the analytical spot, it was not possible to measure several spots in one single grain and each REE spectrum is relevant of measurements in one analysed grain.

## Geochemistry of quartz-pebble conglomerates

Major and trace element concentrations in sedimentary rocks are generally rather heterogeneous and difficult to compare because they derived from the mixing of different source lithologies. However, the composition of the conglomerates must be characteristic of the precursor rock composition and of the detrital and alteration mineral assemblage.

### **Major Elements**

The whole-rock major element composition of the mineralized Witwatersrand conglomerates is summarized in Table **3.1.1**.

The total of bulk composition for most of the individual samples from the CRG is low which is inferred to the LOI values that could not be determined because of the high sulphur content due to massive concentrations of sulphides. However, when it was possible to measure the LOI in the conglomerates, values range between 0.42 and 2.10 % which reflects the variations in the organic matter compound, elevated values corresponding to a higher organic content.

The major whole-rock composition variations between the Dominion and Central Rand group reefs are well illustrated in the Figure **3.1.8**. The DG and CRG conglomerates present high SiO<sub>2</sub> contents but quite highly variable, ranging between 63.20 and 96.70 % (mean SiO<sub>2</sub> for DG: 85.64 ± 4.80 % and for CRG: 83.99 ± 9.69 %) depending on quartz pebble abundance.

The DG reefs are generally characterized by higher contents in Al<sub>2</sub>O<sub>3</sub> (2.66-9.19 % for DG and 0.50-3.61 % for CRG) and P<sub>2</sub>O<sub>5</sub> (0.04-0.60 % for DG and <0.015-0.09 % for CRG) associated to aluminium-rich and phosphate accessory mineral accumulation, and to principally very abundant garnet and monazite grains. Enrichment in Al, Mg and K (MgO = 0.11-0.99 % for DG and <0.01-0.63 % for CRG - K<sub>2</sub>O = 0.56-2.30 % for DG and <0.05-0.80 % for CRG) are also inferred to be due to the presence of muscovite and chlorite in the matrix of conglomerates.

**Table 3.1.1.** Comparative chemical analyses of the major elements (ICP-OES) in the Dominion and Central Rand Group conglomerates

Stratigraphy	Dominion Group (DG)																			
	Lower DG Reef			Upper DG Reef																
Reef Bore Hole Depth Sample	DRT070 621.9 m AO8042	DDR077 393.0 m CO5602	DRT131 906.5 m EO3058	DRT050 185.5 m AO1618	DRT058 182.5 m AO3883	DRT103 BO518	DRT090 823.2 m BO8981	DDR077 371.7 m CO5512	DRT113 807.8 m CO6778	DRT113 810.0 m CO6789	DRT095 790.7 m CO7744	DDR23 39.2 m DO1525	DRT024 206.8 m DO1823	DRT034 342.1 m DO8629	DRT101 485.8 m EO1040	DRT131 EO3027	DRT164 794.3 m EO4924	DRT094 840.0 m EO5611	DRT179 699.8 m FO921	DRT108 726.6 m FO5732
%																				
SiO <sub>2</sub>	90.96	91.86	93.08	87.56	86.71	86.48	89.24	77.63	83.77	83.03	74.75	82.53	88.17	88.11	86.39	87.93	88.91	84.84	78.25	82.57
Al <sub>2</sub> O <sub>3</sub>	4.06	2.66	3.89	3.70	4.43	4.57	3.52	4.73	5.55	4.85	7.12	5.46	3.72	3.94	3.99	3.65	4.61	4.19	9.19	5.41
Fe <sub>2</sub> O <sub>3t</sub>	1.51	2.25	0.81	2.78	4.21	3.70	2.75	10.57	5.09	5.30	8.50	5.22	3.18	3.17	4.50	4.15	3.57	7.11	6.67	4.53
MnO	0.02	0.01	0.01	0.06	0.29	0.03	0.18	0.58	0.39	0.19	0.34	0.18	0.18	0.22	0.05	0.26	0.22	0.15	0.23	0.07
MgO	0.12	0.11	0.15	0.39	0.39	0.41	0.62	0.65	0.80	0.70	0.62	0.73	0.23	0.43	0.49	0.30	0.65	0.35	0.39	0.99
CaO	0.04	0.06	0.06	1.16	0.14	0.30	0.09	0.36	0.67	0.36	0.80	0.15	0.03	0.10	0.11	0.09	0.15	0.09	<D.L.	0.77
Na <sub>2</sub> O	<D.L.	<D.L.	<D.L.	<D.L.	<D.L.	<D.L.	<D.L.	<D.L.	<D.L.	<D.L.	<D.L.	<D.L.	<D.L.	<D.L.	<D.L.	<D.L.	<D.L.	<D.L.	<D.L.	<D.L.
K <sub>2</sub> O	1.26	0.72	1.19	0.87	0.89	1.22	0.65	0.56	1.02	0.90	1.58	1.06	0.86	0.88	0.91	0.66	0.98	0.92	2.30	1.52
TiO <sub>2</sub>	0.07	0.19	0.13	0.66	0.33	0.43	0.34	0.61	1.21	0.59	1.15	1.03	0.28	0.22	0.37	0.42	0.32	0.49	1.01	1.17
P <sub>2</sub> O <sub>5</sub>	0.06	0.07	0.04	0.56	0.16	0.25	0.10	0.24	0.32	0.32	0.60	0.15	0.21	0.22	0.11	0.15	0.07	0.16	0.31	0.31
LOI	0.42	0.98	0.47	1.20	1.21	1.77	1.02	N.D.	1.18	1.90	2.18	2.10	1.14	1.16	2.07	1.09	0.93	0.96	1.97	1.20
Total	98.51	98.91	99.81	98.94	98.75	99.16	98.51	95.93	100.00	98.16	97.64	98.61	97.99	98.44	98.98	98.69	100.41	99.25	100.31	98.54

Stratigraphy	Central Rand Group (CRG)													
	Lower CRG		Middle CRG						Upper CRG					
Reef Sample	Carbon Leader Reef BP86-13		Vaal Reef BP86-11	Leader Reef BP86-05-A	Leader Reef BP86-05-B	Middle Reef BP86-04	Basal Reef BP86-03	A Reef BP86-12	Elsberg Reef BP86-07	VCR BP86-06	VCR BP86-08	VCR BP86-09	VCR BP86-10	
%														
SiO <sub>2</sub>		91.27	88.30	85.38	85.15	79.09	63.20	86.89	85.15	91.64	67.83	96.70	87.28	
Al <sub>2</sub> O <sub>3</sub>		0.50	0.67	0.87	2.26	1.36	3.04	1.96	2.95	3.61	2.87	0.55	0.76	
Fe <sub>2</sub> O <sub>3t</sub>		3.35	4.86	7.87	6.80	12.73	20.70	3.10	6.74	1.72	17.42	1.77	6.03	
MnO		<D.L.	<D.L.	<D.L.	0.01	<D.L.	0.01	<D.L.	0.02	0.01	0.02	0.01	<D.L.	
MgO		0.17	<D.L.	0.03	0.07	0.05	0.19	0.03	0.59	0.42	0.63	0.22	0.01	
CaO		<D.L.	<D.L.	<D.L.	<D.L.	<D.L.	0.04	<D.L.	<D.L.	<D.L.	<D.L.	<D.L.	<D.L.	
Na <sub>2</sub> O		<D.L.	<D.L.	<D.L.	<D.L.	<D.L.	<D.L.	<D.L.	<D.L.	<D.L.	<D.L.	<D.L.	<D.L.	
K <sub>2</sub> O		<D.L.	<D.L.	0.06	0.09	0.25	0.27	0.47	0.48	0.80	0.42	<D.L.	<D.L.	
TiO <sub>2</sub>		0.08	0.05	0.08	0.13	0.10	0.14	0.47	0.19	0.09	0.18	0.03	0.06	
P <sub>2</sub> O <sub>5</sub>		0.05	0.05	0.07	0.07	0.06	0.06	0.04	0.07	0.04	0.09	<D.L.	0.07	
LOI		N.D.	N.D.	N.D.	N.D.	N.D.	N.D.	N.D.	N.D.	0.76	N.D.	0.62	N.D.	
Total		95.42	93.92	94.34	94.57	93.63	87.65	92.97	96.18	99.08	89.46	99.90	94.21	

Notes: Analyses realised by SARM (CRPG-CNRS, Nancy, France); LOI = loss on ignition; N.D. = not determined; <D.L. = below detection limits (CaO = 0.02%; Na<sub>2</sub>O = 0.07%; K<sub>2</sub>O = 0.05%; P<sub>2</sub>O<sub>5</sub> = 0.015%; MnO = 0.001%; MgO = 0.01%).

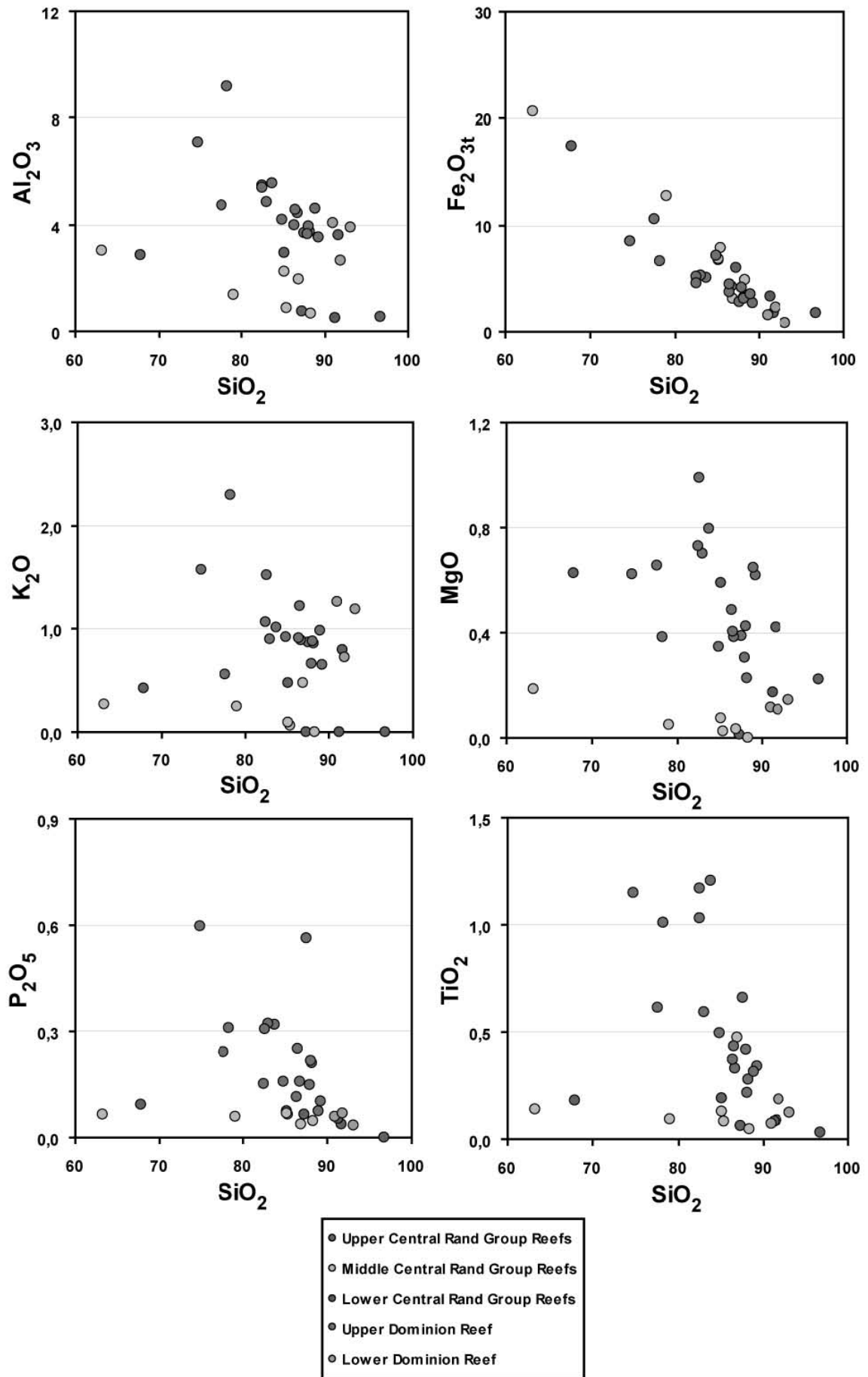


**Figure 3.1.8.** Binary diagrams showing whole rock  $\text{SiO}_2$  content vs.  $\text{Al}_2\text{O}_3$ ,  $\text{K}_2\text{O}$ ,  $\text{P}_2\text{O}_5$ ,  $\text{Fe}_2\text{O}_{3t}$ ,  $\text{MgO}$  and  $\text{TiO}_2$  contents in weight percent (wt%).

The amount of  $\text{TiO}_2$  is more prominent in the DG reefs and is related to the occurrence of ilmenite and Ti-oxides (0.07-1.21 % for DG and 0.03-0.47 % for CRG). The iron content is quite elevated in all reefs but is on average higher in the CRG ones (mean  $\text{Fe}_2\text{O}_{3t}$ :  $4.48 \pm 2.35\%$  for DG and  $7.76 \pm 6.12\%$  for CRG). The  $\text{Fe}_2\text{O}_{3t}$  vs.  $\text{SiO}_2$  plot for all samples shows principally a linear negative trend the slope of which is more inclined for the CRG samples (around -0.7). The  $\text{SiO}_2$  content controlled by quartz pebble abundance and  $\text{Fe}_2\text{O}_{3t}$  content controlled mostly by the sulphide abundance, correlate negatively. The calcium content is generally below or close to the detection limit value (0.02%) in the CRG reefs but in some DG samples CaO can rise up to 1.16% suggesting the presence of carbonates which have however not been observed. The sodium content in all analysed samples is always under the detection limit (0.07 %) and the manganese content is also very low with a maximum of 0.58 % MnO in the upper DG reef probably contained in garnet and Fe-Ti oxide accumulations. The chemical composition is variable between the reefs but when the major mineral composition is evaluated using the Q vs. A diagram (Fig. 3.1.9), it reveals that the bulk mainly corresponds to a mixture between quartz and phyllosilicates (muscovite-illite + chlorite) which probably derive from the alteration of detrital feldspars. The DG reefs have a distinct higher A parameter ( $A = \text{mol Al}-(\text{K}+\text{Na}+2\text{Ca}) = 12.6$  to  $131.4$  for DG and  $9.7$  to  $53.7$  for CRG) indicative of elevated alumino-silicate mineral concentrations associated to abundant garnet accumulation.

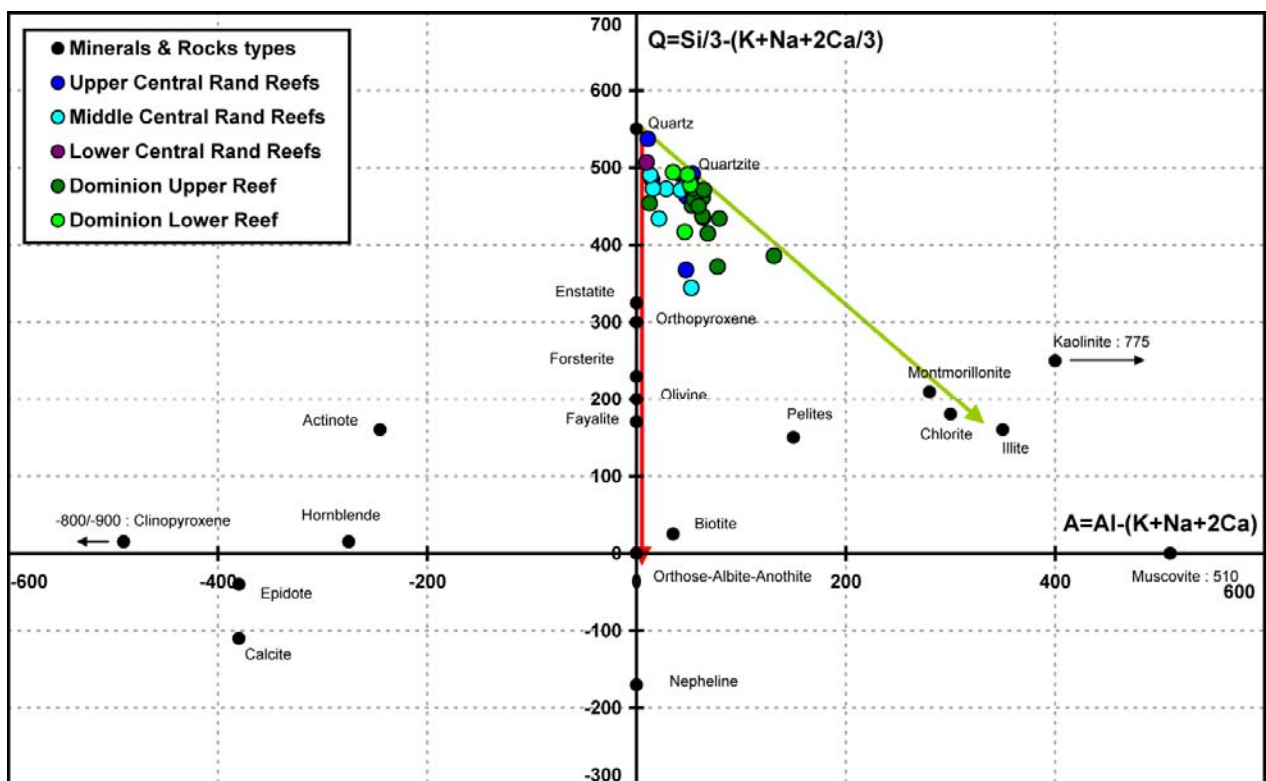


**Figure 3.1.9.** Variations of the Q  $[(\text{Si}-(\text{K}+\text{Na}+2\text{Ca}))/3]$  vs. A  $[\text{Al}-(\text{K}+\text{Na}+2\text{Ca})]$  parameters (in cations) for the Witwatersrand Reefs compared to mineral and igneous rock type compositions. The red arrow corresponds to the axis between quartz and feldspar trend and the green arrow between quartz and phyllosilicates.

### Trace elements

The sedimentary rocks sharing the same metamorphic history and alteration processes and the same source areas show commonly the same trace element patterns (McLennan, 1989). This is consistent with the results obtained for samples collected within the same stratigraphic level in the Witwatersrand Basin. The trace element composition of the Witwatersrand reefs is summarized in Table 3.1.2 for the Dominion Group and in Table 3.1.3 for the Central Rand Group.

Most Th and U concentrations of the Witwatersrand reefs (Fig. 3.1.10) are mainly higher than the Clarke values representative of the average of the upper continental crust (2.8 ppm U and 10.7 ppm Th after Taylor and McLennan, 1985). The Th/U ratios are mostly between 0.1 and 1 which indicates the presence of uranium oxides (Th/U ratios between 0.1 and 0.03 represent those of uraninite symbolize by the grey field). The most enriched sample is from the upper Dominion reef reaching up to 3454 ppm U and 1498 ppm Th. The upper DG conglomerates are the most enriched and the CRG reefs have much lower concentrations with 10 times less U and 100 times less Th for similar U contents which should reflect a different mineralogy for both elements. The upper Dominion reef trend indicates the mixing between a low Th/U phase (uraninite) with a high Th/U ratio and high Th phase (monazite). The CRG reefs define a trend without a significant contribution of the Th/U rich end member whereas the lower Dominion reef presents an intermediate position.

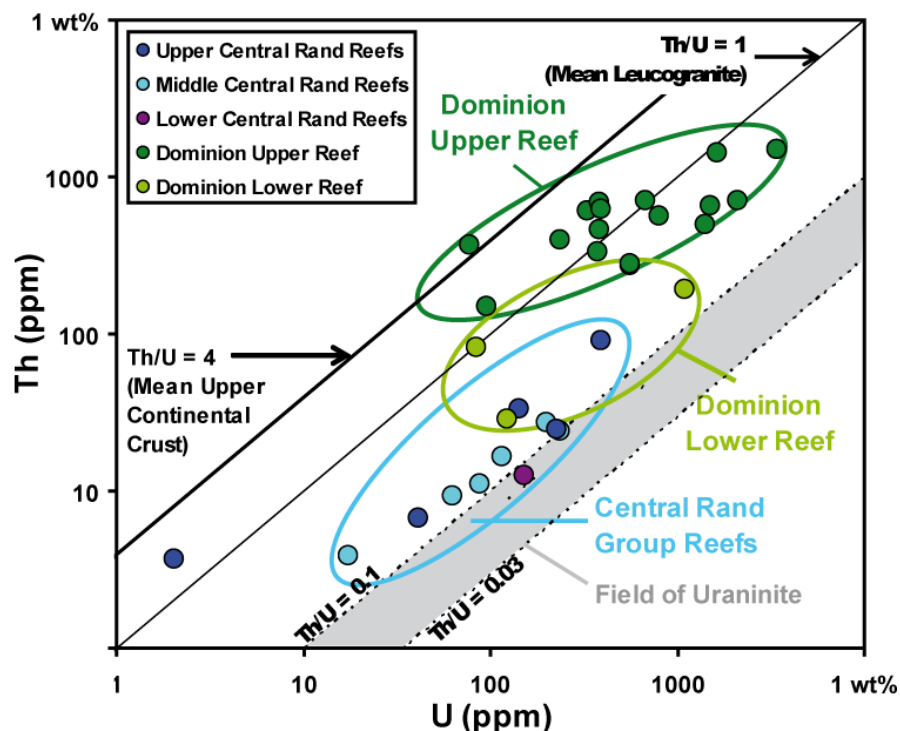


Figure 3.1.10. Th vs. U concentrations (in ppm) in the Witwatersrand reefs.

**Table 3.1.2.** Trace element composition (ICP-MS) of the Dominion Group conglomerates

Stratigraphy	Dominion Group																			
	Lower DG Reef			Upper DG Reef																
Reef Bore Hole Depth Sample	DRT070	DDR077	DRT131	DRT050	DRT058	DRT103	DRT090	DDR077	DRT113	DRT113	DRT095	DDR23	DRT024	DRT034	DRT101	DRT131	DRT164	DRT094	DRT179	DRT108
	621.9 m	393.0 m	906.5 m	185.5 m	182.5 m		823.2 m	371.7 m	807.8 m	810.0 m	790.7 m	39.2 m	206.8 m	342.1m	485.8 m		794.3 m	840.0 m	699.8 m	726.6 m
	AO8042	CO5602	EO3058	AO1618	AO3883	BO518	BO8981	CO5512	CO6778	CO6789	CO7744	DO1525	DO1823	DO8629	EO1040	EO3027	EO4924	EO5611	FO921	FO5732
<b>ppm</b>																				
<b>As</b>	10.73	87.60	5.04	124.70	47.51	88.75	67.15	37.60	135.20	390.90	287.90	54.32	712.20	81.19	312.10	52.55	72.52	126.80	74.92	36.73
<b>Ba</b>	51.63	98.91	54.64	437.00	101.60	131.80	39.84	55.68	132.80	55.62	138.90	460.10	59.38	55.02	63.14	49.10	49.61	39.77	60.66	133.70
<b>Be</b>	<D.L.	<D.L.	1.60	2.20	<D.L.	<D.L.	<D.L.	<D.L.	1.57	1.61	2.13	1.92	<D.L.	<D.L.	<D.L.	<D.L.	<D.L.	<D.L.	2.51	2.68
<b>Bi</b>	0.46	6.89	0.17	102.60	9.73	25.89	11.59	4.94	9.87	6.74	45.50	8.94	30.82	2.25	4.72	6.39	4.00	4.28	17.56	14.41
<b>Cd</b>	0.16	8.05	0.74	1.66	2.19	1.09	0.30	0.53	0.92	70.22	2.02	0.58	1.52	3.46	2.08	0.41	1.54	0.98	5.89	0.65
<b>Co</b>	6.92	60.17	4.70	101.70	58.83	77.09	43.06	156.70	36.51	97.47	115.60	39.97	100.40	36.30	71.32	41.92	15.48	49.41	46.70	40.52
<b>Cr</b>	33.20	873.40	349.20	476.50	385.70	299.40	336.10	995.70	858.90	860.50	778.50	391.90	352.90	293.30	419.70	571.40	440.40	311.90	515.00	581.90
<b>Cs</b>	2.23	2.59	1.28	6.87	2.83	8.20	1.35	3.16	2.04	1.74	3.27	2.21	3.26	1.67	3.07	0.61	1.29	1.16	2.27	7.40
<b>Cu</b>	21.44	104.90	16.84	57.00	73.10	89.61	68.21	421.20	386.10	118.50	254.60	212.40	65.96	34.35	190.30	163.10	110.10	181.20	307.50	324.60
<b>Ga</b>	5.90	5.41	6.30	36.16	13.19	18.22	8.91	14.14	24.07	24.56	38.67	10.68	15.61	13.96	8.75	10.63	8.60	11.30	24.82	28.24
<b>Ge</b>	0.94	1.46	0.98	8.22	3.26	3.82	2.26	3.91	5.53	5.11	8.47	2.26	3.29	3.23	2.00	2.46	2.07	2.68	4.55	5.21
<b>Hf</b>	1.96	3.49	5.60	45.02	17.61	9.71	5.51	16.87	24.47	13.12	36.49	18.71	10.30	6.09	5.18	7.01	6.75	6.80	17.21	21.51
<b>In</b>	<D.L.	<D.L.	<D.L.	<D.L.	<D.L.	<D.L.	<D.L.	<D.L.	<D.L.	<D.L.	<D.L.	<D.L.	<D.L.	<D.L.	<D.L.	<D.L.	<D.L.	<D.L.	<D.L.	<D.L.
<b>Mo</b>	7.21	34.89	14.82	5.26	49.60	3.57	41.77	27.40	23.28	20.64	24.83	11.08	15.17	9.19	22.28	19.12	15.97	11.07	5.69	74.29
<b>Nb</b>	24.39	90.98	17.42	527.50	439.90	371.20	164.20	506.00	204.70	501.20	540.00	147.80	462.50	219.80	244.10	219.70	57.36	204.10	263.30	246.20
<b>Ni</b>	29.18	76.21	11.74	317.90	113.60	196.60	66.82	204.70	99.93	134.20	275.90	115.90	190.20	86.93	120.00	100.10	53.12	85.86	123.20	128.80
<b>Pb</b>	177.34	2706.44	85.25	1845.00	1102.60	740.86	656.17	626.15	334.13	1713.36	1572.26	501.29	1628.28	752.16	573.58	269.20	275.82	356.63	661.46	252.36
<b>Rb</b>	60.00	46.53	52.64	55.84	49.47	76.82	34.04	34.20	52.54	42.60	75.16	68.50	46.15	48.79	46.20	28.51	42.42	37.47	84.14	103.90
<b>Sb</b>	8.92	9.62	0.24	2.31	12.94	1.23	10.12	11.50	0.40	1.12	1.64	11.16	1.27	11.30	9.81	9.74	0.30	1.23	0.55	1.33
<b>Sn</b>	3.51	77.67	2.65	81.55	58.75	53.93	13.35	42.88	9.74	40.09	58.56	21.78	56.33	30.70	37.70	22.26	7.58	12.66	18.46	14.86
<b>Sr</b>	6.29	11.51	7.96	205.60	20.15	60.58	18.09	27.36	62.87	41.95	78.93	22.37	11.19	9.15	18.14	12.36	14.39	14.56	11.56	85.16
<b>Ta</b>	8.49	62.56	2.53	358.00	197.00	194.10	67.72	222.80	69.87	184.70	250.10	69.87	241.40	87.55	107.10	90.64	17.98	80.91	95.59	93.76
<b>Th</b>	28.85	190.30	80.93	1498.00	501.40	656.30	274.40	565.50	610.00	694.70	1435.00	365.30	703.80	461.30	280.10	331.60	147.80	394.00	625.70	699.70
<b>U</b>	123.00	1097.00	85.13	3454.00	1420.00	1512.00	565.00	802.60	330.00	387.90	1645.00	77.97	2098.00	381.60	564.00	378.60	95.01	239.20	390.30	684.60
<b>V</b>	5.08	43.08	15.87	16.84	38.89	13.74	37.40	47.09	33.54	28.38	27.46	47.81	19.29	24.78	33.57	39.59	19.46	15.09	20.58	18.60
<b>W</b>	0.50	2.50	1.75	4.62	3.93	1.52	1.90	3.18	2.30	1.87	4.40	1.88	3.20	2.13	1.61	3.55	1.87	1.63	2.09	3.36
<b>Y</b>	29.16	143.20	44.02	542.80	305.50	356.70	208.30	424.40	354.20	323.60	573.90	229.80	294.30	225.50	223.10	196.40	94.71	180.70	345.30	415.40
<b>Zn</b>	77.46	5853.00	79.56	30.15	593.30	80.63	116.40	111.00	78.48	10510.00	168.30	250.20	183.70	1272.00	466.40	99.25	195.80	175.40	805.70	58.77
<b>Zr</b>	63.63	83.56	217.30	1617.00	312.20	296.40	183.50	433.50	773.40	398.90	1190.00	618.80	292.70	195.60	155.60	224.30	236.80	220.80	532.40	729.40

Notes: Analyses realised by SARM (CRPG-CNRS, Nancy, France); <D.L. = below detection limits (Be = 0.2 ppm; In = 0.06 ppm)

**Table 3.1.3.** Trace element composition (ICP-MS) of the Central Rand Group conglomerates

Stratigraphy	Central Rand Group (CRG)											
	Lower CRG	Middle CRG						Upper CRG				
Reef Sample	Carbon Leader Reef BP86-13	Vaal Reef BP86-11	Leader Reef BP86-05-A	Leader Reef BP86-05-B	Middle Reef BP86-04	Basal Reef BP86-03	A Reef BP86-12	Elsberg Reef BP86-07	VCR BP86-06	VCR BP86-08	VCR BP86-09	VCR BP86-10
<b>ppm</b>												
As	31.18	946.30	1867.00	321.70	417.70	395.40	85.11	347.90	15.65	795.80	17.60	1226.00
Ba	3.55	6.72	8.31	21.82	35.22	55.32	83.54	44.99	53.42	47.08	2.54	6.79
Be	<D.L.	<D.L.	<D.L.	<D.L.	<D.L.	<D.L.	<D.L.	<D.L.	<D.L.	<D.L.	<D.L.	<D.L.
Bi	0.27	1.55	2.99	0.45	0.77	0.74	1.03	1.16	0.15	1.63	0.59	1.83
Cd	0.27	0.23	0.13	<D.L.	0.36	0.15	1.01	0.35	<D.L.	0.58	<D.L.	0.16
Co	48.06	85.29	130.60	39.46	87.96	91.64	67.95	84.45	6.69	156.40	12.31	118.90
Cr	141.70	141.50	324.00	146.20	232.10	258.30	799.70	311.10	52.91	783.20	94.45	236.30
Cs	<D.L.	<D.L.	0.70	1.05	0.31	1.21	1.27	0.82	0.68	1.17	<D.L.	0.39
Cu	94.79	24.64	34.16	14.80	26.67	24.45	57.13	48.85	15.48	76.33	<D.L.	48.36
Ga	0.81	1.25	1.55	3.02	1.89	3.37	2.59	4.24	4.60	5.60	1.29	1.52
Ge	0.60	1.03	0.82	0.98	1.02	0.94	0.94	1.20	1.33	1.58	0.77	0.93
Hf	2.17	2.07	2.71	1.39	3.31	2.99	17.67	4.97	1.86	8.83	2.12	2.53
In	<D.L.	<D.L.	<D.L.	<D.L.	<D.L.	<D.L.	<D.L.	<D.L.	<D.L.	<D.L.	<D.L.	<D.L.
Mo	0.67	1.39	3.31	1.35	2.38	2.52	5.60	2.35	0.81	4.33	2.89	2.77
Nb	1.87	6.48	3.49	3.01	1.56	3.81	7.04	5.67	1.84	8.35	1.30	3.39
Ni	66.43	64.36	103.90	89.65	218.30	134.70	99.79	100.10	23.47	131.50	22.63	80.62
Pb	42.27	45.66	87.42	49.81	77.29	112.46	91.70	397.23	3.46	635.19	26.02	79.40
Rb	0.58	1.47	2.69	4.08	8.31	9.73	17.15	18.88	28.76	17.52	<D.L.	2.30
Sb	7.71	9.39	4.34	6.49	14.23	28.02	18.54	2.39	0.32	16.76	0.39	12.78
Sn	0.35	16.85	0.54	0.66	0.41	2.32	0.73	0.69	0.45	0.78	<D.L.	1.08
Sr	9.17	12.20	9.58	9.25	10.31	29.21	21.10	4.63	3.72	7.83	1.97	9.31
Ta	0.74	3.47	1.61	0.72	0.66	3.01	1.10	1.89	0.22	5.79	0.45	1.70
Th	12.47	16.68	27.04	9.27	3.85	11.16	24.23	33.22	3.67	91.40	6.72	24.36
U	153.60	115.00	201.20	62.82	17.31	88.94	238.20	142.40	2.02	393.50	41.24	227.90
V	4.95	3.43	6.50	11.40	9.71	18.00	19.20	21.21	14.53	21.04	2.32	5.24
W	0.72	0.89	1.01	0.40	0.43	0.51	1.77	0.48	0.37	1.10	<D.L.	0.85
Y	9.07	9.06	16.22	10.62	6.97	11.62	24.96	23.77	7.48	62.87	6.40	12.64
Zn	62.21	33.86	32.42	9.86	20.73	22.71	30.67	88.36	49.34	92.91	<D.L.	30.90
Zr	105.80	87.89	112.80	51.47	129.80	116.90	738.80	205.60	68.34	363.20	85.73	101.10

*Notes:* Analyses realised by SARM (CRPG-CNRS, Nancy, France); <D.L. = below detection limits (Be = 0.2 ppm; Cd = 0.15 ppm; Cs = 0.1 ppm; Cu = 3 ppm; In = 0.06 ppm; Rb = 0.3 ppm; Sn = 0.2 ppm; W = 0.15 ppm; Zn = 6 ppm).

High field strength elements (HFSE) are more enriched in the DG reefs than in the CRG conglomerates: Nb (mean: 273 ppm for DG and 4 ppm for CRG), Ta (mean: 125 ppm for DG and 2 ppm for CRG) reflecting the abundance of detrital Nb-Ta oxides, Rb (mean: 54 ppm for DG and 9 ppm for CRG) reflecting the abundance of K-micas, Y (mean: 276 ppm for DG and 17 ppm for CRG) corresponding mainly to xenotime, U (mean: 817 ppm for DG and 140 ppm for CRG) for the abundance of U-oxides, Th (mean: 527 ppm for DG and 22 ppm for CRG) for abundance of monazite and uraninite, Zr (mean: 439 ppm for DG and 181 ppm for CRG) and Hf (mean: 14 ppm for DG and 4 ppm for CRG) for zircon. The HFSE concentrations in sediments are mainly controlled by the heavy mineral phases and the eroded rocks tributary of the detritus in the Dominion Group are therefore presumably HFSE-rich mineral sources such as granites or pegmatites. On the other hand, the DG and CRG reefs are characterized by heavy metals enrichment in As (up to 391 ppm for DG and 712 ppm for CRG), Co (up to 157 ppm for DG and 156 ppm for CRG), Cr (up to 873 ppm for DG and 800 ppm for CRG), Cu (up to 421 ppm for DG and 95 ppm for CRG), Ni (up to 318 ppm for DG and 218 ppm for CRG), Pb (up to 0.3 % for DG and 635 ppm for CRG) and Zn (up to 1.05 % for DG and 93 ppm for CRG) which are generally relevant of heavy minerals from mafic or ultramafic sources. High contents of As, Co and Cu are associated to the abundance of sulphides and Cr to detrital chromite. Highest Pb concentrations are relevant of radiogenic lead and to the presence of galena. The source area of the Dominion Group sediments was probably an Archean composite terrain made of both granitic and greenstone rocks with a major contribution of quartz, feldspar altered to illite and heavy accessory minerals. The low HFSE concentrations in CRG indicate that the sediments probably derived from terrains dominated by HFSE-poor mafic rock suites and were composed of less felsic rocks than for DG with a main composition of quartz, micas and minor heavy minerals.

The rare earth element composition of the Witwatersrand reefs is synthesised in Table 3.1.4 for the Dominion Group and in Table 3.1.5 for the Central Rand Group. The chondrite-normalized REE patterns of the conglomerates (Fig. 3.1.11) show the same general trend with strong high fractionation between light rare earth elements (LREE) and heavy rare earth elements (HREE) and negative Eu anomalies. However, the DG reefs have much higher REE concentrations than the CRG reefs: the average of  $\Sigma$ REE is 3,431 ppm for DG and only 152 ppm for CRG. Moreover, the REE patterns for the distinct reefs within the two sedimentary groups show REE abundances that increase toward the top of the sequence: from 94 ppm in the lower DG reef to a maximum of 1.12 wt% in the upper DG reef, and from 47 ppm for the lower Carbon Leader Reef in CRG to up to 607 ppm in the Ventersdorp Contact Reef.

The REE patterns of the upper DG reef show also stronger fractionation than for the other conglomerates, especially in comparison of the flattened CRG reef trends. The heavy vs. light REE fractionation ( $La_N/Yb_N$ ) ranges from 8.31 to 23.17 in CRG, from 3.42 to 14.98 in the lower DG reef and from 12.35 to 46.34 in the upper DG reef. This reflects the decreasing contribution of REE-rich minerals such as monazite for the LREE and zircon and xenotime for the HREE.

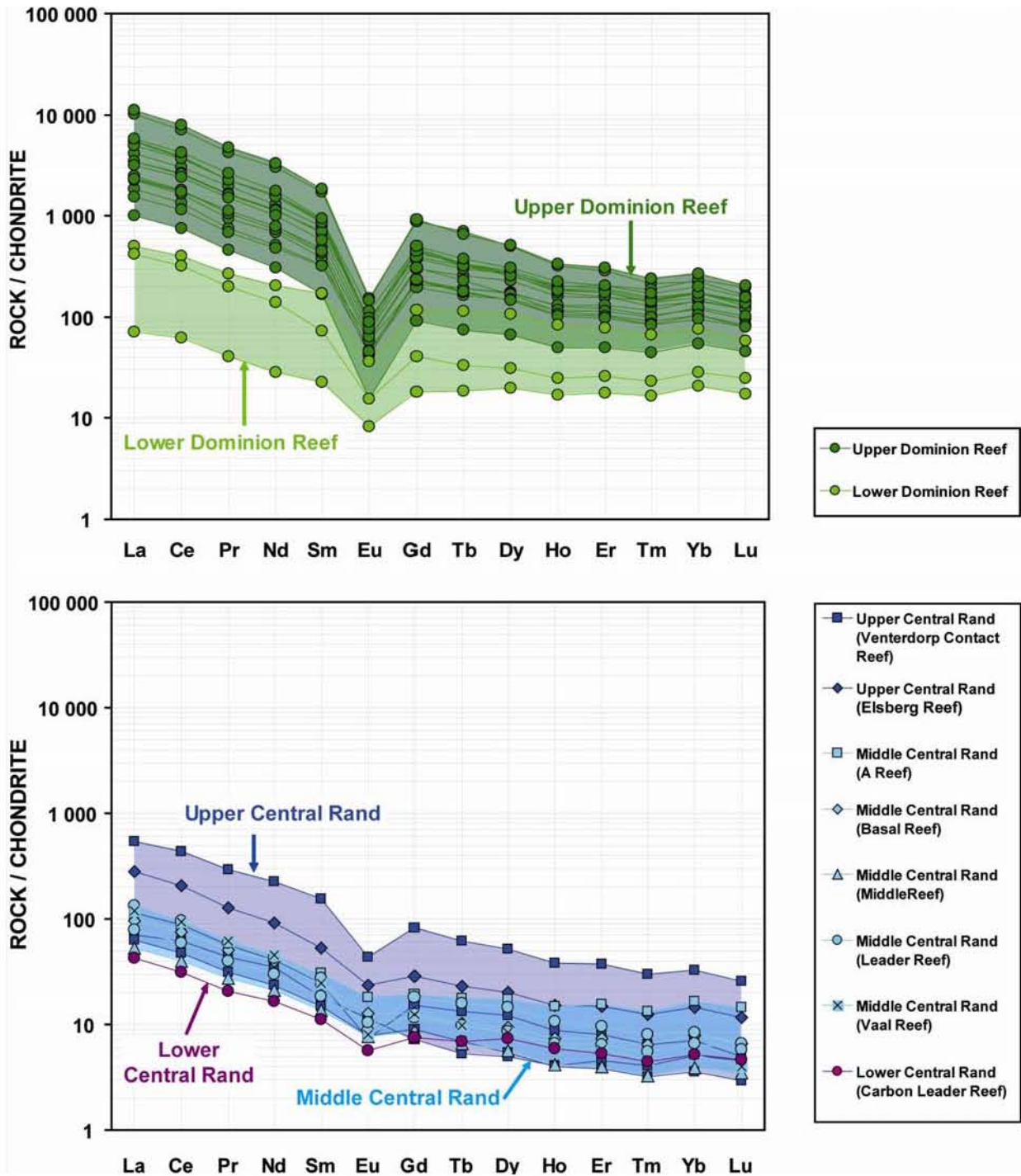


Figure 3.1.11. Chondrite normalized REE patterns of the Witwatersrand reefs (normalized to chondrite values after Anders and Grevesse, 1989).

**Table 3.1.4.** Rare Earth Element concentrations (ICP-MS) in the Dominion Group conglomerates

Stratigraphy	Dominion Group																			
	Lower DG Reef			Upper DG Reef																
Reef	DRT070	DDR077	DRT131	DRT050	DRT058	DRT103	DRT090	DDR077	DRT113	DRT113	DRT095	DDR23	DRT024	DRT034	DRT101	DRT131	DRT164	DRT094	DRT179	DRT108
Bore Hole	621.9 m	393.0 m	906.5 m	185.5 m	182.5 m		823.2 m	371.7 m	807.8 m	810.0 m	790.7 m	39.2 m	206.8 m	342.1m	485.8 m		794.3 m	840.0 m	699.8 m	726.6 m
Depth																				
Sample	AO8042	CO5602	EO3058	AO1618	AO3883	BO518	BO8981	CO5512	CO6778	CO6789	CO7744	DO1525	DO1823	DO8629	EO1040	EO3027	EO4924	EO5611	FO921	FO5732
<b>ppm</b>																				
<b>La</b>	17.14	120.10	101.50	2438.00	565.70	992.80	437.70	827.20	1332.00	1285.00	2659.00	545.50	824.60	765.70	367.40	591.60	239.30	555.20	1175.00	1385.00
<b>Ce</b>	38.08	245.60	195.80	4364.00	1081.00	1852.00	825.60	1602.00	2371.00	2326.00	4780.00	993.80	1586.00	1460.00	697.30	1097.00	457.70	1051.00	2230.00	2603.00
<b>Pr</b>	4.06	26.97	20.14	425.60	112.00	194.80	75.56	164.40	227.10	224.70	475.30	94.14	160.30	149.00	68.80	105.90	45.51	113.40	224.40	262.80
<b>Nd</b>	13.27	95.22	64.88	1409.00	365.60	608.10	243.00	535.80	756.70	759.10	1561.00	321.40	531.20	472.30	226.40	343.20	143.90	367.20	720.80	827.30
<b>Sm</b>	3.43	25.35	10.93	257.40	71.20	117.30	48.81	100.90	132.50	138.40	275.10	56.91	105.30	85.69	47.59	63.51	24.99	67.34	127.50	142.30
<b>Eu</b>	0.49	2.20	0.93	9.15	3.60	5.65	3.49	4.24	5.08	6.85	8.76	2.47	5.78	3.82	2.64	2.78	0.92	2.73	4.57	5.33
<b>Gd</b>	3.81	24.39	8.54	184.60	62.94	90.10	43.94	78.46	95.42	101.10	191.80	47.49	81.97	63.97	40.90	48.34	19.03	49.52	93.00	104.20
<b>Tb</b>	0.74	4.59	1.33	27.93	10.27	13.35	7.70	11.99	13.29	13.37	26.25	7.55	12.85	9.23	6.53	6.96	2.97	7.15	12.92	14.92
<b>Dy</b>	4.93	26.92	7.67	124.90	57.25	71.14	43.31	67.55	68.30	65.06	127.30	42.91	67.98	41.93	37.47	36.60	16.44	36.43	64.45	76.71
<b>Ho</b>	1.01	4.96	1.47	19.39	9.60	12.21	7.72	12.08	11.50	10.40	19.92	7.87	11.28	6.89	7.04	6.44	3.00	6.16	10.96	13.27
<b>Er</b>	2.98	13.16	4.42	48.50	26.43	32.56	20.92	34.96	31.05	26.94	51.66	22.14	29.49	17.60	19.52	17.32	8.38	16.45	29.65	34.43
<b>Tm</b>	0.50	2.01	0.70	6.35	4.40	4.68	3.12	5.64	4.50	3.78	7.16	3.46	4.20	2.71	2.99	2.56	1.34	2.48	4.28	5.14
<b>Yb</b>	3.49	13.01	4.86	37.74	29.96	29.64	20.45	39.58	29.57	24.45	45.02	24.89	26.70	17.73	21.34	17.52	9.30	16.33	28.94	33.94
<b>Lu</b>	0.52	1.73	0.74	4.91	3.84	4.15	2.84	5.81	4.30	3.61	6.16	3.55	3.59	2.37	3.05	2.49	1.37	2.40	4.12	4.63
<b>Σ REE</b>	94.43	606.20	423.91	9357.47	2403.79	4028.47	1784.15	3490.60	5082.31	4988.75	10234.42	2174.07	3451.23	3098.94	1548.97	2342.22	974.15	2293.78	4730.59	5512.98
<b>(La/Sm)<sub>N</sub></b>	3.23	3.06	5.99	6.11	5.13	5.46	5.79	5.29	6.49	5.99	6.24	6.19	5.06	5.77	4.98	6.01	6.18	5.32	5.95	6.28
<b>(Tb/Yb)<sub>N</sub></b>	0.90	1.50	1.17	3.15	1.46	1.91	1.60	1.29	1.91	2.32	2.48	1.29	2.05	2.21	1.30	1.69	1.36	1.86	1.90	1.87
<b>(La/Yb)<sub>N</sub></b>	3.52	6.62	14.98	46.34	13.54	24.03	15.35	14.99	32.31	37.70	42.37	15.72	22.15	30.98	12.35	24.22	18.45	24.39	29.12	29.27
<b>Eu/Eu*</b>	0.42	0.27	0.29	0.13	0.16	0.17	0.23	0.15	0.14	0.18	0.12	0.15	0.19	0.16	0.18	0.15	0.13	0.14	0.13	0.13
<b>(Gd/Yb)<sub>N</sub></b>	0.90	1.55	1.45	4.04	1.73	2.51	1.77	1.64	2.66	3.41	3.52	1.57	2.53	2.98	1.58	2.28	1.69	2.50	2.65	2.53

Notes: Analyses realised by SARM (CRPG-CNRS, Nancy, France); Eu/Eu\* =  $Eu_N/\sqrt{(Sm.Gd)_N}$ ; (X)<sub>N</sub> = normalized to chondrite C1 values after Anders and Grevesse (1989)

**Table 3.1.5.** Rare Earth Element concentrations (ICP-MS) in the Central Rand Group conglomerates

Stratigraphy	Central Rand Group (CRG)											
	Lower CRG	Middle CRG						Upper CRG				
Reef Sample	Carbon Leader Reef BP86-13	Vaal Reef BP86-11	Leader Reef BP86-05-A	Leader Reef BP86-05-B	Middle Reef BP86-04	Basal Reef BP86-03	A Reef BP86-12	Elsberg Reef BP86-07	VCR BP86-06	VCR BP86-08	VCR BP86-09	VCR BP86-10
<b>ppm</b>												
<b>La</b>	10.15	28.72	31.84	18.96	12.64	23.01	24.65	67.23	17.07	129.40	15.22	27.66
<b>Ce</b>	19.11	56.89	58.72	36.37	24.54	45.58	47.89	124.50	37.38	266.80	29.20	53.42
<b>Pr</b>	2.08	6.17	5.94	3.96	2.74	5.09	5.22	12.78	4.37	29.51	3.16	5.60
<b>Nd</b>	7.72	21.24	20.14	14.03	9.90	18.77	19.06	42.92	16.48	106.50	11.08	19.13
<b>Sm</b>	1.66	3.65	4.08	2.79	2.04	3.61	4.54	7.93	2.70	23.10	2.24	3.70
<b>Eu</b>	0.34	0.49	0.53	0.63	0.46	0.77	1.09	1.40	0.69	2.61	0.47	0.44
<b>Gd</b>	1.59	2.63	3.82	2.45	1.78	2.66	4.05	6.06	1.52	17.31	1.87	3.22
<b>Tb</b>	0.28	0.39	0.63	0.39	0.27	0.41	0.71	0.92	0.21	2.45	0.27	0.53
<b>Dy</b>	1.85	2.10	3.60	2.16	1.42	2.35	4.35	5.04	1.24	13.06	1.35	3.08
<b>Ho</b>	0.36	0.37	0.64	0.40	0.25	0.45	0.90	0.91	0.25	2.28	0.24	0.53
<b>Er</b>	0.91	0.98	1.62	1.10	0.68	1.25	2.65	2.53	0.77	6.37	0.65	1.36
<b>Tm</b>	0.13	0.14	0.24	0.17	0.10	0.19	0.40	0.38	0.12	0.89	0.10	0.19
<b>Yb</b>	0.88	0.89	1.44	1.11	0.66	1.35	2.79	2.47	0.86	5.57	0.60	1.19
<b>Lu</b>	0.14	0.12	0.20	0.17	0.10	0.20	0.44	0.35	0.14	0.77	0.09	0.15
<b>Σ REE</b>	47.18	124.78	133.43	84.69	57.58	105.67	118.73	275.40	83.79	606.62	66.53	120.20
<b>(La/Sm)<sub>N</sub></b>	3.96	5.08	5.03	4.39	4.00	4.12	3.50	5.47	4.08	3.62	4.39	4.83
<b>(Tb/Yb)<sub>N</sub></b>	1.34	1.88	1.87	1.49	1.71	1.30	1.09	1.59	1.04	1.87	1.93	1.89
<b>(La/Yb)<sub>N</sub></b>	8.31	23.17	15.85	12.21	13.72	12.24	6.34	19.56	14.20	16.66	18.07	16.66
<b>Eu/Eu*</b>	0.65	0.48	0.41	0.74	0.74	0.76	0.78	0.62	1.04	0.40	0.70	0.39
<b>(Gd/Yb)<sub>N</sub></b>	1.49	2.44	2.19	1.82	2.22	1.63	1.20	2.03	1.45	2.56	2.55	2.23

Notes: Analyses realised by SARM (CRPG-CNRS, Nancy, France); Eu/Eu\* =  $Eu_N / \sqrt{(Sm.Gd)_N}$ ; (X)<sub>N</sub> = normalized to chondrite C1 values after Anders and Grevesse (1989).

The negative Eu anomaly is more important in the DG reefs ( $\text{Eu}/\text{Eu}^*=0.18\pm 0.07$ ) than in the CRG conglomerates ( $\text{Eu}/\text{Eu}^*=0.64\pm 0.20$ ). Usually, the Archean sediments have a typical REE trend with weak to no Eu anomaly corresponding to  $\text{Eu}/\text{Eu}^*$  ratios upper than 0.85 and a strong depletion in HREE with high  $(\text{Gd}/\text{Yb})_N$  ratios (after Taylor and McLennan, 1995; Fig. 3.1.12). Recent sediments differ generally by a notable increase in the negative Eu anomaly at the end of Archean Eon (smaller  $\text{Eu}/\text{Eu}^*$  ratios). Archean sediments may have inherited of a sizable negative Eu anomaly if they are derived from felsic igneous rocks (Gao and Wedepohl, 1995; Condie, 1997). The negative Eu anomaly in rocks of the upper continental crust is unlike the Archean TTG granitoids but more characteristic of fractionated K-rich granites appearing generally at the end of Archean time (Moyen et al., 2003; Champion and Smithies, 2004).

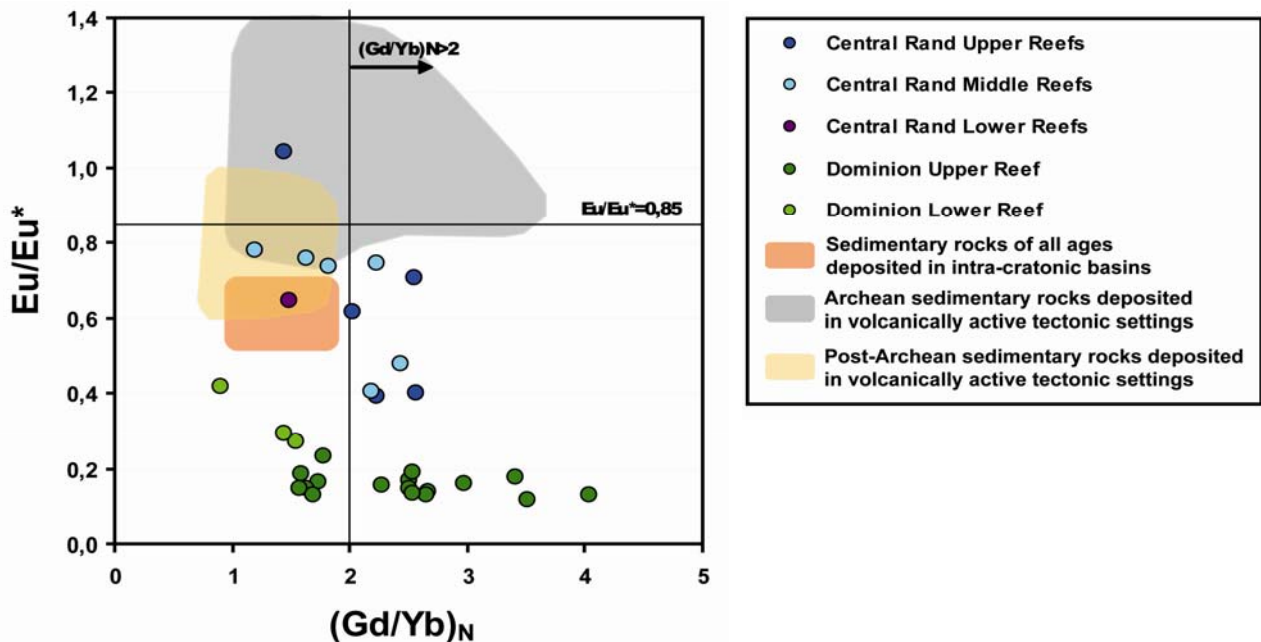


**Figure 3.1.12.**  $\text{Eu}/\text{Eu}^*$  ( $=\text{Eu}_N/\sqrt{(\text{Sm}.\text{Gd})_N}$ ) vs.  $(\text{Gd}/\text{Yb})_N$ . The fields of typical Archean and post-Archean sedimentary rocks deposited in volcanically active tectonic settings are from Taylor and McLennan (1995) and the field of “cratonic” sediments is adapted from McLennan and Taylor (1991).

The REE patterns of sediments are most likely associated to the abundance in high-REE minerals such as zircon (HREE) or monazite (LREE). The upper DG reef is again the more enriched in REE and notably in LREE. Figure 3.1.13 illustrates the total bulk of REE abundances in function of U and Th contents and shows a positive correlation between all of these elements. This clearly demonstrates that the mineral assemblage controls the chemistry of trace elements in the reefs and that REE, U and Th were transported together. The enriched DG reefs are related to accumulation of uraninite and monazite whereas the CRG reefs show different correlations because of decreasing contribution of magmatic REE-rich uraninite and monazite and higher abundances of Th- and REE-poor hydrothermal uraninite.

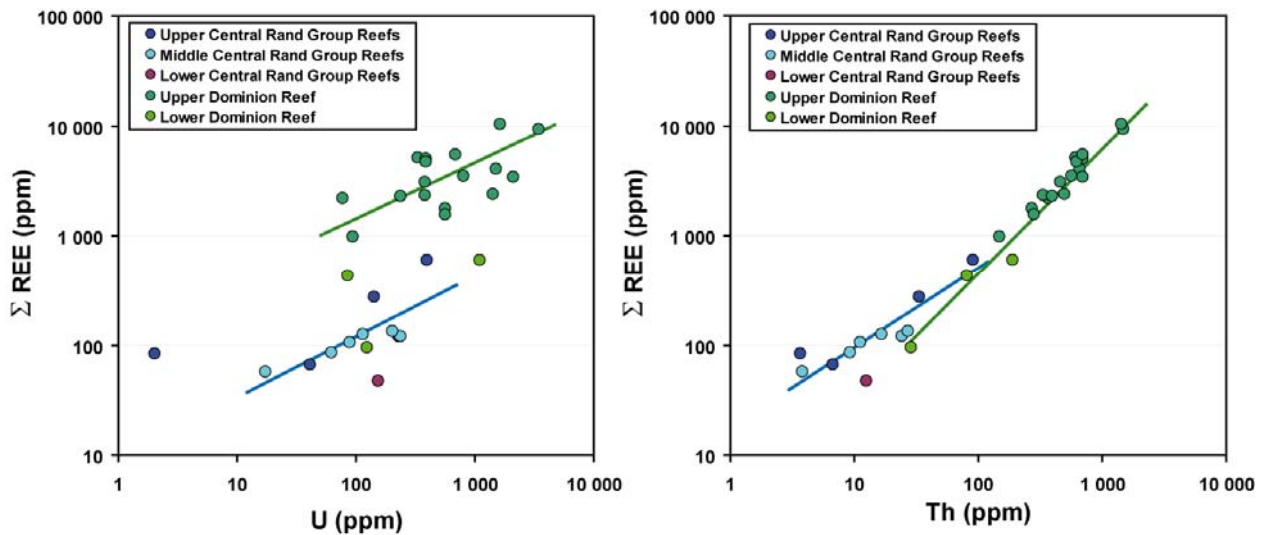


Figure 3.1.13.  $\Sigma$ REE vs. U and Th concentrations (in ppm).

## Textural aspects and chemistry of U-bearing minerals and some associated accessories

### *Dominion Group reefs*

The DG reefs are clast-supported, dominated by well packed rounded to angular and often fractured quartz pebbles (Fig. 3.1.14). Sometimes these pebbles show recrystallized edges at the contact with other quartz clasts. Pebbles are emplaced within a sericitic and chloritic matrix showing occasionally a metamorphic foliation oblique to the lithologic layering. Phyllosilicates frequently embed the pebbles (Fig. 3.1.15) confirming that white micas were produced by the alteration of feldspar initially present in quartz-feldspar clasts ( $K\text{-Feldspar} + H^+ \rightarrow \text{muscovite} + \text{quartz} + K^+$ ). Heavy minerals are disseminated within the matrix between the quartz pebbles and are largely comprised of pyrite and garnet rounded grains with minor monazite, zircon, uraninite, ilmenite, titano-magnetite, chromite, and rare cassiterite and niobium-tantalum minerals. However, secondary pyrite veinlets crosscutting bedding and pebbles are common and show clearly at least one post-dating generation of sulphide

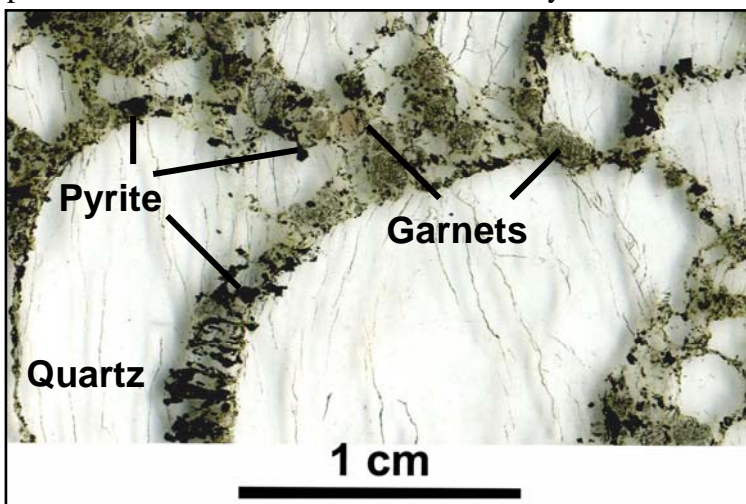
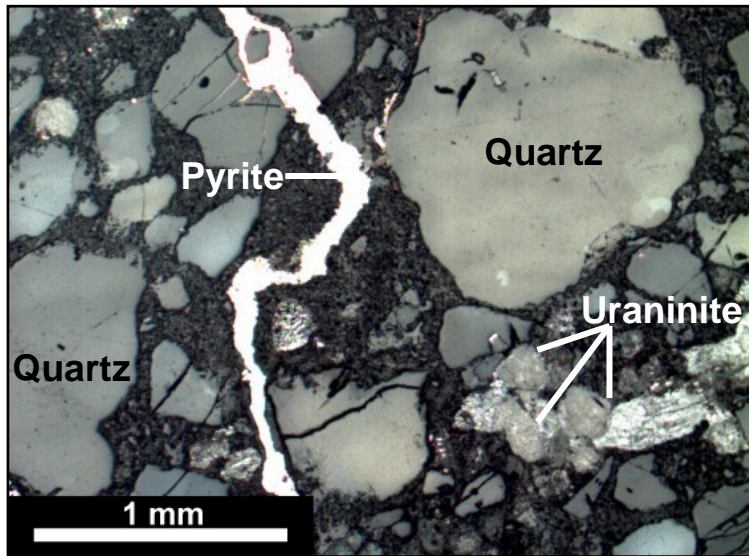
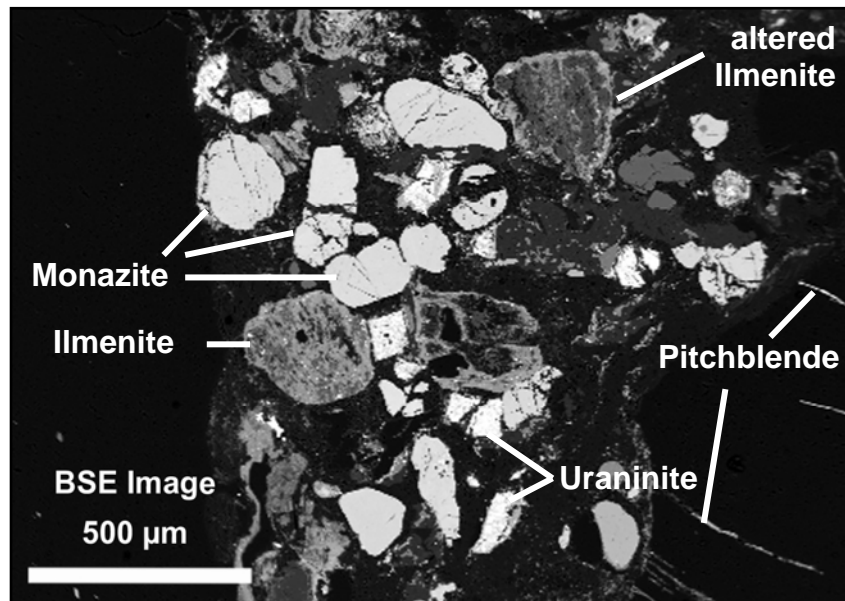


Figure 3.1.14. Picture of a thin section (upper DG reef: DRT034-DO8628-342m depth) showing the relative proportion of fractured quartz pebbles and matrix composed mainly of chlorite and sericite with disseminated heavy minerals (opaque pyrite and pink to brownish garnet in well rounded grains).



**Figure 3.1.15.** Photomicrograph in reflected light showing a veinlet of pyrite crosscutting the sericitic matrix and quartz pebbles (lower DG reef: DRT179-FO948). The lighter grains are primary uraninite.

Two stages of U mineralization could also be distinguished, namely a primary stage that comprises subhedral to well rounded grains of monazite and uraninite and a secondary stage associated with uranium dispersed within the matrix coating primary heavy minerals and filling fractures (Fig. 3.1.16). The chemical compositions of the various phases are reported in Tables 3.1.6 and 3.1.7.



**Figure 3.1.16.** SEM-BSE image showing accumulation of heavy minerals, uraninite, monazite and ilmenite, with secondary mineralization, U-Ti phases coating primary grains and pitchblende filling fractures of quartz pebbles (upper DG reef: DRT034-DO8628-342m depth).

Monazite grains from the Dominion Group upper reef have an average composition dominated by LREE (23.8-34.8 wt%  $\text{Ce}_2\text{O}_3$ , 10.2-23.4 wt%  $\text{La}_2\text{O}_3$ , 24.1-30.5 wt%  $\text{Pr}_2\text{O}_3$  -  $11.58 \pm 2.275$ -17 wt%  $\text{Nd}_2\text{O}_3$ ) and phosphorous (24.1-30.5 wt%  $\text{P}_2\text{O}_5$ ) with small amounts of calcium (up to 1.28 wt%  $\text{CaO}$ ), yttrium (up to 2.84 wt%  $\text{Y}_2\text{O}_3$ ) and silicium (up to 3.27 wt%

SiO<sub>2</sub>). High contents in radioelements are also noticed from 0.16 to 14.76 wt% ThO<sub>2</sub> and up to 5.22 wt% UO<sub>2</sub> and 2.43 wt% PbO corresponding to radiogenic lead. The U-Th-Pb chemical ages calculated from the radioelement contents yield wide range of variation between 802 Ma and 4544 Ma with a Gaussian repartition centred on an average value of 3.1 Ga but with a major peak at 2.7 Ga (Fig. 3.1.17). The oldest age probably corresponds to local radiogenic lead accumulation. The 2.7 Ga peak represents a major thermal event associated with the ~2.71 Ga rifting event causing the Ventersdorp Supergroup volcanism and finally the ages older than 3.1 Ga clearly demonstrates the detrital origin of monazite grains.

The binary diagram representing the monazite composition (Fig. 3.2.18) plots mostly along the cheralite-(Ce) group with a slight tendency to the huttonitic compositions probably because of some REE and P losses during alteration. Cheralite-(Ce) is a solid solution between brabantite and monazite-(Ce) minerals and is characteristic of highly differentiated and strongly peraluminous granites deriving from low temperature residual melts of S-type affinity (Förster, 1998).

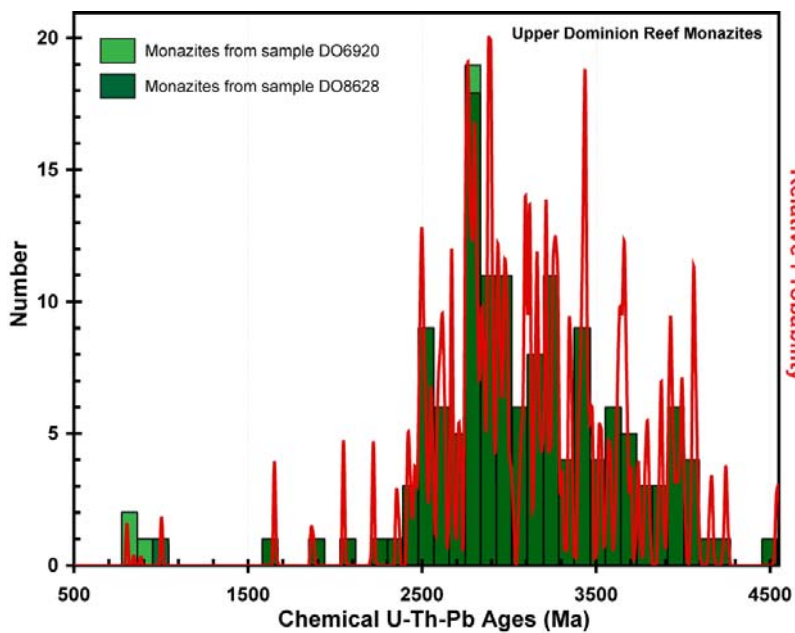


Figure 3.1.17. Histogram and relative probability curve representing the distribution of U-Th-Pb chemical ages calculated in monazite grains from two samples of the upper Dominion reef.

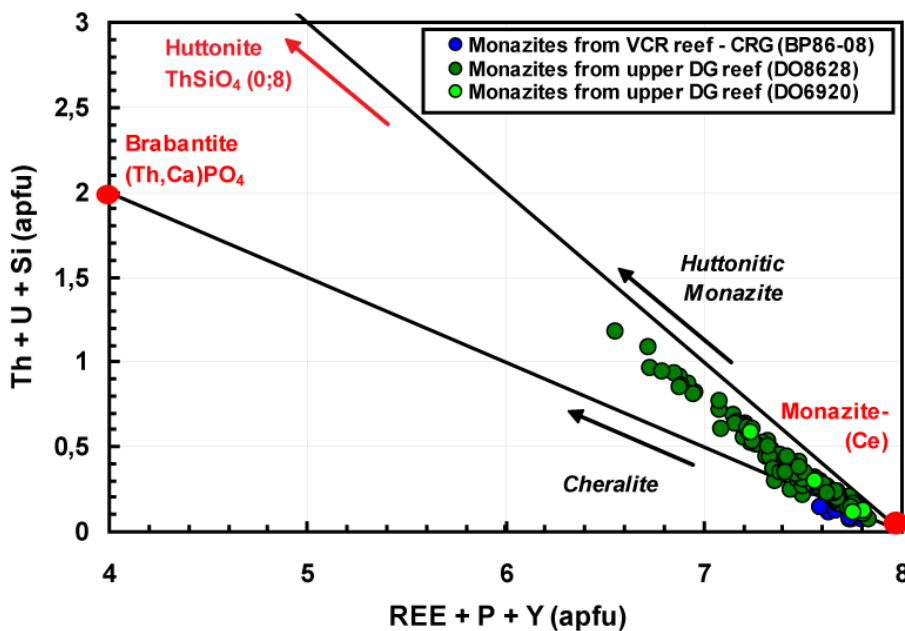


Figure 3.1.18. Plot of (Th+U+Si) vs. (REE+Y+P) calculated in formula proportions on the basis of 16 O atoms after Förster (1998). Monazite group minerals are reported in red circles with molar abundance of huttonite, brabantite and monazite-(Ce).

**Table 3.1.6.** Representative average composition of primary detrital U-bearing minerals from the Upper Dominion Reef analysed by electron microprobe.

Paragenesis	Primary (detrital)									
Mineral	Monazite		Uraninite							
Form	Detrital grains (sub-rounded)		Detrital grains (subhedral to well rounded)							
Sample	DO6920	DO8628	AO3883		AO5268		DO8628		AO5686	
Bore hole	DRT039	DRT034	DRT058		DRT079		DRT034		DRT070	
Depth	337.5 m	342 m	182.5 m		328 m		342 m		608.25 m	
EMPA	4	143	Well preserved 52	Coffinitized 21	Well preserved 41	Coffinitized 2	Well preserved 50	Coffinitized 4	Well preserved 58	Coffinitized 16
Al <sub>2</sub> O <sub>3</sub>	0.17 ± 0.18	<D.L.	0.09 ± 0.17	1.77 ± 0.36	0.19 ± 0.14	0.82 ± 0.11	<D.L.	<D.L.	<D.L.	0.31 ± 0.16
SiO <sub>2</sub>	1.01 ± 0.60	1.01 ± 0.62	1.88 ± 1.07	11.37 ± 1.99	2.24 ± 0.97	8.46 ± 0.54	0.74 ± 0.53	3.19 ± 0.68	1.47 ± 0.73	5.61 ± 2.27
SO <sub>2</sub>	N.D.	N.D.	1.09 ± 1.00	1.85 ± 1.47	1.33 ± 0.93	2.70 ± 0.24	0.63 ± 0.71	1.59 ± 0.63	1.19 ± 0.67	2.09 ± 0.81
K <sub>2</sub> O	N.D.	N.D.	0.21 ± 0.04	0.21 ± 0.09	N.D.	N.D.	N.D.	N.D.	0.18 ± 0.05	0.18 ± 0.04
CaO	0.55 ± 0.34	0.47 ± 0.24	1.21 ± 0.34	0.59 ± 0.24	1.17 ± 0.33	0.78 ± 0.25	1.82 ± 1.05	1.71 ± 0.63	2.27 ± 0.86	1.75 ± 0.29
FeO	<D.L.	<D.L.	0.83 ± 0.12	0.48 ± 0.19	0.78 ± 0.20	0.49 ± 0.05	0.69 ± 0.19	0.62 ± 0.20	0.35 ± 0.22	0.29 ± 0.10
PbO	0.35 ± 0.28	0.82 ± 0.38	6.98 ± 4.38	8.86 ± 6.12	9.21 ± 4.84	13.17 ± 0.12	12.59 ± 4.41	11.33 ± 2.43	14.85 ± 3.44	17.06 ± 3.82
UO <sub>2</sub>	1.53 ± 2.47	0.22 ± 0.12	70.17 ± 5.12	53.49 ± 5.78	70.16 ± 4.94	60.09 ± 3.93	67.88 ± 4.66	57.42 ± 3.19	64.19 ± 3.51	55.68 ± 4.06
MgO	N.D.	N.D.	<D.L.	<D.L.	N.D.	N.D.	N.D.	N.D.	<D.L.	<D.L.
TiO <sub>2</sub>	<D.L.	<D.L.	<D.L.	0.41 ± 1.07	0.33 ± 0.33	0.13 ± 0.15	0.25 ± 0.39	1.75 ± 1.50	0.17 ± 0.25	0.25 ± 0.29
ThO <sub>2</sub>	1.36 ± 0.90	4.99 ± 2.66	5.88 ± 1.72	6.05 ± 1.97	5.14 ± 1.90	5.68 ± 3.45	5.34 ± 1.93	5.35 ± 1.16	6.54 ± 1.93	5.26 ± 1.63
MnO	<D.L.	<D.L.	1.33 ± 0.23	<D.L.	1.49 ± 0.41	1.02 ± 0.08	0.76 ± 0.37	0.56 ± 0.23	0.62 ± 0.19	0.48 ± 0.18
Y <sub>2</sub> O <sub>3</sub>	0.28 ± 0.54	1.30 ± 0.55	3.55 ± 1.12	2.01 ± 0.53	1.99 ± 0.75	1.84 ± 0.62	2.32 ± 1.11	2.63 ± 0.95	2.58 ± 1.09	2.89 ± 0.70
P <sub>2</sub> O <sub>5</sub>	28.18 ± 1.35	28.09 ± 1.10	<D.L.	<D.L.	<D.L.	<D.L.	<D.L.	0.32 ± 0.28	<D.L.	<D.L.
La <sub>2</sub> O <sub>3</sub>	20.69 ± 2.52	16.43 ± 1.91	<D.L.	0.20 ± 0.06	<D.L.	0.27 ± 0.14	<D.L.	<D.L.	<D.L.	0.25 ± 0.11
Ce <sub>2</sub> O <sub>3</sub>	31.54 ± 2.64	29.97 ± 2.20	<D.L.	0.98 ± 0.25	0.30 ± 0.25	0.32 ± 0.10	<D.L.	0.61 ± 0.33	<D.L.	0.65 ± 0.36
Pr <sub>2</sub> O <sub>3</sub>	2.05 ± 0.35	2.43 ± 0.15	N.D.	N.D.	N.D.	N.D.	N.D.	N.D.	N.D.	N.D.
Nd <sub>2</sub> O <sub>3</sub>	6.95 ± 1.62	8.60 ± 0.76	<D.L.	0.63 ± 0.21	<D.L.	<D.L.	<D.L.	<D.L.	<D.L.	<D.L.
SmO	0.87 ± 0.16	1.55 ± 0.38	N.D.	N.D.	N.D.	N.D.	N.D.	N.D.	N.D.	N.D.
Gd <sub>2</sub> O <sub>3</sub>	<D.L.	0.83 ± 0.31	N.D.	N.D.	<D.L.	<D.L.	<D.L.	<D.L.	N.D.	N.D.
Dy <sub>2</sub> O <sub>3</sub>	N.D.	N.D.	<D.L.	<D.L.	<D.L.	<D.L.	<D.L.	<D.L.	<D.L.	<D.L.
Yb <sub>2</sub> O <sub>3</sub>	N.D.	N.D.	N.D.	N.D.	<D.L.	<D.L.	<D.L.	<D.L.	<D.L.	<D.L.
Nb <sub>2</sub> O <sub>3</sub>	N.D.	N.D.	N.D.	N.D.	0.26 ± 0.23	<D.L.	0.22 ± 0.31	1.66 ± 0.97	N.D.	N.D.
Ta <sub>2</sub> O <sub>5</sub>	N.D.	N.D.	<D.L.	<D.L.	<D.L.	<D.L.	<D.L.	<D.L.	<D.L.	<D.L.
F	N.D.	N.D.	N.D.	N.D.	<D.L.	<D.L.	0.27 ± 0.19	0.18 ± 0.15	N.D.	N.D.
Total	96.12 ± 1.18	96.80 ± 0.72	94.71 ± 1.85	89.99 ± 3.34	96.22 ± 1.41	97.15 ± 0.88	95.33 ± 1.83	91.42 ± 1.29	94.17 ± 2.44	91.42 ± 1.29

**Notes:** All average values are reported in weight percent ± the standard deviation from EMPA (electron microprobe CAMECA SX100); Abbreviations: EMPA = number of EMPA measurements; <D.L. = beyond Detection Limit (Al=0.05wt%, Si=0.06wt%, S=0.10wt%, K=0.10wt%, Ca=0.12wt%, Fe=0.20wt%, Pb=0.31wt%, U=0.09wt%, Mg=0.04wt%, Ti=0.05wt%, Th=0.11wt%, Mn=0.20wt%, Y=0.12wt%, P=0.06wt%, La=0.07wt%, Ce=0.29wt%, Pr=0.14wt%, Nd=0.62wt%, Sm=0.15wt%, Gd=0.66wt%, Dy=0.70wt%, Yb=0.43wt%, Nb=0.13wt%, Ta=0.26wt%, F=0.12wt%); N.D. = Not Determined.

**Table 3.1.7.** Representative average composition of secondary U-bearing minerals from the Upper Dominion Reef analysed by electron microprobe.

Paragenesis	Secondary (hydrothermal remobilization)										
Mineral	Pitchblende	Coffinite				U-Ti phases			U-Th phases		
Form	Around detrital grains or along fractures	Around detrital uraninite grains				Around detrital grains or in "ghost" minerals			Patchy in "ghost" minerals		
Sample	DO6920	AO3883	AO5268	DO6920	AO5686	AO3883	AO5268	DO8628	AO3883	DO6920	AO5686
Bore hole	DRT039	DRT058	DRT079	DRT039	DRT070	DRT058	DRT079	DRT034	DRT058	DRT039	DRT070
Depth	337.5 m	182.5 m	328 m	337.5 m	608.25 m	182.5 m	328 m	342 m	182.5 m	337.5 m	608.25 m
EMPA	4	10	2	3	37	13	2	4	9	8	4
Al <sub>2</sub> O <sub>3</sub>	0.49 ± 0.52	2.15 ± 0.57	2.55 ± 0.31	0.36 ± 0.11	1.75 ± 0.55	1.51 ± 0.38	1.57 ± 1.12	0.97 ± 0.84	1.56 ± 0.21	0.16 ± 0.03	1.08 ± 0.22
SiO <sub>2</sub>	1.80 ± 0.87	18.93 ± 3.77	22.87 ± 3.01	13.49 ± 0.54	20.56 ± 4.26	10.44 ± 2.56	6.86 ± 1.40	10.26 ± 1.98	19.79 ± 1.52	10.31 ± 0.77	20.45 ± 1.80
SO <sub>2</sub>	<D.L.	1.64 ± 0.99	0.75 ± 0.48	0.79 ± 0.38	1.84 ± 0.97	1.16 ± 1.52	0.79 ± 0.29	1.83 ± 1.28	2.17 ± 1.17	1.82 ± 1.85	2.77 ± 1.48
K <sub>2</sub> O	N.D.	0.15 ± 0.09	N.D.	N.D.	0.18 ± 0.07	0.13 ± 0.04	N.D.	N.D.	<D.L.	N.D.	<D.L.
CaO	2.01 ± 0.41	0.75 ± 0.24	<D.L.	0.52 ± 0.06	1.20 ± 0.17	0.94 ± 0.27	0.24 ± 0.08	0.60 ± 0.22	0.29 ± 0.08	1.10 ± 0.20	2.51 ± 0.25
FeO	0.79 ± 0.18	<D.L.	<D.L.	0.25 ± 0.22	<D.L.	1.65 ± 0.29	2.17 ± 1.04	1.64 ± 1.28	<D.L.	1.17 ± 2.06	<D.L.
PbO	1.46 ± 0.57	10.19 ± 7.07	4.50 ± 2.44	1.75 ± 0.35	9.75 ± 4.00	5.54 ± 6.58	3.81 ± 0.67	15.03 ± 4.63	10.38 ± 6.04	4.39 ± 3.02	10.93 ± 4.16
UO <sub>2</sub>	81.79 ± 1.62	32.27 ± 7.06	39.95 ± 6.23	48.56 ± 1.21	39.15 ± 8.51	23.99 ± 5.48	21.88 ± 0.82	20.93 ± 2.75	12.49 ± 2.85	27.53 ± 7.78	5.41 ± 0.92
MgO	N.D.	0.08 ± 0.04	N.D.	N.D.	<D.L.	<D.L.	N.D.	N.D.	<D.L.	N.D.	<D.L.
TiO <sub>2</sub>	<D.L.	1.32 ± 1.60	0.28 ± 0.17	<D.L.	0.52 ± 1.49	29.29 ± 5.07	33.32 ± 3.73	10.16 ± 4.84	<D.L.	0.26 ± 0.49	<D.L.
ThO <sub>2</sub>	<D.L.	13.98 ± 6.28	9.50 ± 4.58	7.38 ± 1.17	6.98 ± 4.48	3.58 ± 2.23	1.98 ± 0.48	7.32 ± 1.86	40.65 ± 2.93	21.03 ± 12.40	47.31 ± 3.31
MnO	0.33 ± 0.11	<D.L.	<D.L.	<D.L.	<D.L.	<D.L.	0.47 ± 0.10	<D.L.	<D.L.	<D.L.	<D.L.
Y <sub>2</sub> O <sub>3</sub>	0.45 ± 0.13	6.52 ± 2.59	4.73 ± 0.27	8.65 ± 0.19	4.28 ± 0.91	2.18 ± 1.35	4.14 ± 0.25	8.25 ± 6.04	3.56 ± 0.78	9.15 ± 2.38	2.08 ± 0.21
P <sub>2</sub> O <sub>5</sub>	<D.L.	0.70 ± 0.26	0.17 ± 0.04	4.71 ± 0.18	0.31 ± 0.33	0.15 ± 1.44	<D.L.	3.63 ± 2.08	0.81 ± 0.13	7.51 ± 1.79	1.06 ± 0.07
La <sub>2</sub> O <sub>3</sub>	0.27 ± 0.05	0.09 ± 0.05	0.35 ± 0.13	<D.L.	1.07 ± 0.38	0.66 ± 0.26	0.76 ± 0.16	<D.L.	0.35 ± 0.12	<D.L.	0.25 ± 0.08
Ce <sub>2</sub> O <sub>3</sub>	1.55 ± 0.41	0.35 ± 0.23	1.63 ± 0.20	0.34 ± 0.11	2.60 ± 0.91	2.69 ± 0.56	3.69 ± 0.20	0.35 ± 0.14	0.55 ± 0.28	0.56 ± 0.13	0.39 ± 0.17
Pr <sub>2</sub> O <sub>3</sub>	N.D.	N.D.	N.D.	N.D.	N.D.	N.D.	N.D.	N.D.	N.D.	N.D.	N.D.
Nd <sub>2</sub> O <sub>3</sub>	0.94 ± 0.12	<D.L.	1.06 ± 0.54	0.76 ± 0.51	1.30 ± 0.36	1.18 ± 0.48	2.39 ± 0.10	<D.L.	<D.L.	1.03 ± 0.39	<D.L.
SmO	N.D.	N.D.	N.D.	N.D.	N.D.	N.D.	N.D.	N.D.	N.D.	N.D.	N.D.
Gd <sub>2</sub> O <sub>3</sub>	<D.L.	N.D.	<D.L.	1.52 ± 0.28	N.D.	N.D.	1.28 ± 0.14	1.05 ± 0.63	N.D.	1.61 ± 0.29	N.D.
Dy <sub>2</sub> O <sub>3</sub>	<D.L.	<D.L.	<D.L.	1.29 ± 0.18	<D.L.	<D.L.	<D.L.	1.16 ± 0.74	<D.L.	1.37 ± 0.38	<D.L.
Yb <sub>2</sub> O <sub>3</sub>	<D.L.	N.D.	<D.L.	0.78 ± 0.07	N.D.	N.D.	<D.L.	0.66 ± 0.45	N.D.	0.63 ± 0.21	N.D.
Nb <sub>2</sub> O <sub>3</sub>	<D.L.	N.D.	0.31 ± 0.15	<D.L.	N.D.	N.D.	3.43 ± 0.53	5.38 ± 1.79	N.D.	<D.L.	N.D.
Ta <sub>2</sub> O <sub>5</sub>	<D.L.	0.31 ± 0.28	<D.L.	<D.L.	<D.L.	1.91 ± 1.29	0.81 ± 0.04	1.30 ± 1.35	<D.L.	<D.L.	<D.L.
F	<D.L.	N.D.	<D.L.	0.72 ± 0.06	N.D.	N.D.	<D.L.	<D.L.	N.D.	1.02 ± 0.20	N.D.
Total	92.99 ± 0.98	90.93 ± 2.31	90.63 ± 0.54	92.08 ± 0.36	92.62 ± 2.45	87.70 ± 3.79	90.90 ± 0.59	91.28 ± 2.51	93.93 ± 3.08	90.92 ± 3.88	95.61 ± 0.68

**Notes:** All average values are reported in weight percent ± the standard deviation from EMPA (electron microprobe CAMECA SX100); Abbreviations: EMPA = number of EMPA measurements; <D.L. = beyond Detection Limit (Al=0.05wt%. Si=0.06wt%. S=0.10wt%. K=0.10wt%. Ca=0.12wt%. Fe=0.20wt%. Pb=0.31wt%. U=0.09wt%. Mg=0.04wt%. Ti=0.05wt%. Th=0.11wt%. Mn=0.20wt%. Y=0.12wt%. P=0.06wt%. La=0.07wt%. Ce=0.29wt%. Pr=0.14wt%. Nd=0.62wt%. Sm=0.15wt%. Gd=0.66wt%. Dy=0.70wt%. Yb=0.43wt%. Nb=0.13wt%. Ta=0.26wt%. F=0.12wt%); N.D. = Not Determined.

Uranium mineralization occurs mostly in primary uraninite grains with sub-euhedral to well-rounded shapes, ranging between 50 and 300  $\mu\text{m}$  in width and averaging around 100  $\mu\text{m}$ . In reflected light (Fig. 3.1.19), grains display zones of variable reflectance, the darker domains correspond to more altered areas which follow the intense microfracturation. The same pattern is observed in BSE-SEM imaging (Fig. 3.1.20) showing relatively lower brightness enriched in lighter elements along the fractures associated to alteration into (U,Th)-silicates. Pristine uraninite (bright areas) and altered domains (dark grey) have been distinguished for determination of chemical compositions (Table 3.1.6). Plots in binary diagrams follow the chemical evolution between major elements and the U content (Fig. 3.1.21). Altered uraninite domains result from a transformation into coffinite with increasing Si content and leaching of Pb and U by chemical interaction with silica-bearing fluids that circulated after sedimentation and burial during diagenesis, metamorphism and/or hydrothermal alteration. Where ilmenite grains are closely associated with primary uraninite (as in Fig. 3.1.16), U leached from uranium oxides combines with Ti to form secondary U-Ti phases that coat the primary grains resulting in a leucoxene/brannerite admixture (Table 3.1.7). This reaction has also been observed in the Pongola Basin close to the Witwatersrand and in the Elliot Lake quartz pebble conglomerates from the Pronto mine in Ontario (Saager and Stupp, 1983).

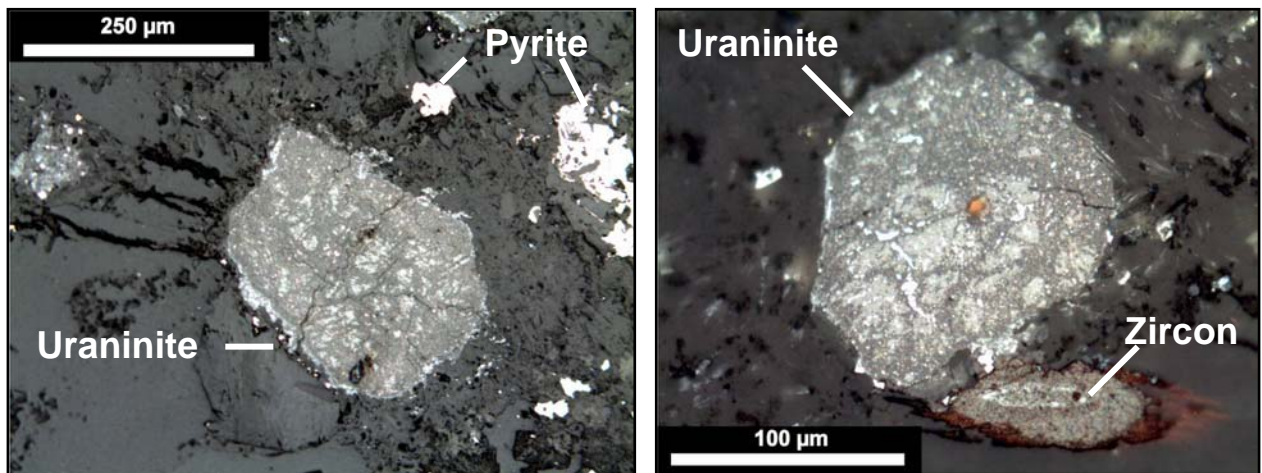


**Figure 3.1.19.** Photomicrographs in reflected light showing primary uraninite grains with xenomorphic grains of pyrite and zircon surrounded by red internal reflection material that corresponds to hematite (lower DG reef: DRT179-FO948).

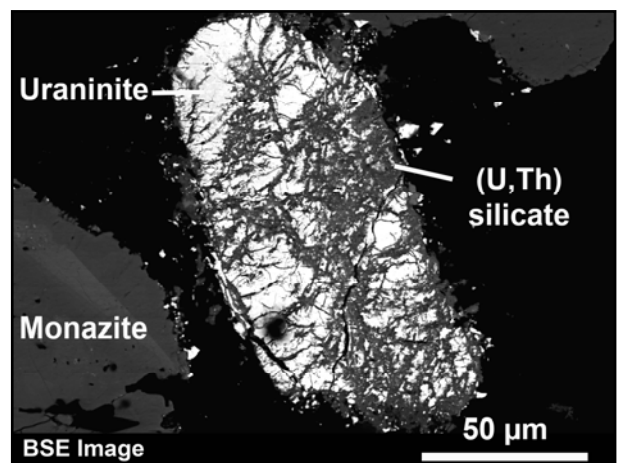


**Figure 3.1.20.** SEM-BSE image showing primary uraninite rounded grain with monazite (upper DG reef: DRT034-DO8628-342m depth).

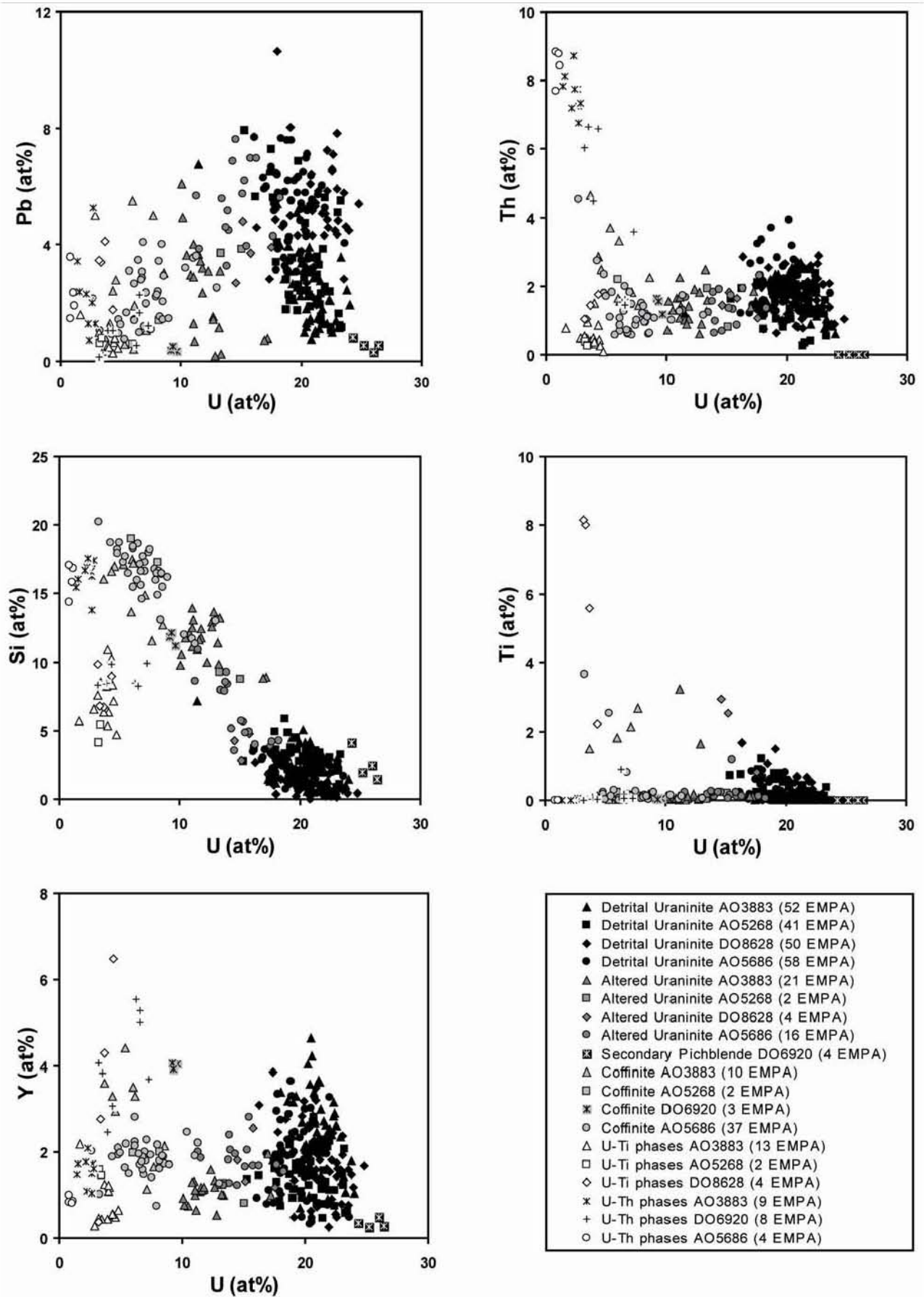


**Figure 3.1.21.** U versus Pb, Th, Si, Ti and Y contents (in atomic percent) of different U-bearing minerals from the Dominion Reefs. The name of mineral species, sample reference and number of EMPA measurements are respectively quoted in the legend.

Primary uraninite grains are characterized by highly variable U, Th and Pb contents: 49.99-80.53 wt%  $\text{UO}_2$ , 2.20-28.89 wt%  $\text{PbO}$  and 0.95-12.21wt%  $\text{ThO}_2$ . The chemical ages of these uraninite yield wide variations from 73 to 2620 Ma with a major peak of the probability curve at 1300 Ma (Fig. 3.1.22). Most of ages are below 1600 Ma suggesting that uraninite has lost radiogenic lead. Beside these alteration effects, pristine uraninite areas are characterized by high Th contents that are characteristic of uraninite that formed at high temperature in a granitic magma. Based on their Th concentrations (Fig. 3.1.23), at least two families of grains can be distinguished. The low Th contents are typical for highly fractionated leucogranites (e.g. the peraluminous Tanco pegmatite; this work chapter 2, part 2.3) whereas high Th contents are normally related to partial melting of metasediments at higher temperatures (e.g. uraninite formed in S-type granites as in the Mustalampi pegmatites in Karelia or the Kola Peninsula Archean pegmatites; part 2.4). This is also consistent with their high yttrium and manganese contents ranging between 0.31 and 6.42wt%  $\text{Y}_2\text{O}_3$  and between 0.8 and 2.19 wt%  $\text{MnO}$ , respectively. In comparison, secondary pitchblende that formed by hydrothermal fluid circulation and precipitated within pebble fractures has no Th (always below detection limit:  $\text{Th} < 0.11$  wt%) and very low contents of  $\text{Y}_2\text{O}_3$  ( $m = 0.45 \pm 0.13$  wt%) and  $\text{MnO}_2$  ( $m = 0.33 \pm 0.11$  wt%).

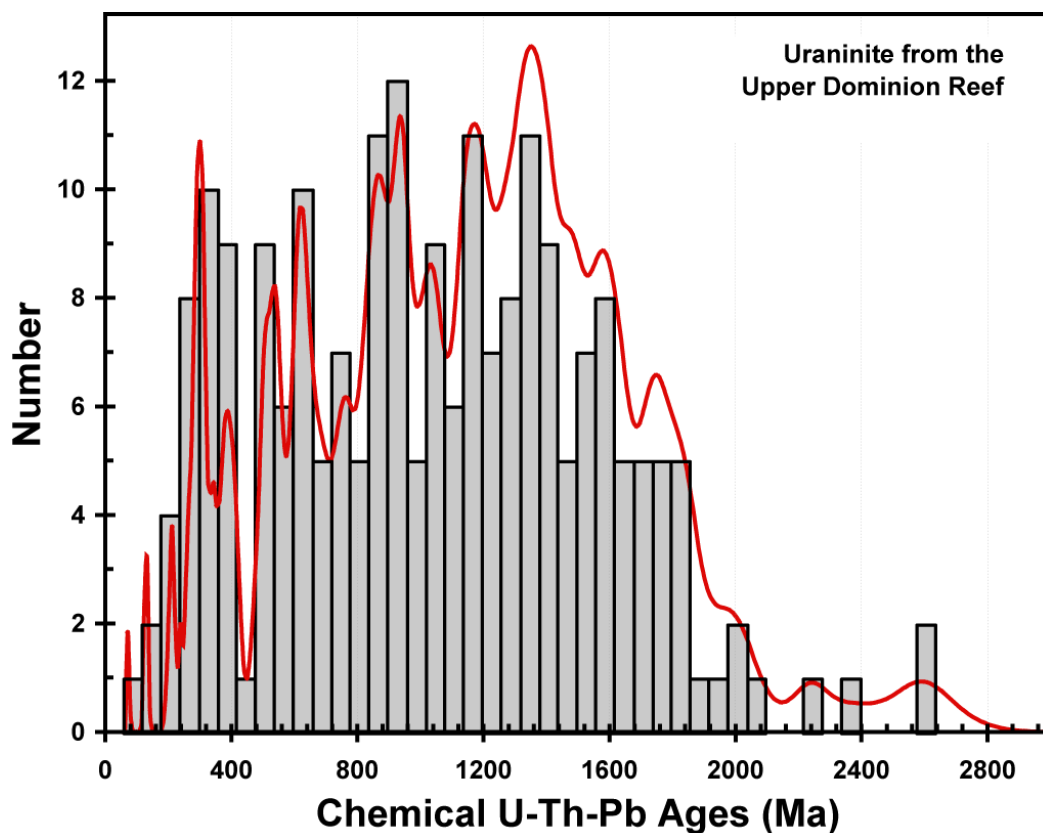


**Figure 3.1.22.** Histogram and relative probability curve representing the distribution of U-Th-Pb chemical ages calculated in uraninite grains from the upper Dominion reef (both pristine areas and coffinitized:  $N = 243$ ).

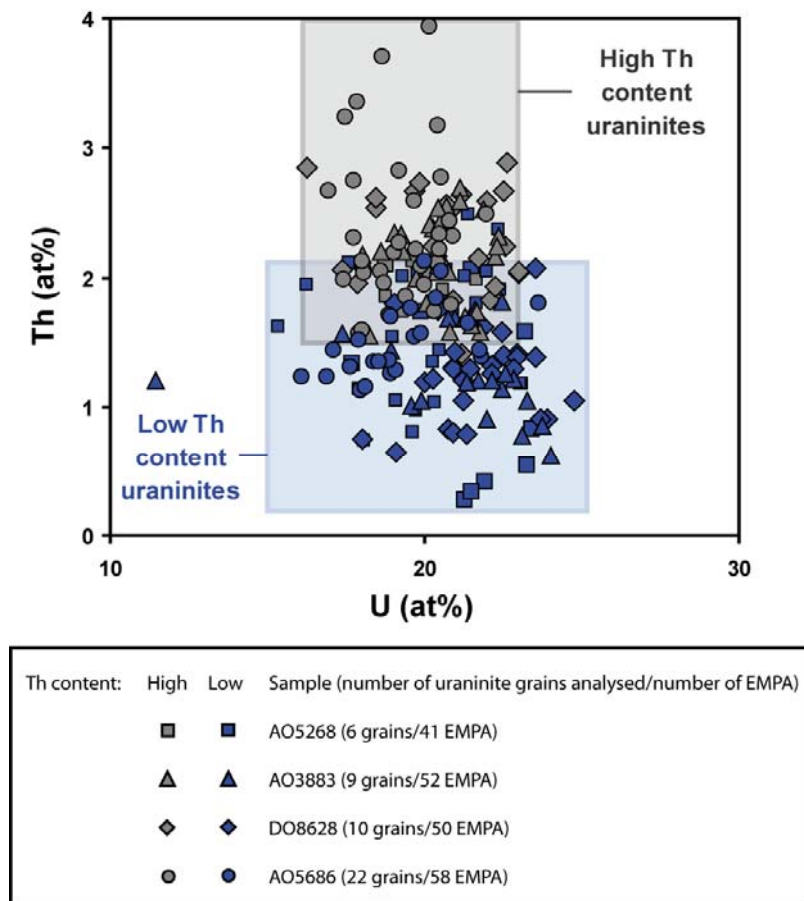


**Figure 3.1.23.** Binary diagram showing Th vs. U contents (in atomic percent) in pristine primary uraninite showing two distinct family of grains with low Th contents below 2 at% and an second group with high Th contents up to 4 at%.

REE concentrations of La, Ce and Nd are sometimes detected by EMPA in primary uraninite grains (Table 3.1.6). In situ REE isotope analyses were performed by SIMS on nine distinct uraninite grains from two samples of the upper Dominion reef (Table 3.1.8). REE concentrations are very high reaching a maximum for cerium (0.27-1.39 wt% Ce) and a  $\Sigma$ REE content ranging between 1.3 wt% and 5.22 wt% ( $m = 2.88$  wt%). The chondrite-normalized REE patterns (Fig. 3.1.24) show consistent weakly fractionated shapes ( $0.30 < [\text{La}/\text{Sm}]_N < 1.25$  and  $0.60 < [\text{Gd}/\text{Yb}]_N < 1.74$ ) centred on a strong negative europium anomaly with  $[\text{Eu}/\text{Eu}^*]_N$  ranging from 0.13 to 0.34. Most REE abundances are higher than  $10^4$  times compared with the chondrites.

**Table 3.1.8.** SIMS determinations of REE contents (ppm) in the primary uraninite grains from the Dominion Group quartz pebble conglomerates compared to the composition of other uranium oxides formed during magmatic process in S-type Rössing pegmatite from Namibia and hydrothermal uraninite (pitchblende) from the Cigar Lake unconformity-type deposit of the Athabasca Basin in Canada (data from Bonhoure, 2007)

Sample	N°	La	Ce	Pr	Nd	Sm	Eu	Gd*	Tb	Dy	Ho	Er	Tm	Yb*	Lu	Σ REE	[La/Sm] <sub>N</sub>	[Gd/Yb] <sub>N</sub>	[Eu/Eu*] <sub>N</sub>
<i>Primary uraninites from the upper Dominion Group reef (Witwatersrand Basin, South Africa) – this study</i>																			
AO3883	1	447	2 689	411	1 724	859	126	1 250	240	1 896	343	1 181	314	1 405	105	12 991	0.33	0.74	0.37
m depth	2	639	3 664	544	2 069	1 328	112	2 578	550	3 914	593	2 250	671	2 814	168	21 893	0.30	0.76	0.18
	3	2 307	9 442	1 146	3 869	1 713	124	2 817	569	3 810	593	2 310	579	2 539	178	31 996	0.84	0.92	0.17
	4	3 697	7 548	920	4 230	2 446	339	3 742	735	5 574	952	3 644	780	3 258	191	38 055	0.95	0.95	0.34
	5	630	3 843	584	2 338	1 287	91	2 067	414	3 931	635	2 494	684	2 851	166	22 016	0.31	0.60	0.17
<b>Average</b>		<b>1 544</b>	<b>5 437</b>	<b>721</b>	<b>2 846</b>	<b>1 527</b>	<b>158</b>	<b>2 491</b>	<b>501</b>	<b>3 825</b>	<b>623</b>	<b>2 376</b>	<b>606</b>	<b>2 574</b>	<b>161</b>	<b>25 390</b>	<b>0.55</b>	<b>0.79</b>	<b>0.25</b>
AO5686	1	4 193	13 902	1 816	7 412	3 049	147	4 876	974	6 288	974	3 894	840	3 563	222	52 150	0.86	1.13	0.12
	2	2 285	5 798	688	2 998	1 445	196	2 863	614	3 922	697	2 632	661	2 792	171	27 762	0.99	0.85	0.29
	3	2 872	8 015	926	3 842	1 444	116	2 373	479	3 191	484	1 656	394	1 725	120	27 637	1.25	1.14	0.19
	4	1 982	6 208	781	3 259	1 547	113	2 673	550	3 525	502	1 652	250	1 268	128	24 440	0.80	1.74	0.17
<b>Average</b>		<b>2 833</b>	<b>8 481</b>	<b>1 053</b>	<b>4 378</b>	<b>1 871</b>	<b>143</b>	<b>3 196</b>	<b>654</b>	<b>4 232</b>	<b>664</b>	<b>2 459</b>	<b>536</b>	<b>2 337</b>	<b>160</b>	<b>32 997</b>	<b>0.98</b>	<b>1.21</b>	<b>0.19</b>
<i>Magmatic uraninites from the Rössing Alaskite (Namibia) – data from Bonhoure (2007)</i>																			
<b>Rössing</b>	1	320	4 301	518	2 718	1 505	94	2 440	490	3 796	769	2 401	398	1 582	73	21 404	0.13	1.27	0.15
	2	268	3 909	494	2 643	1 541	88	2 670	549	4 259	889	2 852	446	1 770	81	22 460	0.11	1.25	0.13
	3	802	9 506	430	1 444	1 885	86	4 057	891	7 652	155	5 606	026	4 257	243	39 039	0.27	0.79	0.09
	4	270	3 581	429	2 659	1 386	75	1 987	379	3 144	694	1 903	318	1 254	56	18 135	0.12	1.31	0.14
<b>Average</b>		<b>415</b>	<b>5 324</b>	<b>468</b>	<b>2 366</b>	<b>1 579</b>	<b>86</b>	<b>2 788</b>	<b>577</b>	<b>4 712</b>	<b>877</b>	<b>3 190</b>	<b>547</b>	<b>2 215</b>	<b>114</b>	<b>25 259</b>	<b>0.16</b>	<b>1.15</b>	<b>0.13</b>
<i>Hydrothermal uraninite (pitchblende) from the Cigar Lake unconformity-type deposit (Athabasca Basin, Saskatchewan, Canada) – data from Bonhoure (2007)</i>																			
	1	11	116	25	134	91	25	283	67	450	62	136	15	87	11	1 512	0.08	2.68	0.48
	2	7	89	21	125	80	26	275	66	480	72	146	16	97	13	1 513	0.05	2.35	0.53
	3	8	104	25	146	91	32	365	90	609	82	184	22	122	14	1 893	0.06	2.47	0.53
	4	9	106	25	146	89	27	352	86	590	79	175	21	118	14	1 839	0.06	2.45	0.47
	5	13	140	32	186	99	31	380	93	637	86	191	23	129	15	2 055	0.08	2.45	0.49
	6	16	139	31	168	82	29	299	73	477	69	153	18	87	8	1 649	0.13	2.83	0.56
	7	11	141	34	201	114	39	424	103	705	96	214	26	144	17	2 270	0.06	2.43	0.54
	8	16	113	23	119	64	22	248	61	424	58	131	16	89	10	1 394	0.16	2.30	0.53
<b>Average</b>		<b>11</b>	<b>119</b>	<b>27</b>	<b>153</b>	<b>89</b>	<b>29</b>	<b>328</b>	<b>80</b>	<b>546</b>	<b>76</b>	<b>166</b>	<b>20</b>	<b>109</b>	<b>13</b>	<b>1 766</b>	<b>0.08</b>	<b>2.49</b>	<b>0.52</b>

\* Gd and Yb are calculated from Sm-Tb and Tm-Lu concentrations respectively because of analytical interferences forbidding their accurate measurements:  $Gd^* = Sm + 2/3Tb$  and  $Yb^* = (Tm + Lu)/2$   
[X]<sub>N</sub> = normalized to chondrite values;  $[Eu/Eu^*]_N = Eu_N / \sqrt{[Sm.Gd]_N}$

The high REE abundances in the Dominion uraninite grains and the flat patterns with strong negative Eu anomalies are typical of uranium oxides that formed at high temperatures in a granitic magma originating from partial melting of sediments. Uraninites from the Rössing alaskite in Namibia display exactly the same patterns (Fig. 3.1.24) and have an equivalent composition with a high thorium content ranging 3.3-8.0 wt% ThO<sub>2</sub>, elevated Y and REE contents with 1.6-7.14 wt% Y<sub>2</sub>O<sub>3</sub> and 2.3 wt%  $\Sigma$ REE (Cuney and Kyser, 2008). Some of the Dominion uraninites are even more enriched in Th, Y and REE. In comparison, hydrothermal uraninite (pitchblende) hosts much lower REE abundances than magmatic uraninites ( $m = 1.77$  wt%  $\Sigma$ REE) and its chondrite-normalized REE distribution is characterized by a bell-shape pattern centered on medium REE (maximum for Tb and Dy), and are strongly depleted in LREE with no evident Eu anomaly. This confirms the detrital origin of primary uraninites from the upper Dominion reef and their derivation from fractionated granitic rocks with the typical REE signature of S-type granites.

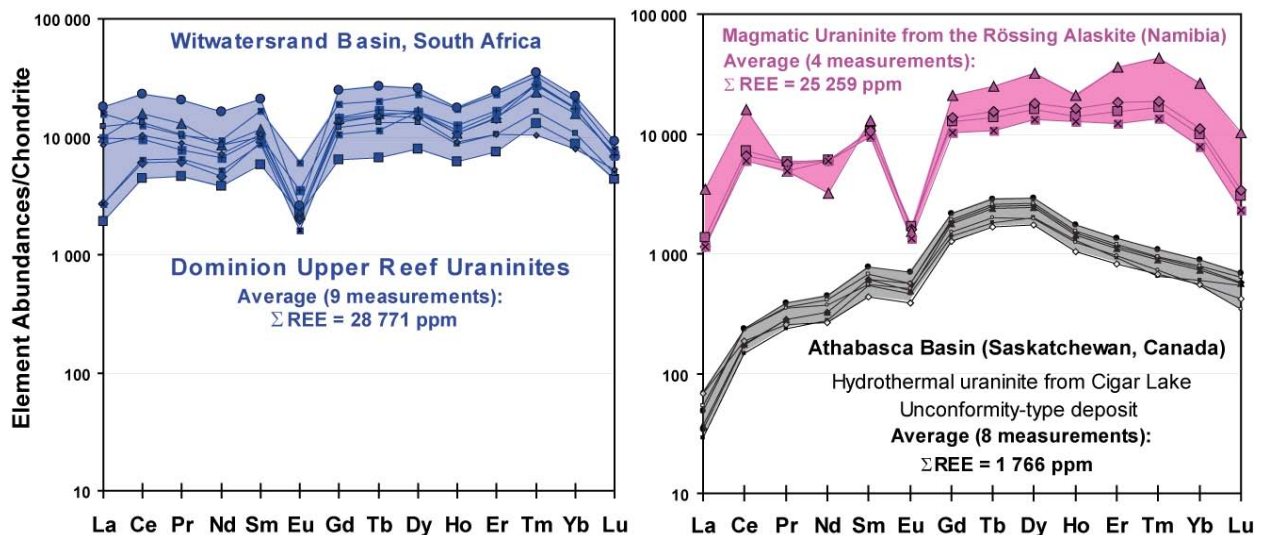


**Figure 3.1.24.** Chondrite-normalized REE patterns of primary uraninite grains from the Dominion quartz pebble conglomerates compared to magmatic uraninites from the Rössing deposit in Namibia and hydrothermal pitchblende from the Athabasca Basin in Canada (data in Table 3.1.8).

Chemical analyses of detrital heavy minerals accompanying the primary uranium ore are also used to constrain the provenance of the sediments and nature of the source rock(s). As uraninite usually formed in granitic-pegmatitic rocks and that the mafic to ultramafic rocks are depleted in U, studies have focussed also on two other minerals: garnets, which originate from granites or metamorphic rocks, and columbite-tantalite that formed in differentiated granites/pegmatites.

The upper DG reef is very rich in detrital garnets, which are highly fractured but generally not altered (Fig. 3.1.25). They are always well rounded and reach up to 5 mm in

diameter. Chemical compositions of 5 grains from two samples (DRT024-DO1823 at 206.7 metres depth and DRT70-AO5686 at 608.2 metres depth) have been obtained from 48 EMPA (Table 3.1.9). Garnets are mainly composed of aluminium (20.88-22.26 wt%  $\text{Al}_2\text{O}_3$  representing  $\sim 2$  apfu  $\text{Al}^{\text{vi}}$ ), silicium (36.26-37.65 wt%  $\text{SiO}_2$  equivalent to  $\sim 3$  apfu Si) and iron (28.87-33.62 wt% FeO corresponding to 1.96-2.27 apfu  $\text{Fe}^{2+}$ ) with relatively high contents of manganese (0.75-6.12 wt% MnO), and lower contents of magnesium (0.88-3.97 wt% MgO) and calcium (1.33-5.39 wt% CaO) totalling less than 1 apfu (Mn+Mg+Ca). Chemical variations are represented by ternary diagrams in Figure 3.1.26. The Dominion garnets have compositions close to the almandine end-member (66.3-77.5 mol% Alm) with variable pyrope (3.6-16.3 mol% Py), spessartite (1.8-14.2 mol% Sps) and grossular (3.0-15.8 mol% Grs) components. Almandine garnets are typically found in granites/pegmatites or low grade to amphibolite facies metamorphic rocks (Okuzawa and Hisada, 2008) but those with high Mn and Fe contents are generally typical of fractionated leucogranites.

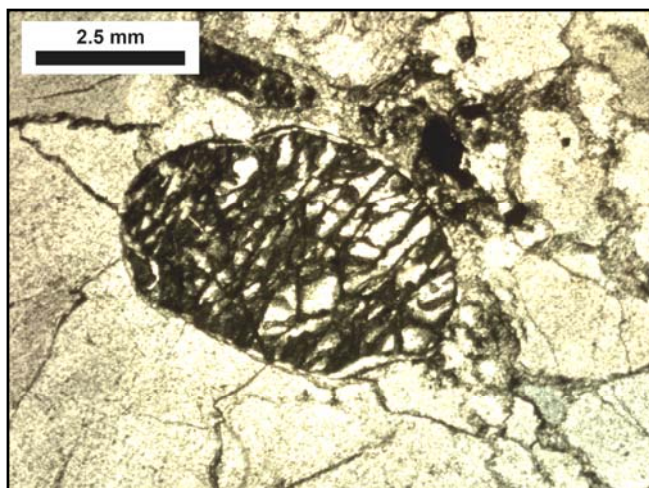


**Figure 3.1.25.** Detrital garnet showing high fracturation and relief within quartz in natural transmitted light (DRT024-DO1823 at 206.7m depth).

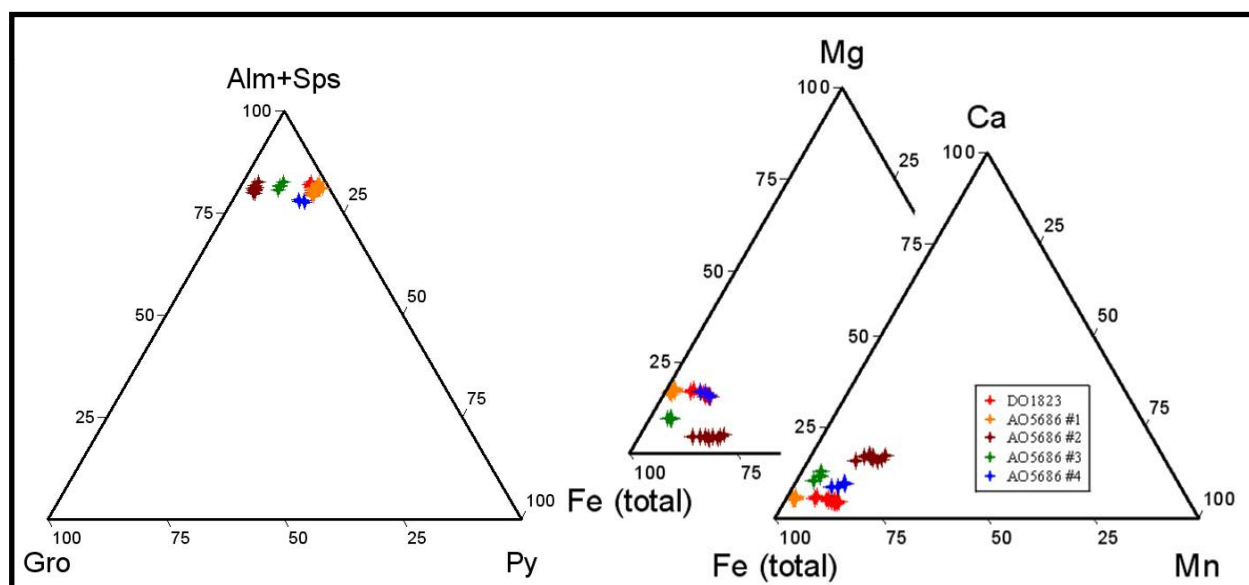


**Figure 3.1.26.** Ternary diagrams showing the compositions of detrital garnets from the upper Dominion reef. The garnet end members mostly represented by the EMP chemical compositions (Table 3.1.9) are: Alm = almandine, Sps = spessartite, Gro = grossular and Py = pyrope.

**Table 3.1.9.** Representative average composition of detrital garnets from the Dominion Group reefs.

Location Rock type Sample	Upper Dominion Reef, Witwatersrand Basin, South Africa Conglomerate				
	DO1823	AO5686			
EMPA measurements	15	#1 15	#2 10	#3 4	#4 4
SiO <sub>2</sub>	37.60	36.26	37.06	37.27	37.65
TiO <sub>2</sub>	0.02	0.02	0.09	0.05	0.02
Al <sub>2</sub> O <sub>3</sub>	21.34	22.26	20.88	20.92	21.52
Cr <sub>2</sub> O <sub>3</sub>	0.08	0.03	0.03	0.12	0.05
Y <sub>2</sub> O <sub>3</sub>	0.00	0.00	0.00	0.00	0.00
Fe <sub>2</sub> O <sub>3</sub> *	0.00	0.44	0.00	0.00	0.00
FeO	31.53	33.62	28.87	33.43	30.18
MnO	4.04	0.75	6.12	1.86	4.06
MgO	3.80	3.97	0.88	2.08	3.70
CaO	1.33	1.49	5.39	3.54	2.60
Σ oxides (wt%)	99.75	98.84	99.31	99.27	99.78
Atomic contents normalized to 12 oxygen atoms and 8 cations per formula unit					
Si	3.009	2.926	3.013	3.018	3.004
Al iv	0.000	0.074	0.000	0.000	0.000
Al vi	2.013	2.043	2.000	1.996	2.023
Ti	0.001	0.001	0.005	0.003	0.001
Cr	0.005	0.002	0.002	0.008	0.003
Y	0.000	0.000	0.000	0.000	0.000
Fe <sup>3+</sup>	0.000	0.027	0.000	0.000	0.000
Fe <sup>2+</sup>	2.111	2.269	1.963	2.265	2.013
Mn	0.274	0.051	0.421	0.128	0.275
Mg	0.454	0.478	0.106	0.251	0.440
Ca	0.114	0.129	0.469	0.307	0.223
Σ cations	7.981	8.000	7.981	7.976	7.982
End member molecules					
Pyrope	15.4	16.3	3.6	8.5	14.9
Almandine	71.5	77.5	66.3	76.8	68.2
Spessartite	9.3	1.8	14.2	4.3	9.3
Andradite	0.0	1.3	0.0	0.0	0.0
Uvarovite	0.2	0.1	0.1	0.4	0.2
Grossular	3.6	3.0	15.8	10.0	7.4
Σ	100.0	100.0	100.0	100.0	100.0

\* Fe<sub>2</sub>O<sub>3</sub> calculated to eliminate excess cations over 8.

Detrital columbite-tantalite grains are rare in the Dominion reefs. One grain has been analysed from the upper Dominion reef (DRT70-AO5686 at 608.2 metres depth). It has an elongated form, 150 µm long and 30-50 µm wide, and displays a zoning in BSE mode (Fig. 3.1.27). The internal core of the grain has an homogeneous composition (Table 3.1.10) dominated by tantalum (53.42-57.46 wt% Ta<sub>2</sub>O<sub>5</sub>), niobium (25.20-29.06 wt% Nb<sub>2</sub>O<sub>5</sub>) and iron (total as Fe<sup>2+</sup> averaging 10.11-11.24 wt% FeO) with some minor amounts of manganese (3.03-4.04 wt% MnO), magnesium (1.22-1.60 wt% MgO) and titan (0.59-1.12 wt% TiO<sub>2</sub>). The chemical profile carried out by electron microprobe through the grain (Fig. 3.1.27) reveals that the lower BSE brightness aureole can be attributed to increase of Ti, Ca, U and Y concentrations and lower contents of Ta, Nb, Fe, Mn and Mg. Analyses in the rim show a wide range of compositions with high contents in TiO<sub>2</sub> (8.63-29.70 wt%), Y<sub>2</sub>O<sub>3</sub> (5.21-9.68 wt%), CaO (3.62-5.73 wt%), UO<sub>2</sub> (0.54-9 wt%) and PbO (0.27-2.87 wt%) associated with a major decrease in Nb<sub>2</sub>O<sub>5</sub> (from 24.64 to 10.95 wt%), Ta<sub>2</sub>O<sub>5</sub> (from 40.45 to 6.48 wt%) and FeO (from 4.71 to 0.91 wt%) contents. The very low analytical totals in the rim varying between 75 and 90 wt% are related to the metamictization and hydration of mineral. This rim is considered as an alteration

zone due to diagenetic or hydrothermal fluids that circulated in the matrix, that have affected primary ilmenite and uraninite grains.

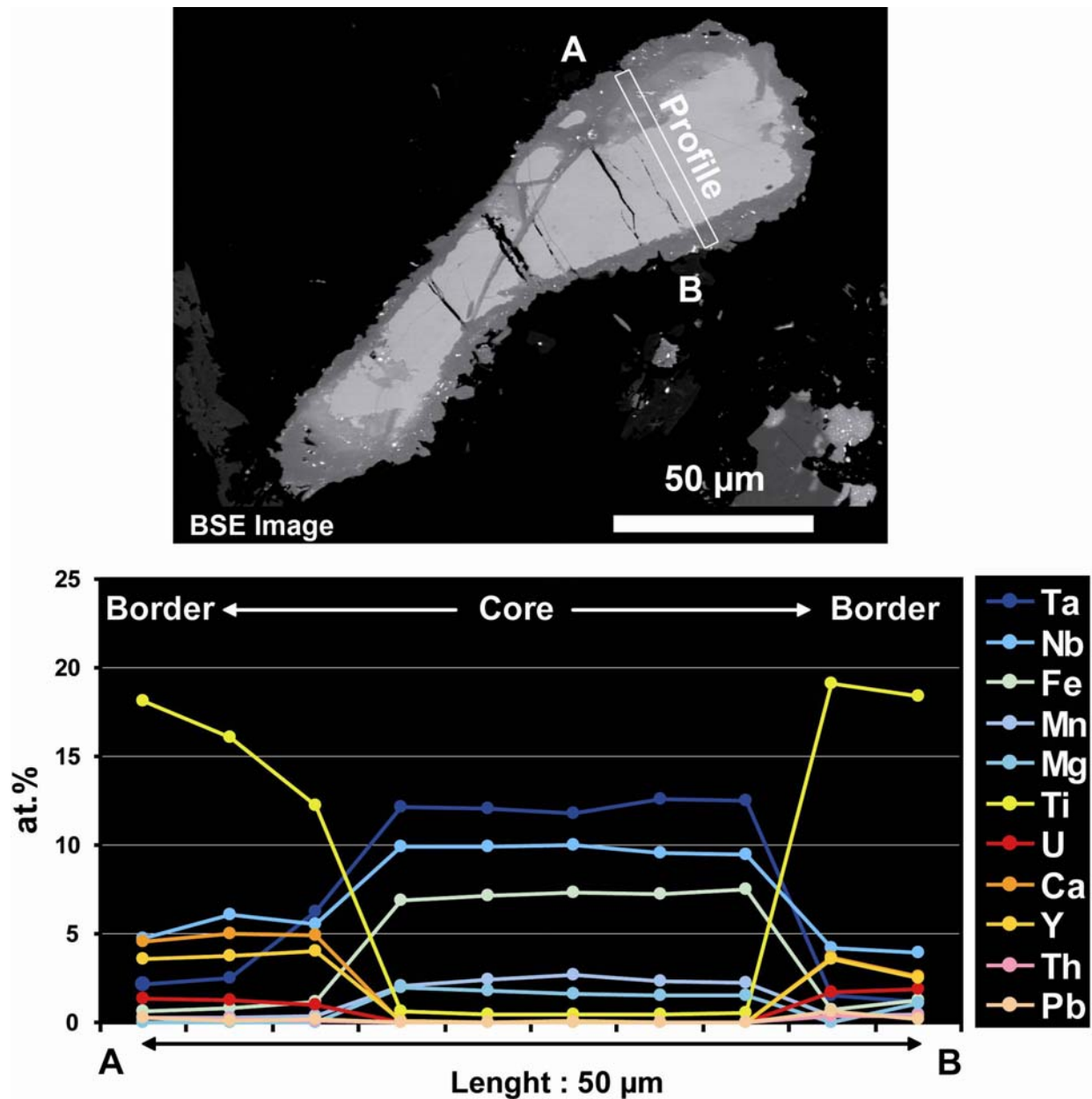


Figure 3.1.27. BSE image of a detrital columbite-tantalite crystal from the upper Dominion reef (sample DRT70-AO5686) and chemical EMP profile showing variations in element concentrations (atom percent) across the grain.

**Table 3.1.10.** Average chemical composition of a columbite-tantalite mineral from the upper Dominion reef.

<i>Drill hole DRT70</i>	<i>Ferro-tantalite</i>	
	Pristine core	Altered aureole
<i>Depth 608.2m</i>	Mean $\pm$ Std. Devi.	Mean $\pm$ Std. Devi.
<i>Sample AO5686</i>	Mean $\pm$ Std. Devi.	Mean $\pm$ Std. Devi.
EMPA	(19)	(8)
Na <sub>2</sub> O	<D.L.	0.14 $\pm$ 0.10
CaO	<D.L.	4.84 $\pm$ 0.70
FeO	10.56 $\pm$ 0.30	2.12 $\pm$ 1.50
MnO	3.52 $\pm$ 0.25	0.83 $\pm$ 0.73
MgO	1.44 $\pm$ 0.12	<D.L.
TiO <sub>2</sub>	0.85 $\pm$ 0.16	20.92 $\pm$ 12.65
Nb <sub>2</sub> O <sub>5</sub>	26.99 $\pm$ 1.06	13.63 $\pm$ 6.54
Ta <sub>2</sub> O <sub>5</sub>	55.37 $\pm$ 0.97	16.54 $\pm$ 4.76
SnO <sub>2</sub>	<D.L.	<D.L.
PbO	<D.L.	0.84 $\pm$ 0.87
ThO <sub>2</sub>	<D.L.	0.72 $\pm$ 0.72
UO <sub>2</sub>	<D.L.	4.94 $\pm$ 3.19
Y <sub>2</sub> O <sub>3</sub>	<D.L.	7.80 $\pm$ 1.61
Sb <sub>2</sub> O <sub>3</sub>	<D.L.	<D.L.
Bi <sub>2</sub> O <sub>3</sub>	<D.L.	<D.L.
Sc <sub>2</sub> O <sub>3</sub>	<D.L.	<D.L.
WO <sub>3</sub>	<D.L.	<D.L.
ZrO <sub>2</sub>	<D.L.	<D.L.
F	<D.L.	<D.L.
<i>Total</i>	99.19 $\pm$ 1.47	80.93 $\pm$ 4.92

*Structural Formula in atomic contents normalized to 6 oxygen atoms*

Fe	0.63 $\pm$ 0.01
Mn	0.21 $\pm$ 0.02
Mg	0.15 $\pm$ 0.01
$\Sigma$ Cations in A site	1.00 $\pm$ 0.02
Ti	0.05 $\pm$ 0.01
Nb	0.88 $\pm$ 0.02
Ta	1.08 $\pm$ 0.02
$\Sigma$ Cations in B site	2.01 $\pm$ 0.01
$\Sigma$ Cations	3.04 $\pm$ 0.01
Mn/(Mn+Fe)	0.25 $\pm$ 0.01
Ta/(Ta+Nb)	0.55 $\pm$ 0.01

**Notes :** CAMECA SX100 electron microprobe analysis in wt%; <D.L. = below Detection Limit (Na = 0.09 wt%, Ca = 0.10 wt%, Fe = 0.15 wt%, Mn = 0.15 wt%, Mg = 0.06 wt%, Ti = 0.06 wt%, Nb = 0.48 wt%, Ta = 0.28 wt%, Sn = 0.15 wt%, Pb = 0.17 wt%, Th = 0.29 wt%, U = 0.17 wt%, Sb = 0.21 wt%, W = 0.48 wt%, F = 0.11 wt%, Bi = 0.54 wt%, Sc = 0.06 wt%, Y = 0.25 wt%, Zr = 0.36 wt%).

The pristine core plots in the ferro-tantalite field with Ta/(Nb+Ta) ratio between 0.54 and 0.57 and Mg/(Fe+Mg) between 0.23 and 0.28 (Fig. 3.1.28), that are distinct from the ferro-columbite of the Pilbara late-orogenic potassic granites (part 2.2) or from the mangano-tantalite of the Tanco peraluminous rare-element pegmatite (part 2.3). Ferro-tantalite occurs as a primary mineral in highly fractionated beryl or petalite pegmatites (Wang et al., 1997; Tindle and Breaks, 1998) or in highly evolved peraluminous rare-element leucogranites (Linnen and Cuney, 2005; Chudík et al., 2008).

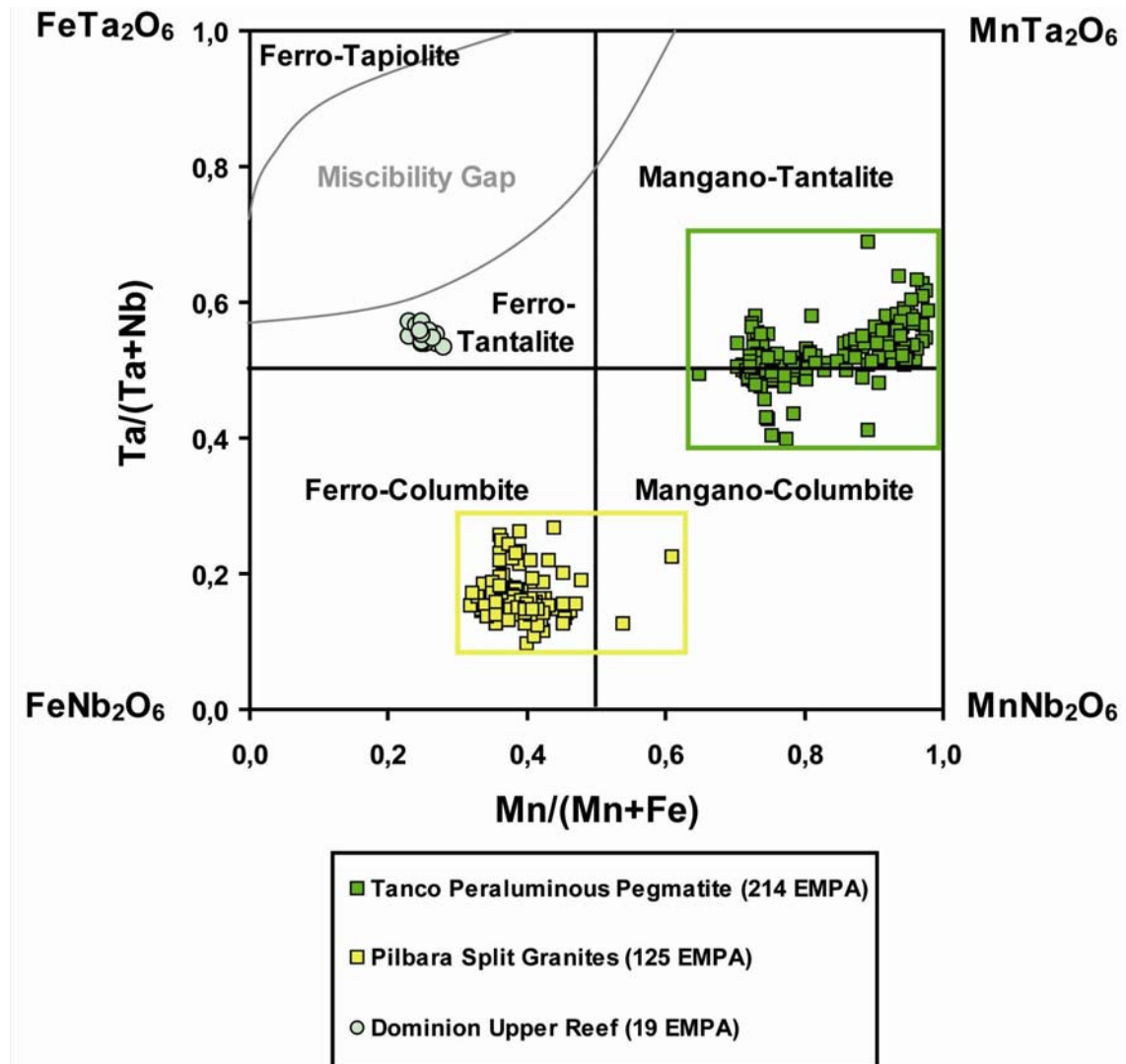


**Figure 3.1.28.** Chemical composition of detrital ferro-tantalite in the upper Dominion reef compared to the composition of mangano-tantalite minerals from the Tanco peraluminous pegmatite (Manitoba, Canada) and ferro-columbite from late-orogenic potassic granites from the Pilbara Craton (Western Australia) represented in the typical end-member quadrilateral (Ercit et al., 1995).

### Central Rand Group reefs

Uranium occurs in several quartz pebble conglomerates of the Central Rand Group but is much more scattered and less abundant than in the Dominion reefs. Consequently, it is rarely mined and only produced as a by-product of gold. All uranium-bearing minerals encountered during microscopic and SEM observations were included within carbonaceous matter.

The most uraniferous reefs analysed are the Beisa and Carbon Leader conglomerates located in the Johannesburg Subgroup at the base of the Central Rand Group. The Carbon Leader reef was deposited during a transgressive stage of the basin and reflect a tidal marine environment (Robb and Robb, 1998). Numerous small uraninite grains are present in the carbonaceous seams which are very abundant in these two basal reefs. Carbonaceous seams are apparently continuous laterally, remain parallel to bedding of the conglomerates and can reach thicknesses of several centimetres. Uraninite is very finely grained with subhedral shape and sizes of approximately 5 to 10  $\mu\text{m}$ , although some of the grains can reach sizes of up to 50-100  $\mu\text{m}$  particularly in the Beisa reef (Fig. 3.1.29). Uraninite is accompanied by pyrite and occasionally zircon and is often surrounded by secondary (U,Th)-silicates.

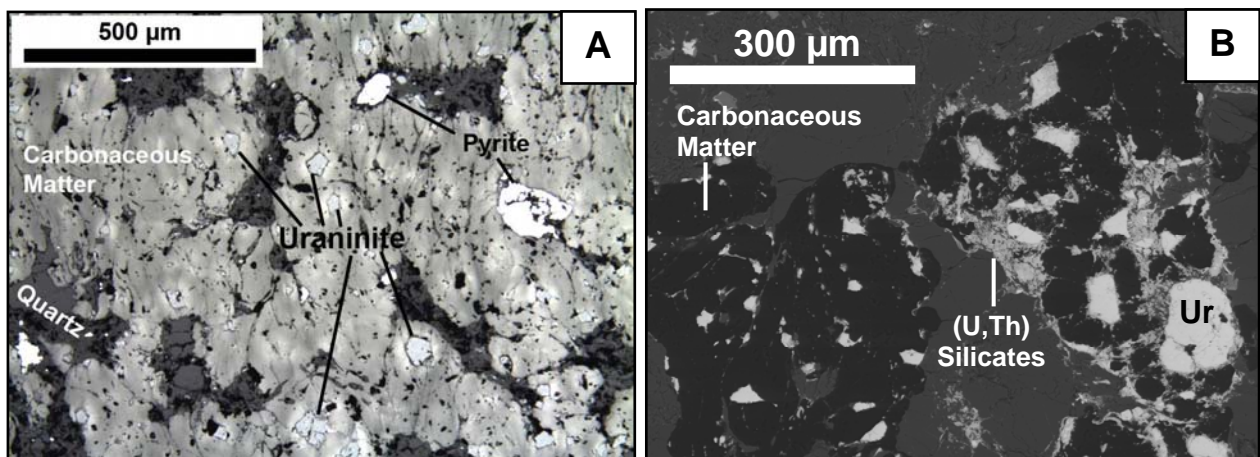


**Figure 3.1.29.** Carbonaceous matter layer in the Beisa reef (Welkom Goldfield) with incorporated spread uraninite and pyrite grains, A: reflected light and B: SEM-BSE image.

Pyrite occurs mostly as fractured well-rounded grains (Fig. 3.1.30-A). Spherulites reaching up to 1.5 mm in diameter with a radial structured core and concentric external laminations have been observed in the Carbon Leader reef (Fig. 3.1.30-B). Similar spherulites have been observed in Early Paleoproterozoic shales from the northern Transvaal Basin (Bekker et al., 2004) and seem to originate from marcasite that is latterly altered to pyrite during diagenesis. Post-depositional transformation of the lower CRG reefs is evidenced by compaction of quartz grains, intense fracturation and sometimes stockworks of pyrite or galena veinlets cutting the strata and passing through the primary grains of pyrite and the carbonaceous seams (Fig. 3.1.30-A and D).

Carbonaceous matter also infiltrates the fractures of quartz grains. The textures suggest pressure solution during ductile deformation (Fig. 3.1.30-C).

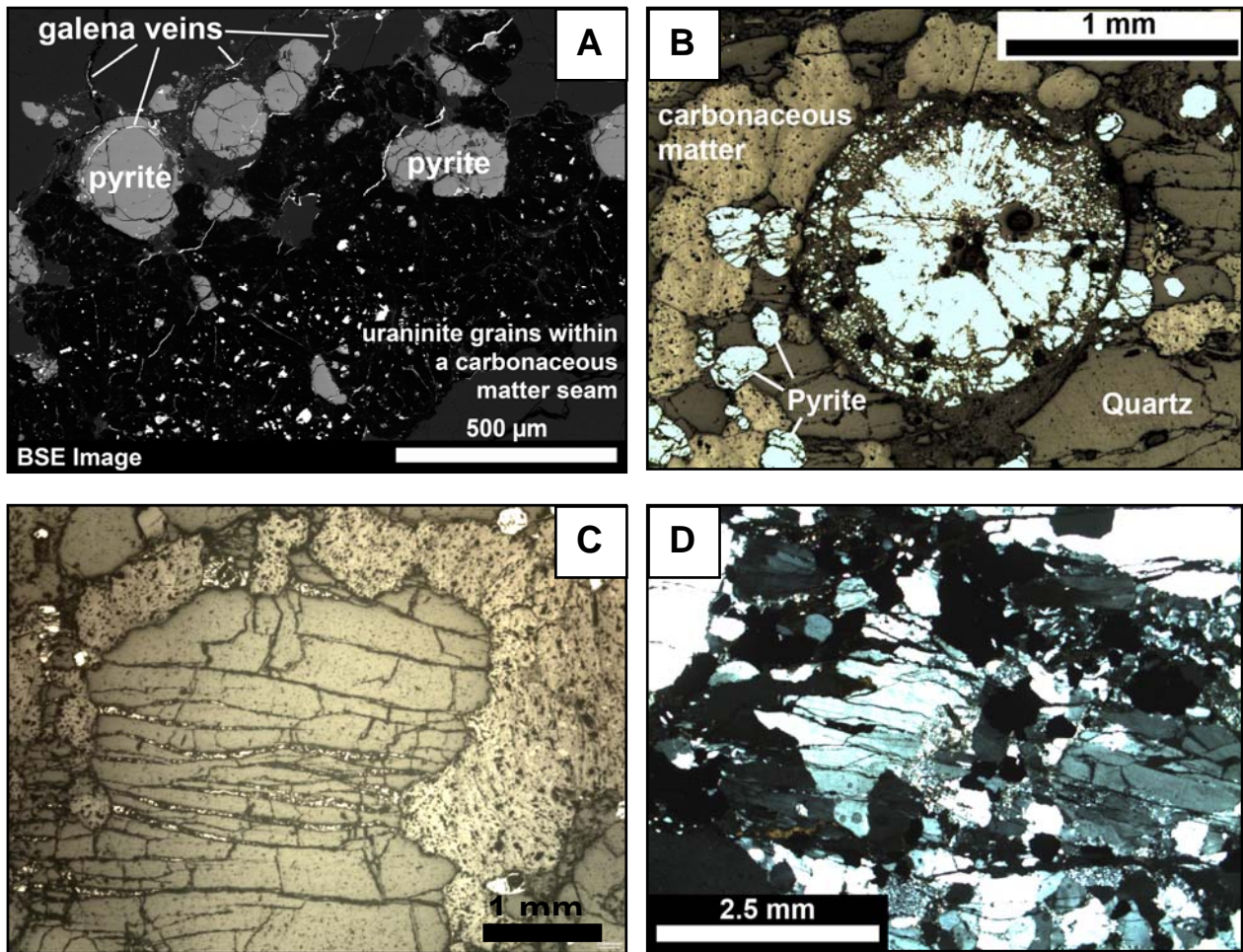


**Figure 3.1.30.** Photomicrographs of the Carbon Leader conglomerates (West Rand Goldfield): **A-** carbonaceous matter seam with disseminated uraninite grains and pyrite globules with secondary galena veinlets (SEM-BSE image); **B-** spherulite of pyrite probably replacing marcasite (reflected light); **C-** carbonaceous matter filling microfractures within quartz grain (reflected light); **D-** well-packed quartz grains truncated by fractures (cross nicols transmitted light).

Uraninite grains in the Beisa reef are characterized by high Th and Y contents (2.66-7.43 wt%  $\text{ThO}_2$  and 0.34-2.84wt%  $\text{Y}_2\text{O}_3$ ) that indicate their detrital origin from granitic source rocks. Nevertheless, the low analytical totals ( $m = 93.77 \pm 0.94$  wt%) and low lead contents (1.94-10.31 wt%  $\text{PbO}$ ) indicate the hydration of minerals and leaching of radiogenic lead (Table 3.1.11). This is confirmed by the chemical U-Th-Pb ages spread between 178 and 952 Ma with a peak at 600-700 Ma suggesting a relatively late post-depositional alteration event (Fig. 3.1.31). Uraninite grains in the Carbon Leader reef are also typical of uranium oxides that grew in a magma with high Th contents (1.29-8.70 wt%  $\text{ThO}_2$ ) but less Y (0.32-1.56 wt%  $\text{Y}_2\text{O}_3$ ) suggesting a more fractionated source. The higher lead contents ranging from 4.71-22.9 wt%  $\text{PbO}$  yield older chemical ages ranging from 628 to 2044 Ma but, nevertheless, indicate radiogenic lead loss during late hydrothermal alteration.

**Table 3.1.11.** Representative average composition of U-minerals associated to carbonaceous matter in the Central Rand Group reefs.

Stratigraphy Reef	Lower Central Rand		Middle Central Rand						Upper Central Rand
	Beisa Reef	Carbon Leader Reef	Vaal Reef	Middle Reef	Middle Reef	Basal Reef	A Reef	A Reef	VCR
Goldfield	Welkom	West Rand	Klerksdorp	Welkom	Welkom	Welkom	Klerksdorp	Klerksdorp	Klerksdorp
Samples	Beisa2	WR78-1A, 1B, 1C and 7	BP86-11A	BP86-4A	BP86-4A	BP86-3A	BP86-12B	BP86-12B	BP86-10
Mineral	Uraninite	Uraninite	Uraninite	Uraninite	U-Ti phases	U-Ti phases	U-Ti phases	(U,Th)- Silicates	Uraninite
Paragenesis	Primary	Primary	Primary	Primary	Secondary	Secondary	Secondary	Secondary	Primary
EMPA	93	30	13	2	8	5	6	5	6
Al <sub>2</sub> O <sub>3</sub>	<D.L.	<D.L.	0.12 ± 0.17	<D.L.	1.05 ± 0.13	1.08 ± 0.30	0.77 ± 0.23	0.35 ± 0.18	<D.L.
SiO <sub>2</sub>	1.52 ± 0.45	0.94 ± 0.55	2.05 ± 1.53	0.66 ± 0.23	8.23 ± 2.82	10.37 ± 5.89	3.81 ± 1.30	15.70 ± 1.50	1.14 ± 0.32
SO <sub>2</sub>	0.32 ± 0.34	1.47 ± 0.81	0.88 ± 0.54	0.48 ± 0.09	0.47 ± 0.61	1.25 ± 1.07	0.44 ± 0.62	1.33 ± 0.60	<D.L.
K <sub>2</sub> O	0.16 ± 0.04	0.21 ± 0.04	0.21 ± 0.03	0.24 ± 0.01	<D.L.	0.11 ± 0.05	<D.L.	<D.L.	0.24 ± 0.06
CaO	1.07 ± 0.17	1.16 ± 0.30	0.73 ± 0.16	1.13 ± 0.11	1.04 ± 0.42	1.03 ± 0.39	0.55 ± 0.21	1.81 ± 0.40	1.04 ± 0.08
Na <sub>2</sub> O	<D.L.	<D.L.	<D.L.	<D.L.	0.19 ± 0.13	0.12 ± 0.14	0.22 ± 0.11	<D.L.	<D.L.
FeO	0.34 ± 0.10	0.36 ± 0.17	0.33 ± 0.29	<D.L.	0.87 ± 0.29	0.84 ± 0.25	0.55 ± 0.15	0.31 ± 0.18	<D.L.
PbO	6.96 ± 1.72	14.90 ± 4.51	11.11 ± 2.69	15.12 ± 1.26	2.48 ± 2.75	4.56 ± 4.53	2.09 ± 2.32	4.61 ± 1.40	10.02 ± 1.60
UO <sub>2</sub>	74.38 ± 1.62	73.48 ± 3.88	75.62 ± 3.17	69.18 ± 4.91	32.22 ± 6.24	36.15 ± 2.43	34.61 ± 10.40	13.17 ± 6.99	70.07 ± 2.12
ThO <sub>2</sub>	5.32 ± 1.15	3.92 ± 1.73	3.27 ± 0.35	3.93 ± 0.38	5.60 ± 2.83	3.80 ± 1.14	1.72 ± 0.69	55.78 ± 8.72	2.85 ± 0.99
MgO	<D.L.	<D.L.	<D.L.	<D.L.	<D.L.	<D.L.	<D.L.	<D.L.	<D.L.
TiO <sub>2</sub>	0.85 ± 0.55	0.34 ± 0.26	0.88 ± 0.62	2.99 ± 3.73	39.52 ± 6.06	32.30 ± 6.25	49.89 ± 12.30	<D.L.	0.70 ± 0.13
MnO	<D.L.	<D.L.	<D.L.	<D.L.	0.30 ± 0.20	0.24 ± 0.16	<D.L.	<D.L.	<D.L.
Y <sub>2</sub> O <sub>3</sub>	1.70 ± 0.53	0.66 ± 0.30	0.99 ± 0.18	1.25 ± 0.22	1.41 ± 0.85	0.24 ± 0.22	<D.L.	0.36 ± 0.04	1.32 ± 0.28
P <sub>2</sub> O <sub>5</sub>	<D.L.	<D.L.	0.21 ± 0.33	<D.L.	0.15 ± 0.23	0.13 ± 0.21	<D.L.	<D.L.	<D.L.
La <sub>2</sub> O <sub>3</sub>	N.D.	<D.L.	<D.L.	<D.L.	<D.L.	<D.L.	<D.L.	<D.L.	<D.L.
Ce <sub>2</sub> O <sub>3</sub>	<D.L.	<D.L.	<D.L.	<D.L.	<D.L.	0.34 ± 0.22	<D.L.	<D.L.	<D.L.
Nd <sub>2</sub> O <sub>3</sub>	N.D.	<D.L.	<D.L.	<D.L.	<D.L.	<D.L.	<D.L.	<D.L.	<D.L.
Dy <sub>2</sub> O <sub>3</sub>	<D.L.	<D.L.	<D.L.	<D.L.	<D.L.	<D.L.	<D.L.	<D.L.	<D.L.
Ta <sub>2</sub> O <sub>5</sub>	<D.L.	<D.L.	<D.L.	<D.L.	<D.L.	<D.L.	<D.L.	<D.L.	<D.L.
Total	93.77 ± 0.94	98.46 ± 2.05	97.12 ± 2.10	96.12 ± 2.29	94.67 ± 1.61	95.63 ± 1.62	93.93 ± 0.69	95.86 ± 0.80	96.49 ± 0.90

**Notes:** All average values are reported in weight percent ± the standard deviation from EMPA (electron microprobe CAMECA SX100); Abbreviations: EMPA = number of EMPA measurements; <D.L. = beyond Detection Limit (Al=0.06wt%, Si=0.06wt%, S=0.07wt%, K=0.11wt%, Ca=0.09wt%, Na=0.11wt%, Fe=0.21wt%, Pb=0.12wt%, U=0.57wt%, Th=0.11wt%, Mg=0.04wt%, Ti=0.07wt%, Mn=0.20wt%, Y=0.12wt%, P=0.06wt%, La=0.17wt%, Ce=0.29wt%, Nd=0.54wt%, Dy=0.63wt%, Ta=0.22wt%); N.D. = Not Determined.

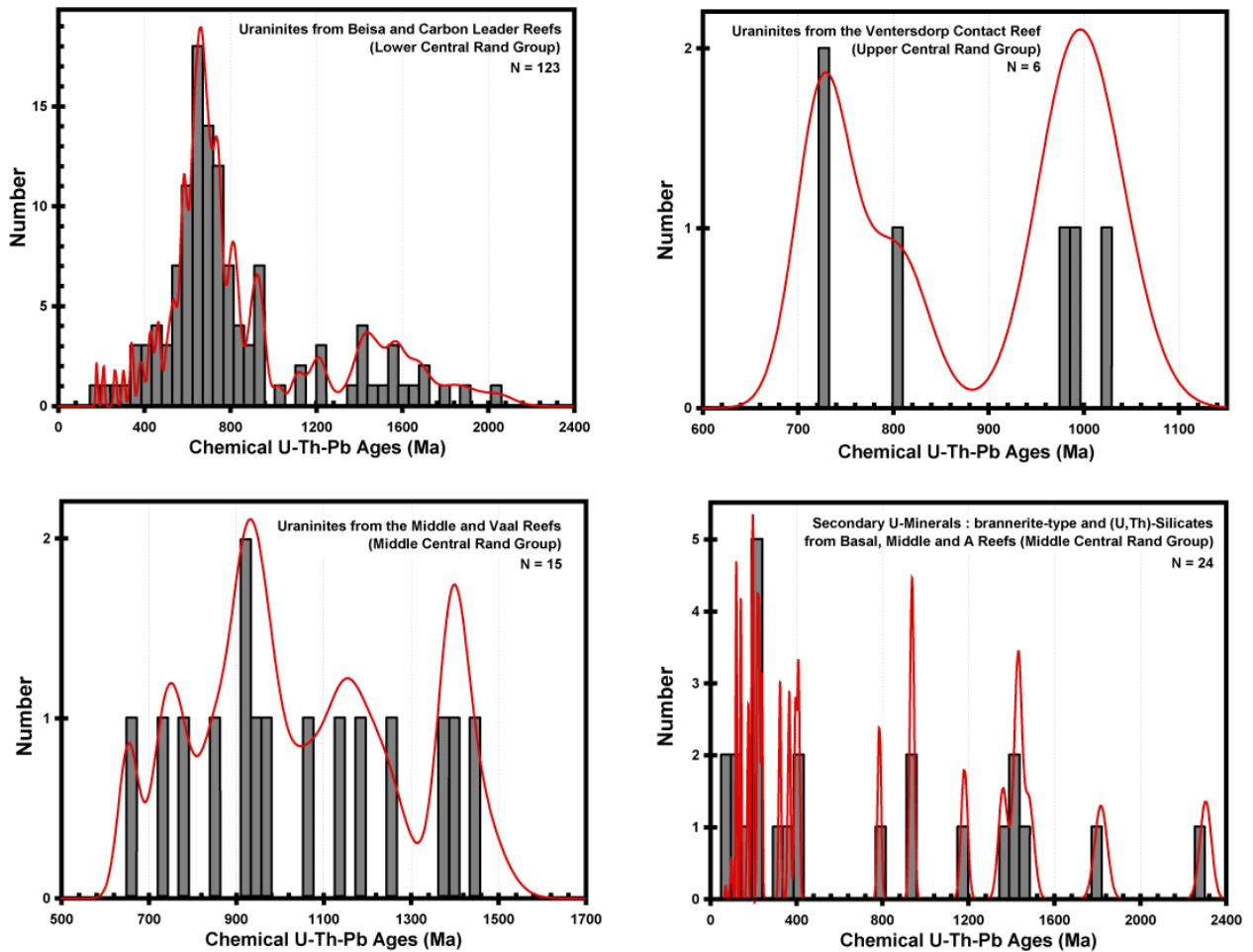


**Figure 3.1.31.** Histograms and relative probability curves representing the distribution of chemical U-Th-Pb ages of U-minerals from various Central Rand Group reefs.

Reefs occurring within the middle and upper units of the CRG sedimentary sequence are characterized by a relatively high amount of matrix minerals (prevailing much more than in the well packed Dominion reefs) composing muscovite, pyrophyllite and chloritoid (Fig. 3.1.32-A and -B). No feldspar has been observed during our petrographic study however it is known to occur sporadically in quartzites of the CRG and feldspar grains are more abundant in the quartzarenites and quartz-feldspar wakes from the West Rand Group (Law et al., 1990). The CRG mineralization occurs as well sorted heavy mineral beds with a thickness of up to several centimetres (Fig. 3.1.32-C) or as disseminated grains between pebbles in the less sorted layers (Fig. 3.1.32-D). Sulphides are by far the most abundant heavy minerals and are dominated by well rounded grains of pyrite and minor arsenopyrite coated by post-depositional crystallisation of secondary pyrite (Fig. 3.1.32-E and -F). Authigenic pyrite growth can be inferred from the presence of cubes disseminated in the matrix (Fig. 3.1.32-G). Veinlets of pyrite, generally associated with chalcopyrite and sporadically pyrrhotite, have also been observed cutting detrital grains and sedimentary layers similar to the textures observed in the Dominion reefs. Zircon with inclusions of xenotime, titanium oxides, Cr-spinels with minor monazite are other detrital minerals found in association with rounded sulphides (Fig. 3.1.32-D and -H).

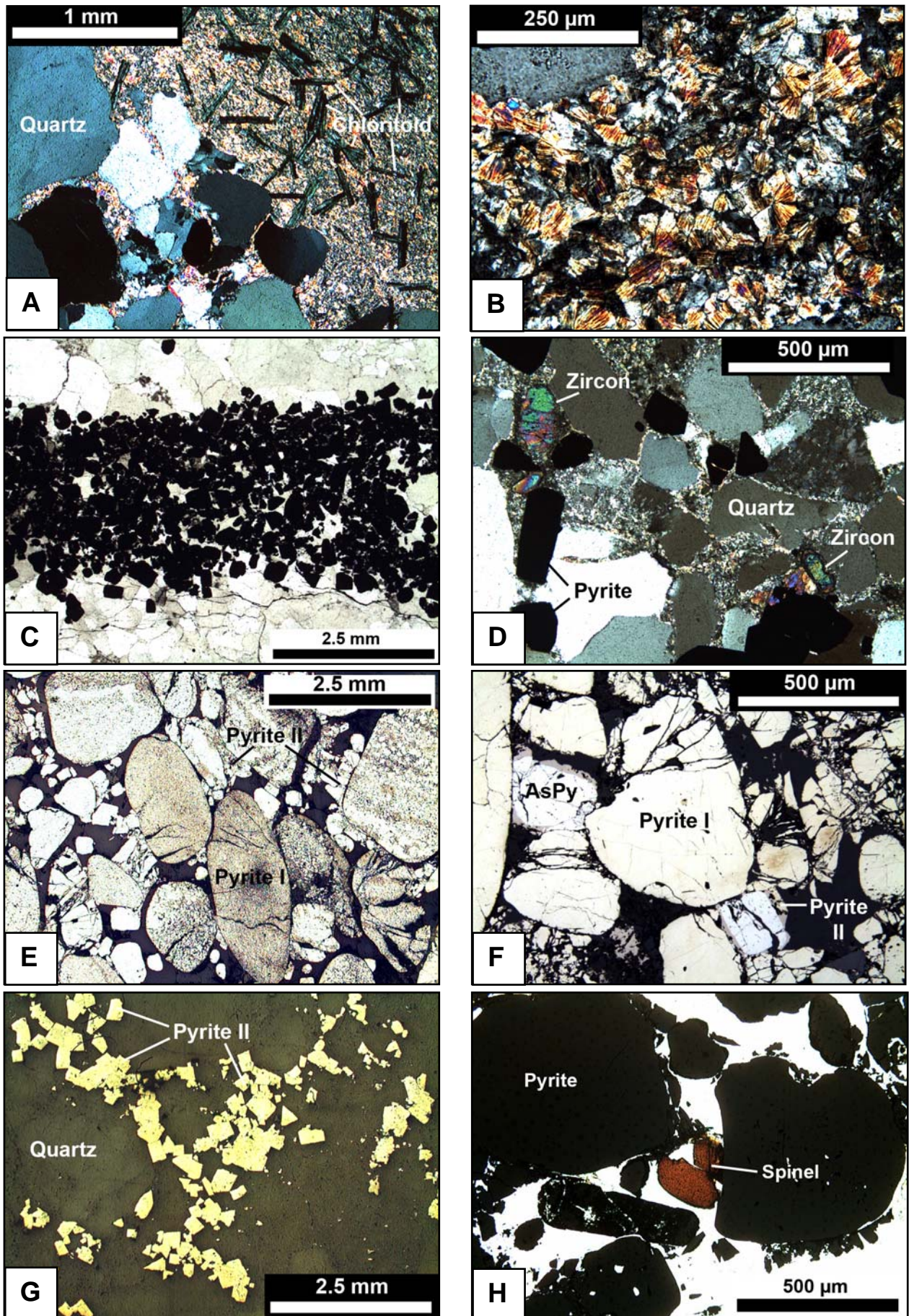


**Figure 3.1.32.** Photomicrographs of the Central Rand Group conglomerates : **A-** quartz grains supported by sericitic matrix and chloritoid (cross nicols-Basal reef); **B-** muscovite fan-like sheets (cross nicols-Leader reef); **C-** 3 mm thick layer of heavy minerals (plane light-Leader reef); **D-** disseminated zircon and opaque grains (cross nicols-VCR); **E-** rounded pyrite (I) grains and later recrystallization (II) (reflected light-Basal reef); **F-** rounded pyrite and arsenopyrite with overgrowths of pyrite II (reflected light-VCR); **G-** cubes of authigenic pyrite (reflected light-Middle reef); **H-** rounded spinel between pyrite grains (plane light-Vaal reef).

Within the middle and upper CRG reefs, carbonaceous matter is abundant but occurs generally as isolated carbonaceous nodules displaying well rounded shapes and diameters ranging between 30 and 300  $\mu\text{m}$  (Fig. **3.1.33**). Globules are generally disseminated within the matrix between quartz pebbles but locally can occur as drop-like inclusions in quartz together with pyrite, in that instance being often surrounded by radial fractures (Fig. **3.1.33-A** and **B**). Uraninite is less abundant than in the lower stratigraphic levels and is more scattered within the carbonaceous matter (Fig. **3.1.33-B**). It appears as highly fractured sub-rounded grains of which sizes never exceed 30  $\mu\text{m}$  (Fig. **3.1.33-C**) and commonly are smaller than 5  $\mu\text{m}$ . Uraninite compositions (Table **3.1.11**) are indicative for their granitic origin similar to those originating from the lower DG, Beisa and Carbon Leader reefs, with moderate thorium contents: 2.71-3.81 wt%  $\text{ThO}_2$  ( $m = 3.27 \pm 0.35$  wt%) in uraninite from the Vaal reef, 3.66-4.19 wt%  $\text{ThO}_2$  ( $m = 3.93 \pm 0.38$  wt%) in grains from the Middle reef and 1.84-3.79 wt%  $\text{ThO}_2$  ( $m = 2.85 \pm 0.99$  wt%) in uraninite from the Ventersdrop Contact reef. Primary uraninites are also characterized by high Y contents ranging between 0.68 and 1.68 wt%  $\text{Y}_2\text{O}_3$ . High Si and Ca contents, traces of S, Ti and K, and low EMP analytical totals suggest alteration and hydration of minerals. Lead contents ranging from 6.43 to 16.48 wt% PbO yield a wide variation of chemical ages ranging from 653 to 1443 Ma (Fig. **3.1.31**).

The most abundant U-bearing mineral in middle and upper CRG reefs is not uraninite but a range of microcrystalline U-Ti phases with wide compositional variations (Table **3.1.10**) dominated by titanium (24.60-69.85 wt%  $\text{TiO}_2$ ), uranium (25.5-41.74 wt%  $\text{UO}_2$ ), silica (5.04-20.86 wt%  $\text{SiO}_2$ ) and thorium (0.60-10.2 wt%  $\text{ThO}_2$ ). Textural associations within fractures of primary rutile or uraninite grains, coating of carbonaceous matter nodules or disseminated within the sericitic matrix support a secondary origin (Fig. **3.1.33-D**, **E** and **F**). The various stoichiometric proportions of U-Ti phases correspond to a mixture of leucoxene, brannerite and coffinite (Fig. **3.1.34**). This suggests U mobilization due to alteration of primary uranium oxides as also observed in the Elliot Lake conglomerate deposits (Saager and Stupp, 1983). The U-Th-Pb chemical ages of U-Ti phases are extremely scattered ranging from 68 to 2304 Ma (Fig. **3.1.31**), and are younger than the youngest VCR reef overlying unconformably the Witwatersrand Supergroup, but at the base of the Ventersdorp volcanics aged ca 2.71 Ga (Armstrong et al., 1991), which confirms that uranium was redistributed during post-sedimentary alteration event(s). It can be noticed that U-Ti phases are also associated with gold mineralization in pore spaces within carbonaceous matter (Fig. **3.1.33-F**). The gold occurs as electrum alloy and no detrital gold particles have been observed during the present petrographic investigation.

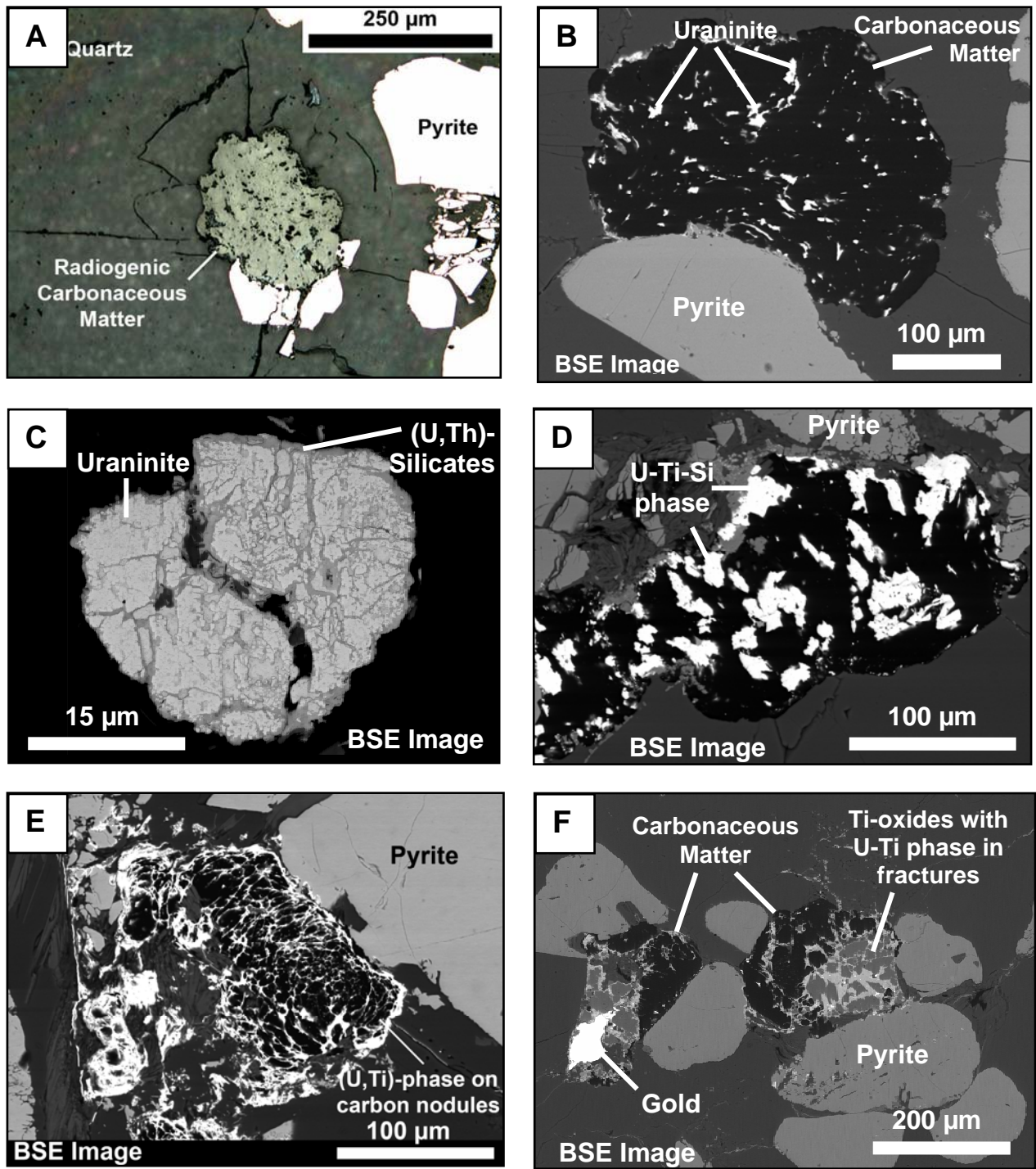


**Figure 3.1.33.** U mineralization in the Central Rand Group conglomerates : **A-** uraniferous carbonaceous matter globule surrounded by pyrite and inducing radial fractures in the host-quartz (reflected light-Vaal reef); **B-** same mineral paragenese than A with inclusions of uraninite (BSE-Vaal reef); **C-** uraninite in carbonaceous nodule with (U,Th)-silicates coating grain and fractures (BSE-Vaal reef); **D-** U-Ti-Si phase in carbonaceous matter (BSE-A reef); **E-** U-Ti phase deposited on carbonaceous globules (BSE-Basal reef); **F-** Carbonaceous matter coating primary Ti-oxides highly fractured and altered into brannerite (BSE-A reef).

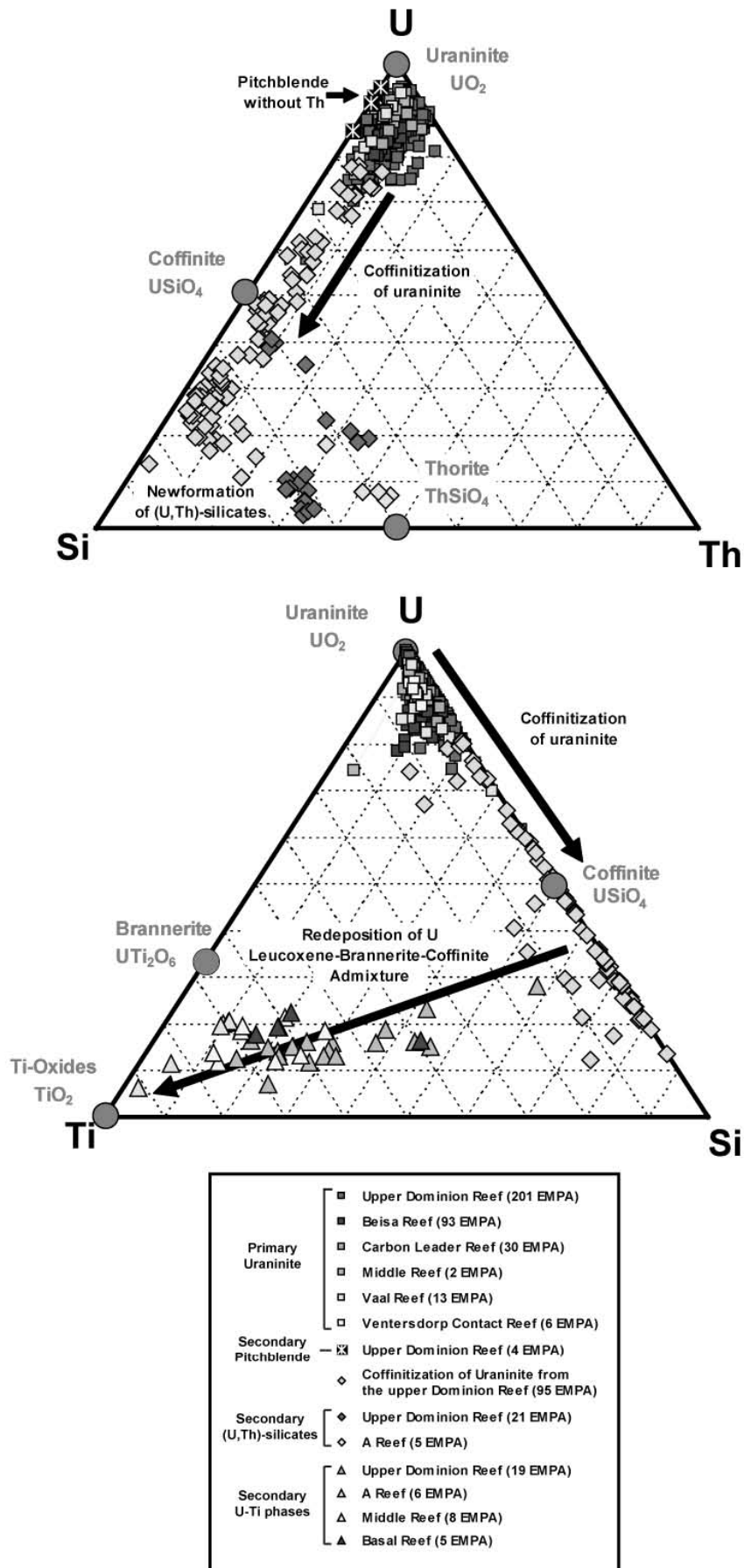


**Figure 3.1.34.** Ternary diagrams showing the stoichiometric proportions of the U mineralization from the Witwatersrand conglomerates in the various reefs studied.

Other accessory minerals account for an extremely low radioelement contents in the CRG conglomerates. Uranium and thorium contents of zircon grains through the sedimentary sequence are below the detection limits of the microprobe (U and Th < 0.08 wt%; Table 3.1.12). Monazite grains host locally up to a few hundreds of ppm U ( $m = 0.09 \pm 0.06$  wt%  $UO_2$ ) and high Th contents ( $m = 2.05 \pm 0.98$  wt%  $ThO_2$ ) in the Ventersdorp Contact reef but they are very rare compared to uraninite and the secondary brannerite-leucoxene association. The analysed monazite grains have a composition plotting on the trend of cheralite-(Ce) group which suggests that detrital grains derive from peraluminous S-type granite(s) as for the Dominion monazites (Förster, 1998; Fig. 3.1.18). Chemical U-Th-Pb dating yield ages comprised between 2095 and 2848 Ma (total of 17 measurements) with the exception of one analysis providing an age of ca. 646 Ma. The sediment deposition is constrained between 2894 and 2714 Ma (Zhao et al., 2006). This implies that late hydrothermal alteration have also affected the Ventersdorp monazite grains.

**Table 3.1.12.** Average composition of zircon and monazite from the Central Rand Reefs

Stratigraphy Reef Goldfield	Middle Central Rand Group			Upper Central Rand Group	
	Leader Reef Welkom	Middle Reef Welkom	A Reef Klerksdorp	Ventersdorp Contact Reef Klerksdorp	Ventersdorp Contact Reef Klerksdorp
Sample	BP86-05	BP86-04	BP86-12	BP86-08	BP86-08
Mineral	Zircon	Zircon	Zircon	Zircon	Monazite
EMPA	72	7	15	38	17
ZrO <sub>2</sub>	64.44 ± 4.20	65.18 ± 0.30	63.84 ± 2.87	64.24 ± 3.87	N.D.
HfO <sub>2</sub>	0.57 ± 0.39	0.51 ± 0.12	0.51 ± 0.10	0.44 ± 0.05	N.D.
SiO <sub>2</sub>	32.14 ± 1.48	32.77 ± 0.22	31.80 ± 1.29	31.86 ± 2.02	0.54 ± 0.30
Al <sub>2</sub> O <sub>3</sub>	<D.L.	<D.L.	<D.L.	<D.L.	<D.L.
CaO	<D.L.	<D.L.	<D.L.	<D.L.	0.57 ± 0.30
FeO	<D.L.	<D.L.	<D.L.	<D.L.	<D.L.
PbO	<D.L.	<D.L.	<D.L.	<D.L.	0.26 ± 0.13
UO <sub>2</sub>	<D.L.	<D.L.	<D.L.	<D.L.	0.09 ± 0.06
ThO <sub>2</sub>	<D.L.	<D.L.	<D.L.	<D.L.	2.05 ± 0.98
TiO <sub>2</sub>	<D.L.	<D.L.	<D.L.	<D.L.	<D.L.
MnO	N.D.	N.D.	N.D.	N.D.	<D.L.
Y <sub>2</sub> O <sub>3</sub>	<D.L.	<D.L.	<D.L.	<D.L.	1.67 ± 0.82
P <sub>2</sub> O <sub>5</sub>	<D.L.	<D.L.	<D.L.	<D.L.	29.86 ± 0.50
La <sub>2</sub> O <sub>3</sub>	<D.L.	<D.L.	<D.L.	<D.L.	13.62 ± 2.18
Ce <sub>2</sub> O <sub>3</sub>	N.D.	N.D.	N.D.	N.D.	20.66 ± 1.53
Pr <sub>2</sub> O <sub>3</sub>	N.D.	N.D.	N.D.	N.D.	2.60 ± 0.24
Nd <sub>2</sub> O <sub>3</sub>	N.D.	N.D.	N.D.	N.D.	13.68 ± 2.45
SmO	N.D.	N.D.	N.D.	N.D.	2.34 ± 0.90
Gd <sub>2</sub> O <sub>3</sub>	N.D.	N.D.	N.D.	N.D.	1.79 ± 1.03
Dy <sub>2</sub> O <sub>3</sub>	<D.L.	<D.L.	<D.L.	<D.L.	N.D.
Er <sub>2</sub> O <sub>3</sub>	<D.L.	<D.L.	<D.L.	<D.L.	N.D.
Yb <sub>2</sub> O <sub>3</sub>	<D.L.	<D.L.	<D.L.	<D.L.	N.D.
Total	97.57 ± 4.87	98.64 ± 0.46	96.73 ± 3.54	97.15 ± 4.83	97.85 ± 0.82

**Notes:** All average values are reporter in weigh percent ± the standard deviation from EMPA (electron microprobe CAMECA SX100); Abbreviations: EMPA = number of EMPA measurements; <D.L. = beyond Detection Limit (Zr=0.20wt%, Hf=0.08wt%, Si=0.06wt%, Al=0.05wt%, Ca=0.06wt%, Fe=0.13wt%, Pb=0.14wt%, U=0.08wt%, Th=0.08wt%, Ti=0.04wt%, Mn=0.18wt%, Y=0.08wt%, P=0.08wt%, La=0.15wt%, Ce=0.23wt%, Pr=0.15wt%, Nd=0.20wt%, Sm=0.15wt%, Gd=0.25wt%, Dy=0.16wt%, Er=0.25wt%, Yb=0.22wt%); N.D. = Not Determined.

## Discussion

The Dominion Group, which sedimentation is comprised between  $3086 \pm 3$  Ma (Westerdam granite after Robb et al., 1992) and  $3074 \pm 6$  Ma (Armstrong et al., 1991), and which is located at the bottom of the Witwatersrand Basin, hosts the most uraniferous quartz pebble conglomerates. Grades can reach up to 0.35 wt% U and 0.15 wt% Th in the upper Dominion reef. The actual inferred resources for the Dominion reefs are estimated at 55,460 tU with grades from 0.05 to 0.10 wt% U (after Uranium One Ltd. for the Dominion and Rietkuil deposits). The average composition in our sampling (20 samples) is 817 ppm U and 527 ppm Th. Conglomerates are also enriched in REE ( $\Sigma\text{REE} = 94\text{-}11219$  ppm) and other HFSE (273 ppm Nb, 125 ppm Ta, 276 ppm Y, 439 ppm Zr) associated with uraninite, monazite, zircon and ferro-tantalite accumulation.

The Central Rand Group reefs, which deposition is constrain between 2894 and 2714 Ma (Zhao et al., 2006), host much lower radioelement concentrations, meaning 140 ppm U and 22 ppm Th (30 samples) on average, lower rare earth element contents with  $\Sigma\text{REE}$  ranging between 47-607 ppm and are depleted in HFSE. Conglomerates have a lower A parameter (Fig. **3.1.9**) corresponding to a less abundant phyllosilicates derived from feldspar alteration.

Therefore, bulk geochemistry of the conglomerates is mainly controlled by the accessory mineral abundances and to a lower extend by later alteration that has diminished the K, Na and Ca contents with feldspar alteration.

The uranium ore in the Witwatersrand quartz pebble conglomerate deposits consist mainly of primary uraninite grains that are either disseminated in the heavy mineral layers dominated by sulphides in the Dominion reefs or within carbonaceous matter in the Central Rand reefs. Secondary uranium mineralization also occurs in various stratigraphic units and is represented by coffinite, (U,Th)-silicates, brannerite and rutile or anatase admixture that can also coat primary grains, or occur finely disseminated in the matrix, filling pores, or are trapped as fine nets on the carbonaceous matter. Evidence of a late ore deposition is finally provided by pitchblende, sulphides and galena veinlets cross cutting the two previous mineralization stages.

***Primary ore and evidences for a detrital origin***

The shape of round pyrite and uraninite primary grains probably results from a long transportation and can be taken as a first evidence for their detrital origin. However, epigenetic uraninite can occasionally occur in the form of rounded grains as observed in the unconformity-type deposits of the Athabasca Basin (Phillipe et al., 1993). To this point, the shape of grains cannot unequivocally be used to indicate the origin of minerals.

Uraninite from the Witwatersrand occur with other heavy minerals accumulated in sedimentary beds more or less sorted which can also be debated because hydrothermal fluid infiltration can occur along stratigraphic beds through porosity or fractures (Law and Phillips, 2006).

In the Central Rand Group reefs, uraninite only occurs within carbonaceous nodules disseminated in the matrix or as inclusions in quartz pebbles with pyrite. Many hypotheses on the origin of the carbonaceous matter have been advanced:

- i) the organic rich bands following sedimentary beds, as observed in the Beisa and Carbon Leader reefs, are thought to derive from the decomposition of carbon organisms living as microbial mat covers (Schidlowski, 1981; Hallbauer, 1986; Mossman et al., 2008);
- ii) the little droplets or carbon as found in the upper and middle Central Rand Group reefs are supposedly eroded kerogen nodules removed from older channels (Engelbrecht et al., 1986);
- iii) however, it should also be noticed that similar uraninite-bearing bituminous nodules have been observed in peraluminous granites from the Barberton Mountain Land (Drennan, 1988; Robb et al., 1994) which could be considered either as possible source-rocks or as a confirmation that kerogen migration has affected both the sedimentary basin and the granites;
- iv) finally, vein-like kerogen cutting stratification are inferred to be formed by thermal maturation of migrated hydrocarbons (Gray et al., 1998; Jolley et al., 2004; Mossman et al., 2008).

Thus, the uraninite associated with carbonaceous matter could have two origins: detrital with secondary precipitation of migrated hydrothermal carbon material that polymerized around uraninite (Parnell, 1999; England et al., 2001 and 2002) or epigenetic implying the hydrothermal remobilization of uranium latterly trapped on the reduced material (Law and Phillips, 2006).

However, this work brings new geochemical constraints demonstrating that the primary uraninite grains in both the Dominion and Central Rand Groups are allogenic and have initially crystallized from granitic melts. They have variable but high thorium contents, an extremely weakly soluble element in aqueous solution, incorporated in uranium oxides crystallizing in a cooling magma. This feature has also been already advanced by Grandstaff (1974) among others as an evidence for the uraninite detrital origin. The variation of Th contents between uraninite grains (Fig. 3.1.35) reflects certainly different parental-rocks from composite source areas when grains are from the same reef for the upper Dominion Group conglomerates, or simply reflects variation in the source areas feeding the different Goldfields and the various Central Rand Group reefs during time. The chondrite-normalized REE patterns of single uraninite grains from the upper Dominion reef also unambiguously demonstrate the detrital origin of primary uraninite (Fig. 3.1.24). They have characteristic weakly fractionated shapes with high REE abundances ( $\sim 10^4$  times that of chondrites) and negative Eu anomalies, specificities of magmatic uranium oxides (Bonhoure, 2007).

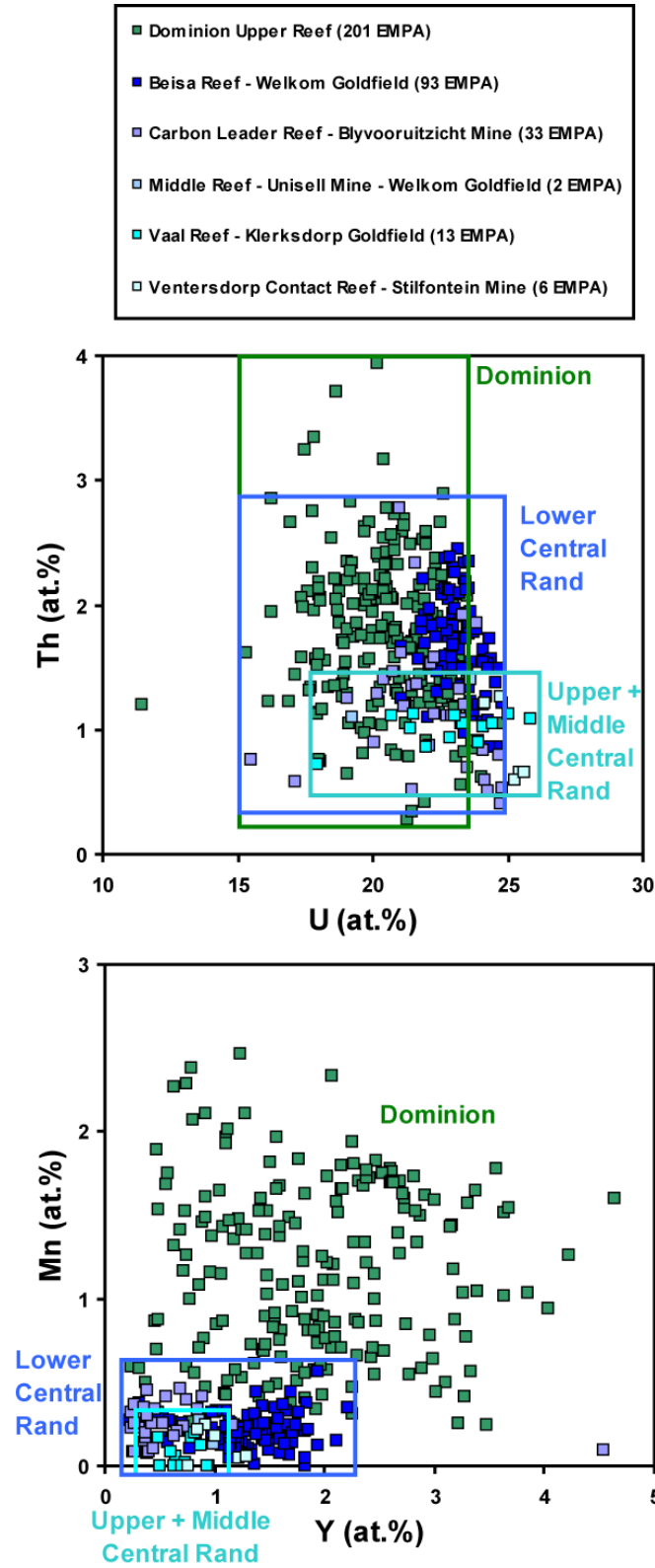


**Figure 3.1.35.** Binary diagrams Th vs. U and Mn vs. Y (in atomic percent) characterizing the primary uraninite grains from the various reefs sampled in the Dominion and Central Rand Groups.

### ***Provenances of the primary uraninite grains***

All the detrital accessory minerals present in the conglomerates derive from diverse source-rocks composing the different eroded areas with time and each reef sampled vertically in the various units of the Witwatersrand sedimentary record represents a different time interval of transportation and deposition.

The Dominion Group sediments are coeval with mafic volcanic series and contemporaneous of a volcanic arc (Stanistreet and McCarthy, 1991; Frimmel, 2005). This is expressed by the abundance in detrital chromite, pyrite and titanium oxides that correspond to the dismantlement of a volcanic arc complex that also may be older. However, the mineral assemblage with detrital grains of low to high Th-contents (0.95-12.21 wt% ThO<sub>2</sub>) uraninite, zircon, cheralite-(Ce) monazite, cassiterite, almandine-garnets and ferro-tantalite is characteristic of the erosion of extremely fractionated granites. The highly variable uraninite composition of the upper Dominion Group reef supports at least two different source-rock types:

1) Uraninite grains characterized by low to moderate Th contents, high Mn concentrations (up to 2.19 wt% MnO) and lower Y and REE contents (Fig. **3.1.35**) are typical of peraluminous rare metal pegmatites (e.g. the Tanco pegmatite, Canada – this work part **2.3**). Moreover, cheralite-type monazite and ferro-tantalite support highly fractionated rare-element leucogranites as parental source rocks, beryl-type pegmatites (e.g. Separation Lake, Canada – Tindle and Breaks, 1998; Scheibengraben pegmatite in Check Republic – Novák et al., 2003) or Li- and F-rich granitic pegmatites (Černý 1989). The Barberton Mountain Land in eastern Kaapvaal Craton constitutes a potential source area for this type of leucogranites. The Sinceni pegmatites located therein are fractionated beryl-type rare element granites aged ca. 3.0 Ga with occurrences of primary cassiterite and high Ta concentrations (Trumbull, 1995). These pegmatites are genetically linked to early (3.3 to 3.1 Ga age) granitic plutons they intrude and are emplaced in late-tectonic settings. Therefore, this type of pegmatites probably exists before 3.09 Ga, the maximal age of the Dominion sedimentation.

2) A second source type is provided by uraninite grains characterized by very high Th, Y and REE contents. This uraninite composition is typical of uranium oxides grown in anatectic melts from partial melting of metasediments as the Archean and Paleoproterozoic pegmatites of the Karelia and Kola crustal blocks from the Baltic Shield (this work part **2.4**) or the Rössing alaskites in Namibia (Cuney and Kyser, 2008).

These results show that at the time of the Dominion Reef deposition (3.09-3.07 Ga), highly differentiated felsic rocks were already present and represent the source for the primary detrital uraninite from the basal reefs of the Witwatersrand basin.

Because only a few occurrences of uraninite are known in the West Rand Group (Frimmel and Minter, 2002), a major change in the provenance of sediments has probably induced the almost total disappearance of detrital uraninite until the Beisa Reef deposition at the base of the Central Rand Group. This change is observed stratigraphically with a major discordance between the Dominion and the Witwatersrand Supergroup series, as well as by the very different bulk geochemistry of the sedimentary rocks. This change may be caused either because U rich-granites/pegmatites were totally eroded, or more likely because of the uplift related to the continental collision during the Limpopo Orogen (Fig. 3.1.2; Catuneanu and Biddulph, 2001) associated with continuous flexural deformation forming the foreland basin (Fig. 3.1.3; Eriksson et al., 2009). These events have induced a major change in the hydrodynamic processes and the nature of eroded terranes. The HFSE depleted compositions of the Central Rand Group reefs indicate that the sediments derived mostly from terranes dominated by mafic rocks with less felsic compounds than in the time of the Dominion deposition. The Central Rand uraninite composition evolves depending of the reef provenance. In the lower Central Rand Group, the Beisa and Carbon Leader Reefs host uraninite moderate ThO<sub>2</sub> (1.29-8.70 wt%) and Y<sub>2</sub>O<sub>3</sub> (0.32-2.84 wt%) contents and no manganese (Fig. 3.1.35) possibly formed in high-K calc-alkaline granites (e.g. the Eburnean granite from Guinea which uraninite has ThO<sub>2</sub> contents ranging 3.11-6.59 wt%, Y<sub>2</sub>O<sub>3</sub> = 0.59-0.88 wt% and no Mn – this work part 2.1). These granites form generally in a convergent geodynamic setting upon a subducting slab with mantle wedge interaction, a modern geodynamic process supposedly starting at the end of Mesoarchean but is still debated (Martin and Moyen, 2005; Martin *et al.*, 2005). The upper sedimentary reefs, the Vaal, Middle and Ventersdorp Contact conglomerates, host less abundant uraninite grains characterized by low Th and Y contents (1.84-4.19 wt% ThO<sub>2</sub> and 0.68-1.68 wt% Y<sub>2</sub>O<sub>3</sub>) and still no Mn which suggests parental granitic rocks derived from less U enriched source melts. When the reefs produced by the progressive erosion of a continental relief are from the same goldfield and from the same source area, there was probably a vertical gradient of differentiation for the source rocks with highly differentiated U-enriched granitoids on top of more mafic to intermediate rocks, latterly eroded. However, hydrodynamic systems evolve with space and time and the reefs which were sampled from various goldfields and sedimentary sequences are necessarily from multiple source areas composed with mixed rocks of accreted terrains.

***Paleo-placer Genetic Model and secondary remobilizations***

The data provided by the present study provides new constraints on the detrital origin of uraninite and that the crystals derive from the erosion of Archean granitic rocks of various types. This work also supports the modified paleo-placer theory (Reimer and Mossman, 1990; Frimmel and Gartz, 1997; Minter, 1976 and 1999; Meyer et al., 1994b; Frimmel and Minter, 2002; Minter, 2006). Uraninite crystals were extracted by purely mechanical processes from the Archean granitic plutons, they were sometimes broken into several pieces and were abraded during their transportation to finally acquire a dominant rounded shape. Grains were sorted by hydraulic processes and accumulated in the conglomerates as layers with other heavy minerals of approximately equivalent size versus density.

Post-sedimentary processes (diagenesis, metamorphism associated with kerogen migration and hydrothermalism) induced basinal fluid circulation in the porous conglomerates and primary grains were submitted to intense low temperature hydrothermal alteration. Several stages of sulphide mineral deposition have been observed, coating primary rounded grains, authigenic cubes of pyrite free in the matrix between pebbles or simply as veins cutting clearly the stratification layering. Alteration of uraninite with U and Pb leaching by fluids is demonstrated by young and very scattered chemical U-Th-Pb ages. Primary uraninite is mostly affected by coffinitization in the Dominion conglomerates but when it occurs with detrital titanium oxides, very abundant in the Central Rand Group reefs, U extracted from uraninite react with Ti and forms uraniferous titanates with variable stoichiometric composition between brannerite and leucoxene. Uraninite gradually disintegrated into smaller size grains with alteration and time. Uranium re-deposition happened in association with reduced carbonaceous matter material derived from the decomposition of organic bacterial mats along some local stratigraphic layers or from maturation and migration of kerogen from other stratigraphic levels through the basin forming veins filling fractures. The uranium mobilisation seems to be more intense in the Central Rand Group reefs where brannerite-type mineralization is more abundant and primary uraninite grains are rare. However, it is also possible that the source rocks were less enriched in uranium oxides during time of the Central Rand Group deposition compared to the Dominion Group. The uranium and lead released from the alteration of uraninite can also crystallize locally as pitchblende and galena veinlets. Secondary hydrothermal uranium oxides have a distinct chemical composition from the primary uraninite with no thorium content and very low Y and Mn contents.

The following paragenetic sequence can be drawn from all these previous mineralogical and textural observations (Fig. 3.1.36).

Mineral	Syn-depositional (Detrital Origin)	Post-depositional (Hydrothermal Origin)	
	Stage I Derived from mechanic erosion of Archean Terranes	Stage II disseminated in the matrix coating primary grains or trapped on organic matter	Stage III filling fractures or vein-like
Quartz			
Feldspar	Not observed (transformed to phyllosilicates)		
Pyrite			
Arsenopyrite			
Rutile			
Ilmenite			
Chromite			
Ferro-Tantalite (only DG)			
Garnet (only DG)			
Uraninite			
Zircon+Xenotime			
Monazite (mainly DG)			
Carbonaceous Matter (mainly CRG)	?		
Gold (mainly CRG)			
Brannerite			
Leucoxene/Anatase			
(U,Th)-Silicates			
Chalcopyrite			
Pyrrhotite			
Galena			
Pitchblende			

**Figure 3.1.36.** List of the ore minerals observed during our petrographic study of the Witwatersrand conglomerates from the Dominion and Central Rand Groups and their paragenetic sequence of deposition. The question mark for the detrital origin of the carbonaceous matter suggests possible recycling of older sedimentary units.

As a final conclusion, this work provides unequivocal evidences for the detrital origin of primary uraninites from the Witwatersrand quartz-pebble conglomerates. The Dominion uraninite grains have been eroded from granites of peraluminous affinity such as rare metal enriched leucogranites and S-type granites formed within the Kaapvaal Craton in early Archean time, at least older than 3.1 Ga. The Central Rand uraninite composition is more characteristic of uranium oxides formed in granites with high-K calc-alkaline affinity. These results have two major implications for the early Earth geodynamic and environmental characteristics: 1) the existence of highly differentiated magmas generated in convergent margin setting or by late

orogenic crustal anatexis attests that modern plate-tectonic processes were already operating at the time of the basin deposition and 2) considering the chemical instability of uraninite under oxidizing conditions, the Archean atmosphere between 3.1 and 2.7 Ga necessarily contained significantly less oxygen than the modern atmosphere and reducing conditions were prevailing on Earth surface to have permitted the preservation of uraninite during its transport and deposition in the Witwatersrand Basin.

## Acknowledgements

Authors are grateful to the following persons for their welcome in South Africa, the help provided during field trips and for sampling assistance: Judith Kinnaird, Laurence Robb, Carl Anhaeusser and Gillian Drennan from the Witwatersrand University (Johannesburg) and Richard Stewart (Uranium One, Dominion Mine). We want also to thanks Bernard Poty and Falk Koenemann permitting to access to their own rock-collection from the Central Rand Goldfields. The author thanks finally Alain Kohler, Johann Ravaux and Sandrine Mathieu for their invaluable assistance with the scanning electron microscopy and electron microprobe work at the SCMEM laboratory. Michel Champenois and Denis Mangin are also grateful for their support with the ion microprobe instrument at the CRPG-CNRS. This work was financially supported by AREVA.

## References

- Alexandre, P. and Kyser, T.K., 2005, Effects of cationic substitutions and alteration in uraninite, and implications for the dating of uranium deposits, *The Canadian Mineralogist* 43, p. 1005-1017.
- Anders, E. and Grevesse, N., 1989, Abundances of the elements: Meteoritic and solar. *Geochimica and Cosmochimica Acta* 57, p. 197-214.
- Anhaeusser, C. R. and Burger, A. J., 1982, An interpretation of U-Pb zircon ages for Archean tonalite gneisses from the Johannesburg-Pretoria granite dome, *Trans. Geological Society of South Africa* 85, p. 111-116.
- Armstrong, R. A., Compston, W., Retief, E. A., Willimas, I. S. and Welke, H. J., 1991, Zircon ion microprobe studies bearing on the age of the Witwatersrand triad, *Precambrian Research*, Vol. 53, p. 243-266.
- Barton, E. S., Barton, J. M. Jr., Callow, M. J., Allsopp, H. L., Evans, I. B. W. and Welke, H. J., 1986, Emplacement ages and implications for the source region of granitoid rocks associated with the Witwatersrand Basin, *Ext. Abstract Geocongress '86*, Geological Society of South Africa, Johannesburg, p. 93-97.
- Bekker, A. Holland, H. D., Wang, P.-L., Rumble III, D., Stein, H. J., Hannah, J. L., Coetzee, L. L. and Beukes, N. J., 2004, Dating the rise of atmospheric oxygen, *Nature*, Vol. 427, p. 117-120.

- Bonhoure, J., 2007, Géochimie des éléments de terres rares et du plomb dans les oxydes d'uranium naturels. Thèse de Doctorat, Université de Nancy, France (unpublished).
- Bonhoure, J., Kister, P., Cuney, M. and Deloule, E., 2007, Methodology for Rare Earth Element determinations of uranium oxides by ion microprobe, *Geostandards and Geoanalytical Research*, Vol. 31, No. 3, p. 209-225.
- Bowles, J. F. W., 1990, Age dating of individual grains of uraninite in rocks from electron microprobe analyses, *Chemical Geology*, Vol. 83, Issues 1-2, p. 47-53.
- Buick, I.S., Maas, R. and Gibson, R., 2001, Precise U-Pb titanite age constraints on the emplacement of the Bushveld Complex, South Africa. *Journal of the Geological Society*, London, 158, p. 3-6.
- Burger, A. J., Nicolaysen, L. O. and de Villiers, J. W. L., 1962, Lead isotopic compositions of galenas from the Witwatersrand and Orange free State, and their relation to the Witwatersrand and Dominion Reef uraninites, *Geochimica et Cosmochimica Acta*, Vol. 26, Issue 1, p. 25-50.
- Button, A. and Tyler, N., 1981, The character and economic significance of Precambrian paleoweathering and erosion surfaces in southern Africa. *Econ. Geol.* 75th Ann. Vol.: 686-709.
- Brynard, H. L. and Andreoli, M. A. G., 1988, The overview of the regional geological and structural setting of the uraniferous granites of the Damara Orogen, Namibia; In: *Recognition of uranium provinces*, IAEA, Vienna, p. 195-212.
- Carignan J., Hold, P., Mevelle, G. Morel, J. and Yeghichevan, D., 2001, Routine analysis of trace elements in geological samples using flow injection and low pressure on line liquid chromatography coupled to ICP-MS: a study of geochemical reference materials BR, DR-N, UB-N, AN-G and GH, *Geostandards Newsletter* 25, p. 187-198.
- Catuneanu, O., 2004, Retroarc foreland systems - evolution through time; *Geological Society of Africa Presidential Review No. 7*, *Journal of African Earth Sciences*, Vol. 38, p. 225-242.
- Catuneanu, O. and Biddulph, M.N., 2001 Sequence stratigraphy of the Vaal Reef facies associations in the Witwatersrand foredeep, South Africa, *Sedimentary Geology* 141-142, 113-130.
- Champion, D. C. and Smithies, R. H., 2004, Archaean granites, *The Ishihara Symposium: Granites and Associated Metallogensis*, *Geoscience Australia*, p. 13-17.
- Chudík, P., Uher, P., Kohút, M. and Bačík, P., 2008, Accessory columbite to tantalite, tapiolite and zircon: products of extreme fractionation in highly peraluminous pegmatitic granite from the Považský Inovec Mountains, Western Carpathians, Slovakia; *Journal of Geosciences*, Vol. 53, p. 323-334.
- Clemens, J. D., Yearron, L. M. and Stevens, G., 2006, Barberton (South Africa) TTG magmas: Geochemical and experimental constraints on source-rock petrology, pressure of formation and tectonic setting, *Precambrian Research*, Vol. 151, Issues 1-2, p. 53-78.
- Cocherie, A. and Albarède, F., 2001, An improved U-Th-Pb age calculation for electron microprobe dating of monazite, *Geochimica et Cosmochimica Acta*, Vol. 65, p. 4509-4522.
- Compston, W. and Kröner, A., 1988, Multiple zircon growth within early Archaean tonalitic gneiss from the Ancient Gneiss Complex, Swaziland: Croissance multiple du zircon dans un gneiss tonalitique de l'Archéen inférieur du Complexe Ancient Gneiss, Swaziland; *Earth and Planetary Science Letters*, Vol. 87, n°1-2, p. 13-28.
- Condie, K. C., 1997, *Plate Tectonics and Crustal Evolution*, 4<sup>th</sup> Edition, Butterworth Heinemann, Oxford, 282 p.

- Cuney, M. and Kyser, K., 2008, Chapter 5: Deposits related to Partial Melting, In: Cuney, M. and Kyser, K. (eds.) Recent and not-so-recent developments in uranium deposits and implications for exploration, Mineralogical Association of Canada, Short Course Series, Vol. 39, p 79-95.
- Davidson, C. F., 1957, On the occurrence of uranium in ancient conglomerates. *Economic Geology*, Vol. 52, p. 668-693.
- de Ronde, C. E. J. and de Wit, M. J., 1994, The tectonothermal evolution of the Barberton greenstone belt, South Africa: 490 million years of crustal evolution; *Tectonics*, Vol. 13, p. 983-1005.
- de Wit, M. J., Armstrong, R. A., Kamo, S. L. and Erlank, A. J., 1993, Gold-bearing sediments in the Pietersburg greenstone belt: age equivalents to the Witwatersrand Supergroup sediments, South Africa; *Economic geology*, Vol. 88, p. 1242-1252.
- de Wit, M. J., Roering, C., Hart, R. J., Armstrong, R. A., De Ronde, C. E. J., Green, R. W. E., Tredoux, M., Peberdy, E., Hart, R. A., 1992, Formation of an Archaean continent; *Nature*, Vol. 357, p. 553-562.
- Drennan, G. R., 1988, The nature of the Archean basement in the hinterland to the Welkom Goldfield. M. Sc. Thesis (unpublished), University of Witwatersrand, Johannesburg, 187 p.
- Engelbrecht, C. J., Baumbach, G. W. S., Matthysen, J. L. and Fletcher, P., 1986, The West Wits Line, In: Anhaeusser, C. R. and Maske, S. (eds.) *Mineral Deposits of Southern Africa*, Geological Society of South Africa, Johannesburg, p. 599-648.
- England, G. L., Rasmussen, B., Krapez, B. and Groves, D. I., 2001, The origin of uraninite, bitumen nodules and carbon seams in Witwatersrand gold-uranium-pyrite ore deposits, based on a Permo-Triassic analog; *Economic Geology*, Vol. 96, No. 8, p. 1907-1920.
- England, G. L., Rasmussen, B., Krapez, B. and Groves, D. I., 2002, Archaean oil migration in the Witwatersrand Basin of South Africa, *Journal of the Geological Society*, Vol. 159, Issue 2, p. 189-201.
- Ercite, T. S., Wide, M. A., Černý, P., 1995, Compositional and structural systematics of the columbite group, *American Mineralogist*, Vol. 80, p. 613-619.
- Eriksson, P. G., Banerjee, S., Nelson, D. R., Rigby, M. J., Catuneanu, O., Sarkar, S., Roberts, R. J., Ruban, D., Mtimkulu, M. N. and Raju, P. V. S., 2009, A Kaapvaal craton debate: Nucleus of an early small supercontinent or affected by an enhanced accretion event? *Gondwana Research*, Vol. 15, Issues 3-4, p. 354-372.
- Ferraz, M. F., 1989, The nature of the Archean basement in the provenance areas of the East Rand and Evander Goldfields. M. Sc. Thesis (unpublished), University of Witwatersrand, Johannesburg, 145 p.
- Ford, M. A., 1993, Uranium in South Africa, *Journal of The South African Institute of Mining and Metallurgy*, Vol. 93, No. 2., p. 37-58.
- Förster, H.-J., 1998, The chemical composition of REE-Y-Th-U-rich accessory minerals in peraluminous granites of the Erzgebirge-Fichtelgebirge region, Germany, Part I: The monazite-(Ce)-brabantite solid solution series, *American Mineralogist*, Vol. 83, p. 259-272.
- Frimmel, H. E., 2005, Archaean atmospheric evolution: evidence from the Witwatersrand gold fields, South Africa. *Earth-Science Reviews* 70, p. 1-46.
- Frimmel, H. E. and Minter, W. E. L., 2002, Recent Developments Concerning the Geological History and Genesis of the Witwatersrand Gold Deposits, South Africa, *Society of Economic Geologists Special Publication* 9, 2002, p. 17-45.

- Frimmel, H. E. and Gartz, V. H., 1997, Witwatersrand gold particule chemistry matches model of metamorphosed, hydrothermally altered placer deposits. *Mineralium Deposita*, Vol. 32, p. 523-530.
- Gao, S. and Wedepohl, K. H., 1995, The negative Eu anomaly in Archean sedimentary rocks: Implications for decomposition, age and importance of their granitic sources; *Earth and Planetary Science Letters*, Vol. 133, No. 1, p. 81-94.
- Gibson, R. L., Armstrong, R. A. and Reimold, W. U., 1997, The age and thermal evolution of the Vredefort impact structure: A single-grain U-Pb zircon study. University of the Witwatersrand, Johannesburg; *Economic Geology Research Unit Information Circular 309*, 18 p.
- Grandstaff, D. E., 1974, Microprobe analyses of uranium and thorium in uraninite from the Witwatersrand, South Africa, and Blind River, Ontario, Canada. *Transactions. Geol. Soc. of S. A.* 77, p. 291-294.
- Gray, G. J., Lawrence, S. R., Kenyon, K. and Cornford, C., 1998, Nature and origin of "carbon" in the Archean Witwatersrand basin; *Journal of the Geological Society*, Vol. 155, p. 39-59.
- Harley, M. and Dixon, R., 2006, Dominion Uranium Project, North-West Province, Republic of South Africa. Independent Technical Report: prepared by SRK Consulting for srx Uranium One Inc., p. 1-138.
- Hallbauer, D. K., 1986, The mineralogy and geochemistry of Witwatersrand pyrite, gold, uranium and carbonaceous matter, In: Anhaeusser, C. R. and Maske, S. (eds.) *Mineral Deposits of Southern Africa*, Geological Survey of South Africa, Johannesburg, p. 731-752.
- Hallbauer, D. K., 1984, Archean granitic sources for detrital mineral assemblage in the Witwatersrand conglomerates. Abstract Geocongress '84, Geological Society of South Africa, Potchefstroom, p. 53-56.
- Hallbauer, D. K., 1982, A review of some aspects of the geochemistry and mineralogy of the Witwatersrand gold deposits, *Proc., 12<sup>th</sup> CMMI Congr. Ed. H. W. Glen. S. Afr. Inst. Min. Metall.*, Johannesburg, p. 957-964.
- Hiemstra, S. A., 1968, The mineralogy and petrology of the uraniferous conglomerate of the Dominion Reefs Mine, Klerksdorp area. *Transactions. Geol. Soc. of S.A.* 71, p. 1-65.
- Hirdes, W., 1978, Small-scale gold distribution patterns in the Precambrian Kimberley Reef placer: A case-study at marievale GMC., East Rand Goldfield, South Africa, *Mineralium Deposita*, Vol. 13, N<sup>o</sup>. 3, p. 313-328.
- Jolley, S. J., Freeman, S. R., Barnicoat, A. C., Phillips, G. M., Knipe, R. J., Pather, A., Fox, N. P. C., Strydom, D., Birch, M. T. G., Henderson, I. H. C. and Rowland, T. W., 2004, Structural controls on Witwatersrand gold mineralization; *J. Struct. Geol.*, Vol. 26, Issues 6-7, p. 1067-1086.
- Kamo, S. L. and Davis, D. W., 1994, Reassessment of Archaean crustal development in the Barberton Mountain Land, South Africa, based on U-Pb dating, *Tectonics* Vol. 13, p. 167-192.
- Kempe, U., 2003, Precise electron microprobe age determination in altered uraninite: consequences on the intrusion age and the metallogenic significance of the Kirchberg granite (Erzgebirge, Germany), *Contributions to Mineralogy and Petrology* 145, p. 107-118.
- Kish, L. and Cuney, M., 1981, Uraninite-albite veins from Mistamisk Valley of the Labrador Through, Quebec. *Mineralogical Magazine* 44, p. 471-483.

- Klemd, R. and Hallbauer, D. K., 1987, Hydrothermally altered peraluminous Archean granites as a provenance model for Witwatersrand sediments, *Mineralium Deposita* 22, p. 227-235.
- Kositcin, N. and Krapez, B., 2004, SHRIMP U-Pb detrital zircon geochronology of the Late Archean Witwatersrand Basin of South Africa: relation between zircon provenance age spectra and basin evolution; *Precambrian Research*, Vol. 129, p. 141-168.
- Kröner, A., Byerly, G. R. and Lowe, D. R., 1991, Chronology of Early Archean granite-greenstone evolution in the Barberton Mountain Land, South Africa, based on precise dating by single zircon evaporation, *Earth and Planetary Science Letters*, Vol. 103, p. 41-54.
- Kyser, K. and Cuney, M., 2008, Chapter 10: Other types of uranium deposits, In: Cuney, M. and Kyser, K. (eds.) *Recent and not-so-recent developments in uranium deposits and implications for exploration*, Short Course 39, Mineralogical Association of Canada, p. 241-252.
- Law, J. and Phillips, N., 2006, Witwatersrand gold-pyrite-uraninite deposits do not support a reducing Archean atmosphere, *Geological Society of America Memoirs*, Vol. 198, p. 121-141.
- Law, J. D. M., Bailey, A. C., Cadle, A. B., Phillips, G. N. and Stanistreet, I. G., 1990, Reconstructive approach to the classification of Witwatersrand 'quartzites', *South African Journal of Geology*, Vol. 93, p. 83-92.
- Liebenberg, W. R., 1955, The occurrence and origin of gold and radioactive minerals in the Witwatersrand System, the Dominion Reef, the Ventersdorp Contact Reef and the Black Reef. *Transactions, Geological Society of South Africa* 58, p. 101-227.
- Linnen, R. L. and Cuney, M., 2005, Granite-Related Rare-Element Deposits and Experimental Constraints on the Ta-Nb-W-Sn-Zr-Hf Mineralization, In: Linnen, R. L. and Samson, I. M. (eds.), *Rare-Element Geochemistry and Mineral Deposits*, Geological Association of Canada, GAC Short Course Notes 17, p. 45-67.
- Ludwig, K.R., 1999, Isoplot/Ex version 2.00 – A geochronological toolkit for Microsoft Excel, Berkeley Geochronology Center, Special Publication No. 2.
- McCourt, S., 1995, The crustal architecture of the Kaapvaal between 3.5 and 2.0 Ga, *Mineralium Deposita*, Vol. 30, p. 89-97.
- McLennan, S. M., 1989, Rare earth elements in sedimentary rocks: influence of provenance and sedimentary processes; *Geochemistry and Mineralogy of Rare Earth Elements* (Lipin, B. R. and McKay, G. A., eds.), *Reviews in Mineralogy*, Vol. 21, p. 169-200.
- McLennan, S. M. and Taylor, S. R., 1991, Sedimentary rocks and crustal evolution: Tectonic setting and secular trends; *The Journal of Geology*, Vol. 99, p. 2-21.
- McLennan, S. M. and Taylor, S. R., 1979, Rare earth element mobility with associated with uranium mineralization; *Nature*, Vol. 282, p. 247-250.
- Meyer, M., Robb, L. J. and Anhaeusser, C. R., 1986, Uranium and thorium contents of Archean granitoids from the Barberton Mountain Land, South Africa, *Precambrian Research* 33, p. 303-321.
- Meyer, F. M., Robb, L. J., Reimold, W. U. and DeBruijn H., 1994a, Contrasting low- and high-Ca granites in the Barberton Mountain Land, southern Africa. *Lithos*, 32, p. 63-76.
- Meyer, F. M., Möller, P., Debruin, D., Przybylowicz, W. J. and Prozesky, V. M., 1994b, The gold-pyrite association in Witwatersrand reefs: Evidence for electrochemical precipitation of gold; *Exploration and Mining Geology*, Vol. 3, p. 207-217.
- Minter, W. E. L., 2006, The sedimentary setting of Witwatersrand placer mineral deposits in an Archean atmosphere, *Geological Society of America Memoirs*, Vol. 198, p. 105-119.

- Minter, W. E. L., 1999, Irrefutable detrital origin of Witwatersrand gold and evidence of eolian signatures. *Econ. Geol.* 94, 665-670.
- Minter, W. E. L., 1976, Detrital gold, uranium, and pyrite concentrations related to sedimentology in the Precambrian Vaal Reef placer, Witwatersrand, South Africa. *Econ. Geol.* 94, 665-670.
- Minter, W.E.L. and Loen, J.S., 1991, Palaeocurrent dispersal patterns of Witwatersrand gold placers: *South African Journal of Geology*, v. 94, p. 70-85.
- Montel, J. M., Foret, S., Veschambre, M., Nicollet, C. and Provost, A., 1996, Electron microprobe dating of monazite, *Chemical Geology*, 131, p. 37-53.
- Mossman, D.J., Minter, W.E.L., Dutkiewicz, A., Hallbauer, D.K., George, S.C., Hennigh, Q., Reimer, T.O. and Horscroft F.D. (2008) The indigenous origin of Witwatersrand “carbon”, *Precambrian Research*, Vol. 164, p. 173-186.
- Martin, H., 2005, Genesis and Evolution of the Primitive Earth Continental Crust, In: M. Gargaud et al. (Ed.), *Lectures in Astrobiology*, Springer-Verlag Berlin Heidelberg, Vol. I, p. 113-163.
- Martin, H. and Moyen, J. F., 2005, The Archaean-Proterozoic transition: Sanukitoid and Closepet type magmatism, *Polskie Towarzystwo Mineralogiczne – Prace Specjalne Mineralogical Society of Poland – Special Papers*, Vol. 26, p. 57-68.
- Moyen, J. F., Martin, H., Jayananda, M. and Auvray, B., 2003, Late Archaean granites : typology based on the Dharwar Craton (India), *Precambrian Research*, Vol. 127, p. 103-123.
- Nedachi, M., Yamanouchi, H. and Ohmoto, H., 1998, Detrital and hydrothermal origins for quartz, pyrite, and uraninite in Au-U-rich conglomerates of the Witwatersrand gold field, South Africa, *Goldschmidt Conference Toulouse 1998*, *Mineralogical Magazine*, Vol. 62A, p. 1060-1061.
- Novák, M., Černý, P. and Uher P., 2003, Extreme variation and apparent reversal of Nb-Ta fractionation in Columbite group minerals from the Scheibengraben beryl-columbite granitic pegmatite, Maršíkov, Czech Republic; *Eur. J. Mineral.*, Vol. 15, p. 565-574.
- Okuzawa, K. and Hisada, K., 2008, Temporal changes in the composition of Miocene sandstone related to collision between the Honshu and Izu Arcs, Japan, In; Draut, A.E., Clift, P.D. and Scholl, D.W. (eds.), *Formation and Applications of the Sedimentary Record in Arc Collision Zones*, Geological Society of America, Special Paper 436, p. 185-198.
- Parnell, J., 1999, Petrographic evidence for emplacement of carbon into Witwatersrand conglomerates under high fluid pressure, *Journal of Sedimentary Research*, Vol. 69, No. 1, p. 164-170.
- Phillipe, S., Lancelot, J. R., Clauer, N. and Pacquet, A., 1993, Formation and evolution of the Cigar Lake uranium deposit based on U-Pb and K-Ar isotope systematics, *Canadian Journal of Earth Sciences*, Vol. 30, p. 720-730.
- Phillips, G. N., 1987, Metamorphism of the Witwatersrand goldfields: conditions during peak metamorphism. *J. Metamor. Geol.*, Vol. 5, p. 307-322.
- Ramdohr, P., 1958, New observations on the ores of the Witwatersrand in South Africa and their genetic significance. *Transaction. Geol. Soc. of S. A.* Vol. 61, p. 1-50.
- Reimer, T. O. and Mossman, D. J., 1990, The Witwatersrand controversy revisited; *Economic Geology*, Vol. 85, No. 2, p. 337-343.

- Robb, L. J. and Robb, V. M., 1998, Gold in the Witwatersrand Basin, In: Wilson, M. G. C. and Anhaeusser, C. R. (eds.), *The Mineral Resources of South Africa, Sixth Edition, Handbook 16*, Council for Geoscience, p. 294-349.
- Robb, L. J. and Meyer, M., 1995, The Witwatersrand Basin, South Africa: Geological framework and mineralization processes, *Ore Geology Reviews* 10, p. 67-94.
- Robb, L. J., Landais, P., Meyer, F. M. and Davis, D. W., 1994, Nodular Organic matter in granites : implications for the origin of « kerogen » in the Witwatersrand Basin, South Africa ; *Exploration Mining Geology*, Vol. 3, p. 219-230.
- Robb, L. J. and Meyer, F. M., 1990, The nature of the Witwatersrand hinterland: Conjectures on the source-area problem, *Economic Geology*, Vol. 85.
- Robb, L. J. and Meyer, M., 1985a, Uranium distribution and concentration mechanism in the hinterland of the Wtwatersrand Basin, Ext. Abstr. Conf. on Concentration Mechanisms of Uranium in Geological Environments, Nancy, France, p. 105-110.
- Robb, L. J. and Meyer, M., 1985b, The nature of the Witwatersrand hinterland: conjectures on the source-area problem. Inform. Circ. Econ. Geol. Res. Unit, University of Witwatersrand, Johannesburg, 178, 25p.
- Robb, L. J., Brandl, G., Anhaeusser, C. R. and Pujol, M., 2006, Archean Granitoids Intrusions, In: Johnson, M. R., Anhaeusser, C. R. and Thomas, R. J. (eds.) *Geology of South Africa*, Council for Geoscience, Geological Society of South Africa, p. 57-94.
- Robb, L., Landais, P. and Drennan, G., 1995, Petrographic, chemical and spectroscopic studies on the metamorphic evolution of the Witwatersrand basin: Information Circular, Economic Geology Research Unit, University of the Witwatersrand, Vol. 296, p. 38-43.
- Robb, L. J., Landais, P., Meyer, F. M. and Davis, D. W., 1994, Nodular hydrocarbons in granites: implications for the origim of kerogen in the Witwatersrand Basin, South Africa. *Explor. Min. Geol.* 3, p.219-230.
- Robb, L. J., Davis, D. W., Kamo, S. L. and Meyer, F. M., 1992, Ages of altered granites adjoining the Witwatersrand Basin with implications for the source of gold uranium; *Nature*, Vol. 357, p. 677-680.
- Robb, L.J., Davis, D.W. and Kamo, S.L., 1991, Chronological framework for the Witwatersrand Basin and environs: towards a time constrained depositional model, *S. Afr. J. Geol.* 94, 86-95.
- Robb, L. J., Meyer, F. M., Ferraz, M. F. and Drennan, G. R., 1990a, The distribution of radioelements in Archean granites of the Kaapvaal Craton, with implications for the source of uranium in the Witwatersrand Basin, *South African Journal of Geology* 93 (1), p. 5-40.
- Robb, L. J., Davis, D. W. and Kamo, S. L., 1990b, U-Pb ages on single detrital zircon grains from the Witwatersrand Basin, South Africa: Constraints on the age of sedimentation and on the evolution of granites adjacent to the basin, *J. of Geol.*, Vol. 98, p. 311-328.
- Rundle, C. C. and Snelling, N. J., 1977, The geochronology of uraniferous minerals in the Witwatersrand Triad; an interpretation of new and existing U-Pb age data on rocks and minerals from the Dominion Reef, Witwatersrand and Ventersdorp Supergroups, *Phil. Trans. Royal Society of London*, Vol. 286, p. 567-583.
- Saager, R. and Stupp, H. D., 1983, U-Ti phases from Precambrian quartz-pebble conglomerates of the Elliot Lake area, Canada, and the Pongola basin, South Africa, *Mineralogy and Petrology*, Vol. 32, No. 2-3, p. 83-102.

- Safonov, Y. G. and Prokof'ev, V. Y., 2006, Gold-bearing reefs of the Witwatersrand Basin: a model of synsedimentation hydrothermal formation, *Geology of Ore Deposits*, Vol. 48, No. 6, p. 415-447.
- Schidlowski, M., 1981, Uraniferous constituents of the Witwatersrand conglomerates: ore-microscopic observations and implications for the Witwatersrand metallogeny, In: Armstrong, F. (ed.) *Genesis of uranium and gold-bearing quartz pebble conglomerates*, Professional Paper, United States Geological Survey, Vol. 1161, p. 1-29.
- Schmitz, M. D., Bowring, S. A., de Wit, M. J. and Gartz, V., 2004, Subduction and terrane collision stabilize the western Kaapvaal craton tectosphere 2.9 billion years ago; *Earth and Planetary Science Letters*, Vol. 222, p. 363-376.
- Simpson, P.R. and Bowles, J. F. W., 1977, Uranium mineralization of the Witwatersrand and Dominion Reef systems: *Phil. Trans. Royal Soc. London. Series A, Mathematical and Physical Sciences*, Vol. 286, p. 527-548.
- Stanistreet, I. S. and McCarthy, T. S., 1991, Changing tectono-sedimentary scenarios relevant to the development of the late Archaean Witwatersrand Basin. *Journal of African Earth Sciences*, Vol. 13, p. 65-81.
- Suzuki, K., Adachi, M. and Kazjizuka, I., 1994, Electron microprobe observations of Pb diffusion in metamorphosed detrital monazites, *Earth and Planetary Science Letter*, 128, p. 391-405.
- Taylor, S. R. and McLennan, S. M., 1995, The geochemical evolution of the continental crust; *Rev. Geophys.*, Vol. 33, p. 241-265.
- Taylor, S. R. and McLennan, S. M., 1985, *The Continental Crust: Its Composition and Evolution*, Blackwell, Oxford, 312 p.
- Tindle, A. G. and Breaks, F. W., 1998, Oxide minerals of the Separation rapids Rare-Element Granitic Pegmatite Group, Northwestern Ontario, *The Canadian Mineralogist*, Vol. 36, p. 609-635.
- Trumbull, R. B., 1993, A petrological and Rb-Sr isotopic study of an early Archean fertile granite-pegmatite system: the Sinceni pluton in Swaziland, *Precambrian Research*, Vol. 61, p. 89-116.
- Trumbull, R. B., 1995, Tin mineralization in the Archean Sinceni rare element pegmatite field, Kaapvaal Craton, Swaziland; *Economic Geology*; Vol. 90, No. 3, p. 648-657.
- Wallmach, T. and Meyer, F. M., 1990, A petrogenetic grid for metamorphosed aluminous Witwatersrand shales, *S. Afr. J. Geol.*, Vol. 93, p. 93-102.
- Wallmach, T., Meyer, F. M., Schweitzer, J. K. and Henkel, J., 1990, The stability of chloritoid, andalusite and pyrophyllite during very low grade metamorphism in metasediments of the Witwatersrand; *Ext. Abstr. Gecongress '90*, UCT, Cape Town.
- Wang, R. C., Fontan, F., Xu, S. J., Chen, X. M. and Monchoux, P., 1997, The Association of Columbite, Tantalite and Tapiolite in the Suzhou Granite, China, *The Canadian Mineralogist*, Vol. 35, p. 699-706.
- Williams, M. L., Jercinovic, M. J. and Hetherington, C. J., 2007, Microprobe Monazite Geochronology: Understanding Geologic Processes by Integrating Composition and Chronology, *Annual Review of Earth and Planetary Sciences*, Vol. 35, p. 137-175.
- Zhao, B., Robb, L. J., Harris, C. and Jordaan, L. J., 2006, Origin of hydrothermal fluids and gold mineralization associated with the Ventersdorp Contact Reef, Witwatersrand Basin, South Africa: Constraints from S, O, and H isotopes; *GSA Special Papers*, Vol. 405, p. 333-352.

## PARTIE 3.2

# Hydrothermal vs. detrital uraninite origin in the Elliot Lake quartz pebble conglomerates, Ontario, Canada: a chemical characterization using EMPA and SIMS

Isabelle Duhamel and Michel Cuney

*G2R, Nancy-Université, CNRS, CREGU, BP 239, 54506, Vandœuvre-lès-Nancy, France*

---

### Abstract

The Elliot Lake-Blind River uranium deposits from south-eastern Ontario are hosted in the basal quartz pebble conglomerates of the Huronian Supergroup deposited between 2.45 and 2.2 Ga. The detailed mineralogical study of 20 samples from the Quirke syncline in the Denison ores provides the recognition of four major stage of U mineralization. The earliest stage occurs as abundant angular to sub-rounded uraninite grains 100 to 300µm wide within heavy mineral beds composed of detrital pyrite, zircon, monazite and titanium oxides. These primary uraninite grains are then altered during a second mineralization stage with leaching of U and Pb from the crystal lattice mostly replaced by Si, and recrystallized into coffinite. The third stage is represented by micrometer-scale euhedral uraninite grains disseminated mostly within 100-500 µm large bitumen globules, and less commonly within the matrix of conglomerates. The last stage corresponds to (U,Th)-silicates and -titanates widespread in the clay matrix between the detrital grains with textural features showing clearly that these ultimate U-bearing phases are formed after sedimentation by alteration of the primary ores. In situ chemical characterization by electron microprobe revealed that stage I uraninite has moderate to high Th contents (3.89 to 10.60 wt% ThO<sub>2</sub>) and therefore derived from the erosion of a granitic source. On the contrary, uraninite from stage III has no Th and is formed by precipitation from hydrothermal aqueous solutions mainly on kerogen acting as a reducing trap. The primary uraninite has undergone alteration that partly reset its U-Pb isotopic system at  $1766 \pm 39$  Ma (SIMS), an age corresponding to the regional metamorphism during the Penokean orogeny (~1.9-1.7 Ga). The high thorium, yttrium (mY = 3.13 wt%) and rare earth element (mΣREE = 1.64 wt%) concentrations measured by SIMS and the chondrite-normalized REE patterns of primary uraninite grains demonstrate that the magmatic source was highly fractionated and corresponds most probably to partial melting of metasediments. The source area was possibly from the north-western Ontario where Late Archean peraluminous S-type granites of the Superior Province have preserved magmatic uraninite.

---

### Keywords

Ontario, Elliot Lake, Paleoproterozoic, Huronian, Paleoplacer, detrital uraninite, rare earths, hydrothermal remobilization, kerogen.

## Introduction

Quartz-pebble conglomerate-type uranium deposits are hosted in fluvial sedimentary sequence which deposition is restricted from 3.1 to 2.22 Ga and lie on Archean crystalline, metasedimentary and metavolcanic basement rocks. The uranium ores are represented mainly by euhedral to sub-rounded uraninite grains occurring in basal channel facies with other heavy minerals dominated by pyrite. The detrital origin of uraninite and pyrite in conglomerates has long been used as a strong argument to decipher the reducing character of the Archean atmosphere. The rounded shape of pyrite and uraninite, the radiometric ages of the grains indicating older data than the sedimentation and the lack of Mass Independent Fractionation (MIF) of sulphur isotopes strongly support the detrital origin (Frimmel, 2005). However, the origin of uraninite has remained controversial because even if the mineralization seems to be sedimentological controlled, post-sedimentary hydrothermal remobilizations have been evidenced as secondary alteration minerals related to diagenesis (brannerite, thucholite, pitchblende) or vein-like structures parallel to shears or thrusts (Kyser and Cuney, 2008).

The scope of this work is to better constrain the discrimination between sedimentary versus hydrothermal origin of uranium mineralization in the quartz pebble conglomerate uranium deposits. The Blind River-Elliot Lake district located in southern Ontario (Canada) represents the best chance to find uraninite concentrations because of the high grade uranium-bearing conglomerate averaging 0.08-0.09 %U and the good preservation of the rocks only weakly metamorphosed. Textural and mineralogical characteristics of the ore, U-Pb isotopic dating of uraninite and chemical composition of U-bearing minerals are used to identify the processes involved in the formation of the deposits. The geochemical signature of uraninite from conglomerates measured in situ with high precision instruments (EMPA and SIMS) is compared to other uranium oxides crystallized in well constrained geological conditions and provide clues to constrain the characteristics of the uranium source. The ultimate issue of this study is to contribute to the debate of the oxygen level in the pre 2.2 Ga atmosphere on the Earth.

## Geological setting

The Elliot Lake quartz pebble conglomerates are located in the Canadian Shield within the Matinenda Formation which forms the basal unit of the Paleoproterozoic Huronian Supergroup. The Huronian sequence is exposed as a long folded belt along the northern shore of the Lake Huron at the boundary between the Archean Southern and Superior Provinces (Fig. 3.2.1).

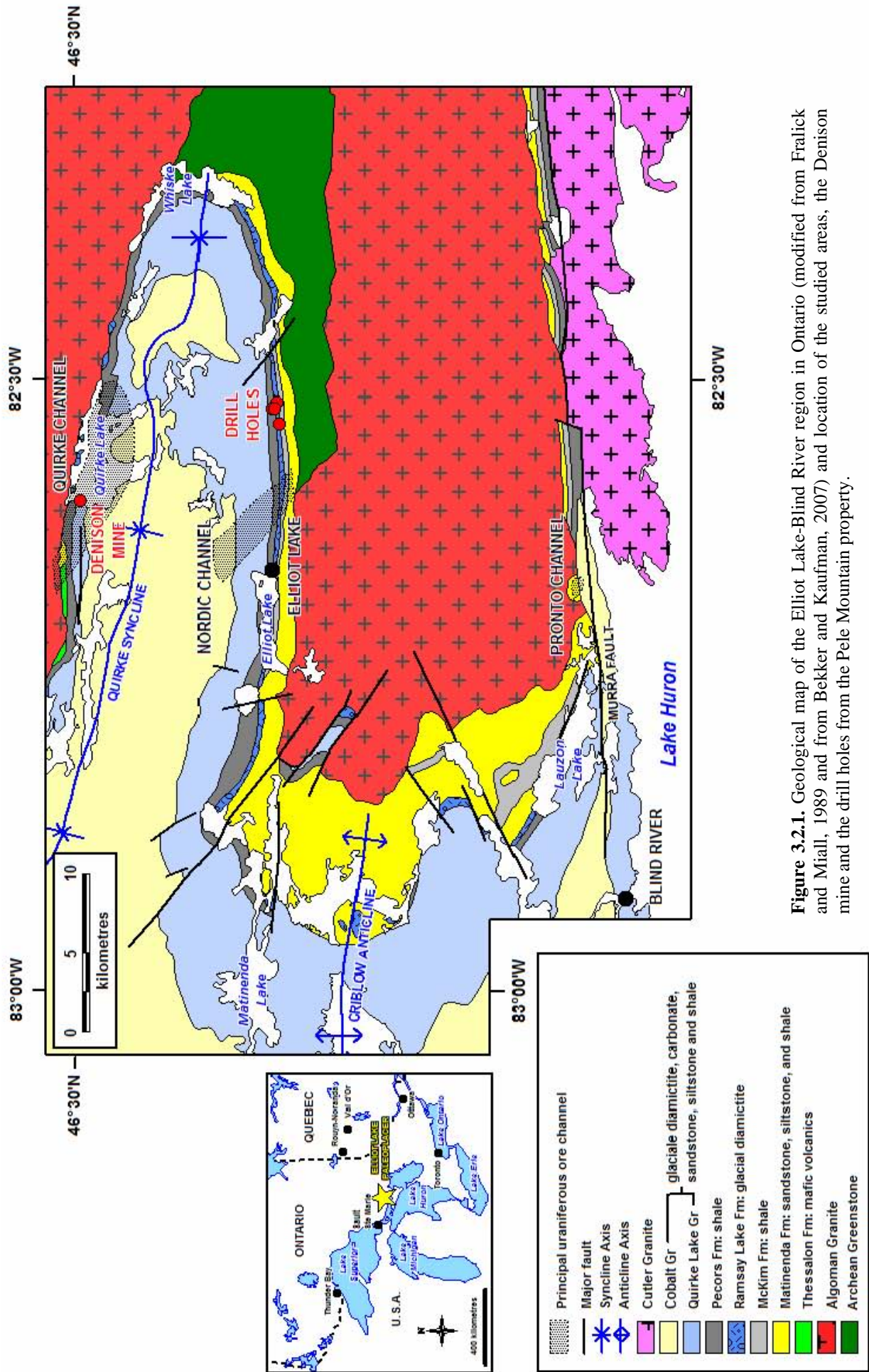


Figure 3.2.1. Geological map of the Elliot Lake-Blind River region in Ontario (modified from Fralick and Miall, 1989 and from Bekker and Kaufman, 2007) and location of the studied areas, the Denison mine and the drill holes from the Pele Mountain property.

The clastic sediments lie unconformably upon the erosional surface of Archean greenstone (metavolcanic and metasedimentary) rocks and granites. The lower Huronian Group starts with the basal bimodal volcanics of the Livingstone Creek and Thessalon formations and is overlain by the fluvial quartzites of the Matinenda Formation (conglomerates, sandstones and siltstones) and the turbidites of the upper McKim Formation (Fig. 3.2.2; Young, 1995; Bekker and Kaufman, 2007).

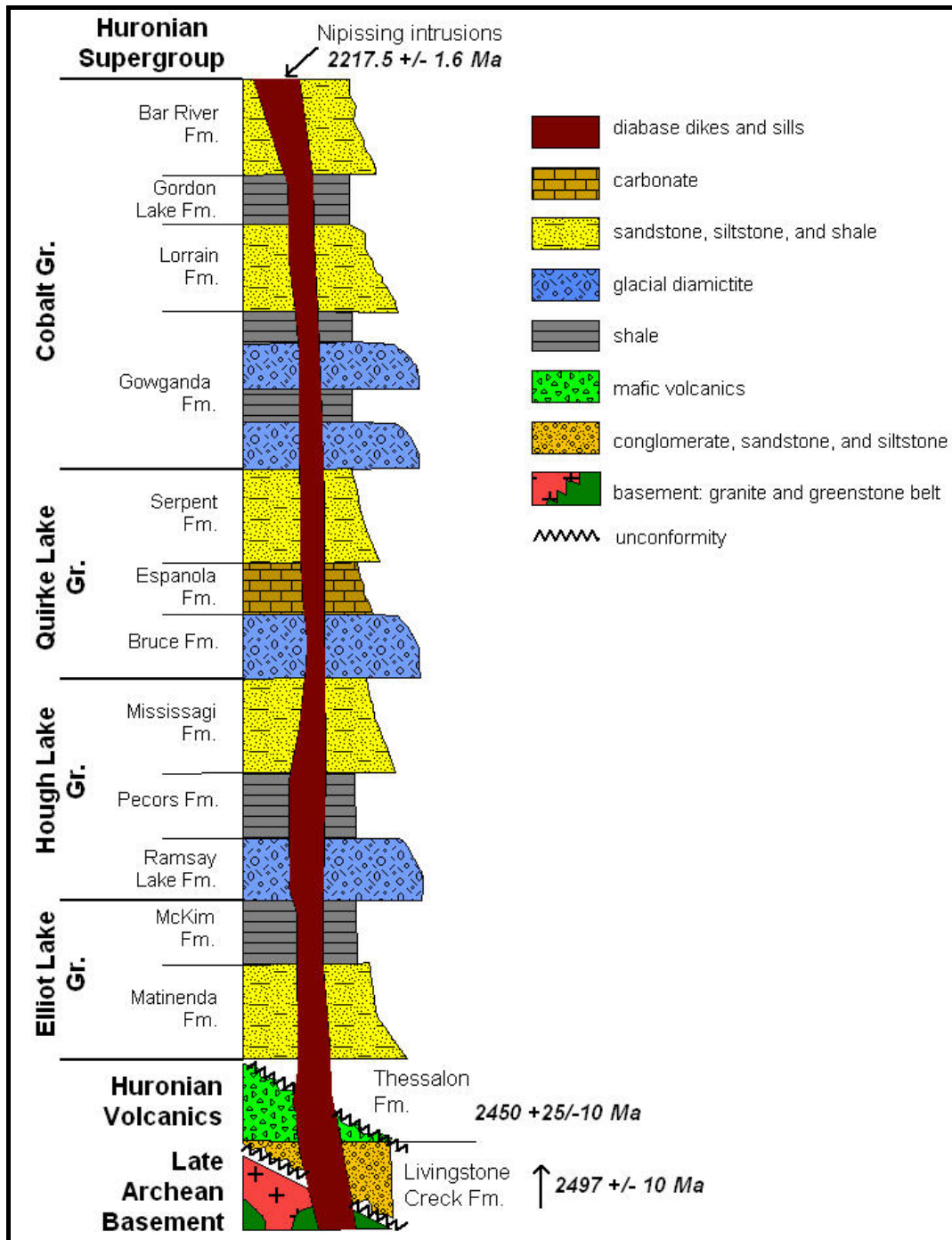


Figure 3.2.2. Stratigraphic column of the Huronian Supergroup in the Elliot Lake-Blind River area (modified from Bekker and Kaufman, 2007). Ages correspond to isotopic dating provided in the volcanic rocks that constrain the Huronian deposition between 2.45 and 2.22 Ga (data from Krogh et al., 1984, Andrews et al., 1986, Buchan et al., 1998 and Rainbird and Davis, 2006).

The lower Huronian formations are interpreted to be deposited during passive rifting of a continental margin during the breakup of the Archean supercontinent Kenorland (Bennett et al., 1991; Young, 1995). The age of deposition of the Huronian formations is bracketed by the basal volcanics dated at ca. 2,450 +25/-10 Ma (Andrews et al., 1986) and the intrusion of dykes and sills of the Nipissing diabase which crosscut them ca. 2,217-2,210 Ma (Krogh et al., 1984; Buchan et al., 1998). The area is deformed with pluri-kilometric folds striking east-west and shallowly dipping to the west. These large-scale folds are formed during an extensional regime resulting in gravity-controlled mass movements (Young, 1995). The extensional event happens prior to ~2.22 Ga because the Nipissing dykes are not deformed. Then, low-grade metamorphism occurred during the Penokean Orogeny (~1.9-1.7 Ga) which corresponds to a northwest-directed compressional regime induced by the collision between the Wisconsin magmatic arc, bordering the southern ancient North America Craton, and the northern Superior Craton, which actual suture is located along the Niagara fault zone (Sims et al., 1989). This orogen involves shearing, secondary folding and major faulting in the back-arc basin where the deposits are located. The Huronian sedimentary formations filling the basin are then truncated to the east by the Grenville Front (ca. 1.3-1.0 Ga) and are covered to the south by Paleozoic sediments and the Great Lakes.

The uraniferous quartz pebble conglomerates of the Elliot Lake-Blind River area, south-east of Sault St-Marie, have been discovered in 1947 (Abraham, 1953). They have produced 138,500 tons of uranium metal between 1958 and 1996 with an average grade of 0.08 to 0.09%U. Reserves are about 450,000 tonnes U. The uranium ore is located within various quartz pebble conglomerate horizons interbedded with arkose and sandstone forming the Matinenda Formation deposited in high energy braided fluvial systems during several regressive cycles (Bennett, 2006). The paleocurrents measured in the lower part of the Huronian Supergroup, in both McKim and Matinenda formations, indicate paleoslope to the south-southeast (Fralick and Miall, 1982 and 1989; Long, 1995; Bekker and Kaufman, 2007). The basal conglomerate unit is discontinuous laterally because of complex fault systems through the basement rocks dislocating the sedimentary cover. Uranium mineralization is confined to conglomerates consisting of well-rounded and well-sorted quartz (> 95% of the pebble fraction) and chert pebbles in a matrix of quartz, feldspar, sericite and pyrite (Cuney and Kyser, 2008).

The radioactive minerals are mostly represented by uraninite, brannerite and uranothorite accompanying heavy mineral beds with pyrite, monazite and zircon (Roscoe, 1969). Minor coffinite, xenotime and gummite have also been observed (Mossman 1999). Heavy minerals yielded U/Pb ages of  $2550 \pm 50$  Ma for uraninite (Meddaugh and Holland, 1981), 2500 Ma for monazite and 2450 Ma for zircon (Mair et al. 1960), all indicative of an Archean granitic source.

Uraninite occurs primarily as small clusters of grains between pebbles and in monomineralic subparallel bands of well-sorted angular grains concentrated proximal to the base of small-scale depositional units within conglomerate (Cuney and Kyser, 2008). Brannerite is amorphous U-Ti-oxides supposedly resulting from the reaction between altered ilmenite and uraninite grains. Highly radioactive bitumen called thucholite (Ellsworth, 1928) is also common in the ore but represent a small proportion of the U mineralization. Two origins for thucholite have been advanced: one considering it as fossil algal mats of cyanobacteria or a methanogenic source biota that were trapped by rapid sediment deposition and transformed in situ into kerogen with burial of the sedimentary pile and the other as remobilized compounds resulting from the hydrous pyrolysis of kerogen derived from the maturation of organic matter initially present in the McKim Formation and having migrated during diagenesis contemporaneously with U-rich fluids (Willingham et al., 1985; Goodarzi et al., 1993; Mossman et al., 1993a). U-Pb isotopic dating of kerogen yielded an upper intercept at  $2139 \pm 100$  Ma corresponding to the Nipissing thermal event (Mossman et al., 1993b). A late stage of mineralization is also supported by the presence of abundant euhedral autigenic pyrite which secondary origin has been proven by sulphur isotopic composition in  $\delta^{34}\text{S}$  and  $\delta^{32}\text{S}$  showing large variations of the mass-independent fractionation or MIF (Yamaguchi and Ohmoto, 2006).

U enrichment in conglomerates correlates with the increase of quartz-pebble size and with abundance of pyrite (Theis 1979, Roscoe 1969). The distribution of the uranium ores are sedimentary controlled within major channels corresponding to topographic depressions during time of deposition (Abraham, 1953; Roscoe, 1969) and considering the previous mineralogical observations and geochronological works the deposits are considered to be modified paleoplacer-type with hydrothermal remobilization of U (Derry, 1960; Robertson and Steenland, 1960; Robinson and Spooner, 1982; Mock and Ohmoto, 1997; Ono et al., 1998; Yamaguchi et al., 1998).

### **Sampling and analytical methods**

Twenty samples were collected in the Quirke syncline from two occurrences (see location in Fig. 3.2.1): (1) an underground exposure at the Denison mine (shaft 2 ~ 800 m depth) in the main uraniferous Quirke channel and (2) four drill holes from the Pele Mountain property between the Whiske and Elliot lakes. Each occurrence is located along a side of the Quirke syncline, the northern and southern flanks respectively. All the samples belong to the Matinenda Formation which is mainly represented by quartzite interlayered with 10 cm to 5 m thick

conglomeratic beds. In this region, the Matinenda Formation lies directly on the Archean basement and its total thickness may reach 300 m. The four drill cores collected in 2007 are : PM25 (UTM: 381865.5 Easting, 5137661.0 Northing) which reaches the basal regolith at 129.95 m depth, PM36 (UTM: 382842.7 Easting, 5137945.0 Northing) showing a basal conglomerate in contact with the Archean volcanics just above a clay-rich shear zone at a depth of 130.56 m, PM45 (UTM: 383208.1 Easting, 5137827.5 Northing) with the main mineralized conglomerate reef localized between 66.04 m and 66.45 m depth, and PM53 (UTM: 382846.3 Easting, 5138117.9 Northing) reaching Archean volcanics at a depth of 203.3 m. The drill holes, which are located in an area of less than 2 kilometres, indicate a large variation of the thickness of the Huronian which is relevant of block movements along complex tectonic structures conducting to differential erosion of certain areas. Drill-core samples were selected according to their high radioactivity measured with a SPP2 scintillometer in counts per second (cps). The background of the Matinenda quartzite was comprised between 100 and 120 cps. The conglomeratic beds were always more radioactive with an average around 200-250 cps and rising up to 450 cps in the main mineralized conglomerate reef (sample 138553 from drill hole PM45 at 66.2 m depth).

Samples were sawn and thirty one polished thin sections have been prepared at the lithopreparation laboratory of the Nancy University (France). The mineralogy of the uraniferous quartz pebble conglomerates has been studied in transmitted and reflected lights using a polarizing microscope Olympus BX51.

Chemical composition and textures of the U-bearing minerals were analysed at the SCMEM laboratory (Nancy-University) using both scanning electron microscope Hitachi-FEG S4800 coupled with an energy dispersive spectrometer Noran Vantage (SEM-EDS) and an electron microprobe (CAMECA-SX100). Polished thin sections were carbon-coated and backscattered electron (BSE) imaging was performed with the SEM-EDS to reveal composition variations. The variations of average atomic number in the minerals give a corresponding variation of grey intensities in the BSE images: the brighter domains corresponding to higher atomic weight average number. Semi-quantitative analyses by scanning the sample surface during 15 minutes with the SEM-EDS were also performed to map major element distribution. The quantitative major and trace element composition of the minerals were then determined by in situ electron microprobe analyses (EMPA). They were performed with an accelerating voltage of 20 kV for monazite and 15 kV for other minerals, a beam current of 10 nA, and a 2  $\mu$ m beam diameter. Four wavelength-dispersive spectrometers (WDS) equipped of analyser crystals (TAP: thallium acid phthalate, LPET: large pentaerythriol, PET: pentaerythriol, LIF: LiF and PC1: multilayered W-Si) have been used to analyse a large series of elements selected according to the

nature of the analyzed mineral (Al, Si, S, K, P, Ca, Na, V, Fe, Mg, Mn, Mo, Ta, Ti, Zr, Y, Pb, U, Th, La, Ce, Pr, Nd, Sm, Gd and Dy). The accurate composition of the minerals was determined using comparison with both natural and synthetic standards (albite, orthose, hematite, wollastonite, olivine, Mo metal, V metal, SrSO<sub>4</sub>, ZrO<sub>2</sub>, UO<sub>2</sub>, ThO<sub>2</sub>, PbCrO<sub>4</sub>, LiTaO<sub>3</sub>, MnTiO<sub>3</sub>, LaPO<sub>4</sub>, YPO<sub>4</sub>, CePO<sub>4</sub>, PrPO<sub>4</sub>, NdPO<sub>4</sub>, SmPO<sub>4</sub>, GdTIGe and DyRu<sub>2</sub>Ge<sub>2</sub>). The counting times was between 5 and 30 seconds per element, the longer time being used for the low concentrations and especially to obtain a higher precision on the determination of U, Th and Pb contents. The relative errors on each element measurements are below 1%.

To take into account the proportions of the elements in the structural formulae, the results in weight percent (wt.%) have been recalculated in atomic percent (at.%). The chemical ages of U-bearing minerals for each EMPA were calculated using the following equation derived from the radioactive decay law (modified from Bowles, 1990 after Cocherie and Albarède, 2001 and Pommier et al., 2002):

$$C_{Pb} = C_{Th} \left[ \frac{M_{208Pb}}{M_{232Th}} (e^{\lambda_{232}t} - 1) \right] + C_U \left[ 0.9928 \frac{M_{206Pb}}{M_{238U}} (e^{\lambda_{238}t} - 1) + 0.0072 \frac{M_{207Pb}}{M_{235U}} (e^{\lambda_{235}t} - 1) \right]$$

where  $t$  is the age of mineral crystallisation,  $C_{Pb}$ ,  $C_{Th}$  and  $C_U$  are concentrations (in ppm) converted from the Pb, Th and U contents measured by EMPA in weight percent,  $M_{206Pb}$  (205.97445 g.mol<sup>-1</sup>),  $M_{207Pb}$  (206.97588 g.mol<sup>-1</sup>),  $M_{208Pb}$  (207.97664 g.mol<sup>-1</sup>),  $M_{232Th}$  (232.03805 g.mol<sup>-1</sup>),  $M_{235U}$  (235.04392 g.mol<sup>-1</sup>),  $M_{238U}$  (238.05078 g.mol<sup>-1</sup>) are molar masses, and  $\lambda_{232}$  ( $0.049475 \times 10^{-9} \text{ y}^{-1}$ ),  $\lambda_{238}$  ( $0.155125 \times 10^{-9} \text{ y}^{-1}$ ) and  $\lambda_{235}$  ( $0.98485 \times 10^{-9} \text{ y}^{-1}$ ) are the decay constants of <sup>232</sup>Th, <sup>238</sup>U and <sup>235</sup>U respectively. This relation is used assuming that <sup>235</sup>U, <sup>238</sup>U and <sup>232</sup>Th produce the totality of the lead present in the analyzed spot (<sup>207</sup>Pb+<sup>206</sup>Pb+<sup>208</sup>Pb) so Pb is considered to be entirely of radiogenic origin, there was no common lead incorporated in the mineral during its crystallization. The detailed methodology is generally described for monazite chemical dating (Suzuki et al., 1994; Montel et al., 1996; Cocherie and Albarède, 2001, Williams et al., 2007) but it is also available for other uraniumiferous minerals as uraninite (Kempe, 2003; Alexandre and Kyser, 2005). The U, Th and Pb concentrations measured by EMPA permit to solve the equation by iteration determining one chemical age for each single spot analysed. The main limitations of this method is the uncertainty on the presence of common lead and the open system behaviour of lead in some uranium bearing minerals but its interest is to provide a test on the homogeneity of radioelement distribution within the minerals for the selection of the best preserved areas and a first estimation of an age which can be close to the crystallization of the mineral if the crystal has remained a closed system.

Ion microprobe analyses by secondary ion mass spectrometry (SIMS) of U and Pb isotopes for the dating of uranium minerals were performed at the CRPG (CNRS, Nancy, France) using a CAMECA IMS-3f instrument. A beam of negatively charged oxygen atoms is focused on to the gold-coated surface of the polished sample. Ions sputtered from a spot size between 20  $\mu\text{m}$  to 50  $\mu\text{m}$  of the uraninite grain are accelerated by an electrical field and separated magnetically into the different atom species by the mass spectrometers. The precise isotopic composition is quantified using a specific standard presenting the closest analogy with the analyzed mineral, for each set of isotopes or elements. U and Pb isotopes were measured using a Katanga uraninite standard from Zambia dated by TIMS and SIMS at  $540 \pm 4$  Ma (Holliger, 1988; Cathelineau et al., 1990). The  $^{206}\text{Pb}/^{238}\text{U}$  and  $^{207}\text{Pb}/^{235}\text{U}$  ratios of each analysis were plotted in a Concordia diagram using the ISOPLOT flowsheet of Ludwig (1999) with the Microsoft EXCEL software. The discordia line intersections were calculated in order to define the lowermost MSWD (mean square weighted deviation) value. The isotopic ages are given with uncertainties at the  $1\sigma$  level.

A recent technique, the in situ determination of Y and REE abundances by SIMS using the same previous ion microprobe has been developed successfully by Bonhoure and co-authors (Bonhoure et al., 2007) to characterize the uranium oxide chemistry from different uranium occurrences. The concentrations and the REE distribution patterns appear to be characteristic from the processes involved in the formation of the crystals and differ for each type of uranium deposits (unconformity-type deposits, syn-metamorphic deposits related to albitisation, vein-type deposits, volcanic caldera-related deposits, magmatic deposits in granitoids). A uraninite standard from the Mistamisk Valley in Canada (Kish and Cuney, 1981) was used to calculate the Y and REE concentrations of uraninite from the Elliot Lake quartz pebble conglomerates. REE fractionation in uraninite is of major importance because these elements can be incorporated in the lattice during crystallisation thanks to their equivalent ion radii with  $\text{U}^{4+}$  (close to 1 Å) and most of them are not sensitive to changes in redox conditions (Bonhoure et al., 2007). The experimental procedure, the instrument calibration and the calculation methodology are exposed in detail by Bonhoure et al. (2007). Two mass molecular interferences cannot be resolved with the elements Gd and Yb, their abundances were thus calculated using the concentrations of the two rare earth elements having the closest ionic radii as follow:  $\text{Gd}^* = \text{Sm} + 2/3\text{Tb}$  and  $\text{Yb}^* = (\text{Tm} + \text{Lu})/2$ . The REE abundances are then normalized to chondrite values from Anders and Grevesse (1989) for the drawing of the REE patterns.

## Mineralogy of the uranium ore

The conglomerates of the Matinenda Formation hosting the U mineralization are mainly composed of quartz pebbles within a matrix represented by a mixture of more or less altered feldspar (plagioclase, orthoclase and microcline) quartz and sericite and dispersed heavy minerals (Fig. 3.2.3). The conglomerates are very poorly sorted, well packed with pebbles generally elongated along the strata, but phyllosilicates within the matrix are sometimes oriented across the stratigraphy. The heavy minerals and mainly opaques form sometimes dark layers a few millimetres to three centimetres thick. The most radioactive beds are very rich in sulphides, mostly pyrite with minor chalcopyrite and galena.

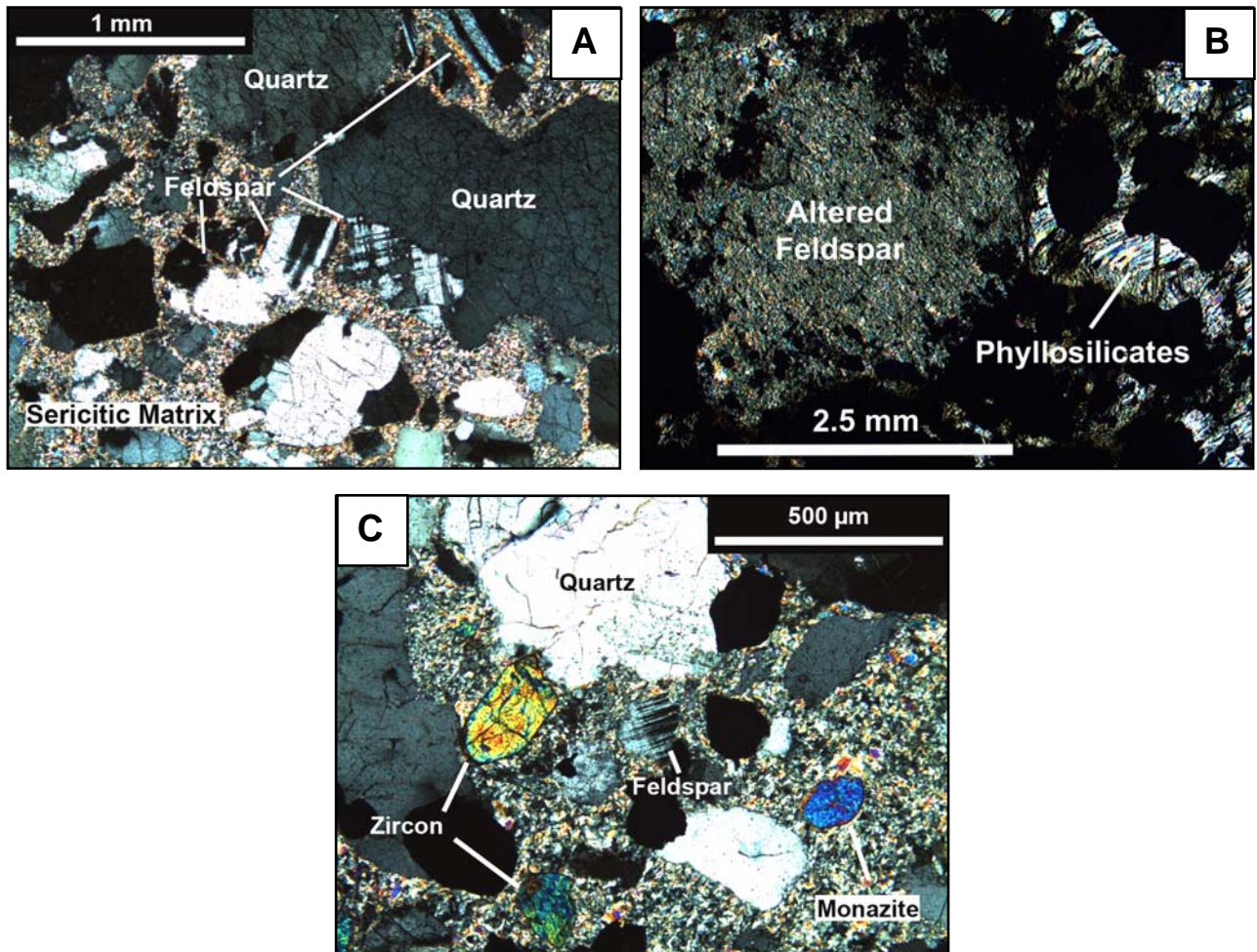


**Figure 3.2.3.** Petrographic images in polarized transmitted light showing (A) the different grain sizes of the common minerals constituting the matrix of the Matinenda conglomerates: quartz, orthoclase feldspar and plagioclase in a sericitic groundmass (sample 138538, drill hole PM53, depth 181.1 m), (B) a sericitized feldspar phenocrystal and opaque accessories within an oriented phyllosilicate matrix (sample BP72-102 from the Denison mine) and (C) zircon and monazite grains dispersed with opaque minerals, quartz and feldspar in the argillaceous fine-grained matrix (sample 138538).

On the basis of the petrographic study, the textural relations observed by SEM and the nature of the uranium mineral assemblage, four stages are distinguished:

(1) The first stage, only observed in the main Quirke channel sampled at the Denison mine, is represented by uraninite grains disseminated in the matrix between the quartz pebbles together with sub-rounded to subhedral grains of quartz, pyrite, titanium oxides and minor amounts of zircon and monazite. The heavy mineral laminations may contain up to 30% of uraninite grains (Fig. 3.2.4). The uraninite grains are angular to sub-rounded and are 100  $\mu\text{m}$  to 300  $\mu\text{m}$  large (Fig. 3.2.5). Some of these uraninite grains are surrounded by overgrowths of secondary idiomorphic pyrite and chalcopyrite (Fig. 3.2.6). The zircon grains show a distinct zoning related to the crystal growth and sometime underlined by metamictized zones (Fig. 3.2.7). Monazite grains show homogeneous average atomic number in BSE mode with however widespread lighter grey domains corresponding to Th- and Si-rich areas along fractures (Fig. 3.2.8). The titanium oxides have a  $\text{TiO}_2$  stoichiometry in SEM-EDS analysis and a distinct internal texture in BSE images showing typical rutile twinning defining angles of  $60^\circ$  between three sets of elongated needles that derive probably from the alteration of ilmenite crystals (Fig. 3.2.9). This texture may be inherited from the dissolution of titano-magnetite as observed in the Witwatersrand Basin deposits (Law and Phillips, 2006).

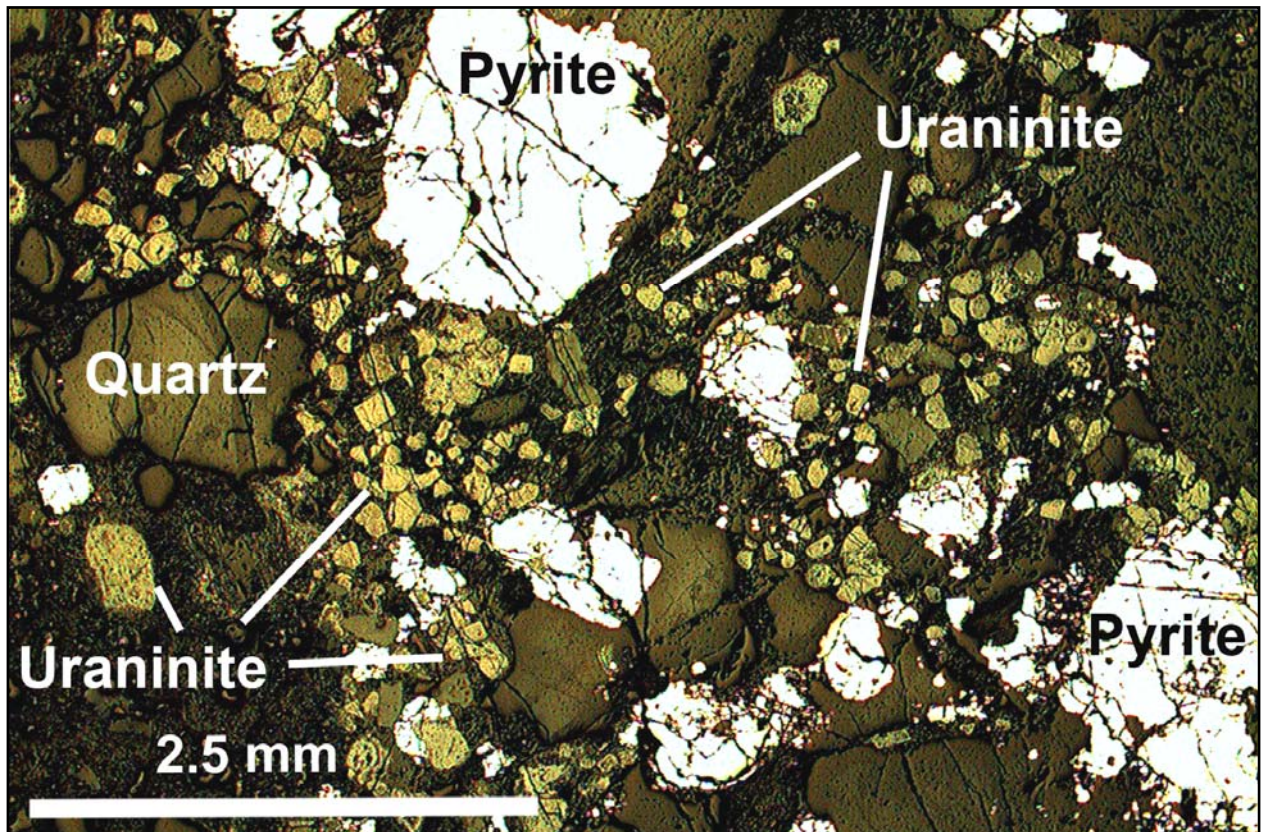


**Figure 3.2.4.** Petrographic image in reflected light showing abundant angular to well rounded uraninite grains with pyrite and quartz (sample BP72-102 from the Denison mine).

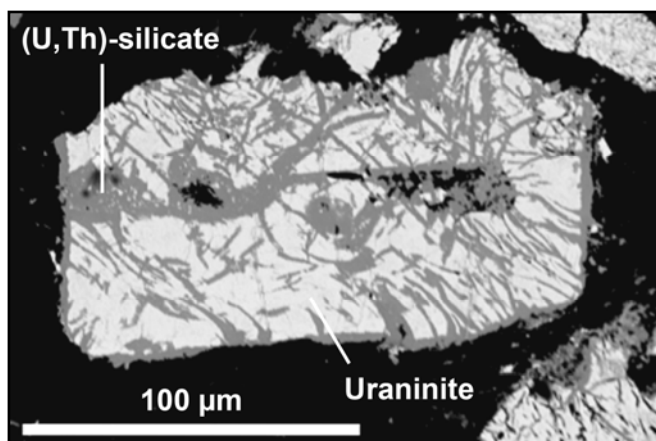


**Figure 3.2.5.** BSE image of an early uraninite grain (sample BP72-102 from the Denison mine). The medium grey areas correspond to lower average atomic number domains associated to alteration and recrystallization into (U,Th)-silicates.

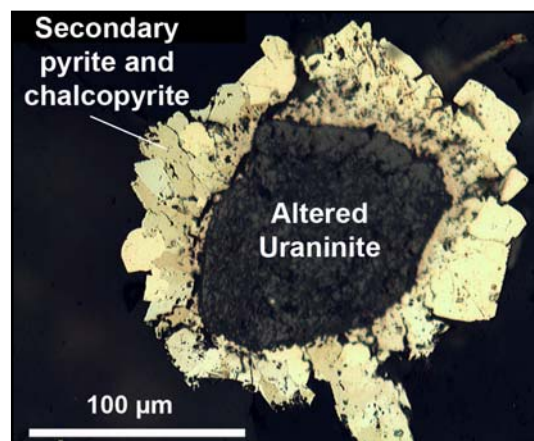


**Figure 3.2.6.** Petrographic image in reflected light of a sub-rounded early uraninite grain (dark grey mineral in the middle) and secondary crystallization of pyrite (light yellowish reflection) and chalcopyrite (darker brownish reflection) coming from a fracture at the bottom of the picture (sample BP72-102 from the Denison mine).

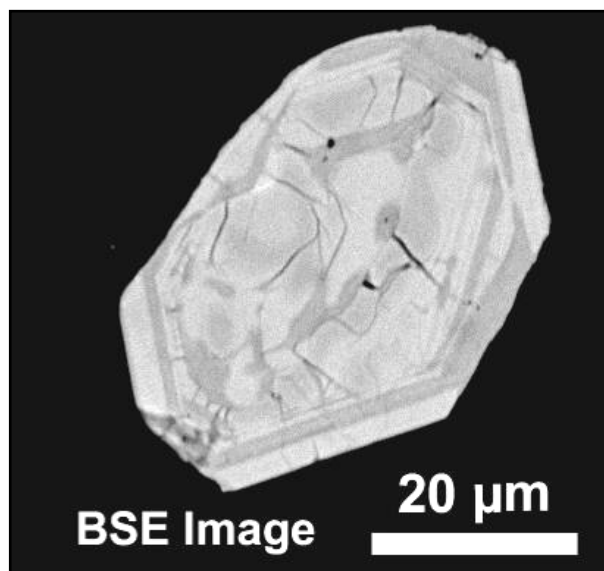
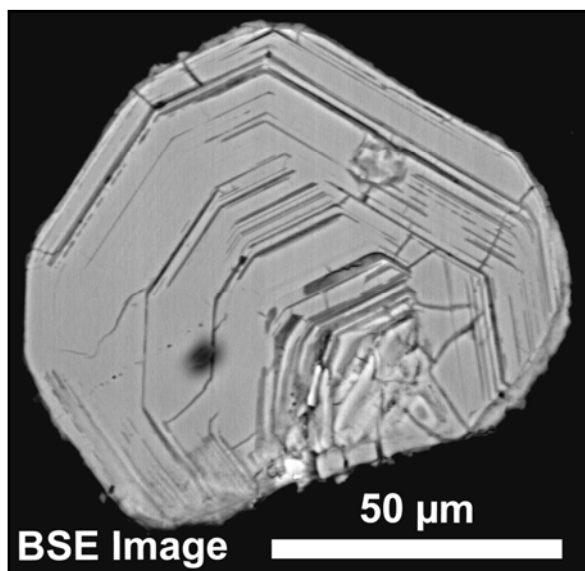


**Figure 3.2.7.** Two zircon grains showing well developed crystal growth zonation in BSE mode imaging (left: sample 138547 from drill hole PM25 at 103.8m depth; right: sample 138538 from drill hole PM53 at 181.1m depth).

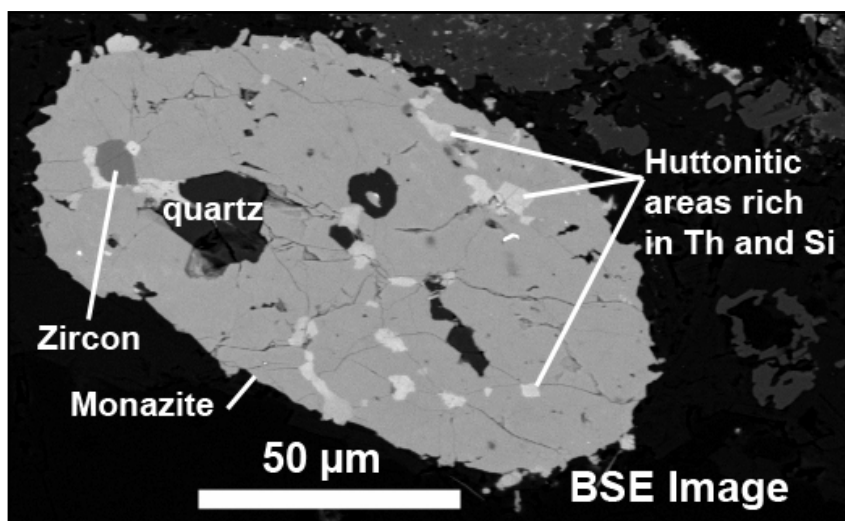


**Figure 3.2.8.** Monazite grain showing huttonitic areas (lighter grey) associated to microfracturation and inclusions of quartz (darker grey) and zircon (medium grey) in BSE mode (sample 138538 from drill hole PM53 at 181.1m depth).

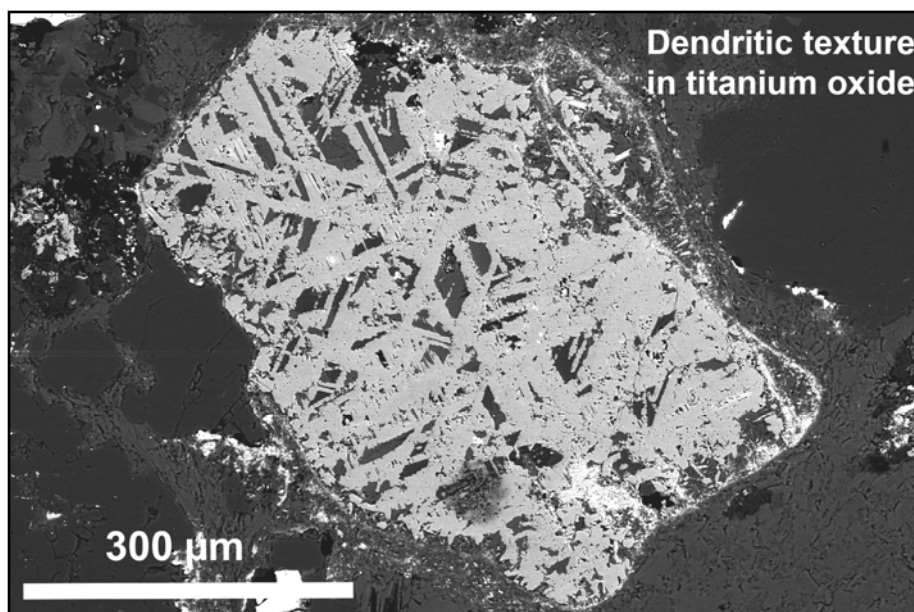


**Figure 3.2.9.** Titanium oxide showing a typical dendritic texture in BSE mode corresponding to web of rutile silks (sample 138553 from drill hole PM45 at 66.2m depth).

(2) The second stage corresponds to the alteration of the uraninite crystals. The alteration is particularly visible in BSE images with darker grey zones mainly at the margin of the crystals and along microcracks (Fig. 3.2.5). These darker grey areas are richer in light element abundances, mostly in Si and poorer in U and Pb.

(3) The third stage corresponds to uranium associated with carbonaceous matter generally named thucholite by previous authors. The carbonaceous matter appears generally globular ranging between 100  $\mu\text{m}$  and 500  $\mu\text{m}$  in diameter and is composed of low reflectivity, amorphous and isotropic material (Fig. 3.2.10). Most of time globules show a surrounding shrinkage gap and internal shrinkage microcracks suggesting that they were probably initially oil droplets converted into solid bitumen (Fig. 3.2.12). Euhedral uraninite grains ranging between 1 to 3  $\mu\text{m}$  large are commonly widespread within the carbonaceous matter (Fig. 3.2.11 and 3.2.12). This association has been observed in all studied samples and the globules are widespread within the conglomerates with no clear relation with the sedimentation bedding. Therefore, the carbonaceous matter is interpreted as being of secondary origin compared to the carbonaceous-free uraninite grains which represent an early mineralization deposited along sedimentary beds in sample BP72-102 from the Denison mine (Fig. 3.2.4) where no carbonaceous seam has been observed although they have been described by previous authors in this locality (Willingham et al., 1985). Authigenic pyrite overgrowths generally occur around the bitumen with galena filling microcracks (Fig. 3.2.13).

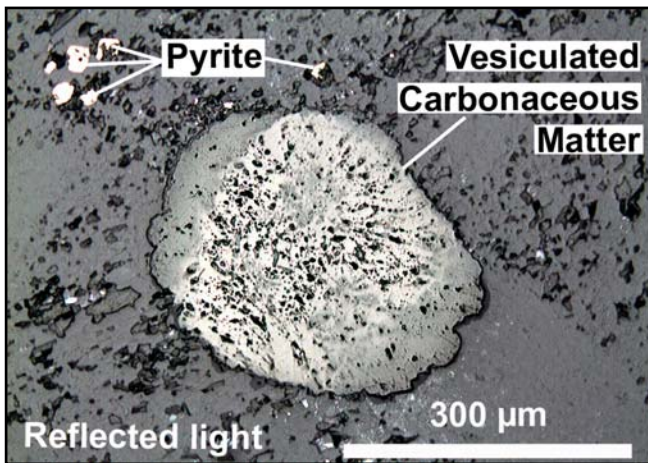


**Figure 3.2.10.** Petrographic image of a vuggy carbonaceous matter globule in reflected light (sample 138547 from drill hole PM25 at 103.8m depth).

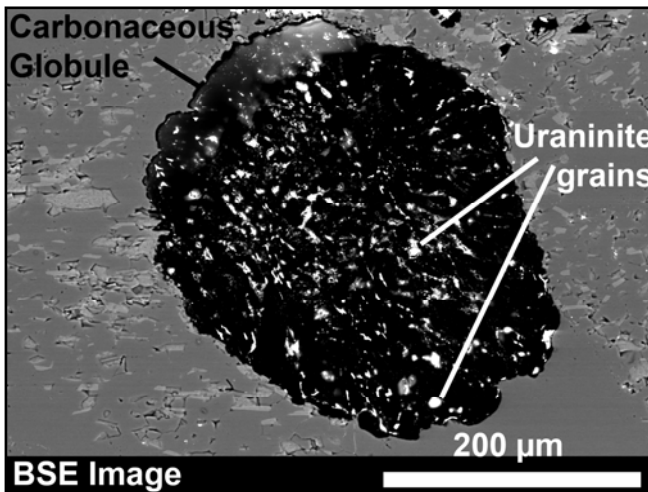


**Figure 3.2.11.** BSE image of previous carbonaceous matter globule showing disseminated uraninite crystals (sample 138547).

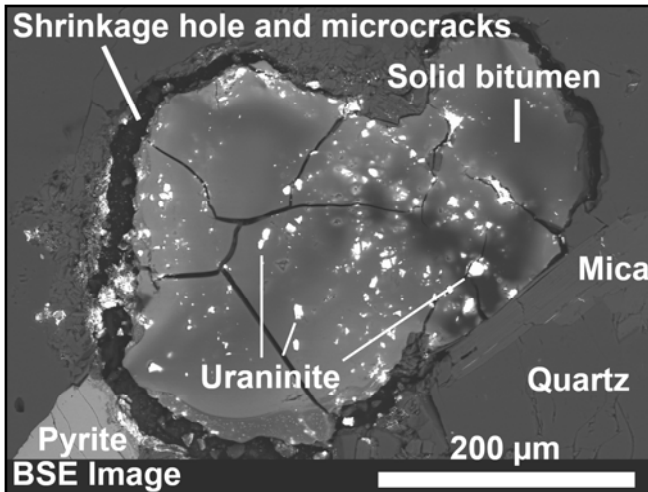


**Figure 3.2.12.** BSE image of solid bitumen showing a surrounding retraction gap, shrinkage microcracks and small uraninite crystals (sample 138553 from drill hole PM45 at 66.2m depth).

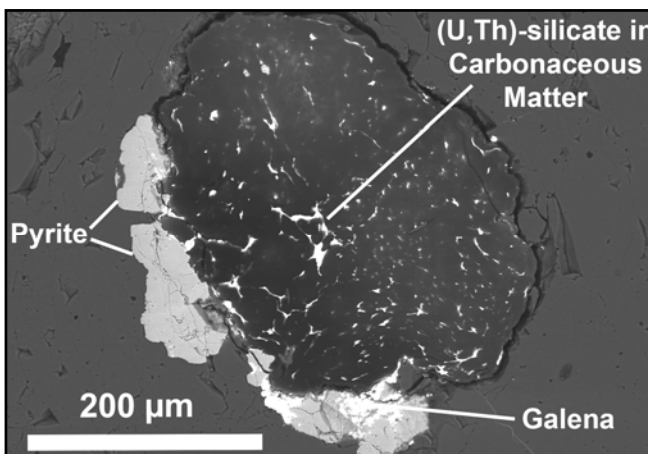


**Figure 3.2.13.** BSE image of kerogen with widespread (U,Th)-silicates and later crystallisation of pyrite and galena (sample 138548 from drill hole PM25 at 128.8m depth).

(4) A last type of U mineralization is represented by (U,Th)-silicates and -titanates widespread within the matrix but are preferentially concentrated around the earlier uranium phases.

The U-Th-Si phases surround the small euhedral uraninite grains within carbonaceous matter or fill cavities within the globules but are generally poorly crystallized (Fig. 3.2.13). In the matrix, amorphous U-silicates impregnated by hematite fill the intergranular space between epigenetic idiomorphic pyrite crystals (Fig. 3.2.14) and interfingered within clay minerals (Fig. 3.2.15). U-silicates are often observed intimately mixed with hematite which suggests a late hydrothermal oxidizing fluid circulation. Some minor occurrences can be better crystallized as the little pseudo-hexagonal globular overgrowths around pyrite crystals (Fig. 3.2.16). EDS analyses indicate a mixture between U, Ca, Si and P that probably reflects coffinite pseudomorphs after ningyoite  $[\text{CaU}(\text{PO}_4)_2 \cdot 1-2\text{H}_2\text{O}]$  a common epigenetic U mineralization observed in other sediment-hosted deposits (Boyle, 1982; Hansley and Fitzpatrick, 1989; Utsunomiya et al., 2008).

The (U,Th)-titanates are preferentially located close to the association between early uraninite and titanium oxide grains. The textures observed by SEM in the elementary mapping (Fig. 3.2.17) clearly shows a relation between the primary grains and the intergranular U-titanates. The subhedral uraninite grains show variations of grey colour intensity, the darker grey areas correspond to higher K, P and Ca contents with traces of Fe, Ti, S, Si and Al, but with low U and Pb contents. The large Ti-oxide phase (about the same size as the uraninite crystals) is strongly altered with no internal structure but presents widespread inclusions of galena crystals aggregate as nodules. Uraninite and Ti-oxides are embedded in a clay matrix with elevated K, Al and Si contents probably related to the presence of illite. The U-Th-Ti phases deposited around the U- and Ti-oxides detrital grains have a heterogeneous composition and present minor amounts of K and P. The (U,Th)-titanate phase seems to result from the redeposition of uranium and titanium leached out from the primary minerals by fluids. This phenomenon  $\text{UO}_2 + 2\text{TiO}_2 \rightarrow \text{UTi}_2\text{O}_6$  associated with the newformation of brannerite has been named the Pronto reaction by Ramdhor and has been described previously in the deposit (Saager and Stupp, 1983; Farrow and Mossman, 1988).

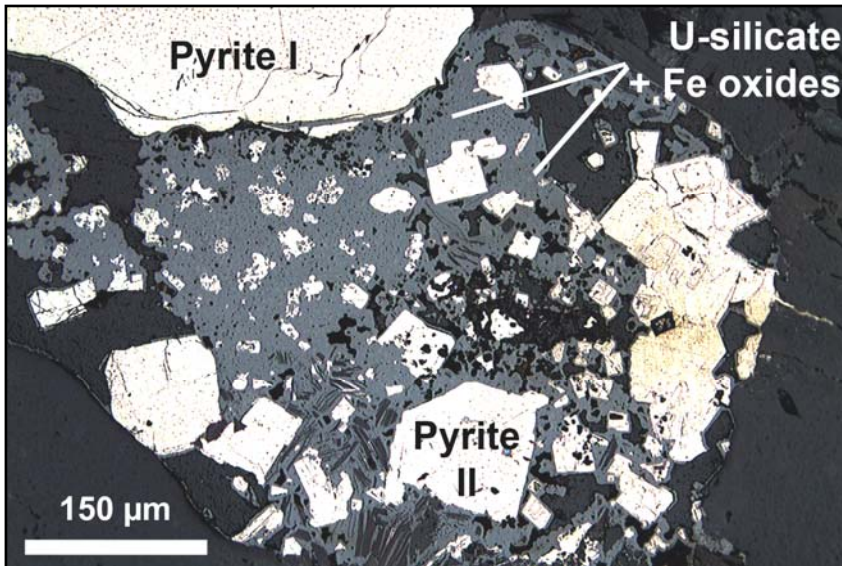


**Figure 3.2.14.** Petrographic image in reflected light of two generations of pyrite (stage I: rounded detrital grain and stage II: epigenetic idiomorphic crystals) with interstitial mixture of U-silicate and hematite (sample 138549 from drill hole PM25 at 128.3m depth).

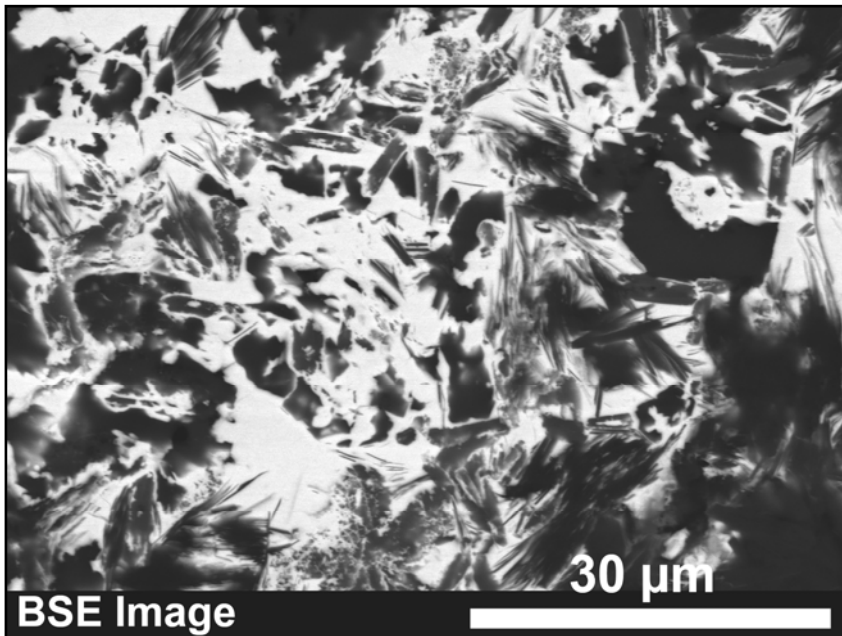


**Figure 3.2.15.** BSE image of U-Th-Si phase (light) interfingers with clay minerals in the matrix of conglomerate (sample 138553 from drill hole PM45 at 66.2m depth).

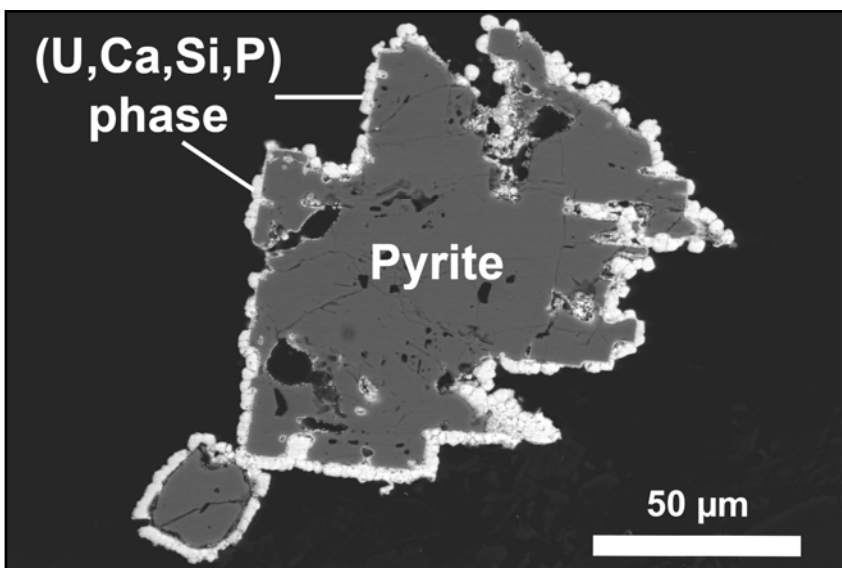


**Figure 3.2.16.** BSE image of pyrite with overgrowing globular crystals of complex U-bearing phase (sample 138548 from drill hole PM25 at 128.8m depth).

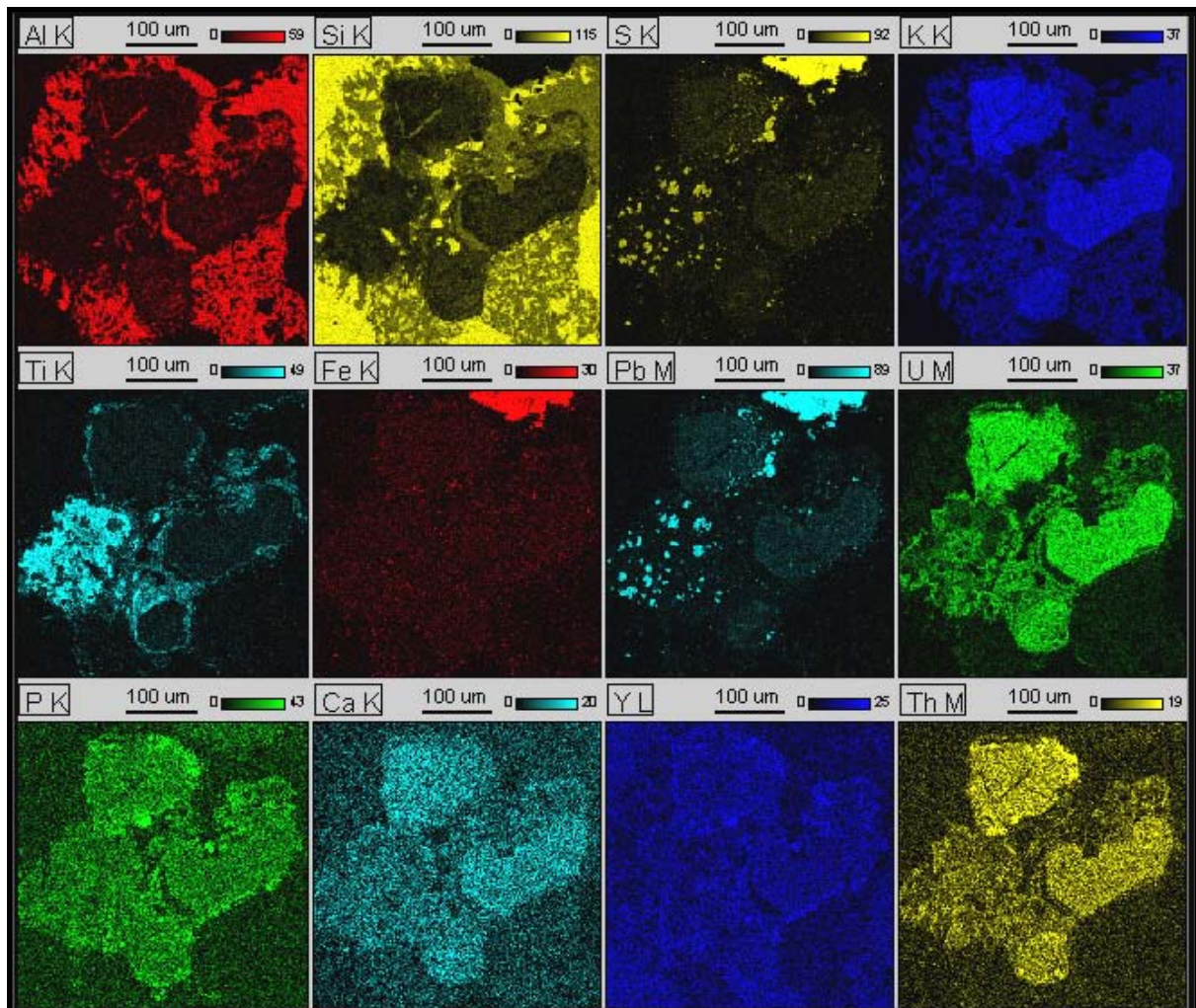
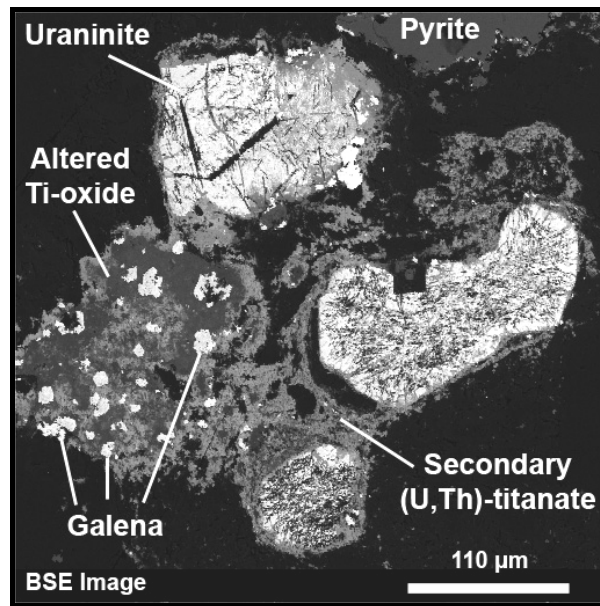


**Figure 3.2.17.** BSE image and related elementary mapping by SEM-EDS of the Pronto reaction occurring between early uraninite and Ti-oxide grains producing interstitial (U,Th)-titanates when altered together (sample BP72-102 from the Denison mine).

## Chemical characterization of the uranium mineralization

The electron microprobe analysis performed in the different U-bearing minerals from the Matinenda Formation have been synthesised in Table **3.2.1** and classified by their order of appearance in the paragenetic sequence.

Monazite grains accompanying the early uraninite in the first stage of mineralization display generally two distinct zones in BSE imaging (Fig. **3.2.8**), a large homogeneous grey part associated to main mineral areas and small light grey zones corresponding to local enrichment in Th and Si contents. The main monazite has an average composition dominated by LREE ( $15.55 \pm 2.83$  wt%  $\text{La}_2\text{O}_3$  -  $30.93 \pm 2.11$  wt%  $\text{Ce}_2\text{O}_3$  -  $2.54 \pm 0.38$  wt%  $\text{Pr}_2\text{O}_3$  -  $11.58 \pm 2.27$  wt%  $\text{Nd}_2\text{O}_3$ ) and phosphorous ( $28.49 \pm 1.02$  wt%  $\text{P}_2\text{O}_5$ ) with minor amounts of yttrium ( $0.54 \pm 0.39$  wt%  $\text{Y}_2\text{O}_3$ ), silicium ( $1.00 \pm 0.57$  wt%  $\text{SiO}_2$ ) and calcium ( $0.35 \pm 0.17$  wt%  $\text{CaO}$ ). It host also minor thorium contents ranging from 0.45 to 5.53 wt%  $\text{ThO}_2$  ( $m = 2.75 \pm 1.25$  wt%). The lightest areas show an increase of Th and Si contents with up to 15.93 wt%  $\text{ThO}_2$  and 16.20 wt%  $\text{SiO}_2$  and a decrease of the analytical total ( $m = 91.16 \pm 3.97$  wt%) associated probably to hydration of the mineral. In the binary diagram (Th+U+Si) vs. (REE+Y+P) (Fig. **3.2.18**) monazite composition plots almost perfectly along the line between monazite-(Ce) for the darker homogeneous domain and the light areas tend to the huttonite composition. This vector represents huttonitic substitution  $(\text{Th,U})\text{SiREE}_{-1}\text{P}_{-1}$  with REE and P losses (Förster, 1998). Huttonitic-rich monazite-(Ce) is commonly found in transitional I-S type biotite and two-mica granites or in post-collision A-type affinity granites (Förster, 1998 and reference therein). The high  $\text{ThO}_2$  contents in monazite are generally characteristic of low-Ca peraluminous granites ranging generally from 6 to 12 wt% and exceptionally up to 15 wt% (Cuney and Friedrich, 1987).

The chemical ages calculated from the U, Th and total-Pb contents of the monazite crystals show a wide range repartition ranging from 0 to 907 Ma for huttonitic composition and between 531 Ma and 2931 Ma with a peak at about 1.8 Ga for main Monazite-(Ce) (Fig. **3.2.19**). The enrichment in Th and Si in huttonitic areas is clearly related to a late event. The four oldest ages obtained in the main monazite-(Ce) areas ( $2561 \pm 11$  Ma,  $2571 \pm 11$  Ma,  $2596 \pm 10$  Ma and  $2931 \pm 11$  Ma) prove the detrital origin of the monazite grains and their derivation from a source rock older than the Huronian sedimentation (maximum age of deposition  $\sim 2.45$  Ga) but the scattered younger results show the high degree of alteration of the monazite crystals. Nevertheless, the number of monazite analyses (42) is not sufficient to be representative of the detrital monazite grain populations within the Matinenda Formation and further EMPA analyses of individual grains would be necessary to discriminate accurate ages for the source rocks or alteration events.

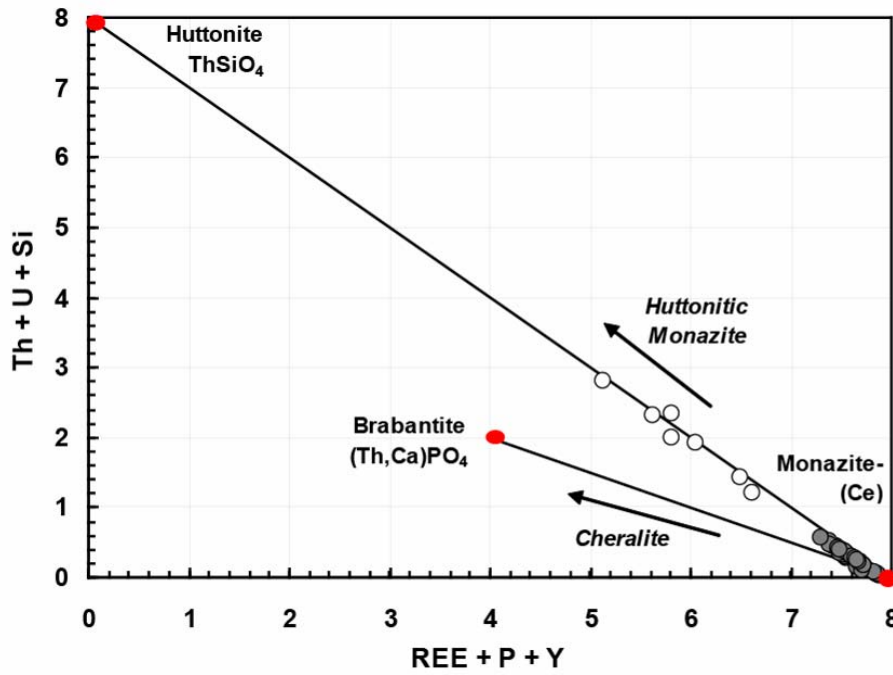


**Figure 3.2.18.** Plot of (Th+U+Si) vs. (REE+Y+P) calculated in formula proportions on the basis of 16 O atoms after Förster (1998). Monazite group minerals are reported in red circles with molar abundance of huttonite, brabantite and monazite-(Ce). Filled grey circles represent sain monazite from the Elliot Lake conglomerates whereas open circles represent lighter zones with huttonitic composition (sample 138538 from drill hole PM53 at 181.1m depth).

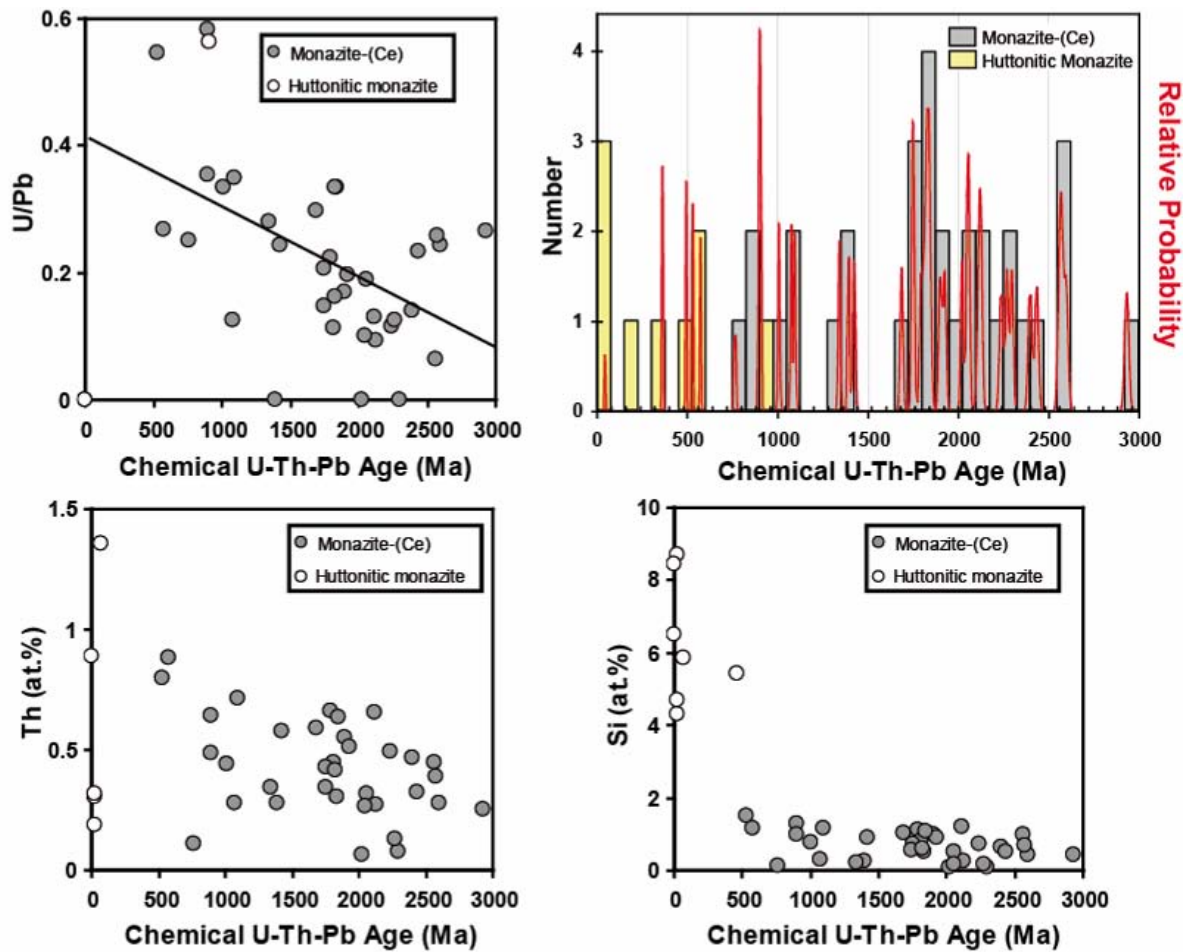


**Figure 3.2.19.** U/Pb ratio, Th and Si contents (in atomic percent) vs. chemical ages (Ma) calculated after the methodology of Cocherie and Albarede (2001) from in situ EMPA measurements of U, Th and Pb contents in 20 monazite grains and relative probability histogram showing the scattered results.

**Table 3.2.1.** Average chemical composition of the different U-bearing phases observed in the quartz pebble conglomerates of the Matinenda Formation (EMPA in weight percent measured by electron microprobe CAMECA SX100).

Mineralization Phase	STAGE I		STAGE II		STAGE III		STAGE IV		
	Monazite		Early Uraninite	Alteration and recrystallization of Early Uraninite		Secondary Uraninite		(U,Th)-silicates	U-Ti phases
Form and Occurrence	Sub-rounded grains		Angular to sub-rounded grains	Altered areas in Early Uraninite (low BSE)	Coffinite surrounding the Early Uraninite	Small euhedral crystals (1-3 µm large)		Widespread filling porosity of the matrix and the vesicles of bitumen	Filling intergranular space and quoting grains exclusively close to early uraninite and Ti-oxides
Average	Monazite-(Ce) (low BSE)	Huttonitic Monazite (high BSE)	Well preserved areas (high BSE)	11 EMPA ± 1σ	11 EMPA ± 1σ	within the Solid Bitumen Globules (very common)	within the matrix (more rarely)	45 EMPA ± 1σ	12 EMPA ± 1σ
Average	35 EMPA ± 1σ	7 EMPA ± 1σ	212 EMPA ± 1σ	11 EMPA ± 1σ	11 EMPA ± 1σ	26 EMPA ± 1σ	7 EMPA ± 1σ	45 EMPA ± 1σ	12 EMPA ± 1σ
wt. %									
Al <sub>2</sub> O <sub>3</sub>	<D.L.	1.81 ± 4.84	<D.L.	1.03 ± 0.57	2.28 ± 2.21	0.11 ± 0.09	0.12 ± 0.11	0.78 ± 0.66	0.68 ± 0.28
SiO <sub>2</sub>	1.00 ± 0.57	9.59 ± 3.34	0.88 ± 0.71	10.04 ± 3.40	16.52 ± 3.04	0.67 ± 0.41	0.48 ± 0.17	12.80 ± 5.13	5.83 ± 2.16
SO <sub>2</sub>	N.D.	N.D.	0.67 ± 0.73	0.64 ± 0.58	0.84 ± 1.09	0.21 ± 0.35	0.15 ± 0.23	0.93 ± 0.77	0.57 ± 1.11
K <sub>2</sub> O	N.D.	N.D.	0.19 ± 0.04	0.23 ± 0.08	0.41 ± 0.43	0.28 ± 0.09	0.24 ± 0.03	0.19 ± 0.08	<D.L.
P <sub>2</sub> O <sub>5</sub>	28.49 ± 1.02	20.06 ± 2.85	<D.L.	0.95 ± 0.88	1.62 ± 1.87	1.00 ± 0.89	0.89 ± 0.85	6.68 ± 3.83	<D.L.
CaO	0.35 ± 0.17	0.68 ± 0.27	1.13 ± 0.36	0.90 ± 0.21	0.73 ± 0.22	1.20 ± 0.81	1.43 ± 0.11	2.07 ± 1.07	1.64 ± 0.45
Na <sub>2</sub> O	N.D.	N.D.	<D.L.	<D.L.	<D.L.	0.23 ± 0.13	0.17 ± 0.10	<D.L.	<D.L.
V <sub>2</sub> O <sub>3</sub>	N.D.	N.D.	<D.L.	<D.L.	<D.L.	<D.L.	<D.L.	<D.L.	<D.L.
FeO	<D.L.	<D.L.	<D.L.	<D.L.	<D.L.	0.38 ± 0.27	1.51 ± 0.95	0.55 ± 0.68	1.45 ± 1.31
MgO	N.D.	N.D.	<D.L.	<D.L.	<D.L.	<D.L.	<D.L.	<D.L.	<D.L.
MnO	<D.L.	<D.L.	<D.L.	<D.L.	<D.L.	<D.L.	<D.L.	<D.L.	<D.L.
MoO <sub>3</sub>	N.D.	N.D.	<D.L.	<D.L.	<D.L.	<D.L.	<D.L.	<D.L.	<D.L.
Ta <sub>2</sub> O <sub>5</sub>	N.D.	N.D.	<D.L.	<D.L.	<D.L.	<D.L.	<D.L.	<D.L.	<D.L.
TiO <sub>2</sub>	<D.L.	<D.L.	0.09 ± 0.12	2.46 ± 4.55	7.64 ± 6.06	<D.L.	<D.L.	0.11 ± 0.16	42.71 ± 4.68
ZrO <sub>2</sub>	<D.L.	<D.L.	<D.L.	<D.L.	<D.L.	<D.L.	<D.L.	<D.L.	<D.L.
Y <sub>2</sub> O <sub>3</sub>	0.54 ± 0.39	1.24 ± 0.10	2.04 ± 0.80	2.32 ± 1.60	3.66 ± 3.20	<D.L.	<D.L.	4.40 ± 1.20	0.61 ± 0.35
PbO	0.22 ± 0.10	<D.L.	15.23 ± 2.73	6.39 ± 4.90	1.84 ± 2.63	5.82 ± 2.19	5.63 ± 2.80	1.61 ± 2.71	1.47 ± 0.94
UO <sub>2</sub>	0.06 ± 0.04	0.53 ± 0.43	66.13 ± 2.84	55.70 ± 8.81	48.78 ± 10.65	84.44 ± 4.55	85.90 ± 0.65	45.80 ± 16.12	32.14 ± 3.54
ThO <sub>2</sub>	2.75 ± 1.25	7.17 ± 5.89	7.06 ± 0.93	7.28 ± 5.18	1.94 ± 1.44	0.29 ± 0.49	<D.L.	10.82 ± 11.44	2.36 ± 0.72
La <sub>2</sub> O <sub>3</sub>	15.55 ± 2.83	11.63 ± 2.46	<D.L.	<D.L.	<D.L.	<D.L.	<D.L.	0.10 ± 0.05	<D.L.
Ce <sub>2</sub> O <sub>3</sub>	30.93 ± 2.11	23.46 ± 3.26	<D.L.	0.35 ± 0.15	0.21 ± 0.20	<D.L.	<D.L.	0.81 ± 0.21	1.15 ± 0.53
Pr <sub>2</sub> O <sub>3</sub>	2.54 ± 0.38	1.73 ± 0.19	N.D.	N.D.	ND.	ND.	ND.	ND.	ND.
Nd <sub>2</sub> O <sub>3</sub>	11.58 ± 2.27	8.09 ± 1.15	<D.L.	<D.L.	<D.L.	<D.L.	<D.L.	1.03 ± 0.29	0.86 ± 0.53
Sm <sub>2</sub> O <sub>3</sub>	1.67 ± 0.80	1.28 ± 0.38	N.D.	N.D.	ND.	ND.	ND.	ND.	ND.
Gd <sub>2</sub> O <sub>3</sub>	0.82 ± 0.42	0.77 ± 0.25	N.D.	N.D.	ND.	ND.	ND.	ND.	ND.
Dy <sub>2</sub> O <sub>3</sub>	N.D.	N.D.	<D.L.	<D.L.	<D.L.	<D.L.	<D.L.	0.74 ± 0.20	<D.L.
<b>Total</b>	96.84 ± 1.48	91.16 ± 3.97	95.03 ± 1.31	89.89 ± 3.61	88.67 ± 2.30	95.55 ± 3.84	97.63 ± 2.80	89.57 ± 3.24	92.52 ± 2.13

**Notes:** N.D. = not determined; <D.L. = below detection limit (for monazite: Al = 0.09 wt%; Si = 0.05 wt%; P = 0.06 wt%; Ca = 0.07 wt%; Fe = 0.15 wt%; Mn = 0.16 wt%; Ti = 0.04 wt%; Zr = 0.20 wt%; Y = 0.12 wt%; Pb = 0.14 wt%; U = 0.04 wt%; Th = 0.04 wt%; La = 0.16 wt%; Ce = 0.19 wt%; Pr = 0.14 wt%; Nd = 0.19 wt%; Sm = 0.14 wt%; Gd = 0.24 wt% - for other U-bearing phases: Al = 0.06 wt%; Si = 0.06 wt%; S = 0.11 wt%; K = 0.11 wt%; P = 0.06 wt%; Ca = 0.08 wt%; Na = 0.11 wt%; V = 0.16 wt%; Fe = 0.20 wt%; Mg = 0.04 wt%; Mn = 0.21 wt%; Mo = 0.12 wt%; Ta = 0.21 wt%; Ti = 0.07 wt%; Zr = 0.20 wt%; Y = 0.12 wt%; Pb = 0.12 wt%; U = 0.57 wt%; Th = 0.11 wt%; La = 0.07 wt%; Ce = 0.29 wt%; Nd = 0.54 wt%; Dy = 0.65 wt%); « low » and « high » BSE refer to low and high average atomic number areas in BSE imaging respectively.

The uraninite grains from the first stage have also shown distinct zones with different average atomic number domains in BSE images (example in Fig. 3.2.5) that were analysed separately by electron microprobe (Table 3.2.1). A total of 212 EMPA were performed in the brightest domains which are the richest in U and Pb and correspond to the best preserved parts of the uraninite crystals. The average composition of these uraninites present high concentrations of uranium ( $66.13 \pm 2.84$  wt%  $\text{UO}_2$ ), lead ( $15.23 \pm 2.73$  wt%  $\text{PbO}$ ), thorium ( $7.06 \pm 0.93$  wt%  $\text{ThO}_2$ ) and yttrium ( $2.04 \pm 0.80$  wt%  $\text{Y}_2\text{O}_3$ ). Small but significant concentrations of calcium, silicium, sulphur, potassium and titanium have been also measured in some analytical spots and explain the high standard deviation values obtained for these elements. The P, Na, V, Fe, Mg, Mn, Mo, Ta, Zr and REE concentrations are always under the detection limits of the electron microprobe. The Th and Y concentrations in the pristine areas range from 3.89 to 10.60 wt%  $\text{ThO}_2$  and from 0.36 to 4.56 wt%  $\text{Y}_2\text{O}_3$ . The plot of Th vs. Y concentrations measured in individual grains of pristine uraninite domains (Fig. 3.2.20) shows a predominant family of crystals with both high Th and Y contents (Th >2 at% or  $\text{ThO}_2$  >6 wt% and Y >1 at% or  $\text{Y}_2\text{O}_3$  > 1.5 wt%) and only rare crystals with lower concentrations. The high Th contents in uraninite is symptomatic of its crystallization at high temperature in magmatic melt (Cuney and Friedrich, 1987). It is remarkable to find only one grain (#2 in red) with both low Th and Y contents (m =  $1.38 \pm 0.09$  wt%  $\text{ThO}_2$  and  $0.5 \pm 0.10$  wt%  $\text{Y}_2\text{O}_3$ ) that suggest a distinct source.

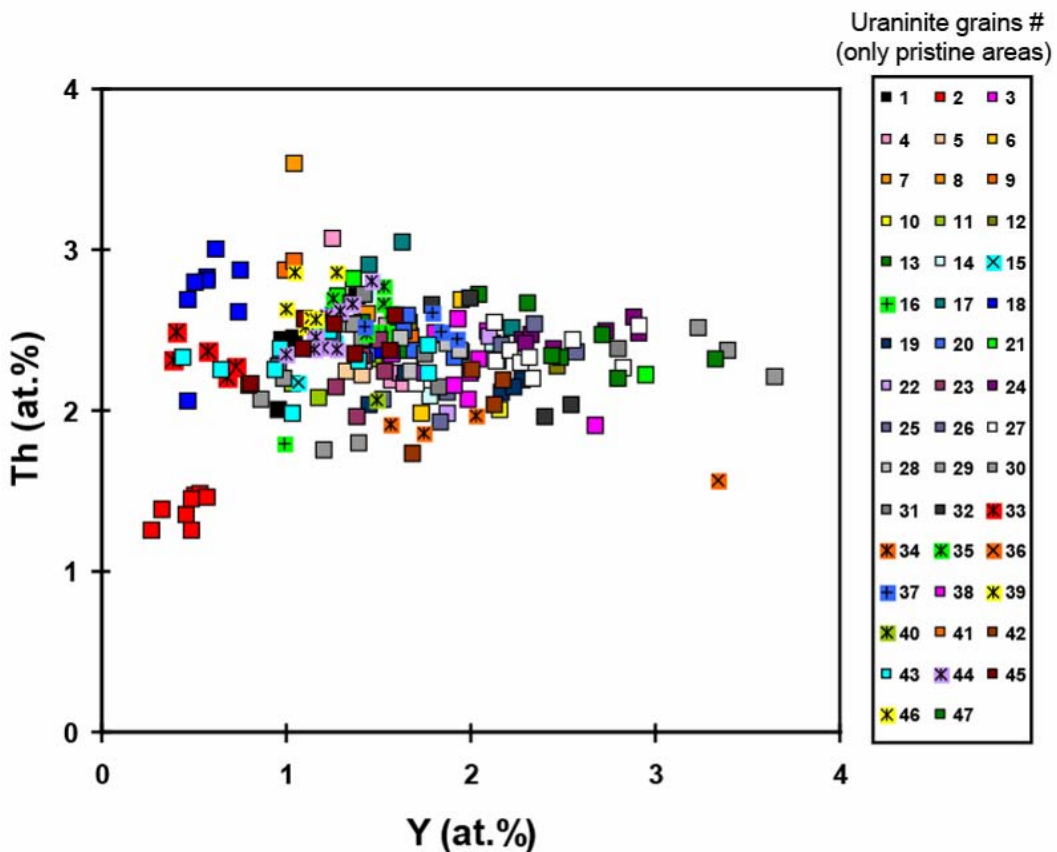


Figure 3.2.20. Binary diagram showing Th vs. Y contents (in atomic percent) of individual grains of uraninite.

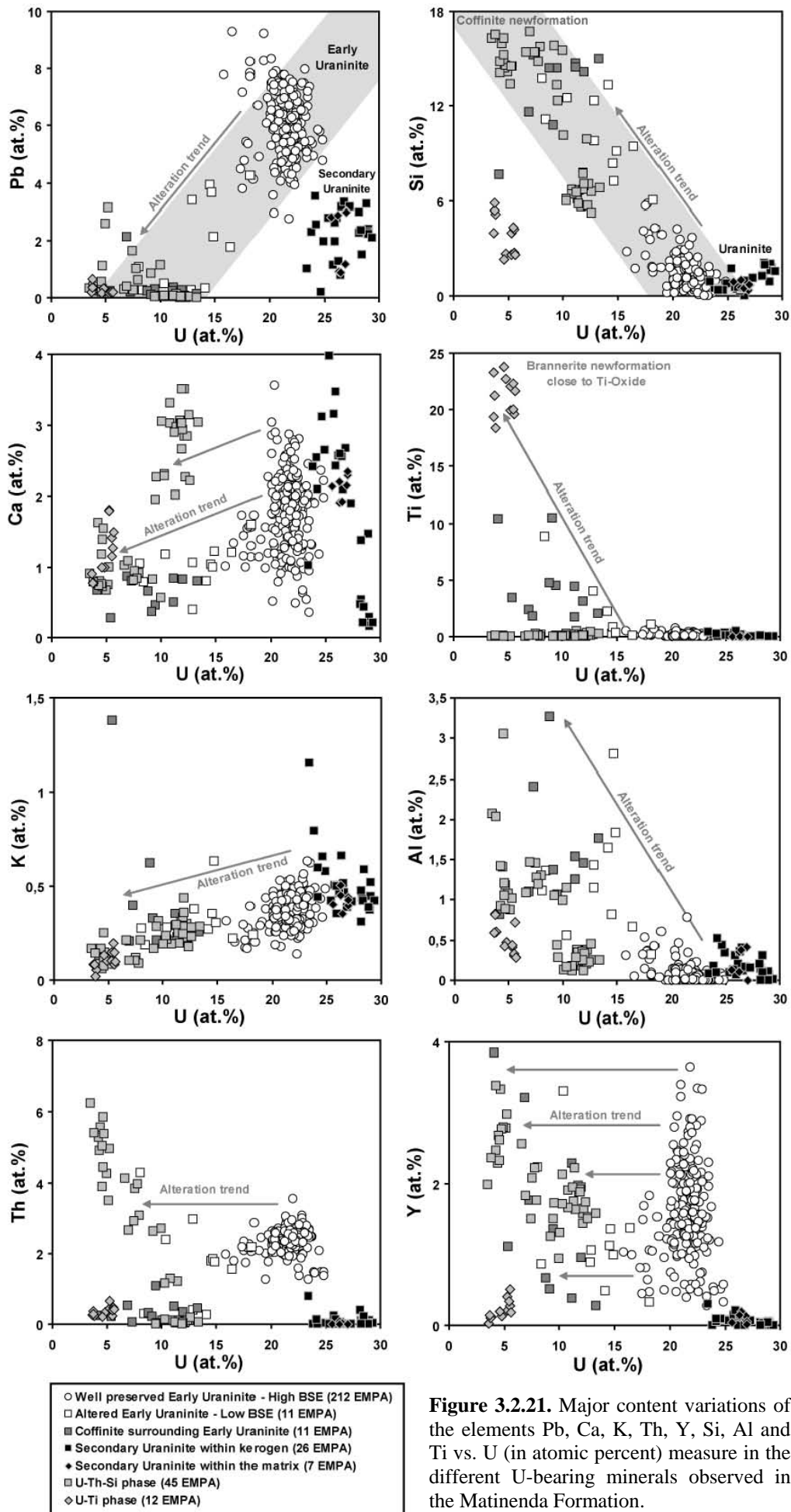
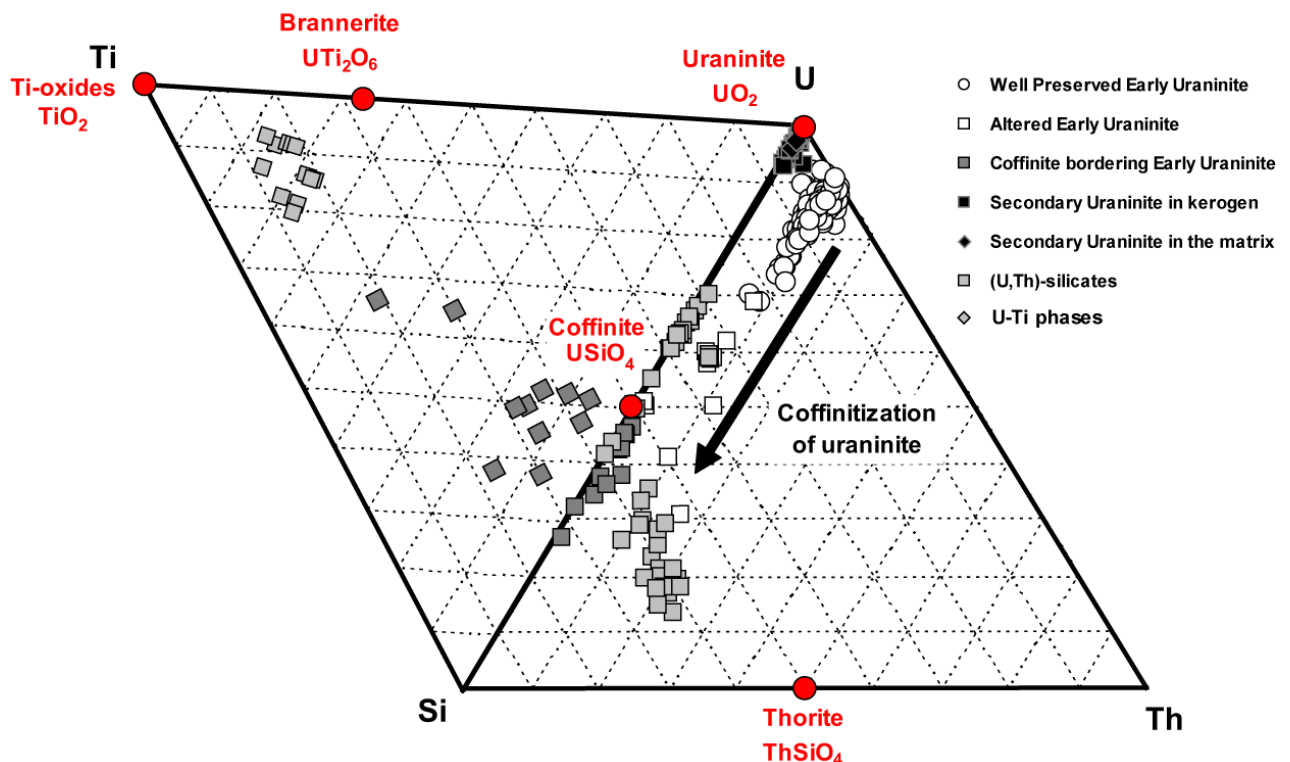


Figure 3.2.21. Major content variations of the elements Pb, Ca, K, Th, Y, Si, Al and Ti vs. U (in atomic percent) measure in the different U-bearing minerals observed in the Matinda Formation.

The average composition of the darker grey domains in BSE mode within the early uraninite grains has been calculated from 22 EMPA. They show higher silicium contents ( $10.04 \pm 3.40$  wt%  $\text{SiO}_2$ ) that partly compensates the decrease in U ( $55.70 \pm 8.81$  wt%  $\text{UO}_2$ ) and Pb ( $6.39 \pm 4.90$  wt%  $\text{PbO}$ ) concentrations (Fig. 3.2.21). The average composition at the margin of the uraninite crystals have been distinguished because they reach the silicium content of coffinite with an average at  $16.52 \pm 3.04$  wt%  $\text{SiO}_2$  and lower  $\text{UO}_2$  ( $48.78 \pm 10.65$  wt%) and  $\text{PbO}$  ( $1.84 \pm 2.63$  wt%) contents. The low analytical totals (from  $96.54 \pm 1.81$  in the freshest uraninite domains, down to  $89.89 \pm 3.61$  wt% in the inner altered areas and to  $88.67 \pm 2.30$  wt% for the coffinitized border) are considered to be relevant of OH and/or water incorporation in the mineral structure. The titanium content is also increasing from the pristine uraninite areas where the value is close to the detection limit ( $0.09 \pm 0.12$  wt%  $\text{TiO}_2$ ) to the edge of the crystals with a value reaching 20.92 wt%  $\text{TiO}_2$  in one spot (average  $7.64 \pm 6.06$  wt%  $\text{TiO}_2$ ) clearly showing that Ti is incorporated in the uranium oxides during their alteration but only when titanium oxides are present in the neighbour minerals. At their margin intermediate compositions between coffinite and brannerite are observed (Fig. 3.2.22). Some elements which are below the detection limits of the EMP in the preserved uraninite domains are present in the altered areas, such as Al, P and Ce. The S, K and Ca contents are low and under one weight percent. (Fig. 3.2.21).



**Figure 3.2.22.** Ternary plots showing U-Si-Th and U-Si-Ti (in relative cation proportions) for the various U-bearing minerals observed in the Matinenda Formation

Th contents range from 1.20 to 19.19 wt% in the darker uraninite domains. Thorium remains mostly in situ during alteration of the crystals; the higher Th contents mostly correspond to local reconcentrations whereas the average value is unchanged (7.06 wt% for preserved uraninite vs. 7.28 wt% for altered parts). This feature is confirmed by the composition of the darker margin depleted in thorium ( $1.94 \pm 1.44$  wt%  $\text{ThO}_2$ ). The yttrium content variations are also quite large in the different areas with  $\text{Y}_2\text{O}_3$  ranging between 0.36 and 4.56 wt% in the pristine uraninite (average  $2.04 \pm 1.60$  wt%), between 0.48 and 6.18 wt% in the Si-rich areas (average  $2.32 \pm 1.60$  wt%) and between 0.55 and 10.96 wt% in the coffinite-type boundary (average  $3.66 \pm 3.20$  wt%).

The Pb/U ratios in the earlier uraninite are between 0.13 and 0.56 in the least altered domains corresponding to chemical U-Th-Pb ages ranging between  $709 \pm 27$  Ma and  $2493 \pm 54$  Ma. Only the oldest age is older than the age of the Matinenda Formation and may indicate a detrital origin for this uraninite grain. The chemical age distribution in the histogram (Fig. 3.2.23) shows a well defined Gaussian distribution with an average weighted age of  $1441 \pm 35$  Ma symptomatic of a major event affecting the uraninite. The coffinitized areas have much lower Pb/U ratios between 0.01 and 0.31 corresponding to chemical ages between 58 Ma and 1574 Ma. Three main age groups are distinguished at circa 1300 Ma, 700 Ma and 200 Ma suggesting that early uraninite have undergone multi-generation of alteration events.

The small euhedral uraninite grains occurring mostly within the kerogen globules and less commonly in the matrix have completely different average composition compared to the early uraninite crystals (Table 3.2.1). Only 33 EMPA have been obtained because the size of grains is generally smaller than the size of the analytical spot ( $2\mu\text{m}$ ). Small cubes of uraninite are mainly characterized by high uranium concentrations ( $84.44 \pm 4.55$  wt%  $\text{UO}_2$ ), low lead concentrations ( $5.82 \pm 2.19$  wt%  $\text{PbO}$ ), and Y and Th contents close or lower than the detection limit ( $\text{Y} < 0.12$  wt%). Only two uraninite grains have provided greater  $\text{ThO}_2$  contents of 1.19 and 2.25 wt%. Locally low amounts of phosphorous ( $1.00 \pm 0.89$  wt%  $\text{P}_2\text{O}_5$ ), sodium ( $0.23 \pm 0.13$  wt%  $\text{Na}_2\text{O}$ ) and iron ( $0.38 \pm 0.27$  wt%  $\text{FeO}$ ) have also been detected whereas they were under the EMP detection limits in the early uraninite. The other elements show globally the same abundance in both uraninite types. The Pb/U ratios measured in euhedral uraninite included in the bitumen are between 0.01 and 0.15 corresponding to ages of 52 Ma to 833 Ma which indicate that the uraninite depleted in Th and Y has probably crystallized after the primary Th-Y-rich uraninite grains (Fig. 3.2.24).

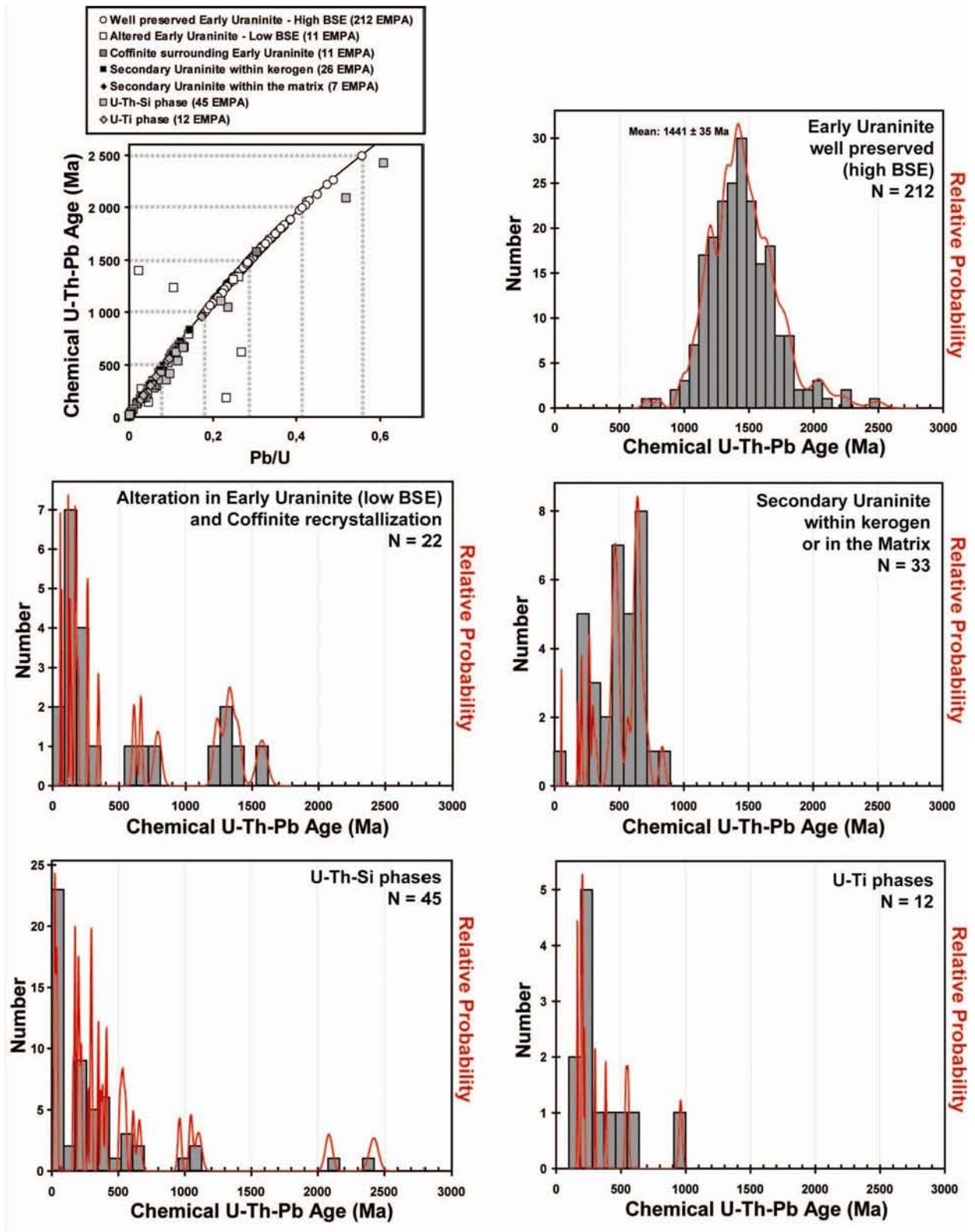
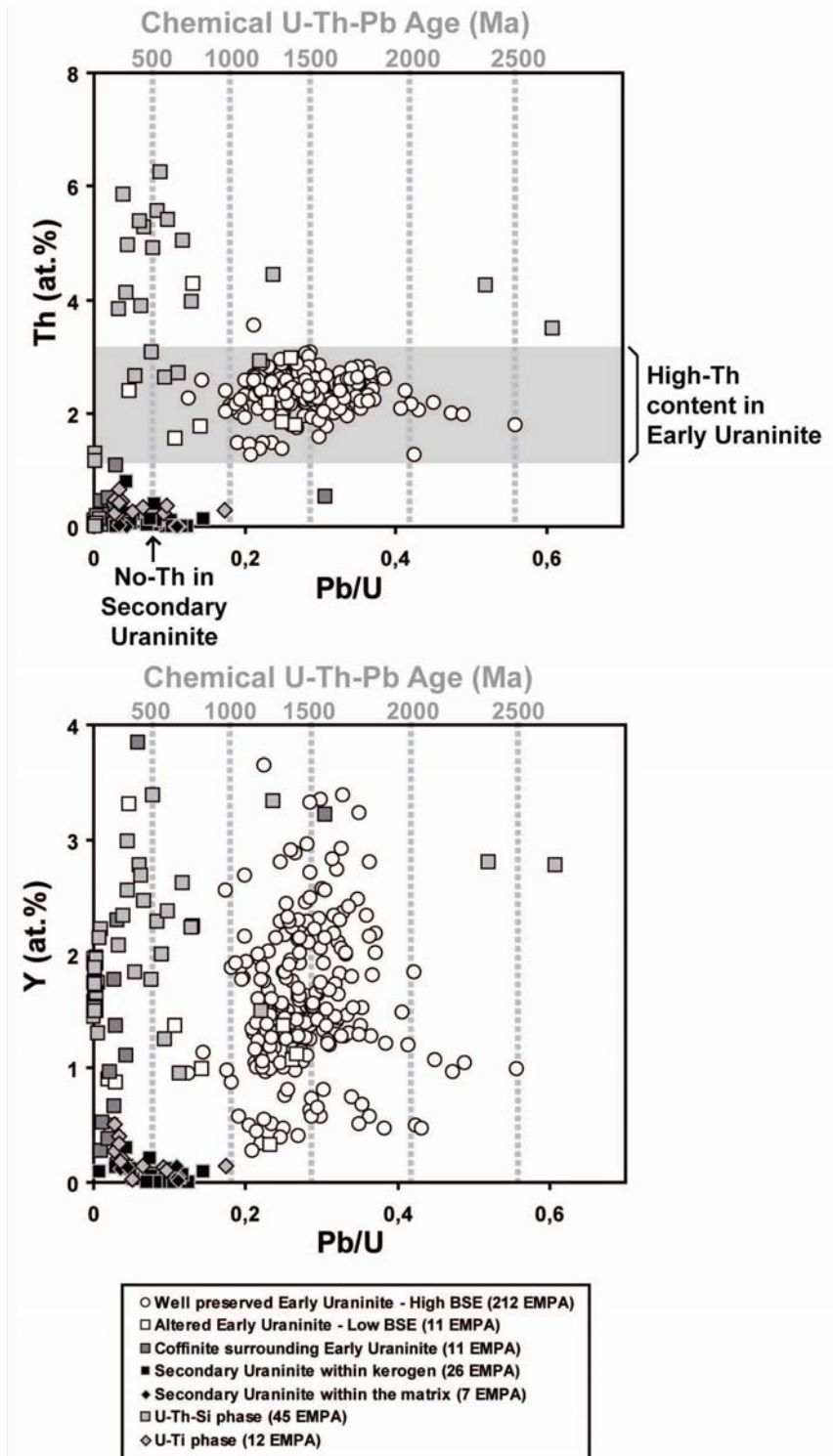


Figure 3.2.23. Relative probability histogram of chemical U-Th-Pb ages (Ma) of the main U-bearing phases from the Matinda Formation.



**Figure 3.2.24.** Th and Y contents (in atomic percent) vs. chemical U-Th-Pb ages (Ma) derived from the Pb/U ratios in the U-bearing phases of the Matinenda Formation.

The U-Th-Si phases occurring within the matrix have a highly variable composition probably resulting from a mixture of different phases as indicated by the large standard deviation values, with : 19.05 to 64.96 wt%  $\text{UO}_2$  ( $m = 45.80 \pm 16.12$  wt%), 0.01 to 33.24 wt%  $\text{ThO}_2$  ( $m = 10.82 \pm 11.44$  wt%) and 5.18 to 20.31 wt%  $\text{SiO}_2$  ( $m = 12.80 \pm 5.13$  wt%). The analytical totals are low ( $m = 89.57 \pm 3.24$  wt%), and probably result from the presence of hydroxide or water components. Phosphorous content may be very high (1.09 to 11.93 wt%  $\text{P}_2\text{O}_5$ ,  $m = 6.68 \pm 3.83$  wt%) as well as yttrium (1.95 to 7.35 wt%  $\text{Y}_2\text{O}_3$  and  $m = 4.40 \pm 1.20$  wt%). Low contents of REE (0.10  $\pm$  0.05 wt%  $\text{La}_2\text{O}_3$ ; 0.81  $\pm$  0.21 wt%  $\text{Ce}_2\text{O}_3$ ; 1.03  $\pm$  0.29 wt%  $\text{Nd}_2\text{O}_3$ ; 0.74  $\pm$  0.20 wt%  $\text{Dy}_2\text{O}_3$ ) are also detected suggesting a REE enrichment during alteration. Iron and sulphur contents are high in some spots up to 3.60 wt% FeO and 3.67 wt%  $\text{SO}_2$  which probably reflect the presence of micron-scale pyrite grains. Lead contents are also highly variable (<0.12 wt% to up to 12.99 wt% PbO) corresponding to chemical ages from less than 20 Ma (age limit under which the lead content is below the detection limit of the EMP) to  $2421 \pm 34$  Ma. However, the histogram of chemical ages (Fig. 3.2.23) shows that most of the ages are younger than 700 Ma (40/45 analyses).

The U-Ti phases encountered between primary uraninite and rutile grains have between 36.39 and 51.83 wt%  $\text{TiO}_2$  ( $m = 42.71 \pm 4.68$  wt%) and between 27.48 and 36.84 wt%  $\text{UO}_2$  ( $m = 32.14 \pm 3.54$  wt%) corresponding to a composition close to the stoichiometry of brannerite (Fig. 3.2.22). They have low analytical totals averaging  $92.52 \pm 2.13$  wt% indicating the presence of water. They contain minor amounts of Si ( $5.83 \pm 2.16$  wt%  $\text{SiO}_2$ ), Th ( $2.36 \pm 0.72$  wt%  $\text{ThO}_2$ ) and Ca ( $1.64 \pm 0.45$  wt% CaO). The brannerite-type phases have also incorporated traces of Y ( $0.61 \pm 0.35$  wt%  $\text{Y}_2\text{O}_3$ ) and REE ( $1.15 \pm 0.53$  wt%  $\text{Ce}_2\text{O}_3$ , and  $0.86 \pm 0.53$  wt%  $\text{Nd}_2\text{O}_3$ ). Fe and S contents are sometimes very high as in the U-Th-Si phases and range between 0.69-5.48 wt% FeO and 0-3.65 wt%  $\text{SO}_2$  which may reflect the presence of microgranular iron oxides or pyrite grains. The very low lead contents (average  $1.47 \pm 0.94$  wt% PbO) give Pb/U ratios ranging between 0.03 and 0.17 corresponding to young chemical ages mostly close to 250 Ma.

## U-Pb isotopic dating

U-Pb isotopic dating of early uraninite grains from the Elliot Lake deposits has been performed in the less altered sample from the Denison mine (BP72-102-1). The small size of the secondary uraninite grains in the other samples prevents their analysis using this method. Six crystals have been selected from the Quirke channel because of their large size. The internal textures were characterized with SEM-BSE mode but it was impossible to find homogeneous areas for the analytical spot size (20-30  $\mu\text{m}$  in diameter) for in situ U-Pb isotopic analyses. Indeed, the microprobe beam spot enclose both pristine uraninite and partly coffinitized areas analysed previously by EMPA as Si-enriched and (U+Pb)-depleted zones. Therefore the results represent a mixing between both materials. The isotopic measurement results are presented in Table 3.2.2.

**Table 3.2.2.** Ion microprobe U-Pb isotopic composition of six uraninite grains from the Matinenda Formation, Quirke channel, sampled at the Denison mine.

Sample Uraninite Crystal Spot number	$\frac{^{204}\text{Pb}}{^{206}\text{Pb}}$	$\frac{^{207}\text{Pb}}{^{206}\text{Pb}}$	$\frac{^{208}\text{Pb}}{^{206}\text{Pb}}$	$\frac{^{207}\text{Pb}}{^{206}\text{Pb}}$	Age (Ma)	$\frac{^{206}\text{Pb}}{^{238}\text{U}}$	Age (Ma)
<i>BP72-102 (Plot A-C2)</i>							
<b>Grain 1</b>							
Spot 1	0.000058 (0)	0.103 (9)	0.055 (24)		1687 $\pm$ 17		1408 $\pm$ 51
Spot 2	0.000020 (0)	0.096 (2)	0.032 (6)		1553 $\pm$ 3		1400 $\pm$ 40
Spot 3	0.000006 (0)	0.094 (2)	0.030 (9)		1514 $\pm$ 5		1493 $\pm$ 43
Spot 4	0.000014 (0)	0.087 (6)	0.032 (16)		1368 $\pm$ 11		1729 $\pm$ 51
<i>Sample BP72-102 (Plot B-C9a)</i>							
<b>Grain 2</b>							
Spot 1	0.000151 (1)	0.110 (3)	0.040 (10)		1803 $\pm$ 5		1366 $\pm$ 40
Spot 2	0.000104 (0)	0.103 (2)	0.034 (6)		1677 $\pm$ 3		1783 $\pm$ 51
<i>Sample BP72-102 (Plot B-C9b)</i>							
<b>Grain 3</b>							
Spot 1	0.000218 (2)	0.103 (4)	0.036 (21)		1675 $\pm$ 6		1718 $\pm$ 50
<b>Grain 4</b>							
Spot 1	0.000280 (2)	0.114 (8)	0.042 (17)		1868 $\pm$ 13		1575 $\pm$ 46
Spot 2	0.000298 (2)	0.103 (4)	0.037 (19)		1687 $\pm$ 4		1344 $\pm$ 39
Spot 3	0.000226 (1)	0.104 (3)	0.039 (15)		1692 $\pm$ 4		1568 $\pm$ 46
<b>Grain 5</b>							
Spot 1	0.000123 (1)	0.107 (3)	0.032 (8)		1741 $\pm$ 5		1885 $\pm$ 54
Spot 2	0.000202 (1)	0.104 (2)	0.042 (10)		1695 $\pm$ 3		1225 $\pm$ 36
Spot 3	0.000140 (2)	0.104 (4)	0.042 (19)		1705 $\pm$ 4		1434 $\pm$ 42
<b>Grain 6</b>							
Spot 1	0.000274 (1)	0.109 (2)	0.043 (8)		1784 $\pm$ 2		1564 $\pm$ 45
Spot 2	0.000425 (1)	0.106 (3)	0.045 (12)		1725 $\pm$ 3		1668 $\pm$ 48
Spot 3	0.000373 (1)	0.105 (2)	0.046 (9)		1714 $\pm$ 2		1809 $\pm$ 52
Spot 4	0.000105 (1)	0.105 (2)	0.034 (7)		1710 $\pm$ 3		1596 $\pm$ 46

**Notes:** numbers in brackets indicate errors ( $1\sigma \cdot 10^{-6}$  for  $^{204}\text{Pb}/^{206}\text{Pb}$ ,  $1\sigma \cdot 10^{-3}$  for  $^{207}\text{Pb}/^{206}\text{Pb}$  and  $^{208}\text{Pb}/^{206}\text{Pb}$ ),  $^{207}\text{Pb}/^{206}\text{Pb}$  ages are corrected from the common Pb.

The  $^{207}\text{Pb}/^{206}\text{Pb}$  ages calculated for the different spots within the individual grains are reported in Figure 3.2.25 and show as expected a wide scatter of the data. The youngest Pb-Pb ages and the largest age variations are recorded in the grain 1, with four Pb-Pb ages from 1368  $\pm$  11 Ma to 1687  $\pm$  17 Ma. The oldest Pb-Pb age is found in grain 4 at 1868  $\pm$  13 Ma. The youngest ages probably represent a mixing dominated by coffinitized darker domains whereas the oldest ages are dominated by better preserved uraninite. The 17 measurements have a weighted Pb-Pb age average of 1699  $\pm$  38 Ma.

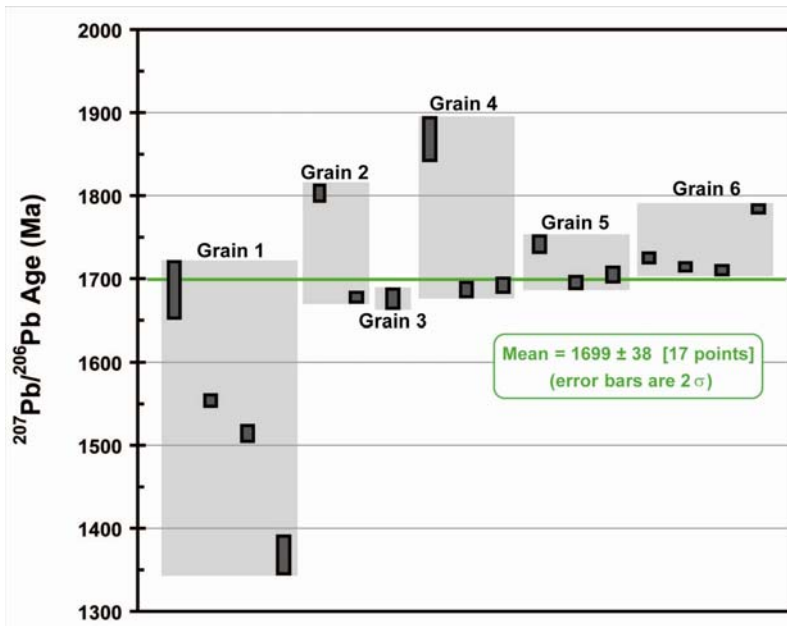


**Figure 3.2.25.** Distribution of  $^{207}\text{Pb}/^{206}\text{Pb}$  ages measured in 6 early uraninite grains from the Denison mine ore showing (Quirke channel – sample BP72-102) using ion microprobe instrument (SIMS).

The  $^{206}\text{Pb}/^{238}\text{U}$  versus  $^{207}\text{Pb}/^{235}\text{U}$  ratios are plotted in a Concordia diagram (Fig. 3.2.26). The 17 measurements from 6 uraninite grains are relatively well aligned along a single discordia line. The intercepts of the discordia line with the concordia curve gives a lower age at  $103 \pm 63$  Ma that cannot be distinguished significantly from zero and an upper age at  $1766 \pm 39$  Ma. Even if the MSWD value (16) is high because of the large uncertainties on each measurement, the good alignment of the points for all the analyzed spots allow considering the age of the upper intercept as meaningful with respect to the geological history of the area. This age probably corresponds to an alteration event that has induced the lead loss from the uraninite crystal lattice, which is coeval with vaning stages of the Penokean orogeny (1.9 to 1.7 Ga). This orogeny is responsible of a low grade metamorphic event in the region. The thermal effect Penokean orogeny was sufficient to completely reset the U-Pb isotopic system of the early uraninite crystals.

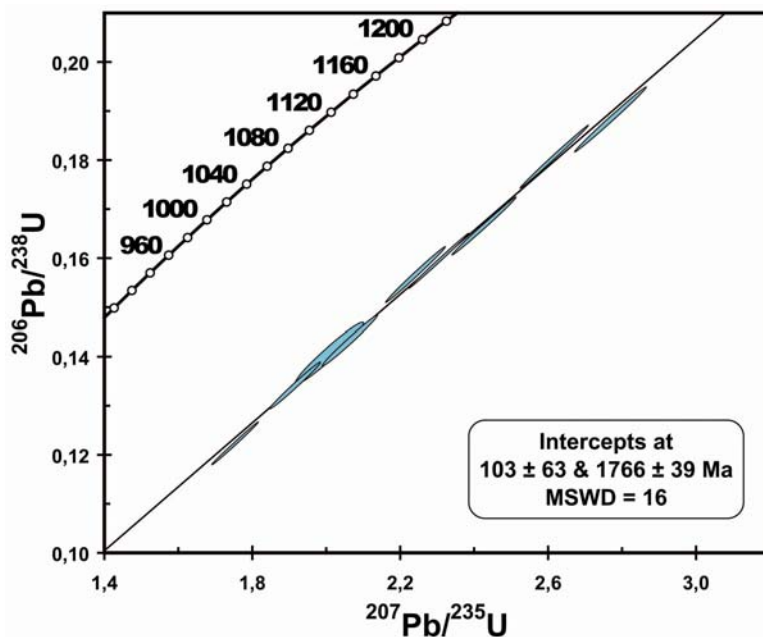


**Figure 3.2.26.** Concordia diagram for the six uraninite grains from the Quirke channel (BP72-102). The error ellipse for each analytical measurement is plotted in blue. The ages corresponding to the Discordia intercepts with the Concordia curve were calculated using the software of Ludwig (1999).

### **In situ Y and REE measurements (SIMS)**

Ten REE and yttrium analyses have been performed by SIMS on nine distinct early uraninite grains from the Denison mine (sample BP72-102). Only one grain had the size permitting to analyse 2 spots (1 and 2 in Table **3.2.3**). Y contents in the Elliot Lake uraninites are highly variable but quite high in all grains and ranges between 1.09 wt% and 5.75 wt% with a mean of 3.13 wt%. Average  $\Sigma$ REE content reaches 1.64 wt% (1.07 to 2.27 wt%).

The chondrite-normalized REE abundances of the nine spots (Fig. **3.2.27**) show consistent global patterns centred on a strong negative europium anomaly with  $[\text{Eu}/\text{Eu}^*]_{\text{N}}$  ranging from 0.09 to 0.40 ( $m = 0.19$ ). Most REE have abundances higher than  $10^4$  times the chondrites. The HREE distribution is quite flat ( $1.18 < [\text{Gd}/\text{Yb}]_{\text{N}} < 2.86$ ,  $m = 1.96$ ) but a small depletion in LREE and notably in La is noted with  $[\text{La}/\text{Sm}]_{\text{N}}$  ranging from 0.04 to 0.16 (average 0.09).

**Table 3.2.3.** SIMS determinations of Y and REE contents (ppm) in the early uraninite grains (stage I) from the Elliot Lake quartz pebble conglomerates compared to the composition of other uranium oxides formed during magmatic processes in different granitoids and hydrothermal uraninite (pitchblende) from the Cigar Lake unconformity-type deposit of the Athabasca Basin in Canada (data from this study and Bonhoure, 2007)

Sample	N°	Y	La	Ce	Pr	Nd	Sm	Eu	Gd*	Tb	Dy	Ho	Er	Tm	Yb*	Lu	Σ REE	[La/Sm] <sub>N</sub>	[Gd/Yb] <sub>N</sub>	[Eu/Eu*] <sub>N</sub>
<i>Early uraninites from the Denison Mine deposit in the Quirke channel (Elliot Lake, Ontario, Canada) – this study</i>																				
BP72-102-1	1	33 992	173	1 559	335	1 761	1 532	80	2 191	418	3 424	644	1 711	376	1 473	63	15 741	0.13	2.51	0.40
underground exposure	2	16 867	220	2 651	563	2 909	1 540	121	1 632	262	1 693	321	706	102	471	38	13 230	0.12	2.47	0.37
Shaft 2 ~800m depth	3	25 409	327	2 350	396	2 094	1 250	69	1 876	365	2 361	416	1 092	170	760	57	13 582	0.05	2.23	0.15
	4	57 479	127	1 820	438	3 051	2 144	114	3 609	735	5 017	872	2 217	468	1 981	123	22 714	0.11	1.40	0.09
	5	41 880	216	2 231	479	2 917	2 090	141	2 953	560	3 521	627	1 813	526	2 074	92	20 240	0.06	2.15	0.10
	6	35 510	195	1 767	398	2 371	2 047	83	2 919	556	3 622	615	1 604	273	1 124	62	17 636	0.04	1.51	0.12
	7	12 934	254	2 055	394	2 233	1 265	176	1 427	239	1 292	208	575	101	471	39	10 728	0.16	2.04	0.14
	8	42 802	191	2 701	603	3 483	2 313	130	2 929	526	3 894	740	1 911	255	1 088	69	20 833	0.07	1.23	0.13
	9	10 856	240	1 985	373	2 185	1 282	165	1 460	246	1 319	179	591	108	489	38	10 659	0.09	2.86	0.23
	10	35 660	359	2 565	442	2 701	2 012	67	2 680	494	2 954	556	1 447	385	1 583	87	18 332	0.06	1.18	0.17
<b>Average</b>		<b>31 339</b>	<b>230</b>	<b>2 168</b>	<b>442</b>	<b>2 570</b>	<b>1 747</b>	<b>115</b>	<b>2 368</b>	<b>440</b>	<b>2 910</b>	<b>518</b>	<b>1 367</b>	<b>276</b>	<b>1 152</b>	<b>67</b>	<b>16 370</b>	<b>0.09</b>	<b>1.96</b>	<b>0.19</b>
<i>Magmatic uraninites from a S-type pegmatite of the Karelian region (Baltic Shield, Finland) – this study</i>																				
9375-3	1	14 841	217	1 581	345	2 214	1 205	141	1 469	258	1 545	292	831	96	490	50	10 734	0.13	0.95	0.30
	2	16 531	301	1 898	393	2 292	1 364	453	1 711	306	1 884	357	1 027	133	642	58	12 818	0.15	0.86	0.84
	3	18 981	865	4 470	911	5 436	2 472	412	2 763	460	2 703	504	1 421	153	801	86	23 455	0.21	1.19	0.40
<b>Average</b>		<b>16 784</b>	<b>461</b>	<b>2 649</b>	<b>550</b>	<b>3 314</b>	<b>1 680</b>	<b>335</b>	<b>1 981</b>	<b>341</b>	<b>2 044</b>	<b>384</b>	<b>1 093</b>	<b>127</b>	<b>644</b>	<b>65</b>	<b>15 669</b>	<b>0.16</b>	<b>1.00</b>	<b>0.51</b>
<i>Magmatic uraninites from the Rössing Alaskite (Namibia) – data from Bonhoure (2007)</i>																				
Rössing	1	61 702	320	4 301	518	2 718	1 505	94	2 440	490	3 796	769	2 401	398	1 582	73	21 404	0.13	1.27	0.15
	2	68 134	268	3 909	494	2 643	1 541	88	2 670	549	4 259	889	2 852	446	1 770	81	22 460	0.11	1.25	0.13
	3	110 383	802	9 506	430	1 444	1 885	86	4 057	891	7 652	1 155	5 606	1 026	4 257	243	39 039	0.27	0.79	0.09
	4	45 505	270	3 581	429	2 659	1 386	75	1 987	379	3 144	694	1 903	318	1 254	56	18 135	0.12	1.31	0.14
<b>Average</b>		<b>71 431</b>	<b>415</b>	<b>5 324</b>	<b>468</b>	<b>2 366</b>	<b>1 579</b>	<b>86</b>	<b>2 788</b>	<b>577</b>	<b>4 712</b>	<b>877</b>	<b>3 190</b>	<b>547</b>	<b>2 215</b>	<b>114</b>	<b>25 259</b>	<b>0.16</b>	<b>1.15</b>	<b>0.13</b>
<i>Hydrothermal uraninite (pitchblende) from the Cigar Lake unconformity-type deposit (Athabasca Basin, Saskatchewan, Canada) – data from Bonhoure (2007)</i>																				
	1	3 965	11	116	25	134	91	25	283	67	450	62	136	15	87	11	1 512	0.08	2.68	0.48
	2	4 268	7	89	21	125	80	26	275	66	480	72	146	16	97	13	1 513	0.05	2.35	0.53
	3	5 092	8	104	25	146	91	32	365	90	609	82	184	22	122	14	1 893	0.06	2.47	0.53
	4	4 760	9	106	25	146	89	27	352	86	590	79	175	21	118	14	1 839	0.06	2.45	0.47
	5	5 298	13	140	32	186	99	31	380	93	637	86	191	23	129	15	2 055	0.08	2.45	0.49
	6	4 577	16	139	31	168	82	29	299	73	477	69	153	18	87	8	1 649	0.13	2.83	0.56
	7	5 854	11	141	34	201	114	39	424	103	705	96	214	26	144	17	2 270	0.06	2.43	0.54
	8	3 514	16	113	23	119	64	22	248	61	424	58	131	16	89	10	1 394	0.16	2.30	0.53
<b>Average</b>		<b>4 666</b>	<b>11</b>	<b>119</b>	<b>27</b>	<b>153</b>	<b>89</b>	<b>29</b>	<b>328</b>	<b>80</b>	<b>546</b>	<b>76</b>	<b>166</b>	<b>20</b>	<b>109</b>	<b>13</b>	<b>1 766</b>	<b>0.08</b>	<b>2.49</b>	<b>0.52</b>

\* Gd and Yb are calculated from Sm-Tb and Tm-Lu concentrations respectively because of analytical interferences forbidding their accurate measurements:  $Gd^* = Sm + 2/3Tb$  and  $Yb^* = (Tm + Lu)/2$   
 $[X]_N$  = normalized to chondrite values;  $[Eu/Eu^*]_N = Eu_N / \sqrt{[Sm.Gd]_N}$

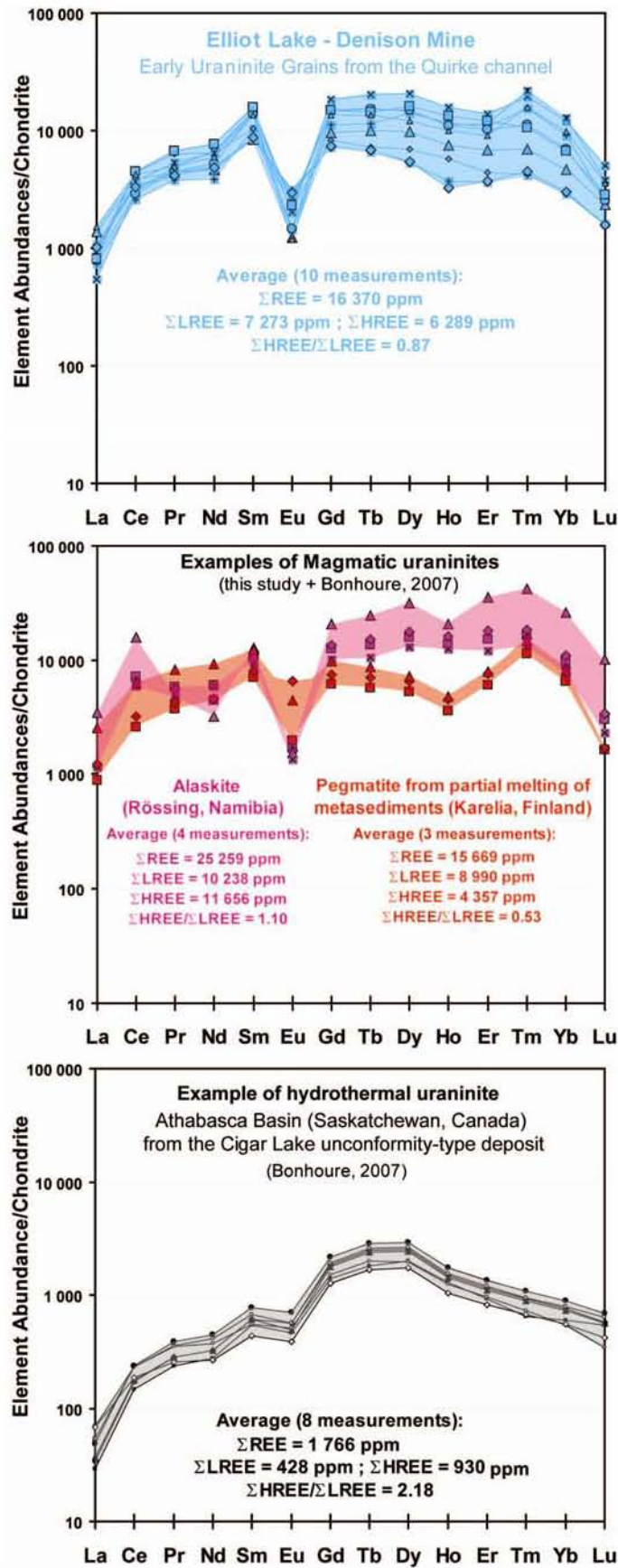


**Figure 3.2.27.** Chondrite-normalized REE abundances measured in situ in nine uraninite grains from the Quirke channel in the Matinenda Formation (sample BP72-102 from the Denison mine). Sums of REE, LREE (=La+Ce+Pr+Nd+Sm+Eu) and HREE (=Gd+Tb+Dy+Ho+Er+Tm+Yb+Lu) are calculated before chondrite normalization.

## Discussion

### ***Origin of early uraninite grains***

The uranium ore within the main mineralized channel of the Elliot Lake deposit is mainly composed of thorian uraninite associated to monazite and other heavy minerals (stage I).

The detrital origin of uraninite I from the Quirke channel of the Denison mine is supported by the following features:

#### (i) the high Th contents

The best preserved domains of euhedral to sub-rounded uraninite grains present Th concentrations ranging between 3.89 to 10.60 wt% ThO<sub>2</sub> that are characteristic of a crystallization in a highly differentiated melt at elevated temperature during magmatic processes.

#### (ii) the high Y and REE contents, and the characteristics of REE patterns (weak global fractionation and negative Eu anomaly)

The detrital origin of thorian uraninite grains is strongly supported by the REE patterns measured in situ by SIMS. The composition of the Elliot Lake uraninite is comparable to those determined by Bonhoure (2007) on magmatic uraninite from S-type pegmatites, one from the Karelia region in the Baltic Shield of Finland (data from this study, **chapter 2 - part 2.4**) and an other occurrence from the Rössing alaskite ore showing in Namibia (Bonhoure, 2007) whereas the hydrothermal uraninite (pitchblende) from the Athabasca Basin unconformity-type deposits have a completely distinct REE pattern. Both types of uraninite (hydrothermal vs. magmatic origin) have very distinctive Y content and chondrite-normalized REE patterns (Table **3.2.3** and Fig. **3.2.27**). The hydrothermal pitchblende formed under low temperature (<200°C) is characterized by lower Y and REE concentrations (average Athabasca: Y = 0.47 wt% and ΣREE = 0.17 wt%, less than 10<sup>3</sup> the chondrites), and present a bell-shape REE pattern centred on middle-REE and are LREE-depleted ([La/Sm]<sub>N</sub> = 0.08). The magmatic uraninites have much higher Y and REE abundances compared to the hydrothermal ones (Karelia: Y = 1.68 wt% and ΣREE = 1.57 wt%; Rössing: Y = 7.14 wt% and ΣREE = 2.53 wt%, more than 10<sup>4</sup> the chondrites) with a distinctive weakly fractionated REE pattern and a negative Eu anomaly inherited from plagioclase fractionation in the silicate melt (Karelia: [Eu/Eu\*]<sub>N</sub> = 0.51; Rössing: [Eu/Eu\*]<sub>N</sub> = 0.13). The comparison of the REE patterns and abundances of the Elliott Lake uraninites with other uranium occurrences show that the Quirke channel uraninites have clearly a magmatic signature.

The early uraninite grains from Elliot Lake have crystallized at a high temperature melt from a magmatic source similar to peraluminous granitoids.

(iii) the chemical U-Th-Pb dating

The uraninite and monazite chemical dating yields only a few ages older than the maximal age of deposition of the Huronian sedimentary sequence (basal volcanics at  $2450 \pm 25/-10$  Ma, Andrews et al., 1986): up to  $2493 \pm 54$  Ma in uraninite and  $2931 \pm 11$  Ma in monazite, implying a detrital origin from an older source rock for these crystals and at least older than 2.5 Ga for uraninite. These ages are consistent with the previous isotopic age determination in detrital zircon from the Huronian sediments which yield mostly pre-2.8 Ga ages and some older ages between 3.6-2.9 Ga (Rainbird et al., 2006).

**Potential Archean U-sources**

The detrital accessory mineral assemblage reveals clearly that the mineralized quartz pebble conglomerates from the Matinenda Formation derive from the erosion of felsic rocks (zircon, monazite, large amount of quartz) and mafic rocks (large amount of pyrite and titanium oxides). The low maturity of the rock (abundant detrital feldspar grains), the poor sorting of the conglomerates and the angular shape of the uraninite grains suggest that the source area is proximal from the deposition area. These observations are concordant with the previously measured paleocurrents indicating that the source area was located to the northwest (Fralick and Miall, 1982 and 1989; Long, 1995; Bekker and Kaufman, 2007) and corresponds to the Archean granite-greenstone terrains of the Superior Province.

The composition of detrital uraninite and monazite grains show distinct signatures relevant of at least three types of granitic rock sources.

The Th vs. Y contents measured by EMPA (Fig. 3.2.20) and the Y and REE concentrations measured by SIMS (Table 3.2.3) allow to classify the individual grains of uraninite in two distinct families: a dominant group very rich in Th ( $>6$  wt% to up to 10.6 wt%  $\text{ThO}_2$ ), Y ( $\sim 2.5$ -4 wt% Y) and REE ( $\Sigma\text{REE} \sim 1.5$ -2 wt%) which is generally characteristic of a crystallization during partial melting in **S-type granites** (ex: Rössing or Karelia Mustalampi pegmatite in Finland with 7.4 and 11.8 wt%  $\text{ThO}_2$  in magmatic uraninite - chapter 2, part 2.4) and a less abundant fraction with moderate Th contents ( $<6$  wt%  $\text{ThO}_2$ ) and one grain composed of  $1.38 \pm 0.09$  wt%  $\text{ThO}_2$  and  $0.5 \pm 0.10$  wt%  $\text{Y}_2\text{O}_3$  characterizing uraninite formed in **highly fractionated**

**leucrogranites** (ex: in Manitoba, the peraluminous Tanco pegmatite host uraninite with ThO<sub>2</sub> ranging from 1.6 to 5.9 wt% and m = 0.03 wt% Y and 0.02wt%  $\Sigma$ REE - chapter 2, part 2.3).

Besides the thorium content measured by EMP in the monazite grains suggests that the source area was composed of **metaluminous to mid-peraluminous A-type granitic rocks** and the U-Th-Pb chemical dating yields a minimum age of 2.93 Ga for the source rock.

Considering the chemical composition characteristic of the uraninite, the minimal age of the source rocks and the paleocurrent directions, the dyke swarms of uranium-rich pegmatites from the Late Archean Superior Province located in north-western Ontario (Fig. 3.2.28) represent the ideal sources for the detrital U mineralization of the Elliot Lake-Blind River deposits. U-rich plutonic rocks are located near the Manitoba boundary, 600 to 800 km from the actual position of the paleoplacer deposits. Anorogenic leucogranites and pegmatites are issued from the partial melting of supra-crustal metasedimentary rocks from the greenstone belts of the Bird River, Winnipeg River and Wabigoon sub-provinces (Černý, 1990; Larbi et al., 1999). They have a peraluminous composition, are rich in REE, they display uraninite occurrences and are aged between 2.63 and 2.67 Ga (Fyon et al., 1992). Older A- and I-type affinity granites are associated locally to the uranium and thorium rich S-type pegmatites and those terranes may have fed the Matinenda Formation.

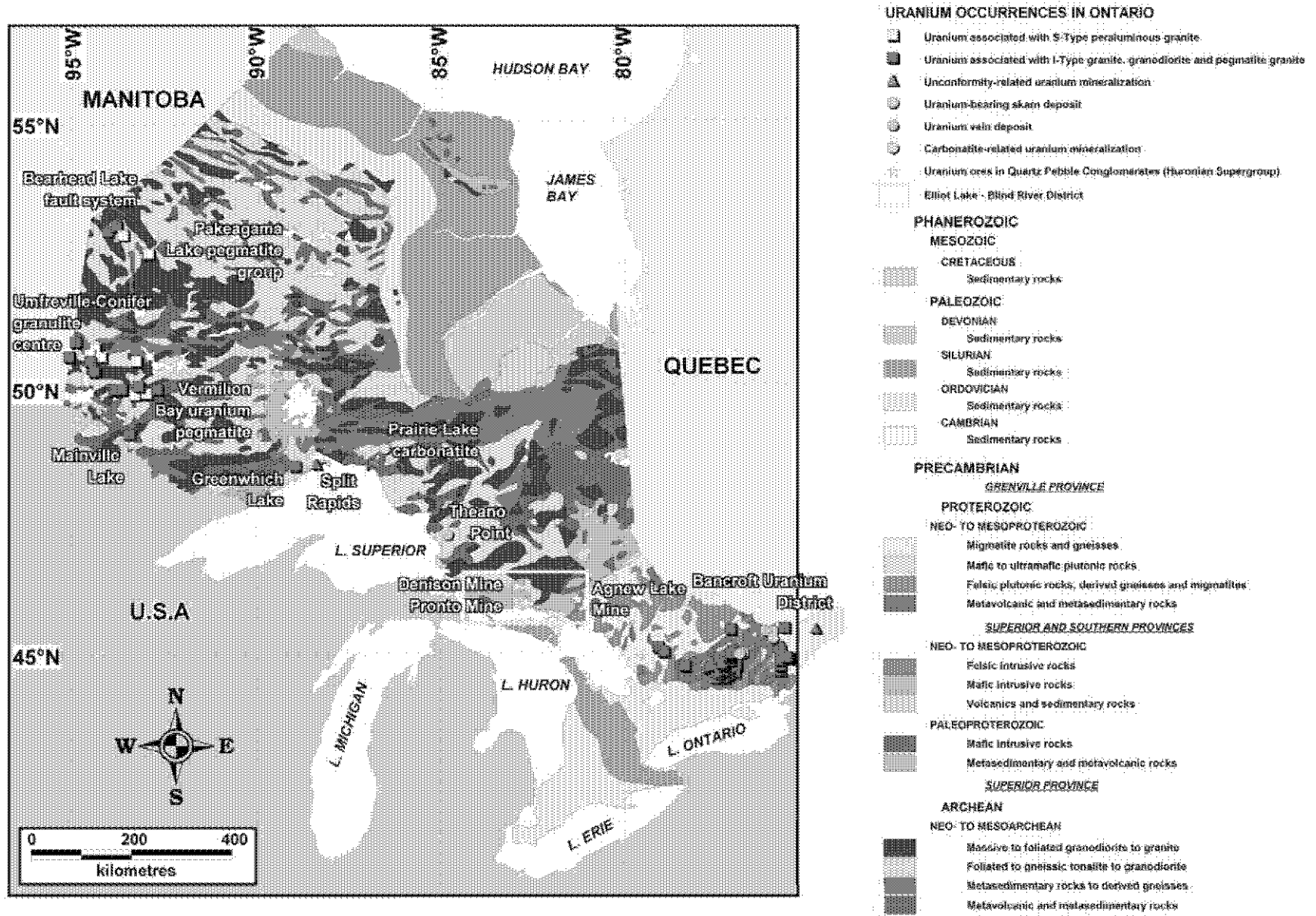
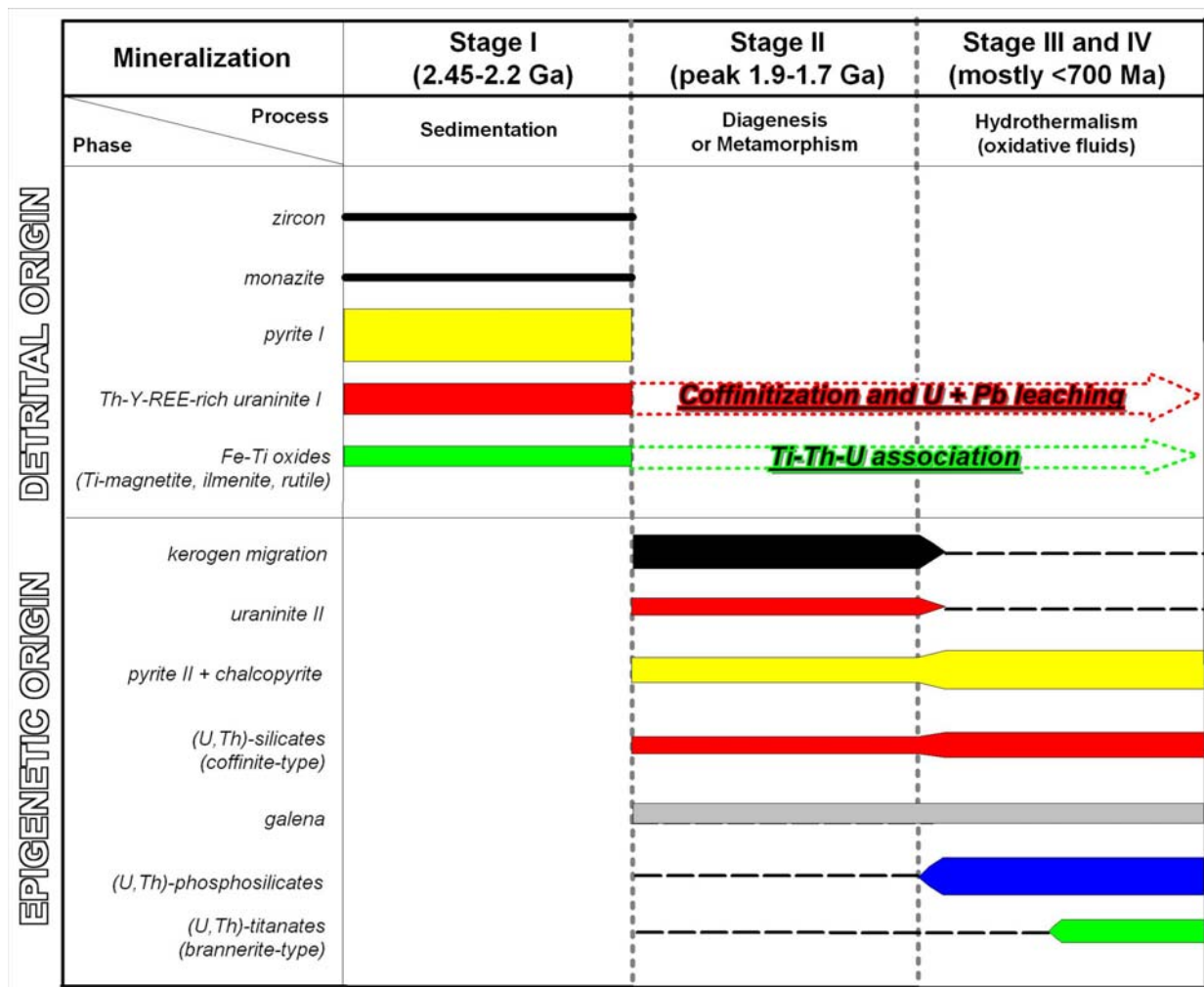


Figure 3.2.28. Location of U occurrences in Ontario (modified from the Ontario Geological Survey).

***Late episodes of uranium remobilisation and U-mineral newformation***

The SEM observations in BSE mode and the electron microprobe measurements reveal textural and chemical complexities within early uraninite that are associated to post-sedimentary alteration. The alteration has induced the uranium and lead departure from the crystal lattice mostly replaced by silicium and involving transformation into (U,Th)-silicates and coffinite (stage II). This recrystallization results in the resetting of the U-Th-Pb chemical and U-Pb isotopic systems. The oldest ages at circa 1.8 Ga and 1.4-1.5 Ga have been obtained in the earlier mineralization. The oldest may correspond to the radioelement mobilization during metamorphism of the Penokean orogeny (~1.9-1.7 Ga). The uranium mobilized from the primary ore has migrated through the porosity of the conglomerates but seems to have been largely redeposited as secondary uranium phases in the interspaces between minerals within the clay matrix. Part of it has precipitated with kerogen acting as a reducing chemical trap and formed the secondary hydrothermal uraninite depleted in Th, Pb and Y (stage III). An other part of the U mobilized has formed complex phases with Si, P and/or Ti such as urano-titanates with alteration of detrital Fe-Ti oxides (ilmenite, Ti-magnetite, rutile) and (U,Th)-phosphosilicates mixed with iron oxides and minor sulfides from the alteration of monazite (stage IV). The phosphorous derives possibly from the alteration of monazite as indicated by the presence of small amounts of light REE in the analyses. This last stage of uranium remobilization must have happened until recently because of the very young chemical ages determined in these uraniferous phases (mostly < 700 Ma). The presence of widespread hematite also suggests that the later hydrothermal brines should be oxidant but further complementary studies on the composition of interstitial clays or fluid inclusions in quartz would provide more information on the nature of the fluids.

The paragenetic sequence presented in Figure 3.2.29 has been deduced from the detail mineralogical and chemical studies and summarizes the behaviour of U-mineralization observed in the Matinenda Formation.



**Figure 3.2.29.** Paragenetic sequence of U mineralization in the Elliot Lake paleoplacer-type deposits. The thickness of bars represents the relative abundance for each accessory mineral and dashed lines when occurrences are not confident.

**Implication for the oxygen-free level in the Early Proterozoic environment**

In the modern oxygen-rich atmosphere and hydrosphere, uranium oxides in contact with the sub-surface oxidized waters are rapidly dissolved because tetravalent uranium ( $U^{4+}$ ) present in the uranium oxides is oxidized into its hexavalent state ( $U^{6+}$ ) which form highly solubles complexes and then can be transported as uranyl ions by meteoric waters. Grandstaff (1980) has shown that uraninite is thermodynamically unstable at oxygen pressure ( $pO_2$ ) greater than  $\sim 10^{-21}$  atm. If the atmosphere was oxygenated at the present level during Early Proterozoic, the time of the Elliot Lake paleoplacer deposition, the uraninite crystals deriving from the erosion of the Archean granites would have been rapidly destroyed during the weathering of outcropping rocks, and their transportation by fluvial systems until their ultimate sedimentation within channels and their burial under younger clastic sediments would have not been possible. From the kinetic of dissolution experiments of Grandstaff (1980), the oxygen partial pressure should have been at least lower than  $10^{-2}$  PAL (Present Atmospheric Level).

The atmosphere probably gets enriched in oxygen progressively, firstly by photodissociation and latterly by photosynthesis after the evolution of living organisms (Candfield, 2005; and reference therein). Significant evidences of an oxygenic alteration in the upper Huronian formations have been formulated by previous workers as the positive carbon isotope composition of organic matter and the phosphates presence in the Pecors Formation (Bekker and Kaufman, 2007). Therefore, the Great Oxidation Event (GOE) must have occurred between 2.45 and 2.22 Ga which is generally the timing proposed by other authors (Holland, 2002; Bekker et al., 2004).

## Conclusions

Detrital and hydrothermal uraninites from the different deposits of the Elliot Lake Quartz Pebble Conglomerates are for the first time characterized thoroughly using a combination of BSE imaging for textural and compositional variation features, electron microprobe analysis for major chemical composition and chemical dating and SIMS for isotopic U-Pb dating and trace element (Y and REE) analyses. This study provides undisputable geochemical evidences that the early Th-Y-REE-rich uraninite grains from the Matinenda Formation were eroded mechanically from proximal peraluminous granitoids and have accumulated within the heavy mineral beds in the basal Huronian sedimentary sequence. The detrital origin of these uranium oxides with regards to the instability of uraninite under the actual high oxygen pressure level fully supports the reduced nature of the Early Proterozoic atmosphere. Chemical U-Th-total Pb ages and isotopic U-Pb ages allowed identifying multi-stage of uranium (and lead) remobilization from the primary ore and subsequent hydrothermal redepositions, but the primary age of uraninite deposition is strongly altered by these alterations events. The new precipitates have a highly variable composition that depends of the fluid composition and of the nature of the other heavy minerals locally altered together. Secondary uraninite is deposited with kerogen which has probably acted as a chemical reduced trap. In summary, our results support one of the previous models proposing that the Elliot Lake deposits are modified paleoplacers.

## Acknowledgement

Drill-hole samples and data have been provided by the mining company Pele Mountain Ltd (Toronto, Ontario, Canada) and we are grateful to the geological staff that permits to complete this work and validate our observations and results. We will thanks more precisely Patrick Enright and Mark Smethurst for there warm welcome at there office in Toronto. We want

also to thanks Professor Bernard Poty permitting to access to his own rock-collection from the Denison mine. The author thanks Alain Kohler, Johann Ravaux and Sandrine Mathieu for their invaluable assistance with the scanning electron microscopy and electron microprobe work at the SCMEM laboratory. Michel Champenois and Denis Mangin are also grateful for their support with the ion microprobe instrument at the CRPG-CNRS. This work was financially supported by AREVA.

## References

- Abraham, E. M., 1953, Geology of parts of long and spragge townships Blind River uranium area, district of Algoma, Ontario Department of Mines, PR-1953-2, 10 p.
- Alexandre, P. and Kyser, T.K., 2005, Effects of cationic substitutions and alteration in uraninite, and implications for the dating of uranium deposits, *The Canadian Mineralogist* 43, p. 1005-1017.
- Anders, E. and Grevesse, N., 1989, Abundances of the elements: Meteoritic and solar. *Geochimica and Cosmochimica Acta* 57, p. 197-214.
- Andrews, A.J., Masliwec, A., Morris, W. A., Owsiacki, L. and York, D., 1986, The silver deposits at Cobalt and Gowganda, Ontario. II: an experiment in age determinations employing radiometric and paleomagnetic measurements, *Canadian Journal of Earth Sciences* 23, p. 1507-1518.
- Bekker, A. and Kaufman, A. J., 2007, Oxidative forcing of global climate change: A biochemical record across the oldest Paleoproterozoic ice age in North America, *Earth and Planetary Science Letters* 258, p. 486-499.
- Bekker, A., Holland, H. D., Wang, P.-L., Rumble III, D., Stein, H. J., Hannah, J. L., Coetzee, L. L. and Beukes, N. J., 2004, Dating the rise of atmospheric oxygen, *Nature*, Vol. 427, p. 117-120.
- Bennett, G., 2006, The Huronian Supergroup between Sault Ste Marie and Elliot Lake, *Field Trip Guidebook*, Vol. 52, Part 4 Institute on Lake Superior Geology Sault Ste Marie, Ontario, 65 p.
- Bennett, G., Dressler, B. O. and Robertson, J. A., 1991, The Huronian Supergroup and associated intrusive rocks, In: P. C. Thurston, H. R. Williams, R. H. Sutcliffe and G. M. Stott (Eds.) *Geology of Ontario*, Ontario Geological Survey, Special Vol. 4 (1), p. 549-592.
- Bonhoure, J., 2007, *Géochimie des éléments de terres rares et du plomb dans les oxydes d'uranium naturels*. Thèse de Doctorat, Université de Nancy, France (unpublished).
- Bonhoure, J., Kister, P., Cuney, M. and Deloule, E., 2007, Methodology for Rare Earth Element determinations of uranium oxides by ion microprobe, *Geostandards and Geoanalytical Research*, Vol. 31, No. 3, p. 209-225.
- Bowles, J.F.W., 1990, Age dating of individual grains of uraninite in rocks from electron microprobe analyses, *Chemical Geology* 83, p. 47-53.
- Boyle, D. R., 1982, The formation of basal-type uranium deposits in South Central British Columbia, *Economic Geology*, Vol. 77, No. 5, p. 1176-1209.

- Buchan, K. L., Mortensen, J. K., Card, K. D. and Percival, J. A., 1998, Paleomagnetism and U-Pb geochronology of diabase dyke swarms of Minto block, Superior Province, Quebec, Canada, *Canadian Journal of Earth Sciences*, Vol. 35 (9), p. 1054-1069.
- Candfield, D. E., 2005, The Early Earth History of Atmospheric Oxygen: homage to Robert M. Garrels, *Annu. Rev. Earth Planet. Sci.* 33, p. 1-36.
- Cathelineau, M., Boiron, M.-C., Holliger, P. and Poty, B., 1990, Metallogenesis of the French part of the Variscan orogen. Part II: Time-space relationship between U, Au and Sn-W ore deposition and geodynamic events-mineralogical and U-Pb data. *Tectonophysics* 177, p. 59-79.
- Černý, P., 1990, Distribution, affiliation and derivation of rare-element granitic pegmatites in the Canadian Shield, *International Journal of Earth Sciences*, Vol. 79, Issue 2, p. 183-226.
- Cocherie, A. and Albarede, F., 2001, An improved U-Th-Pb age calculation for electron microprobe dating of monazite, *Geochimica et Cosmochimica Acta*, Vol. 65, No. 24, p. 4509-4522.
- Cuney, M. and Kyser, K., 2008, Deposits related to Partial Melting, In: M. Cuney and K. Kyser (eds.) *Recent and not-so-recent developments in uranium deposits and implications for exploration*, Short Course Series Vol. 39, Mineralogical Association of Canada, p. 79-95.
- Cuney, M. and Friedrich, M., 1987, Physicochemical and crystal-chemical controls on accessory mineral paragenesis in granitoids: implications for uranium metallogenesis, *Bull. Minéral.*, 110, p. 235-247.
- Derry, D. R., 1960, Evidence of the origin of the Blind River uranium deposits, *Economic Geology*, Vol. 55, No. 5, p. 906-927.
- Ellsworth, H.V., 1928, I. Thucholite, a remarkable primary carbon mineral from the vicinity of Parry Sound, Ontario. II. Cyrtolite intergrowth associated with the Parry Sound thucholite, *American Mineralogist* 13, p. 419-441.
- Farrow, C. E. G. and Mossman, D. J., 1988, Geology of Precambrian paleosols at the base of the Huronian Supergroup, Elliot Lake, Ontario, Canada, *Precambrian Research*, Vol. 42, Issues 1-2, p. 107-139.
- Förster, H.-J., 1998, The chemical composition of REE-Y-Th-U-rich accessory minerals in peraluminous granites of the Erzgebirge-Fichtelgebirge region, Germany, Part I: The monazite-(Ce)-brabantite solid solution series, *American Mineralogist*, Vol. 83, p. 259-272.
- Fralick, P. W. and Miall, A. D., 1989, Sedimentology of the Lower Huronian Supergroup (Early Proterozoic), Elliot Lake area, Ontario, Canada, *Sediment. Geol.* 63, p. 127-153.
- Fralick, P. W. and Miall, A. D., 1982, Sedimentology of Huronian deposits, including Uranium bearing rocks, Ontario Geological Survey, OFR 5375, 35 p.
- Fyon, J. A., Breaks, F. W., Heather, K. B., Jackson, S. L., Muir, T. L., Stott, G. M. and Thurston, P. C., 1992, Metallogeny of Metallic Mineral Deposits in the Superior Province of Ontario, In: P.C. Thurston, H.R. Williams, R.H. Sutcliffe and G.M. Stott (Eds.), *Geology of Ontario*, Ontario Geological Survey, Special Vol. 4, Part 2, p. 1091-1176.
- Goodarzi, F., Gentzis, T., Mossman, D. and Nagy, B., 1993, Petrography and Genesis of Organic Matter in the Paleoproterozoic Uraniferous Conglomerates of the Elliot Lake Region, Ontario, *Energy Sources*, Part A: Recovery, Utilization, and Environmental Effects, Vol. 15, Issue 2, p. 339-357.
- Grandstaff, D. E., 1980, Origin of uraniumiferous conglomerates at Elliot Lake, Canada and Witwatersrand, South Africa: Implications for oxygen in the Precambrian atmosphere, *Precambrian Research*, Vol. 13, Issue 1, p. 1-26.

- Hansley P. L. and Fitzpatrick, J. J., 1989, Compositional and crystallographic data on REE-bearing coffinite from the Grants uranium region northwestern New Mexico, *American Mineralogist*, Vol. 74, p. 263-270.
- Holland, H.D., 2002, Volcanic gases, black smokers, and the Great Oxidation Event, *Geochimica et Cosmochimica Acta* 66, p. 3811-3826.
- Holliger, P., 1988, Ages U-Pb définis in situ sur oxydes d'uranium à l'analyseur ionique: méthodologie et conséquences géochimiques. *Comptes rendus de l'Académie des Sciences de Paris* 307, p. 367-373.
- Kempe, U., 2003, Precise electron microprobe age determination in altered uraninite: consequences on the intrusion age and the metallogenic significance of the Kirchberg granite (Erzgebirge, Germany), *Contributions to Mineralogy and Petrology* 145, p. 107-118.
- Kish, L. and Cuney, M., 1981, Uraninite-albite veins from Mistamisk Valley of the Labrador Through, Quebec. *Mineralogical Magazine* 44, p. 471-483.
- Krogh, T. E., Davis, D. W. and Corfu, F., 1984, Precise U-Pb zircon and badelleyite ages for the Sudbury area, In: E.G. Pye, A.J. Naldrett, P.E. Giblin (Eds.), *The Geology and Ore Deposits of the Sudbury Structure*, Ontario Geol. Surv. Spec., vol. 1, p. 431-446.
- Larbi, Y., Stevenson, R., Breaks, F., Machado, N. and Gariépy, C., 1999, Age and isotopic composition of late Archean leucogranites: implications for continental collision in the western Superior Province, *Canadian Journal of Earth Sciences* 36(4), p. 495-510.
- Law and Phillips, 2006, Witwatersrand gold-pyrite-uraninite deposits do not support a reducing Archean Atmosphere, In: S.E. Kesler and H. Ohmoto (eds.), *Evolution of Early Earth's Atmosphere, Hydrosphere and Biosphere – Constraints from ore deposits*, Geological Society of America, Memoir 198, p. 121-141.
- Long, 1995, Huronian sandstone thickness and paleocurrent trends as a clue to the tectonic evolution of the Southern Province, *The Canadian Mineralogist*, Vol. 33, p. 922-923.
- Ludwig, K. R., 1999, Isoplot/ex version 2.10. A geochronological toolkit for Microsoft Excel. Special Publication n° 1a, Berkeley Geochronological Center.
- Mair, J. A., Maynes, A. D., Patchett, J. E. and Russel, R. D., 1960, Isotopic evidence on the origin and age of the Blind River uranium deposits, *Journal of Geophysical Research*, Vol. 65, p. 341-348.
- Meddaugh, W. S. and Holland, H. D., 1981, Age and origin of uraninite in the Elliot Lake, Ontario, uranium deposits, *Geological Society of America*, Abstract with Program 12, 509 p.
- Mock, R. L. and Ohmoto, H., 1997, Nondetrital origins of uranium-bearing minerals and pyrites in Early Proterozoic quartz-pebble conglomerates of the Elliot Lake district, Ontario, 7<sup>th</sup> Annual V. M. Goldschmidt Conference Abstract (2273), *LPI Contrib.* 921, p. 143.
- Montel, J. M., Foret, S., Veschambre, M., Nicollet, C. and Provost, A., 1996, Electron microprobe dating of monazite, *Chemical Geology*, 131, p. 37-53.
- Mossman, D. J., 1999, Carbonaceous substances in mineral deposits; implications for geochemical exploration, *Geochemical exploration 1997, selected papers from the 18<sup>th</sup> international Geochemical exploration symposium*, *Journal of Geochemical Exploration*, Vol. 66, p. 279-293.
- Mossman, D. J., Goodarzi, F. and Gentzis, T., 1993a, Characterization of insoluble organic matter from the Lower Proterozoic Huronian Supergroup, Elliot Lake, Ontario, *Precambrian research*, vol. 61, n° 3-4 (2 p.), p. 279-293

- Mossman, D. J., Nagy, B. and Davis, D. W., 1993b, Hydrothermal alteration of organic matter in uranium ores, Elliot Lake, Canada: Implications for selected organic-rich deposits, *Geochimica et Cosmochimica Acta*, Vol. 57, Issue 14, p. 3251-3259.
- Ono, S., Mock, R. and Ohmoto, H., 1998, Two-fluids (oxic and reduced) model for the formation of uraninite in Early Proterozoic quartz-pebble conglomerates of the Elliot Lake District, Ontario, Canada, Goldschmidt Conference, *Mineralogical Magazine* Vol. 62A, p. 1110-1111.
- Pommier, A., Cocherie, A. and Legendre, O., 2002, EPMA Dating User's manual: Age calculation from electron probe microanalyser measurements of U-Th-Pb, BRGM, 9 p.
- Rainbird, R. H. and Davis, W. J., 2006, Sampling superior: detrital zircon geochronology of the Huronian, *Geological Association of Canada Abstract with Programs*, Vol. 31, p. 125.
- Rainbird, R. H., Heaman, L. M., Davis, W. J. and Simonetti, A., 2006, Coupled Hf and U-Pb isotope analysis of detrital zircons from the Paleoproterozoic Huronian Supergroup *Geological Society of America Abstracts with Programs*, Vol. 38, No. 7, p. 410.
- Robertson, D. S. and Steenland, N. C., 1960, On the Blind River uranium ores and their origin, *Economic Geology*, Vol. 55, No. 4, p. 659-694.
- Robinson, A. and Spooner, E.T.C., 1982, Source of detrital components of uraniferous conglomerates, Quike ore zone, Elliot Lake, Ontario, Canada, *Nature* 299, 622-624.
- Roscoe, S. M., 1969, Huronian rocks and uraniferous conglomerates, *Geological Survey of Canada*, Paper 68-40, 205 p.
- Saager, R. and Stupp, H. D., 1983, U-Ti phases from Precambrian quartz-pebble conglomerates of the Elliot Lake area, Canada, and the Pongola basin, South Africa *Mineralogy and Petrology*, Vol. 32, Numbers 2-3, p. 83-102.
- Sims, P. K., Van Schmus, W. R., Schulz, K. J. and Peterman, Z. E., 1989, Tectono-stratigraphic evolution of the Early Proterozoic Wisconsin magmatic terranes of the Penokean Orogen, *Canadian Journal of Earth Sciences*, Vol. 26 (10), p. 2145-2158.
- Suzuki, K., Adachi, M. and Kazjizuka, I., 1994, Electron microprobe observations of Pb diffusion in metamorphosed detrital monazites, *Earth and Planetary Science Letter*, 128, p. 391-405.
- Theis, N. J., 1979, Uranium-bearing and associated minerals in their geochemical and sedimentological context, Elliot Lake, Ontario, *Geological Survey of Canada Bulletin* Vol. 304, 50 p.
- Tropper, P. and Manning, C.E., 2005, Very low solubility of rutile in H<sub>2</sub>O at high pressure and temperature, and its implications for Ti mobility in subduction zones, *American Mineralogist*, Vol. 90, No. 2-3, p. 502-505.
- Utsunomiya, S., Deditius, A. P., Pointeau, V. and Ewing, R. C., 2008, Coffinite and ningyoite from the natural reactor at Bangombé, Gabon, *Geochimica et Cosmochimica Acta*, Vol. 72, Issue 12, p. A968.
- Williams, M. L., Jercinovic, M. J. and Hetherington, C. J., 2007, Microprobe Monazite Geochronology: Understanding Geologic Processes by Integrating Composition and Chronology, *Annual Review of Earth and Planetary Sciences*, Vol. 35, p. 137-175.
- Willingham, T.O., Nagy, B., Nagy, L.A., Krinsely, D.H. and Mossman, D.J., 1985, Uranium-bearing stratiform organic matter in paleoplacers of the lower Huronian Supergroup, Elliot Lake – Blind River, Canada. *Canadian Journal of Earth Sciences* 22, p. 1930-1944.

- Yamaguchi, K. E. and Ohmoto, H., 2006, Evolution from sulphur-isotope and trace elements in pyrite for their multiple post-depositional processes in uranium ores at the Stanleigh Mine, Elliot Lake, Ontario, Canada, In: S.E. Kesler and H. Ohmoto (eds.), *Evolution of Early Earth's Atmosphere, Hydrosphere and Biosphere – Constraints from ore deposits*, Geological Society of America, Memoir 198, p. 143-156.
- Yamaguchi, K. E., Ono, S. and Ohmoto, H., 1998, Diverse origins of pyrites in Palaeoproterozoic uraniferous quartz-pebble conglomerates, Elliot Lake, Canada: evidence from laser-microprobe sulphur isotope analyses, *Goldschmidt Conference Toulouse, Mineralogical Magazine*, Vol. 62A, Issue 3, p. 1673-1674.
- Young, G.M., 1995, The Huronian Supergroup in the context of a Paleoproterozoic Wilson cycle in the Great Lakes region, *The Canadian Mineralogist*, Vol. 33, p. 921-922.

## PARTIE 3.3

# Geochemistry and Mineralogy of post-GOE Quartz Pebble Conglomerates: example of the thoriferous Jatulian Formation from the Baltic Shield (2.3-2.15 Ga)

Isabelle Duhamel and Michel Cuney

*G2R, Nancy-Université, CNRS, CREGU, BP 239, 54506, Vandœuvre-lès-Nancy, France*

---

### Abstract

The rise of oxygen in the Earth's atmosphere also called the Great Oxidation Event (GOE) as drastically influenced the uranium cycle with the disappearance of major quartz-pebble conglomerate (QPC)-type U deposits after 2.2 Ga. The Jatulian Formation deposited between 2.3 and 2.1 Ga is a basal sedimentary unit unconformably overlying Archean basement granites of the Karelian Craton (Baltic Shield) where occurrence of uraninite-bearing pegmatites have been reported. Lower Jatulian comprises QPC horizons from few centimetres to 3 meters thick interbedded with quartzite and sandstones and totalizing a sequence of 200 m thick. Jatulian quartzite-sandstones are immature and arkosic in composition with high potassium content associated to abundant plagioclase, orthoclase and microcline with rounded quartz, matrix-supported in clays with occasional carbonates. Coarser lenses of QPC represent paleo-channels enriched in thorium (Th up to 0.29 wt%), rare earth elements ( $\Sigma$ REE up to 1385 ppm) and slightly in uranium (U up to 20.3 ppm) that can be ascribed to refractory mineral concentrations. The radiogenic minerals occur as detrital accumulation of monazite and zircon between the feldspar and quartz grains, which suggest that Jatulian QPC derives from the erosion of an Archean potassic-rich granitic source. Post-depositional alteration associated to intense hematization led to alteration of monazite and newformation of abundant ferrithorites mostly responsible of the anomalous radioactivity. Chemical U-Th-Pb age dating indicates that the oxidative weathering of phosphate minerals is a relatively late event happening approximately in the last 500 Ma. The absence of either uraninite or boxwork point to the presence of sufficient amounts of oxygen in the atmosphere at the time of the Archean Baltic Shield erosion.

---

### Keywords

Finland, Jatulian, quartz pebble conglomerates, paleo-placer, Great Oxidation Event, monazite, zircon, alteration.

## Introduction

Quartz-pebble conglomerate (QPC) uranium deposits are hosted in basal units of large Archean to Early Paleoproterozoic basins formed within old relief depressions by fluvial to deltaic braided stream systems and overlie eroded Archean cratons. The U mineralization is mainly represented by accumulation of uraninite grains in heavy mineral beds associated with pyrite, titanium oxides, gold, zircon and monazite that form the typical accessory mineral assemblage of Archean granite and greenstone terrains. This type of ore occurrences is hosted by sedimentary units generally older than 2.2 Ga and supposedly deposited under anoxic conditions, as the well documented Witwatersrand deposits in South Africa or the Elliot Lake conglomerates in Canada. The youngest QPC-deposits, as the Jacobina conglomerates in Brazil (Ledru et al., 1007; Milesi et al., 2002) which deposition is bracketed between 2086 Ma (the youngest isotopic U-Pb age measured in detrital zircon grains) and 1883 Ma (age of younger intrusive granites), only host detrital gold particles and secondary sulphide minerals deposited from post-sedimentation hydrothermal activity.

The disappearance of detrital uraninite and pyrite, both redox sensitive minerals, from the sedimentary rocks younger than Paleoproterozoic would be the result of oxidant reactions in the atmosphere and/or hydrosphere. Other geochemical and sedimentological evidences suggest the existence of a drastic change in the Earth surface environment at the beginning of the Paleoproterozoic Eon: as the disappearance of mass-independent sulphur isotope variations (Bekker et al., 2004), the decrease of the atmospheric methane content (Kasting, 2005), the abrupt end of the worldwide deposition of banded iron formations after 2.4 Ga (Klein, 2005), and the rise of sulphate in shallow marine environments with deposition of evaporitic basins inexistent before 2.2 Ga (Grotzinger and Kasting, 1993 ; Pope and Grotzinger, 2003; Evans, 2006). The cause of this major environmental change remain unclear but is generally inferred to the emergence of photosynthetic life starting with cyanobacteria development (Cloud 1968; Kirschvink and Kopp 2008) or to the dissociation of atmospheric methane coupled to H<sub>2</sub> escape (Catling et al., 2001; Catling and Claire, 2005). The combined geochemical and geological data give the Great Oxidation Event (GOE) timing between 2.4 and 2.3 (Holland, 2002).

The large majority of the QPC deposited after the GOE host no detrital uraninite or pyrite as the gold-bearing paleo-placer of Tarkwa in Ghana formed ca. 1.9 Ga ago (Sestini, 1973). Only few post-GOE occurrences of detrital uraninite are known and occur in very specific environment at high altitude where pressure of free-oxygen is low and high erosion rate is associated to rapid

sediment deposition that burial and protect the minerals from late weathering alteration (Maynard et al., 1991; Maynard, 1992). However, no more gigantic QPC-deposits ever been formed since Archean and Paleoproterozoic Eons. Thus, evolution from a reduced environment to an oxygen level has influenced drastically the redox sensitive mineral compartment during sub-aerial transportation.

The Jatulian sediments focused our interest because they display a favourable context for the discovery of uraniferous QPC deposits. Jatulian Formation has been deposited between 2.3 and 2.1 Ga exactly at the time of the oxygen rise in the atmosphere. Jatulian sediments form the basal unit of the Karelian Supergroup overlying the Baltic Shield and are directly in contact with the Archean granitic and metasedimentary gneisses forming the southern Karelian Craton. Uraninite occurrences have been described in the neighbour granitic domes within the Mustalampi pegmatite aged  $> 2338 \pm 2$  Ma (maximal isotopic Pb-Pb age obtained on altered uraninite, this work chapter 2-part 2.4) or in quartz veins dated at  $2322 \pm 15$  Ma (Pekkarinen, 1979). These fertile granitic sources are thus almost coeval to slightly older with the deposition of the basal Jatulian unit composed of interlayered QPC with sandstones and quartzite. This work provides a geochemical and mineralogical characterization of the basal Jatulian sediments lying upon these fertile granitic sources to investigate the presence of U and Th mineralization.

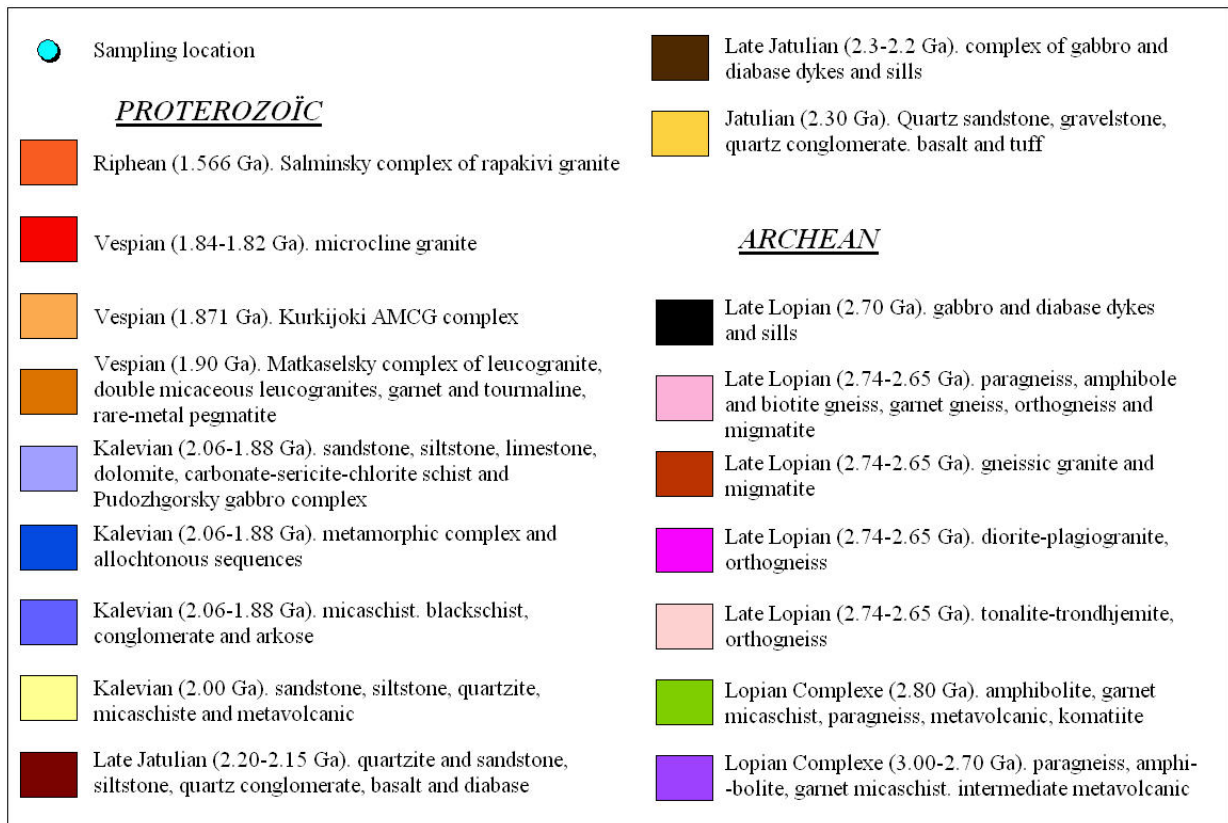
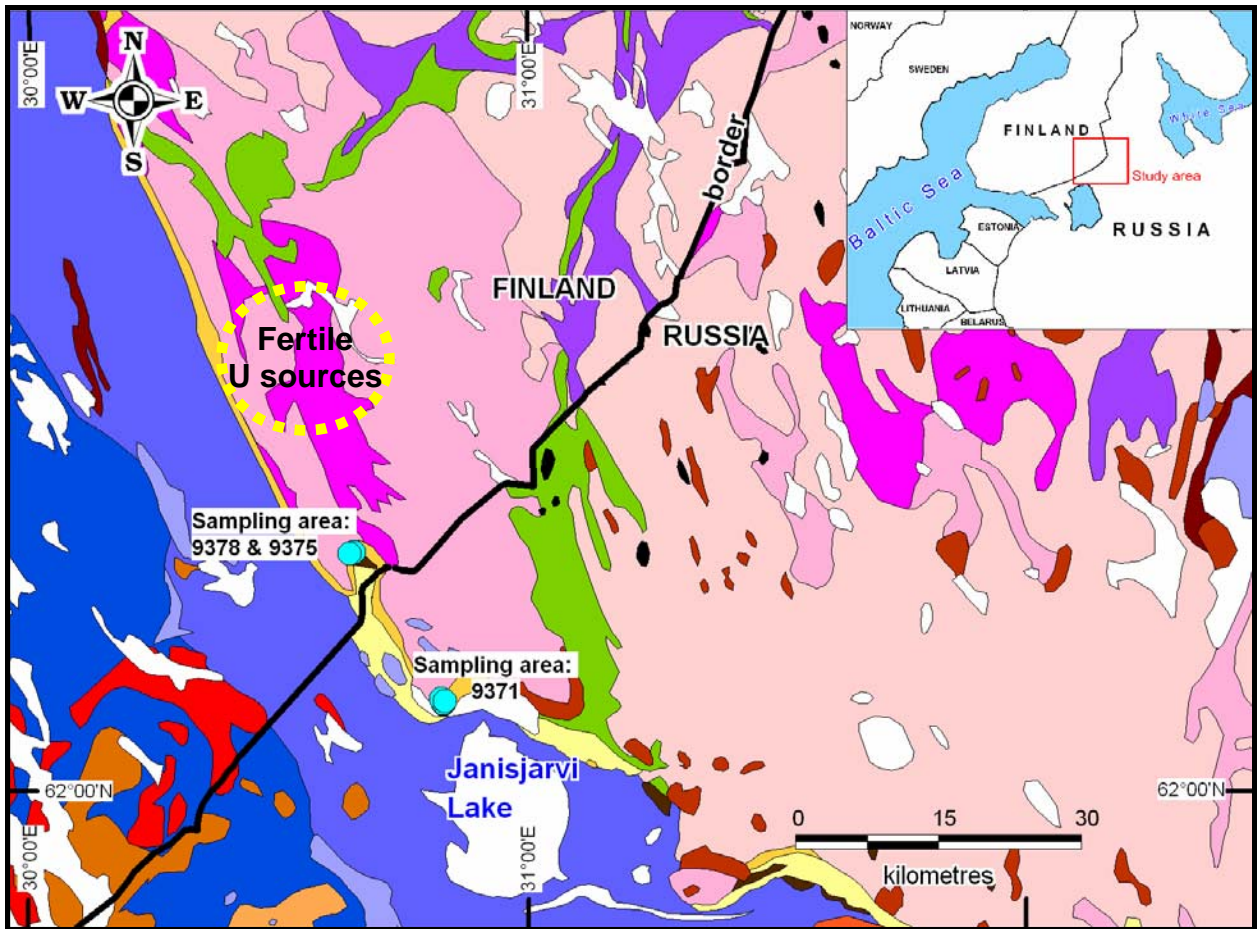


Figure 3.3.1. Geological map of the southeast Karelia at the boundary between Finland and Russia elaborated from the data of the Geological Survey of Finland.

## Geological Setting

The Karelian Supergroup represents the supracrustal cover located on the southern margin of the Baltic Shield. In the Maloye Janisjarvi-Kuhilaslampi area (Fig. 3.3.1), the sediments fill a depression created by the major Janisjarvi fault zone oriented NW-SE and form a band of 150 km long for approximately 500 m to 2000 m in thickness (Äikäs and Sarikkola, 1987). This band is penetrated by mafic volcanic dykes associated to a succession of rifting events occurring between 2.45 and 1.98 Ga that have fractioned the Baltic Shield into several blocks and probably formed the graben (Kohonen, 1995; Iljina and Hanski, 2005; Vuollo and Huhma, 2005). The Jatulian Formation is the basal unit of the Karelian Supergroup unconformably overlaying the Archean basement of the Karelian block aged ca. 3.0-2.7 Ga (Lopian) with regolith development at its contact (Paavola and Kallio, 1986). The remanant paleo-weathered basement occurring locally under the unconformity with the Jatulian sediments represents few-meters thick brecciated quartz-feldspar crystalline rocks altered to sericite, carbonate and chlorite (Pekkarinen, 1979).

The stratigraphic subdivisions of the Karelian sedimentary cover between Finland and Russia are not named the same. The Russian distinguish the following Paleoproterozoic units (Fig. 3.3.2):

- the Sarioli Group which refers to the brecciated basement regolith;
- basement is unconformably overlain by the basal Jatuli Group corresponding to the Finnish Lower Jatulian Formation (2.3-2.15 Ga) and composed of interlayered quartzite, sandstones, gritstones and conglomerates with rare dolomite lenses;
- followed upward by the Ludicovi Group mainly composed of massive dolostones and shales that corresponds to the Finnish Upper Jatulian member (dolostones) and Lower Kalevian Formation (micaschists) deposited approximately ca. 2.06-1.88 Ga.

The GOE in this sedimentary sequence is evidenced by the deposition of abundant calcium sulphates, red beds and stromatolites forming carbonate platforms in marine environments (Lahtinen et al., 2008). Moreover, the Jatulian dolomitic rocks possess high and positive  $\delta^{13}\text{C}$  values deriving from the diagenesis of organic matter and necessarily implying a developed biosphere in aerobic conditions (Karhu 1993; Melezhik et al., 2000, 2005 and 2007).

Finally, the Karelian formations were metamorphosed to the greenschist facies, faulted and folded into a NW to NNW oriented synclinorium during the compressional Svecofennian Orogeny and intruded by syn-tectonic Vespian granitic plutons about 1.8-1.95 Ga ago (Nironen, 1997; Ovchinnikova et al., 2007).

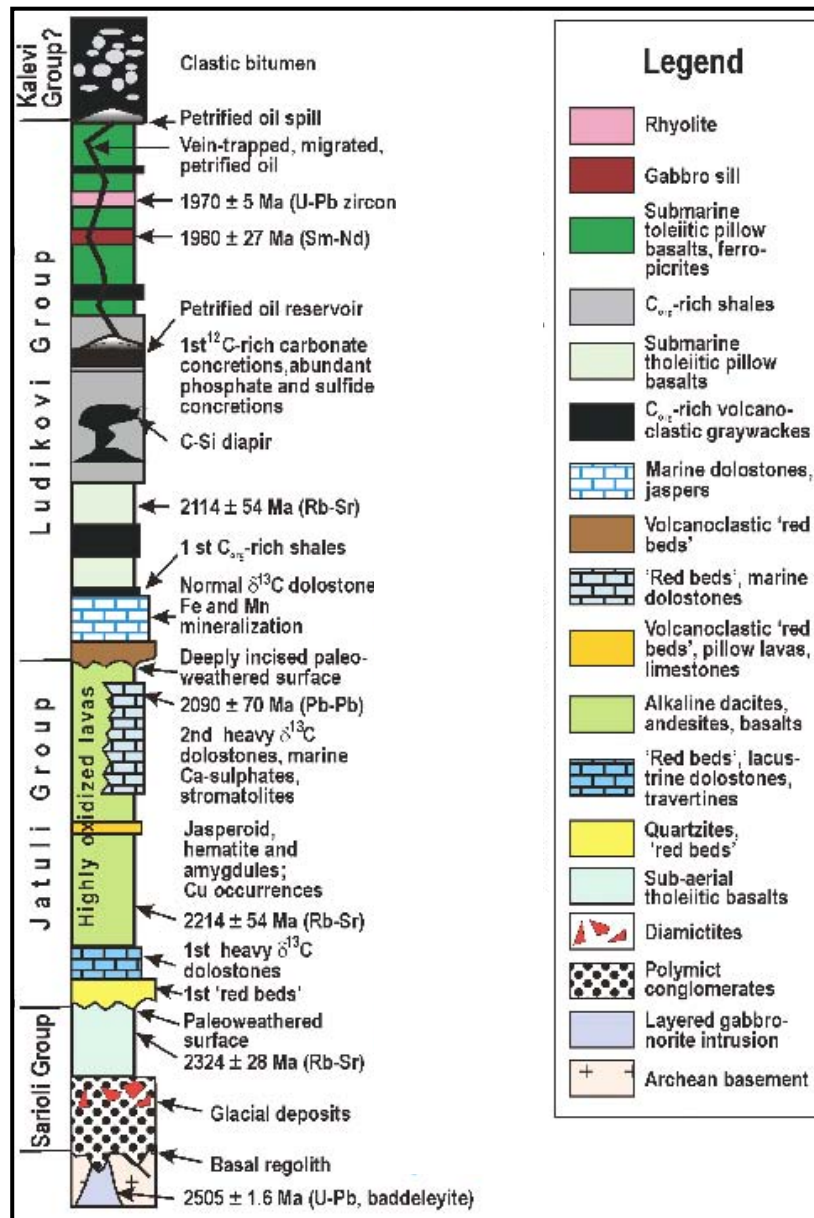


**Figure 3.3.2.** Paleoproterozoic sedimentary succession with stratigraphic appellation used in Russia (modified from Melezhik et al., 2005). The radiometric dates are from Hanski (1992), Amelin et al. (1995), and Balashov (1996).

This study focused on the Lower Jatulian Formation or Jatuli Group directly in contact with the Archean basement. The Jatulian deposition age is constrained by U-Pb and Sm-Nd ages established for volcanogenic rocks ca. 2325 Ga and the age of the Upper Jatulian dolomitic member, the Tulomozero Formation, which has been estimated by isotopic Pb-Pb dating at 2090 ± 70 Ma (Ovchinnikova et al., 2007) and 2058 ± 2 Ma (Melezhik et al., 2007). This Jatulian sequence represents ~200 m which terrigene, littoral and shallow marine sediments filling a paleo-basin at the margin of a stable Archean crustal block (Paavola and Kallio, 1986; Ovchinnikova et al., 2007). The quartzite and sandstones often have obliquely lamination of littoral type and the presence of more abundant dolomite upward suggests a transgressive succession with marine-environment sedimentation.

The Jatulian sediments host U and Th anomalies. The supposedly placer-type occurrences (Shurilov et al., 2007; Shurilov, 2008) are localized in small-thick interlayers of conglomerates in the basal parts of the obliquely laminated series. Thickness of mineralized layers ranges between 0.5 cm and 40 cm. Mineralization corresponds to concentrations of accessories in the basal parts of the conglomeratic beds: zircon, rutile, leucoxene, apatite, hematite, pyrite (with jarosite pseudomorphs), monazite and ferrithorite. The main radioactive mineral is supposedly Th-rich monazites with average bulk rock content of 0.03-0.06% Th to up to 0.7 % and a maximum of 0.005% U. Other U occurrences have also been discovered in the Ludicovian dolomitic series in the Russian border, north of the Ladoga Lake (Upper Jatulian). Uranium mineralization corresponds to pitchblende spherulites associated to graphite in the dolostones and is probably associated to hydrothermal processes (Caillat et al., 2006). Only the first type of occurrences (placer-type) will be studied in this work.

### Sampling and macroscopic description

The Jatulian Formation is outcropping to the southeast of the Baltic Shield, at the limit between Archean Karelian Craton and Proterozoic sedimentary cover. Samples from the basal sediments of the Jatulian Formation have been collected during field trip in 2006 (Caillat et al., 2006) in the northeast of the Janisjarvi Lake at the boundary between Finland and Russia (Fig. 3.3.1). Location of sampling with GPS coordinates and a short description of the lithologies and radioactivity measured by scintillometer for each outcrop are given in Table 3.3.1. A total of eleven samples have been collected, 6 in Russia and 5 in Finland along two parallel transects across the Jatulian unit, both transects separated ~20 km from each other (Fig. 3.3.1).

**Table 3.3.1.** Description and location of the studied samples

Sample	Lithology	Location	Radioactivity		Description	GPS Coordinates (Finish system : KKKJ3)	
			Outcrop (SPPγ in cps)	Sample (SPP2 in cps)		X	Y
9371-2	Quartzite	Russia, Janisjarvi	170	50-70	Jatulian grey quartzite with red surface	3700366	6892127
9371-3	Quartzite	Russia, Janisjarvi	120	40-55	Jatulian black quartzite	3700366	6892127
9371-4	Quartzite	Russia, Janisjarvi	140	45-65	Jatulian black quartzite	3700336	6892204
9371-5	Quartzite + Conglomerate	Russia, Janisjarvi	500	60-100	Jatulian black quartzite and conglomerate	3700336	6892204
9371-6	Conglomerate	Russia, Janisjarvi	600	110-240	Jatulian red conglomerate	3700083	6892602
9371-7	Quartzite (albitized)	Russia, Janisjarvi	130	45-65	Pink albite in contact with green Jatulian quartzite with quartz vein	3700483	6892428
9375-11	Sandstone	Finland, Miljoonakallio roadcut	140	40-60	Medium grained feldspathic sandstone	3690099	6907320
9375-12	Sandstone	Finland, Miljoonakallio roadcut	120	45-55	Coarse-grained to fin grained sandstone displaying a slightly higher radioactivity	3690099	6907320
9375-13	Quartzite	Finland, Miljoonakallio roadcut	140	50-60	Pure quartzite	3690099	6907320
9375-14	Quartz-Pebble Conglomerate	Finland, Miljoonakallio roadcut	900	350-600	Radioactive quartz pebble conglomerate	3689675	6907161
9378-14	Conglomerate	Finland, Miljoonakallio roadcut	300	85-120	Strongly radioactive conglomerate	3689675	6907161

The Lower Jatulian Formation corresponds mainly to light-grey coarse-grained quartzite and sandstones progressively becoming middle-grained and dark coloured upward (samples 9371-3 and 4 in Fig. **3.3.3** and samples 9375-11, 12 and 13 in Fig. **3.3.4**). Quartzite and sandstones generally display herringbone cross-bedding that form zig-zag structures by the superposition of oblique laminations, as in sample 9371-3 (Fig. **3.3.3**), which are characteristic of littoral and tidal sedimentation with alternating flow directions. Some ferruginized coarser-grained lenses are sometimes present in the obliquely laminated quartzite-sandstone beds as samples 9371-2 and 9371-7. Locally, quartz veins intrude the sediments and sometimes display a well defined but irregular contact associated to albitization of the host rock (pink albite layer in quartzite 9371-7).

Conglomerate lenses occur sporadically in the quartzite-sandstone unit and are interpreted as coarse and poorly sorted sediments filling channels. Conglomerates are composed of quartz pebbles, feldspar-quartz and quartz-biotite pebbles up to 10 cm large (Fig. **3.3.3**: 9371-6A+6B; Fig. **3.3.4**: 9375-14 and 9378-14 sampled at a few meters distance laterally). The coarser conglomerates are located at the base of the channels and always display reddish ferruginous cement with darker red to brown coloration more pronounced around the pebbles. Upward in the channels, the pebbles are smaller and float in coarse quartzite-sandstones, as sample 9371-5 (Fig. **3.3.3**).

The variation in the coloration of the sedimentary sequence mainly grey with ferruginous coarser lenses suggests either that the detrital material filling the fluvial/deltaic channels has been transported under an oxygen-rich atmosphere or that the ferric alteration may be post-sedimentary with oxidant fluid circulation affecting preferentially the coarser beds which are more porous. It should be noticed although that the peaks of radioactivity are measured on the reddish and coarser conglomerates, up to 600 cps on the outcrop 9371-6 and 900 cps in the outcrop 9375-14 (Table **3.3.1**).

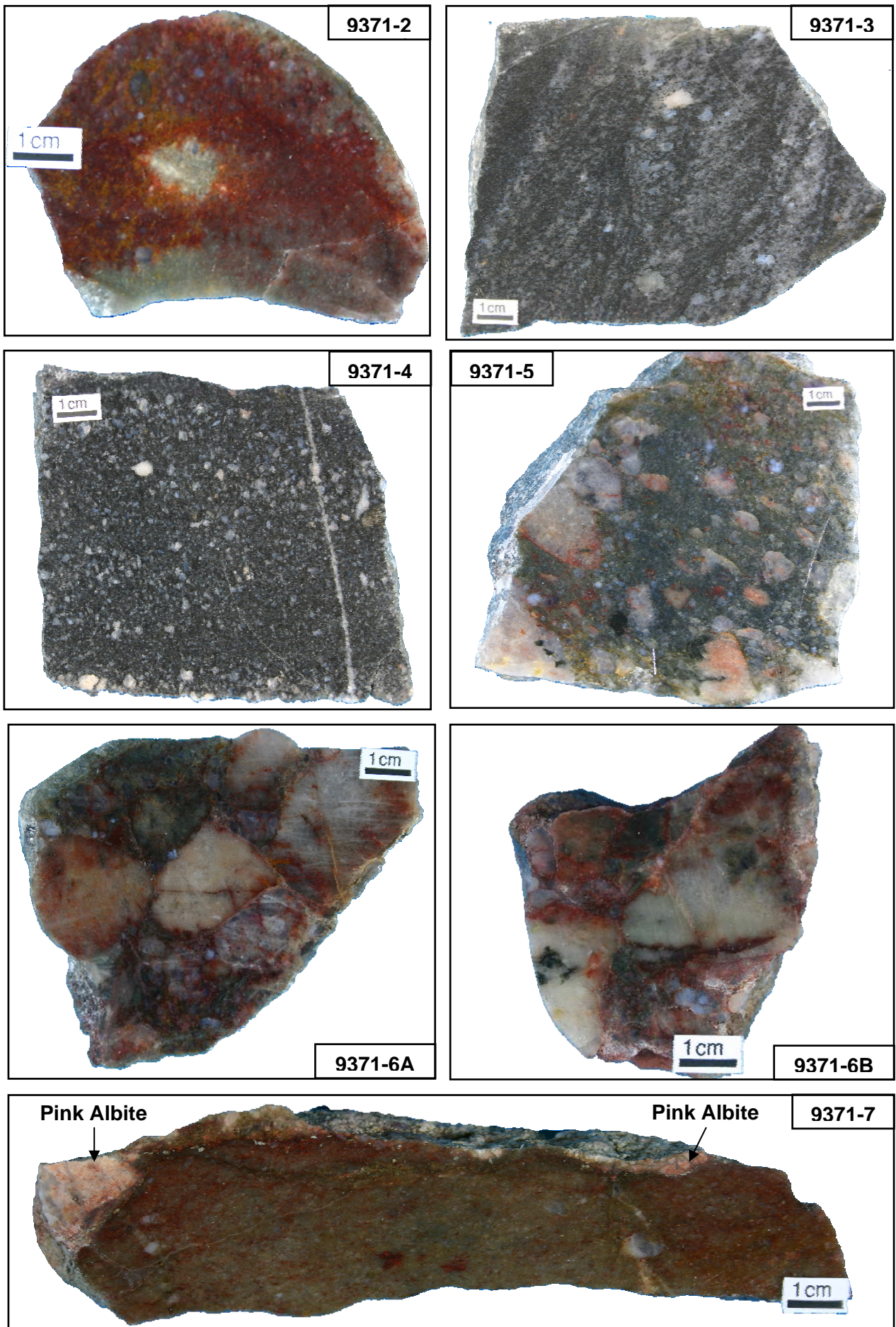


**Figure 3.3.3.** Samples of the Lower Jatulian sequence collected in the southern transect 9371 (location in Fig. 3.3.1) north of the Janisjarvi Lake in Russia.

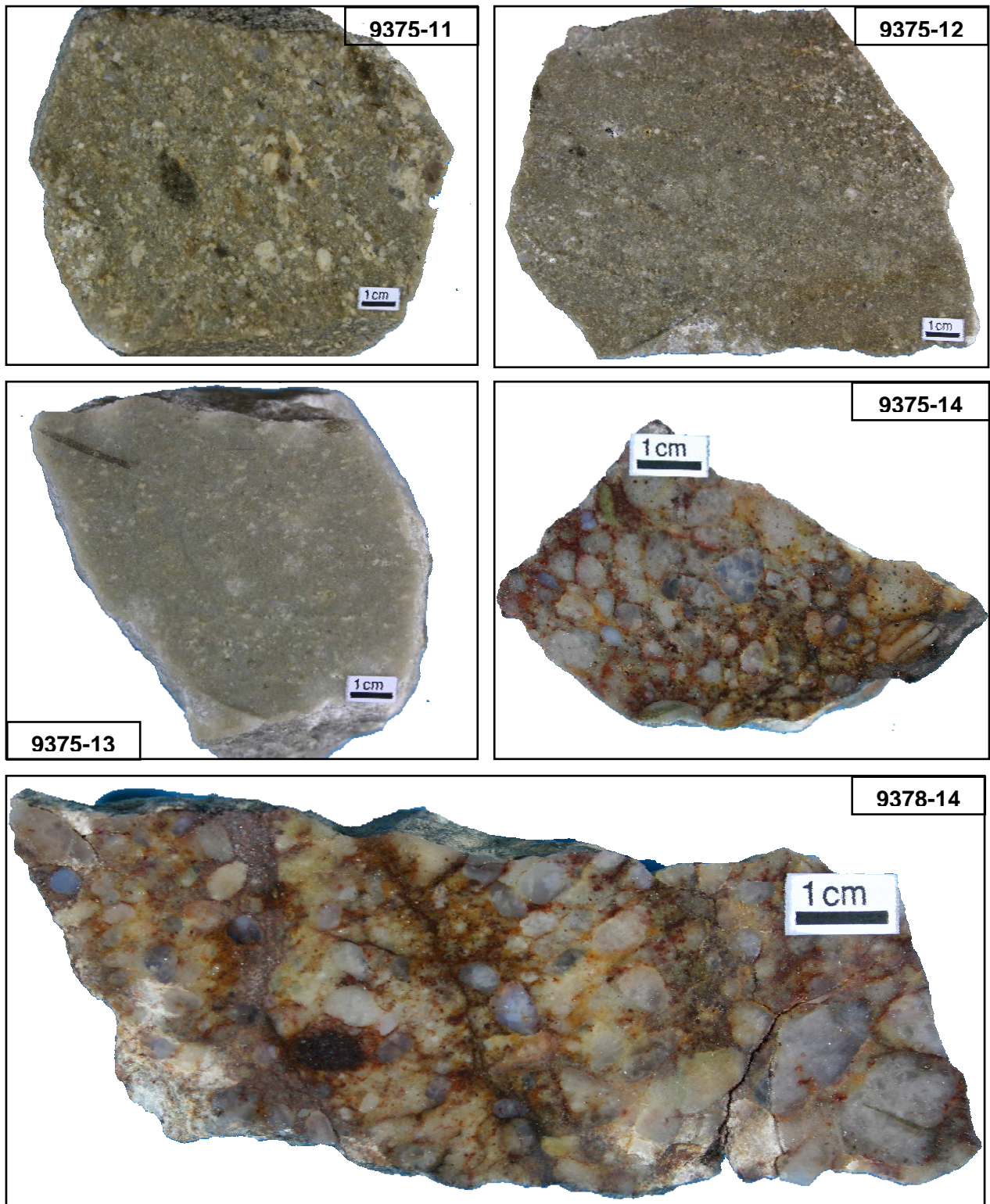


**Figure 3.3.4.** Samples of the Lower Jatulian sequence collected in the northern transect 9375-9378 (location in Fig. 3.3.1) south of the Karelian fertile granitoids in Finland.

## Analytical techniques

### Whole-rock geochemistry

Eleven samples were crushed and powdered to a granulometry below 80  $\mu\text{m}$  using successively a jaw crusher, a roller mill and an agate planetary micro-mill at the G2R laboratory (University of Nancy, France). For sample 9371-7, the albitized zone in contact with the quartz vein was separated to avoid contamination of the quartzite bulk composition. The whole-rock geochemical analyses were performed at the SARM laboratory (Nancy, France) using inductively coupled plasma spectroscopy techniques, ICP-OES (emission) for detection of 10 major elements and ICP-MS (mass) for 29 trace elements and 14 rare earth elements. The analytical procedure and the international standards used for calibration are described by Carignan et al. (2001). The detection limits are low in order to 1  $\text{ng}\cdot\text{g}^{-1}$  and uncertainties on measurements are <1% for Si, <2% for Fe, <5-10% for Al, Mn, Mg and Ti, <5% for Th and rare earth elements (REE) and <8% for U. Results are presented in the two following tables.

**Table 3.3.2.** Whole-rock chemical analyses of the major elements (ICP-OES) in the basal Jatulian sediments

Sample	9371-2	9371-3	9371-4	9371-5	9371-6	9371-7	9375-11	9375-12	9375-13	9375-14	9378-14
Lithology	Quartzite	Quartzite	Quartzite	Quartzite + Conglomerate	Conglomerate	Quartzite (albitized)	Sandstone	Sandstone	Quartzite	Conglomerate	Conglomerate
SiO <sub>2</sub> (%)	96.54	96.96	94.67	98.70	97.07	91.07	86.98	88.34	90.97	91.50	96.84
Al <sub>2</sub> O <sub>3</sub>	0.97	1.05	3.00	1.19	1.19	5.04	8.12	7.19	4.73	2.25	1.79
CaO	<L.D.	<L.D.	<L.D.	<L.D.	<L.D.	<L.D.	<L.D.	<L.D.	<L.D.	0.04	<L.D.
Na <sub>2</sub> O	<L.D.	<L.D.	<L.D.	<L.D.	<L.D.	<L.D.	<L.D.	<L.D.	<L.D.	<L.D.	<L.D.
K <sub>2</sub> O	0.28	0.32	0.89	0.35	0.35	1.57	3.72	2.59	1.48	0.64	0.58
P <sub>2</sub> O <sub>5</sub>	<L.D.	<L.D.	<L.D.	0.02	0.06	<L.D.	<L.D.	<L.D.	<L.D.	0.29	0.08
Fe <sub>2</sub> O <sub>3</sub>	0.44	0.08	0.14	0.31	0.43	0.37	0.66	0.78	0.28	2.76	0.73
MnO	0.00	<L.D.	<L.D.	0.00	0.00	0.00	0.00	0.00	0.00	0.01	0.00
MgO	0.03	0.01	0.03	<L.D.	<L.D.	0.12	0.25	0.26	0.10	0.06	0.06
TiO <sub>2</sub>	0.03	0.03	0.04	0.08	0.06	0.14	0.10	0.14	0.07	0.09	0.13
LOI	0.21	0.35	0.55	0.23	0.24	0.67	1.12	1.35	0.94	1.00	0.62
Total	98.50	98.80	99.32	100.89	99.39	98.98	100.95	100.66	98.57	98.63	100.82
A/CNK	3.23	2.98	3.11	3.16	3.17	2.96	2.01	2.56	2.94	2.94	2.87
Q	530.23	531.55	506.81	540.75	531.69	472.26	403.91	435.53	473.64	494.03	525.51
P	5.89	6.89	18.92	7.38	7.36	33.45	79.14	55.07	31.56	12.98	12.26
A	13.16	13.63	40.02	15.96	16.00	65.51	80.17	86.05	61.30	29.09	22.90
B	6.53	1.71	2.94	4.94	6.04	9.35	15.69	17.99	6.75	37.28	12.10

*Notes:* Analyses realised by SARM (CRPG-CNRS, Nancy, France); LOI = loss on ignition; <D.L. = below detection limits (CaO = 0.02%; Na<sub>2</sub>O = 0.07%; K<sub>2</sub>O = 0.05%; P<sub>2</sub>O<sub>5</sub> = 0.015%; MnO = 0.001%; MgO = 0.01%); A/CNK [= Al/(Na+K+2Ca)] index calculated in moles whereas Q [= Si/3-(K+Na+2Ca/3)], P [= K-(Na+Ca)], A [= Al-(K+Na+2Ca)] and B [= Fe+Ti+Mg] parameters are calculated in thousands of cations.

**Table 3.3.3.** Whole-rock chemical analyses of the trace elements (ICP-MS) in the basal Jatulian sediments

Sample	9371-2	9371-3	9371-4	9371-5	9371-6	9371-7	9375-11	9375-12	9375-13	9375-14	9378-14
Lithology	Quartzite	Quartzite	Quartzite	Quartzite + Conglomerate	Conglomerate	Quartzite (albitized)	Sandstone	Sandstone	Quartzite	Conglomerate	Conglomerate
As (ppm)	2.71	<L.D.	<L.D.	<L.D.	4.03	<L.D.	<L.D.	<L.D.	<L.D.	7.13	3.31
Ba	35.22	33.61	119.10	54.06	58.61	353.60	376.30	263.50	114.90	119.70	100.40
Be	0.22	<L.D.	0.23	0.22	0.26	0.94	0.78	0.91	0.55	0.52	0.25
Bi	0.12	<L.D.	<L.D.	0.15	0.14	0.36	0.12	0.12	0.20	0.11	<L.D.
Cd	0.17	<L.D.	<L.D.	0.22	0.20	<L.D.	<L.D.	<L.D.	<L.D.	0.67	0.75
Co	0.54	<L.D.	<L.D.	<L.D.	<L.D.	<L.D.	0.76	0.75	0.51	1.42	<L.D.
Cr	15.41	14.87	13.83	37.70	33.62	23.43	21.88	18.09	16.85	48.46	34.96
Cs	<L.D.	<L.D.	<L.D.	<L.D.	<L.D.	0.17	0.59	0.56	0.25	0.17	0.11
Cu	4.46	4.85	42.09	12.25	46.00	29.27	<L.D.	<L.D.	<L.D.	92.51	30.09
Ga	1.88	1.60	4.26	1.89	2.24	9.16	9.61	9.18	5.79	6.47	3.41
Ge	0.67	0.54	0.56	0.68	0.88	0.84	0.68	0.70	0.56	1.96	1.00
Hf	5.16	2.35	1.53	7.25	4.61	2.88	2.51	2.46	1.18	21.28	24.35
In	<L.D.	<L.D.	<L.D.	<L.D.	<L.D.	<L.D.	<L.D.	<L.D.	<L.D.	<L.D.	<L.D.
Mo	0.47	<L.D.	<L.D.	0.45	0.65	0.70	<L.D.	<L.D.	<L.D.	0.91	0.45
Nb	2.13	1.47	1.68	20.72	15.62	5.61	4.64	6.60	2.74	45.73	21.92
Ni	5.29	9.08	5.15	6.71	7.45	7.77	8.97	7.22	7.67	6.49	3.74
Pb	5.90	1.80	1.89	13.60	23.11	5.06	7.48	4.66	3.74	98.86	77.62
Rb	8.60	9.34	29.39	12.10	12.25	47.42	125.80	108.10	58.56	21.07	17.13
Sb	<L.D.	<L.D.	<L.D.	<L.D.	0.12	<L.D.	<L.D.	<L.D.	<L.D.	<L.D.	<L.D.
Sn	0.56	0.46	0.77	1.03	0.72	0.96	0.74	1.18	0.55	51.88	15.93
Sr	3.72	<L.D.	6.52	4.27	7.84	2.91	30.38	29.42	27.47	706.80	64.37
Ta	2.12	0.30	0.40	8.75	7.51	0.74	0.74	0.94	0.38	46.00	16.40
Th	153.30	4.04	24.25	409.80	941.10	8.68	25.54	6.88	4.06	2928.00	860.30
U	1.70	1.16	1.35	2.80	4.13	1.94	1.03	1.19	0.87	20.25	8.27
V	7.71	5.78	8.21	18.72	15.02	26.57	8.28	10.63	5.80	45.56	25.93
W	0.40	0.31	0.36	0.62	0.51	0.61	0.35	0.39	0.25	1.55	0.78
Y	7.76	2.35	2.28	15.71	37.54	12.92	8.81	15.21	5.18	118.10	54.35
Zn	<L.D.	7.11	28.13	7.74	19.87	21.61	6.81	6.99	<L.D.	<L.D.	<L.D.
Zr	218.70	87.02	57.14	293.80	194.00	104.70	91.51	92.23	42.52	973.50	917.00
Th/U	90.44	3.48	18.00	146.62	228.15	4.48	24.84	5.78	4.66	144.59	103.99
La (ppm)	11.88	1.07	1.01	4.67	9.63	12.92	8.68	26.08	6.43	303.60	83.35
Ce	28.06	2.37	2.20	13.82	26.88	25.83	23.46	54.33	12.66	618.10	181.70
Pr	3.43	0.27	0.27	1.63	3.19	2.93	2.32	6.40	1.41	62.39	20.84
Nd	12.89	1.11	1.08	6.68	13.32	11.32	8.74	23.77	5.08	222.90	79.61
Sm	2.77	0.30	0.32	2.54	5.28	2.83	1.97	4.49	0.94	54.62	20.88
Eu	0.28	0.04	0.05	0.29	0.58	0.58	0.38	0.97	0.21	10.57	3.77
Gd	2.15	0.33	0.37	2.92	6.45	2.85	1.67	3.31	0.75	47.68	17.49
Tb	0.30	0.06	0.06	0.54	1.18	0.46	0.26	0.49	0.12	6.55	2.45
Dy	1.60	0.38	0.38	3.31	7.08	2.51	1.57	2.65	0.77	31.16	12.46
Ho	0.28	0.08	0.07	0.61	1.29	0.43	0.30	0.50	0.16	4.95	2.12
Er	0.72	0.24	0.23	1.72	3.51	1.08	0.87	1.40	0.50	11.60	5.50
Tm	0.11	0.04	0.04	0.29	0.52	0.15	0.14	0.22	0.08	1.43	0.78
Yb	0.71	0.31	0.29	2.05	3.38	1.02	0.95	1.44	0.58	8.17	5.15
Lu	0.12	0.05	0.05	0.31	0.47	0.17	0.14	0.21	0.09	1.10	0.77
ΣREE	65.29	6.64	6.42	41.37	82.77	65.07	51.45	126.25	29.77	1384.82	436.86
[La/Sm] <sub>N</sub>	1.04	0.86	0.75	0.44	0.44	1.10	1.06	1.40	1.66	1.34	0.96
[Gd/Yb] <sub>N</sub>	2.45	0.87	1.03	1.15	1.54	2.27	1.43	1.86	1.06	4.72	2.75
Eu/Eu*	0.35	0.42	0.42	0.33	0.30	0.63	0.65	0.77	0.76	0.63	0.60

Notes: Analyses realised by SARM (CRPG-CNRS, Nancy, France); ΣREE in ppm, [X]<sub>N</sub> = normalized to chondrites and Eu/Eu\* = Eu<sub>N</sub>/√(Gd<sub>N</sub>×Sm<sub>N</sub>).

**Mineralogical study**

Mineralogical studies were performed at the University of Nancy (France) on a set of 15 polished thin sections representative of the various lithologies in the basal Jatulian sedimentary unit, quartzite, sandstones and conglomerates. Detailed petrographic, textures and assemblage of the minerals were carried out using both polarized microscope Olympus BX51 and scanning electron microscope Hitachi FEG-S4800 (SEM). Semi-quantitative analyses were performed by a coupled energy dispersive spectrometer Noran Vantage with the SEM. They allow element repartition mapping to evaluate the composition variations associated to average atomic number differences in backscattered electron images (BSE). High brightness areas in BSE mode correspond to heavy atomic weight element concentrations whereas darker domains are associated to lighter element accumulations.

Electron microprobe analyses (EMPA) in the refractory minerals bearing U and/or Th, zircon and monazite, were conducted on CAMECA SX100 instrument at the SCMEM laboratory (Nancy University). The measurements were performed with a current intensity of 10 nA, an accelerating voltage of 20 kV and a beam spot size of approximately 2  $\mu\text{m}$  wide. The standards, crystal analyser and counting times for each analysed element are given in Table 3.3.4. The relative errors on each measurement are below 1%. To allow comparison between the different minerals, the results given in weight percent (wt.%) have been recalculated for the plots in atomic percent (at.%).

The U and Pb concentrations in zircon grains are mostly below detection limits; however, U, Th and Pb contents over instrument limitation have been measured in monazite grains and the chemical ages were calculated for each EMPA by iteration resolving the following equation derived from the radioactive decay law (modified from Bowles, 1990 after Cocherie and Albarède, 2001):

$$C_{Pb} = C_{Th}[0.897(e^{\lambda_{232} \cdot t} - 1)] + C_U[0.859(e^{\lambda_{238} \cdot t} - 1) + 0.006(e^{\lambda_{235} \cdot t} - 1)]$$

where  $C_{Pb}$ ,  $C_{Th}$ , and  $C_U$  are concentrations of Pb, Th, and U (in ppm) measured in situ in the uraninite;  $\lambda_{232}$  ( $0.049475 \times 10^{-9} \text{ y}^{-1}$ ),  $\lambda_{238}$  ( $0.155125 \times 10^{-9} \text{ y}^{-1}$ ) and  $\lambda_{235}$  ( $0.98485 \times 10^{-9} \text{ y}^{-1}$ ) are the decay constants for  $^{232}\text{Th}$ ,  $^{238}\text{U}$ , and  $^{235}\text{U}$  respectively; and  $t$  is age (in year). This relation is used assuming that  $^{235}\text{U}$ ,  $^{238}\text{U}$  and  $^{232}\text{Th}$  produce the totality of the lead present in the analyzed spot ( $^{207}\text{Pb} + ^{206}\text{Pb} + ^{208}\text{Pb}$ ), thus Pb is considered to be entirely of radiogenic origin and there was no common lead incorporated in the mineral during its crystallization. This method is commonly

used for monazite dating (Suzuki et al., 1994; Montel et al., 1996; Cocherie and Albarède, 2001, Williams et al., 2007). The chemical age results are finally plotted in histograms with the Isoplot program (Ludwig, 1999) providing a probability curve for the more confident age population and showing the distribution of chemical ages calculated in the various samples.

**Table 3.3.4.** Overview of the element set-up for the CAMECA SX100 electron microprobe including analysed line, calibration standard, and background positions used during integrated analysis of zircon and monazite grains.

<i>Mineral analysed</i>	<i>Element</i>	<i>Line</i>	<i>Spectrometer crystal</i>	<i>Standard</i>	<i>High Back-ground</i>	<i>Low Back-ground</i>	<i>Slope</i>	<i>Peak counting time (s)</i>
<i>Zircon</i>	La	L $\alpha$	PET	LaPO <sub>4</sub>	500		1.1	20
	Ca	K $\alpha$	PET	Wollastonite	700		1.1	10
	P	K $\alpha$	PET	KTiP	400	-400		20
	Zr	L $\alpha$	TAP	Zircon	700		1.2	10
	Y	L $\alpha$	TAP	YPO <sub>4</sub>	625	-450		40
	Al	K $\alpha$	TAP	Albite	800		1.2	10
	Yb	L $\alpha$	LIF	YbCo <sub>2</sub> Si <sub>2</sub>	474	-943		20
	Er	L $\alpha$	LIF	ErNi <sub>2</sub> Si <sub>2</sub>	600		1.05	20
	Dy	L $\alpha$	LIF	DyRu <sub>2</sub> Ge <sub>2</sub>	320	-1200		40
	Fe	K $\alpha$	LIF	Fe metal	600		1.1	10
	Si	K $\alpha$	TAP	Zircon	500		1.2	20
	Hf	M $\alpha$	TAP	Hf metal	600	-550		30
	Ti	K $\alpha$	LPET	MnTiO <sub>3</sub>	600		1.1	10
	U	M $\beta$	LPET	UO <sub>2</sub>	793	-1447		30
	Th	M $\alpha$	LPET	ThO <sub>2</sub>	726	-1274		30
Pb	M $\beta$	LPET	PbCrO <sub>4</sub>	970	-900		30	
<i>Monazite</i>	Ce	L $\alpha$	PET	CePO <sub>4</sub>	450		1.2	10
	La	L $\alpha$	PET	LaPO <sub>4</sub>	500		1.1	10
	Ca	K $\alpha$	PET	Wollastonite	700		1.1	20
	Pb	M $\beta$	PET	PbCrO <sub>4</sub>	1700		1.05	60
	Zr	L $\alpha$	TAP	ZrO <sub>2</sub>	700		1.2	20
	Y	L $\alpha$	TAP	YPO <sub>4</sub>	625	-450		30
	Al	K $\alpha$	TAP	Albite	800		1.2	20
	Gd	L $\beta$	LIF	GdTiGe	450	-400		60
	Fe	K $\alpha$	LIF	Hematite	700		1.1	20
	Mn	K $\alpha$	LIF	MnTiO <sub>3</sub>	600		1.1	20
	Sm	L $\alpha$	LIF	SmPO <sub>4</sub>	600	-600		60
	P	K $\alpha$	TAP	CePO <sub>4</sub>	800		1.2	20
	Si	K $\alpha$	TAP	Orthose	800		1.2	20
	Nd	L $\beta$	LPET	NdPO <sub>4</sub>	700		1.15	20
	Pr	L $\beta$	LPET	PrPO <sub>4</sub>	750	-370		20
	Ti	K $\alpha$	LPET	MnTiO <sub>3</sub>	600		1.1	10
	U	M $\beta$	LPET	UO <sub>2</sub>	793	-1447		60
	Th	M $\alpha$	LPET	ThO <sub>2</sub>	726	-1247		30

**Notes:** TAP – thallium acid phthalate crystal; LPET – large pentaerythriol crystal; PET – large pentaerythriol crystal; LIF – Lif crystal; PCI – multilayered W-Si crystal; Background positions refer to number of wavelength, expressed as  $\sin \theta \cdot 10^5$ , above and below the peak position or derived by line regression with the slope indicated. Background counting time is equivalent to half of the peak counting time for each element.

## Results

### Geochemistry

Major element data are presented in Table 3.3.2. The Jatulian sediments show very high silica content ranging 87-88% SiO<sub>2</sub> in sandstones, 91-97% for conglomerates and 95-99% in quartzite corresponding to the high abundance in detrital quartz. In the Q-A diagram of Debon and Le Fort (Fig. 3.3.5), sediment compositions plot in the ternary domain between quartz, feldspar and phyllosilicates mixture with very high Q parameter (404-532) and a slightly aluminous composition (13-86) maximal in the sandstones hosting higher aluminium contents (up to 8.12% Al<sub>2</sub>O<sub>3</sub> in 9375-11). Sodium and calcium contents are almost always under detection limits. The femic minerals are rare (1.71<B<37.38) and generally correspond to iron oxides with rare biotite (maximum 2.76% Fe<sub>2</sub>O<sub>3</sub> in conglomerate 9375-14).

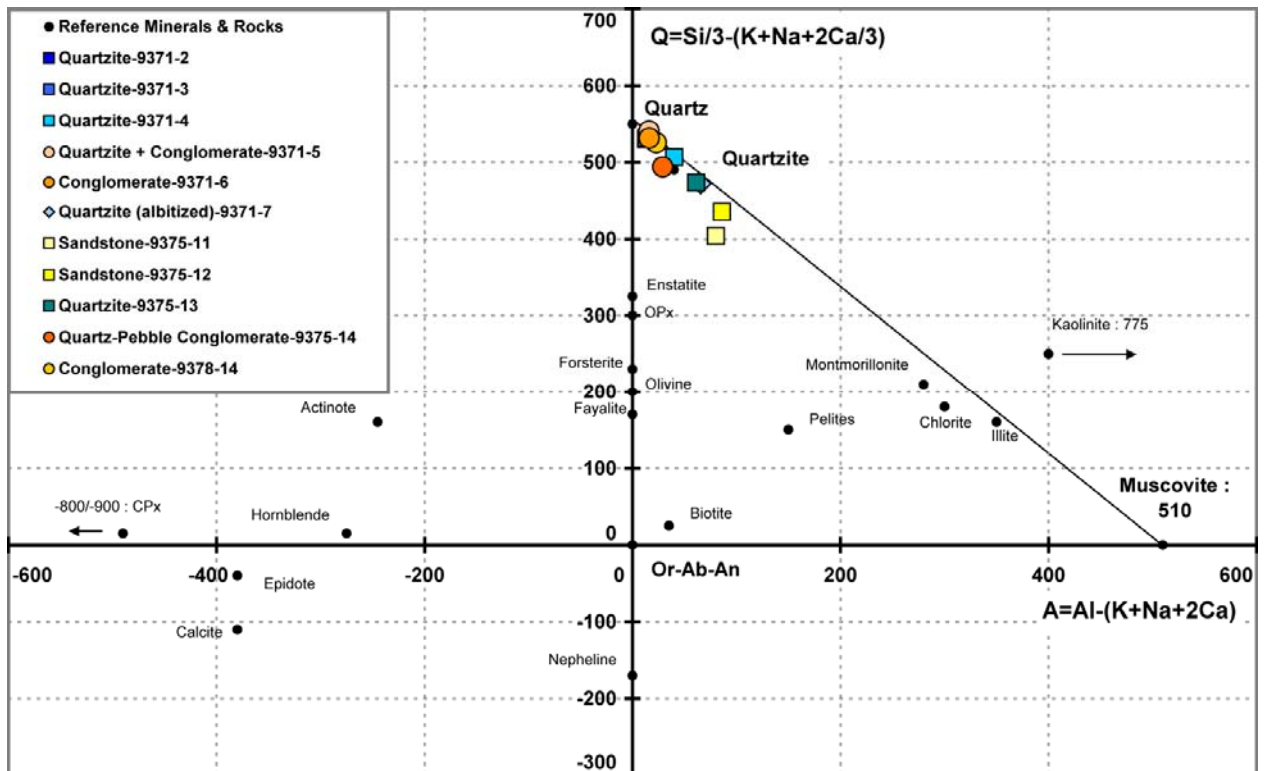


**Figure 3.3.5.** Binary diagram showing Q [= (Si - (K + Na + 2Ca)) / 3] vs. A [= Al - (K + Na + 2Ca)] parameters (in thousands of cations) of the basal Jatulian sediments with reference sedimentary rocks and minerals (modified from Debon and Le Fort, 1982).

Jatulian sediments have a highly feldspathic composition plotting in the arkosic domain of de La Roche diagram (Fig. 3.3.6) typical of clastic material derived from the alteration of granitic basement rocks. Sandstones have the highest potassic contents, 3.72 wt% and 2.59 wt% K<sub>2</sub>O in samples 9375-11 and 9375-13, respectively.

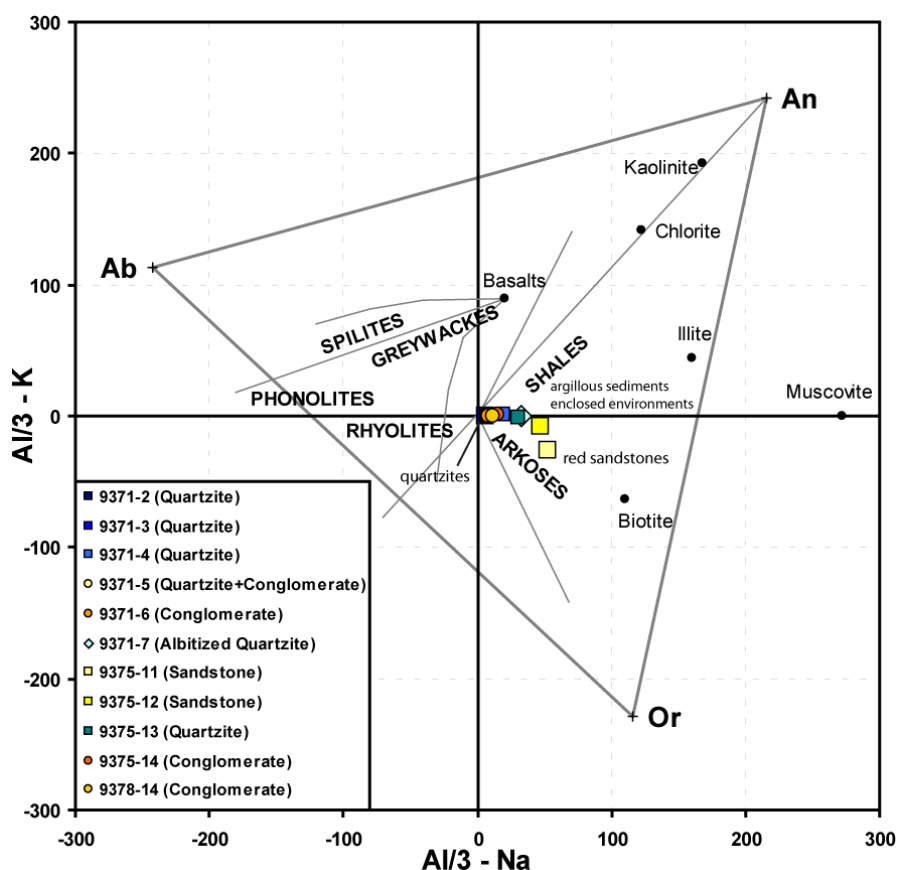


**Figure 3.3.6.** Al/3-K vs. Al/3-Na diagram (from de La Roche, 1968) showing the composition of Jatulian sediments with main rocks domains and minerals.

Trace element concentrations presented in Table 3.3.3 also suggest that sediments originate mainly from felsic rocks because of the low contents in As (< 7 ppm), Ni (< 9 ppm), Co (< 2 ppm), Cr (< 50 ppm) and the variable but high amounts in Ba (33-376 ppm), Rb (9-126 ppm), Th (4 ppm to 0.3 wt%), U (0.87-20.25 ppm), Zr (87-974 ppm), Hf (1.53-24.35 ppm) and Y (2-118 ppm). Lowest HFSE contents are in quartzite and increase with the granulometry, reaching maximal values in the conglomerate layers. The most HFSE-enriched sample, conglomerate 9375-14 (also the most radioactive), has also high Nb (45.73 ppm) and Ta (46 ppm) contents and is highly anomalous in Sr (706.8 ppm) and Th (2928 ppm).

The chondrite-normalized REE spidergrams of the Jatulian sediments (Fig. 3.3.7) have all flat patterns associated to low fractionation between LREE and HREE ( $0.44 < [La/Sm]_N < 1.40$  and  $0.87 < [Gd/Yb]_N < 4.72$ ). However, the strongest REE fractionation is again recorded by the most radioactive conglomerate 9375-14. The REE patterns also display slightly negative Eu anomalies ( $0.30 < Eu/Eu^* < 0.76$ ) probably related to detrital material reflecting the granitic parental-rock compositions from which they derive.

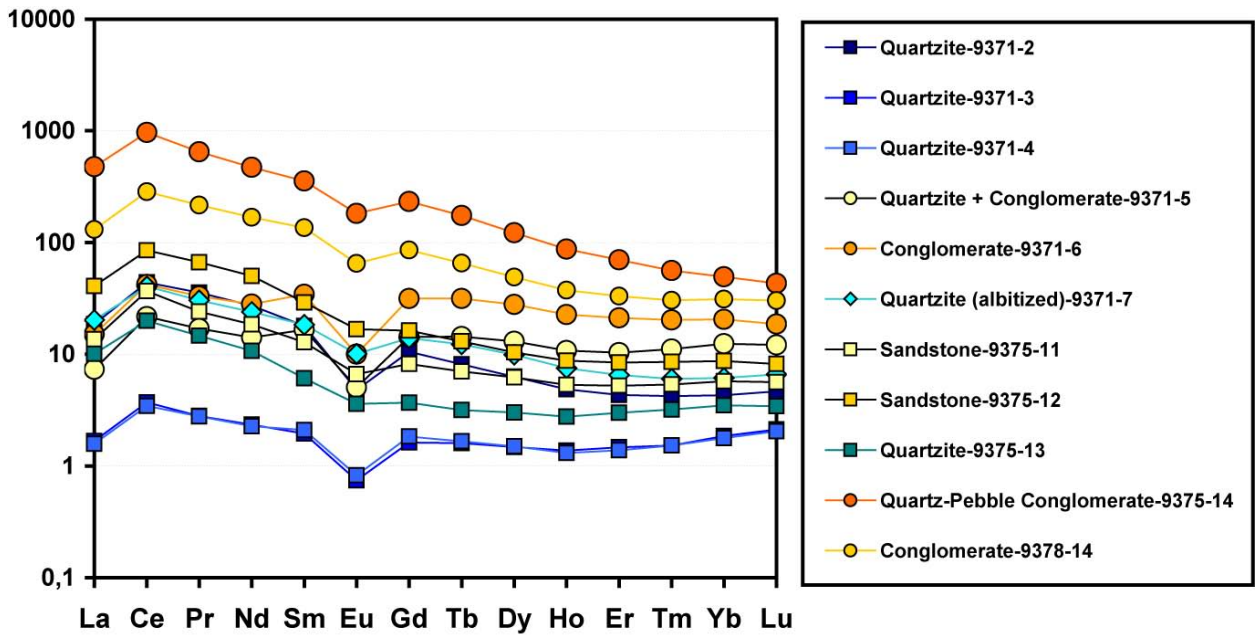


Figure 3.3.7. Chondrite-normalized REE patterns of the basal Jatulian sediments (normalized to Chondrite values of Anders and Grevesse, 1989).

The binary diagram presenting the Th vs. U contents of the rocks (Fig. 3.3.8) shows that the conglomerates are highly enriched in Th (from 410 ppm to 0.3%) and only slightly in U (2.8-20.25 ppm) implying very high Th/U ratios from 104 to 248. Quartzite and sandstones have much scattered Th contents (4-153 ppm) for an almost invariant U content meaning 1.32 ppm which provides wide range of Th/U ratios between 3.48 and 90.44.

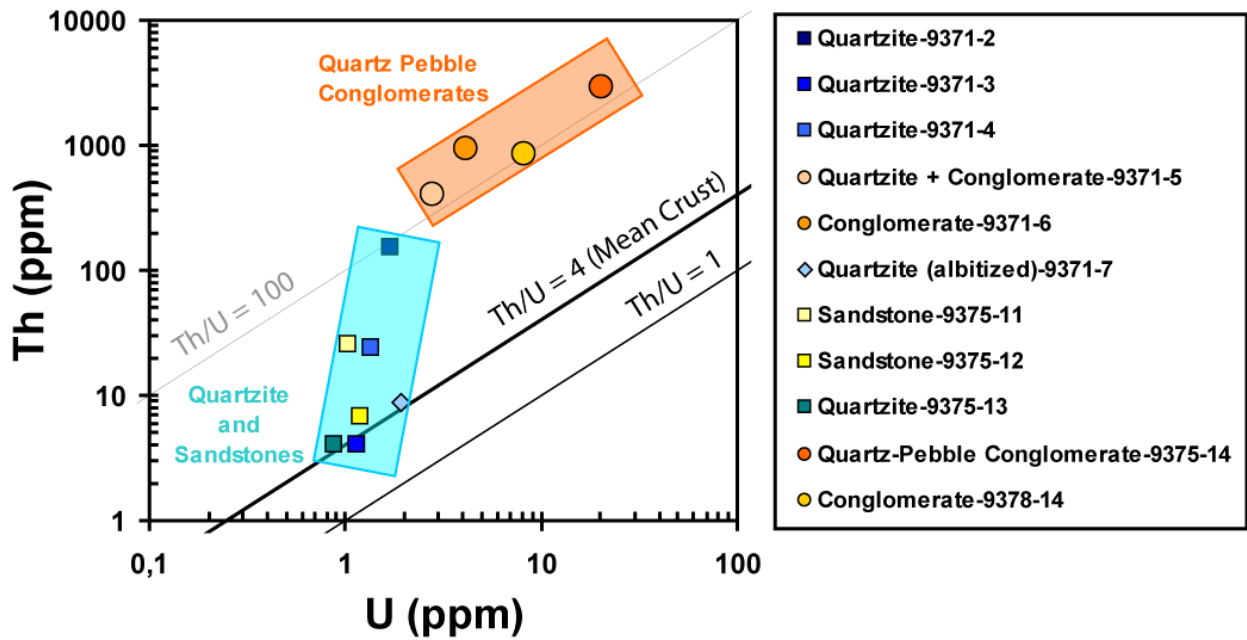
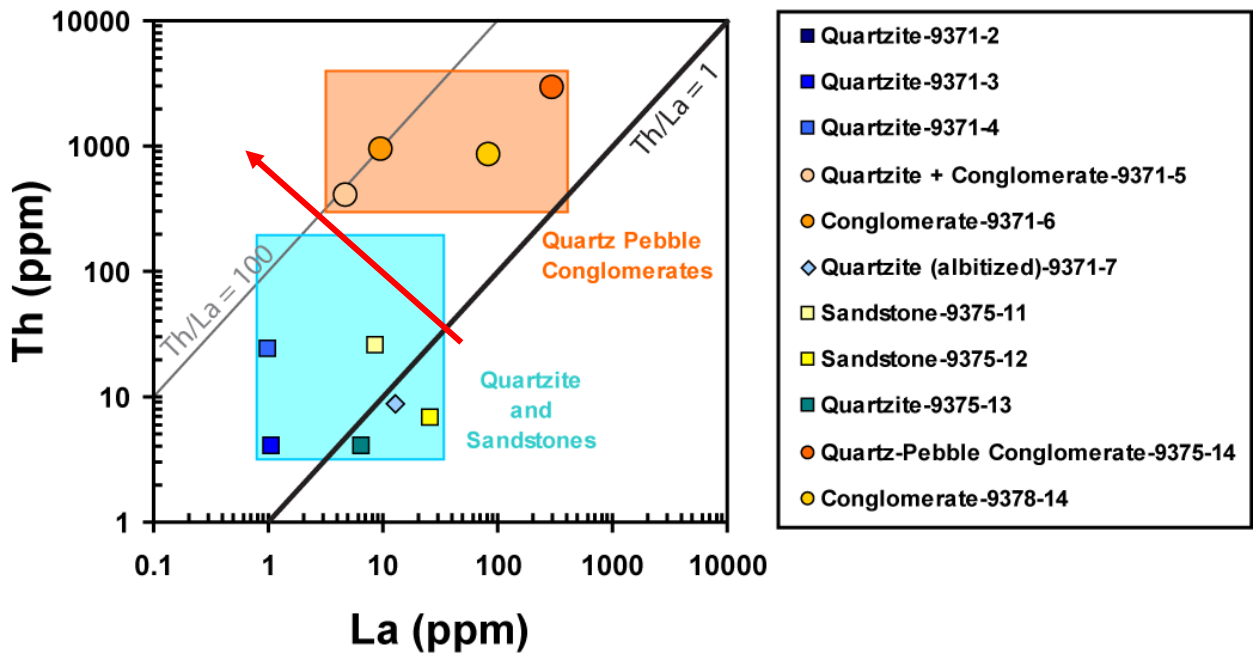


Figure 3.3.8. Binary diagram showing Th vs. U contents (in ppm) of the basal Jatulian sediments.

Considering the Th vs. La content variations (Fig. 3.3.9), the Th enrichment in the conglomerates probably reflects monazite accumulation in heavy mineral layers as mentioned by Shurilov and co-authors (2007 and 2008) whereas monazite are probably more disseminated in quartzite and

sandstones. Moreover, the very high Th/La ratios suggest that monazite grains are highly altered which is generally associated to LREE leaching (symbolized by the decreasing La contents) and Th re-concentration.



**Figure 3.3.9.** Binary diagram showing Th vs. La contents. (ppm) in Jatulian sediments. The red arrow represents the trend of increasing monazite alteration generally associated with La leaching vs. Th enrichment.

Finally, the binary diagram presenting U vs. Zr contents of the Jatulian sediments (Fig. 3.3.10) shows a strong and positive correlation between uranium enrichment in the conglomerates with increasing Zr content obviously representative of the zircon grain concentration in the channels. The trend follow mostly the ratio Zr/U= 100.

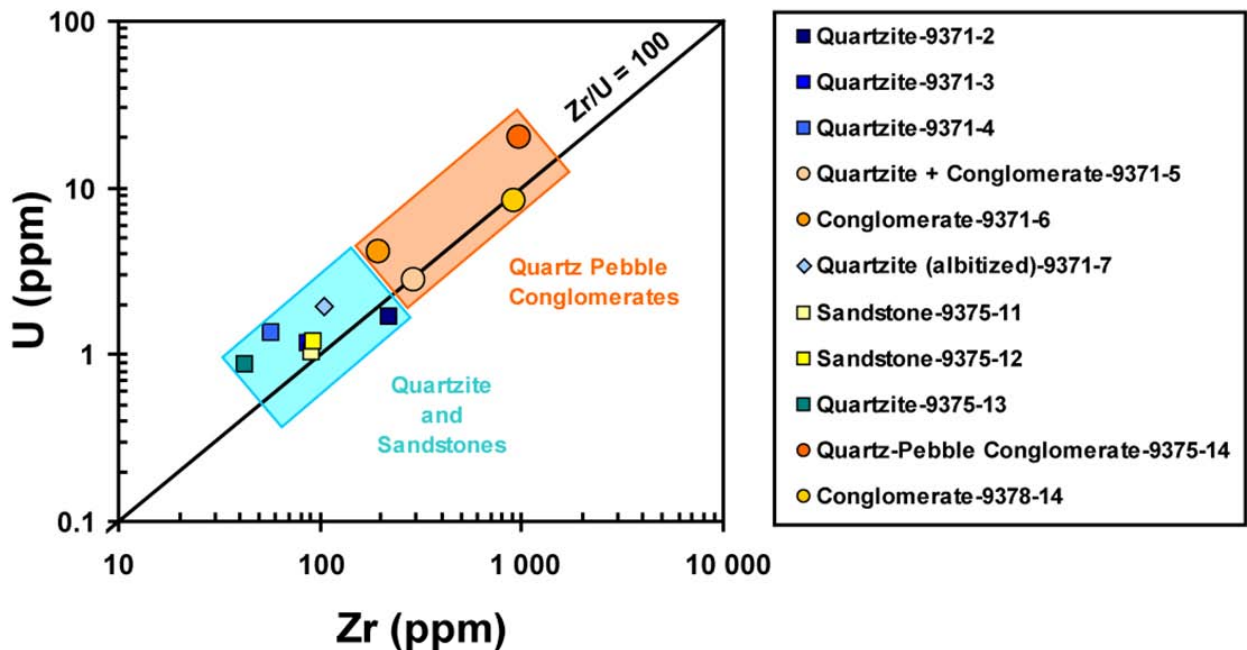


**Figure 3.3.10.** Binary diagram showing U vs. Zr contents (ppm) in Jatulian sediments.

## MINERALOGY

### Lower Jatulian Quartzite-Sandstones

The grey quartzite and sandstones are highly heterogeneous in grain size (fine to coarse) and are poorly sorted. They are composed of abundant K-feldspar (orthoclase and microcline), plagioclase and quartz grains with rare biotite generally cemented by sericite of fine-grained phyllosilicates, chiefly muscovite, illite and minor chlorite in a random orientation (Fig. **3.3.11** and **3.3.12**). Phyllosilicates probably derived from the plagioclase and biotite destruction. Detrital grains are generally unetched in the sandstones and float in the sericitic cement but some quartzite sediments are slightly better packed as sample 9371-13. Feldspar grains remain sometimes elongated with angular shape which suggests low mechanical abrasion during a short period of transportation before deposition. Quartz grains are mostly sub-rounded, sometimes polycrystalline but no deformation has been evidenced. The original detrital quartz boundary rarely displays secondary thin quartz overgrowth. These observations infer low diagenetic processes and immature arkosic sediments.

Quartzite 9371-7 is atypical compare to other samples because it hosts very abundant feldspar fraction and has partly carbonate cement with minor muscovite (Fig. **3.3.13-A**). Feldspar is strongly albitized and displays a typical chessboard texture (Fig. **3.3.13-B**). These alterations (albitization, carbonatization and sericitization) have been observed in other basal Early Proterozoic metasedimentary belts overlying Archean basement rocks in northern Finland, as in the Pyhätunturi quartzites from the Kumpu Group in Central Lapland (Laajoki, 1988; Räsänen and Huhma, 2001) but this Finish sedimentary unit is considered post-Jatulian because they contain pebbles of calc-alkaline volcanic rocks aged ca. 1.88 Ga (Rastas et al., 2001).

Some accessory minerals are disseminated in the cement, mainly zircon and monazite with rare titanium oxides, tourmaline and garnet (Fig. **3.3.14** and **3.3.15**). Green-kind tourmaline is generally elbaite or schorlite, species enriched in Ca, Na, Fe and Li (Henry and Dutrow, 1992) which indicates a Li-rich granitoids as a likely source.

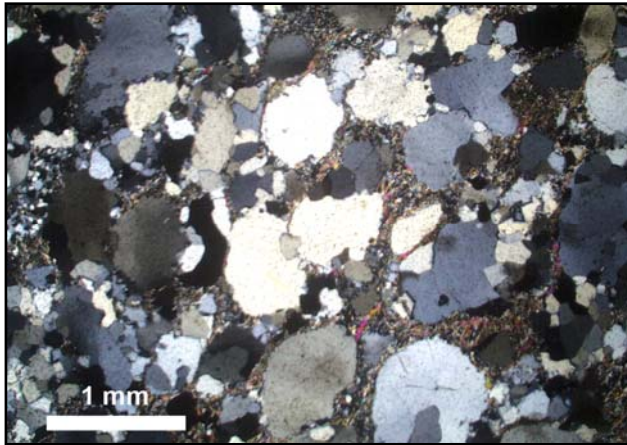


**Figure 3.3.11.** Photomicrograph of a Jatulian quartzite (9375-13-cross nicols) showing etched quartz grains with a sericitic cement.

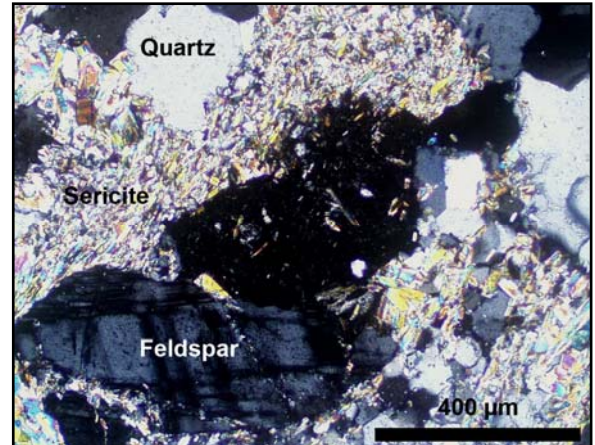


**Figure 3.3.12.** Photomicrograph of a Jatulian sandstone (9375-11, cross nicols) showing quartz and feldspar grains floating in a sericite composed of fine-grained laths of white phyllosilicates.

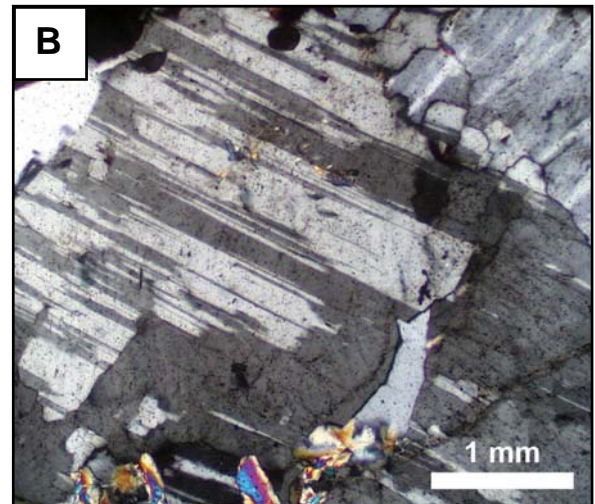
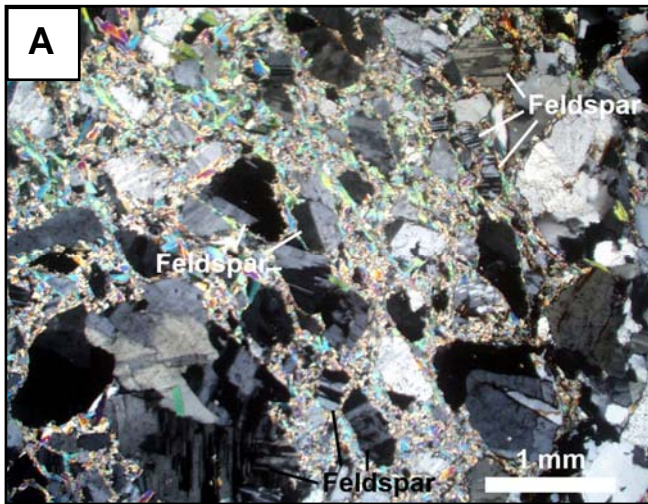


**Figure 3.3.13.** Photomicrographs of a Jatulian quartzite (9371-7) showing **A**- carbonate-cement between feldspar and quartz grains, and **B**- closer view of a feldspar with typical chessboard texture of albitization (cross-nicols).

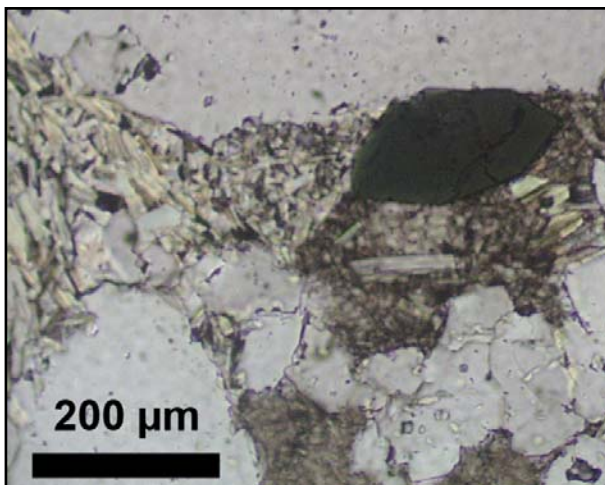


**Figure 3.3.14.** Photomicrograph of a detrital green tourmaline with hexagonal crystal shape surrounded by muscovite and quartz grains (sandstone 9375-12; plane light).

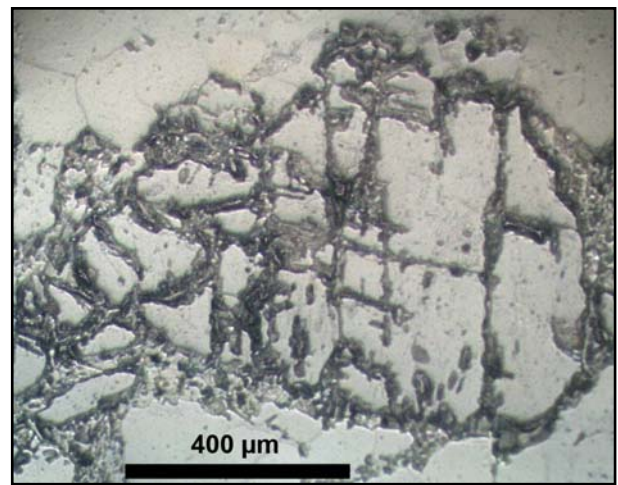


**Figure 3.3.15.** Photomicrograph of a detrital garnet with rounded shape and fractures filled by chlorite (sandstone 9375-12; reflected light).

**Lower Jatulian Conglomerates**

Conglomerates are rather more mature than the quartzite and sandstones with less K-feldspar and almost no plagioclase remaining. K-feldspar are well preserved and mainly represented by orthoclase. Quartz pebbles are surrounded by abundant etched quartz grains with interstitial muscovite and illite elongated in the same direction (probably diagenetic or hydrothermal fluid pathways) and more rarely carbonate cement (Fig. 3.3.16).

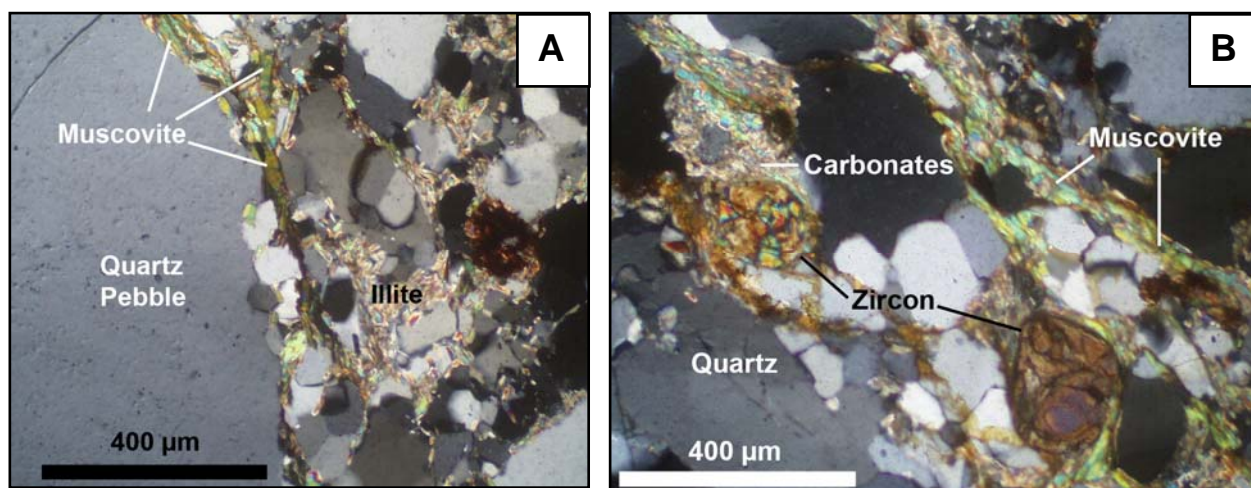


**Figure 3.3.16.** Photomicrographs of the most radioactive quartz pebble conglomerate (9375-14, cross nicols) showing **A-** well compacted polycrystalline quartz grains with muscovite and illite and **B-** detrital zircon and locally carbonate cement.

Detrital grains are poorly sorted with various grain size mixed together but are well compacted with low cement proportion compare to sandstones. Quartz pebbles and coarse grains generally show undulous extinction and smaller etched grains often display triple-joint boundaries (Fig. 3.3.17). The conglomerate are highly ferruginous with lots of fine-grained hematite peppered everywhere in the rock cement but most preferentially clusters on refractory minerals (Fig. 3.3.17, 3.3.18 and 3.3.19). Monazite seems to be more affected, become totally opaque and sometimes display radial fractures in the adjacent quartz grains which suggest that they possibly expand in volume (Fig. 3.3.17 and 3.3.20). In reflected light, refractory minerals show strong reddish internal reflections typical of intensive hematization (Fig. 3.3.21 and 3.3.22).

No pyrite, no uraninite and even no boxwork have been observed in any of the 15 thin sections. The U and Th enrichments of the Jatulian sediments are therefore associated to the refractory minerals that can be very abundant in the quartz pebble conglomerates.

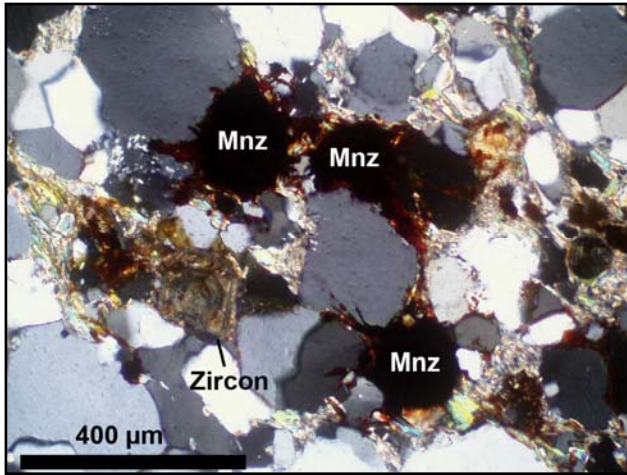


**Figure 3.3.17.** Refractory minerals between quartz grains showing multiple triple-joint boundaries and disseminated interstitial white micas (conglomerate 9375-14, cross nicols).

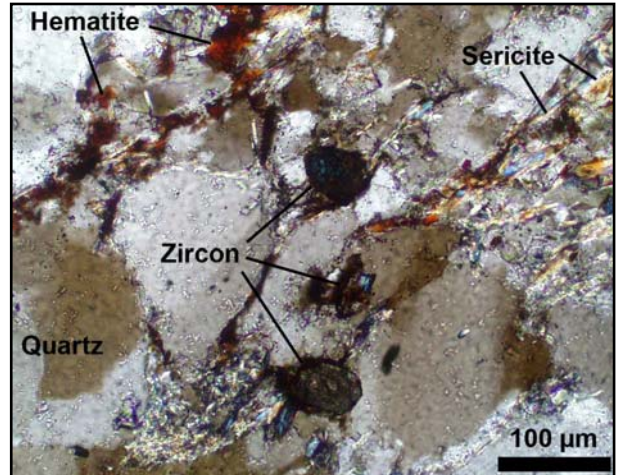


**Figure 3.3.18.** Zircon grains disseminated between quartz grains in the sericite (conglomerate 9371-5, cross nicols). Note the disseminated hematite giving its brownish to reddish colour to the rock.

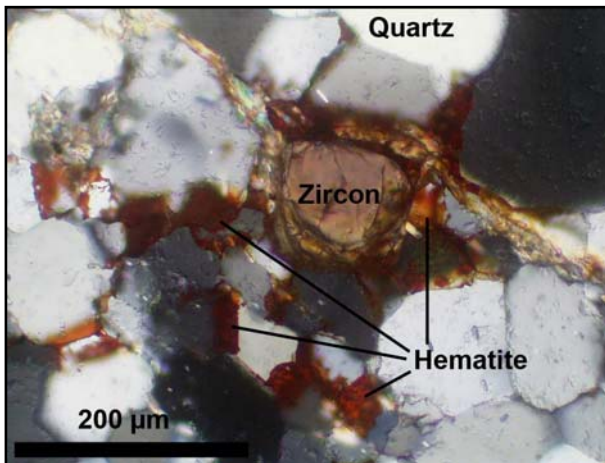


**Figure 3.3.19.** Refractory minerals between quartz grains showing multiple triple-joint boundaries and disseminated interstitial white micas (conglomerate 9375-14, cross nicols).

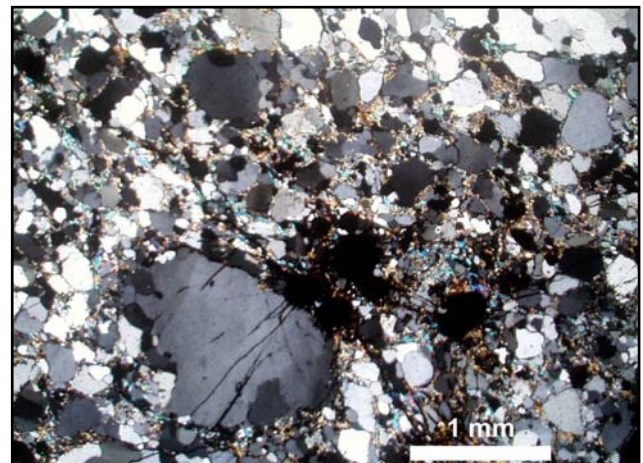


**Figure 3.3.20.** Refractory minerals between quartz grains showing multiple triple-joint boundaries and disseminated interstitial white micas (conglomerate 9375-14, cross nicols).

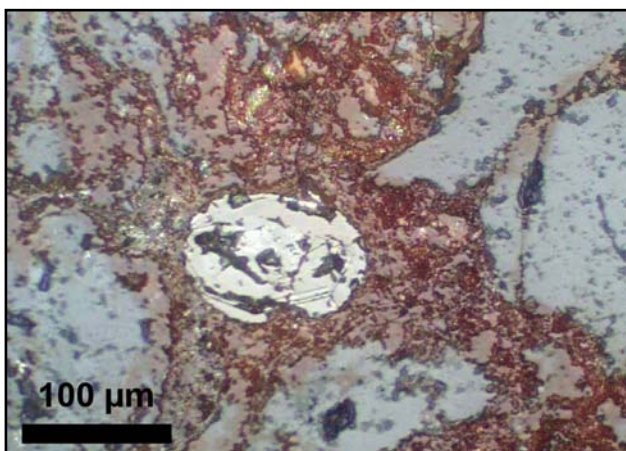


**Figure 3.3.21.** Photomicrograph of a detrital zircon surrounded by hematized sericitic cement showing red internal reflections (conglomerate 9371-5; reflected light).

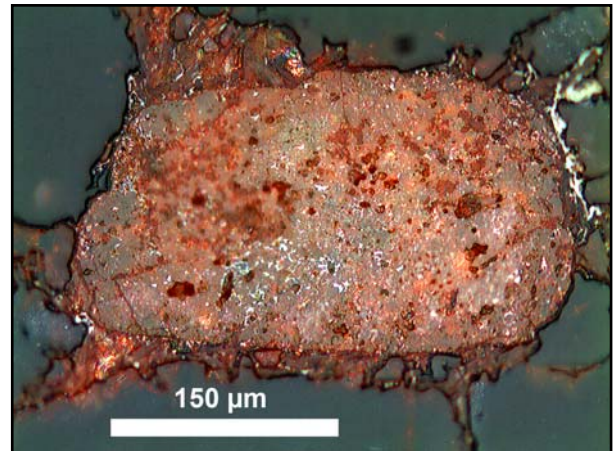


**Figure 3.3.22.** Photomicrograph of an altered monazite coated by small hematite red crystals (conglomerate 9378-14; reflected light).

## Composition of U and Th bearing minerals

### *Detrital zircon grains*

Zircon composition is highly heterogeneous considering the wide average atomic number variations revealed in BSE imaging (Fig. 3.3.23). Grains are generally subhedral, average 100  $\mu\text{m}$  in size and primary magmatic grow zoning is well developed. However, alteration textures are visible with decreasing BSE grey intensity following microcracks induced by metamictization.

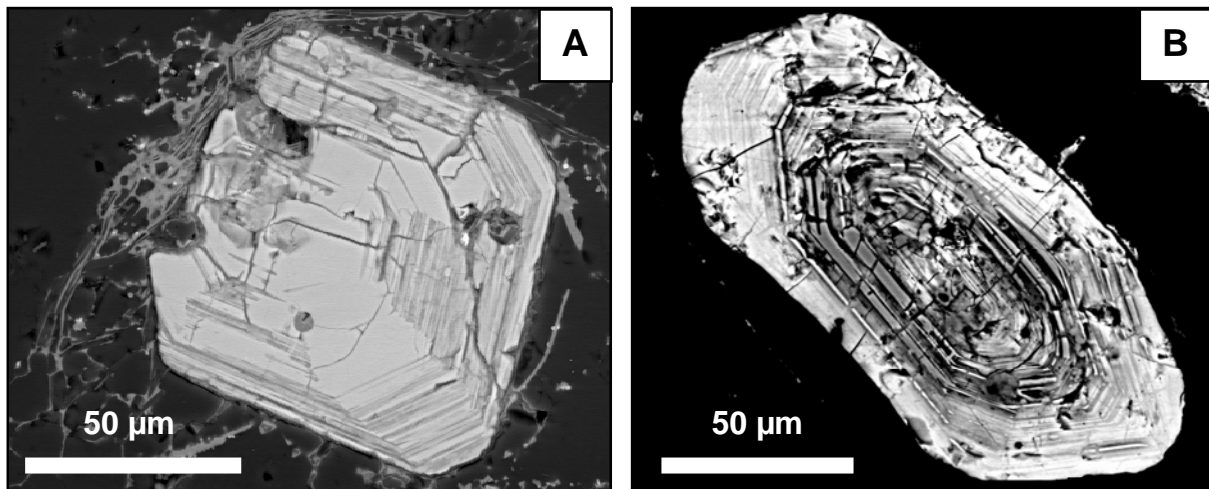


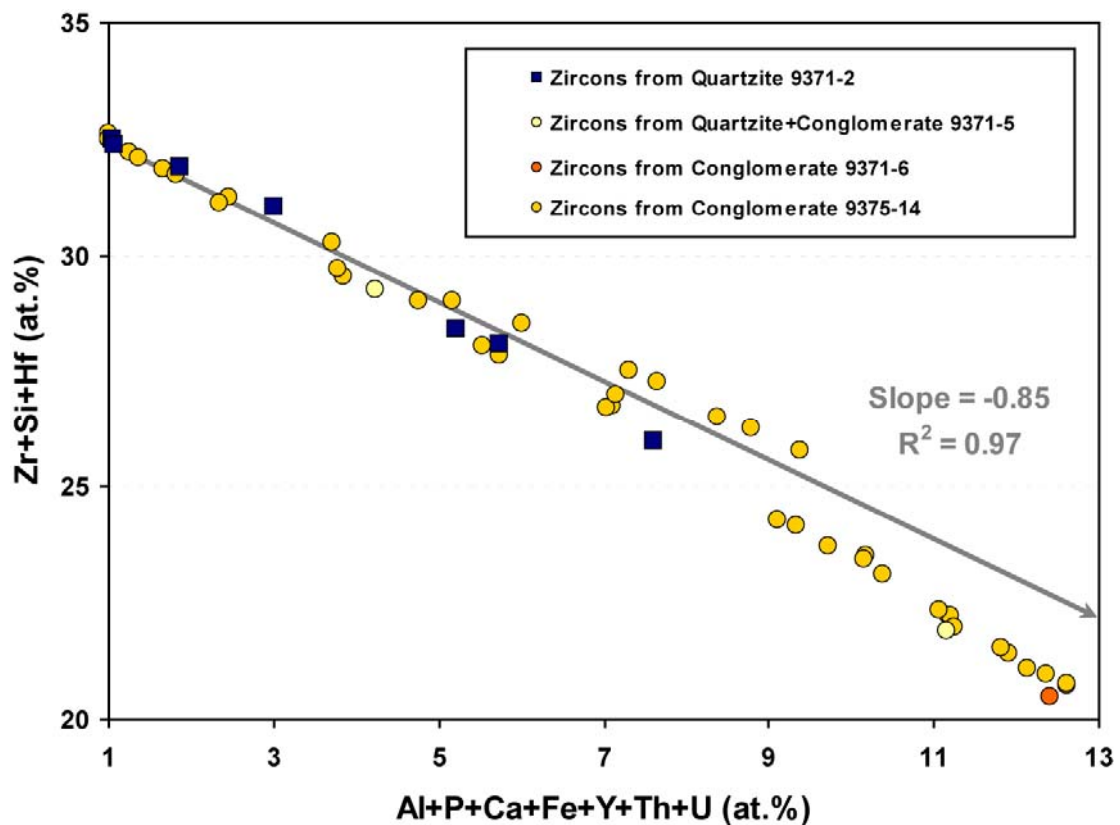
**Figure 3.3.23.** BSE mode images of individual zircon grain **A**- in quartzite 9371-2 and **B**- in conglomerate 9375-14.

Zircon composition measured in 36 grains from 4 samples is presented in Table 3.3.5. Major elements correspond to zirconium, silica and hafnium representing more than 95% of the chemistry. However, high contents in Fe and Th and traces of Al, P, Ca, Y and sometimes U have been detected and increase significantly in the conglomerates reaching maximum values in the most radioactive sample 9375-14. The binary plot of major element variations (Fig. 3.3.24) shows a negative correlation between abundances in Zr, Hf and Si with substituting elements almost perfectly plotting on a line with a slope of - 0.85 ( $R^2 = 0.97$ ). Introduction of iron is probably related to late alteration or weathering linked to the pervasive hematization shown by the petrographic observations. The negative correlation between Ca, U and Th contents opposite to major element contents is inferred to the zirconium replacement by radioelements in the crystal lattice during magmatic crystallization in the parental rocks with cationic exchanges following the reaction  $2\text{Zr}^{4+} \leftrightarrow 2\text{Ca}^{2+} + (\text{U,Th})^{4+}$  which is only possible because of the close ionic radii of these elements (1.12 Å for  $\text{Ca}^{2+}$ , 1 Å for  $\text{U}^{4+}$ , 1.05 Å for  $\text{Th}^{4+}$  and 0.84 Å for  $\text{Zr}^{4+}$ ).

**Table 3.3.5.** Average composition of zircon from the Jatulian sediments measured by electron microprobe

Sample	9371-2	9371-5	9371-6	9375-14
Lithology	Quartzite	Quartzite+Conglomerate	Conglomerate	Conglomerate
EMPA	65/9 grains	26/8 grains	10/1 grains	96/18 grains
	Mean ± $\sigma$	Mean ± $\sigma$	Mean ± $\sigma$	Mean ± $\sigma$
Al <sub>2</sub> O <sub>3</sub>	0.08 ± 0.25	0.11 ± 0.39	0.15 ± 0.46	0.28 ± 0.49
SiO <sub>2</sub>	31.50 ± 3.09	31.73 ± 3.82	30.62 ± 6.57	29.09 ± 5.95
P <sub>2</sub> O <sub>5</sub>	0.32 ± 1.14	0.68 ± 2.51	1.38 ± 4.31	0.96 ± 1.87
CaO	0.12 ± 0.34	0.14 ± 0.42	0.20 ± 0.62	0.21 ± 0.36
FeO	0.27 ± 0.64	0.24 ± 0.38	0.22 ± 0.58	1.10 ± 2.20
Y <sub>2</sub> O <sub>3</sub>	<D.L.	0.13 ± 0.51	0.42 ± 1.33	0.85 ± 1.55
ZrO <sub>2</sub>	65.37 ± 3.37	64.75 ± 4.27	64.25 ± 7.13	60.53 ± 9.97
HfO <sub>2</sub>	1.09 ± 0.19	1.33 ± 0.16	1.22 ± 0.09	1.21 ± 0.19
PbO	<D.L.	<D.L.	<D.L.	<D.L.
ThO <sub>2</sub>	0.19 ± 0.66	0.39 ± 1.60	0.56 ± 1.68	2.06 ± 6.10
UO <sub>2</sub>	<D.L.	<D.L.	<D.L.	0.15 ± 0.25
TiO <sub>2</sub>	<D.L.	<D.L.	<D.L.	<D.L.
Dy <sub>2</sub> O <sub>3</sub>	<D.L.	<D.L.	<D.L.	0.20 ± 0.31
Er <sub>2</sub> O <sub>3</sub>	<D.L.	<D.L.	<D.L.	<D.L.
Yb <sub>2</sub> O <sub>3</sub>	<D.L.	<D.L.	<D.L.	<D.L.
La <sub>2</sub> O <sub>3</sub>	<D.L.	<D.L.	<D.L.	<D.L.
Total	99.23 ± 3.14	99.78 ± 2.24	99.47 ± 3.92	96.97 ± 6.20

Notes: <D.L. = below detection limit (Al = 0.05 wt%; Si = 0.04 wt%; P = 0.08 wt%; Ca = 0.07 wt%; Fe = 0.13 wt%; Y = 0.08 wt%; Zr = 0.20 wt%; Hf = 0.08 wt%; Pb = 0.15 wt%; Th = 0.09 wt%; U = 0.11 wt%; Ti = 0.04 wt%; Dy = 0.16 wt%; Er = 0.25 wt%; Yb = 0.22 wt%; La = 0.15 wt%).


**Figure 3.3.24.** Zircon composition of the Jatulian sediments represented in a binary diagram showing major constituents (Zr+Hf+Si) substitute to (Al+P+Ca+Fe+Y+Th+U) in atomic percents.

The radioelement concentrations in zircon remains however low and this mineral does not contribute significantly to the whole rock abundances. The most radioactive conglomerate 9375-14 contains 20.25 ppm U and 2928 ppm Th for 973.5 ppm Zr (Table 3.3.3). Considering that zircon  $ZrSiO_4$  represents only 50% of the bulk rock Zr concentration, zircon grains in this conglomerate contain 0.13 wt% U and 1.85 wt% Th (means) so the total U and Th budget hosted in zircon is approximately 2.53 ppm U  $[(973.5 \times 10^{-6}) \times 2 \times (1300 \times 10^{-6})]$  and 36 ppm Th  $[(973.5 \times 10^{-6}) \times 2 \times (1300 \times 10^{-6})]$ . Consequently, zircon contributes to 11% of total U content in the rock and only 1.23% of the total Th.

### ***Altered monazite grains***

Monazite display very complex chemical composition and microtextural heterogeneities by BSE imaging. The crystals have almost always irregular shapes rising up to 600  $\mu\text{m}$  wide. They have a general high BSE intensity in the core reflecting high average atomic number but with variable darker light-grey domains indicating that the composition is quite heterogeneous (Fig. 3.3.25). They are often coated by iron oxides, darker in the BSE images, that fill the porosity, fractures and cleavage of phyllosilicates probably used as pathways by the oxidant fluid responsible for the alteration (Fig. 3.3.26).

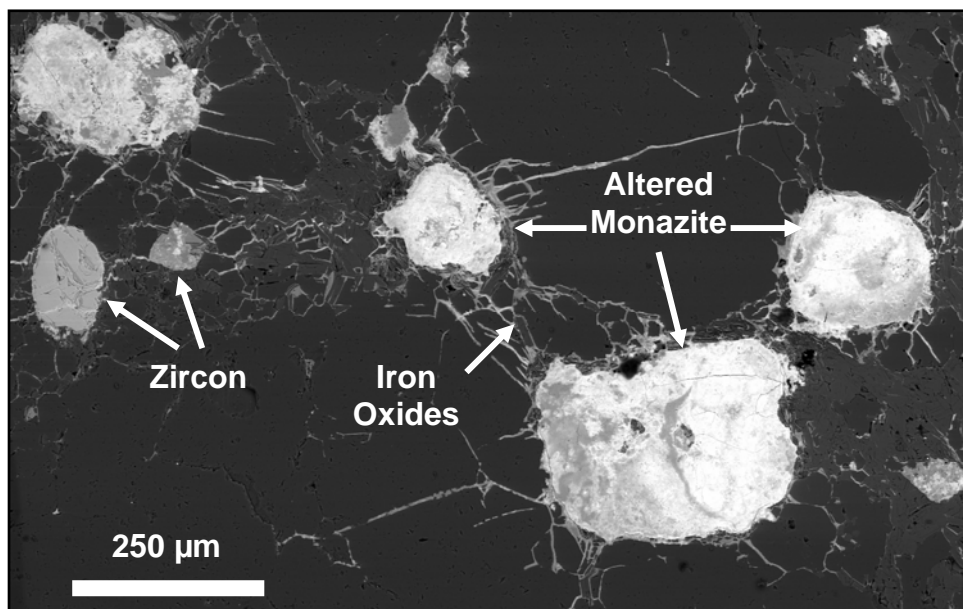


**Figure 3.3.25.** BSE mode image of numerous altered monazite grains and zircons with iron oxides along fractures in quartz pebbles (Conglomerate 9375-14).

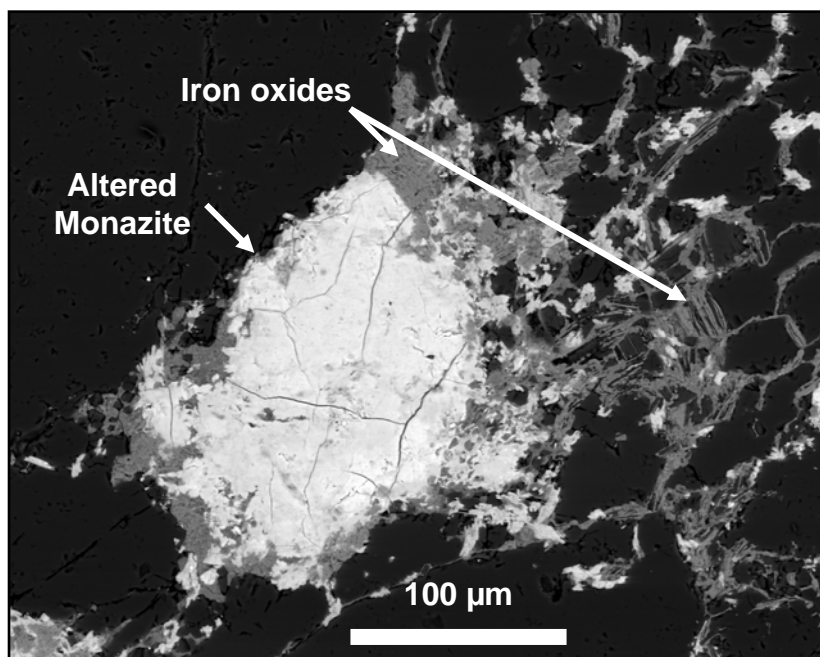


**Figure 3.3.26.** BSE mode image of an altered monazite grain coated by iron oxides filling porosity between phyllosilicate laths (Quartzite+Conglomerate 9371-5).

A total of 38 grains of monazite have been analysed in the same 4 samples than the zircons. Results presented in Table 3.3.6 show very low concentrations in REE and very high Th contents. Monazite grains from quartzite 9371-2 are the less altered with slightly higher La, Ce and Nd contents ( $m = 0.75 \text{ wt\% La}_2\text{O}_3$ ,  $1.95 \text{ wt\% Ce}_2\text{O}_3$  and  $0.94 \text{ wt\% Nd}_2\text{O}_3$ ) and lower but widely variable Th contents ( $m = 25.26 \pm 10.03 \text{ wt\% ThO}_2$ ). Alteration is much more intense in the conglomeratic units with major increase of Th, Fe and Si contents and minor increase in U and Ca whereas REE and P contents decrease abruptly. Concentrations of  $\text{UO}_2$  in monazite generally never exceed 1 wt% with some few analytical point exceptions in sample 9375-14 with up to 1.42 wt%, which is high for monazite. Content in  $\text{ThO}_2$  can reach up to 67.7 wt% in pseudomorphic minerals replacing altered monazite from this high radioactive conglomerate. To this point, monazite is transformed to thorite by huttonitic substitutions of LREE and P by Si and Th (Fig. 3.3.27). The very high Fe contents are related to the intense and pervasive hematization observed petrographically and in BSE imaging. Both iron elevated contents and very low analytical totals are probably associated to iron hydroxides mixed with thorite and forming ferrithorite.

**Table 3.3.6.** Average composition of monazite from the Jatulian sediments measured by electron microprobe

Sample	9371-2	9371-5	9371-6	9375-14
Lithology	Quartzite	Quartzite+Conglomerate	Conglomerate	Conglomerate
EMPA	19/5 grains	37/11 grains	10/5 grains	75/17 grains
	Mean ± σ	Mean ± σ	Mean ± σ	Mean ± σ
Al <sub>2</sub> O <sub>3</sub>	1.65 ± 1.27	0.96 ± 0.32	1.06 ± 0.36	0.42 ± 0.26
SiO <sub>2</sub>	0.80 ± 0.45	1.08 ± 4.86	0.06 ± 0.11	6.20 ± 4.08
P <sub>2</sub> O <sub>5</sub>	16.88 ± 6.12	23.21 ± 4.50	23.43 ± 3.75	8.45 ± 4.44
CaO	5.95 ± 2.44	7.12 ± 2.13	7.47 ± 1.38	1.89 ± 1.97
TiO <sub>2</sub>	3.75 ± 8.12	0.11 ± 0.26	0.08 ± 0.13	0.49 ± 0.68
MnO	0.15 ± 0.17	<D.L.	<D.L.	0.32 ± 0.25
FeO	21.60 ± 11.48	6.26 ± 3.69	6.59 ± 3.03	13.59 ± 10.14
Y <sub>2</sub> O <sub>3</sub>	0.33 ± 0.11	0.19 ± 0.11	0.22 ± 0.12	1.11 ± 0.81
ZrO <sub>2</sub>	1.51 ± 0.94	0.45 ± 0.68	0.65 ± 0.67	3.21 ± 2.78
La <sub>2</sub> O <sub>3</sub>	0.75 ± 0.35	0.25 ± 0.89	<D.L.	<D.L.
Ce <sub>2</sub> O <sub>3</sub>	1.95 ± 0.80	0.78 ± 2.25	0.55 ± 0.25	0.69 ± 0.95
Pr <sub>2</sub> O <sub>3</sub>	0.25 ± 0.11	<D.L.	<D.L.	<D.L.
Nd <sub>2</sub> O <sub>3</sub>	0.94 ± 0.41	0.32 ± 1.33	0.22 ± 0.13	0.30 ± 0.49
SmO	0.22 ± 0.10	0.21 ± 0.73	<D.L.	0.17 ± 0.14
ThO <sub>2</sub>	25.26 ± 10.03	43.33 ± 9.61	40.57 ± 5.53	46.13 ± 12.19
UO <sub>2</sub>	0.37 ± 0.15	0.49 ± 0.18	0.40 ± 0.14	0.58 ± 0.22
PbO	<D.L.	0.44 ± 0.25	0.41 ± 0.20	<D.L.
Gd <sub>2</sub> O <sub>3</sub>	<D.L.	<D.L.	<D.L.	<D.L.
Total	82.61 ± 8.20	85.46 ± 9.62	82.25 ± 7.29	84.19 ± 4.81

*Notes:* <D.L. = below detection limit (Al = 0.06 wt%; Si = 0.04 wt%; P = 0.04 wt%; Ca = 0.07 wt%; Ti = 0.04 wt%; Mn = 0.11 wt%; Fe = 0.11 wt%; Y = 0.09 wt%; Zr = 0.16 wt%; La = 0.23 wt%; Ce = 0.25 wt%; Pr = 0.12 wt%; Nd = 0.15 wt%; Sm = 0.13 wt%; Th = 0.10 wt%; U = 0.10 wt%; Pb = 0.30 wt%; Gd = 0.24 wt%).

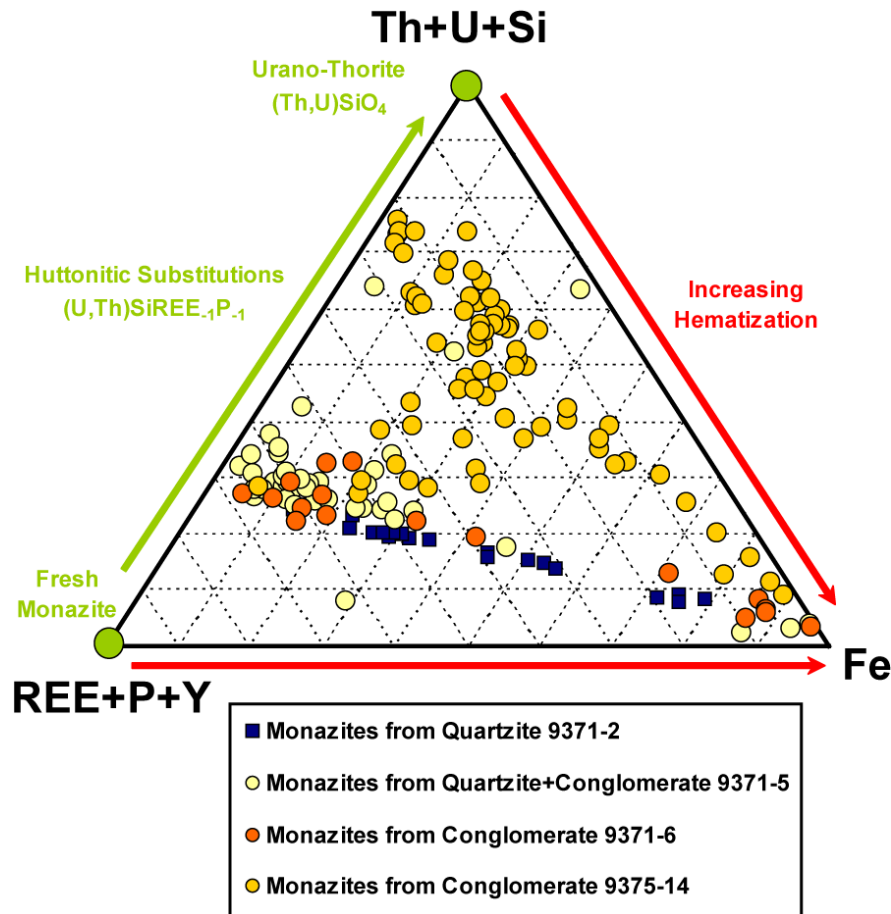


**Figure 3.3.27.** Ternary diagram showing the monazite compositions in the Jatulian sediments showing normally fresh monazite major constituents (REE+P+Y) substitute to (Th+U+Si) during huttonitic transformation and intensive hematization with Fe incorporation.

Dating of altered monazites using electron microprobe analyses of U, Th and Pb yields scattered results from actual time to approximately the age of the sediment deposition (Fig. 3.3.28). Most of chemical ages are close to 0 because Pb content is generally below detection limit of the instrument ( $\text{Pb} < 0.3 \text{ wt\%}$ ). There are four results older than 1 Ga at 1490 Ma in monazite from sample 9371-5, at 1105 Ma and 2060 Ma in two distinct grains from sample 9371-6 and at 2141 Ma in one grain from conglomerate 9375-14. This wide range is inferred to the strong alteration event affecting monazites in all the Lower Jatulian sedimentary layers. Because most of ages are below 500 Ma, it is postulated that alteration affecting the basal Jatulian sequence is associated to late weathering by meteoric alteration.

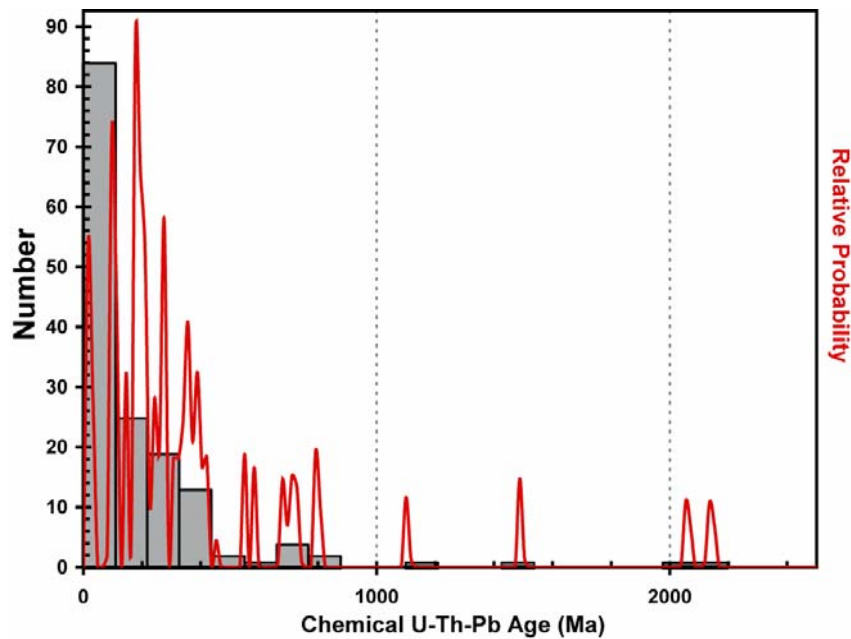


**Figure 3.3.28.** Histogram and relative probability curve representing the distribution of chemical age dating on the 28 grains of altered detrital monazites from the Lower Jatulian sediments.

## Conclusions

Proterozoic Jatulian sediments aged ca. 2.3-2.15 Ga are poorly sorted, highly feldspathic siliciclastic material deposited in a paleo-basin at the margin of the Karelian crustal block of the Baltic Shield. Whole-rock geochemistry and mineralogical study confirm that Jatulian sediments are directly issued from the erosion of Archean felsic granitic rocks. These source rocks are rather fertile in U with occurrences of uraninite discovered in quartz-feldspar pegmatites close to the Jatulian sediments but however, only zircon and monazite have been discovered in the Jatulian quartzite, sandstones and quartz-pebble conglomerates as primary detrital phases. The detrital mineral association (quartz, K-feldspar with minor plagioclase, green tourmaline, garnet, zircon and monazite) composing the Lower Jatulian sediments with the HFSE enrichment and the flat REE patterns with negative Eu anomalies suggest that the parental rock was most

probably fractionated granitic rocks. Zircon grains are well zoned with composition variation corresponding to metamictization and with relatively low U and Th contents that cannot account for the high U and Th concentrations of the rocks rising up to 0.002% U and 0.3%Th. However, monazite grains are highly altered with LREE and P leaching and new formation of a Th, Si and Fe-rich phase with minor amounts of U, corresponding to ferrithorite, a mixture of huttonitic monazite and iron hydroxides. This last phase is the dominant Th- and U-bearing mineral which most likely give the radioactive anomalies detected in Jatulian series. No boxwork has been observed which suggests that if uraninite were eroded from the Archean basement rocks, they were probably oxidized by oxygen-rich atmosphere or hydrosphere before sedimentation and only refractory minerals such as monazite and zircon have survived during the transportation under such conditions. The abundance of hematite within the Jatulian sediments is consistent with post-sedimentary oxidizing fluid circulation, which may correspond to the oxidation of formed detrital Fe-Ti oxides. The monazite chemical dating yields very young ages mostly < 500 Ma that suggests the weathering was probably caused by meteoric water infiltration and alteration.

## References

- Aikäs, O. and Sarikkola, R., 1987, Uranium in Lower Proterozoic conglomerates of the Koli Area, Eastern Finland, Uranium deposits in quartz pebble conglomerates, IAEA-TECDOC-427, p. 189-234.
- Amelin, Yu. V., Heaman, L. M. and Semenov, V. S., 1995, U-Pb geochronology of layered mafic intrusions in the eastern Baltic Shield: implications for the timing and duration of Palaeoproterozoic continental rifting; *Precambrian Research*, Vol. 75, p. 31-46.
- Anders E. and Grevesse N., 1989, Abundances of the elements: Meteoritic and solar. *Geochimica and Cosmochimica Acta* 57, 197-214.
- Balashov, Yu. A., 1996, Geochronology of Early Proterozoic rocks from the Pechenga-Varzuga structure in the Kola Peninsula; *Petrology*, Vol. 4, p. 3-25.
- Bekker, A., Holland, H. D., Wang, P. L., Rumble, D., Stein, H. J., Hannah, J. L., Coetzee, L. L. and Beukes. N. J., 2004, Dating the rise of atmospheric oxygen, *Nature* 427, p. 117-120.
- Bowles, J. F. W., 1990, Age dating of individual grains of uraninite in rocks from electron microprobe analyses, *Chemical Geology* 83, p. 47-53.
- Caillat, C., Kister, P. and Chemillac, R., 2006, *Compte Rendu de Mission: Puruvesi (Finland) – Northern Ladoga (Russia) Field Trip 26.09.06-04.10.06*, Internal Report AREVA NC/BUM/DEX/PN 06-FIN-CRM-03, 41 p.
- Catling, D. C. and Claire, M. W., 2005, How Earth's atmosphere evolved to an oxic state: a status report, *Earth and Planetary Science Letters*, Vol. 237, p. 1-20.
- Catling, D. C., Zahnle, K. J. and McKay, C. P., 2001, Biogenic methane, hydrogen escape, and the irreversible oxidation of early Earth, *Science*, Vol. 293, p. 839-843.
- Carignan J., Hold, P., Mevelle, G. Morel, J. and Yeghichevan, D., 2001, Routine analysis of trace elements in geological samples using flow injection and low pressure on line liquid

- chromatography coupled to ICP-MS: a study of geochemical reference materials BR, DR-N, UB-N, AN-G and GH, *Geostandards Newsletter* 25, p. 187-198.
- Cocherie, A. and Albarède, F., 2001, An improved U-Th-Pb age calculation for electron microprobe dating of monazite, *Geochimica et Cosmochimica Acta*, Vol. 65, p. 4509-4522.
- Cloud, P. E., 1968, Atmospheric and hydrospheric evolution on the primitive Earth, *Science*, Vol. 160, p. 729-736.
- Debon, F. and Le Fort, P., 1982, A chemical-mineralogical classification of common plutonic rocks and associations; *Trans. Royal Soc. Edinburg Earth Sci.*, Vol. 73, p. 135-139.
- de La Roche, H., 1968, Comportement géochimique différentiel de Na, K et Al dans les formations volcaniques et sédimentaires : un guide pour l'étude des formations métamorphiques et plutoniques ; *Comptes Rendus de l'Académie des Sciences (Paris)*, Vol. 267, p. 39-42.
- Evans, D. A. D., 2006, Proterozoic low orbital obliquity and axial-dipolar geomagnetic field from evaporite palaeolatitudes, *Nature*, Vol. 444, p. 51-55.
- Grotzinger, J. P. and Kasting, J. F., 1993, New constraints on Precambrian ocean composition, *Journal of Geology*, Vol. 101, p. 235-243.
- Hanski, E. J., 1992, Petrology of the Pechenga ferropicrites and cogenetic Ni-bearing gabbro-wehrlite intrusions, Kola Peninsula, Russia; *Geological Survey of Finland Bulletin*, Vol. 367, 192 p.
- Henry, D. J. and Dutrow, B. L., 1992, Tourmaline in a Low-Grade Clastic Metasedimentary Rock - an Example of the Petrogenetic Potential of Tourmaline; *Contributions to Mineralogy and Petrology*, Vol. 112, Issue 2-3, p. 203-218.
- Holland, H. D., 2002, Volcanic gases, black smokers, and the Great Oxidation Event, *Geochimica et Cosmochimica Acta*, Vol. 66, p. 3811-3826.
- Hölttä, P., Balagansky, V., Garde, A. A., Mertanen, S., Peltonen, P., Slabunov, A., Sorjonen-Ward, P. and Whitehouse, M., 2008, Archean of Greenland and Fennoscandia, *Episodes*, Vol. 31, No. 1, p. 13-19.
- Iijina, M. and Hanski, E., 2005, Layered mafic intrusions of the Tornio-Näränkäväära belt, In: Lehtinen, M., Nurmi, P. A., Rämö, O. T. (eds.), *The Precambrian Geology of Finland – Key to the Evolution of the Fennoscandian Shield*, *Developments in Precambrian Geology* 14, Elsevier Science B. V., Amsterdam.
- Karhu, J., 1993, Paleoproterozoic evolution of the carbon isotope ratios of sedimentary carbonates in the Fennoscandian Shield, *Geological Survey of Finland, Bulletin* 371, 87 p.
- Kasting, J. F., 2005, Methane and climate during the Precambrian era, *Precambrian Research*, Vol. 137, p. 119-129.
- Kirschvink, J. L. and Kopp, R. E., 2008, Palaeoproterozoic ice houses and the evolution of oxygen-mediating enzymes: the case for a late origin of photosystem II; *Philosophical Transactions of the Royal Society B: Biological Sciences*, Vol. 363, p. 2755-2765.
- Klein, C., 2005, Some Precambrian banded iron-formations (BIFs) from around the world: Their age, geologic setting, mineralogy, metamorphism, geochemistry, and origins, *American Mineralogist*, Vol. 90, p. 1473–1499.
- Kohonen, J., 1995, From continental rifting to collisional crustal shortening – Paleoproterozoic Kaleva metasediments of the Höytiäinen area in North Karelia, Finland, *Geological Survey of Finland, Bulletin* 380.
- Kouvo, O. and Tilton, G. R., 1966, Mineral Ages from the Finnish Precambrian, *The Journal of Geology*, Vol. 74, No. 4, p. 421-442.

- Lahtinen, R., Huhma, H., Kontinen, A., Kohonen, J. and Sorjonen-Ward, P., 2009, New constraints for the source characteristics, deposition and age of the 2.1-1.9 Ga metasedimentary cover at the western margin of the Karelian Province, Precambrian Research (in press).
- Lahtinen, R., Garde, A. A. and Melezhik, V. A., 2008, Paleoproterozoic evolution of Fennoscandia and Greenland, Episodes, Vol. 31, No. 1, p. 20-28.
- Lahtinen, R., Korja, A. and Nironen, M., 2005, Palaeoproterozoic tectonic evolution of the Fennoscandian Shield; In: Lehtinen, M., Nurmi, P.A., Rämö, O.T. (Eds.), The Precambrian Bedrock of Finland-Key to the Evolution of the Fennoscandian Shield. Elsevier Science B.V., p. 418-532.
- Laajoki, K., 1988, Nenäkangas-type conglomerates – evidence of a major break in sedimentation of the early Proterozoic (Karelia) quartzites in Kainuu, northern Finland; In: Laajoki, K. and Paakkola, J. (eds.) Sedimentology of the Precambrian formations in eastern and northern Finland; Proceedings of IGCP 160 Symposium at Oulu, January 21-22, 1986; Geological Survey of Finland, Special Paper 5, p. 91-107.
- Ledru, P., Milesi, J.-P., Johan, V., Sabaté, P. and Maluski, H., 1997, Foreland basins and gold-bearing conglomerates: a new model for the Jacobina Basin (São Francisco province, Brazil), Precambrian Research, Vol. 86, Issues 3-4, p. 155-176.
- Lehtinen, M., Nurmi, P. A. and Rämö, T., 2005, Precambrian geology of Finland: key to the evolution of the Fennoscandian shield, C. K. Condie Editor Series, Elsevier, Development in Precambrian Geology Vol. 14, 736 p.
- Lobaev, V., 2005, Caractéristiques minéralogiques et géochimiques du bassin sédimentaire mésoprotérozoïque de Pasha–Ladoga et de son socle (Bouclier Balte, Russie). Implications pour la genèse des gisements d'uranium de type discordance. Thèse présentée pour l'obtention de titre de Docteur en Sciences de la Terre et de l'Univers de l'Université Henry Poincaré, Nancy-I, France, 318 p.
- Ludwig, K.R., 1999, Isoplot/Ex version 2.00 – A geochronological toolkit for Microsoft Excel, Berkeley Geochronology Center, Special Publication No. 2.
- Maynard, J. B., 1992, Chemistry of modern soils as a guide to interpreting Precambrian paleosols, J. Geol. 100, p. 279-289.
- Maynard, J. B., Ritger, S. D. and Sutton, S. J., 1991, Chemistry of sands from the modern Indus River and the Archean Witwatersrand basin: Implications for the composition of the Archean atmosphere, Geology 19, p. 265-268.
- Melezhik, V. A., Fallick, A. E., Hanski, E., Kump, L. R., Lepland, A., Prave, A. R. and Strauss, H., 2005, Emergence of the aerobic biosphere during the Archean-Proterozoic transition: Challenges of the future research; GSA Today, Vol. 15, No. 1, p. 4-11.
- Melezhik, V. A. and Fallick, A. E., 2007, A widespread positive  $\delta^{13}\text{C}_{\text{carb}}$  anomaly at around 2.33-2.06 Ga on the Fennoscandian Shield: a paradox?, Terra Nova, Vol. 8, Issue 2, p. 141-157.
- Melezhik, V. A., Huhma, H., Condon, D. J., Fallick, A. E., Whitehouse, M. J., 2007, Temporal constraints on the Paleoproterozoic Lomagundi-Jatuli carbon isotopic event, Geology, Vol. 35, No. 7, p. 655-658.
- Melezhik, V. A., Fallick, A. E., Medvedev, P. V. and Makarikhin, V. V., 2000, Palaeoproterozoic magnesite-stromatolite-dolostone-'red bed' association, Russian Karelia: palaeoenvironmental constraints on the 2.0 Ga-positive carbon isotope shift; Norsk Geologisk Tidsskrift, 0029-196X, Vol. 80, Issue 3, p. 163-186.
- Milesi, J.-P., Ledru, P., Marcoux, E., Mougeot, R., Johan, V., Lerouge, C., Sabaté, P., Bailly, L., Respaut, J. P. and Skipwith, P., 2002, The Jacobina Paleoproterozoic gold-bearing

- conglomerates, Bahia, Brazil: a “hydrothermal shear-reservoir” model, *Ore Geology Reviews*, Vol. 19, Issues 1-2, p. 95-136.
- Montel, J. M., Foret, S., Veschambre, M., Nicollet, Ch. And Provost, A., 1996, Electron microprobe dating of monazite; *Chemical Geology*, Vol. 131, p. 37-53.
- Nironen, M., 1997, The Svecofennian Orogen: a tectonic model, *Precambrian Research* 86, p. 21-44.
- Ohmoto, H., Watanabe, Y., Ikemi, H., Poulson, S. R. and Taylor, B. E., 2006, Sulphur isotope evidence for an oxic Archaean atmosphere, *Nature*, Vol. 442, p. 908.
- Ovchinnikova, G. V., Kuznetsov, A. B., Melezhik, V. A., Gorokhov, I. M., Vasil’eva, I. M. and Gorokhovskii, B. M., 2007, Pb-Pb Age of Jatulian Carbonate Rocks : The Tulomozero Formation of the Southeast Karelia, *Stratigraphy and Geological Correlation*, Vol. 15, No. 4, p. 359-372 ; Original Russian Text published in *Stratigrafiya Geologicheskaya Korrelyatsiya*, 2007, Vol. 15, No. 4, p. 20-33.
- Paavola, J. and Kallio, P., 1986, *Geology of eastern Finland: Joint excursion of Swedish and Finnish Geologist (Excursion Guide)*, Report 2281, 27 p.
- Pekkarinen, L., 1979, The Karelian formations and their depositional basement in the Kiihtelysvaara-Värtsilä area, East Finland. *Geological Survey of Finland Bulletin* 301, 141 p.
- Pope, M. C. and Grotzinger, J. P., 2003, Paleoproterozoic Stark Formation, Athapuscow Basin, Northwest Canada: record of cratonic-scale salinity crisis; *Journal of Sedimentary Research*, Vol. 73, p. 280-295.
- Räsänen, J. and Huhma, H., 2001, U-Pb datings in the Sodankylä schist area, Central Finnish Lapland; *Geological Survey of Finland, Special Paper* 33, p. 153-188.
- Rastas, P., Huhma, H., Hanski, E., Lehtonen, M.I., Paakkola, J., Mänttari, I. & Härkönen, I. 2001. U-Pb isotopic studies on the Kittilä greenstone area, central Lapland, Finland. In: Vaasjoki, M. (ed.) *Radiometric Age Determinations from Finnish Lapland and Their Bearing on the Timing of Precambrian Volcano-Sedimentary Sequences*; *Geological Survey of Finland, Special Paper* 33, 95-141.
- Sestini, G., 1973, Sedimentology of a paleoplacer: The gold-bearing Tarkwaian of Ghana, *In: Amstutz, G.C., and Bernard, A.J., eds., Ores in sediments*, Heidelberg, Springer-Verlag, p. 275-305.
- Shurilov, A.V., 2008, *Métallogenèse de l’uranium dans la région de Ladoga (Karélie, Russie)*, thèse pour l’obtention du diplôme de doctorat de l’Université Henry Poincaré, Nancy, France, 463 p.
- Shurilov, A.V., Cuney, M. and Polekhovsky, Yu.S., 2007, Evolution of uranium enrichment in the Ladoga region (Russia), 9th biennial SGA meeting, 20th-23rd august 2007, Dublin, Session 17a, 4 p.
- Suzuki, K., Adachi, M. and Kazjizuka, I., 1994, Electron microprobe observations of Pb diffusion in metamorphosed detrital monazites, *Earth and Planetary Science Letter*, 128, p. 391-405.
- Vuollo, J. and Huhma, H., 2005, Paleoproterozoic mafic dikes in NE Finland, *In: Lehtinen, M., Nurmi, P. A., Rämö, O. T. (eds.) Precambrian Geology of Finland – Key to the Evolution of the Fennoscandian Shield*, Elsevier B. V., Amsterdam, p. 195-236.
- Williams, M. L., Jercinovic, M. J. and Hetherington, C. J., 2007, Microprobe Monazite Geochronology: Understanding Geologic Processes by Integrating Composition and Chronology, *Annual Review of Earth and Planetary Sciences*, Vol. 35, p. 137-175.

## **SYNTHESE ET DISCUSSION SUR LES MINERALISATIONS URANIFERES DES CONGLOMERATS A GALETS DE QUARTZ**

### **Origine de l'uranium des paléo-placers (magmatique-détritique et hydrothermale)**

Cette étude prouve de façon indéniable qu'entre 3.1 et 2.2 Ga, les dépôts sédimentaires continentaux formés dans les grands systèmes fluviaux ou deltaïques étaient porteurs de concentrations importantes de grains détritiques d'uraninite provenant de l'érosion de roches granitiques archéennes. Les arguments présentés dans ce chapitre sont à la fois les caractéristiques morphologiques des grains (plus ou moins arrondis), leur distribution suivant des structures sédimentaires (lits de minéraux lourds), la nature de la paragenèse minérale associée, les caractéristiques géochimiques des conglomérats mais surtout, les arguments chimiques qui sont principalement la teneur en Th des uraninites et les signatures magmatiques en éléments des terres rares.

D'autre part, la présence de minéraux uranifères d'origine hydrothermale est elle aussi caractéristique. Lors de la diagenèse ou du métamorphisme, des fluides circulent dans la porosité des sédiments et les grains d'uraninite primaire sont altérés. L'uranium semble réagir de façon différente suivant la nature des fluides, des minéraux présents à proximité et probablement aussi en fonction du pH de la solution. Les fluides riches en silice vont altérer l'uraninite et former de la coffinite en libérant une partie de l'uranium et du plomb radiogénique. L'uranium semble re-précipiter préférentiellement sur les grains de rutile ou d'ilménite avoisinant pour former un mélange entre brannérite et leucoxène. L'uranium est aussi présent sous la forme de pechblende sans Th formée à basses températures dans les fissures qui recourent la stratification.

Ces deux origines soutiennent donc le modèle de paléo-placers remaniés qui est généralement avancé pour ce type de gisements.

## Conditions de genèse d'un gisement à l'Archéen

Un gisement d'uranium est un système actif très complexe qui voit le jour à l'Archéen uniquement grâce à une combinaison exceptionnelle d'objets et d'évènements géologiques dans l'espace (source et moteur à proximité) et dans le temps (pré-GOE). Le modèle conceptuel en métallogénie pour la formation d'un gisement peut être représenté par une chaîne dont les maillons se succèdent dans un ordre précis : source → mobilisation → transport → piège → concentration → remobilisation / enrichissement → altération/conditions de préservation.

### 1) Une source pré-enrichie

La signature chimique des grains détritiques d'uraninite des paléo-placers étudiés varie d'un grain à l'autre dans un même gisement suivant le niveau stratigraphique du dépôt sédimentaire hôte (reef). Cela traduit une évolution au cours de l'enregistrement sédimentaire qui dépend de la nature de la roche source. Une source granitique peut disparaître progressivement avec l'érosion, être remplacée par les nouveaux granites qui sont mis à l'affleurement au cours de la sédimentation ou tout simplement par l'évolution du réseau hydrographique au cours du temps en fonction d'évènements tectoniques et n'affecte plus les mêmes domaines du socle. La chimie des uraninites peut varier aussi au sein d'un même reef lorsque que les grains proviennent de plusieurs sources érodés en même temps.

La Figure 3-A reprend la teneur moyenne en Th des différents reefs étudiés dans gisements du Witwatersrand et d'Elliot Lake. Le ou les magmas parents des uraninites des paléo-placers étaient nécessairement pré-enrichis en U pour pouvoir cristalliser de l'uraninite et devaient être très fractionnés. On peut distinguer trois grands types de source fertile potentielle : 1) le type faiblement peralumineux (pegmatoïdes des zones anatectiques) issu de la fusion à très hautes températures de roches sédimentaires qui génère des uraninites très riches en Th, Y et REE, 2) le type calco-alkalin fortement potassique (A2) issu du fractionnement de roches ignées à températures élevées et donnant des uraninites à teneurs élevées en Th, et 3) le type L (leucogranites) donnant des uraninites pauvres en Th et REE, résultant de la fusion de sédiments très peralumineux à basses températures. Les gros grains détritiques anguleux d'uraninite à Elliot Lake semblent provenir de sources magmatiques de type pegmatoïdes anatectiques alors que les petites uraninites analysées dans les nodules isolés de matière organique sont d'origine hydrothermale et sans Th. Les uraninites du Groupe de Dominion associées aux lits de minéraux lourds et celles de Beisa reef associées à des lits de matières carbonées à la base du Bassin du

Witwatersrand sont légèrement moins riches en Th que celles d'Elliot Lake et dérivent probablement de granites fractionnés formés à hautes températures. En remontant dans la séquence du Witwatersrand, les paléo-placers du Group du Central Rand sont de plus en plus pauvres en Th, ce qui reflète un fractionnement de plus en plus important entre Th et U dans la croûte continentale. Cela démontre aussi certainement que ces uraninites sont issues de magmas fractionnés formés à plus basses températures pour les uraninites du Carbon Leader reef, du Middle reef, du Vaal reef et du Ventersdorp Contact reef (VCR).

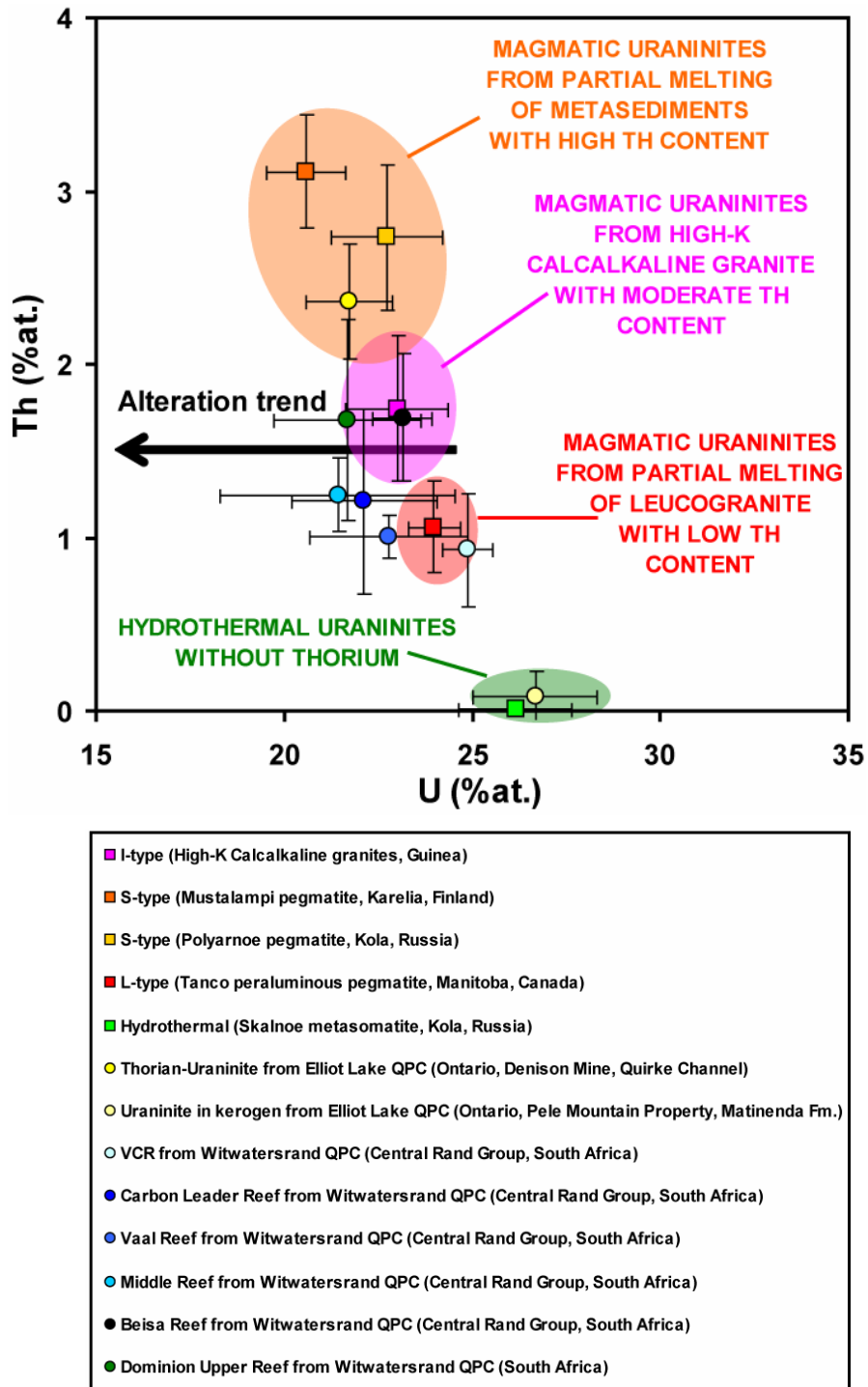


**Figure 3-A.** Diagramme récapitulatif présentant les teneurs moyennes en Th et U (at.%) des uraninites des paléo-placers du Witwatersrand et d'Elliot Lake en comparaison de celles formées dans roches magmatiques étudiées au chapitre 2.

## 2) Conditions de transport (atmosphère réductrice)

Dans les conditions atmosphériques actuelles très oxydantes, l'ion uraneux ( $U^{4+}$ ) des uraninites s'oxyde très rapidement dans les eaux météoriques naturelles et passe sous la forme d'ion uranyle ( $U^{6+}$ ) très mobile. Cet ion hexavalent forme ensuite des complexes stables en solution aqueuse en se liant avec  $P$ ,  $CO_3^-$ ,  $F$  ou  $Cl$  suivant les ions disponibles et le pH de la solution qui peut évoluer dans une gamme extrêmement large (Fig. 3-B). L'uranium peut re-précipiter sous sa forme d'oxyde uniquement en conditions réductrices à faible Eh, de l'ordre de 0.2 pour des pH acides < 6 et Eh nécessairement encore plus faible pour des pH plus élevés. L'atmosphère archéenne était donc réductrice pour que les grains d'uraninite ne soient pas altérés par des processus chimiques lorsque les plutons granitiques affleuraient ou lors de leur transport dans les rivières. Le taux d'oxygène libre dans l'atmosphère et dissous dans les eaux de surface devait donc être beaucoup plus faible qu'actuellement.

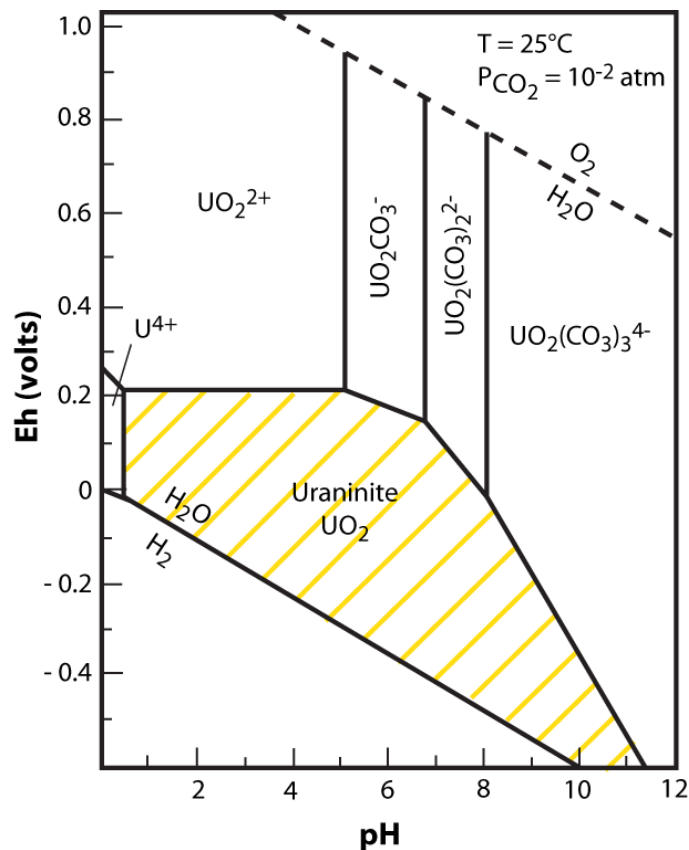


**Figure 3-B.** Diagramme Eh vs. pH (modifié de Langmuir, 1978) pour des conditions spécifiques à 25°C et une pression  $CO_2$  atmosphérique de  $10^{-2}$  atm.

Les conglomérats Archéens du Witwatersrand se distinguent aussi des sédiments huroniens et jatuliens par l'absence de feldspath détritique et par l'abondance des galets et grains de quartz. Les feldspaths ont pu disparaître lors de la diagenèse en se transformant en phyllosilicates dont la

matrice est constituée mais leur disparition peut aussi refléter des conditions de transport impliquant des eaux de surface à l'Archéen probablement acides. La Figure 3-C présente les courbes de solubilité de différentes espèces minérales uranifères et thorifères en fonction du pH. Les courbes de solubilité de l'uraninite et de la thorianite sont très basses et varient peu pour des pH compris entre 6 et 8 (concentrations :  $\log[U, Th] = -15$  à  $-16$  moles/litre). Le point de solubilité minimale des minéraux uranifères hexavalents dont la courbe est de forme parabolique est environ  $10^{10}$  fois plus important que pour les oxydes d'uranium (concentrations :  $\log[U, Th] \sim -6$  moles/litre). Ceci implique que les grains d'uraninite thorifère pouvaient être transportés sur de longues distances sans être altérés. Seul un pH extrême aux alentours de 2 aurait pu permettre de dissoudre les cristaux d'uraninite.

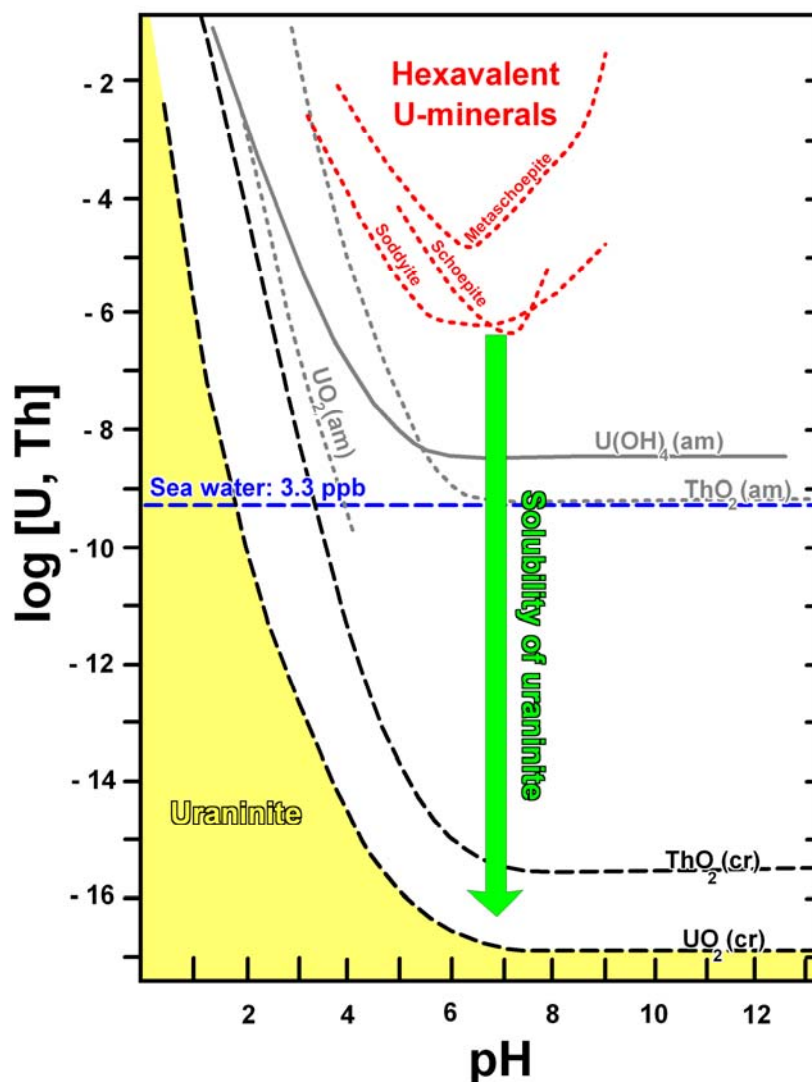


**Figure 3-C.** Solubilité de différentes espèces minérales à U(VI), U(IV) et Th(IV) : amorphes, oxydes bien cristallisés et hydroxydes à  $\sim 20^\circ\text{C}$  en fonction du pH compilé de plusieurs sources par Fanghänel and Neck (2002). Les données de l'uraninite (pechblende incluse)  $\text{UO}_2$  bien cristallisée sont pour 1 M NaCl en solution aqueuse à pH faible et la courbe est extrapolée pour les pH plus grands suivant la valeur de solubilité de  $10^{-17}$  proposée par Rai et al. (2003) pour un  $\text{pH} > 4$ . Les données pour les phases bien cristallisées et amorphes (colloïdes inclus) de  $\text{UO}_2$  et  $\text{ThO}_2$  sont tirées de données expérimentales obtenues dans des solutions à 0.5 M NaCl mais pour  $\text{ThO}_2$  bien cristallisé à  $\text{pH} > 3$ , la courbe de solubilité a été calculée (Rai et al., 1997). Les données pour la schoepite ( $\text{UO}_2)_4\text{O}(\text{OH})_6 \cdot 6(\text{H}_2\text{O})$  sont de Jang et al. (2006), pour la metaschoepite  $\text{UO}_3(\text{H}_2\text{O})_2$  de Gorman-Lewis et al. (2008) et pour la sodybite :  $(\text{UO}_2)_2\text{SiO}_4 \cdot 2(\text{H}_2\text{O})$  de Gorman-Lewis et al. (2007).

L'uranium ayant une densité de 18.7 proche de celle de l'or (19.3), les grains d'uraninite dans le Bassin du Witwatersrand se concentrent par des processus purement mécaniques dans les bancs aurifères avec les autres minéraux lourds dont la pyrite prédomine largement.

### 3) Conditions de préservation

Les âges isotopiques U-Pb des uraninites détritiques reflètent rarement les âges de cristallisation de leur magma source car U et Pb sont facilement mobilisés lors des percolations de fluides. La circulation de fluides hydrothermaux ultérieurs à leur dépôt et la remontée en surface des gisements après l'oxyatmersion (GOE) ont pu altérer ces minéraux. Si par des mouvements tectoniques la couverture sédimentaire surplombant les reefs est érodée, les uraninites ne sont plus protégées et peuvent soit être reprises dans les nouveaux dépôts terrigènes si l'atmosphère est encore suffisamment réductrice, soit être mis en solution si l'atmosphère est oxydante.

Après 2.2 Ga, le cycle de l'uranium change drastiquement. Le taux d'oxygène dans l'atmosphère augmente progressivement avec la prolifération des cyanobactéries et des stromatolites. Les uraninites formées dans les magmas sont altérées rapidement en surface lorsque les batholithes sont exposés à l'atmosphère oxydante. L'uranium très soluble est alors transporté dans les eaux de ruissèlement, par les rivières ou dans l'eau de mer sous la forme de l'ion uranyle. L'uranium peut aussi être d'origine diagénétique et transporté par les eaux de bassin, par les fluides métasomatiques lors du métamorphisme.

On pourra noter que tous les grains d'uraninite analysés dans les nodules ou les bancs de matières carbonés du Super-Groupe du Witwatersrand sont des uraninites d'origine détritique à la différence de celles d'Elliot Lake qui sont présentes dans les nodules de kérogène mais d'origine hydrothermale. La matière carbonée qui englobe les uraninites du Witwatersrand semble donc s'être fixée autour des grains primaires pour former les nodules, ce qui a dû protéger les grains du passage des fluides métamorphiques ou diagénétiques ultérieurs et limiter les phénomènes de remobilisation.

Enfin, l'altération des grains détritiques peut engendrer *in fine* la précipitation de minéralisations secondaires qui peuvent former des niveaux plus riches que la minéralisation primaire disséminée, et participer à la genèse des nouveaux types de gisement (discordance par exemple).

**Références citées dans la synthèse sur les paléo-placers**

- Fanghänel, Th., and Neck, V., 2002, Aquatic chemistry and solubility phenomena of actini oxides/hydroxides: Pure Applied Chemistry, v. 74, p. 1895-1907.
- Langmuir, D., 1978, Uranium solution-mineral equilibria at low temperatures with applications to sedimentary ore deposits: Geochimica Cosmochimica Acta, v. 42, p. 547-569.
- Rai, D., Felmy, A.R., Sterner, S.M., More, D.A., Mason, M.J., and Novak, C.F., 1997, The solubility of Th(IV) and U(IV) hydrous oxides in concentrated NaCl and MgCl<sub>2</sub> solutions: Radiochimica Acta, Vol. 79, p. 239.
- Rai, A., Yui, M., and Moore, D.A., 2003, Solubility product at 22°C of UO<sub>2</sub> precipitated from aqueous U(IV) solutions: Journal of Solution Chemistry, v. 32, p. 1-17.
- Jang, J.H., Dempsey, B.A. and Burgos, W.D., 2006, Solubility of schoepite: Comparison and selection of complexation constants for U(VI): Water Research, v. 40, p. 2738-2746.
- Gorman-Lewis, D., Mazeina, L., Fein, J.B., Szymanowski, J.E.S., Burns, P.C., and Navrotsky, A., 2007, Thermodynamic properties of soddyite from solubility and calorimetry measurements: Journal of Chemical Thermodynamics, Vol. 39, p.568-575.
- Gorman-Lewis, D., Fein, J.B., Burns P.C., Szymanowski, J.E.S. and Converse, J., 2008, Solubility measurements of the uranyl oxide hydrate phases metaschoepite, compregnacite, Na-compregnacite, becquerelite, and clarkeite: Journal of Chemical Thermodynamics, Vol. 40, p. 980-990.



---

# **CONCLUSIONS GENERALES**

---



L'enrichissement de la croûte terrestre en uranium commence à l'Archéen entre 3.5 et 2.7 Ga avec la formation des premiers cratons constitués principalement de TTG (tonalites-trondhjémites-granodiorites) dont les teneurs en U restes faibles (1.5 ppm en moyenne), mais cependant plus importantes que les grands domaines de roches basaltiques qui les entourent (quelques dizaines de ppb). L'origine des TTG serait l'aboutissement de la fusion de grand volume de roches mafiques hydratées produisant des résidus riches en grenat et hornblende, soit dans un contexte de subduction par fusion du slab à de grandes profondeurs dans le manteau, soit par fusion à la base de la croûte océanique lors de remontée de grands panaches mantelliques (cf. chapitre 1).

Les premiers granitoïdes capables de cristalliser de l'uraninite, les granites calco-alcalins potassiques de type Closepet, n'apparaîtraient qu'à la fin de l'Archéen vers 2.7 Ga, grâce à l'enrichissement du manteau en radioéléments par fusion du slab. Cependant, les résultats de cette thèse incitent à penser qu'un tel processus de formation était déjà en place avant 3.1 Ga et que par conséquent la tectonique des plaques existait déjà dès le Mésoarchéen.

En effet, l'étude des plus anciens gisements d'uranium connus sur Terre, les conglomérats à uraninites du Groupe de Dominion déposés dès 3.09 Ga à la base du Bassin de Witwatersrand en Afrique du Sud, a montré que les uraninites qu'ils contiennent possèdent des caractéristiques géochimiques distinctes (teneurs en Th, Y, REE et signature des spectres en REE) qui prouvent sans ambiguïté leur origine détritique. Ces uraninites proviendraient donc de l'érosion de granitoïdes vieux d'au moins 3.1 Ga et déjà capables de cristalliser de l'uraninite. D'après la chimie des uraninites et la paragenèse en minéraux accessoires détritiques qui les accompagnent, les roches sources étaient composées de leucogranites peralumineux enrichis en métaux rares et formés à relativement basses températures (~600°C) comme la pegmatite de Tanco du Bouclier Canadien et de granites formés à très hautes températures (800-1000°C) comme les granites calco-alcalins fortement potassiques de Guinée et ceux issus de la fusion partielle de la croûte et des ceintures volcano-sédimentaires comme les pegmatites de la péninsule de Kola ou de la région de Carélie du Bouclier Baltique. L'uranium de ces roches granitiques archéennes était mobilisé par érosion éolienne ou par le réseau hydrographique dégradant les plutons en surface par pure effet mécanique. Les grains d'uraninite arrachés aux granites n'étaient pas oxydés puisque l'atmosphère était réductrice à l'Archéen et ils étaient ainsi transportés pour s'accumuler finalement avec les autres minéraux lourds dans les chenaux des grands systèmes fluviaux ou à la base des fans deltaïques qui se jetaient dans la mer.

L'uranium des uraninites ou des autres minéraux accessoires (zircon, monazite, uranothorite, uranmicrolite...) présents dans les paléo-placers ou les granites archéens pouvait cependant être remobilisé ultérieurement, soit par le passage de fluides météoriques ou hydrothermaux oxydants, soit par métasomatisme le plus souvent calcique ou sodique, ou encore lors du passage de la fenêtre à huile en se fixant sur les kérogènes (en quantités peu significatives par rapport aux précédents processus). Les remobilisations ultérieures peuvent finalement conduire à la formation de nouvelles concentrations dans des contextes très variés (discordances, veines...) et effacer partiellement ou totalement l'origine primaire magmatique ou détritique des minéralisations.

Bien que les terrains archéens apparaissent comme peu fertiles de prime abord et que les bassins Paléoprotérozoïques sont les cibles les plus prisées dans l'exploration pour la découverte de nouvelles concentrations uranifères, les plus grands gisements actuels ont pris naissance dans les domaines archéens. La croûte continentale archéenne représente donc le tout premier maillon du cycle d'enrichissement de l'uranium dans l'histoire géologique de la Terre. Les granitoïdes archéens qui en sont la source originelle demandent à être beaucoup plus étudiés afin d'appréhender les processus de leur genèse qui restent encore obscurs.

---

# **LISTE DES ABREVIATIONS**

---

## Liste des abréviations

---

Toutes les abréviations utilisées dans ce rapport sont conformes au système international métrique (SI).

<b><math>\sigma</math></b>	écart-type (en anglais « <i>standard deviation</i> ») $\sigma = \sqrt{\frac{\sum_1^n (x_n - m)^2}{n - 1}}$ ou n correspond au nombre de mesures et m à la moyenne arithmétique
<b><math>\pm</math></b>	plus ou moins
<b><math>\sim</math></b>	environ
<b><math>&lt;</math></b>	inférieur à
<b><math>=</math></b>	égal à
<b><math>&gt;</math></b>	supérieur à
<b><math>\mu</math></b>	micro ( $10^{-6}$ )
<b><math>\alpha</math></b>	alpha (utilisé pour les rayonnements)
<b><math>\beta</math></b>	beta (utilisé pour les rayonnements)
<b>P</b>	pression
<b>Pa</b>	Pascal (unité de la pression)
<b>T</b>	température
<b>t</b>	tonne
<b>°C</b>	degrés Celsius (unité de la température)
<b>A</b>	ampères
<b>kV</b>	kilo volt
<b>keV</b>	kilo électron volt
<b>Ma</b>	méga années (1 Ma = $10^6$ années = 1 million d'années)
<b>M</b>	mole
<b>Ga</b>	giga années (1 Ga = $10^9$ années = 1 milliard d'années)
<b>m</b>	mètre
<b>m<sup>2</sup></b>	mètre carré
<b>km</b>	kilomètre ( $10^3$ m)
<b>cm</b>	centimètre ( $10^{-2}$ m)
<b>mm</b>	millimètres ( $10^{-3}$ m)
<b>REE</b>	éléments des terres rares (de l'anglais « <i>Rare Earth Elements</i> »)
<b>g/t</b>	gramme par tonne
<b>US\$</b>	dollar des Etats Unis d'Amérique
<b>k</b>	kilo ( $10^3$ = mille)

---

# **LISTE DES FIGURES**

---

---

**INTRODUCTION GENERALE**


---

<b>Figure 1.</b> Production mondiale d'uranium jusqu'en 2007 et estimation des réserves (prouvées « <i>Reasonably Assured Resources</i> » et spéculatives « <i>Inferred Resources</i> ») en fonction des différents types de gisements (les valeurs sont exprimées en tonnes U ; compilation effectuée par l'IAEA 2007 d'après Cuney, 2009 ; les gisements classés dans la catégorie « <i>Other</i> » comprennent les gisements de type métamorphique, superficiel, cheminée bréchique collapsée, phosphorite, lignite et shales noirs) .....	10
<b>Figure 2.</b> Répartition géographique des provinces archéennes et protérozoïques dans le monde (modifiée de Rämö and Haapala, 1996) et localisation des granitoïdes et paléo-placers échantillonnés dans cette étude .....	12

---

**CHAPITRE 1 : CONNAISSANCES SUR L'ARCHÉEN ET TRANSITION VERS LE PALÉOPROTÉROZOÏQUE**


---

<b>Figure 1.1.</b> Chronologie de l'Archéen .....	17
<b>Figure 1.2.</b> Le principe de sagduction (d'après Gorman <i>et al.</i> , 1978 et Martin., 2005) permet d'expliquer les mouvements lithosphériques verticaux observés à l'Archéen entre les unités granito-gneissiques anciennes de type TTG formant des dômes par mouvements ascendants (flèches noires) dans des roches volcaniques plus jeunes et plus denses constituant les ceintures de roches vertes qui s'enfoncent par mouvements gravitaires .....	19
<b>Figure 1.3.</b> Diagramme pression-température et coupes schématiques des zones de subduction montrant la formation de la croûte continentale à l'Archéen et à notre époque (modifié de Martin, 2005) .....	20
<b>Figure 1.4.</b> Schéma simplifié d'une délamination crustale .....	21
<b>Figure 1.5</b> Schéma simplifié d'une remontée de plume mantellique .....	21
<b>Figure 1.6.</b> Reconstitution du supercontinent Columbia au paléo-mésoproterozoïque issu de collisions entre les blocs cratoniques archéens et protérozoïques lors des orogènes entre 2,1 et 1,8 Ga (modifié de Zhao <i>et al.</i> , 2002). La localisation des zones d'étude est reportée par des étoiles : en rouge les zones de socle archéen et en vert les paléo-placers .....	23
<b>Figure 1.7.</b> Diagramme ternaire K <sub>2</sub> O-Na <sub>2</sub> O-CaO montrant l'évolution de la composition des granitoïdes archéens (TTG, sanukitoïdes et granites de type Closepet) modifié de Martin and Moyen (2005) .....	27
<b>Figure 1.8.</b> Spectre des REE normalisées aux chondrites (valeurs chondritiques C1 de Sun and McDonough, 1989) pour les granitoïdes archéens (TTG, sanukitoïdes et granites de type Closepet) d'après les compositions du Tableau 1.2 (Martin <i>et al.</i> , 2005) comparés à la composition moyenne de la croûte continentale actuelle (Taylor and McLennan, 1985) .....	27
<b>Figure 1.9.</b> Teneurs en uranium et thorium (ppm) des roches archéennes d'après une compilation des analyses géochimiques des différents cratons référencées dans la base de données « GEOROC » (3094 analyses: 2236 roches mafiques, 649 roches acides et 209 roches sédimentaires, extrait du site <a href="http://georoc.mpch-mainz.gwdg.de/georoc/">http://georoc.mpch-mainz.gwdg.de/georoc/</a> ) .....	29
<b>Figure 1.10.</b> Composition de l'atmosphère au cours du temps (d'après Yamaguchi, 2005) : en bleu - modèle pour une atmosphère archéenne réduite avec la courbe de l'évolution de pO <sub>2</sub> augmentant progressivement avec la complexification des organismes vivants et l'oxyatmoversion entre 2,2 et 1,9 Ga dès l'apparition des organismes phototrophes (hypothèse soutenue par Kasting, 1987 et 2001, Rye and Holland, 2000, Pavlov <i>et al.</i> , 2001, Bekker <i>et al.</i> , 2004, Barley <i>et al.</i> , 2005, Holland, 2006), et en vert - modèle pour une atmosphère archéenne oxygénée (d'après Ohmoto, 1996, 2003 et 2004 ; Lasaga and Ohmoto, 2002) .....	31
<b>Figure 1.11.</b> Résumé des « évidences » de l'oxyatmoversion, l'augmentation de l'oxygène libre dans l'atmosphère entre 2,2 et 1,85 Ga symbolisée par les traits bleus (extrait de Yamaguchi, 2005 ; modifié de Holland, 1994 et Phillips <i>et al.</i> , 2001) .....	32
<b>Figure 1.12.</b> Répartition des paléo-placers archéens à paléoproterozoïques (en orange) et des formations de fer rubanées (BIF de l'anglais « <i>Banded Iron Formation</i> » ; en bleu) modifiée de Houston and Karlstrom, (1979) d'après la reconstitution des continents de Piper (1976) et la distribution des BIF de Goodwin (1973) .....	35

**CHAPITRE 2 : SOURCES MAGMATIQUES ARCHEENNES DE L'URANIUM**

**Partie 2.1 Craton de Kénéma Man, Guinée**

<b>Figure 2.1.1</b>	Simplified geological map of the West African Craton (modified from Egal et al., 2002) .....	50
<b>Figure 2.1.2.</b>	Geological map of south-east Guinea (modified from Thiéblemont et al., 2001) and location of studied samples .....	53
<b>Figure 2.1.3.</b>	Binary diagram showing the K <sub>2</sub> O vs. SiO <sub>2</sub> contents (wt%) of the Guinean magmatic rocks. The composition limits and fields are from Peccerillo and Taylor (1976) and rock composition references are from Debon and Lefort (1983) .....	61
<b>Figure 2.1.4.</b>	Binary diagram showing the K <sub>2</sub> O vs. Na <sub>2</sub> O contents (wt%) of the Guinean magmatic rocks .....	61
<b>Figure 2.1.5.</b>	Variation of P versus Q parameters for magmatic rocks from south-east Guinea (diagram from Debon and Lefort, 1988) .....	62
<b>Figure 2.1.6.</b>	Variation in the peraluminous index A with the fractionation parameter B (coloration index) for Guinean magmatic rocks (diagram from Debon and Lefort, 1988) .....	63
<b>Figure 2.1.7.</b>	Binary diagram showing Rb versus Y+Nb contents (in ppm) of the Guinean magmatic rocks (diagram from Pearce, 1982) .....	64
<b>Figure 2.1.8.</b>	Variation of Th/Yb ratio with Ta/Yb ratio for Guinean magmatic rocks (diagram from Pearce, 1983) .....	65
<b>Figure 2.1.9.</b>	A/NK vs. A/CNK diagram of the magmatic rocks from south-east Guinea (data from Table 2.1.1) .....	65
<b>Figure 2.1.10.</b>	Th-U variations in the magmatic rocks from south-east Guinea .....	66
<b>Figure 2.1.11.</b>	Th* and U* variations versus K <sub>2</sub> O/Na <sub>2</sub> O ratio for the Guinean magmatic rocks .....	67
<b>Figure 2.1.12.</b>	Chondrite-normalized REE spectra of the U-Th-rich samples collected from south-east Guinea .....	68
<b>Figure 2.1.13.</b>	Photomicrographs of Leonian orthogneiss NZE2328: cross nicols transmitted light A - perthitic feldspar and quartz with lobate contacts, B - myrmekite exsolutions at the border of a feldspar, C - zoned zircon within biotite, D - Monazite rimmed by epidote, E - elongated zircon, F - titanite with typical wedge-shape and high polarization colours; reflected light G - euhedral magnetite crystal with ilmenite lamellae; natural transmitted light H - residual magnetite crystal surrounded by hematite .....	70
<b>Figure 2.1.14.</b>	Photomicrographs of Liberian granitoids: crossed nicols transmitted light A- deformed twinning plagioclase and fractured feldspar with polycrystalline quartz (NZE2600), B- sericitized feldspar and quartz with undulous extinction (DTMAC12*), C- biotite and epidote outlining the schistosity and following curvature of deformed quartz lamellae (NZE2615); natural transmitted light D- biotite altered to chlorite (DTMAC12*); crossed nicols transmitted light E- epidotization of biotite and altered feldspar (DTMAC23*), F- monazite and zircon aggregates (DTMAC12*), G- apatite (DTMAC12*); reflected light: H- reddish internal reflection around zircon due to hematite (DTMAC12*) .....	71
<b>Figure 2.1.15.</b>	Photomicrographs of Paleoproterozoic samples: crossed nicols transmitted light A- quartz with wavy extinction surrounded by K-feldspar phenocrysts (NZE2381), B- zircon associated with iron oxides within biotite (NZE2393), C- apatite crystals within plagioclase (NZE2381); reflected light D- residual euhedral uraninite surrounded by carbonate, hematite and pyrite (NZE2381); transmitted light: E- brown titanite crystals with green hornblende (DTNZE31a); crossed nicols transmitted light: F- perthitic K-feldspar surrounded by hornblende (green) and epidote (orange to violet) (DTNZE31a), G- apatite in typical hexagonal cross section between hornblende and polycrystalline quartz (DTNZE 31a); reflected light H- Cubes of pyrite and iron oxides (DTNZE31a) .....	73
<b>Figure 2.1.16.</b>	BSE-SEM images of zoned zircon A - from Leonian gneiss (NZE2328) showing distinctive average atomic number zones and radial fractures and B - from a Liberian granite (DTMAC12*) .....	74

<b>Figure 2.1.17.</b> BSE-SEM images of different monazite grains from the Liberian Macenta batholith (DTMAC12*) and showing various alteration stages presented in increasing order: A - relatively pristine monazite with urano-thorianite inclusions, B - porous monazite surrounded by a radiation damage rim and C - completely altered monazite with huttonite newly formed crystals (light grey).	75
<b>Figure 2.1.18.</b> Variations in the major element content composing zircon (Zr+Hf+Si) with minor element content (Al+P+Y+Ca+Fe+U+Th) in atomic percent and increasing radioelement content (U+Th) substitute to Zr .....	77
<b>Figure 2.1.19.</b> Distribution of monazite compositions from the Liberian granite DTMAC12* represented in the ternary system of the end-member molecules (diagram from Bowie and Horne, 1953 and Förster, 1998) .....	79
<b>Figure 2.1.20.</b> BSE-SEM image of an altered monazite grain surrounded by an epidote aureole in the Leonian gneiss (sample NZE2328). Note the radial fractures in Fe-oxides and the fibrous allanite crystals developed from monazite and elongated along the biotite's cleavage .....	80
<b>Figure 2.1.21.</b> BSE images of uraninite grains from the Paleoproterozoic granite NZE2381: A - almost entirely dissolve grain leaving a boxwork with epidote and pyrite, B - partly dissolved uraninite rimmed by a radiation damaged ring and C - highly fractured uraninite .....	81
<b>Figure 2.1.22.</b> Distribution of the chemical age dating in uraninite from the Eburnean granite NZE2381 .....	82
 <b>Partie 2.2 Craton de Pilbara, Australie</b>	
<b>Figure 2.2.1</b> Geological map of the Pilbara Craton showing the Archean granite-greenstone terranes and the location of samples (modified from Hickman, 1983) .....	94
<b>Figure 2.2.2.</b> Generalised stratigraphic column of the Pilbara Supergroup (after Van Kranendonk et al., 2004) .....	95
<b>Figure 2.2.3.</b> Schematic diagram showing various stages in the development of Paleoproterozoic crust of the Pilbara Craton (after Smithies et al., 2009) .....	96
<b>Figure 2.2.4.</b> Granitic samples from the Pilbara Craton: A- 142879 Spear Hill Monzogranite (core sample of the Shaw Granitic Complex), B- 169044 Moolyella Monzogranite (core sample of the Mount Edgar Granitic Complex), C- 178011 Cooke Creek Monzogranite (hand sampling) and D- 178014 Bonney Downs Monzogranite (hand sampling) .....	99
<b>Figure 2.2.5.</b> Hornblende geobarometer relations (modified from Anderson and Smith, 1995) .....	102
<b>Figure 2.2.6.</b> Binary diagram showing the K <sub>2</sub> O vs. SiO <sub>2</sub> contents (wt%) of the Split Rock Supersuite from the Pilbara Craton .....	104
<b>Figure 2.2.7.</b> A/NK versus A/CNK diagram (Maniardi and Piccoli, 1989) .....	104
<b>Figure 2.2.8.</b> Q-P chemical-mineralogical diagram of Debon and Le Fort (1988) representing variations of the proportions of quartz relative to plagioclase and K-feldspar for the granitoids of the Split Rock Supersuite from the Eastern Pilbara Terrane .....	105
<b>Figure 2.2.9.</b> A-B chemical-mineralogical diagram of Debon and Le Fort (1988) representing the variations of the peraluminous index (A) versus a differentiation index (B) for the granitoids of the Eastern Pilbara Terrane .....	106
<b>Figure 2.2.10.</b> Chondrite-normalized spectra of whole-rock REE abundances in the Split Rock Supersuite granitoids sampled in this study compare to the average upper continental crust composition (Taylor and McLennan, 1985) .....	106
<b>Figure 2.2.11.</b> Binary diagram showing whole-rock Th vs. U contents (in ppm) of the Split Rock Supersuite granitoids from the East Pilbara Terrane .....	107
<b>Figure 2.2.12.</b> Polarized transmitted light image of the well preserved primary magmatic assemblage of quartz, feldspar and muscovite phenocrysts ( <i>sample 169044</i> ) .....	108
<b>Figure 2.2.13.</b> Myrmekite in microcline (the plaid twinning) observed in polarized transmitted light ( <i>sample 142879</i> ) .....	108
<b>Figure 2.2.14.</b> Quartz with rolling extinction, feldspar and muscovite partly replaced by chlorite observed in polarized transmitted light ( <i>sample 169044</i> ) .....	108

## Liste des Figures

<b>Figure 2.2.15.</b> Biotite partly altered to chlorite observed in natural transmitted light ( <i>sample 178014</i> ) .....	108
<b>Figure 2.2.16.</b> Titanite (stage I) observed in polarized transmitted light ( <i>sample 178011</i> ) .....	109
<b>Figure 2.2.17.</b> Hornblende A- in polarized transmitted light and B- in BSE mode ( <i>sample 178011</i> ) showing ilmenite inclusions and the typical crossing cleavage .....	110
<b>Figure 2.2.18.</b> BSE image of apatite crystals occurring in Fe-Ti oxide ( <i>sample 178014</i> ) .....	111
<b>Figure 2.2.19.</b> Fragmented garnet phenocryst in natural transmitted light ( <i>sample 169044</i> ) .....	112
<b>Figure 2.2.20.</b> BSE image of a garnet showing a darker zoning at the edge of the crystal and along microcracks ( <i>sample 169044</i> ) .....	112
<b>Figure 2.2.21.</b> Ternary diagrams representative of the end member molecules (Alm = Almandine; Sps = Spessartite; Gro = Grossular; And = Andradite; Py = Pyrope; Uv = Uvarovite) and the Fe, Mn and Ca contents in two phenocrysts of garnet ( <i>sample 169044</i> ) .....	112
<b>Figure 2.2.22.</b> BSE image showing the complex texture and composition heterogeneities in a columbite crystal ( <i>sample 169044</i> ). Chemical profile through the grain was realized by electron microprobe analysis along the A-B line approximately each 3.5 $\mu\text{m}$ .....	115
<b>Figure 2.2.23.</b> Columbite-Tantalite quadrilateral representing binary plot of Mn/(Mn+Fe) against Ta/(Ta+Nb) in atom per formula unit (apfu) for the pristine columbite observed in sample 169044 .	116
<b>Figure 2.2.24.</b> Zircon and monazite grains in polarised transmitted light showing a radiation damage halo in the surrounding muscovite ( <i>sample 178011</i> ) .....	117
<b>Figure 2.2.25.</b> Euhedral zircons showing the crystal grow zoning and altered areas (darker grey) in BSE mode ( <i>sample 178014</i> ) .....	118
<b>Figure 2.2.26.</b> Euhedral zircon with a complex heterogeneous texture in BSE mode associated to metamictization ( <i>sample 169044</i> ) .....	118
<b>Figure 2.2.27.</b> Fractured and altered zircon surrounded by fluorocarbonate in BSE mode ( <i>sample 142879</i> ) .....	118
<b>Figure 2.2.28.</b> Binary diagram showing the element substitutions occurring during alteration of zircon with the decreasing average atomic number in BSE mode .....	120
<b>Figure 2.2.29.</b> Monazite (Mnz) in BSE mode showing porosity at the edge of the grain corresponding to dissolution cavities and surrounding zircon (Zrn) and ilmenite-rutile association ( <i>sample 178014</i> ) .....	120
<b>Figure 2.2.30.</b> BSE image of an altered monazite completely replaced by fluorocarbonate ( <i>sample 142879</i> ). Secondary ilmenite and epidote surround the cavity .....	120
<b>Figure 2.2.31.</b> Euhedral zircon and xenotime crystals in BSE mode showing small inclusions of uranothorite and secondary fluorocarbonate adjacent to the assemblage ( <i>sample 169044</i> ) .....	122
<b>Figure 2.2.32.</b> Saussuritization of the feldspar phenocrysts partly to totally replace by finely grained micas and epidote, observed in polarized transmitted light ( <i>sample 142879</i> ) .....	122
<b>Figure 2.2.33.</b> Classification of chlorite crystals after Hey (1954) .....	124
<b>Figure 2.2.34.</b> Fluorocarbonate within a cavity of altered monazite observed in BSE mode ( <i>sample 142879</i> ) .....	124
<b>Figure 2.2.35.</b> BSE image of fibrous fluorocarbonate developed in intergrain space ( <i>sample 178014</i> ) .....	124
<b>Figure 2.2.36.</b> Epidote and later pumpellyite associated to chlorite in polarized transmitted light ( <i>sample 142879</i> ) .....	126
<b>Figure 2.2.37.</b> BSE image showing primary magmatic ilmenite, titanite I, zircon and altered monazite replaced to REE-fluorocarbonates (white) surrounded by epidote aureole and disseminated apatite crystallization ( <i>sample 178011</i> ) .....	127
<b>Figure 2.2.38.</b> Titanite (stage II) overgrowing on ilmenite (Ilm) in reflected light ( <i>sample 178011</i> ). Note the development of crystals along the biotite cleavage .....	127
<b>Figure 2.2.39.</b> Fluorite overgrowing on ilmenite along muscovite-chlorite cleavage planes in natural polarised light ( <i>sample 169044</i> ) .....	128

<b>Figure 2.2.40.</b> BSE image of pseudocubic fluorite crystals between two feldspar phenocrysts ( <i>sample 169044</i> ) .....	128
<b>Figure 2.2.41.</b> amygdales of pumpellyite superimposed to chlorite and epidote between quartz and feldspar phenocrysts in polarised transmitted light ( <i>sample 142879</i> ) .....	128
<b>Figure 2.2.42.</b> Pumpellyite affecting a muscovite phenocryst ( <i>sample 178011</i> ) .....	128
<b>Figure 2.2.43.</b> Mineral paragenesis following the evolution of the high-K granites from the eastern Pilbara Craton .....	130

### Partie 2.3 Pegmatite de Tanco, Manitoba, Canada

<b>Figure 2.3.1.</b> Location and geological setting of the Tanco pegmatite .....	142
<b>Figure 2.3.2.</b> East-west section showing the general geology of the Tanco Lower pegmatite and location of the studied samples .....	144
<b>Figure 2.3.3.</b> Optical microscopic and SEM images of the euhedral uraninite crystals in the Tanco Lower pegmatite .....	148
<b>Figure 2.3.4.</b> Binary diagrams illustrating the various chemical compositions of the different BSE brightness parts in the less altered uraninite crystals from samples 2-22 and 2-57 versus the Pb/U ratios and correspondent calculation of U-Pb-Th chemical ages .....	151
<b>Figure 2.3.5.</b> Variations of U + Pb contents relatively to Si + Ca + K + P (in atom percent) in the brighter and darker grey zones of the uraninite crystals in BSE images .....	152
<b>Figure 2.3.6.</b> Optical microscopic and SEM images of the accessory minerals associated to the paragenesis of uraninite crystals in the Tanco pegmatite .....	154
<b>Figure 2.3.7.</b> BSE image of a broken uranmicrolite crystal showing a complex internal zoning ( <i>sample LP-16</i> ) and plots of the EMP analysis results across the chemical profile drawn in the picture showing variations in major and trace elements (in atom percent) .....	158
<b>Figure 2.3.8.</b> Chemical compositions of columbite-tantalite minerals from the three samples of the Tanco Lower Pegmatite represented in the typical end-member quadrilateral .....	159
<b>Figure 2.3.9.</b> Distribution of $^{207}\text{Pb}/^{206}\text{Pb}$ ages in three uraninite grains from the Tanco Lower Pegmatite .....	164
<b>Figure 2.3.10.</b> Concordia diagram with the U-Pb isotopic of three uraninite crystals from the Tanco Lower Pegmatite .....	165
<b>Figure 2.3.11.</b> Secondary electron imaging of the different ion spots in uraninite 2 ( <i>sample 2-22</i> ) analysed by SIMS (ion probe CAMECA IMS-3f) .....	166
<b>Figure 2.3.12.</b> Chondrite-normalized REE abundances in uraninite from the Tanco pegmatite (this study), the Rössing deposit and the Otish Mounts pegmatite (data after Bonhoure, 2007) .....	168

### Partie 2.4 Bouclier Baltique: Cratons de Carélie et de Kola (Russie et Finlande)

<b>Figure 2.4.1.</b> Sketch map of the Archean crust in the Baltic Shield (after Hölttä et al., 2008) showing the location of the studied areas (red squares): (a) Principal tectonic units of the Baltic shield; (b) Geological representation of the main Archean terranes, and greenstone, schist and paragneiss belts .....	180
<b>Figure 2.4.2.</b> Geological map of the southeast Karelia at the boundary between Finland and Russia elaborated from the data of the Geological Survey of Finland .....	184
<b>Figure 2.4.3.</b> Macroscopic pictures of the various Archean lithologies sampled in the Mustalampi area .....	186
<b>Figure 2.4.4.</b> Granoblastic texture in Archean amphibolite ( <i>sample 9375-1</i> , crossed nicols transmitted light) .....	185
<b>Figure 2.4.5.</b> Hornblende, feldspar and biotite within Archean amphibolite ( <i>sample 9375-1</i> , crossed nicols transmitted light) .....	185

## Liste des Figures

<b>Figure 2.4.6</b> Binary diagram showing the K <sub>2</sub> O vs. SiO <sub>2</sub> contents (wt%) of the Baltic Shield basement rocks .....	188
<b>Figure 2.4.7.</b> Feldspar porphyroblast (center) indicating a dextral sense of shearing with the schistosity define by biotite elongation (sample 9375-5, crossed polarized light) .....	188
<b>Figure 2.4.8.</b> Chondrite-normalized REE patterns of the Karelian basement rocks .....	189
<b>Figure 2.4.9.</b> Th vs. U contents (ppm) of the Karelian basement rocks .....	189
<b>Figure 2.4.10</b> BSE-SEM image of two monazite crystals within biotite (sample 9375-5) .....	190
<b>Figure 2.4.11</b> BSE-SEM image of zoned zircon grain within biotite (sample 9375-5) .....	190
<b>Figure 2.4.12</b> BSE-SEM image of pyrite and molybdenite vein-like deposition (light grey) along biotite (sample 9375-5) .....	190
<b>Figure 2.4.13</b> BSE-SEM image of a monazite crystal (left) and detail textural features in the same grain (right) showing white cubes of uranothorite (sample 9375-5) .....	191
<b>Figure 2.4.14.</b> Biotite, sericitized feldspar and quartz pegmatite containing two isolated uraninite grains (sample 9375-3, crossed nicols transmitted light) .....	192
<b>Figure 2.4.15.</b> Quartz vein cutting the two-mica pegmatite (sample 9375-3, crossed nicols transmitted light) .....	192
<b>Figure 2.4.16.</b> BSE-SEM image of three apatite grains displaying typical hexagonal shape (sample 9375-2) .....	192
<b>Figure 2.4.17.</b> BSE-SEM image of a monazite fractured grain showing uranothorite inclusions (white) and internal porosity (sample 9375-2) .....	192
<b>Figure 2.4.18.</b> BSE-SEM image of cubic uraninite crystal in biotite selvage and elongated quartz (sample 9375-3) .....	193
<b>Figure 2.4.19.</b> BSE-SEM image of small anatase crystal aggregates lining pore space on the surface of biotite lamellae (sample 9375-3) .....	193
<b>Figure 2.4.20.</b> BSE-SEM images of uraninite crystals (sample 9375-3) showing highly fracturation, galena (white) coating grain boundary and filling fractures (A+C) and alteration zones (grey) corresponding to recrystallization into coffinite or remobilization within hosting biotite cleavage (B) .....	195
<b>Figure 2.4.21.</b> Binary diagrams Th, Pb, Si, Al, Ca and LREE vs. U (in atomic percent) illustrating the variations of the chemical composition in uraninite crystals from the Mustalampi pegmatite 9375-3 with alteration .....	196
<b>Figure 2.4.22.</b> Histogram showing the repartition of chemical U-Th-Pb ages determined from 117 EMPA in uraninite grains from the Mustalampi pegmatite (sample 9375-3) .....	197
<b>Figure 2.4.23.</b> Concordia diagram for the five isotopic measurements realized in 2 uraninite grains from the Mustalampi pegmatite (sample 9375-3) .....	198
<b>Figure 2.4.24.</b> Distribution of <sup>207</sup> Pb/ <sup>206</sup> Pb ages (Ma) measured in 2 uraninite grains from the Mustalampi pegmatite (sample 9375-3 from Karelia, Finland) .....	199
<b>Figure 2.4.25.</b> Chondrite-normalized spectra of REE abundances in magmatic uraninites from S-type granitoids .....	200
<b>Figure 2.4.26.</b> Huhtilampi granite samples characterized by a red coloration (scale bar = 1 cm) .....	201
<b>Figure 2.4.27.</b> Granoblastic texture of quartz and feldspar with minor interstitial biotite (sample 9375-17, crossed polarized transmitted light) .....	202
<b>Figure 2.4.28.</b> Quartz with undulous extinction and feldspar xenomorphic grains with recrystallized borders (sample 9375-17, crossed polarized transmitted light) .....	202
<b>Figure 2.4.29.</b> Plagioclase altered to sericite and muscovite with late carbonate minerals (sample 9375-16, crossed polarized transmitted light) .....	202
<b>Figure 2.4.30.</b> Biotite altered to chlorite and associated with pyrite (opaque) and disseminated hematite giving a reddish coloration (sample 9375-16, natural transmitted light) .....	202
<b>Figure 2.4.31.</b> BSE-SEM image of a zircon grain (sample 9375-16) .....	202

## Liste des Figures

<b>Figure 2.4.32.</b> BSE-SEM image of monazite with thorite inclusions (sample 9375-17) .....	202
<b>Figure 2.4.33.</b> Variation of P versus Q parameters for Kola and Karelia basement rocks from the Baltic Shield (diagram from Debon and Lefort, 1988) .....	203
<b>Figure 2.4.34.</b> Variation in the peraluminous index A with the fractionation parameter B (coloration index) for Kola and Karelia basement rocks (diagram from Debon and Lefort, 1988) ....	203
<b>Figure 2.4.36.</b> Geological map and location of the uranium occurrences from the Litsa region in northeastern Kola Peninsula, Russia (modified from Afanasieva et al., 2007) .....	206 -207
<b>Figure 2.4.37.</b> Outcrop picture (104) of the Dikoe Archean leucogranite cross cut by anastomosing muscovite-bearing fractures (dark shearing zones) .....	208
<b>Figure 2.4.38.</b> Macroscopic image of different rock pieces of the Dikoe samples (104-3) showing leucocrate quartz-feldspar pegmatite .....	208
<b>Figure 2.4.39.</b> Shear zone showing biotite muscovitization and disappearance of quartz (sample 59, crossed polarized transmitted light) .....	209
<b>Figure 2.4.40.</b> Acicular brown rutile needles issued from the chloritization of biotite (sample 104-3, natural transmitted light) .....	209
<b>Figure 2.4.41.</b> Progressive developpement of albitization (right) in a plagioclase with local sericite dust (sample 59, crossed polarized transmitted light) .....	209
<b>Figure 2.4.42.</b> Green to bluish tourmaline crystals within muscovite-rich shear zone (sample 104-3, crossed polarized transmitted light) .....	209
<b>Figure 2.4.43.</b> Chondrite-normalized REE patterns of the Kola pegmatite samples .....	210
<b>Figure 2.4.44.</b> Zircon and xenotime preserved crystals within the muscovite-rich shear zone (sample 104-3, crossed polarized transmitted light) .....	210
<b>Fig. 2.4.45.</b> U versus Th contents (ppm) in individual pegmatite samples from the uranium occurrences Dikoe, Skalnøe and Polyarnøe .....	212
<b>Fig. 2.4.46.</b> BSE-SEM image of a primary monazite grain with cubic uraninite inclusions .....	213
<b>Fig. 2.4.47.</b> BSE-SEM image of isolated Th-rich uraninite (white) altered to hexavalent-U mineralization (darker material with microcracks) .....	213
<b>Figure 2.4.48.</b> Histogram showing the repartition of chemical U-Th-Pb ages determined from EMPA measurements in uraninite and monazite grains from the Dikøe metasomatite (sample 104-3) .....	214
<b>Figure 2.4.49.</b> A- Outcrop 88 showing folding and shearing in quartz-feldspar granitoid of the Skalnøe ore and B- various rock-sections of sample 88a extracted from this outcrop revealing silicification along the muscovite-rich shear zones (dark) .....	215
<b>Figure 2.4.50.</b> Perthitic feldspar with a sigmoidal shape surrounded by micro-granular quartz and muscovite clusters (sample 88a; crossed nicols) .....	216
<b>Figure 2.4.51.</b> Albitized microcline crystal surrounded by orthoclase and recrystallized patches of quartz (sample 88a; crossed nicols) .....	216
<b>Figure 2.4.52.</b> Outcrop 89 at Skalnøe showing the sharp contact between vein-like intrusion of quartz-feldspar granitoid (right) and the darker fine grained mylonitic gneisses (left) where coarse grained biotite restite occur .....	217
<b>Figure 2.4.53.</b> Picture of a rock-section from the migmatitized paragneiss at Skalnøe (sample 89b) .....	217
<b>Figure 2.4.54.</b> Migmatitic gneiss at Skalnøe (sample 89b, crossed nicols): A- nematoblastic texture of biotite and B- a closer view showing muscovitization of biotite and recrystallized feldspar and quartz grains with ternary junctions .....	217
<b>Figure 2.4.55.</b> A- Outcrop 90 showing intrusive quartz-feldspar pegmatoid dyke <1m wide with quartz-boudinage structures, B- sample 90a: strongly cataclased feldspar and quartz with interstitial biotite schlirens and boxwork filled by hexavalent uranium minerals, C- sample 90b: more silicified .....	218

<b>Figure 2.4.56.</b> Photomicrographs of Skalnøe pegmatites showing A- quartz recrystallization and altered biotite (90b, crossed nicols), B- pethitic feldspar (90a, crossed nicols), C- plagioclase enclosed in the biotite-rich restite (90a, crossed nicols), D- muscovitization of chloritized biotite (90a, crossed nicols), E- cubic boxwork in biotite selvage (90a, transmitted light), F- boxwork surrounded by a pleochroic halo in biotite (90b, transmitted light) .....	219
<b>Figure 2.4.57.</b> BSE-SEM images of A- primary molybdenite and B- secondary U-mineralization represented by pitchblende coating microcracks mixed with iron oxides and euhedral cubes of galena (sample 90a) .....	220
<b>Fig. 2.4.58.</b> Polyarnøe granitoid dyke intruding biotite-quartz-feldspar gneiss .....	221
<b>Figure 2.4.59.</b> A- Biotite selvage with zircon and opaque minerals (transmitted light) and B- quartz and biotite (crossed nicols) in Polyarnøe pegmatite (sample 58-1) .....	222
<b>Figure 2.4.60.</b> SEM-BSE images of various zircon and uraninite grains in biotite selvages of the Polyarnøe pegmatite (sample 58-2) showing intergrow relation (A-B-C) and small uranorthite inclusions in zircon (D) .....	222
<b>Figure 2.4.61.</b> Binary diagram showing element substitutions Zr+Hf+Si vs. U+Pb+Ca+Fe (in atomic %) in zircon from the Polyarnøe pegmatite (sample 58-2) .....	223
<b>Figure 2.4.62.</b> Distribution of $^{207}\text{Pb}/^{206}\text{Pb}$ ages (Ma) measured in 2 uraninite grains of the Polyarnøe pegmatite (sample 58-2) .....	226
<b>Figure 2.4.63.</b> Concordia diagram for the two uraninite grains from Polyarnøe (sample 58-2) .....	226

## SYNTHESE ET DISCUSSION SUR LES SOURCES MAGMATIQUES ARCHEENNES DE L'URANIUM

<b>Figure 2-A.</b> Diagramme binaire de synthèse montrant l'évolution des lignées magmatiques étudiées en fonction de l'indice de peraluminosité (A) et de l'indice de différenciation (B) d'après Debon and Lefort (1988) .....	234
<b>Figure 2-B.</b> Diagramme binaire des concentrations Th vs. U (en pourcentage atomique) des uraninites dans les roches magmatiques étudiées dans ce chapitre .....	234
<b>Figure 2-C.</b> Comparaison entre les spectres des éléments des Terres Rares normalisés aux chondrites, d'oxydes d'uranium cristallisés par des processus hydrothermaux protérozoïques (données de Bonhoure, 2007) et des uraninites magmatiques cristallisées à hautes températures dans des pegmatites archéennes (cette étude) .....	236

---

## CHAPITRE 3 : PALEO-PLACERS URANIFERES

---

### Partie 3.1 Bassin du Witwatersrand, Afrique du Sud

<b>Figure 3.1.1.</b> Geological map of the Witwatersrand Basin and surrounding Archean granite-greenstone terranes with location of the principal goldfields .....	247
<b>Figure 3.1.2.</b> Sketch model of the tectonic setting during the deposition of the Witwatersrand Basin (after Catuneanu and Biddulph, 2001; modified from Robb et al., 1991) .....	248
<b>Figure 3.1.3.</b> Schematic representation of the postulated model for accretion of intra-oceanic obduction complexes onto the Kaapvaal nucleus related to an underplating mantle superplume (modified from Eriksson et al., 2009) .....	249
<b>Figure 3.1.4.</b> Simplified stratigraphic column for the Dominion Group (after the Uranium One Ltd. data) and Central Rand Group (modified from Frimmel and Minter, 2002) with relative stratigraphic position of the various reefs sampled in this study .....	252
<b>Figure 3.1.5.</b> Drill core showing the upper quartzite and conglomerate member succession of the Dominion Group: (up) grey quartzite, (middle) conglomerate with sub-angular to rounded quartz pebbles (down) pale green to yellowish pyritic and sericitic conglomerate .....	256
<b>Figure 3.1.6.</b> Sample from the Beisa reef (Welkom Goldfield) at the base of the Central Rand Group. Note the large carbonaceous matter beds following the elongation of the white to black coloured quartz pebbles .....	256

## Liste des Figures

<b>Figure 3.1.7.</b> Sample from the Carbon Leader reef (West Rand Goldfield) at the base of the Central Rand Group .....	256
<b>Figure 3.1.8.</b> Binary diagrams showing whole rock SiO <sub>2</sub> content vs. Al <sub>2</sub> O <sub>3</sub> , K <sub>2</sub> O, P <sub>2</sub> O <sub>5</sub> , Fe <sub>2</sub> O <sub>3t</sub> , MgO and TiO <sub>2</sub> contents in weight percent (wt%) .....	262
<b>Figure 3.1.9.</b> Variations of the Q [= (Si-(K+Na+2Ca))/3] vs. A [=Al-(K+Na+2Ca)] parameters (in cations) for the Witwatersrand Reefs compared to mineral and igneous rock type compositions ...	263
<b>Figure 3.1.10.</b> Th vs. U concentrations (in ppm) in the Witwatersrand reefs .....	264
<b>Figure 3.1.11.</b> Chondrite normalized REE patterns of the Witwatersrand reefs (normalized to chondrite values after Anders and Grevesse, 1989) .....	268
<b>Figure 3.1.12.</b> Eu/Eu* (=Eu <sub>N</sub> /√(Sm.Gd) <sub>N</sub> ) vs. (Gd/Yb) <sub>N</sub> The fields of typical Archean and post-Archean sedimentary rocks deposited in volcanically active tectonic settings are from Taylor and McLennan (1995) and the field of “cratonic” sediments is adapted from McLennan and Taylor (1991) .....	271
<b>Figure 3.1.13.</b> ΣREE vs. U and Th concentrations (in ppm) .....	272
<b>Figure 3.1.14.</b> Picture of a thin section (upper DG reef: DRT034-DO8628-342m depth) showing the relative proportion of fractured quartz pebbles and matrix composed mainly of chlorite and sericite with disseminated heavy minerals (opaque pyrite and pink to brownish garnet in well rounded grains) .....	272
<b>Figure 3.1.15.</b> Photomicrograph in reflected light showing a veinlet of pyrite crosscutting the sericitic matrix and quartz pebbles (lower DG reef: DRT179-FO948). The lighter grains are primary uraninite .....	273
<b>Figure 3.1.16.</b> SEM-BSE image showing accumulation of heavy minerals, uraninite, monazite and ilmenite, with secondary mineralization, U-Ti phases coating primary grains and pitchblende filling fractures of quartz pebbles (upper DG reef: DRT034-DO8628-342m depth) .....	273
<b>Figure 3.1.17.</b> Histogram and relative probability curve representing the distribution of U-Th-Pb chemical ages calculated in monazite grains from two samples of the upper Dominion reef .....	274
<b>Figure 3.1.18.</b> Plot of (Th+U+Si) vs. (REE+Y+P) calculated in formula proportions on the basis of 16 O atoms after Förster (1998) .....	274
<b>Figure 3.1.19.</b> Photomicrographs in reflected light showing primary uraninite grains with xenomorphic grains of pyrite and zircon surrounded by red internal reflection material that corresponds to hematite (lower DG reef: DRT179-FO948) .....	277
<b>Figure 3.1.20.</b> SEM-BSE image showing primary uraninite rounded grain with monazite (upper DG reef: DRT034-DO8628-342m depth) .....	277
<b>Figure 3.1.21.</b> U versus Pb, Th, Si, Ti and Y contents (in atomic percent) of different U-bearing minerals from the Dominion Reefs .....	278
<b>Figure 3.1.22.</b> Histogram and relative probability curve representing the distribution of U-Th-Pb chemical ages calculated in uraninite grains from the upper Dominion reef (both pristine areas and coffinitized: N = 243) .....	279
<b>Figure 3.1.23.</b> Binary diagram showing Th vs. U contents (in atomic percent) in pristine primary uraninite showing two distinct family of grains with low Th contents below 2 at% and an second group with high Th contents up to 4 at% .....	280
<b>Figure 3.1.24.</b> Chondrite-normalized REE patterns of primary uraninite grains from the Dominion quartz pebble conglomerates compare to magmatic uraninites from the Rössing deposit in Namibia and hydrothermal pitchblende from the Athabasca Basin in Canada .....	282
<b>Figure 3.1.25.</b> Detrital garnet showing high fracturation and relief within quartz in natural transmitted light (DRT024-DO1823 at 206.7m depth) .....	283
<b>Figure 3.1.26.</b> Ternary diagrams showing the compositions of detrital garnets from the upper Dominion reef .....	283
<b>Figure 3.1.27.</b> BSE image of a detrital columbite-tantalite from the upper Dominion reef (sample DRT70-AO5686) and chemical EMP profile showing variations in element concentrations (atom percent) across the grain .....	285

<b>Figure 3.1.28.</b> Chemical composition of detrital ferro-tantalite in the upper Dominion reef compare to composition of columbite-tantalite minerals from the Tanco peraluminous pegmatite (Manitoba, Canada) and late-orogenic potassic granites from the Pilbara Craton (Western Australia) represented in the typical end-member quadrilateral (Ercit et al., 1995) .....	287
<b>Figure 3.1.29.</b> Carbonaceous matter layer in the Beisa reef (Welkom Goldfield) with incorporated spread uraninite and pyrite grains, A: reflected light and B: SEM-BSE image .....	288
<b>Figure 3.1.30.</b> Photomicrographs of the Carbon Leader conglomerates (West Rand Goldfield) .....	289
<b>Figure 3.1.31.</b> Histograms and relative probability curves representing the distribution of chemical U-Th-Pb ages of U-minerals from various Central Rand Group reefs .....	291
<b>Figure 3.1.32.</b> Photomicrographs of the Central Rand Group conglomerates .....	292
<b>Figure 3.1.33.</b> U mineralization in the Central Rand Group conglomerates .....	294
<b>Figure 3.1.34.</b> Ternary diagrams showing the stoichiometric proportions of the U mineralization from the Witwatersrand conglomerates in the various reefs studied .....	295
<b>Figure 3.1.35.</b> Binary diagrams Th vs. U and Mn vs. Y (in atomic percent) characterizing the primary uraninite grains from the various reefs sampled in the Dominion and Central Rand Groups .....	300
<b>Figure 3.1.36.</b> List of the ore minerals observed during our petrographic study of the Witwatersrand conglomerates from the Dominion and Central Rand Groups and their paragenetic sequence of deposition .....	304

### Partie 3.2 Elliot Lake-Blind River, Ontario, Canada

<b>Figure 3.2.1.</b> Geological map of the Elliot Lake-Blind River region in Ontario (modified from Fralick and Miall, 1989 and from Bekker and Kaufman, 2007) and location of the studied areas, the Denison mine and the drill holes from the Pele Mountain property .....	315
<b>Figure 3.2.2.</b> Stratigraphic column of the Huronian Supergroup in the Elliot Lake-Blind River area (modified from Bekker and Kaufman, 2007) .....	316
<b>Figure 3.2.3.</b> Petrographic images in polarized transmitted light showing (A) the different grain sizes of the common minerals constituting the matrix of the Matinenda conglomerates: quartz, orthoclase feldspar and plagioclase in a sericitic groundmass (sample 138538, drill hole PM53, depth 181.1 m), (B) a sericitized feldspar phenocrystal and opaque accessories within an oriented phyllosilicate matrix (sample BP72-102 from the Denison mine) and (C) zircon and monazite grains dispersed with opaque minerals, quartz and feldspar in the argillaceous fine-grained matrix (sample 138538) .....	322
<b>Figure 3.2.4.</b> Petrographic image in reflected light showing abundant angular to well rounded uraninite grains with pyrite and quartz (sample BP72-102 from the Denison mine) .....	323
<b>Figure 3.2.5.</b> BSE image of an early uraninite grain (sample BP72-102 from the Denison mine) ....	324
<b>Figure 3.2.6.</b> Petrographic image in reflected light of a sub-rounded early uraninite grain (dark grey mineral in the middle) and secondary crystallization of pyrite (light yellowish reflection) and chalcopyrite (darker brownish reflection) coming from a fracture at the bottom of the picture (sample BP72-102 from the Denison mine) .....	324
<b>Figure 3.2.7.</b> Two zircon grains showing well developed crystal grow zonation in BSE mode imaging (left: sample 138547 from drill hole PM25 at 103.8m depth; right: sample 138538 from drill hole PM53 at 181.1m depth) .....	324
<b>Figure 3.2.8.</b> Monazite grain showing huttonitic areas (lighter grey) associated to micro-fracturation and inclusions of quartz (darker grey) and zircon (medium grey) in BSE mode (sample 138538 from drill hole PM53 at 181.1m depth) .....	324
<b>Figure 3.2.9.</b> Titanium oxide showing a typical dentritic texture in BSE mode corresponding to web of rutile silks (sample 138553 from drill hole PM45 at 66.2m depth) .....	325
<b>Figure 3.2.10.</b> Petrographic image of a vuggy carbonaceous matter globule in reflected light (sample 138547 from drill hole PM25 at 103.8m depth) .....	326
<b>Figure 3.2.11.</b> BSE image of previous carbonaceous matter globule showing disseminated uraninite crystals (sample 138547) .....	326

<b>Figure 3.2.12.</b> BSE image of solid bitumen showing a surrounding retraction gap, shrinkage microcracks and small uraninite crystals (sample 138553 from drill hole PM45 at 66.2m depth) .....	326
<b>Figure 3.2.13.</b> BSE image of kerogen with widespread (U,Th)-silicates and later crystallisation of pyrite and galena (sample 138548 from drill hole PM25 at 128.8m depth) .....	326
<b>Figure 3.2.14.</b> Petrographic image in reflected light of two generations of pyrite (stage I: rounded detrital grain and stage II: epigenetic idiomorphic crystals) with interstitial mixture of U-silicate and hematite (sample 138549 from drill hole PM25 at 128.3m depth) .....	328
<b>Figure 3.2.15.</b> BSE image of U-Th-Si phase (light) interfingers with clay minerals in the matrix of conglomerate (sample 138553 from drill hole PM45 at 66.2m depth) .....	328
<b>Figure 3.2.16.</b> BSE image of pyrite with overgrowing globular crystals of complex U-bearing phase (sample 138548 from drill hole PM25 at 128.8m depth) .....	328
<b>Figure 3.2.17.</b> BSE image and related elementary mapping by SEM-EDS of the Pronto reaction occurring between early uraninite and Ti-oxide grains producing interstitial (U,Th)-titanates when altered together (sample BP72-102 from the Denison mine) .....	329
<b>Figure 3.2.18.</b> Plot of (Th+U+Si) vs. (REE+Y+P) calculated in formula proportions on the basis of 16 O atoms after Förster (1998) .....	331
<b>Figure 3.2.19.</b> U/Pb ratio, Th and Si contents (in atomic percent) vs. chemical ages (Ma) calculated after the methodology of Cocherie and Albarede (2001) from in situ EMPA measurements of U, Th and Pb contents in 20 monazite grains and relative probability histogram showing the scattered results .....	331
<b>Figure 3.2.20.</b> Binary diagram showing Th vs. Y contents (in atomic percent) of individual grains of uraninite .....	333
<b>Figure 3.2.21.</b> Major content variations of the elements Pb, Ca, K, Th, Y, Si, Al and Ti vs. U (in atomic percent) measure in the different U-bearing minerals observed in the Matinenda Formation .	334
<b>Figure 3.2.22.</b> Ternary plots showing U-Si-Th and U-Si-Ti (in relative cation proportions) for the various U-bearing minerals observed in the Matinenda Formation .....	335
<b>Figure 3.2.23.</b> Relative probability histogram of chemical U-Th-Pb ages (Ma) of the main U-bearing phases from the Matinenda Formation .....	337
<b>Figure 3.2.24.</b> Th and Y contents (in atomic percent) vs. chemical U-Th-Pb ages (Ma) derived from the Pb/U ratios in the U-bearing phases of the Matinenda Formation .....	338
<b>Figure 3.2.25.</b> Distribution of $^{207}\text{Pb}/^{206}\text{Pb}$ ages measured in 6 early uraninite grains from the Denison mine ore showing (Quirke channel – sample BP72-102) using ion microprobe instrument (SIMS) .....	341
<b>Figure 3.2.26.</b> Concordia diagram for the six uraninite grains from the Quirke channel (BP72-102)	341
<b>Figure 3.2.27.</b> Chondrite-normalized REE abundances measured in situ in nine uraninite grains from the Quirke channel in the Matinenda Formation (sample BP72-102 from the Denison mine) ...	344
<b>Figure 3.2.28.</b> Location of U occurrences in Ontario (modified from the Ontario Geological Survey) .....	348
<b>Figure 3.2.29.</b> Paragenetic sequence of U mineralization in the Elliot Lake paleoplacer-type deposits. The thickness of bars represents the relative abundance for each accessory mineral and dashed lines when occurrences are not confident .....	350
 <b>Partie 3.3 Formation Jatulienne, Carélie (Russie-Finlande)</b>	
<b>Figure 3.3.1.</b> Geological map of the southeast Karelia at the boundary between Finland and Russia elaborated from the data of the Geological Survey of Finland .....	360
<b>Figure 3.3.2.</b> Paleoproterozoic sedimentary succession with stratigraphic appellation used in Russia (modified from Melezhik et al., 2005) .....	362
<b>Figure 3.3.3.</b> Samples of the Lower Jatulian sequence collected in the southern transect 9371 (location in Fig. 3.3.1) north of the Janisjarvi Lake in Russia .....	365
<b>Figure 3.3.4.</b> Samples of the Lower Jatulian sequence collected in the northern transect 9375-9378 (location in Fig. 3.3.1) south of the Karelian fertile granitoids in Finland .....	366

## Liste des Figures

---

<b>Figure 3.3.5.</b> Binary diagram showing Q $[(\text{Si}-(\text{K}+\text{Na}+2\text{Ca}))/3]$ vs. A $[\text{Al}-(\text{K}+\text{Na}+2\text{Ca})]$ parameters (in thousands of cations) of the basal Jatulian sediments with reference sedimentary rocks and minerals (modified from Debon and Le Fort, 1982) .....	371
<b>Figure 3.3.6.</b> Al/3-K vs. Al/3-Na diagram (from de La Roche, 1968) showing the composition of Jatulian sediments with main rocks domains and minerals .....	372
<b>Figure 3.3.7.</b> Chondrite-normalized REE patterns of the basal Jatulian sediments .....	373
<b>Figure 3.3.8.</b> Binary diagram showing Th vs. U contents (in ppm) of the basal Jatulian sediments ..	373
<b>Figure 3.3.9.</b> Binary diagram showing Th vs. La contents. (ppm) in Jatulian sediments .....	374
<b>Figure 3.3.10.</b> Binary diagram showing U vs. Zr contents (ppm) in Jatulian sediments .....	374
<b>Figure 3.3.11.</b> Photomicrograph of a Jatulian quartzite (9375-13-cross nicols) showing etched quartz grains with a sericitic cement .....	376
<b>Figure 3.3.12.</b> Photomicrograph of a Jatulian sandstone (9375-11, cross nicols) showing quartz and feldspar grains floating in a sericite composed of fine-grained laths of white phyllosilicates .....	376
<b>Figure 3.3.13.</b> Photomicrographs of a Jatulian quartzite (9371-7) showing A- carbonate-cement between feldspar and quartz grains, and B- closer view of a feldspar with typical chessboard texture of albitization (cross-nicols) .....	376
<b>Figure 3.3.14.</b> Photomicrograph of a detrital green tourmaline with hexagonal crystal shape surrounded by muscovite and quartz grains (sandstone 9375-12; plane light) .....	376
<b>Figure 3.3.15.</b> Photomicrograph of a detrital garnet with rounded shape and fractures filled by chlorite (sandstone 9375-12; reflected light) .....	376
<b>Figure 3.3.16.</b> Photomicrographs of the most radioactive quartz pebble conglomerate (9375-14, cross nicols) showing A- well compacted polycrystalline quartz grains with muscovite and illite and B- detrital zircon and locally carbonate cement .....	377
<b>Figure 3.3.17.</b> Refractory minerals between quartz grains showing multiple triple-joint boundaries and disseminated interstitial white micas (conglomerate 9375-14, cross nicols) .....	378
<b>Figure 3.3.18.</b> Zircon grains disseminated between quartz grains in the sericite (conglomerate 9371-5, cross nicols) .....	378
<b>Figure 3.3.19.</b> Refractory minerals between quartz grains showing multiple triple-joint boundaries and disseminated interstitial white micas (conglomerate 9375-14, cross nicols) .....	378
<b>Figure 3.3.20.</b> Refractory minerals between quartz grains showing multiple triple-joint boundaries and disseminated interstitial white micas (conglomerate 9375-14, cross nicols) .....	378
<b>Figure 3.3.21.</b> Photomicrograph of a detrital zircon surrounded by hematized sericitic cement showing red internal reflections (sconglomerate 9371-5; reflected light) .....	378
<b>Figure 3.3.22.</b> Photomicrograph of an altered monazite coated by small hematite red crystals (conglomerate 9378-14; reflected light) .....	378
<b>Figure 3.3.23.</b> BSE mode images of individual zircon grain A- in quartzite 9371-2 and B- in conglomerate 9375-14 .....	379
<b>Figure 3.3.24.</b> Zircon composition of the Jatulian sediments represented in a binary diagram showing major constituents (Zr+Hf+Si) substitute to (Al+P+Ca+Fe+Y+Th+U) in atomic percents ..	380
<b>Figure 3.3.25.</b> BSE mode image of numerous altered monazite grains and zircons with iron oxides along fractures in quartz pebbles (Conglomerate 9375-14) .....	381
<b>Figure 3.3.26.</b> BSE mode image of an altered monazite grain coated by iron oxides filling porosity between phyllosilicate laths (Quartzite+Conglomerate 9371-5) .....	382
<b>Figure 3.3.27.</b> Ternary diagram showing the monazite compositions in the Jatulian sediments showing normally fresh monazite major constituents (REE+P+Y) substitute to (Th+U+Si) during huttonitic transformation and intensive hematization with Fe incorporation .....	383
<b>Figure 3.3.28.</b> Histogram and relative probability curve representing the distribution of chemical age dating on the 28 grains of altered detrital monazites from the Lower Jatulian sediments .....	384

---

**SYNTHESE ET DISCUSSION SUR LES MINERALISATIONS URANIFERES DES CONGLOMERATS A GALETS DE QUARTZ**

<b>Figure 3-A.</b> Diagramme récapitulatif présentant les teneurs moyennes en Th et U (at.%) des uraninites des paléo-placers du Witwatersrand et d'Elliot Lake en comparaison de celles formées dans roches magmatiques étudiées au chapitre 2 .....	391
<b>Figure 3-B.</b> Diagramme Eh vs. pH (modifié de Langmuir, 1978) pour des conditions spécifiques à 25°C et une pression CO <sub>2</sub> atmosphérique de 10 <sup>-2</sup> atm .....	392
<b>Figure 3-C.</b> Solubilité de différentes espèces minérales U(VI), U(IV) et Th(IV) : amorphes, oxydes bien cristallisés et hydroxydes à ~20°C en fonction du pH compilé de plusieurs sources par Fanghänel and Neck (2002) .....	393

---

**ANNEXE 1 : METHODOLOGIE ANALYTIQUE**

---

<b>Figure A1.</b> Autoradiographies de deux pegmatites archéennes et de conglomérats porteurs d'uraninite .....	426
<b>Figure A2.</b> Microscope électronique à balayage Hitachi FEG S-4800 .....	427
<b>Figure A3.</b> Schéma de fonctionnement du MEB .....	427
<b>Figure A4.</b> Interactions entre le faisceau électronique et l'échantillon : les différents rayonnements émis (A) apportent des informations sur la nature des atomes excités qui constituent l'échantillon (B) .....	428
<b>Figure A5.</b> Microsonde électronique CAMECA SX100 .....	429
<b>Figure A6.</b> Microsonde ionique CAMECA IMS-3f au CRPG .....	431
<b>Figure A7.</b> Schéma simplifié de fonctionnement de la microsonde ionique du CRPG .....	431
<b>Figure A8.</b> Diagramme Concordia et interprétation des intercepts avec la droite Discordia (d'après Wetherill, 1956) .....	433

---

# **LISTE DES TABLEAUX**

---



---

## CHAPITRE 1 : CONNAISSANCES SUR L'ARCHÉEN ET TRANSITION VERS LE PALÉOPROTÉROZOÏQUE

---

<b>Tableau 1.1.</b> Comparaison des teneurs en uranium et thorium (ppm) de la croûte continentale à l'Archéen par rapport à la composition actuelle .....	25
<b>Tableau 1.2.</b> Composition moyenne des roches de type TTG, des sanukitoïdes et des granites de type Closepet (extrait de Martin <i>et al.</i> , 2005) .....	26

---

## CHAPITRE 2 : SOURCES ARCHEENNES DE L'URANIUM

---

### Partie 2.1 Craton de Kénéma Man, Guinée

<b>Table 2.1.1.</b> Calculated P, Q, A and B parameters (in thousands of cations), A/CNK and A/NK (in moles), K <sub>2</sub> O/Na <sub>2</sub> O ratio, U and Th contents (in ppm), Th/U ratio, initial U* and Th* contents (in ppm) and initial Th*/U* ratio of the Guinean magmatic rocks (all the whole rock geochemical data from BRGM used for calculation of are given in Appendix 2, table A1) .....	55-56
<b>Table 2.1.2.</b> Location and brief description of samples .....	57
<b>Table 2.1.3.</b> Geochemical composition of the studied felsic igneous rocks from south-east Guinea (data from Thiéblemont <i>et al.</i> , 1999 a and b; Goujou <i>et al.</i> , 1999 a and b) .....	57
<b>Table 2.1.4.</b> Overview of the element set-up for the electron microprobe including analysed line, calibration standard, and background positions used during integrated analysis of zircon, monazite and uraninite .....	59
<b>Table 2.1.5.</b> Typical U and Th abundances in accessory minerals (modified from Robb <i>et al.</i> , 1990; data after Wedepohl, 1969) .....	74
<b>Table 2.1.6.</b> Representative electron-microprobe analyses of zircon in magmatic rocks .....	76
<b>Table 2.1.7.</b> Representative electron-microprobe analyses of the monazite group minerals from the Liberian granite DTMAC12* .....	78
<b>Table 2.1.8.</b> Representative electron-microprobe analyses of alteration material within monazite from the Leonian gneiss NZE2328 .....	80
<b>Table 2.1.9.</b> Representative electron-microprobe analyses of uraninite in the Paleoproterozoic granite NZE2381 and calculated chemical ages .....	82

### Partie 2.2 Craton de Pilbara, Australie

<b>Table 2.2.1.</b> Relation between pressure (P in kbar) and the total Al content of hornblende (Al=Al <sup>IV</sup> +Al <sup>VI</sup> in apfu) for melt temperature between approximately 600-800°C .....	102
<b>Table 2.2.2.</b> Whole-rock geochemical composition of the granitoids sampled from the Split Rock Supersuite .....	103
<b>Table 2.2.3.</b> EMPA results (in wt%) of titanite minerals from sample 178011 .....	109
<b>Table 2.2.4.</b> EMPA results (in wt%) of hornblende in sample 178011 .....	110
<b>Table 2.2.5.</b> Average composition of garnets in a late-orogenic Archean granite (sample 169044) from the the Pilbara craton, Australia. ....	113
<b>Table 2.2.6.</b> EMPA results (in wt%) of columbite in sample 169044 .....	114
<b>Table 2.2.7.</b> EMPA results (in wt%) of zircons from the late K-rich granites sampled in the East Pilbara Terrane .....	119
<b>Table 2.2.8.</b> EMPA results (in wt%) of monazite from sample 178014 .....	121
<b>Table 2.2.9.</b> EMPA results (in wt%) of xenotime from sample 169044 .....	122
<b>Table 2.2.10.</b> Representative average chemical compositions of chlorite (EMPA results in wt% ± standard derivative) .....	123
<b>Table 2.2.11.</b> EMPA results (in wt%) of REE-fluorocarbonate .....	125

<b>Table 2.2.12.</b> EMPA results (in wt%) of epidote .....	126
<b>Table 2.2.13.</b> EMPA results (in wt%) of pumpellyite in sample 142879 .....	129
 <b>Partie 2.3 Pegmatite de Tanco, Manitoba, Canada</b>	
<b>Table 2.3.1.</b> Overview of major element set-up for the CAMECA SX100 electron microprobe including analysed line, calibration standard, and background positions used during integrated analysis of uranium and tantalum bearing minerals .....	145
<b>Table 2.3.2.</b> Average chemical compositions of primary uraninite (CAMECA SX100 electron microprobe analysis in wt%) .....	150
<b>Table 2.3.3.</b> Average chemical compositions of secondary U-bearing phases occurring in the vicinity of the primary uraninite (CAMECA SX100 electron microprobe analysis in wt%) .....	153
<b>Table 2.3.4.</b> Average chemical compositions of uranmicrolite (CAMECA SX100 electron microprobe analysis in wt%) .....	156
<b>Table 2.3.5.</b> Average chemical compositions of columbite-tantalite group minerals (CAMECA SX100 electron microprobe analysis in wt%) .....	160
<b>Table 2.3.6.</b> Average chemical compositions of wodginite group minerals (CAMECA SX100 electron microprobe analysis in wt%) .....	161
<b>Table 2.3.7.</b> Average chemical compositions of cassiterite (CAMECA SX100 electron microprobe analysis in wt%) .....	162
<b>Table 2.3.8.</b> Ion probe U-Pb results for three uraninite grains from the Tanco Lower Pegmatite .....	163
<b>Table 2.3.9.</b> SIMS determinations of Y and REE contents (ppm) in the Tanco uraninites (this study) compare to other uranium oxides from pegmatoids of the Rössing ore showing and the Otish Mounts (from Bonhoure, 2007) .....	167
 <b>Partie 2.4 Bouclier Baltique: Cratons de Carélie et de Kola (Russie et Finlande)</b>	
<b>Table 2.4.1.</b> Mustalampi samples from drill hole M52-4241-R324 .....	185
<b>Table 2.4.2.</b> Chemical composition of Archean rocks collected from the Puruvesi region (Karelian Province) .....	187
<b>Table 2.4.3.</b> Average chemical composition of uranothorite hosted in the Mustalampi Archean pegmatite 9375-2 and biotite-rich gneiss 9375-5 .....	191
<b>Table 2.4.4.</b> Average chemical composition of apatite hosted in the Archean granitoids from Karelia .....	193
<b>Table 2.4.5.</b> Average chemical composition (in weight percent) of uraninite crystals hosted in the Archean pegmatite 9375-3 from the Mustalampi area in Karelia .....	195
<b>Table 2.4.6.</b> Ion probe U-Pb results for 2 uraninite grains from the Mustalampi pegmatite 9375-3 ..	197
<b>Table 2.4.7.</b> SIMS determinations of Y and REE contents (ppm) in the uraninite from pegmatites of the Baltic Shield (this study) compare to the chemistry of uraninite from the Rössing alaskite in Namibia (Bonhoure, 2007) .....	200
<b>Table 2.4.8.</b> Location of outcrops sampled during field trip 2007 in the Litsa area, Kola Peninsula (Russia) .....	205
<b>Table 2.4.9.</b> Chemical composition of individual pegmatite samples from the uranium occurrences Polyarnoe, Dikoe and Skalnœ in the Kola Peninsula (Russia) .....	211
<b>Table 2.4.10.</b> Average chemical composition of zircon from the different U-occurrences Dikoe, Skalnœ and Polyarnœ, Kola Peninsula .....	212
<b>Table 2.4.11.</b> Average chemical composition of uraninite hosted in the Archean Dikoe metasomatized leucogranite (sample 104-3) .....	214

## Liste des Tableaux

<b>Table 2.4.12.</b> Average chemical composition of monazite in the Archean Dikoe metasomatized leucogranite (sample 104-3) .....	214
<b>Table 2.4.13.</b> Average chemical composition (in wt%) of pitchblende hosted in the Archean Skalnøe intrusive pegmatites (sample 90a) .....	220
<b>Table 2.4.14.</b> Average chemical composition of uraninite (in weight percent) from the Polyanoë ore showing (sample 58-2) .....	224
<b>Table 2.4.15.</b> Ion probe U-Pb results for 2 uraninite grains from the Polyanoë ore showing .....	225

---

## CHAPITRE 3 : PALEO-PLACERS URANIFERES

---

### Partie 3.1 Bassin du Witwatersrand, Afrique du Sud

<b>Table 3.1.1.</b> Comparative chemical analyses of the major elements (ICP-OES) in the Dominion and Central Rand Group conglomerates .....	261
<b>Table 3.1.2.</b> Trace element composition (ICP-MS) of the Dominion Group conglomerates .....	265
<b>Table 3.1.3.</b> Trace element composition (ICP-MS) of the Central Rand Group conglomerates .....	266
<b>Table 3.1.4.</b> Rare Earth Element concentrations (ICP-MS) in the Dominion Group conglomerates .	269
<b>Table 3.1.5.</b> Rare Earth Element concentrations (ICP-MS) in the Central Rand Group conglomerates .....	270
<b>Table 3.1.6.</b> Representative average composition of primary detrital U-bearing minerals from the Upper Dominion Reef analysed by electron microprobe .....	275
<b>Table 3.1.7.</b> Representative average composition of secondary U-bearing minerals from the Upper Dominion Reef analysed by electron microprobe .....	276
<b>Table 3.1.8.</b> SIMS determinations of REE contents (ppm) in the primary uraninite grains from the Dominion Group quartz pebble conglomerates compared to the composition of other uranium oxides formed during magmatic process in S-type Rössing pegmatite from Namibia and hydrothermal uraninite (pitchblende) from the Cigar Lake unconformity-type deposit of the Athabasca Basin in Canada (data from Bonhoure, 2007) .....	281
<b>Table 3.1.9.</b> Representative average composition of detrital garnets from the Dominion Group reefs .....	284
<b>Table 3.1.10.</b> Average chemical composition of a columbite-tantalite mineral from the upper Dominion reef .....	286
<b>Table 3.1.11.</b> Representative average composition of U-minerals associated to carbonaceous matter in the Central Rand Group reefs .....	290
<b>Table 3.1.12.</b> Average composition of zircon and monazite from the Central Rand Reefs .....	296

### Partie 3.2 Elliot Lake-Blind River, Ontario, Canada

<b>Table 3.2.1.</b> Average chemical composition of the different U-bearing phases observed in the quartz pebble conglomerates of the Matinenda Formation (EMPA in weight percent measured by electron microprobe CAMECA SX100) .....	332
<b>Table 3.2.2.</b> Ion microprobe U-Pb isotopic composition of six uraninite grains from the Matinenda Formation, Quirke channel, sampled at the Denison mine .....	340
<b>Table 3.2.3.</b> SIMS determinations of Y and REE contents (ppm) in the early uraninite grains (stage I) from the Elliot Lake quartz pebble conglomerates compared to the composition of other uranium oxides formed during magmatic processes in different granitoids and hydrothermal uraninite (pitchblende) from the Cigar Lake unconformity-type deposit of the Athabasca Basin in Canada (data from this study and Bonhoure, 2007) .....	343

---

**Partie 3.3 Formation Jatulienne, Carélie (Russie-Finlande)**

<b>Table 3.3.1.</b> Description and location of the studied samples .....	363
<b>Table 3.3.2.</b> Whole-rock chemical analyses of the major elements (ICP-OES) in the basal Jatulian sediments .....	367
<b>Table 3.3.3.</b> Whole-rock chemical analyses of the trace elements (ICP-MS) in the basal Jatulian sediments .....	368
<b>Table 3.3.4.</b> Overview of the element set-up for the CAMECA SX100 electron microprobe including analysed line, calibration standard, and background positions used during integrated analysis of zircon and monazite grains .....	370
<b>Table 3.3.5.</b> Average composition of zircon from the Jatulian sediments measured by electron microprobe .....	380
<b>Table 3.3.6.</b> Average composition of monazite from the Jatulian sediments measured by electron microprobe .....	383

---

**ANNEXE 2 : DONNES GEOCHIMIQUES EXTERNES**

---

<b>Tableau A1.</b> Eléments majeurs (wt.%) dans les roches du socle du Craton de Kénéma Man en Guinée (base de données du BRGM) .....	436 -437
<b>Tableau A2.</b> Eléments majeurs (wt.%) et teneurs en U et Th (ppm) dans les roches de la Supersuite de Split Rock du Craton de Pilbara en Australie (les 4 premiers échantillons ont été analysés au cours de cette thèse et les données suivantes ont été compilées à partir de la base OZCHEM fournie par AGSO et GSWA). Les paramètres A/CNK et A/CNK sont calculés en moles et Q, P, A et B sont donnés en milliers de cations (Chapitre 2 – Partie 2.2) .....	438 -439

---

**ANNEXE 1 :**  
**METHODOLOGIE ANALYTIQUE**

---



## **1. GEOCHIMIE SUR ROCHE TOTALE**

### **1.1 Préparation des échantillons**

Les analyses géochimiques sur roche totale sont effectuées sur seulement 10 grammes de poudre. Afin que les analyses soient les plus représentatives possibles, les parties pouvant biaiser la composition chimique, telles que la croûte d'altération d'une roche prélevée sur un affleurement de surface ou encore les veines de quartz ou de sulfures, ont été retirées lors du sciage à l'aide d'une scie circulaire à disque diamanté.

L'échantillon est ensuite passé successivement au concasseur à mâchoires et au broyeur à cylindre afin de réduire la roche en une poudre grossière (minéraux visibles à l'œil nu). La quantité de poudre nécessaire est obtenue en divisant la quantité de matériel autant de fois que nécessaire à l'aide d'un séparateur équiproportionnel. Enfin, la poudre est passée au micro-broyeur planétaire en agate afin de réduire sa granulométrie à 70-80  $\mu\text{m}$  maximum. Chaque machine est systématiquement nettoyée avant la première utilisation et entre chaque broyage d'échantillon afin d'éviter toute contamination. De plus, la radioactivité des échantillons est mesurée au scintillomètre SPP2 et les échantillons les moins radioactifs sont toujours préparés en premiers pour éviter toute contamination par du matériel plus enrichi.

### **1.2 Protocole chimique**

Les analyses ont été réalisées au Service d'Analyse des Roches et des Minéraux (SARM) du CNRS à Vandœuvre-lès-Nancy. Les échantillons présentés en poudre subissent une fusion au  $\text{LiBO}_2$  puis une mise en solution acide. Les éléments majeurs (Al, Si, P, Na, Mg, K, Ca, Ti, Mn, Fe) sont analysés au spectromètre d'émission (ICP-AES) et les éléments traces (Be, V, Cr, Co, Ni, Cu, Zn, Ga, Ge, As, Rb, Sr, Y, Zr, Nb, Mo, Cd, In, Sn, Sb, Cs, Ba, Hf, Ta, W, Pb, Bi, La, Ce, Pr, Nd, Sm, Eu, Gd, Tb, Dy, Ho, Er, Tm, Yb, Lu, Th, U) au spectromètre de masse (ICP-MS). Le protocole analytique et les standards de référence utilisés ont été décrits par Carignan *et al.* (2001).

## **2. ETUDE MINERALOGIQUE**

### **2.1 Lithopréparation lamellaire**

Les lames minces polies ont de cette étude été réalisées au laboratoire de lithopréparation de l'Université de Nancy. Ces lames minces ont été observées au microscope polarisant en lumière transmise et réfléchi afin de déterminer la composition minéralogique de la roche, sa texture, la taille et la forme des grains, l'état d'altération, etc.

### **2.2 Autoradiographie**

Les zones les plus minéralisées des échantillons ont été rapidement mises en évidence par la mesure au scintillomètre SPP2 de la radioactivité, ainsi qu'en effectuant des autoradiographies soit sur la surface de coupe plane de la roche, soit directement sur la lame mince.

L'autoradiographie consiste à apposer un film sensible aux radiations sur la surface plane de l'échantillon. Après une semaine de temps d'exposition, le film est placé dans une solution révélatrice pendant 2 minutes, puis rincé à l'eau et enfin séché. Des tâches de dégradation du film apparaissent alors sur les zones qui étaient en contact avec des minéraux riches en radioéléments tels que les oxydes d'uranium. Les minéraux accessoires comme le zircon ou la monazite ne contiennent pas assez d'éléments radiogènes (de l'ordre du ppm) pour marquer le

film après une semaine, il faudrait attendre plusieurs mois d'exposition. La figure A1 présente différents résultats d'autoradiographies réalisées avec succès sur des pegmatites et conglomérats.

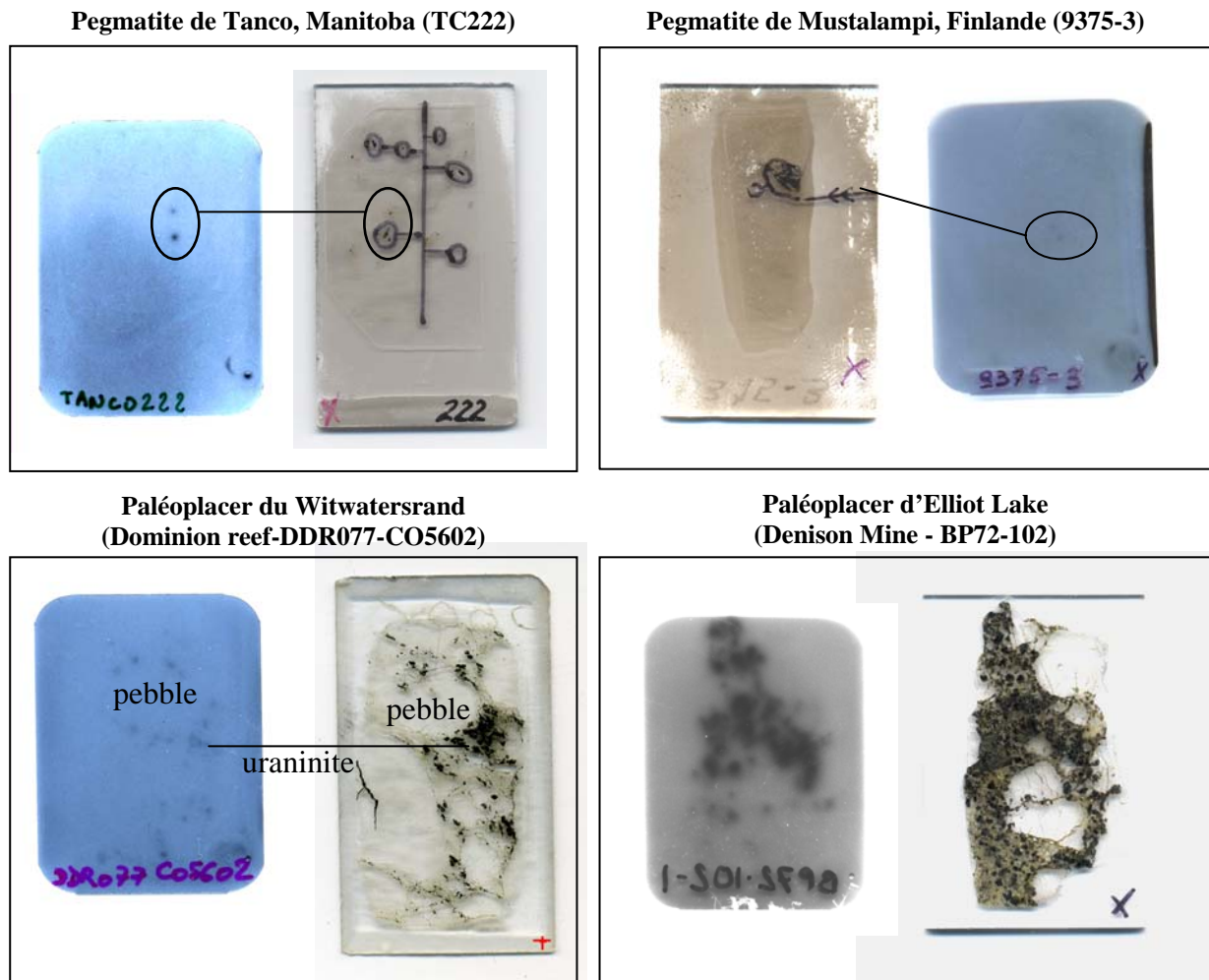


Figure A1. Autoradiographies de deux pegmatites archéennes et de conglomérats porteurs d'uraninite

### 2.3 Microscopie optique

Les lames minces polies de chacun des sites étudiés ont été observées au microscope optique Olympus BX51 muni de deux filtres polarisants : le polariseur, placé avant l'échantillon, sélectionne les raies de lumière incidente afin de les envoyer dans une seule direction de propagation, et l'analyseur, placé après l'échantillon, sélectionne les raies transmises selon leurs teintes de polarisation qui permettent l'identification des minéraux anisotropes. Les espèces minérales qui n'ont pas de biréfringence, tels que les cristaux isotropes cubiques ou encore les minéraux opaques métalliques, sont identifiées en lumière réfléchie ou au microscope électronique à balayage.

### 2.4 Microscopie électronique à balayage (MEB)

Les échantillons analysés sont sous la forme de lames minces polies dont la surface est métallisée au carbone afin de rendre sa surface conductrice. Cette métallisation est effectuée sous une cloche de verre dans laquelle est appliqué un vide secondaire. Deux pointes de graphite situées entre ces deux électrodes sont choquées par des arcs électriques lorsqu'un courant est appliqué. Le graphite libère ses atomes de carbone par sublimation, recouvrant la surface polie de la roche par une très fine pellicule de carbone d'environ 250Å d'épaisseur. L'échantillon est ensuite prêt pour être analysé au MEB.

Deux microscopes électroniques à balayage du laboratoire SCMEM de l'Université de Nancy ont été utilisés au cours de cette étude : le HITACHI FEG S-4800 équipé d'un spectromètre à dispersion d'énergie (EDS de l'anglais « *energy dispersive spectrometer* ») de marque Noran Vantage (Fig. A2), et le PHILIPS XL30 équipé d'un EDS KeveX Sigma.

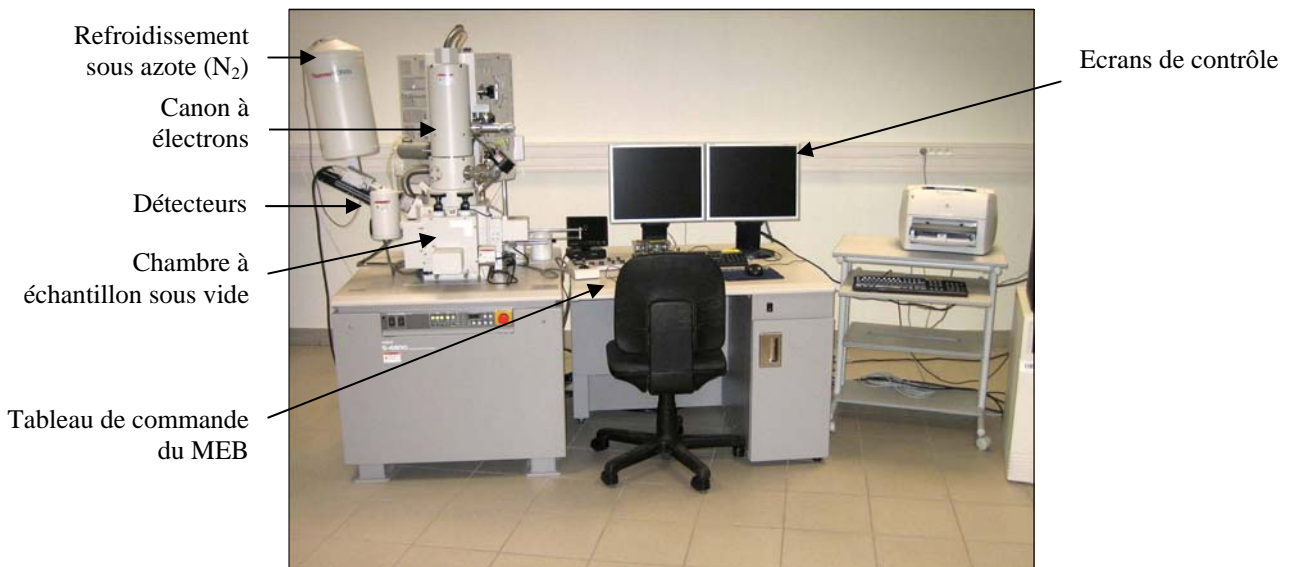


Figure A2. Microscope électronique à balayage Hitachi FEG S-4800

Le MEB est constitué d'une enceinte sous vide secondaire (Fig. A3). Le wehnelt, une plaque percée d'un orifice, est placée à proximité d'un filament de tungstène qui est porté à une tension positive de quelques centaines de volts chauffant ainsi le filament. Cette source émet alors un faisceau d'électrons accélérés par une deuxième plaque percée également d'un orifice, et portée à un potentiel ajustable. Le flux d'électrons est ensuite limité par les diaphragmes et focalisé sur l'échantillon à l'aide de différentes bobines électromagnétiques. Des bobines défectrices en x et en y permettent de déplacer le pinceau électronique à la surface de l'échantillon. Le faisceau d'électrons apparaît sur la lame sous la forme d'une tache (« spot ») qui est déplacée progressivement de façon à balayer une surface rectangulaire ligne après ligne.

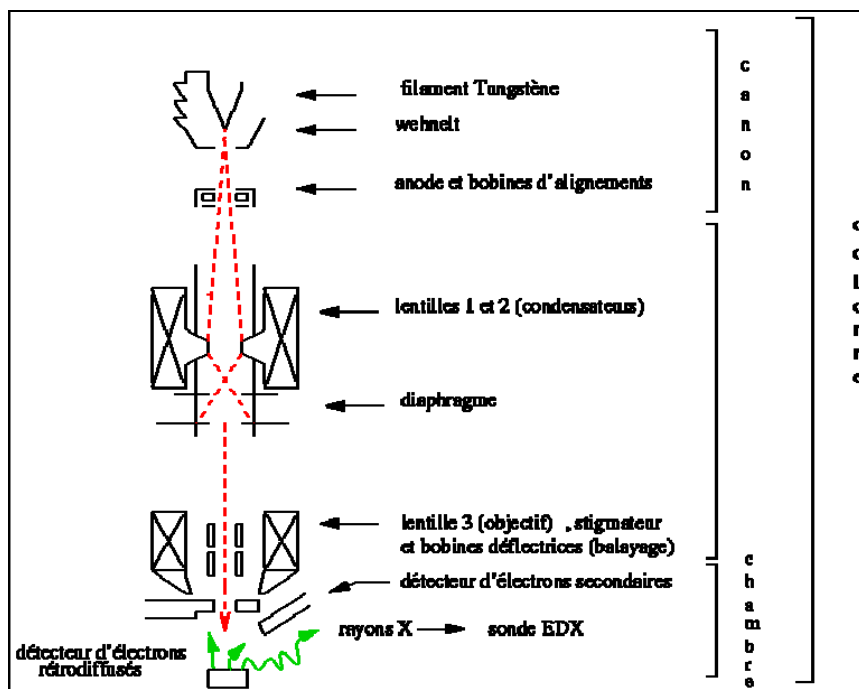
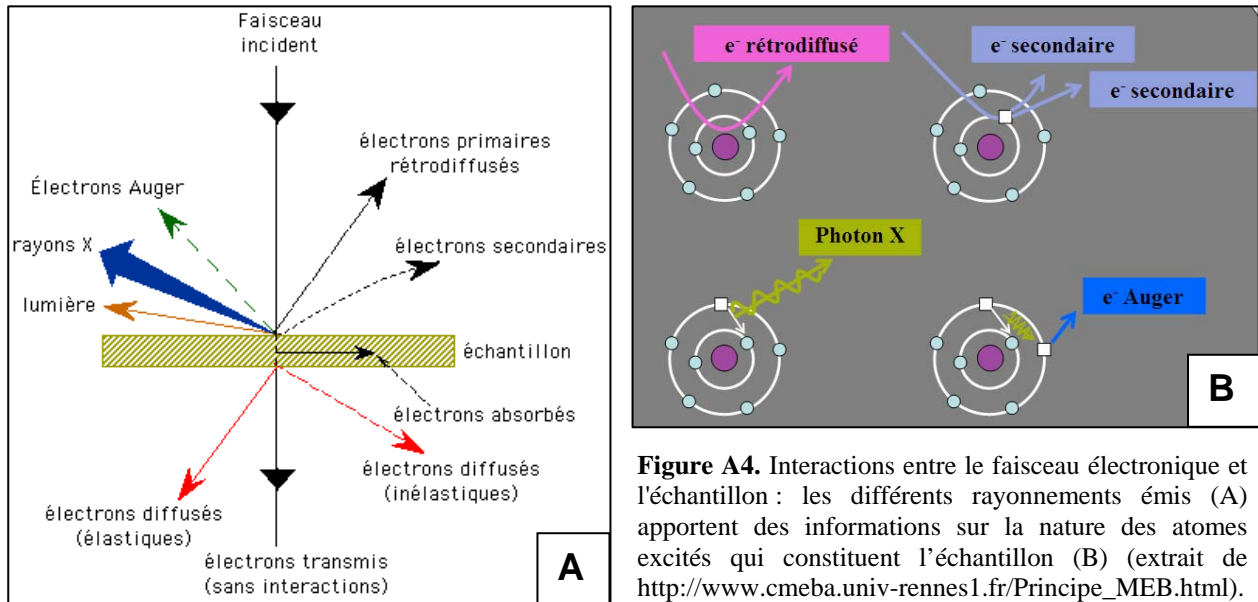


Figure A3. Schéma de fonctionnement du MEB (extrait de : <http://www.enpc.fr/cereve/HomePages/brigitte/MEB/PrincipeMEB/PrincipeMEB.html>)

Le faisceau électronique pénètre ponctuellement dans l'échantillon et s'y diffuse dans un volume qui dépend de la densité de la matrice ainsi que de l'énergie des électrons incidents, donc en partie de la tension d'accélération du microscope. La poire d'interaction varie entre généralement entre  $0,01 \mu\text{m}^3$  et  $100 \mu\text{m}^3$  selon les conditions. L'interaction entre les électrons incidents et l'échantillon produit l'émission d'électrons dont l'énergie dépend de la matière excitée (Fig. A4).



**Figure A4.** Interactions entre le faisceau électronique et l'échantillon : les différents rayonnements émis (A) apportent des informations sur la nature des atomes excités qui constituent l'échantillon (B) (extrait de [http://www.cmeba.univ-rennes1.fr/Principe\\_MEB.html](http://www.cmeba.univ-rennes1.fr/Principe_MEB.html)).

Les électrons secondaires ont une faible énergie cinétique et renseignent sur la texture en surface de l'échantillon (les défauts, fractures, reliefs...). Les électrons secondaires sont détectés par un scintillateur qui restitue l'énergie absorbée sous la forme de photons. Les zones plus claires sur une image en électrons secondaires sont associées à des reliefs positifs alors que les zones plus sombres qui renvoient peu d'électrons correspondent à des creux ou des surfaces planes. Le MEB permet d'obtenir des images très détaillées jusqu'à un grossissement d'au moins 100 000 fois.

Les électrons rétrodiffusés (BSE de l'anglais *Back-Scattered Electrons*) correspondent aux électrons qui sont renvoyés par la force d'attraction des atomes de l'échantillon. Le détecteur BSE renvoie une image dont l'intensité lumineuse est proportionnelle au numéro atomique moyen de la zone excitée. Si la matière est composée d'atomes lourds comme l'uranium ou le plomb, les électrons rétrodiffusés sont renvoyés avec une forte énergie et apparaîtront sur l'image en blanc alors que des phases composées d'éléments plus légers comme l'aluminium et la silice correspondront à des zones plus sombres.

Les rayons X émis par la matière lorsque des électrons de ses atomes sont excités par le bombardement et reviennent à leur état fondamental sont analysés par le spectromètre EDS. Le spectre de rayons X de la zone excitée est caractéristique de sa composition chimique. La position de chaque pic émis est associée à un élément spécifique et les variations de hauteur des pics correspondent aux abondances relatives des éléments entre eux. Il est donc possible pour un point d'analyse d'obtenir une composition semi-quantitative et d'identifier la phase minérale étudiée. Enfin, lorsque l'on balaye une zone entière, il est possible de réaliser une cartographie X de la répartition des éléments et de visualiser les relations entre les phases minérales.

## 2.5 MICROSONDE ELECTRONIQUE (CAMECA SX100 ET SX50)

### 2.5.1 Caractérisation de la composition des minéraux par microanalyses *in situ*

L'analyse quantitative réalisée à la microsonde électronique (EMPA de l'anglais *Electron Micro-Probe Analysis*) est basée sur le même principe que le MEB-EDS et utilise le phénomène résultant de l'interaction entre les électrons de haute énergie et la matière, l'émission X. Un flux d'électrons est émis par un canon à filament de tungstène, puis focalisé sur l'échantillon par une série de lentilles et de bobines induites d'un courant électrique. Les molécules excitées à la surface de l'échantillon émettent des photons afin de revenir à leur stade d'équilibre. Les photons émis sont caractéristiques des éléments constitutifs des minéraux visés par le faisceau et la quantité de photons est proportionnelle à la composition élémentaire de la zone excitée. Ces photons sont analysés par différents spectromètres en dispersion d'énergie (WDS de l'anglais *Wave Length Spectrometers*) dotés chacun de plusieurs cristaux analyseurs (PET, LPET, TAP et LIF) suivant les éléments que l'on veut détecter.

La microsonde CAMECA SX100 du SCMEM la plus utilisée au cours de cette thèse (Fig. A5) est dotée de 5 spectromètres permettant l'analyse des éléments B à U. Une seconde microsonde a été aussi utilisée lorsque les analyses ne nécessitaient pas un champ d'investigation aussi large, la CAMECA SX50 qui possède 4 spectromètres restreignant l'analyse aux éléments N à U. Chaque élément est identifié en fonction de ses raies de longueur d'onde caractéristiques. Le comptage de chaque raie est reporté sur un spectre d'émission qui est comparé à celui d'un standard dans les mêmes conditions d'analyse mais dont la composition est connue. L'intensité de chacun des pics du spectre d'émission peut enfin être convertie en concentrations. Les analyses à la microsonde électronique permettent de déterminer avec précision la composition d'un minéral sur un point dont la taille ne dépasse pas 2  $\mu\text{m}$  de diamètre. Pour chaque phase minérale analysée (oxydes d'uranium, zircon, monazite, ...), un programme d'analyse différent a été établi car les éléments sont en proportions très variables ce qui nécessite un temps de comptage adapté, plus long pour détecter des concentrations plus faibles. D'autre part, le choix des raies sur lesquelles sont basées la quantification a aussi son importance car certaines raies peuvent rentrer en interférences entre elles. Après avoir réglé ses différents paramètres, la limite de détection peut descendre à l'analyse des éléments traces de l'ordre de la centaine de ppm.



**Figure A5.** Microsonde électronique CAMECA SX100

Comme le MEB, la microsonde électronique permet de réaliser des cartographies X de la répartition des éléments, mais aussi des profils d'évolution de la composition chimique dans un échantillon le long d'un axe choisi. Cette méthode s'avère intéressante pour étudier les minéraux zonés.

### 2.5.2 Application à la géochronologie

Ces vingt dernières années, une nouvelle méthode de datation grâce à l'analyse par microsonde électronique a été développée. L'âge d'un minéral porteur d'éléments radiogéniques peut être calculé à partir de sa composition chimique dont les teneurs en éléments fils Pb et Th dérivent de la décroissance de l'élément père U en suivant l'équation :

$$C_{Pb} = C_{Th} \left[ \frac{M_{208Pb}}{M_{232Th}} (e^{\lambda_{232} \cdot t} - 1) \right] + C_U \left[ 0.9928 \frac{M_{206Pb}}{M_{238U}} (e^{\lambda_{238} \cdot t} - 1) + 0.0072 \frac{M_{207Pb}}{M_{235U}} (e^{\lambda_{235} \cdot t} - 1) \right]$$

où  $t$  est l'âge de cristallisation du minéral,  $C_{Pb}$ ,  $C_{Th}$  and  $C_U$  sont les concentrations en Pb, Th et U mesurées à la microsonde électronique en pourcentage massique et converties en ppm,  $M_{206Pb}$  (205.97445 g.mol<sup>-1</sup>),  $M_{207Pb}$  (206.97588 g.mol<sup>-1</sup>),  $M_{208Pb}$  (207.97664 g.mol<sup>-1</sup>),  $M_{232Th}$  (232.03805 g.mol<sup>-1</sup>),  $M_{235U}$  (235.04392 g.mol<sup>-1</sup>),  $M_{238U}$  (238.05078 g.mol<sup>-1</sup>) sont les masses molaires, et  $\lambda_{232}$  ( $0.049475 \times 10^{-9}$  an<sup>-1</sup>),  $\lambda_{238}$  ( $0.155125 \times 10^{-9}$  an<sup>-1</sup>) et  $\lambda_{235}$  ( $0.98485 \times 10^{-9}$  an<sup>-1</sup>) sont les constantes de désintégration de <sup>232</sup>Th, <sup>238</sup>U et <sup>235</sup>U.

La formule simplifiée une fois les constantes appliquées devient :

$$C_{Pb} = C_{Th} [0.897(e^{\lambda_{232} \cdot t} - 1)] + C_U [0.859(e^{\lambda_{238} \cdot t} - 1) + 0.006(e^{\lambda_{235} \cdot t} - 1)]$$

Cette équation est résolue par itérations successives grâce au solveur ou a une série de macro réalisée sous Excel. Cette méthode n'est envisageable que si la teneur en Pb commun est négligeable par rapport à la teneur en Pb radiogénique, la valeur mesurée étant celle du Pb total. Elle est applicable aux minéraux tels que la monazite (Suzuki et al., 1994; Montel et al., 1996; Cocherie and Albarède, 2001), le zircon, le xénotime (Susuki and Adachi, 1991 ; Hetherington *et al.*, 2008) ou encore les oxydes d'uranium (Kempe, 2003; Alexandre and Kyser, 2005). Les analyses ponctuelles itératives sur un même minéral doivent être effectuées dans des zones de composition homogène afin d'obtenir un seul âge calculé par un traitement statistique. Cependant, les minéraux ayant souvent subi différents processus d'altération pouvant affecter leur structure et leur composition depuis leur cristallisation, d'autant plus plausible pour les minéraux archéens, les âges chimiques calculés reflètent le plus souvent des âges d'altération relatifs à des circulations de fluides hydrothermaux ou métasomatiques ultérieurs.

### 3. ETUDES ISOTOPIQUES

#### 3.1 Principe de fonctionnement de la microsonde ionique (CAMECA IMS-3F)

La microsonde ionique utilisée au cours de cette thèse est la CAMECA IMS-3f du CRPG (Centre de Recherches Pétrographiques et Géochimiques) situé à Vandœuvre-lès-Nancy (Fig. A6). Cette microsonde utilise le procédé appelé la spectrométrie de masse à ionisation secondaire (SIMS de l'anglais *Secondary Ion Mass Spectrometry*). L'échantillon est bombardé par un flux d'ions oxygène négatifs avec une tension initiale de 10kV et une intensité de 5-10 nA. La matière ionisée est arrachée de l'échantillon lors du bombardement, induisant la destruction de la zone analysée et la formation d'un petit trou à la surface de l'échantillon. Les ions secondaires sont accélérés à 4500 eV et conduit jusqu'à un spectromètre de masse par une série d'aimants qui génèrent des champs électromagnétiques (Fig. A7). Le spectromètre tri ensuite les éléments suivant leur masse respective et des détecteurs (puits de Faraday et multiplicateurs d'électrons) comptent le nombre d'ions en coups par seconde.



Figure A6. Microsonde ionique CAMECA IMS-3f au CRPG

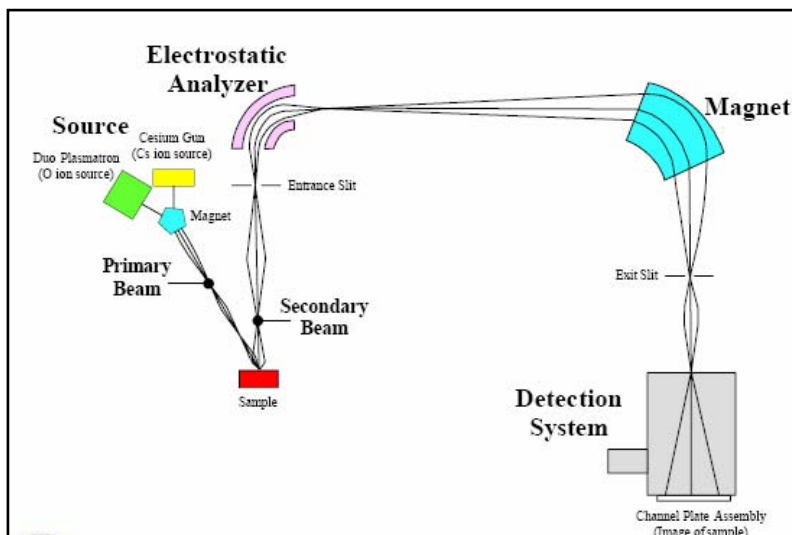


Figure A7. Schéma simplifié de fonctionnement de la microsonde ionique du CRPG

### 3.2 Préparation des échantillons

Dans cette étude, seules les uraninites qui présentaient une surface relativement homogène sur au moins 50  $\mu\text{m}^2$  (pas de fracture, d'altération importante, d'inclusion ou veinule de galène ou de coffinite...) ont été étudiées à la sonde ionique. Cette surface d'analyse minimale qui restreint considérablement le nombre de grains pouvant être étudiés est déterminée par la taille du point d'analyse d'un diamètre d'environ 20 à 30  $\mu\text{m}$  pour une analyses des isotopes de l'uranium et du plomb et de 40 à 50  $\mu\text{m}$  pour une analyses des éléments des terres rares.

De manière générale, les échantillons préalablement étudiées au MEB et à la microsonde électronique se présentent sous la forme de lames minces polies. Les lames minces doivent être taillées en un disque aux dimensions des bagues d'aluminium servant de gabarit pour le porte échantillon de la sonde (diamètre extérieur de 2,5 mm sur 5 mm de hauteur). La mise au gabarit est effectuée à l'aide d'une petite scie à disque de diamant et les minéraux à étudier sont placés autant que possible au centre de ce disque. Une couche de ruban adhésif double face est appliquée sur la face polie de l'échantillon, puis est incéré dans la bague métallique et enfin coulé dans la résine. La résine doit adhérer complètement aux parois de la bague métallique et la bande adhésive permet de ne pas déborder sur la surface de l'échantillon. Lorsque la résine est bien polymérisée, la bande adhésive est décollée de la surface polie, puis l'échantillon est de nouveau poli sur un feutre avec de la pâte diamantée afin d'enlever les traces de résidus de colle. Le plot ainsi confectionné dans la bague en aluminium est métallisé à l'or et l'ensemble garantie la conduction électrique optimale de l'échantillon.

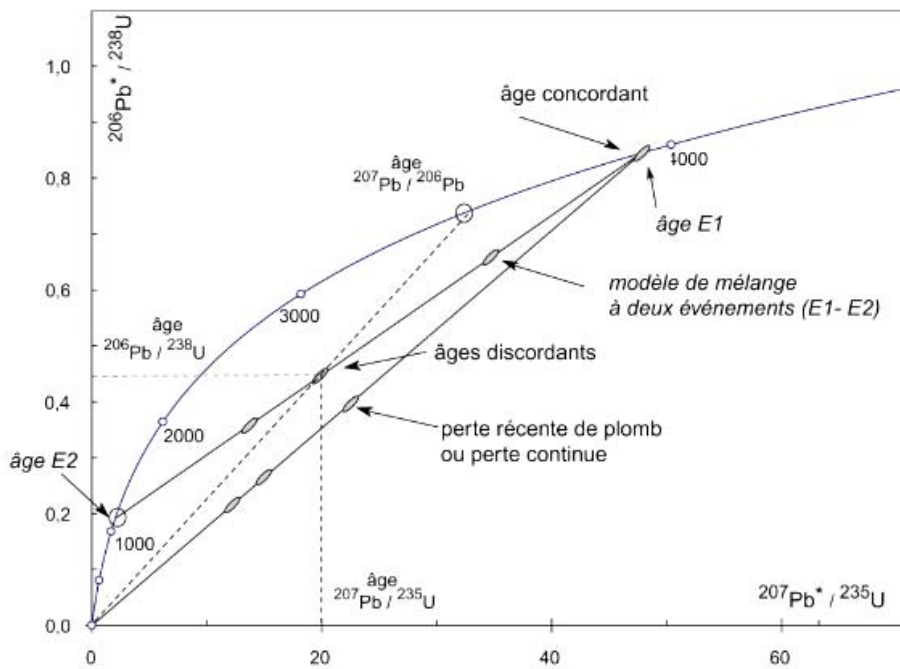
### 3.3 Datation isotopique U-Pb des uraninites

Les intensités des pics de 9 isotopes sont mesurées au spectromètre de masse ( $^{203}\text{Pb}$ ,  $^{204}\text{Pb}$ ,  $^{207}\text{Pb}$ ,  $^{208}\text{Pb}$ ,  $^{232}\text{Th}$ ,  $^{238}\text{U}$ ,  $^{248}\text{ThO}$  et  $^{254}\text{UO}$ ). Le temps de comptage est de 4 s pour chaque isotope, sauf pour  $^{204}\text{Pb}$  mesuré pendant 8s. Un cycle d'analyses correspond à la mesure successive de l'ensemble des masses. Une analyse complète est constituée de 60 cycles et correspond approximativement à 55 min d'analyse pour chaque point. Les résultats de chaque analyse correspondent à la moyenne des cycles effectués. Tous les deux ou trois points d'analyse, une série de mesures est effectuée à partir d'un standard, une uraninite de Mistamisk au Canada (Kish and Cuney, 1981) dont l'âge est connu ( $540 \pm 4$  Ma ; Cathelineau et al., 1990). Les intensités ioniques secondaires mesurées dans l'échantillon sont normalisées à celles du standard dans les mêmes conditions instrumentales ce qui permet de régler les conditions d'analyse pour une mesure optimale, de vérifier qu'il n'y ait pas de problème d'instrumentation en suivant la linéarité et la reproductibilité des mesures et enfin de mesurer un delta-ratio isotopique qui permettra d'évaluer l'erreur sur la mesure.

Trois âges isotopiques peuvent finalement être calculés en fonction des teneurs isotopiques mesurées à la microsonde :

$$\begin{aligned}
 - \quad \text{l'âge} \quad \frac{{}^{206}\text{Pb}}{{}^{238}\text{U}} &= \frac{1}{\lambda_{238}\text{U}} \times \ln \left[ \frac{{}^{206}\text{Pb}}{{}^{238}\text{U}} + 1 \right] \\
 - \quad \text{l'âge} \quad \frac{{}^{207}\text{Pb}}{{}^{235}\text{U}} &= \frac{1}{\lambda_{235}\text{U}} \times \ln \left[ \frac{{}^{207}\text{Pb}}{{}^{235}\text{U}} + 1 \right] \quad \text{avec } \lambda_{238} = 0.155125 \times 10^{-9} \text{ an}^{-1} \\
 - \quad \text{l'âge} \quad \frac{{}^{206}\text{Pb}}{{}^{207}\text{Pb}} &= \frac{e^{\lambda_{238}\text{U} \cdot t} - 1}{e^{\lambda_{235}\text{U} \cdot t} - 1} \times \ln \left[ \frac{{}^{206}\text{Pb}}{{}^{238}\text{U}} + 1 \right] \quad \text{et } \lambda_{235} = 0.98485 \times 10^{-9} \text{ an}^{-1}
 \end{aligned}$$

Si tout le plomb présent dans l'uraninite est d'origine radiogénique et que l'uraninite a évolué depuis sa cristallisation primaire en système clôt, c'est à dire sans perte ni gain en U et Pb (pas de lessivage de U et Pb par altération, ni de cristallisation de galène par exemple), les trois âges doivent normalement être identiques et intersecter la courbe Concordia définie par Wetherill (1956). Cependant, cela est rarement le cas et généralement les âges sont discordants et distribués en dessous de la courbe lorsque le minéral a subi des pertes en U et Pb au cours d'un évènement récent (Fig. A8). Lorsque les âges s'alignent sur une même droite, il est alors possible d'évaluer les âges des évènements associés au déséquilibre isotopique et à l'ouverture du système. Les intersections entre la droite Discordia et la courbe Concordia sont calculées à l'aide de l'outil ISOPLOT développé sous Excel (Ludwig, 1999). L'intercepte supérieur permet parfois de remonter jusqu'à l'âge de cristallisation du minéral. Si les points de mesures ne s'alignent pas suivant une droite mais sont dispersés sans hiérarchie propre, alors il est impossible d'évaluer l'âge de l'uraninite.



### 3.4 Mesures des teneurs en Y et REE des uraninites

Le principe de mesure est le même que pour les isotopes de U et Pb. Les intensités des pics de 31 isotopes sont mesurées au spectromètre de masse ( $^{89}\text{Y}$ ,  $^{139}\text{La}$ ,  $^{140}\text{Ce}$ ,  $^{141}\text{Pr}$ ,  $^{142}\text{Nd}$ ,  $^{143}\text{Nd}$ ,  $^{146}\text{Nd}$ ,  $^{147}\text{Sm}$ ,  $^{149}\text{Sm}$ ,  $^{151}\text{Eu}$ ,  $^{153}\text{Eu}$ ,  $^{154}\text{Gd}$ ,  $^{155}\text{Gd}$ ,  $^{156}\text{Gd}$ ,  $^{157}\text{Gd}$ ,  $^{159}\text{Tb}$ ,  $^{161}\text{Dy}$ ,  $^{162}\text{Dy}$ ,  $^{163}\text{Dy}$ ,  $^{165}\text{Ho}$ ,  $^{166}\text{Er}$ ,  $^{167}\text{Er}$ ,  $^{168}\text{Er}$ ,  $^{169}\text{Tm}$ ,  $^{171}\text{Yb}$ ,  $^{172}\text{Yb}$ ,  $^{173}\text{Yb}$ ,  $^{174}\text{Yb}$ ,  $^{175}\text{Lu}$ ,  $^{235}\text{U}$ ,  $^{251}\text{UO}$ ). Le temps de comptage est de 10 s pour chaque élément des terres rares et de 5 s pour  $^{89}\text{Y}$ ,  $^{235}\text{U}$  et  $^{251}\text{UO}$ . Les mesures sont effectuées successivement sur 16 cycles soit environ 1h45 pour chaque point d'analyse et le résultat correspond à la moyenne des cycles pour chaque isotope. Les intensités ioniques de chaque élément sont normalisées cette fois à celles d'une uraninite du bassin de Katanga en Zambie (Holliger, 1988) dont la composition est connue. Les teneurs en REE sont ensuite calculées selon la méthode développée par Bonhoure et al. (2007) à l'aide d'une feuille de calcul Excel prenant en compte les mesures d'incertitudes. Cependant, les mesures du gadolinium et de l'ytterbium sont soumises à des interférences avec les éléments en terres rares légères (LREE). Les valeurs en Gd et Yb sont donc recalculées en utilisant la méthode des moindres carrés avec les abondances relatives de leurs plus proches voisins :

$$\text{Gd} = 1/3 * \text{Sm} + 2/3 \text{Tb} \text{ (Eu étant souvent anormale elle sera remplacée par Sm)}$$

$$\text{et } \text{Yb} = 1/2 * \text{Tm} + 1/2 * \text{Lu}.$$

## REFERENCES CITEES DANS LES ANNEXES ANALYTIQUES

- Alexandre, P. and Kyser, T.K., 2005, Effects of cationic substitutions and alteration in uraninite, and implications for the dating of uranium deposits, *The Canadian Mineralogist* 43, p. 1005-1017.
- Bonhoure, J., Kister, P., Cuney, M. and Deloule, E., 2007, Methodology for Rare Earth Element Determinations of Uranium Oxides by Ion Microprobe, *Geostandards and Geoanalytical Research* 31, p. 209-225.
- Carignan J., Hold, P., Mevelle, G. Morel, J. and Yeghichevan, D., 2001, Routine analysis of trace elements in geological samples using flow injection and low pressure on line liquid chromatography coupled to ICP-MS: a study of geochemical reference materials BR, DR-N, UB-N, AN-G and GH, *Geostandards Newsletter* 25, p. 187-198.
- Cathelineau, M., Boiron, M.-C., Holliger, P. and Poty, B., 1990, Metallogenesis of the French part of the Variscan orogen; Part II: Time-space relationship between U, Au and Sn-W ore deposition and geodynamic events-mineralogical and U-Pb data, *Tectonophysics* 177, p. 59-79.
- Cocherie, A. and Albarède, F., 2001, An improved U-Th-Pb age calculation for electron microprobe dating of monazite, *Geochimica et Cosmochimica Acta*, Vol. 65, p. 4509-4522.
- Hetherington, C. J., Jercinovic, M. J., Williams, M. L. and Mahan, K., 2008, Understanding geologic processes with xenotime: Composition, chronology, and a protocol for electron probe microanalysis, *Chemical Geology*, Vol. 254, Issues 3-4, p. 133-147.
- Holliger, P., 1988, Ages U-Pb définis in situ sur oxydes d'uranium à l'analyseur ionique: méthodologie et conséquences géochimiques, *Comptes rendus de l'Académie des Sciences de Paris* 307, p. 367-373.
- Kempe, U., 2003, Precise electron microprobe age determination in altered uraninite: consequences on the intrusion age and the metallogenic significance of the Kirchberg granite (Erzgebirge, Germany), *Contributions to Mineralogy and Petrology* 145, p. 107-118.
- Kish, L. and Cuney, M., 1981, Uraninite-albite veins from Mistamisk Valley of the Labrador Through, Quebec. *Mineralogical Magazine* 44, 471-483.
- Ludwig, K.R., 1999, Isoplot/Ex version 2.00 – A geochronological toolkit for Microsoft Excel, Berkeley Geochronology Center, Special Publication No. 2.
- Suzuki, K. and Adachi, M., 1991, Precambrian provenance and Silurian metamorphism of the Tsubono-sawa paragneiss in the South Kitakami terrane, Northeast Japan, revealed by the chemical Th -U-total Pb isochron ages of monazite, zircon and xenotime. *Geochem. Journ.*, 25, p. 357-376.
- Suzuki, K. and Adachi, M., 1994, Middle Precambrian detrital monazite and zircon the Hide gneiss on Oki-Dogo Island, Japan: their origin and implications for the correlation of basement gneiss of Southwest Japan and Korea. *Tectonophysics*, 235, 277-292.
- Montel, J. M., Foret, S., Veschambre, M., Nicollet, Ch. And Provost, A., 1996, Electron microprobe dating of monazite; *Chemical Geology*, Vol. 131, p. 37-53.
- Wetherill, G. H., 1956, An interpretation of the Rhodesia and Witwatersrand age patterns, *Geochimica et Cosmochimica Acta*, Vol. 9, p. 290-292.

---

**ANNEXE 2 :**  
**ANALYSES GEOCHIMIQUES**  
**EXTERNES**

---

Annexe 2 : Données Géochimiques Externes

**Tableau A1.** Eléments majeurs (wt.%) dans les roches du socle du Craton de Kénéma Man en Guinée (base de données du BRGM)

Echantillon	Unité	Facies	SiO <sub>2</sub>	Al <sub>2</sub> O <sub>3</sub>	Fe <sub>2</sub> O <sub>3</sub>	MnO	MgO	CaO	Na <sub>2</sub> O	K <sub>2</sub> O	TiO <sub>2</sub>	P <sub>2</sub> O <sub>5</sub>	PF	Total
KEC-81-12	Paleoarchean	Eclogite	46,7	14,88	15,67	0,31	7,62	11,1	1,85	0,73	1,41	0,16	0	100,4
KEC-81-4	Paleoarchean	Eclogite	48,5	12,63	13,07	0,23	12,6	10,4	1,59	0,23	0,7	0,04	0	99,98
NZE2578	Paléoarchéen	Trondhjemite	74,4	14,6	1,24	0,02	0,18	2,12	5,22	1,25	0,18	0,07	0,49	99,76
NZE2629A	Paléoarchéen	Adamellite	74,2	14,82	1,21	0,03	0,41	0,85	4,16	3,93	0,13	0,02	0,63	100,43
AC.362	Leonian	Gneiss	73,4	14,2	1,8	0,05	0,3	1,2	3,7	5,07	0,21	0,07	0,4	100,4
BEY2462b*	Leonian	Pyrigarnite	51	14,1	16,5	0,24	5,6	9,7	1,5	0,07	1,67	0,14	0	100,52
DL056A	Leonian	Amphibolite	50,5	15,6	11,68	0,18	6,9	8,2	2,7	1,91	0,93	0,11	1,4	100,11
DL086	Leonian	Ultrasite	48,7	15,8	13,24	0,26	18,4	0,2	0,5	0,1	1,2	0,09	1,4	99,89
DL109B	Leonian	Microdiorite	45,4	18,9	15	0,2	3,8	7,8	3,8	1,49	1,07	0,84	0,7	99
DL147	Leonian	Gneiss migmatitique	62,3	14,8	6,09	0,09	3,1	3,9	3,5	4,48	0,75	0,32	0,5	99,83
DL150A	Leonian	Diorite	53,3	13,8	8,01	0,12	6,9	8,4	3,1	3,44	0,86	0,66	0,5	99,09
DL225A	Leonian	Gneiss basique	56,8	17,6	7,18	0,11	2,9	6,3	4,3	2,21	0,59	0,37	0,8	99,16
DL271B	Leonian	Gneiss mylonitique	69,2	15,5	3,86	0,05	1	4,8	4,2	0,32	0,34	0,11	0,5	99,88
DL273	Leonian	Amphibolite	49,5	13,5	15,99	0,25	6,8	10,1	2,1	0,2	1,36	0,12	0,6	100,52
DL279	Leonian	Amphibolite	49,7	14,4	11,99	0,19	8,8	10	1,9	0,67	0,74	0,09	1,3	99,78
DL284	Leonian	Granite	74	13,7	1,67	0,05	0	0,8	3,5	5,53	0	0	0,3	99,55
DL47	Leonian	Amphibolite	49,3	15,7	11,4	0,18	9,2	11,4	1,7	0,22	0,66	0,06	0,6	100,42
DL68	Leonian	Granite migmatitique	72,5	13,8	2,49	0,03	0,4	1,5	3,8	3,85	0,21	0,08	0,4	99,06
DL79B	Leonian	Roche basique	48	14,8	13,45	0,2	7,9	10,3	2,2	0,51	1,04	0,08	0,6	99,08
DTMAC1	Leonian	Orthogneiss	72,6	14,46	2,77	0,04	0,49	2,58	4,19	2,14	0,25	0,09	0,23	99,8
DTMAC2	Leonian	Amphibolite	49,1	15,46	10,64	0,18	8,05	10,9	2,89	1,14	0,59	0,09	0,92	99,98
DTNZE1	Leonian	Amphibolite	48,5	14,69	13,65	0,24	6,05	14,3	1,11	0,27	1,08	0,11	0,41	100,44
DTNZE3	Leonian	Pyrigarnite	48,6	15,14	14,71	0,23	6,79	11,5	2,04	0,18	1,15	0,16	0	100,5
DTTIN1	Leonian	Amphibolite	48,4	15,39	12,65	0,21	7,9	11,2	2,25	0,28	0,89	0,1	0,4	99,59
DTTIN14*	Leonian	Amphibolite	49,5	13,8	14,35	0,21	7	10,8	1,5	0,54	1,14	0,09	0,4	99,33
DTTIN17	Leonian	Amphibolite	50,1	15,65	11,33	0,2	7,56	11,9	1,93	0,48	0,68	0,11	0,43	100,35
EE139	Leonian	Granite	70,9	15,3	2,13	0,03	0,7	2	4,9	3,17	0,3	0,1	0,4	99,93
ID.579	Leonian	Gneiss migmatitique	75,2	13,2	1,41	0,08	0,2	1	2,8	5,83	0,09	0	0,4	100,21
ID113	Leonian	Granite à biotite	71	14,51	2,71	0,06	1,01	2,27	3,91	3,21	0,22	0,07	0,97	99,9
ID125	Leonian	Granite à biotite	68	15,49	3,21	0,11	0,9	1,92	4,5	4,31	0,55	0,15	0,91	100,03
ID234	Leonian	Granite à biotite et amphibole	62,6	16,39	5,29	0,08	2,31	5,1	4,53	1,07	0,5	0,16	0,82	98,89
ID261B	Leonian	Monzogabbro	44,1	11,82	17,54	0,26	9,63	9,76	1,95	1,88	1,25	0,41	1,3	99,92
ID275	Leonian	Granite à biotite	69,6	15,5	3,43	0,05	0,76	2,99	4,67	1,34	0,31	0,11	0,59	99,31
ID277	Leonian	Granite à biotite	73,2	14,26	1,48	0,04	0,32	1,48	4,3	3,61	0,14	0,08	0,5	99,45
ID289A	Leonian	Orthogneiss rubané	71,6	16,11	1,55	0	0,41	3,12	5,44	0,89	0,13	0	0,37	99,59
ID289B	Leonian	Orthogneiss rubané	51,9	17,45	9,64	0,12	4,5	7,87	4,37	1,17	0,84	0,28	1	99,17
ID350	Leonian	Roche Ultrabasique	47,8	9,9	15,34	0,32	8,96	13,9	1,93	0,71	0,8	0,08	0	99,68
ID398	Leonian	Granite à biotite	74,6	13,5	1,23	0	0,21	1,32	3,59	4,22	0,13	0,05	0,56	99,43
ID406	Leonian	Granite à biotite	60,9	17,35	6,33	0,08	2,36	4,32	4,95	1,76	0,69	0,41	0,95	100,11
JLF.114	Leonian	Gneiss migmatitique	76,8	12,8	1,23	0,07	0	0,3	4,5	3,8	0,06	0	0,3	99,86
NZE2033	Leonian	Gneiss à pyroxène	60,1	12,1	11,81	0,44	2,87	7,16	3,03	0,47	0,45	0,08	0,07	98,58
NZE2066a	Leonian	Métatuff	66,2	15,14	4,34	0,08	2,34	3,49	3,81	2,1	0,41	0,1	1,55	99,59
NZE2066c	Leonian	Amphibolite à biotite	46,7	14,41	13,35	0,23	9,01	12,7	1,42	0,14	1,21	0,14	0,44	99,72
NZE2082	Leonian	Amphibolite	49,7	14,22	15,49	0,24	6,53	10,5	0,67	0,61	1,29	0,13	0,64	100,03
NZE2130	Leonian	Amphibolite	60,9	15,19	6,64	0,1	3,87	5,7	3,65	1,58	0,58	0,08	0,65	98,98
NZE2236	Leonian	Gneiss à hornblende et biotite	59,7	14,25	10,77	0,28	3,61	4,64	2,51	2,7	0,8	0,18	0,7	100,13
NZE2239	Leonian	Gneiss à pyroxène	54,8	16,46	8,44	0,15	2,39	8,14	2,92	4,74	0,83	0,47	0,75	100,09
NZE2257	Leonian	Gneiss à pyroxène	61,1	8,93	9,36	0,28	4,04	13,6	1,44	0,29	0,76	0,09	0	99,86
NZE2295	Leonian	Amphibolo-pyroxénite	49,3	14,41	14,45	0,21	6,88	10,7	2,32	0,24	1,05	0,15	0,13	99,88
NZE2317	Leonian	Gneiss à pyroxène	51,1	15,97	10,92	0,18	6,26	10,1	3,08	1,3	0,95	0,28	0,05	100,21
NZE2329b	Leonian	Amphibolo-pyroxénite	47,5	13,65	17,17	0,26	5,25	10,7	2,07	0,56	1,83	0,18	0,75	99,91
NZE2329c	Leonian	Amphibolite mafique	47,8	12,7	11,54	0,32	13,1	10,8	1,48	0,54	0,57	0,05	1,08	99,97
NZE2346	Leonian	Amphibolite	62,7	15,37	6,86	0,09	3,12	4,6	3,09	2,64	0,73	0,27	0,48	99,96
NZE2351d	Leonian	Amphibolite à biotite	49,6	12,99	10,54	0,18	9,85	9,47	2,46	1,63	0,81	0,26	0,87	98,69
NZE2379	Leonian	Amphibolite	53,6	18,8	8,55	0,14	2,11	11,2	3,07	0,67	1,11	0,27	0,45	99,96
NZE2416	Leonian	Métagabbro	48,7	15,16	13,07	0,2	8,47	11,2	1,72	0,2	0,88	0,14	0,17	99,91
NZE2447	Leonian	Amphibolo-pyroxénite	50,5	13,34	18,56	0,25	4,31	8,71	0,5	0,2	2,87	0,32	0	99,52
NZE2467	Leonian	Amphibolite	52	13,64	10,14	0,23	5,97	13,6	1,16	0,38	0,81	0,22	1,13	99,36
NZE2535	Leonian	Amphibolo-pyroxénite	49,2	15,36	12,51	0,21	8	11,6	1,89	0,13	0,94	0,14	0	99,94
NZE2553a	Leonian	Pyrigarnite	49,7	11,96	20,11	0,26	6,08	8,92	0,81	0,29	1,87	0,16	0	100,15
NZE2565	Leonian	Amphibolite	54,1	16,79	9,64	0,15	4,2	7,52	3,77	2,06	0,87	0,26	0,71	100,06
TIN2040	Leonian	Orthogneiss	74,9	13,95	1,14	0,03	0,3	1,81	3,47	3,83	0,07	0	0,47	99,92
NZE2328	Leonian	Gneiss Qtz-Monzonite	63	16,27	4,91	0,07	3,18	3,64	3,4	4,26	0,65	0,24	0,36	99,99

Annexe 2 : Données Géochimiques Externes

**Tableau A1. Suite**

Echantillon	Unité	Faciès	SiO <sub>2</sub>	Al <sub>2</sub> O <sub>3</sub>	Fe <sub>2</sub> O <sub>3</sub>	MnO	MgO	CaO	Na <sub>2</sub> O	K <sub>2</sub> O	TiO <sub>2</sub>	P <sub>2</sub> O <sub>5</sub>	PF	Total
AC.492	Liberian	Qtz-diorite	49,9	14	14,22	0,23	7,4	11,4	1,8	0,19	0,85	0,07	0,6	100,66
AC.497	Liberian	Qtz-Syérite	65,1	14,8	5,07	0,08	2,2	3,4	3,3	4,78	0,39	0,22	0,4	99,74
DL228A	Liberian	Granite	69,2	14,7	3,49	0,03	0,6	1,6	3,3	5,09	0,53	0,16	0,4	99,1
DL247	Liberian	Granodiorite	71,5	14,3	2,37	0,07	0,7	2,7	3,8	3,19	0,26	0,06	0,7	99,65
DL251B	Liberian	Syérite	53,7	16,8	8,31	0,11	3,1	4,6	3,8	5,26	1,89	0,8	0,6	98,97
DL259C	Liberian	Qtz-Monzodiorite	49,8	14,4	15,29	0,14	5,9	6,6	2,6	1,78	1,47	0,16	0,9	99,04
DTMAC20	Liberian	Tonalite	65,7	16,93	4,61	0,07	1,3	3,59	4,76	1,74	0,52	0,11	0,94	100,23
ID179	Liberian	Granodiorite	72,7	14,68	2,53	0,07	0,84	1,18	4,45	2,25	0,2	0,05	1	99,93
ID215	Liberian	Granodiorite	71,3	15,36	2,28	0,06	0,59	2,25	4,42	2,83	0,2	0,07	0,52	99,83
ID260	Liberian	Granodiorite	69,6	15,52	3,35	0,03	0,9	2,86	4,16	2,6	0,34	0,14	0,52	100,01
ID261A	Liberian	Granodiorite	70,5	15,45	2,35	0	0,75	2,14	3,99	3,66	0,26	0,12	0,44	99,69
ID278	Liberian	Granodiorite	72,6	15,36	1,29	0,03	0,25	2,35	4,85	2,62	0,12	0,05	0,33	99,82
ID292	Liberian	Tonalite	70,3	16,01	2,7	0,04	0,82	3,33	4,86	1,48	0,25	0,12	0,26	100,16
ID294	Liberian	Qtz-diorite	55,6	12,1	8,5	0,15	7,59	8,85	2,52	2,09	0,76	0,23	0,86	99,24
ID321	Liberian	Adamellite	73,4	15,06	0,89	0	0,28	1,75	3,91	4,45	0,07	0,06	0,38	100,28
ID333	Liberian	Adamellite	73,9	12,32	3,38	0,05	0,52	1,53	3,4	3,14	0,32	0,07	0,43	99,08
ID341	Liberian	Gabbro	51,3	16,73	10,8	0,17	5,94	8,62	3,7	0,62	0,74	0,31	0,55	99,52
ID371	Liberian	Adamellite	68,4	15,6	2,6	0,05	1,12	2,4	4,01	4,65	0,24	0,11	0,23	99,45
ID392	Liberian	Syérite	59,4	17,05	5,71	0,09	1,99	3,09	5,06	6,2	0,64	0,5	0,33	100,09
ID395	Liberian	Qtz-Monzodiorite	61,3	16,58	5,52	0,07	2,34	4,39	4,48	3,48	0,65	0,55	0,84	100,17
ID436	Liberian	Granodiorite	73,2	13,86	2,01	0	0,28	0,71	5,09	3,95	0,22	0,14	0,23	99,69
ID443	Liberian	Qtz-Monzonite	64,5	15,49	5,12	0,05	1,15	2,75	3,82	4,18	0,67	0,33	0,49	98,54
ID461	Liberian	Granodiorite	70,7	15,71	1,37	0	0,68	2,64	4,11	3,17	0,16	0,07	0,36	98,92
IDEE425	Liberian	Tonalite	68,3	15,63	3,91	0,04	1	3,05	4,83	2,36	0,24	0,14	0,46	99,93
MAC3075	Liberian	Granodiorite	70,1	15,54	2,99	0,04	0,84	2,63	4,26	2,72	0,32	0,14	0,29	99,84
MAC3078a	Liberian	Tonalite	70,2	15,64	2,33	0,05	0,74	2,91	4,59	2,16	0,21	0,04	0,37	99,21
MAC3078e	Liberian	Tonalite	66,4	16,02	4,24	0,11	1,75	4,09	4,76	1,53	0,3	0,09	0,61	99,87
NZE2603	Liberian	Tonalite	66,6	15,52	4,94	0,07	1,59	2,53	4,63	1,79	0,71	0,23	1,02	99,67
NZE2618*	Liberian	Granodiorite	67,9	14,7	4,24	0,06	0,9	2,3	4	3,27	0,35	0,19	1	98,91
NZE2652	Liberian	Adamellite	73,5	14,51	1,4	0,02	0,25	1,59	4,06	3,75	0,14	0,11	0,44	99,79
NZE2659	Liberian	Qtz-diorite	49	14,7	14,72	0,25	6,6	11	2,16	0,14	1,21	0,17	0	100
DTMAC12*	Liberian	Granite	74	13,5	2	0,06	0	0,9	3,4	4,88	0,14	0,06	0,5	99,44
DTMAC15	Liberian	Granite	72,6	13,84	2,61	0,1	0,3	1,07	3	5,63	0,16	0,03	0,62	99,98
DTMAC21	Liberian	Tonalite	68,8	16,76	3,16	0,08	0,78	3,03	5,41	1,38	0,33	0,06	0,49	100,29
DTMAC23*	Liberian	Granodiorite	71,1	15,5	2,4	0,04	0,6	2,4	4,7	2,78	0,32	0,12	0,4	100,36
DTMAC9	Liberian	Adamellite	74,2	14,33	1,42	0,02	0,09	1,44	4,04	4	0,11	0,02	0,43	100,1
NZE2600	Liberian	Granite	74,9	13,77	0,95	0,04	0,16	0,83	3,53	4,98	0,08	0,1	0,3	99,63
NZE2615	Liberian	Adamellite	73,2	14,06	1,71	0,04	0,26	1,38	3,67	4,42	0,19	0,09	0,55	99,54
DTNZE 31a	Rhyacien	Syérite	61,3	15,56	4,16	0,09	1,43	4,47	2,58	9	0,78	0,33	0,26	99,91
NZE2381	Rhyacien	Granite	73,2	14,73	0,88	0,03	0,21	1,45	3,03	5,97	0,02	0,05	0,3	99,89
NZE2393	Rhyacien	Granite	73,4	13,75	2,18	0,02	0,31	1,24	2,4	5,9	0,22	0,05	0,47	99,9
NZE2463	Rhyacien	Granite	74,1	13,87	1,41	0,04	0,17	1,26	3,01	5,37	0,11	0,04	0,19	99,57

## Annexe 2 : Données Géochimiques Externes

**Tableau A2.** Eléments majeurs (wt.%) et teneurs en U et Th (ppm) dans les roches de la Supersuite de Split Rock du Craton de Pilbara en Australie (les 4 premiers échantillons ont été analysés au cours de cette thèse et les données suivantes ont été compilées à partir de la base OZCHEM fournie par AGSO et GSWA). Les paramètres A/CNK et A/NK sont calculés en moles et Q, P, A et B sont donnés en milliers de cations (Chapitre 2 – Partie 2.2).

Echantillon	SiO <sub>2</sub>	Al <sub>2</sub> O <sub>3</sub>	Fe <sub>2</sub> O <sub>3</sub>	MnO	MgO	CaO	Na <sub>2</sub> O	K <sub>2</sub> O	TiO <sub>2</sub>	P <sub>2</sub> O <sub>5</sub>	PF	Total	Q	P	A	B	A/CNK	A/NK	U	Th
Pilbara-178014	72,47	13,62	1,57	0,03	0,29	0,84	3,41	5,43	0,21	0,06	0,72	98,65	167,0	-9,2	11,9	29,5	1,05	1,18	7,54	32,58
Pilbara-178011	69,15	13,99	3,65	0,06	0,55	1,79	3,75	4,38	0,48	0,11	0,77	98,68	148,5	-59,8	-3,7	65,5	0,99	1,28	7,52	29,94
Pilbara-169044	76,42	13,61	0,88	0,06	0,05	0,21	4,23	4,39	0,04	< L.D.	0,53	100,41	191,9	-46,9	29,5	12,7	1,12	1,16	6,23	11,65
Pilbara-142879	74,30	13,36	1,46	0,03	0,19	0,96	3,65	4,80	0,15	0,03	0,64	99,58	181,4	-32,7	8,1	25,0	1,03	1,19	17,82	43,19
Cooglegong-15218	74,60	12,90	0,72	0,07	0,12	0,62	3,60	4,85	0,14	0,01	0,77	98,40	187,6	-24,0	11,6	13,8	1,05	1,15	19,00	45,00
Cooglegong-26308	76,70	12,70	0,46	0,05	0,02	0,39	4,26	4,44	0,04	0,00	1,01	100,07	189,4	-49,9	3,3	6,8	1,01	1,07	17,82	43,19
Cooglegong-142879	72,70	13,79	0,82	0,05	0,20	0,95	3,58	4,97	0,18	0,04	1,83	99,11	171,2	-26,7	15,4	17,5	1,06	1,22	19,00	45,00
Minnamonica-97045009	72,77	13,92	0,52	0,02	0,40	1,36	3,62	4,45	0,24	0,08	0,92	98,30	176,5	-46,4	13,1	19,5	1,05	1,29	14,00	43,00
Minnamonica-97045019	74,02	13,50	0,51	0,02	0,33	0,89	3,49	5,10	0,14	0,07	0,85	98,92	179,4	-19,9	12,0	16,4	1,05	1,20	19,30	48,70
Minnamonica-97045206	73,67	13,67	0,59	0,02	0,27	0,96	3,30	5,68	0,18	0,06	0,84	99,24	170,4	-2,7	6,6	16,4	1,02	1,18	4,40	23,50
Minnamonica-97045209	74,86	13,47	0,45	0,02	0,20	0,88	3,75	4,65	0,13	0,04	0,92	99,37	185,3	-37,7	12,9	12,3	1,05	1,20	6,30	23,90
Minnamonica-98049095	73,69	13,79	0,06	0,05	0,12	0,72	3,68	4,76	0,13	0,05	1,88	98,93	180,7	-30,3	24,8	5,4	1,10	1,23	2,90	30,50
Minnamonica-98049100	74,33	13,05	0,08	0,03	0,06	0,71	3,46	5,15	0,08	0,04	2,03	99,02	183,1	-14,7	9,5	3,5	1,04	1,16	7,20	18,50
Minnamonica-98049104	73,95	13,51	0,00	0,05	0,08	0,81	3,60	4,99	0,10	0,05	1,78	98,92	178,7	-24,4	13,8	3,3	1,05	1,19	2,80	19,70
Minnamonica-98049121	73,87	13,30	0,14	0,04	0,09	0,67	3,57	4,92	0,09	0,05	2,33	99,07	182,4	-22,4	17,2	5,1	1,07	1,19	2,70	16,70
Minnamonica-98049137	73,23	13,72	0,16	0,04	0,23	1,24	3,16	5,16	0,20	0,05	1,41	98,60	180,2	-14,3	13,2	10,3	1,05	1,27	6,50	19,70
Minnamonica-98049138	72,94	13,91	0,02	0,04	0,19	0,93	3,51	5,24	0,16	0,06	1,69	98,69	169,3	-18,3	15,0	7,0	1,06	1,21	5,50	19,10
Minnamonica-98049139	72,88	13,63	0,00	0,05	0,20	0,99	3,17	5,41	0,17	0,06	2,12	98,68	175,6	-4,8	14,7	7,1	1,06	1,23	6,10	30,60
Minnamonica-98049143	75,18	13,09	0,20	0,03	0,03	0,51	3,88	4,83	0,04	0,04	1,66	99,49	183,5	-31,5	10,7	3,8	1,04	1,13	11,60	20,60
Minnamonica-98049145	73,64	14,03	0,34	0,04	0,14	0,98	4,59	3,50	0,12	0,07	1,60	99,05	174,7	-91,1	17,7	9,3	1,07	1,24	9,80	26,00
Minnamonica-98049151	75,99	11,72	1,17	0,04	0,09	1,25	5,10	1,63	0,20	0,02	1,92	99,13	207,9	-152,1	-13,9	19,4	0,94	1,15	9,60	10,80
Minnamonica-98049152	72,69	14,43	0,37	0,04	0,20	1,42	4,22	3,96	0,16	0,05	1,55	99,09	166,4	-77,2	12,0	11,6	1,04	1,28	3,80	12,50
Minnamonica-98049153	73,74	13,44	0,46	0,04	0,17	0,82	3,37	5,23	0,14	0,05	1,58	99,04	179,7	-12,1	14,4	11,8	1,06	1,20	3,70	15,40
Minnamonica-98049154	73,77	13,30	0,36	0,05	0,17	0,89	3,35	4,82	0,17	0,08	2,02	98,98	188,4	-21,4	18,5	10,9	1,08	1,24	8,70	21,00
Minnamonica-98049155	74,68	13,16	0,13	0,04	0,09	0,88	3,65	4,36	0,11	0,05	2,00	99,15	193,7	-40,7	16,3	5,3	1,07	1,23	8,40	25,30
Minnamonica-98049156	74,55	13,30	0,19	0,04	0,07	0,76	3,84	4,48	0,09	0,05	1,96	99,33	185,8	-42,1	14,6	5,3	1,06	1,19	7,30	21,90
Minnamonica-98049157	74,38	13,39	0,09	0,05	0,07	0,67	4,00	4,41	0,06	0,08	2,10	99,30	182,2	-47,1	15,9	3,6	1,06	1,18	7,30	13,40
Minnamonica-98049158	73,76	13,02	0,48	0,04	0,20	0,83	3,21	5,02	0,18	0,08	2,21	99,03	189,4	-11,5	15,4	13,3	1,06	1,21	6,60	12,30
Minnamonica-98049161	72,96	13,57	0,57	0,04	0,23	1,06	3,70	4,85	0,20	0,06	1,78	99,02	170,0	-35,1	5,8	15,4	1,02	1,20	6,20	9,00
Minnamonica-98049164	73,53	13,70	0,48	0,04	0,19	0,92	3,76	4,88	0,17	0,06	1,49	99,22	172,3	-33,9	10,8	12,9	1,04	1,19	8,60	28,60
Minnamonica-98049167	70,97	14,07	1,33	0,05	0,52	1,65	3,81	4,10	0,35	0,09	1,99	98,93	164,3	-65,1	7,0	34,0	1,03	1,31	6,30	24,20
Minnamonica-98049198	74,29	13,19	0,27	0,04	0,07	0,60	3,75	4,95	0,10	0,03	2,03	99,32	179,1	-26,3	11,1	6,4	1,04	1,14	4,40	23,90
Minnamonica-98049211	69,49	14,60	1,53	0,06	0,73	1,89	3,99	4,08	0,35	0,20	1,56	98,48	147,9	-75,6	3,4	41,8	1,01	1,33	2,60	23,30
Minnamonica-98049223	72,42	13,73	0,54	0,03	0,29	1,19	3,77	4,52	0,24	0,06	2,18	98,97	170,2	-46,7	9,1	17,0	1,03	1,24	7,20	16,60
Minnamonica-98049225	74,42	13,39	0,40	0,05	0,19	0,86	3,64	4,81	0,18	0,06	1,03	99,03	183,3	-30,4	12,2	12,0	1,05	1,19	2,10	19,60
Minnamonica-98049226	73,69	13,47	0,32	0,06	0,17	0,88	3,58	4,76	0,14	0,05	2,05	99,17	182,0	-29,9	16,1	10,0	1,06	1,22	3,30	18,70
Minnamonica-98049232	72,91	13,62	0,51	0,05	0,27	1,52	4,06	3,56	0,22	0,06	2,08	98,86	180,1	-82,3	6,2	15,9	1,02	1,29	6,90	21,50
Minnamonica-98049091C	73,93	13,63	0,31	0,05	0,17	0,96	3,90	4,64	0,16	0,04	1,41	99,20	174,6	-44,2	8,6	10,1	1,03	1,19	5,50	22,40

Annexe 2 : Données Géochimiques Externes

**Tableau A2. Suite**

Echantillon	SiO <sub>2</sub>	Al <sub>2</sub> O <sub>3</sub>	Fe <sub>2</sub> O <sub>3</sub>	MnO	MgO	CaO	Na <sub>2</sub> O	K <sub>2</sub> O	TiO <sub>2</sub>	P <sub>2</sub> O <sub>5</sub>	PF	Total	Q	P	A	B	A/CNK	A/NK	U	Th
Moolyella-12586	74,10	13,40	0,45	0,05	0,10	0,82	4,05	4,73	0,09	0,02	0,52	98,33	170,4	-44,6	2,3	9,3	1,01	1,14	3,60	16,80
Moolyella-15228	75,50	13,20	0,44	0,07	0,08	0,74	3,97	4,41	0,06	0,04	0,46	98,97	188,6	-47,4	10,7	8,3	1,04	1,17	5,00	17,40
Moolyella-15267	75,40	13,50	0,16	0,05	0,10	0,52	4,05	4,28	0,06	0,01	0,63	98,76	190,8	-48,8	24,6	5,3	1,10	1,19	18,00	59,00
Moolyella-26269	75,00	13,70	1,40	0,05	0,15	0,70	3,70	4,90	0,07	0,02	0,62	100,31	184,5	-27,6	20,2	22,1	1,08	1,20	12,00	16,00
Moolyella-26270	74,90	13,60	1,30	0,04	0,12	0,81	3,90	5,00	0,07	0,07	0,89	100,70	174,1	-33,9	5,7	20,1	1,02	1,15	6,00	30,00
Moolyella-LTU5593	74,96	13,31	0,07	0,05	0,03	0,77	3,77	4,97	0,10	0,03	1,05	99,11	179,7	-29,6	6,3	2,9	1,02	1,15	12,00	40,00
Moolyella-LTU5594	79,91	13,35	0,00	0,04	0,03	0,80	3,72	5,03	0,13	0,05	1,03	104,09	207,2	-27,2	6,3	2,4	1,02	1,15	15,00	40,00
Moolyella-LTU5595	74,98	13,19	0,00	0,05	0,21	0,74	3,68	4,96	0,11	0,05	0,76	98,73	183,3	-26,4	8,1	6,6	1,03	1,15	15,00	36,00
Moolyella-98047007	74,13	13,76	0,23	0,11	0,04	0,87	3,83	4,69	0,04	0,01	1,74	99,45	178,0	-39,3	15,6	4,4	1,06	1,21	7,00	40,00
Numbana-15241	78,40	12,50	0,33	0,01	0,03	0,92	3,67	4,17	0,04	0,06	0,64	100,77	217,3	-46,1	5,3	5,4	1,02	1,18	15,00	38,00
Numbana-97045023	75,20	13,21	0,32	0,02	0,14	0,73	3,26	5,45	0,06	0,03	0,83	99,25	187,8	-2,2	12,0	8,3	1,05	1,17	7,70	15,40
Numbana-97045035	74,15	13,66	0,58	0,03	0,22	0,85	3,56	5,10	0,12	0,05	0,97	99,29	178,3	-21,5	14,3	14,3	1,06	1,20	6,00	9,00
Numbana-97045053	76,10	12,79	0,43	0,02	0,20	0,67	3,16	5,25	0,11	0,03	0,70	99,46	201,0	-2,2	13,4	11,8	1,06	1,17	6,30	33,00
Numbana-98049005	73,44	13,27	0,43	0,04	0,10	0,86	2,95	5,63	0,16	0,04	1,82	98,74	182,6	9,3	14,7	9,9	1,06	1,21	8,00	30,70
Numbana-98049025	74,50	13,09	0,47	0,05	0,06	0,78	3,25	5,15	0,08	0,02	1,72	99,17	190,0	-9,2	14,5	8,4	1,06	1,20	20,40	31,20
Numbana-98049050	73,20	13,69	0,28	0,05	0,15	1,07	3,42	5,16	0,12	0,04	1,69	98,87	173,6	-19,6	10,3	8,8	1,04	1,22	4,80	48,10
Numbana-98049053	73,60	13,72	0,25	0,04	0,07	0,99	3,35	5,57	0,08	0,03	1,28	98,98	170,3	-7,2	7,2	5,9	1,03	1,19	25,10	50,40
Numbana-142184	74,88	13,14	0,27	0,02	0,20	0,87	3,61	4,75	0,15	0,03	0,84	98,76	187,9	-30,9	9,2	10,3	1,04	1,18	14,90	42,50
Numbana-142185	73,10	13,44	0,55	0,04	0,35	0,86	3,46	5,03	0,25	0,04	0,88	98,00	177,1	-19,9	14,3	18,8	1,06	1,21	14,10	48,00
Numbana-160405	73,49	12,83	0,65	0,07	0,11	0,91	3,76	4,49	0,16	0,02	2,43	98,92	180,4	-42,0	2,4	12,9	1,01	1,16	21,20	29,30
Shaw-A107-1	74,42	13,48	0,30	0,04	0,42	1,00	3,80	4,83	0,16	0,05	0,00	98,50	176,0	-37,7	3,4	16,3	1,01	1,17	12,50	54,00
Shaw-SB580	74,12	13,58	1,27	0,03	0,00	0,94	4,83	5,38	0,13	0,07	0,00	100,35	130,1	-58,1	-37,4	17,5	0,88	0,99	6,60	44,00
Shaw-SB584	74,97	13,15	1,38	0,02	0,00	0,90	3,88	5,09	0,14	0,06	0,00	99,59	172,1	-32,9	-7,6	19,0	0,97	1,10	12,70	46,20
Shaw-SB587	74,48	13,47	1,43	0,03	0,08	1,02	4,26	5,11	0,15	0,05	0,00	100,08	155,3	-46,9	-18,3	21,8	0,93	1,07	15,90	43,80
Shaw-SBS91	73,11	13,53	2,34	0,03	0,18	1,40	4,32	4,54	0,33	0,08	0,00	99,86	153,4	-67,7	-20,5	37,9	0,93	1,12	11,30	65,40
Shaw-SBS93	73,96	13,07	2,10	0,03	0,00	1,06	4,16	4,86	0,23	0,05	0,00	99,52	160,5	-49,7	-19,0	29,1	0,93	1,08	12,00	45,00
<b>Valeur Minimale</b>	<b>69,15</b>	<b>11,72</b>	<b>0,00</b>	<b>0,01</b>	<b>0,00</b>	<b>0,21</b>	<b>2,95</b>	<b>1,63</b>	<b>0,04</b>	<b>0,00</b>	<b>0,00</b>	<b>98,00</b>	<b>130,13</b>	<b>-152,15</b>	<b>-37,42</b>	<b>2,38</b>	<b>0,88</b>	<b>0,99</b>	<b>2,10</b>	<b>9,00</b>
<b>Valeur Maximale</b>	<b>79,91</b>	<b>14,60</b>	<b>3,65</b>	<b>0,11</b>	<b>0,73</b>	<b>1,89</b>	<b>5,10</b>	<b>5,68</b>	<b>0,48</b>	<b>0,20</b>	<b>2,43</b>	<b>104,09</b>	<b>217,31</b>	<b>9,29</b>	<b>29,54</b>	<b>65,48</b>	<b>1,12</b>	<b>1,33</b>	<b>25,10</b>	<b>65,40</b>
<b>Moyenne (64 analyses)</b>	<b>74,09</b>	<b>13,44</b>	<b>0,62</b>	<b>0,04</b>	<b>0,17</b>	<b>0,92</b>	<b>3,74</b>	<b>4,76</b>	<b>0,15</b>	<b>0,05</b>	<b>1,26</b>	<b>99,23</b>	<b>178,51</b>	<b>-35,79</b>	<b>8,73</b>	<b>13,80</b>	<b>1,04</b>	<b>1,19</b>	<b>9,54</b>	<b>29,70</b>
<b>Ecart-type</b>	<b>1,61</b>	<b>0,43</b>	<b>0,65</b>	<b>0,02</b>	<b>0,14</b>	<b>0,30</b>	<b>0,39</b>	<b>0,60</b>	<b>0,08</b>	<b>0,03</b>	<b>0,68</b>	<b>0,83</b>	<b>13,92</b>	<b>25,15</b>	<b>11,07</b>	<b>10,66</b>	<b>0,04</b>	<b>0,06</b>	<b>5,49</b>	<b>13,56</b>



**Titre :** Caractérisation des sources d'uranium à l'Archéen. Mécanismes de genèse des gisements d'uranium les plus anciens (3,0 à 2,2 Ga) et des préconcentrations uranifères paléoprotérozoïques.

**Résumé :** Les plus anciens gisements d'uranium connus sur Terre sont les gisements de type paléoplacer hôtes de conglomérats à cailloux de quartz d'âge compris entre 3,09 et 2,2 Ga. Ces gisements représentent les reliques de l'ancienne croûte continentale archéenne maintenant érodée. L'origine de leurs concentrations primaires, correspondant à des accumulations de grains détritiques d'uraninite, est toujours sujette à controverse et la nature et les processus de formation des roches sources archéennes demeurent incertains.

Ce travail présente l'analyse minéralogique et géochimique détaillée des minéralisations de différents paléoplacers (Witwatersrand en Afrique du Sud, Elliot Lake au Canada et séries Jatuliennes en Russie) ainsi que de granitoïdes archéens et paléoprotérozoïques enrichis en uranium (séries granitiques calco-alkalines à potassiques du craton de Kénéma Man en Guinée, granites tardi-orogéniques du craton de Pilbara en Australie Occidentale, pegmatite peralumineuse de Tanco du Bouclier Canadien et pegmatites à uraninite du Bouclier Baltique en Finlande et Russie). L'étude comparative de ces roches uranifères échantillonnées tout autour du globe prouve à la fois i) l'existence précoce (>3,1 Ga) de granitoïdes différenciés produits par la fusion partielle d'une croûte pré-enrichie tels que des granites peralumineux ou de type S, ii) nécessairement la présence d'un mécanisme permettant de produire ce type de granites comme les zones de subduction ou de collision générées par le mouvement des plaques tectoniques, iii) l'origine magmatique des uraninites thorifères des paléoplacers, iv) la présence d'une atmosphère réductrice avant 2,2 Ga permettant la préservation des uraninites durant leur transport, v) et finalement l'augmentation de l'oxygène libre dans l'atmosphère paléo-protérozoïque à partir de 2,2 Ga provoquant la disparition des paléoplacers uranifères en faveur de l'altération et de l'oxydation des concentrations préexistantes, de la remobilisation de l'uranium et de la formation de dépôts secondaires.

**Mots clés :** uranium, paléoplacer, uraninite détritique, source magmatique, Archéen.

---

**Title :** Characterization of Archean uranium sources. Genetic mechanisms of the oldest uranium deposits (3.0 to 2.2 Ga) and of Paleoproterozoic uraniferous pre-concentrations.

**Abstract :** The oldest known uranium deposits on the Earth are the paleoplacer-type deposits hosted in quartz-pebble conglomerates from 3.09 to 2.2 Ga in age. These deposits are representative of the ancient Archean continental crust now eroded. The origin of the primary ores corresponding to accumulation of detrital uraninite is still controversy and the nature and forming processes of the Archean source rocks remain uncertain.

This work provides the detail mineralogical and geochemical analysis of mineralization from different paleoplacer-type deposits (Witwatersrand in South Africa, Elliot Lake in Canada and the Jatulian series in Russia) and from Archean and Paleoproterozoic U-enriched granitoids (calco-alkaline to potassic granite series from the Kenema Man Craton in Guinea, late-orogenic granites from the Pilbara Craton in West Australia, the Tanco pegmatite from the Canadian Shield and uraninite bearing pegmatites from the Baltic Shield in Finland and Russia). The comparative study of these worldwide uraniferous rocks prove either i) the existence of highly differentiated granitoids produced by the partial melting of a pre-enriched crust as peraluminous and S-type granites in early time (>3.1 Ga), ii) obviously the presence of an effective mechanism to produce such granites as tectonic plate systems with subduction or collisional zones, iii) the magmatic origin of the thorian uraninites in paleoplacers, iv) the efficiency of a reductive atmosphere prior to 2.2 Ga permitting the preservation of uraninite during transportation, v) and finally the rise of the oxygen-free level in the paleoproterozoic atmosphere providing the disappearance of uraniferous paleoplacers in favour of weathering, oxidation of pre-existing concentrations, remobilization of uranium and formation of secondary deposits.

**Key words :** uranium, paleoplacer, detrital uraninite, magmatic source, Archean.